Advances in Science, Technology & Innovation
IEREK Interdisciplinary Series for Sustainable Development

Amjad Kallel · Maurizio Barbieri · Jesús Rodrigo-Comino · Helder I. Chaminé · Broder Merkel · Haroun Chenchouni · Jasper Knight · Sandeep Panda · Nabil Khélifi · Ali Cemal Benim · Stefan Grab · Hesham El-Askary · Santanu Banerjee · Riheb Hadji · Mehdi Eshagh *Editors*

Selected Studies in Environmental Geosciences and Hydrogeosciences

Proceedings of the 3rd Conference of the Arabian Journal of Geosciences (CAJG-3)

IEREK RESEARCH & KNOWLEDGE ENRICHMENT

Springer

Advances in Science, Technology & Innovation

IEREK Interdisciplinary Series for Sustainable Development

Advances in Science, Technology & Innovation (ASTI) is a series of peer-reviewed books based on important emerging research that redefines the current disciplinary boundaries in science, technology and innovation (STI) in order to develop integrated concepts for sustainable development. It not only discusses the progress made towards securing more resources, allocating smarter solutions, and rebalancing the relationship between nature and people, but also provides in-depth insights from comprehensive research that addresses the **17 sustainable development goals (SDGs)** as set out by the UN for 2030.

The series draws on the best research papers from various IEREK and other international conferences to promote the creation and development of viable solutions for a **sustainable future and a positive societal** transformation with the help of integrated and innovative science-based approaches. Including interdisciplinary contributions, it presents innovative approaches and highlights how they can best support both economic and sustainable development, through better use of data, more effective institutions, and global, local and individual action, for the welfare of all societies.

The series particularly features conceptual and empirical contributions from various interrelated fields of science, technology and innovation, with an emphasis on digital transformation, that focus on providing practical solutions to **ensure food, water and energy security to achieve the SDGs.** It also presents new case studies offering concrete examples of how to resolve sustainable urbanization and environmental issues in different regions of the world.

The series is intended for professionals in research and teaching, consultancies and industry, and government and international organizations. Published in collaboration with IEREK, the Springer ASTI series will acquaint readers with essential new studies in STI for sustainable development.

ASTI series has now been accepted for Scopus (September 2020). All content published in this series will start appearing on the Scopus site in early 2021.

Amjad Kallel · Maurizio Barbieri · Jesús Rodrigo-Comino · Helder I. Chaminé · Broder Merkel · Haroun Chenchouni · Jasper Knight · Sandeep Panda · Nabil Khélifi · Ali Cemal Benim · Stefan Grab · Hesham El-Askary · Santanu Banerjee · Riheb Hadji · Mehdi Eshagh
Editors

Selected Studies in Environmental Geosciences and Hydrogeosciences

Proceedings of the 3rd Conference of the Arabian Journal of Geosciences (CAJG-3)

Springer

ISSN 2522-8714 ISSN 2522-8722 (electronic)
Advances in Science, Technology & Innovation
IEREK Interdisciplinary Series for Sustainable Development
ISBN 978-3-031-43802-8 ISBN 978-3-031-43803-5 (eBook)
https://doi.org/10.1007/978-3-031-43803-5

This Springer imprint is published by the registered company Springer Nature Switzerland AG
The registered company address is: Gewerbestrasse 11, 6330 Cham, Switzerland

Paper in this product is recyclable.

About the 2nd Springer Conference of the *Arabian Journal of Geosciences* (CAJG-3), Online November 2–5, 2020

The *Arabian Journal of Geosciences* (AJG) is a Springer journal publishing original articles on the full range of Earth sciences in partnership with the Saudi Society for Geosciences. The journal focuses on, but is not limited to, research themes which have regional significance for the Middle East, the Euro-Mediterranean, Africa, Asia, and some other regions of the world. The journal receives on average 3500 submissions a year and accepts around 800 papers for publication in its 24 annual issues (acceptance rate around 20%). It benefits from the participation of an editorial team of 15 topical chief editors and 100 international associate editors who generously help in evaluating and selecting the best papers.

In 2008, Prof. Abdullah Al-Amri, in close partnership with Springer, founded the *Arabian Journal of Geosciences (AJGS)*. In 2018, the journal celebrated its tenth anniversary. To mark the event, the founder and the editor-in-chief of the AJGS organized the 1st Conference of the *Arabian Journal of Geosciences* (CAJG) in close collaboration with Springer on November 12–15, 2018. The conference was an occasion to endorse the journal's long-held reputation and brought together 450 authors from 70 countries, who work in the wide-ranging fields of Earth sciences. The dynamic four-day conference in a stimulating environment in Hammamet, Tunisia, provided attendees with opportunities to share their latest unpublished findings and learn about the latest geosciences studies. The event also allowed attendees to meet and talk to the journal's editors and reviewers.

In a continuation of the successful 1st CAJG and 2nd CAJG, this year's conference aims to bring geoscientists from all over the world to present and discuss their most recent findings. The 3rd CAJG will continue to publish the newest findings in its proceedings and some special issues by Springer, with a clear mission to drive greater North–South (Europe-Africa) scientific cooperation and to open doors to new and enriching collaborations with geoscientists based in Asia and the Americas. Research studies from the wide-ranging fields of Earth sciences can be submitted for evaluation by the Conference Scientific Committee. In particular, the 3rd CAJG will devote a special session to studies focusing on unraveling the undiscovered oil and gas resources in the Mediterranean and North Africa. Many international experts will be invited to take part in the discussion, in particular we are expecting a massive participation of researchers from North Africa Research Group (NARG) of Manchester University (UK) and other scientists based in North Africa.

Conference Tracks

The scientific committee of the 3rd CAJG invites research papers on all cross-cutting themes of Earth sciences, with a main focus on the following 15 conference tracks:

- Track 1. Atmospheric Sciences, Meteorology, Climatology, Oceanography
- Track 2. Biogeochemistry, Geobiology, Geoecology, Geoagronomy
- Track 3. Earthquake Seismology and Geodesy
- Track 4. Environmental Earth Sciences
- Track 5. Exploration and Theoretical Geophysics, Seismic and Well-Logging Methods, Mathematical Geosciences
- Track 6. Geo-Informatics and Remote Sensing
- Track 7. Geochemistry, Mineralogy, Petrology, Volcanology
- Track 8. Geological Engineering, Geotechnical Engineering
- Track 9. Geomorphology, Geography, Soil Science, Glaciology, Geoarcheology, Geoheritage
- Track 10. Hydrology, Hydrogeology, Hydrochemistry
- Track 11. Marine Geosciences, Historical Geology, Paleoceanography, Paleoclimatology
- Track 12. Numerical and Analytical Methods in Mining Sciences and Geomechanics
- Track 13. Petroleum and Energy Engineering, Petroleum Geochemistry
- Track 14. Sedimentology, Stratigraphy, Paleontology, Geochronology
- Track 15. Structural Geology, Tectonics and Geodynamics, Petroleum Geology

About the Conference Steering Committee

General Chair

Abdullah Al-Amri

Founder and Editor-in-Chief,
Arabian Journal of Geosciences,
King Saud University, Saudi Arabia

Conference Supervisor

Nabil Khélifi

Senior Publishing Editor, MENA program,
Journal Publishing Manager,
Arabian Journal of Geosciences,
Springer, a part of Springer Nature, Germany

Advisory Co-chair

Walter D. Mooney

Guest of Editorial Board,
Arabian Journal of Geosciences,
United States Geological Survey Western Region, USA

Advisory Co-chair

Giovanni Bertotti

Guest of Editorial Board,
Arabian Journal of Geosciences,
Geoscience and Engineering, Delft University of Technology, The Netherlands

Scientific Committee Co-chair

François Roure

Chief Editor—Track 15,
Arabian Journal of Geosciences,
IFP—Energies Nouvelles, France

Scientific Committee Co-chair

Biswajeet Pradhan

Chief Editor—Track 6,
Arabian Journal of Geosciences,
University of Technology Sydney, Australia

Local Organizing Co-chair

Mohamed Soussi

Former Associate Editor,
Arabian Journal of Geosciences,
Tunis El Manar University, Tunis, Tunisia

Local Organizing Co-chair

Mounir Medhioub

Guest of Editorial Board,
Arabian Journal of Geosciences,
University of Sfax, Sfax, Tunisia

Publications Co-chair

Beatriz Bádenas

Chief Editor—Track 14,
Arabian Journal of Geosciences,
University of Zaragoza, Zaragoza, Spain

Publications Co-chair

Marina Rabineau

Chief Editor—Track 11,
Arabian Journal of Geosciences,
University of Brest, Brest, France

Program Co-chair

Amjad Kallel

Chief Editor—Track 4,
Arabian Journal of Geosciences,
ENIS, University of Sfax, Tunisia

Program Co-chair

Sami Khomsi

Georesources Lab,
CERTE, University of Carthage
Tunis, Tunisia

Proceedings Editorial Manager

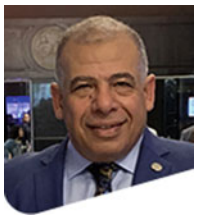

Mourad Amer

Editor of Springer/IEREK ASTI Series,
Guest of Editorial Board of AJGS,
IEREK, Alexandria, Egypt

Communication Chair

Zakaria Hamimi

Associate Editor,
Arabian Journal of Geosciences,
Benha University, Benha, Egypt

Public Relations Chair

Faïez Gargouri

Director of the Higher Institute of Computer Science and Multimedia,
President of the AIG,
University of Sfax, Tunisia

Conference Manager

Mohamed Sahbi Moalla

Journal Coordinator,
Arabian Journal of Geosciences,
ISET, University of Sfax, Tunisia

Preface

The proceedings of the 3rd Springer Conference of the *Arabian Journal of Geosciences* (CAJG-3) which was held online in November 2020 consists of four volumes titled:

Proceedings Volume 1: New Prospects in Environmental Geosciences and Hydrogeosciences
Proceedings Volume 2: Advances in Geophysics, Tectonics, and Petroleum Geosciences
Proceedings Volume 3: Recent Research on Geomorphology, Sedimentology, and Geochemistry
Proceedings Volume 4: Research developments in Geotechnics, Geo-Informatics and Remote Sensing

These volumes are based on the accepted conference papers for either oral/poster presentations or selected for online publication during the CAJG-3.

The first volume offers a broad range of recent studies that discuss the latest advances in geoenvironmental and hydrogeosciences from diverse backgrounds including climate change, geoecology, biogeochemistry, water resources management, and environmental monitoring and assessment. It shares insights of experienced scientists from, but not limited to, research institutes worldwide, focused the Mediterranean and Middle East regions on how the understanding of ecological, climatological, oceanic, and hydrological processes is the key for improving practices in environment management, including the eco-responsibility, scientific integrity, and social and ethical dimensions.

The second volume includes a series of research methods that are nowadays in use for measuring, quantifying, and analyzing the targeted geological domains. Remote sensing with high-resolution satellite imagery, seismology, geochemistry, theoretical geophysics and related profiles with tomographic images, earthquake geology with times series radar interferometry and related geodetic-GPS campaigns, and well-logging contribute to scrutinizing the Earth tectonic architecture. Fundamental questions that address the genesis and evolution of our planet are built upon data collection and experimental investigations under physical constitutive laws which are the conditions for a successful scientific research. These multidisciplinary approaches combined with the geodynamics of tectonic provinces and investigations of potential zones of natural resources (petroleum reservoirs) provide the basis for the economic development.

The third volume presents an updated unique view in conjugating field studies and modeling to better quantify the process-product binomial unusual in geosciences. Earth systems require a comprehensive understanding of processes and dynamics of geology, morphotectonics, sedimentology, stratigraphy, and geochemistry. In the geomorphology section, several studies deal with topics related to fault slip and incision rates, soil science, landslides and debris flows, coastal processes, and geoarcheology and geoheritage. Under the sedimentology section, researchers present recent advances in stratigraphy, environmental, tectonic and diagenetic processes, together with evolutionary, biostratigraphic and paleoenvironmental significance of paleontology are presented. Additionally, this section also contains papers on

marine geosciences, from molecular proxies related to climate to geophysical surveys. Last but not least, the third section on geochemistry focuses on sedimentary geochemistry and mineralogical characterization, magmatic and metamorphic processes and products, and the origin and exploration of mineral deposits. This volume resumes the current situation related to the above-mentioned topics mainly in the Mediterranean realm, testifying the geological importance of this area and surroundings.

The fourth volume contains research studies in the fields of three sections; (1) geological and geotechnical engineering, (2) geomechanical studies based on numerical and analytical methods, and (3) geo-informatics and remote sensing. The content of these research studies would provide new scientific knowledge for further understanding on landslides, new stabilization techniques, importance of geophysics for engineering geology investigations as well as new empirical approaches for easily predicting some physical and hydrogeomechanical properties of geomaterials.

The proceedings of the CAJG-3 is of interest to all researchers, practitioners, and students in all fields of geosciences, including the environmental geosciences.

Sfax, Tunisia — Amjad Kallel
Rome, Italy — Maurizio Barbieri
Granada, Spain — Jesús Rodrigo-Comino
Porto, Portugal — Helder I. Chaminé
Freiberg, Germany — Broder Merkel
Khenchela, Algeria — Haroun Chenchouni
Johannesburg, South Africa — Jasper Knight
Gandhinagar, India — Sandeep Panda
Heidelberg, Germany — Nabil Khélifi
Düsseldorf, Germany — Ali Cemal Benim
Johannesburg, South Africa — Stefan Grab
Orange, USA — Hesham El-Askary
Mumbai, India — Santanu Banerjee
Setif, Algeria — Riheb Hadji
Pilsen, Czech Republic — Mehdi Eshagh
July 2021

Contents

Hydrology, Hydrochemistry, Hydrogeology

About the Editors

Amjad Kallel ENIS, University of Sfax, Sfax, Tunisia

Dr. Amjad Kallel is currently an Associate Professor of Environmental Geology in the Sfax National School of Engineers at the University of Sfax, Tunisia. He holds a B.Eng. in Georesources and Environment (1998) from the University of Sfax (Tunisia) and an M. Sc. degree and a Ph.D. degree in Georesources and Environment (2004) from Hokkaido University (Japan). He joined the Venture Business Laboratory (VBL) at Akita University, Japan (2005–2006) as a researcher focusing on refining and recycling technologies for the recovery of rare elements from natural and secondary sources. On his return to Tunisia, he worked at the University of Gabes from 2006 to 2011, where he contributed to the elaboration of teaching programs at the Higher Institute of Water Sciences and Technologies of Gabes. Since 2011, he has joined the Sfax National School of Engineers. There, he has also been involved in various research projects related to Environmental Geology and Environmental Geotechnics. He has co-organized many prestigious workshops, seminars, and international conferences. In 2016, he joined the *Arabian Journal of Geosciences* (Springer) and the *Euro-Mediterranean Journal for Environmental Integration* (Springer) as Chief Editor and Managing Editor, respectively.

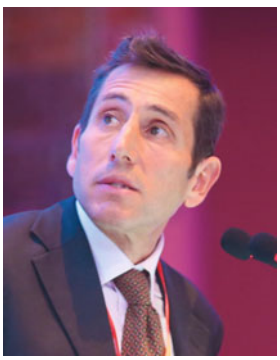

Maurizio Barbieri Department of Chemical Engineering Materials Environment, Faculty of Engineering, Sapienza University of Rome, Italy, Italy

Prof. Barbieri holds a degree in Geological Sciences (1994) and a Ph.D. degree in Earth Sciences (1998) from Sapienza University of Rome, (Italy). He is currently Full Professor of Environmental Geochemistry and Hydrogeochemistry at Sapienza University of Rome (Italy). Job-related skills Geochemical tracers in hydrological studies; interactions between water and the geological and chemical environment; quantitative understanding of chemically based processes in hydrogeochemical environments and complementary physical and biological processes and conditions; kinetics and equilibria of geochemical reactions; the movement of isotopes and soil chemistry; freshwater–seawater interactions in coastal aquifers; basic and applied research on speciation and transformation of trace metals and metalloids during biogeochemical processes in both natural and anthropogenic environments; radiogenic and stable isotope geochemistry. Other fields of expertise are Ion chromatography, ICP-MS, water, soil and

geological mapping, univariate and multivariate analysis of geochemical datasets, Isotope analyses of Sr, H, O, and B. Editorial board member for Springer, Elsevier and MPDI Journals (topics: Geochemistry, Water, and Environment). Water Quality Advisory for the LIFE ACTION GRANTS: Restoration, management and valorization of PRIority habitats of MEDiterranean coastal areas—LIFE17 NAT/GR/000511. Coordinating beneficiary: Hellenic Society for the Protection of Nature (2018–2020). International Project (2018–2020) LIFE17NAT/GR/000511 "Restoration, management, and valorization of PRIority habitats of MEDiterranean coastal areas." Environmental Advisor (Hydrogeochemistry) for the International Project (2016–2019) SECOSUD II—Conservation and equitable use of biological diversity in the SADC region. The project is financed by the Italian Agency for Development Cooperation and implemented through Eduardo Mondlane University, South African National Park, and Sapienza University of Rome. Scientific Coordinator (2014–2016) for the Geochemical model of the Vico Lake (Central Italy), with particular regard to environmental arsenic. Client: Regional Agency for Environmental Protection of Lazio. Environmental Advisor (Hydrogeochemistry) for the International Project (2012-2014) "Institutional Support to the Management of Protected Areas in Albania." Project supported by the International Union for Conservation of Nature (IUCN).

Jesus Rodrigo-Comino University of Granada, Granada, Germany

Dr. Jesús Rodrigo-Comino, graduated in Geography, currently works as Assistant Professor at the University of Granada. He carried out a thesis with an extraordinary degree award with the work: "The soils of the province of Malaga: Revision according to the classification criteria of FAO-WRB (2006)." He holds a master's degree in Territorial Planning and Geographic Information Systems (2013) from the University of Granada, whose final work was divided into three national publications and a monograph. During his predoc stage, he obtained three scholarships for doctoral studies: DAAD (German Academic Exchange Service), La Caixa Foundation, and FPU (Ministry of Education, Spain). During this period, he completed his doctoral thesis between the University of Trier (Germany -2 years-) and Malaga (2 years). Doctor in Geography (2018) from the University of Malaga with a doctoral thesis consisting of eight international publications, international mention and outstanding cum laude: "Actual geomorphological processes in sloping vineyards. A comparison between Ruwer-Mosel Valley (Trier, Germany) and Montes de Málaga (Málaga, Spain)." Currently, he is also preparing a second doctorate in Geomatics engineering at the Polytechnic University of Valencia. His research career consists of four full monographs (Nova, Springer, etc.) and one edited alone (Elsevier), 171 indexed publications (Scopus)/130 JCR, leading international collaborations with research teams from Iran, China, Kazakhstan, Sudan, India, Brazil, Croatia, Iraq, or the USA. Regular reviewer in more than 140 international indexed journals (e.g., *Scientific Reports*, *Science of the Total Environment*,

PLOS One, *Catena*, *Geoderma*, *Agriculture*, *Ecosystem and Environment or Earth-Science Review*), member of the panel of two doctoral theses, evaluator of projects for the Ministries of Science of Chile, Peru, the USA, Serbia, Switzerland, Kazakhstan, or Poland, and postgraduate scholarships for DAAD. He has organized several scientific meetings and congresses (e.g., Action Cost, V Biohydrology, Fire in the Earth, etc.), sessions at international conferences (EGU, TerraEnvision, Conference of the *Arabian Journal of Geosciences*, etc.), oral presentations and conferences magisterial (Germany, Bulgaria, Norway, etc.). Editor-in-Chief of the indexed journal (Scopus and ESCI; Q2) Air Soil and Water Research (SAGE). In addition, he is an associate editor at *Scientific Reports* (Nature-Springer), *Hydrological Science Journal* (Taylor & Francis), *Arabian Journal of Geosciences* (Springer), *Euro-Mediterranean Journal for Environmental Integration* (Springer), and *Journal of Mountain Science* (Springer). He has participated as a researcher in R&D&I projects on social issues related to housing or the census, or transfer and knowledge at European level such as the INTERREG Smart-Light HUB project (light pollution) or COST FIRElinks (fires). He has been invited to give lectures on agriculture, sustainable management, and erosion in several universities. He has supervised five final degree projects and three completed master's degrees in Germany. He has taught regulated and certified teaching at the Universities of Granada, Valencia, Malaga, León, Oviedo, and Trier (in German) on development, geomorphology, Geographic Information Systems, remote sensing, and statistical techniques. He was recently awarded with a Leonardo Grant (BBVA Foundation).

Helder I. Chaminé School of Engineering (ISEP), Polytechnic of Porto, Portugal

Helder I. Chaminé is a skilled Geologist and Professor of engineering geosciences at the School of Engineering (ISEP) of the Polytechnic of Porto, with over 32 years' experience in multidisciplinary geosciences research, consultancy, and practice. He studied geological engineering and geology (B.Sc., 1990) at the Universities of Aveiro and Porto (Portugal), respectively. He received his Ph.D. in geology at the University of Porto in 2000 and spent his postdoctoral research in applied geosciences at the University of Aveiro (2001–2003). In 2011, he received his Habilitation (D.Sc.) in geosciences from the University of Aveiro. Before joining the academy, he worked for over a decade on international projects for mining, geotechnics, groundwater industry and/or academia related to geodynamics and regional geology, hard rock hydrogeology and water resources, engineering geosciences and applied geomorphology, rock engineering and georesources. His research interests span fundamental to applied fields: GIS mapping techniques for applied geology, structural geology and regional geology, engineering geosciences and rock engineering, slope geotechnics, mining geology and hydrogeomechanics, hard rock hydrogeology, exploration hydrogeology, urban groundwater and hydromineral resources. He is interested in mining geoheritage, history of cartography, military geosciences and higher-education dissemination, skills, and core

values. Presently, he is Head of the Laboratory of Cartography and Applied Geology (LABCARGA | ISEP), Senior Researcher at Centre GeoBioTec | U. Aveiro and Centre IDL | U. Lisbon, as well as belongs to the executive board of the M.Sc. + B.Sc. Geotechnical and Geoenvironmental Engineering Programs (OE + EUR-ACE Label) and the Department of Geotechnical Engineering (ISEP). He currently belongs to the board of the Technical Commission of Environmental Geotechnics from SPG. He was a Board Member of APGeom—Portuguese Association of Geomorphologists (2009–2013), SPG—Portuguese Geotechnical Society (2016–2020), APG—Portuguese Association of Geologists (2020–2021), and AIH-GP—Portuguese Chapter of the International Association of Hydrogeologists (2019–2022). He was a consultant and or responsible for over 75 projects of applied geology, hydrogeomechanics, slope geotechnics, mining geology, exploration hydrogeology, hard rock hydrogeology, water resources, urban groundwater, and applied mapping (Mozambique, Portugal, and Spain). He has co-authored over 210 publications in indexed journal articles, conference proceedings/full papers, chapters, technical, and professional papers. He co-edited over 15 special volumes and is presently involved in editing themed issues for some international journals (e.g., *Environmental Earth Sciences*—Springer, *Springer Nature Applied Sciences*, *Discover Water*—Springer, *Arabian Journal of Geosciences*—Springer, *Water*—MDPI). As a referee for several international journals in applied mapping, geosciences, geotechnics, hydrogeology, water resources, and geohazards, he has a broad activity. He served as Invited Expert Evaluator of Bologna Geoscience Program for DGES (Portugal) and Scientific Projects Evaluation for NCST, 2017–2019 (Kazakhstan), and NRF | RISA, 2019 (South Africa), as well as Coordinator of "Geology on Summer| Ciência Viva" Program at ISEP (2005–2019) for geoscience dissemination. He has also been active in teaching and supervising many Ph.D., M.Sc., and undergraduate students. He has been on the editorial board, among others, of the *Arabian Journal of Geosciences* (SSG + Springer), *Hydrogeology Journal* (IAH + Springer), *Euro-Mediterranean Journal for Environmental Integration* (Springer), *Springer Nature Applied Sciences* (Springer), *Mediterranean Geoscience Reviews* (Springer), *Discover Water* (Springer), *Geotechnical Research* (ICE), *Geosciences* (MDPI), *Revista Geotecnia* (Portugal), and *Geología Aplicada a la Ingeniería y al Ambiente* (Argentina). He integrates as Moderator or Session Chair in several conferences, workshops, and meetings. He was the Scientific Chair of the 1st International Conference on Georesources, Geomaterials, Geotechnologies and Geoenvironment, 4GEO (Porto, Portugal, November 7–8, 2019). He is currently on the organizing and scientific committees of the 3rd International Workshop on Natural Hazards—NATHAZ'22 (Terceira Island, Azores, May 2022), supported by Springer.

Broder Merkel TUBAF, Freiberg, Germany

• Dissertation (Ph.D.) Dr. rer.nat. as Hydrogeologist (TU München) • Habilitation (Dr. habil) Christian-Albrechts Universität Kiel • Full Professor for Hydrogeology at TUBAF (1993–2015) Hydrogeology, hydrochemistry, modeling chemical thermodynamics and reactive transport, geo-statistics, GIS and remote sensing • Dean of the Faculty Geoscience, Geotechnics and Mining • DFG liaison officer of TUBAF • Vice-rector of TUBAF • Head of the Scientific Diving Center of TUBAF • Field work in Bolivia, China, Chile, Czech Republic, Iraq, Iran, Israel, Italy, Jordan, Hungary, Mexico, Mozambique, Namibia, Palestine, Russia, Spain, USA • Organization of seven International Conferences Uranium Mining and Hydrogeology

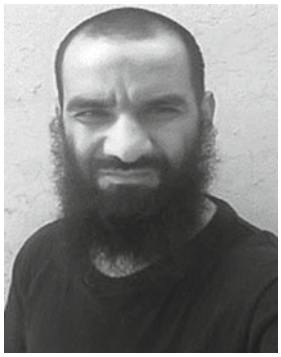

Haroun Chenchouni Higher National School of Forests, Khenchela, Algeria

Dr. Haroun Chenchouni is an associate professor and research scientist (Ecologist) at the Higher National School of Forests (Khenchela, Algeria). He is a former associate professor at the University of Tebessa (Algeria). He holds a M.Sc. (Magister) in Dryland Ecology from the University of Ouargla (Algeria) and a doctorate degree in Ecology and Environment from the University of Batna. He graduated as an engineer in Plant Ecology and Forest Ecosystems from the Department of Biological Sciences (University of Batna, Algeria). His research interests are fairly broad; he uses statistical modeling approaches to understand how natural environments, mainly climatic and edaphic factors, and anthropogenic perturbations influence biological interactions, shape trends in population dynamics, and influence community diversity. He uses various biological models to investigate biological interactions and community ecology of arid and semiarid ecosystems of North Africa. At various universities in Algeria, he teaches forest ecology, biostatistics, and ecological modeling. He has published more than 100 peer-reviewed publications and internationally recognized research papers. He is also involved in national and international research projects. In 2017, he joined the *Arabian Journal of Geosciences* (AJGS) as an associate editor. Then in 2019, he was assigned as a chief editor of Topic 2 (biogeochemistry, geobiology, geoecology, geoagronomy) to handle submissions dealing with various fields of biogeosciences, geoecology, climate change, plant and soil science, agricultural and forest environment, and environmental sciences.

Jasper Knight University of Witwatersrand, South Africa

Professor of Physical Geography, University of the Witwatersrand, Johannesburg, South Africa.

I am a geoscientist with research interests in the spatial and temporal variability in landscape system responses to climate and environmental changes during the late Pleistocene and Holocene, looking at sediments and geomorphology. I focus thematically on glaciers, rivers, coasts, and mountains. I focus geographically on the UK and Ireland, northwest USA, Australia, European Alps, various locations in Asia, and across both southern and northern (Saharan) Africa. I am editor of three major international journals (*Sedimentary Geology*, *Journal of Maps, and Land Degradation & Development*). My teaching and student supervision focuses on the interconnections between the physical and human environments, landscape change, and environmental resources of the past, present, and future.

Dr. Sandeep Panda is currently working as Assistant Professor at the Department of Industrial Biotechnology, Gujarat Biotechnology University, Gujarat, India. His main research areas include (Bio) hydrometallurgical approaches for metal extraction from primary and secondary resources, Bio-desulphurization of Coal, Bio and Chemical approaches for Mine Water treatment and application of eco-friendly approaches for sustainable mineral-metal waste recycling and management. He has been involved as Principal/Co-principal Investigator and as Team Member in several R&D and Industrial research projects (at both national and international levels) since 2009. As of 2023, he has published 55 International journal papers; four book chapters and five Editorial books of high quality and impact that have received nearly 1950 citations (h-index—25). One of his articles published in the journal NATURE related to Tech-Metal supply is receiving much attention and appreciation from global leaders working in his area. His research works have invited the attention of several press and media. He has been featured in the World Ranking of the Top 2% Scientists in the Domain of Mining and Metallurgy (Sub Domain —Environmental Sciences) as per the Stanford University list of top-cited scientists in 2020, 2021, and 2022. He is an active member of several prestigious professional bodies and technical/scientific committee member in several reputed international conferences. He has served as a reviewer in over 40 reputed International Journals and is currently serving as: (1) Associate Editor of the *Arabian Journal of Geosciences* and *Euro-Mediterranean Journal of Environmental Integration* (Springer Nature) and Editorial Board Member of, (2) *Frontiers in Microbiology* and *Frontiers in Environmental Sciences* (Frontiers Publications), (3) *Mineral Processing* and *Extractive Metallurgy Review Journal* (Taylor & Francis Group), and (4) Editorial Advisory Board of *Detritus Journal* (IWWG).

Nabil Khélifi Springer, a part of Springer Nature, Heidelberg, Germany

Dr. Nabil Khélifi undertook fellowships at the System for Analysis, Research and Training (START) in 2005 and the German Academic Exchange Service (DAAD), as part of his Ph.D. studies in Marine Geosciences at the University of Kiel in Germany (2006–2010). After his Ph.D., he received a research grant from the German Science Foundation (DFG) to conduct research projects at the GEOMAR Ocean Research Centre in Kiel, Germany on oceanography and climate reconstructions in the North Atlantic and the Mediterranean (2010–2013). His research findings have been presented at many conferences and published in esteemed journals. He co-organized workshops on the Pliocene climate in Bordeaux, France (2009) and Bristol, UK (2013), funded by the European Science Foundation (ESF). In late 2013, he received the Swiss Government Excellence Scholarship (SGES). In 2014, he joined Springer in Heidelberg, Germany as an Editor, and was promoted to Senior Editor in 2017 responsible for developing their publishing program in the MENA region. He is active in educational seminars for authors, reviewers, and editors to help improve publication output and quality. He is Visiting Lecturer at King Saud University, KSA where he gives M.Sc. lectures on scientific presentations and publishing techniques, as well as career development workshops. He has launched two Springer conferences (more details at www.emcei.net and www.cajg.org). In 2016, he was awarded the Africa Green Future Leadership Award for his promotion of publications from Africa. In 2020, he received the Saudi Society for Geosciences Award for successful management of the *Arabian Journal of Geosciences*.

Ali Cemal Benim Düsseldorf University of Applied Sciences, Düsseldorf, Germany

Prof. Dr.-Ing. habil. Ali Cemal Benim received his B.Sc. and M.Sc. degrees in Mechanical Engineering at the Boğaziçi University, Istanbul, Turkey. He received his Ph.D. degree at the University of Stuttgart, Germany, in 1988, on the topic "Finite Element Modeling of Turbulent Diffusion Flames" with "Degree of Distinction." Following a post-doctoral period at the University of Stuttgart, in 1990 he joined ABB Turbo Systems Ltd. in Baden, Switzerland, where he was the manager of the "Computational Flow and Combustion Modeling" group. Since January 1996, he is Professor for Energy Technology and Head of Center of Flow Simulation at the Duesseldorf University of Applied Sciences, Duesseldorf, Germany.

Stefan Grab School of Geography, Archaeology and Environmental Studies, University of the Witwatersrand, South Africa

Swiss by birth but grew up in Pietermaritzburg, South Africa. Studied geomorphology at the University of Natal with specialization in periglacial geomorphology. Today works in both geomorphology and historical climate change sectors. Research regions include southern and eastern Africa, the mid-Atlantic, and Iran (Middle East).

Hesham El-Askary Chapman University, USA

Prof. El-Askary received his Ph.D. in Computational Sciences and Informatics from George Mason University in 2004. He is the 2015 recipient of the Chapman University's elite Senior Wang-Fradkin Professorship award. In 2016, he was named as the regional coordinator on a $3 million Euro grant from the European Union's (EU) Horizon 2020. The three-year project, known as GEO-CRADLE, deals with Coordinating and integrating state-of-the-art Earth Observation Activities in the regions of North Africa, Middle East, and Balkans and Developing Links with GEO-related initiatives toward GEOSS. Through this work, he with the research team were able to deliver the first analytical solar Atlas of Egypt that is now considered to be the official document of the government for solar investment. This work was recently presented at Planet Earth Institute at the Royal Society in London during a seminar that discussed the future of solar energy in Africa. His research interests include dust storms monitoring and detection using different remote sensing technologies as well as studying other extreme events. He is also involved in studying air pollution problems over mega cities due to natural and man-made effects as well as climate change and its impacts on sea-level rise and coral reefs for coastal areas. His research also included using Earth observations in studying the impact of severe dust storms anomalous chlorophyll outbreaks in the marine environment, hurricanes intensification as well as transport of microbes' causing Kawasaki disease outbreaks. Recently, he has been focusing on using Earth observations for water resources management, precision agriculture along the sustainable development goals. Today he views himself as an Earth System Scientist with a major interest in natural hazards, atmospheric events and using renewable energy as the only way to address global climate change issues. He has published over 100 refereed research publications, conferences full paper and book chapters in these research areas. His research has been supported by the National Science Foundation, NASA, United States Department of Agriculture and European Union. He has received the Saudi Arabia award hosted by the Arab Administrative Development Organization (ARADO) affiliated with the League of Arab states for the best published article in Environmental Management among 150 articles in 2006. He is also member of the Institute of Electrical and Electronics Engineers (IEEE), AGU, EGU, COSPAR, and Phi Beta Delta Honor Society.

Santanu Banerjee Indian Institute of Technology Bombay, Mumbai, India

Santanu Banerjee currently works as a Professor at the Department of Earth Sciences, Indian Institute of Technology Bombay. He does research in sedimentology and petroleum geology. His research areas include authigenic iron silicates, microbially induced sedimentary structures, basin analysis, provenance interpretations, and alternate potash fertilizer. He is on the editorial board of *Journal of Palaeogeography*, *Minerals*, *Arabian Journal of Geosciences*, and *Journal of Earth Systems Science.*

Riheb Hadji University of Sétif 1, Setif, Algeria

Prof. Riheb Hadji is a Professor of Geological Sciences in the Department of Earth Sciences, Institute of Architecture and Earth Sciences, Setif 1 University, Algeria. Specialized in Applied Geology, Geomatics, and Environment, he does research in geomorphology, hydrogeology, and natural hazards. His current project is about risk management in North Africa. He is the head of the Laboratory of Applied Research in Engineering Geology, Geotechnics, Water Sciences, and Environment, Setif 1, University, Algeria, and the co-chairman of the International Association of Water Resources in the Southern Mediterranean Basin. He has published more than 100 scientific papers in peer-reviewed journals, edited two books on Soil mechanics, and has an RG-score of 23.21, an H-index of 24, and an i10 of 34. He has also been involved in four international collaboration projects and several national projects. Editorial Board member in peer-reviewed journals, he is an internationally known expert in RS-GIS, Natural Hazard, and environmental issues.

Mehdi Eshagh University West, Sweden

Mehdi Eshagh, 1977, born in Tehran, Iran, completed his M.Sc. degree in Geodesy from K. N. Toosi University of Technology in Iran and Ph.D. in Geodesy at Royal Institute of Technology (KTH) under supervision of Professor Lars E. Sjöberg in 2009. He became docent (habilitation) in Physical Geodesy and Space Geodesy at KTH and worked there as senior researcher until 2016 and since September 2013 to March 2023 as Professor of Geodesy at University West in the western part of Sweden. He is currently a visiting professor at University of West Bohemia, in Czech Republic. He has about 23 years of activities in teaching diversity of courses in surveying engineering and geodesy, research, and supervision of students at all levels of educations. Author of 129 articles in peer-reviewed international journals and the book *Satellite Gravimetry and the Solid Earth, Mathematical Foundations*, published by Elsevier in 2020. Founder of the *Journal of Geodetic Science* in 2010 and its Editor-in-Chief since 2018. Interested in collaboration in teaching and research internationally, e.g., Affiliated Professor at the Ethiopian Space Science and Technology Institute and Adjunct Professor at the University of Sherbrooke.

Atmospheric Sciences, Meteorology, Climatology, Oceanography

Trend and Variability of Sea Surface Temperature Over the Arabian Gulf

Kamal Aldien Alawad, Abdullah Al-Subhi, Mohammed Alsaafani, and Turki Alraddadi

Abstract

Using the least squares method on a 39-year dataset of sea surface temperature (ECMWF-ERA-Interim), we showed a non-uniform warming spatial trend pattern in winter, but a uniform pattern in summer for the Arabian Gulf region. A distinct warming trend (0.28 °C decade^{-1}) was identified in the time series from the mid-1990s during the summer season, which is approximately three times higher than the global warming trend. Conversely, a non-significant and much weaker warming trend (0.04 °C decade^{-1}) was observed during the winter period. The magnitude of the seasonal cycle is above 10 °C in the southern regions but increases northward and reaches above 20 °C in the far northern region. Our findings support the current non-stationary property of climatic ocean warming. Further analysis is required to investigate the physical drivers of these trends, especially during the summer season.

Keywords

Sea surface temperature • Trend variability • Trend shift • Arabian Gulf

1 Introduction

Ocean warming is a major consequence of climate change and is predicted to continue even if global greenhouse gas emissions decrease. Thus, the need to understand the local effects of global climate change is one of the most urgent topics, since semi-enclosed and shallow basins, such as the Arabian Gulf, tend to warm faster than the open ocean.

Sea surface temperature (SST) is one of the most important oceanographic variables, since it has a great impact on the global ocean and atmospheric circulation phenomena. For example, El Niño/Southern Oscillation, which is the most energetic ocean phenomenon, results from SST variability in the tropical Pacific Ocean.

Due to global warming, global SST has experienced a warming trend (Collins et al., 2013). As the warming trend can be seen at a faster rate over semi-enclosed and shallow basins like the Arabian Gulf (Lima & Wethey, 2012), we aimed to understand the SST variability in this area and predict the long-term trend and magnitude of the seasonal cycle of this basin during the summer and winter seasons.

2 Materials and Methods

In this study, we used 39 years of SST data obtained as a dataset from the European Center for Medium-Range Weather Forecasts (ECMWF-ERA Interim). It is a monthly mean gridded dataset spanning January 1979 to December 2017, with spatial resolutions of 0.25° × 0.25° grids. ECMWF merges the available observations from satellites, ships, drifting buoys and land stations to produce this re-analysis dataset (Dee et al., 2011). We used the least squares method to analyze the spatial and temporal trends in the boreal summer (June–July and August) and winter (December–January and February) seasons. The Mann–Kendall technique was used to test the significance of the results at a 95% significance level.

3 Results and Discussion

Figure 1 shows the spatial SST trends for the summer and winter seasons. It is clear that the Arabian Gulf SST experienced a significant warming trend. The overall Arabian

K. A. Alawad (✉)
Marine Weather Forecast Division, Sudan Meteorological Authority, Khartoum, 574, Sudan
e-mail: kalawad@ersad.gov.sd

K. A. Alawad · A. Al-Subhi · M. Alsaafani · T. Alraddadi
Marine Physics Department, Faculty of Marine Sciences, King Abdulaziz University, Jeddah, 21589, Saudi Arabia

A. Kallel et al. (eds.), *Selected Studies in Environmental Geosciences and Hydrogeosciences*, Advances in Science, Technology & Innovation, https://doi.org/10.1007/978-3-031-43803-5_1

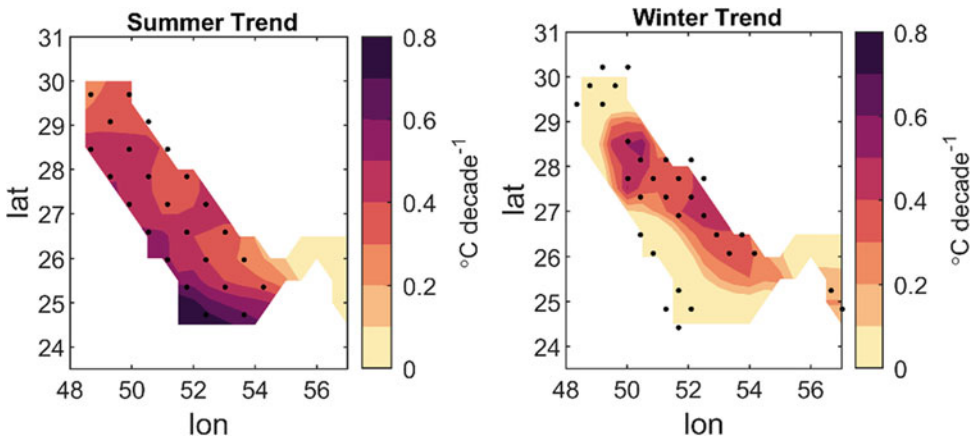

Fig. 1 Spatial SST trend in °C for the summer (left) and winter (right) season. The black dots represent the data at 95% significance level

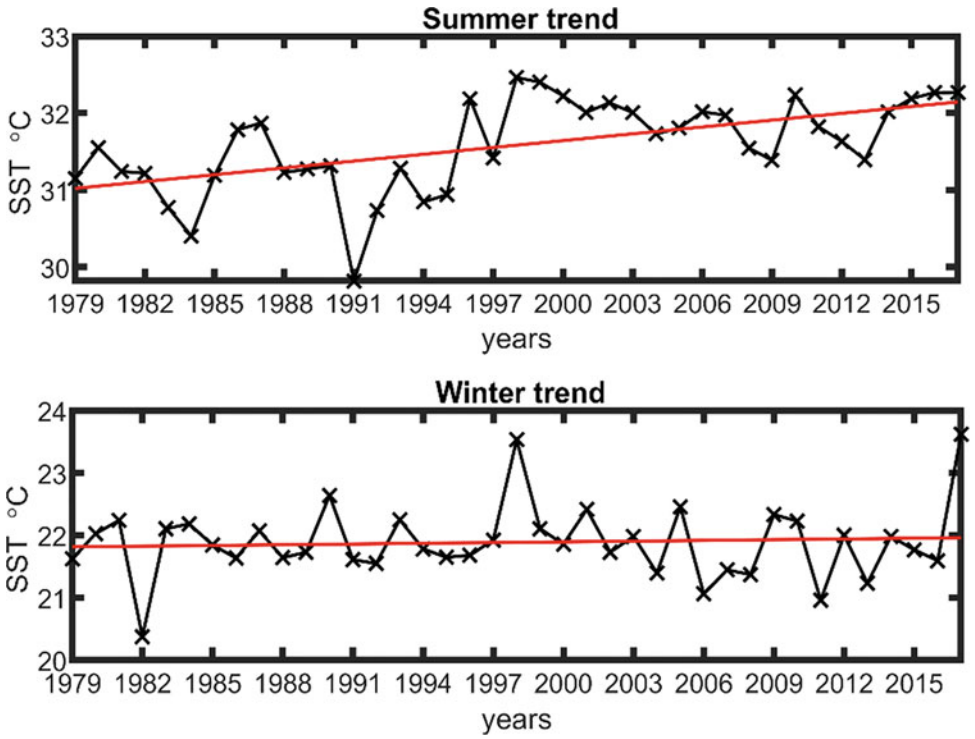

Fig. 2 Time series of the SST trend in °C associated with their corresponding linear trends (red line) for the summer (upper) and winter (lower) seasons

Gulf has a trend value above 0.6 °C decades^{-1} during summer, while it covers a smaller area and shows a smaller trend value during the winter season.

Figure 2 illustrates the SST time series of both summer and winter seasons. In this analysis, we took an average of the Arabian Gulf area as one point. The results revealed a clear shift from the mid-1990s during the summers, showing a significant warming trend of approximately 0.28 °C decade^{-1}, at a 95% significance. This value is approximately three times higher than that of 0.11 °C decade^{-1} of the global SST warming trend between 1980 and 2005 (IPCC, 2014). For the winter season, the trend is much weaker (0.04 °C decade^{-1}) compared to the summer season. Globally, warmer climates can alter tropical marine ecosystems and make the ocean less productive (Behrenfeld et al., 2006; Doney, 2006).

Figure 3 shows the magnitude of the SST seasonal cycle. This map is characterized by a strong meridional gradient with a decreasing pattern toward the south. The gradient range is approximately 8 °C, from 12 °C in the south to 20 °C in the far northern end. Since the Arabian Gulf is a shallow basin (Al-Salem et al., 2018) that opens and connects to the Indian Ocean in the southern end, we expect to observe relatively cold water in the southern part than in the northern region. This explains the occurrence of this strong gradient at such a short distance (approximately 600 km),

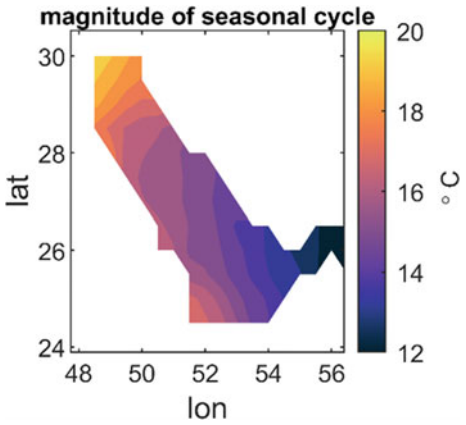

Fig. 3 Magnitude of the seasonal cycle pattern in °C

compared to other semi-enclosed regional seas, such as the Red Sea with approximately 6 °C range along a distance of 1500 km (Alawad et al., 2020a). Furthermore, the high range values, especially over the northern end, suggest that all marine species have high heat tolerance.

4 Conclusion

Similar SST shift has been observed over the Arabian Gulf area (Al-Subhi, 2020) as well as the Red Sea (Alawad et al., 2020b), especially in the last five years (Alosairi et al., 2020) suggesting that similar phenomena and associated mechanisms may have caused the shift and warming trend in both areas. Thus, further analysis is needed to investigate whether the physical drivers of the Red Sea SST trends were extended to the Arabian Gulf, especially during the summer season. Furthermore, using general ocean circulation models over the area may enable us to predict future climate changes.

References

Alawad, K. A., Al-Subhi, A. M., Alsaafani, M. A., & Alraddadi, T. M. (2020a). Atmospheric forcing of the high and low extremes in the sea surface temperature over the Red Sea and associated chlorophyll-a concentration. *Remote Sensing, 12*, 2227.

Alawad, K. A., Al-Subhi, A. M., Alsaafani, M. A., & Alraddadi, T. M. (2020b). Decadal variability and recent summer warming amplification of the sea surface temperature in the Red Sea. *PLoS ONE, 15*, e0237436. https://doi.org/10.1371/journal.pone.0237436

Alosairi, Y., et al. (2020). World record extreme sea surface temperatures in the northwestern Arabian/Persian Gulf verified by in situ measurements. *Marine Pollution Bulletin, 161*, 111766.

Al-Salem, K., Neelamani, S., & Al-Nassar, W. (2018). Wind energy map of Arabian Gulf. *Natural Resources, 9*, 212–228.

Al-Subhi, A. M. (2020). A comprehensive statistical analysis of nearly 35 years AVHRR SST data from the Arabian Gulf: trends, anomalies, and intra- inter-annual seasonality. *Journal of Marine Sciences* (Accepted).

Behrenfeld, M. J., O'Malley, R. T., Siegel, D. A., McClain, C. R., Sarmiento, J. L., Feldman, G. C., Milligan, A. J., Falkowski, P. G., Letelier, R. M., & Boss, E. S. (2006). Climate-driven trends in contemporary ocean productivity. *Nature, 444*, 752–755.

Collins, M., Knutti, R., Arblaster, J., Dufresne, J.-L., Fichefet, T., Friedlingstein, P., Gao, X., Gutowski, W.J., Johns, T., & Krinner, G. (2013). Long-term climate change: projections, commitments and irreversibility. In *Climate change 2013-The physical science basis: Contribution of working group I to the fifth assessment report of the intergovernmental panel on climate change* (pp. 1029–1136). Cambridge University Press

Dee, D.P., Uppala, S.M., Simmons, A.J., Berrisford, P., Poli, P., Kobayashi, S., Andrae, U., & Balmaseda, M. A., Balsamo, G., & Bauer, P. (2011). The ERA-interim reanalysis: Configuration and performance of the data assimilation system. *Quarterly Journal of the Royal Meteorological Society, 137*, 553–597.

Doney, S. C. (2006). Plankton in a warmer world. *Nature, 444*, 695–696.

IPCC. (2014). *Climate change 2013—The physical science basis: Working Group I contribution to the fifth assessment report of the intergovernmental panel on climate change*. Cambridge University Press.

Lima, F. P., & Wethey, D. S. (2012). Three decades of high-resolution coastal sea surface temperatures reveal more than warming. *Nature CommuNications, 3*, 1–13.

A Probabilistic Approach to Estimate Design Wave Parameters and Extreme Wave Return Values for 100 Years in the Indian Ocean

Mourani Sinha and Mrinmoyee Bhattacharya

Abstract

Unexpected, huge, and dangerous rogue or freak waves on calm sea surfaces still remain unpredicted causing destruction to ships and human lives. Probabilistic wave modeling is an approach for long-term operational and extreme wave parameter estimation. Using extreme value distributions like Generalized Extreme Value Distribution (GEV), Generalized Pareto Distribution (GPD), and Weibull Distribution (WD), mathematical equations have been estimated, for the extreme wave height for given return periods, mean maximum wave height, and most frequent wave heights. Using NCEP daily wind data, 37 years (1981–2017) model computed wave height data (SWH) is considered for a grid (72° E, 9° N) in the Indian Ocean through which OCKHI cyclone passed in 2017. The model computed and the distribution of the estimated extreme wave heights were compared over some given return periods 5, 10, 25, 50, and 100 years. The results are not satisfactory due to the coarse and smoothed SWH time series data. To improve the results for the same above grid, NOAA WAVEWATCH III model generated SWH data from 2006–2017 are considered next having better accuracy and finer resolution. At the above location, for a return period of 5 years, the model computed SWH value is 5.56 m, and the GPD, WD, and GEV estimated values are 5.42, 5.59, and 1.89 m, respectively. On comparing computed and estimated extreme wave heights for both normal and cyclonic periods for given return periods, it was found that GPD performed best followed by WD. Different distributions performed with varied accuracy while estimating the mean maximum wave height and most frequent wave heights.

Keywords

Design wave parameters • Probability distributions • Return periods • Indian Ocean • OCKHI cyclone

1 Introduction

Ocean engineering includes onshore and offshore construction activities related to shipping, oil, gas, and other natural resources. For the planning and designing of fixed and floating maritime structures, information on extreme wave conditions is a major requirement (Goda, 2000). The possibility of higher extreme wave heights to be met by ocean-going vessels in the event of global warming and sea-level rise situation for short return periods cannot be neglected. The problem was approached using extreme value distributions (Draper, 1972). The sea surface elevations having inherent randomness were generally assumed to have a normal distribution. A random sample of extreme wave heights has a GEV distribution having location, scale, and shape parameters (Caires, 2011). For modeling the extremes of a probability distribution, there are two parametric approaches, the block maxima, and the threshold exceedances. The former uses GEV, while the latter GPD which models the data exceeding certain peaks over the threshold more efficiently. For more accuracy, the extreme wave heights were derived using the modified WD (Muraleedharan et al., 2007). The expressions for the mean maximum wave height and most frequent wave heights using the modified WD were also estimated. In this paper, extreme wave heights were evaluated and compared for cyclonic and non-cyclonic periods using the expressions estimated for design wave parameters from GEV, GPD, and WD. The

M. Sinha (✉)
Department of Mathematics, Techno India University, Kolkata, West Bengal, India
e-mail: mou510@gmail.com

M. Bhattacharya
Department of Computer Science and Engineering, Techno India University, Kolkata, West Bengal, India

A. Kallel et al. (eds.), *Selected Studies in Environmental Geosciences and Hydrogeosciences*, Advances in Science, Technology & Innovation, https://doi.org/10.1007/978-3-031-43803-5_2

accuracy of the distribution models was tested for the model generated cyclonic and non-cyclonic wave heights.

2 Materials and Methods

WAVEWATCH III model was run for the Indian Ocean region from 1981 to 2017 (37 years) using NCEP daily wind data having a resolution 2.5 degrees. Model computed wave height data was extracted for a grid (72°E longitude and 9°N latitude) in the Arabian Sea through which OCKHI cyclone (November 29, 2017–December 06, 2017) passed. The period 1981–1985 was chosen as the training period for the distributions. At the given location, each of the GEV, GPD, and WD was fitted and the scale, the location, and the shape parameters were calculated for the training period. Computed and predicted extreme wave heights were compared for given return periods 5, 10, 25, 50, and 100 years using the expressions estimated. For the above grid next, NOAA WAVEWATCH III model generated SWH data from 2006 to 2017 was considered as having better accuracy and finer resolution. For the above grid, SWH data for the period 2006–2010 was chosen as the non-cyclonic training period. Data for the period 2017 only was chosen as the cyclonic one. Computed and predicted extreme wave heights were compared for both normal and cyclonic periods for given return periods.

3 Results

Table 1 shows the computed and predicted extreme wave heights (hextreme) calculated for different return periods using the different distributions for the training period 1981–1985 using NCEP wind. Next considering the 5 years non-cyclonic training period from 2006 to 2010, the estimated extreme wave heights encountered for different return periods are given in Table 2. Similar values are given in Table 3 estimating only the cyclonic year 2017. Tables 4 and 5 give the computed and estimated values of the design wave parameters for the non-cyclonic and the cyclonic periods.

Table 1 Computed and predicted hextremes (m) for the training period 1981–1985

Periods Rp (in years)	Computed	GPD	WD	GEV
5	4.74	2.046	6.298	0.3324
10		2.133	6.685	0.3328
25		2.236	7.165	0.3330
50		2.308	7.513	0.3331
100		2.377	7.854	0.3332

Table 2 Computed and predicted hextremes (m) for non-cyclonic condition (2006–2010)

Periods Rp (in years)	Computed	GPD	WD	GEV
5	5.56	5.418	5.592	1.893
10		5.499	5.800	1.896
25		5.583	6.052	1.898
50		5.635	6.234	1.899
100		5.678	6.409	1.9

Table 3 Computed and predicted hextremes (m) for cyclonic condition (2017)

Periods Rp (in years)	Computed	GPD	WD	GEV
1	8.02			
2		5.668	4.147	1.651
5		6.258	4.441	1.659
10		6.629	4.625	1.663
50		7.394	5.006	1.667
100		7.698	5.158	1.668

Table 4 Design wave parameters for non-cyclonic condition

Design wave heights (m)	Computed	GPD	WD	GEV
Mean maximum wave height	1.449	3.212	1.905	2.418
Most frequent maximum wave height	0.81	1.223	0.471	1.110

Table 5 Design wave parameters for cyclonic condition (2017)

Design wave heights (m)	Computed	GPD	WD	GEV
Mean maximum wave height	1.336	1.053	1.732	2.584
Most frequent maximum wave height	0.8	1.116	1.732	1.047

4 Discussion

Analyzing the time series of SWH data from the two sources, it was found the model using the coarse daily NCEP wind fails to capture the cyclonic wave height in December 2017. Thus, the estimated values in Table 1 are underestimated by GPD and GEV. Using a more accurate time series of SWH data, it was seen that extreme wave heights estimated by GPD are closer to the computed value which are followed by WD and GEV. The extreme wave height recorded for the non-cyclonic conditions in a period of 5 years is 5.56 m which is in agreement with the wave height (5.418 m) predicted using GPD in Table 2. Although only a years' data is very little for training any distribution it can be seen from Table 3, GPD performed better than the other distributions for estimating 2017 cyclonic wave heights. From Tables 4 and 5, for the mean maximum wave height, the WD performed better during the non-cyclonic condition, whereas GPD was better during the cyclonic phase. For the most frequent maximum wave height, GEV is estimated more accurately for both cyclonic and non-cyclonic conditions. Thus, different distributions were performed with varied accuracy while estimating the design wave parameters.

5 Conclusion

It is observed, from the results, that the extreme value estimates for both cyclonic and non-cyclonic data seem to deviate for GEV, even though GPD and WD seem to be quite close. It can be said, from the above study, that the estimation of the design wave parameters is dependent on the quality of the data and the chosen distribution model.

References

Caires, S. (2011). Extreme value analysis: wave data. *JCOMM Technical Report No. 57*.

Draper, L. (1972). Extreme wave conditions in British and adjacent water. In *13th International conference on coastal engineering* (pp. 157–165). ASCE Library, Vancouver (1972). https://doi.org/10.1061/9780872620490.009

Goda, Y. (2000). Random seas and design of maritime structures (2nd ed.). 15th Volume of Advanced series on ocean engineering. World Scientific Publishing Company. https://doi.org/10.1142/3587

Muraleedharan, G., Rao, A. D., Kurup, P. G., Nair, N. U., & Sinha, M. (2007). Modified Weibull distribution for maximum and significant wave height simulation and prediction. *Coastal Engineering, 54*(8), 630–638. https://doi.org/10.1016/j.coastang.2007.05.001

On the Formation of Storm Surges in the Azov Sea

Victor Arkhipkin and Stanislav Myslenkov

Abstract

One of the natural hazards associated with the marine environment in the Sea of Azov is storm surges. At present, due to the small number of natural observations on the Azov Sea level, numerical models are used to study surges. The ADCIRC model was chosen to calculate the level fluctuations. This model uses a non-structural computational grid with variable spacing and permits the preservation of fine details of the coastline, channel in river deltas, small islands and shallow shores. The step of the computational grid of the studied sea varies from 50 m to 5 km. Input data for the model were wind and atmospheric pressure fields from the NCEP/CFCR re-analysis, covering the period 1979–2010. To take into account the effect of ice on the formation of surges, the sea concentration ice was set with a daily interval from the OSI-SAF database. The calculated sea level fluctuations were compared to the natural measurements, and a good agreement was found. The largest number of storm surges is observed for the autumn–winter period. Storm surges develop actively from November to February. The number of surges significantly declines during the Spring–Summer period. No inter-annual trend in the occurrence of storm surges in the Azov Sea was identified for the study period. The maximum number of surges was observed in the Taganrog Bay.

Keywords

Azov Sea • Storm surges • ADCIRC model • Numerical modeling

1 Introduction

Storm surges in the Azov Sea are observed regularly. They often occur especially near its eastern coast, with the strongest surges observed in Temryuk Bay (Terziev, 1991). The study of the features of surge formation is necessary for the safety and efficiency of the marine economy, including coastal infrastructure and sea transport. Considering that there are not so many natural observations of the Azov Sea level, a numerical hydrodynamic modeling was used to study the spatial and temporal characteristics of storm surges.

2 Materials and Methods

The ADCIRC model was used to model the storm surges. This model was specially developed for calculating level fluctuations and water circulation in the coastal zone (ADCIRC Homepage, 2020). To assess the effect of wind waves on the level and current fluctuations, the ADCIRC model was applied in conjunction with the SWAN third-generation spectral model of wind waves. The calculations were carried out on non-structural, triangulation grids. For the Azov Sea, two grids were created: without flooding of the adjacent land and with flooding of the mouth of the Don River and adjacent land areas on the eastern coast of the sea. The first contains 53,877 nodes, whereas the second has 65,100 (Fig. 1).

The size of the grid elements varies from 5 km in the central part of the Azov Sea to 25 m in the straits and channels of the Don mouth area. The following boundary conditions were set: on the shore—zero normal flow to the shore and tangential slip; at the bottom—bottom friction according to the quadratic law, while the dimensionless bottom friction coefficient was equal to 0.0025. The horizontal turbulent viscosity coefficient was also taken constant and equal to 2 m^2/s. Drying of the sea and flooding of the adjacent territory were taken into account. River runoff was

V. Arkhipkin (✉) · S. Myslenkov
Lomonosov State University, Leninskie Gory, 1, Moscow, Russian Federation
e-mail: victor.arkhipkin@gmail.com

A. Kallel et al. (eds.), *Selected Studies in Environmental Geosciences and Hydrogeosciences*, Advances in Science, Technology & Innovation, https://doi.org/10.1007/978-3-031-43803-5_3

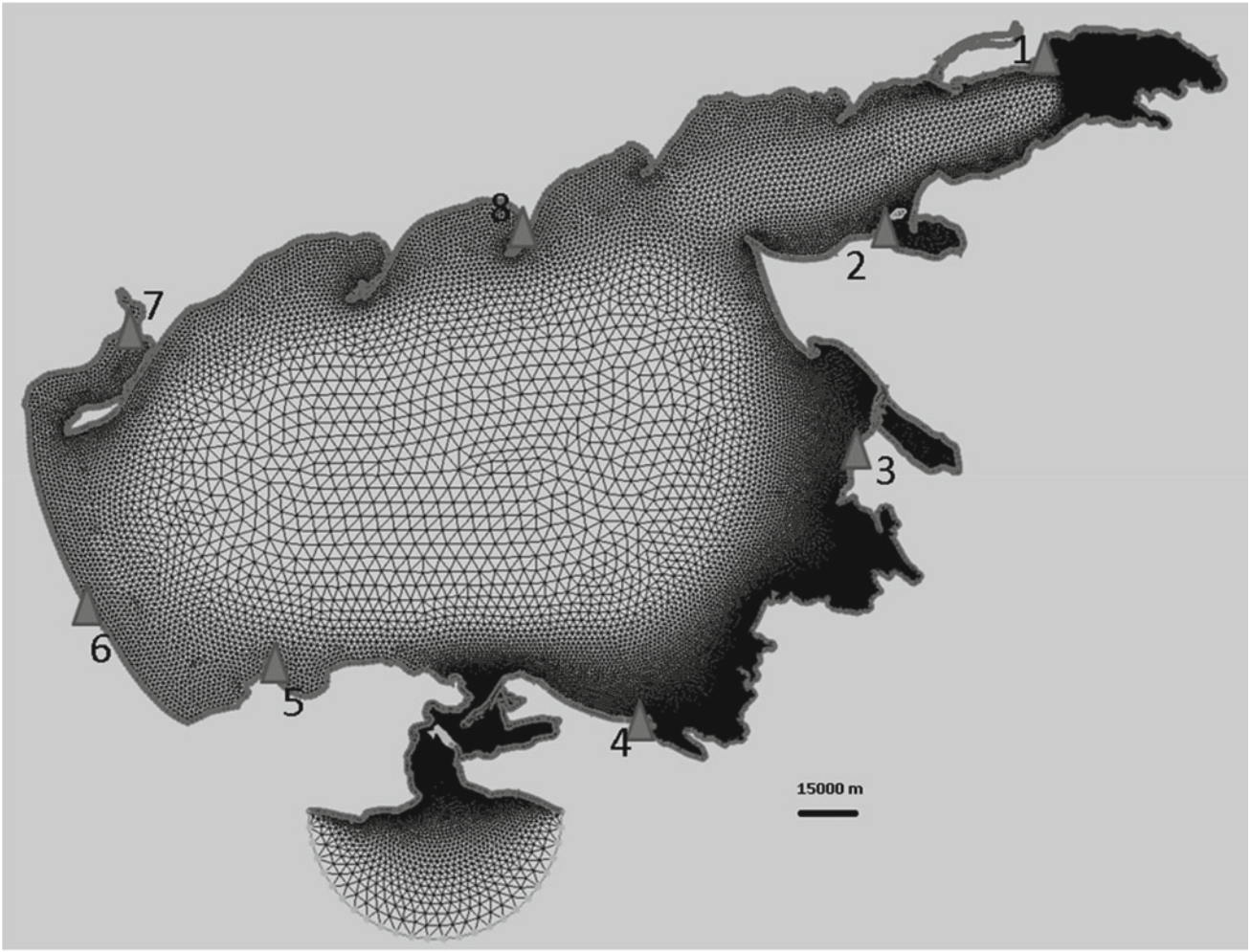

Fig. 1 Unstructured computational grid of the Azov Sea, covering the mouth area of the Don River and some areas of the adjacent land off the east coast. Triangle points where data analysis was performed

not taken into account in mass calculations. However, the river flow was set for some individual numerical experiments in the study of the strongest storm surges in the Don mouth area.

The waves free passage condition—"wave radiation"—was applied at the southern open boundary of the computational region (Fig. 1), located south of the Kerch Strait in the Black Sea. The wind fields (at a height of 10 m) and atmospheric pressure from the NCEP/CFSR re-analysis with a time step of 1 h were set as input data for the period from 1979 to 2010.

The Azov Sea is covered with ice in winter. Thus, the ice concentration fields from the OSI-SAF database with a time step of one day and spatial resolution of 25 km were used for the period from 1979 to 2010.

A more detailed description of the model configuration, the main features of the experiments with the unstructured grid, and the wave model coupling for the different Russian Seas can be found in Pavlova et al. (2020).

3 Results

The results of modeled level fluctuations in the Azov Sea for the period from 1979 to 2010 were analyzed. The analysis was based on the model output data for each node with time step 1 h. The sea level analysis was performed for several individual points—Taganrog (1), Yeisk (2), Primorsko-Akhtarsk (3), Temryuk (4), Mysovoe (5), Arabatskaya Strelka (6), Genichesk (7), and Berdyansk (8) (Fig. 1).

The largest storm surge values are within 0.86–1.98 m (Table 1). In the narrow and shallow Taganrog Bay, the surge is maximum and reaches 1.98 m. Since the surge fluctuations in the Azov Sea level have the form of a single-nodal seiche, the smallest level fluctuations are observed near the nodal line which passes approximately through the center of the sea. The eastern part of Taganrog Bay (the Don River mouth), the southeastern part of

Table 1 Largest calculated storm surge values (m) at these points

1	2	3	4	5	6	7	8
1.98	1.09	1.73	0.96	0.86	1.12	1.11	0.81

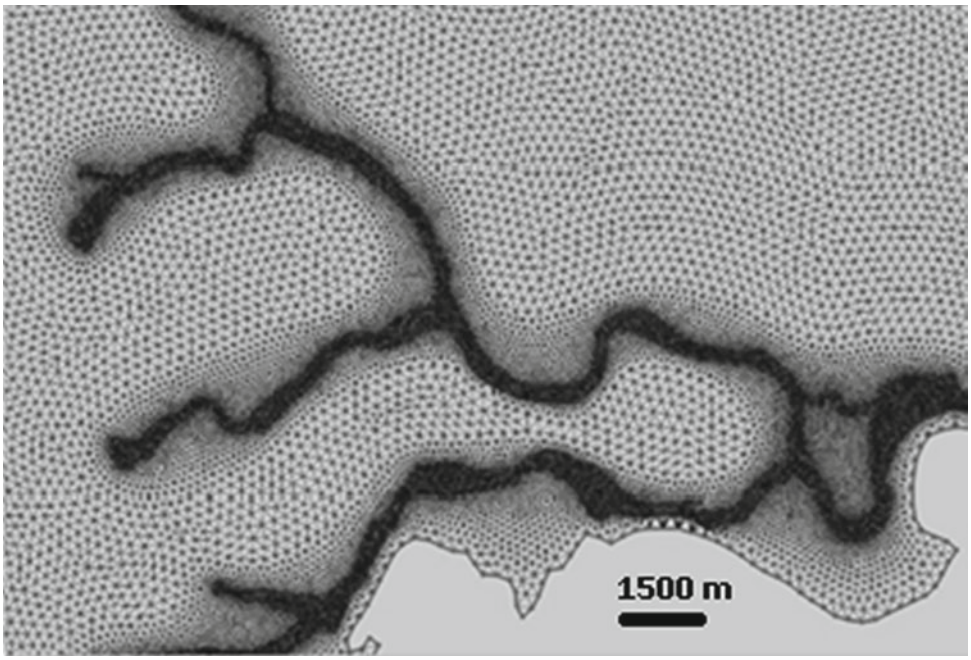

Fig. 2 Fragment of the grid in the Don River mouth area

Temryuk Bay, and the coast of the Arabat Strelka Spit are the dangerous regions for coastal flooding.

Only higher level increases than 0.5 m were taken into account to study the seasonal and long-term variability of surge formation. The 485 cases of storm surges were observed in Taganrog Bay for the period 1979–2010. The recurrence of storm surges in the whole sea was the highest in 1981, 1987, 1997, and 1998. There were no surges more than 0.5 m in the southern part of the Azov Sea (Temryuk, Mysovoe).

The seasonal distribution of surges in the Azov Sea is mainly determined by the peculiarities of synoptic variability in different periods of the year in this area. In general, the greatest number of storm cases occurs in the autumn–winter period of the year, during increased cyclonic activity over the sea.

4 Discussion

It was revealed that storm surges in the western part of the sea are formed during synoptic processes when the eastern and northeastern winds of 10–15 m/s prevail. With south-westerly winds over the entire water area of the sea, surges are formed in Taganrog, Temryuk bays, and Beisugsky estuary.

Due to the fact that the Don mouth area is often flooded by surges, several numerical experiments were modeled to study the characteristics of surge formation in this area. A special computational grid for the Azov Sea was built, which simultaneously covered the entire Don mouth area. The size of the grid elements reached 25 m in the area of the main branches (ducts) (Fig. 2).

The modeling results show that the strongest surges and land floods in the Don mouth area occur at wind speeds above 15 m/s and last more than 10 h. The sea level comes to an equilibrium state on average 20 h after the start of the event.

5 Conclusion

This article introduced new information about storm surges in the Azov Sea based on the results of numerical modeling. The ADCIRC model was implemented with the unstructured grid and NCEP/CFSR re-analysis in the Azov Sea. Sea level database for each node with time step 1 h was created. The maximum surge value reaches 1.98 m in Taganrog Bay. The storm surge recurrence with the level thresholds from 0.5 m was calculated in the Azov Sea for each year. The 485 is maximal number of storm surges which was observed in the Taganrog Bay over the 1979–2010 period.

References

ADCIRC Homepage. (2020). http://www.adcirc.org/. Last accessed August 31, 2020.

Pavlova, A.V., Arkhipkin, V.S., & Myslenkov, S.A. (2020). Storm surge modeling in the Caspian Sea using an unstructured grid. *Russian Journal of Earth Sciences, 20*(1), ES1006.

Terziev, F. (Ed.). (1991). *Hydrometeorology and hydrochemistry of the USSR seas* (Vol. V, Azov Sea). Gidrometeozdat.

Projecting Spatiotemporal Extent of Hydrological Drought in a North African Watershed: Outlooks on Hydrological Response

Youssef Brouziyne, Lahcen Benaabidate, Lhoussaine Bouchaou, Aziz Abouabdilah, and Abdelghani Chehbouni

Abstract

North Africa is considered as the most vulnerable regions regarding climate change impacts. Providing data about the potential responses of hydrological processes to future extreme events (such as drought) will help in designing the fitting adaptation strategies. In this study, the Bouregreg watershed (BW) in Morocco was selected as a typical watershed representing most of the North African watersheds in terms of socioeconomic features, ecological diversities, and the increasing water demand. The semi-distributed model Soil and Water Assessment Tool (SWAT) was forced by two emissions scenario (RCP4.5 and RCP8.5) data from the CNRM-CM5 model of CMIP5 to assess the impact of 2030–2050 dryness on flow regimes. The calibrated SWAT model was used to simulate stream flows of the mid-century period, and the outputs were used to estimate 12 months Streamflow Drought Index (12-SDI) under both RCPs. Results showed the occurrence of several dry years with different severities. During dry years, a significant decrease of water resources availability has been simulated (up to − 69%) with uneven reduction degrees across the study watershed. Hydrologic regimes of sub-basins with high altitudes or benefiting from the ocean effects are supposed to show high resilience levels to future drought impacts. The adopted methodology in this study offers a comprehensive framework by taking benefit of the physical distribution feature of the SWAT model and the statistical representation of Streamflow Drought Index to forecast future droughts and their spatiotemporal extent within the BW.

Keywords

Bouregreg • Flow regimes • SWAT • SDI • Climate change • Drought

1 Introduction

Drought attributes, such as duration and severity, are generally modified from one watershed to another according to the local climate characteristics and the watershed's biophysical features (Brouziyne et al., 2020); understanding the response of vital processes (e.g., hydrology) in a specific watershed is crucial to implement region specific preparedness plan against drought. Drought-focused studies generally rely on drought indices to predict droughts occurrences, whereas most of the climate change impacts on hydrology depend on modeling streamflow under projected climate, as well as interpreting the behavior of the flow attributes compared to baseline situation due to climate extremes (Lopez-Bustins et al., 2013; Rahmani-Rezaeieh et al., 2020). The core objective of this work was to predict the impact of future mid-term dryness on hydrology in a typical North African watershed by combining both semi-distributed hydrologic modeling and a hydrologic drought index.

2 Materials and Methods

2.1 Study Watershed

Being located in the North-western part of Morocco, the Bouregreg watershed (BW) is a typical North African catchment with a high biophysical diversity and several

Y. Brouziyne (✉) · L. Bouchaou · A. Chehbouni
International Water Research Institute, Mohammed VI Polytechnic University (UM6P), 43150 Benguerir, Morocco
e-mail: youssef.brouziyne@gmail.com

L. Benaabidate
Laboratory of Functional Ecology and Environmental Engineering, Faculty of Sciences and Techniques, 30000 Fez, Morocco

A. Abouabdilah
Ecole Nationale d'Agriculture de Meknès, 50001 Meknes, Morocco

A. Kallel et al. (eds.), *Selected Studies in Environmental Geosciences and Hydrogeosciences*, Advances in Science, Technology & Innovation, https://doi.org/10.1007/978-3-031-43803-5_4

natural resources challenges. With a total drainage surface of 9656 km^2, BW has a decreasing elevation gradient from East to Northwest. BW's climate is of a Mediterranean type with an average mean temperature of 16 °C and an annual rainfall average of 460 mm. Rain fed farming lands (28%) and forests (24%) are the dominant land use classes in the study watershed. BW's hydrologic network is formed by four streams: Bouregreg (gauged at downstream by Aguibat Ziar station), Grou (gauged by Ras Fathia station), Machraa (gauged by S. M. Chrif station), and Korifla stream (gauged by Ain Loudah station). The largest streams are Grou and Bouregreg, with average discharges of 5.63 m^3/s and 5.24 m^3/s, respectively.

2.2 Models and Programs

To simulate the hydrological processes in the BW, the Soil and Water Assessment Tool (SWAT) model was used. Before considering the SWAT simulations, calibration efforts are required. To this end, we used the SWAT Calibration and Uncertainty Procedure program (SWAT-CUP) and the uncertainty control algorithm: Sequential Uncertainty Fitting (SUFI-2). Nash-Sutcliff (NSE) and the determination coefficient (R^2) were adopted as indicators of the agreement between simulated and recorded stream flows.

DrinC© software was used to compute the hydrologic drought index Streamflow Drought Index (SDI) (Nalbantis, 2008). The software uses the same concept as the SPI calculation method to compute the SDI over different periods using monthly streamflow data as input. In this study, we calculated 12 months SDI (12-SDI) to capture the regularity of drought events throughout the hydrologic year. The SDI was used owing to its proved ability to replicate historic droughts in the BW in a different study (Brouziyne et al., 2020).

2.3 Datasets

Four dataset categories were used in this study: SWAT input data, calibration data, projected climate data, and DrinC© input data. The input datasets used to build the SWAT project for the BW under baseline scenario are soil data (resolution: 1 km), land use and digital elevation maps (resolution of both: 30 m), and daily maximal and minimal temperature and rainfall (from 1985 to 2005).

To calibrate the SWAT model, recorded monthly streamflow data (from 1985 to 2005) at the four stream gauges were confronted to the simulated stream flows at the same stream gauges. When calibrated, the SWAT model was run using the projected climate data (daily rainfall and daily max and min temperatures) over the period 2030–2050; these data are the downscaled outputs of two emission scenarios (RCP4.5 and RCP8.5) from the Global Circulation Model CNRM-CM5 with 25 km resolution which was used owing to its good accuracy over the North African region (Brouziyne et al., 2020). The Bias-Corrected Spatial Disaggregation method was chosen to bias correct and spatially downscale the GCM simulations, since the first five years of both baseline and future simulation were not considered as they were dedicated to warm up the model. As per the 12-SDI calculation, outputs of the SWAT simulations over the future period (2035–2050) under both RCPs served as inputs for the DrinC© program.

3 Results

3.1 SWAT Calibration

Table 1 represents the SWAT calibration goodness-of-fit at the four stream gauges.

Since NSE and R^2 values exceed 0.5 in all the stream gauges, the satisfactory agreement threshold set by Moriasi et al. (2007), SWAT model can be adopted to study the flow regimes in BW.

3.2 Drought Projections and Hydrologic Response

Figure 1 represents the annual distribution of 12-SDI values over the future simulation period along with the annual Total Water Yield (TWYD) in BW. SWAT simulates TWYD as the sum of all flows (surface and underground) net transmission losses. Projecting hydrologic droughts in the BW revealed that the watershed will experience several dry years with different magnitudes. Under the RCP4.5, two

Table 1 Values of goodness-of-fit indicators during calibration and validation

	Aguibate Ziar		Ras Fathia		S. M. Chrif		Ain Loudah	
	R^2	NSE	R^2	NSE	R^2	NSE	R^2	NSE
Calibration	0.69	0.7	0.73	0.63	0.77	0.87	0.71	0.69
Validation	0.72	0.62	0.69	0.51	0.52	0.46	0.67	0.5

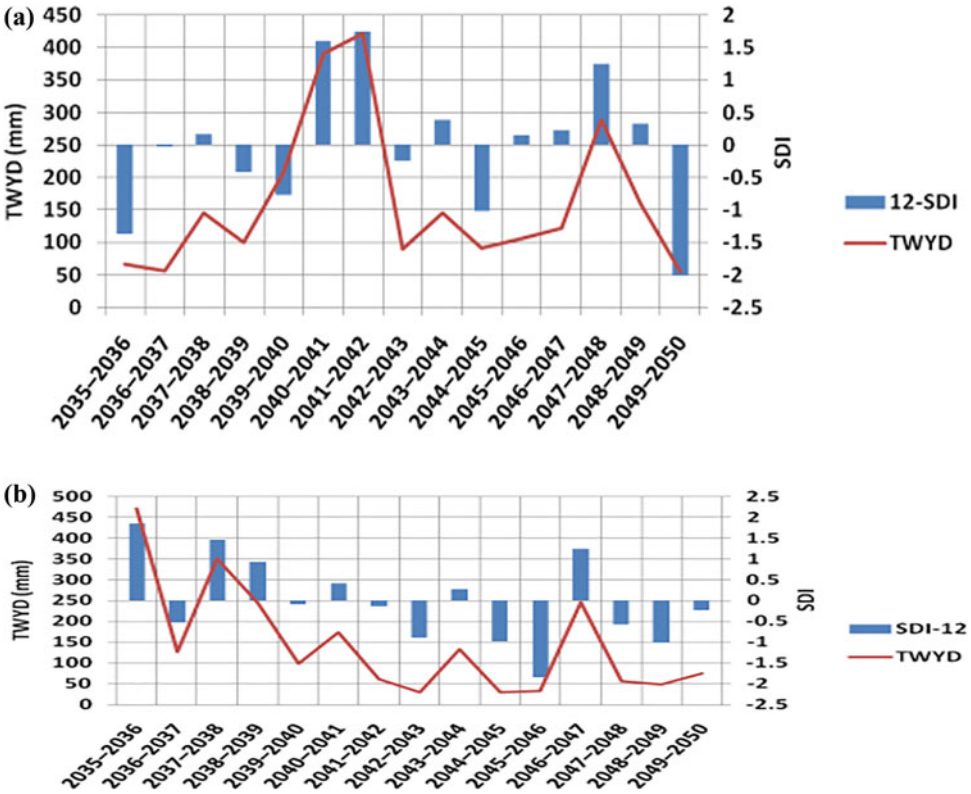

Fig. 1 Annual distribution of 12-SDI and TWYD during 2035–2050 period under **a** RCP4.5 and **b** RCP8.5

moderately dry years and one extremely dry year have been computed; while under the pessimistic scenario, one moderately and one extremely dry year were predicted.

TWYD graphics trends were in agreement with the trend and severity of dryness; very low TWYD values have been simulated during the very dry years. For example, the reduction from the baseline TWYD (130 mm) was around − 57% in the dry year 2049–2050 (RCP4.5) and − 69% in 2045–2046 (RCP8.5). These findings confirm the results of previous attempts to study future droughts in North Africa (Lopez-Bustins et al., 2013).

3.3 Spatial Response of Hydrology

Figure 2 represents the spatial distribution of TWYD reduction by sub-basin during the previously identified dry years: 2049–2050 under RCP4.5 and 2045–2046 under RCP8.5. It can be observed that the sub-basins 2, 1, 3, 5, 8, 9, and 13 are the least affected by the dryness whatever the scenario is. This can be explained by their proximity to the ocean (for the sub-basins located in the extreme Eastern part) and by the altitude effect for sub-basin 13 since it is located over the highest part of BW.

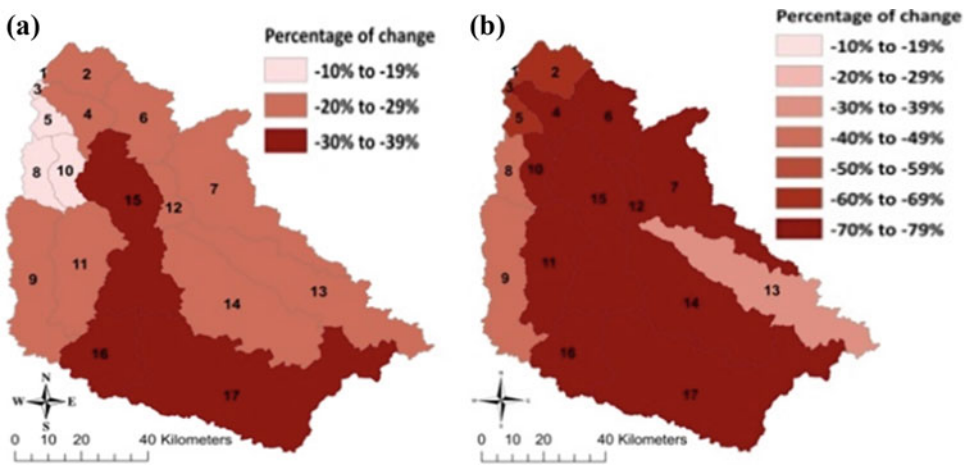

Fig. 2 Sub-basins' TWYD changes during the dry years: **a** 2049–2050 under RCP4.5, **b** 2045–2046 under RCP8.5

4 Conclusion

This study showed that the study watershed will be exposed to drought in the future; several dry years with different severities were predicted during the 2035–2050 period. The TWYD, the selected hydrologic indicator in this study, has shown dramatic decrease in the very dry years. Sub-basins under the ocean or high altitude effects have been revealed less vulnerable to dryness. Any potential drought management strategy has to take into consideration the local characteristics and more urgently the most vulnerable sub-basins in BW.

References

Brouziyne, Y., Abouabdillah, A., Chehbouni, A., Hanich, L., Bergaoui, K., McDonnell, R., & Benaabidate, L. (2020). Assessing hydrological vulnerability to future droughts in a Mediterranean watershed: Combined indices-based and distributed modeling approaches. *Water, 12*. https://doi.org/10.3390/w12092333

Lopez-Bustins, J. A., Pascual, D., Pla, E., & Retana, J. (2013). Future variability of droughts in the Mediterranean catchments. *Natural Hazards, 69*, 1405–1422.

Moriasi, D., Arnold G. J., Van Liew, W. M., Bingner, L. R., Harmel, D. R., & Veith, L. T. (2007). Model evaluation guidelines for systematic quantification of accuracy in watershed simulations. *Transactions of the ASABE, 50*, 885–900. https://doi.org/10.13031/2013.23153

Nalbantis, I. (2008). Evaluation of a hydrological drought index. *European Water, 23*, 67–77.

Rahmani-Rezaeieh, A., Mohammadi, M., & Danandeh Mehr, A. (2020). Climate change impacts on floodway and floodway fringe: A case study in Shahrchay River Basin, Iran. *Arabian Journal of Geosciences, 13*, 494. https://doi.org/10.1007/s12517-020-05444-1

Estimation and Analysis of Global Solar Radiation in Bangkok, Thailand

Siriluk Ruangrungrote

Abstract

Estimations of direct, diffuse and global solar radiation were analytically and numerically achieved via Paltridge and Sabbage methods, yielding the profiles of solar irradiance for Bangkok, in March and April 2009. Both models have different advantages and complications; i.e., eight parameters of cloud and astronomical data were required for running PM and so 15 meteorological parameters were for SM. Daily and monthly solar radiations for 61 consecutive days, representing summertime, were calculated and profiled, together with the statistical tests by RMSE and MABE. Results show that PM was able to provide reasonable predictions of diffuse solar radiation with the RMSE and MABE in a range of 0.18–0.69 and 0.18–0.64 in March, equally for both values around 0.17–0.68 in April. These also showed good agreement with the data from pyranometer (MS 802) measurement. Daily global solar radiation determined by SM indicated similar trend with the actual data. I_{est} values were in a range of 21.46–29.27 MJ/m^2/day with the RMSE and MABE = 6.61 in March and 21.63–29.43 MJ/m^2/day with RMSE and MABE = 5.78, respectively. Moreover, the AODs were achieved at 0.05–0.17 and 0.07–0.75 for the PM and SM, respectively. In summary, the estimations of solar radiation based on computational modeling and empirical equations could practically provide reliable and instantaneous values of solar irradiation components for any location without any constraint of instrumentation or weather condition, meriting the further investigation and challenge in future research.

Keywords

Paltridge model: PM • Sabbage model: SM • AOD

Nomenclature

δ	Declination angle (^{o})
ST	Solar time (hr)
ω	Sunshine hour angle (^{o})
θ_z	Solar zenith angle (^{o})
I_{so}	Extraterrestrial radiation
m_r	Air mass
K_g	Geographical and seasonal factor
L	Latitude of the location
RH	Relative humidity (%)
T_{max}	Monthly average of daily maximum air temperature (^{o}C)
ψ_m	Seasonal factor in month (m)
λ	Wavelength in micron
S	Monthly average of daily real sunshine Duration (hr)
S_0	Monthly average of daily maximum possible sunshine duration (hr)
N	S/S_o

1 Introduction

The available data of solar radiation in terms of direct, diffuse and global components are in demand for many research fields and applications in engineering and renewable energy. Apparently, the number of solar observation sites is still sparse for some locations in Asia, Bangkok, Thailand, in particular. This includes a collection of formulas and methods, being developed for determining daily and monthly data in various places around the world. Then the suitable radiation models for such locations are thought provoking and requisite for atmospheric study. In this work,

S. Ruangrungrote (✉)
Srinakharinwirot University, Bangkok, 10110, Thailand
e-mail: sirilukr@g.swu.ac.th

A. Kallel et al. (eds.), *Selected Studies in Environmental Geosciences and Hydrogeosciences*,
Advances in Science, Technology & Innovation, https://doi.org/10.1007/978-3-031-43803-5_5

Paltridge and Sabbage models (Sabziparvar, 2008) were proposed owing to their various advantages.

2 Materials and Methods

Data collection and site

Daily information of solar radiation in March and April 2009 was collected by pyranometer (MS 802), equipped by the Thai Meteorological Department, Bangkok, 13.40° N, 100.37° E, providing average data as the reliable reference from actual measurement.

Calculation process

Two selected models were applied for instant and total daily solar radiation at the location. Paltridge model (PM) was cloud-based model, governing latitude, cloud data and astronomical parameters (δ), (ST), (ω), (θ_z), (I_{so}), (m_r), eight parameters in total, while modified Sabbage model (SM) was meteorological parameter-based model with 15 required parameters (δ), (ST), (ω), (θ_z), (I_{so}), (m_r). K_g, L, RH, T_{max}, ψ_m, λ, S, S_0 and N. The working process is shown in Fig. 1.

AOD is then calculated by Langley analysis with relation (Alexandrov et al., 2002)

$$I = I_0 \exp(-\tau m), \tag{1}$$

where I is solar intensity at the point of measurement, I_0 is solar intensity at the top of atmosphere, τ = total atmospheric optical depth, and m is the solar air mass relative to unit air mass in zenith direction, using the value 1.142 in this work.

Statistical validation

The obtainable global solar radiation was evaluated and validated by statistical tests which are root mean square error (RMSE) and mean absolute bias error (MABE). For better accuracy of RMSE and MABE values, they should approach to zero (Besharat et al., 2013).

$$RMSE = \sqrt{\frac{1}{n}\sum_{i=1}^{n}(Q_{ic} - Q_{im})^2}$$
$$MABE = \frac{1}{n}\sum_{i=1}^{n}(Q_{ic} - Q_{im}), \tag{2}$$

where n = number of data, Q_{ic} = the estimated solar radiation by modeling, and Q_{im} = the actual measurement of solar radiation.

3 Results

The obtained result of daily solar radiation in terms of I_{est}, direct and diffuse radiation from PM is shown in Fig. 2, data on March 1 and April 1 for instance.

Meanwhile, the same period dataset determined by SM and actual measurement is presented in Fig. 3. As a result, the monthly average of solar radiation and AOD are calculated as given in Table 1.

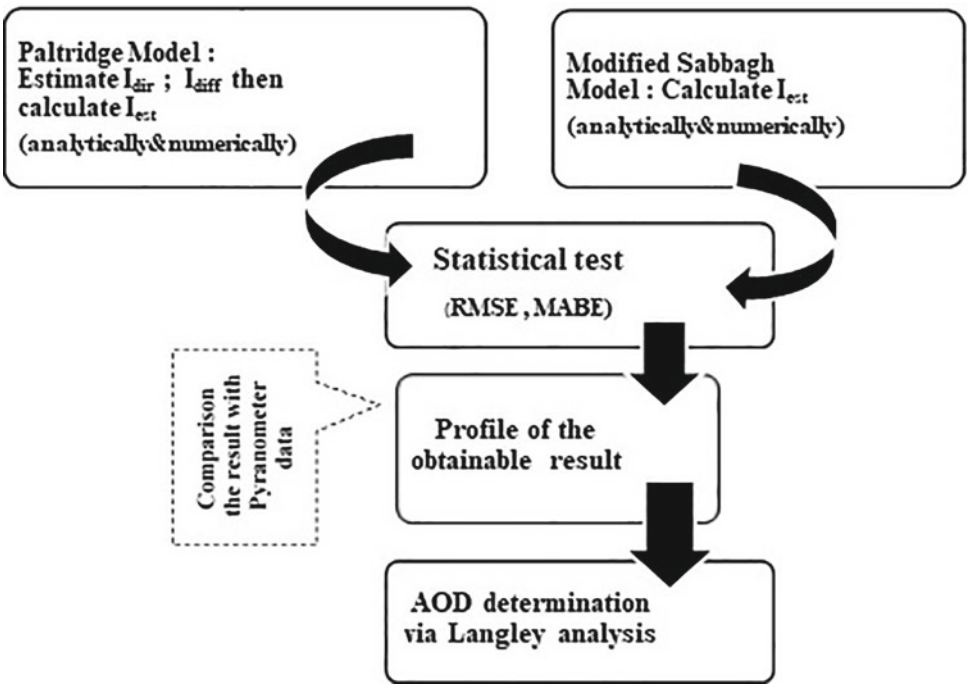

Fig. 1 Flowchart of PM and SM calculation process

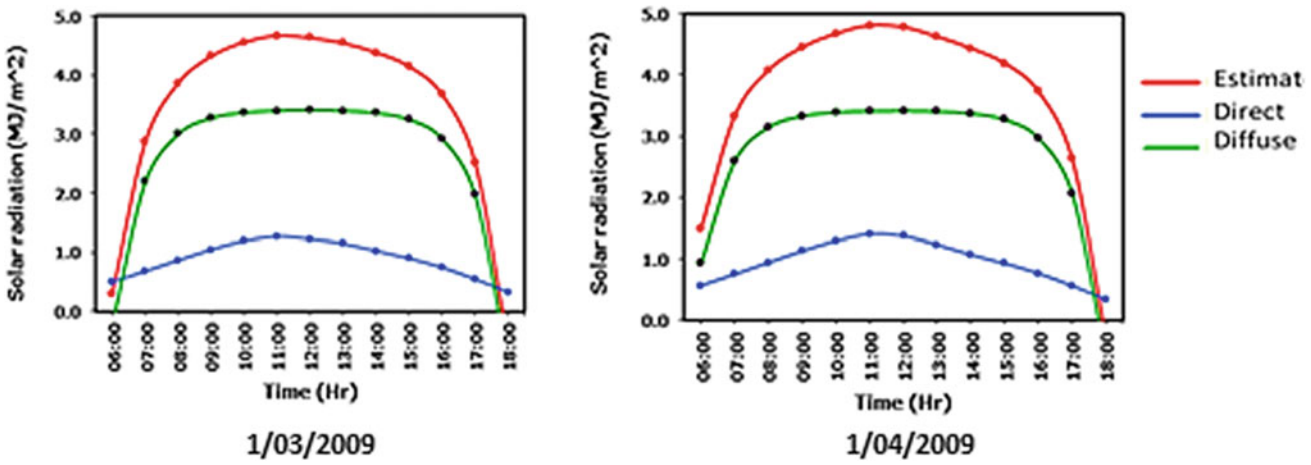

Fig. 2 Example of three components of daily global solar radiation obtained by PM for 2 days in March and April 2009, respectively

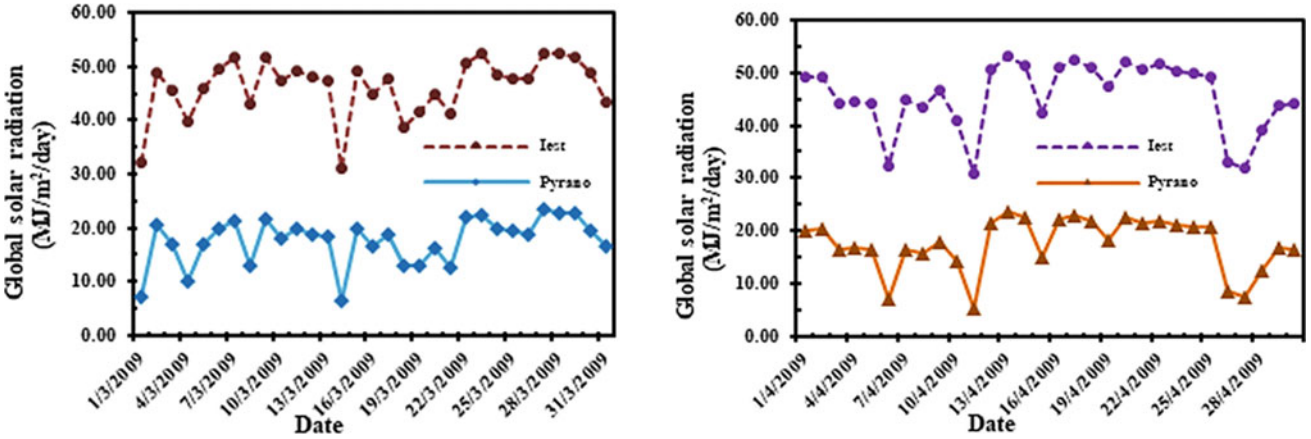

Fig. 3 Comparison of daily global solar radiation obtained by SM and pyranometer measurement in March–April 2009

Table 1 Monthly average of solar radiation and AOD in summer 2009

Month in 2009	I_{est}	I_{diff}	τ_{Total}
March (31 days)	28.679	33.608	0.140
April (30 days)	27.964	12.586	0.698

4 Discussion

Figures 2 and 3 show the performance of two models for estimating solar radiation in Bangkok, Thailand, during the summer of 2009. PM was able to provide reasonable predictions of diffuse solar radiation with the RMSE and MABE in a range of 0.18–0.69 and 0.18–0.64 in March, equally 0.17–0.68 in April for both values. Daily global solar radiation obtained by SM indicated related trend with the real data despite being slightly overestimated. I_{est} values were in a range of 21.46–29.27 MJ/m^2/day with the RMSE and MABE = 6.61 and 21.63–29.43 MJ/m^2/day with RMSE and MABE = 5.78. These showed good agreement with one from other case studies (Khorasanizadeh & Mohammadi, 2013; Shavalipour et al., 2013). Also, the AODs were achieved at 0.05–0.17 and 0.07–0.75 for PM and SM, respectively, to be more specific at 0.140 and 0.698 in average.

5 Conclusion

Two models for simulation of solar radiation based on cloud observation and meteorological data were presented. The greatest advantage of the models is their practical and compatible use without geographical constraints. The correlation and statistical tests were made in order to show the conceivable performance of the best estimation in the site of interest, yielding the alternatives in solar energy research and applications in the regions with similar climate conditions.

References

Alexandrov, M. D., et al. (2002). *Journal of Atmospheric Science, 59*, 524–566.

Besharat, F., Dehghan, A., & Faghih, A. R. (2013). *Renewable and Sustainable Energy Reviews, 21*, 798–821.

Khorasanizadeh, H., & Mohammadi, K. (2013). *Energy, 51*, 257–266.

Sabziparvar, A. (2008). *Renewable Energy, 33*, 1002–1010.

Shavalipour, A., et al. (2013).: *International Journal of Photoenergy*, 174671. https://doi.org/10.1155/2013/174671

Ambient VLF Noise Levels in the Lower Latitude Region

Mario Batubara, Timbul Manik, Musthofa Lathif, Peberlin Sitompul, and Rizal Suryana

Abstract

In this study, the ambient Very Low Frequency (VLF) noise was characterized for a part of tropical of the cancer region above Indonesia longitude using distributed VLF/LF receivers located in Saraburi-Thailand, Pontianak-Indonesia, and Tainan-Taiwan. We introduced an approach to characterize the background VLF noise across the lower latitude. The approach called moving Power Spectral Density where its output was estimated for frequencies ranging from ` ~ 0.01 to 5 Hz for one site at four times of day for each season in both solar maximum and minimum activity of one solar cycle. We selected a large number of 0.5 h waveform segments over 1-year of solar maximum and minimum periods, from continuous data collected by the Indonesian National Institute of Aeronautics and Space (LAPAN) and Asia VLF Observation Network (AVON) system. The ambient noise at the VLF/LF stations is highly variable according to season, time of day and station. Noise spectra for an individual station may vary by four orders of magnitude at any given frequency. Preliminary VLF noise models were defined and used as baselines for evaluating ambient noise at current and future VLF/LF stations. We used this approach to characterize the background noise of all existing stations in the tropical of cancer region. A comparison of full periodic day and season PSDs allows the evaluation for the detection of operational problems and characterization of the performance of the existing VLF/LF stations. The result shows linear relationship between solar activity and the power level of the VLF reception. The median noise levels vary smoothly in the microbaroms band centered on 0.25 Hz and vary smoothly in autumnal equinox after noon time. The noise maps at the wave of low frequencies should be useful for estimating the magnitude threshold for the equatorial networks or conversely for optimizing regional network stations.

Keywords

Noise of very low frequency • Tropical of cancer • Solar activity • And solar cycle

1 Introduction

The term 'noise' is used here to describe all the energy of the signals recorded by a VLF/LF receiver during one full solar cycle period. The total recorded noise is the sum of environmental noise (such as temperature), earth background noise from both natural and cultural sources, and very possibly low-level signals from ground-atmospheric geophysical processes that cannot be visually identified. The noise is measured by the receiver at a single station.

Our objective underlying this work was to characterize the background noise of all existing VLF/LF stations located in the tropical of cancer above the Indonesian longitude using a modified standard methodology. We also intended to evaluate the full range of noise at a given station based on the probability density function (PDFs) computation. Our approach allows us to estimate noise levels over a range of frequencies up to 5 Hz. To this end, the Asia VLF receiver Observation Network (AVON) was used to characterize the frequency-dependent VLF/LF background noise across the tropical of cancer region above the Indonesian longitude. Three stations (PTK, SRB and TWN) were selected. These stations are located in a part of the tropic of cancer, latitude approximately 23°27' N of the terrestrial Equator (Fig. 1). The geographic information of those three stations above are listed in Table 1.These are also useful for supporting data for investigating the full range mechanism on the atmospheric coupling between layers. Three stations will be integrated into the backbone of the AVON (Fig. 1).

M. Batubara (✉) · T. Manik · M. Lathif · P. Sitompul · R. Suryana
Research Center for Space, National Research and Innovation Agency of Indonesia (BRIN), Jl. Sangkuriang, Dago, Kecamatan Coblong, Kota bandung, Bandung, 40135, Indonesia
e-mail: batubaramario@gmail.com

A. Kallel et al. (eds.), *Selected Studies in Environmental Geosciences and Hydrogeosciences*, Advances in Science, Technology & Innovation, https://doi.org/10.1007/978-3-031-43803-5_6

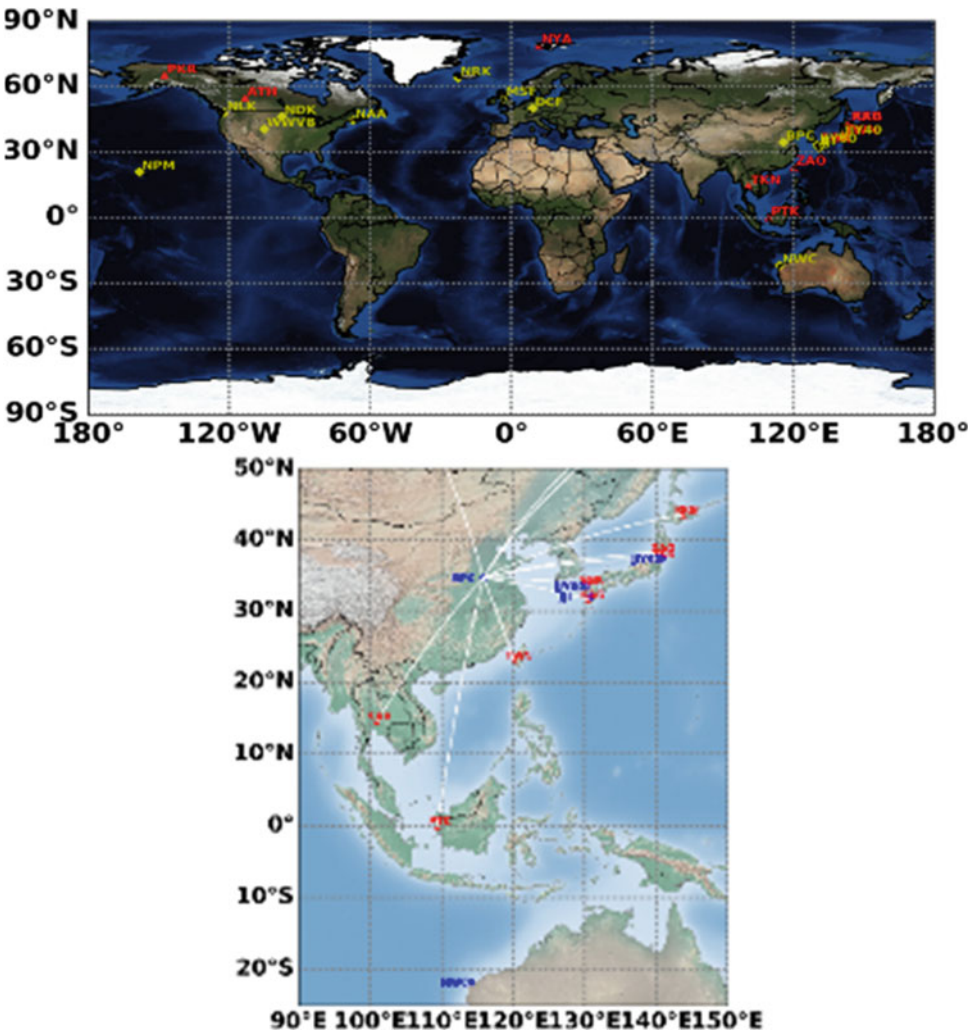

Fig. 1 (Left) Map showing all VLF/LF transmitter (Yellow) and receivers (red). (Right) Zoom in map of the left figure. Our transmitter is BPC located in China and the three used receivers in this study are PTK, TWN, and SRB. Geographic coordinates of these stations are listed in Tables 1 and 2

Table 1 VLF/LF station locations (Transmitter)

Station	Location	Latitude [degree]	Longitude [degree]	Frequency [kHz]
BPC	China	34.63	115.83	68.5

2 Data

Figure 1 (right), Tables 1, and 2 define the locations of the VLF/LF stations of AVON group. Our stations used in this study are star-marked in Tables 1 and 2. The data we used from three stations were analyzed in a period of a solar cycle-24. Each receiver station provides amplitude and phase of the received signals, sampled at 10 Hz. These data were obtained from the AVON FTP server and observation database managed by the National Institute of Aeronautics and Space of Indonesia (LAPAN). The data can be accessed at http://radio.gp.tohoku.ac.jp/db/LF/ and https://bimasakti.sains.lapan.go.id/. In recent years, some studies have focused on the progression and the impact of solar activity through the 11-year cycle of the sunspot number and solar flux, which are the main characteristics of the solar activity variability. The solar cycle 24 was the recent solar cycle, the 24th since 1755. The activity was minimal between 2008 and 2010 and it reached its maximum in 2014. In this study the sunspot number and solar flux were obtained from https://www.swpc.noaa.gov/products/solar-cycle-progression.

3 Methods

Power spectral density was estimated at three stations located in the tropical of cancer latitudes (Fig. 1 right) for data of two-day in each season of peak solar activity (e.g. vernal equinox, summer solstice, autumnal equinox, and winter

Table 2 VLF/LF station locations (Receiver).

Station	Location	Latitude [degree]	Longitude [degree]
PTK	Pontianak/Indonesia	0.003	109.367
SRB	Saraburi/Thailand	14.528	100.9190
TWN	Tainan/ROC	23.070	120.120

solstice). The most common method for estimating the PSD for stationary random VLF data is the "Cooley-Turkey method" (Cooley & Tukey, 1965). For our analysis, the time series components at each station were parsed into 30-secs segments, overlapping by 90%. The observation data were selected four times daily, beginning at 00:00, 06:00, 12:00, and 18:00 local time. The PSD processing of each station component consists of several computations. First, to minimize the variance of the final PSD outputs, each data component was parsed into half-minutes segments, overlapping 90%. Second, in order to suppress the contamination of long-period effect (e.g. large distortion in spectral processing of low frequency quantities), the data were transformed into a zero-mean value, thus long-period data of ambient noise are shown as the noise level above the background noise. Third, a 10% of Hanning taper is used to the ends of each time series segments in order to reduce the side lobe harmonic in the output of FFT and minimize the effect of the discontinuity between the beginning and the end of the time series. These steps were applied to the data recorded at each station on order to get the background noise level of individual station. The PSDs profile output was then used to characterize the frequency source waves. In this work, we investigated all the possible internal waves sources which in general excited from the geophysical processes on the ground.

4 Results

Figure 2, 3 show samples PSD plots for Pontianak station, Indonesia. All spectra calculated for each solar activity, daily and season interval are plotted as blue lines, the 5th and 95th percentiles of the distribution as green and black lines. The red line depicts the median for each interval.

5 Discussion

The entire distribution of the individual PSD curves shows the skewed frequency performance towards higher power at lower frequencies. The effect of solar activity increases the received signal power significantly, especially in the high noise level (95th percentile). The variability of each season's noise level during the minimum solar activity tends to be consistent. However, there is a slight anomaly in the frequency of around 1.5 Hz in the early morning autumnal equinox period. The anomaly is probably thought to be an external force of atmospheric waves drifted up from the lower altitude and the Earth's surface. Widened expansion at high and low noise levels, illustrating the changes in the amplitude of the received waves, which shows the dynamic fluctuation of all seasons and noon times. During this period of expansion, charged particles in the atmosphere undergo an optimal recombination process. In contrast to the conditions when the solar activity is low, the expansion of the lower and upper noise levels widens at night. This confirms the results of previous observations where the VLF signal reception was higher at night (Maurya et al., 2013; Sasmal et al., 2014).

Interestingly, the noise level of the VLF signal in the three seasonal high solar activity in 2015, especially at night, shows anomalies in the variability of the received power. We can see the peak jump of the spectrum at a frequency of about 0.25 Hz in the three noise levels (high, median, and low) starting from 12:00 UT to 21:00 UT, while at other times, this kind of anomaly is not seen. This peak spectrum suggests that the predominant microbarom peak exhibits the highest noise levels in the 0.2–1 Hz band (Pichon et al., 2006), which perturbs the structure of the refraction layer. The propagation of the microbarom waves is substantially affected by the atmosphere thermal and wind structure (Tabulevich, 1995). Depending on the atmospheric wind structure, these signals may propagate in acoustic waveguides between the ground and the troposphere, stratosphere and lower thermosphere (Garcés et al., 2004). Therefore, to confirm the source information, these waves are then valuable potential sources not only for global atmospheric monitoring, since pressure waves can be generated continuously over a long duration, but also for the investigations of the seasonal and diurnal fluctuations of the atmosphere.

6 Conclusion

In this study, VLF signal emitted from man-made transmitter was used as an artificial source of electromagnetic long waves for ionospheric measurements of the structure variability over propagation ranges that exceed several thousands of kilometers. For the studied equatorial ionospheric structures, three stations over the Northern Tropic latitude between peak of solar activity, diurnal, and season were

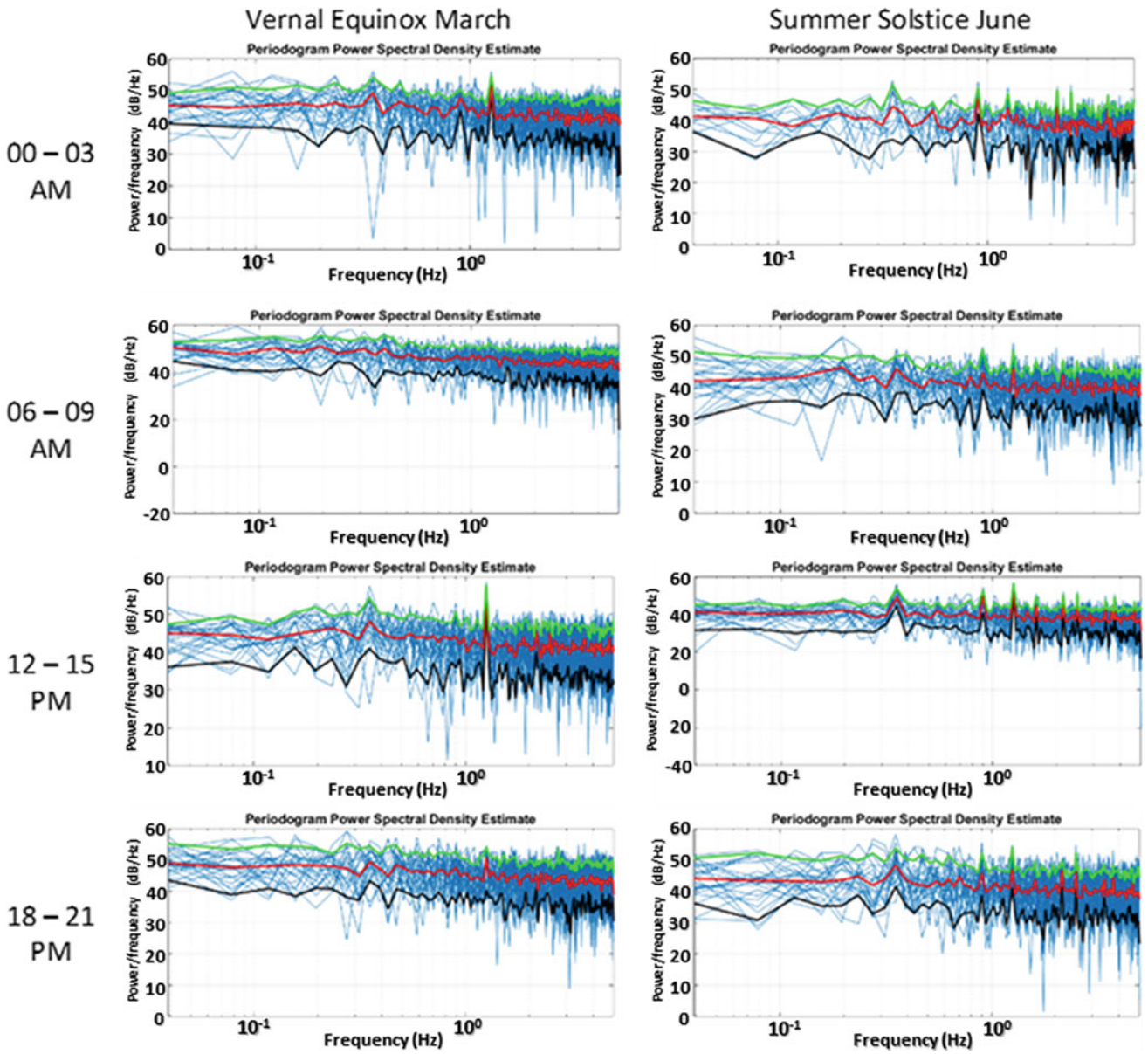

Fig. 2 Power Spectral Density for station at Pontianak, Indonesia for all intervals (blue), the 5th and 95th percentiles (green and black), the median (red) for each time and season in vernal equinox and summer solstice of solar max 24th solar cycle 2015

investigated. A spectral analysis scheme, combined with the distribution probability function was used to investigate the fluctuation of the VLF refraction layer and explain full period trends in the observations and the role of the vertical transport of the atmospheric wave from the bottom area affecting the ionospheric layer. As initial results show, time- and frequency-dependent propagation profiles provide a good correlation between the signal power general changes. We suggest that the solar activity intensifies the refraction layer sensitivity. Their cyclical variations strongly affect the power reception of the VLF signals through the ionosphere refraction process. A clear anomaly of the fluctuation shown in the observed signal power was noted. To interpret these results, we considered the power spectral estimation resulting from each observation time period component. These results confirm the strong influence of the prevailing ocean waves on pressure waves detection capabilities, as microbarom signals almost appear during the night. Further work is needed in order to evaluate the effects of the source (frequency, size, and extent) on the amplitude-scale relations for long propagation ranges. Other stations should also be considered. By taking advantage of new signal processing

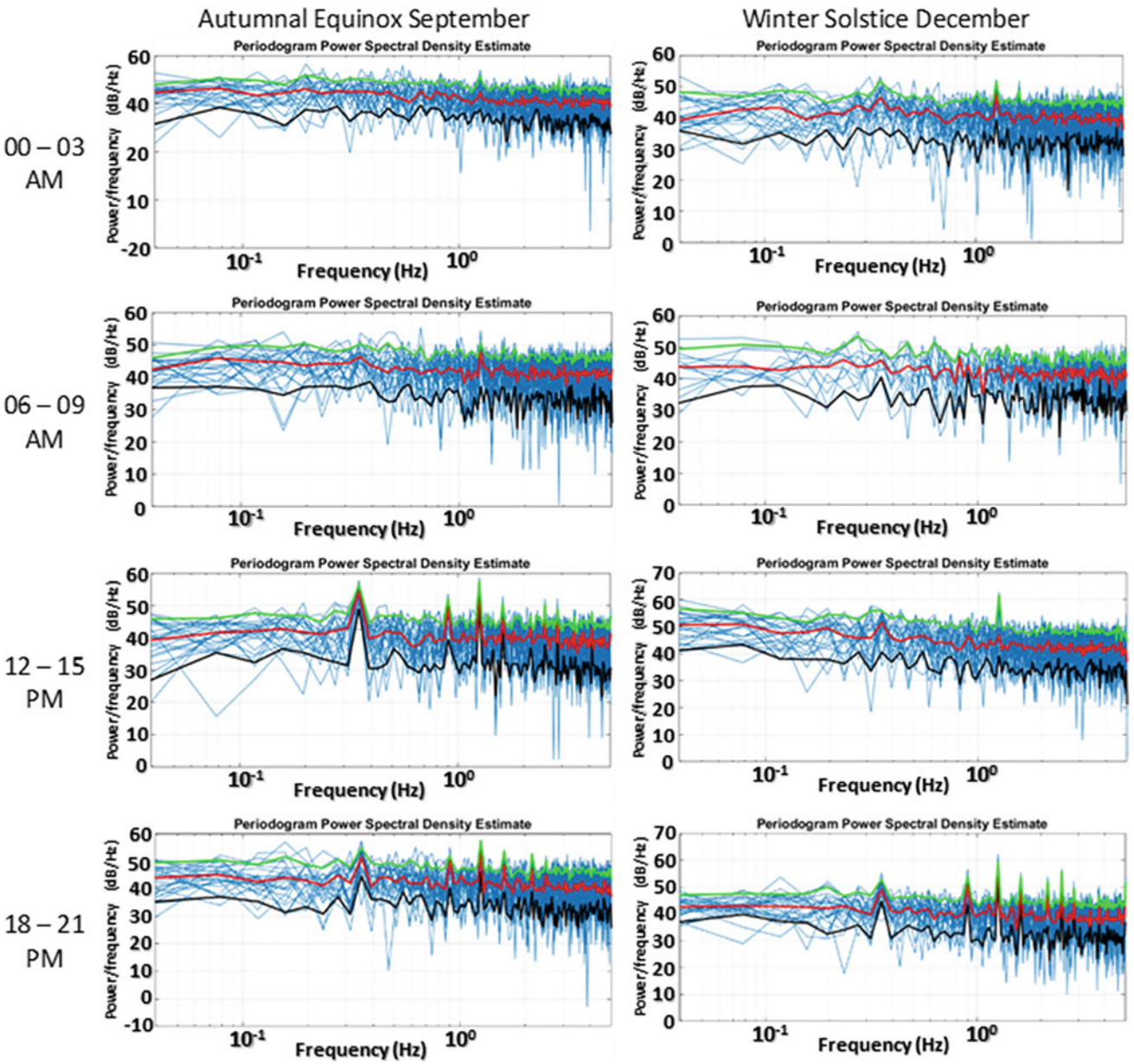

Fig. 3 Power Spectral Density for station at Pontianak, Indonesia for all intervals (blue), the 5th and 95th percentiles (green and black), the median (red) for each time and season in autumnal equinox and winter solstice of solar max 24th solar cycle 2015

methods and recent advances in modeling techniques, continuing the investigations into global monitoring of natural infrasound combine with VLF signals may allow continuous, passive radio-acoustic interaction of the ionosphere.

Acknowledgements The authors are grateful to the Space Science Center of National Institute of Aeronautics and Space of Indonesia (LAPAN) for the helpful support funding of this work we had during the completion of this work. We would also like to thank the Indonesian National Institute of Aeronautics and Space (LAPAN) and Asia VLF Observation Network (AVON) for providing the VLF data. The sunspot number and solar flux are provided by the National Oceanic and Atmospheric Administration (NOAA) Space Weather Prediction Center (SWPC).

References

Cooley, J. W., & Tukey, J. W. (1965). An algorithm for machine calculation of complex fourier series. *Mathmatics of Computation, 19*, 297–301.

Garcés, M., Willis, M., Hetzer, C., Le Pichon, A., & Drob, D. (2004). On using ocean swells for continuous infrasonic measurements of winds and temperature in the lower, middle, and upper atmosphere. *Geophysical Research Letters, 31*, L19304. https://doi.org/10.1029/2004GL020696

Le Pichon, A., Ceranna, L., Garcés, M., Drob, D., & Millet, C. (2006). On using infrasound from interacting ocean swells for global continuous measurements of winds and temperature in the

stratosphere. *Journal of Geophysical Research, 111*, D11106. https://doi.org/10.1029/2005JD006690

Maurya, A., Singh, R., Veenadhari, B., Kumar, S., & Singh, A. (2013). Sub-ionospheric very low frequency perturbations associated with the 12 May 2008 M = 7.9 Wenchuan earthquake. *Natural Hazards and Earth System Sciences., 13*, 2331–2336. https://doi.org/10.5194/nhess-13-2331-2013

Sudipta, S., Sujay, P., Sandip, C. (2014). Study of long path VLF signal propagation characteristics as observed from Indian Antarctic station, Maitri. *Advances in Space Research, 54*.https://doi.org/10.1016/j.asr.2014.06.002

Tabulevich, V. (1995). On recordings of global microseismic vibrations and observations of microseisms in shore zones of oceans. *Physics of the Earth and Planetary Interiors, 91*, 299–305.

Biogeochemistry, Geobiology, Geoecology, Geoagronomy

Estimating Vegetation CO_2 Sequestration in Grombalia Region (Northeastern Tunisia) Using Remote Sensing and GIS

Rim Mehdaoui and Makram Anane

Abstract

The main objective of the research was to estimate the CO_2 sequestration (CDS) of vegetation in Grombalia region using remote sensing and GIS. The research process included (1) mapping land use/land cover (LULC) of Grombalia region during 2016/2017 and 2017/2018 agricultural seasons using supervised maximum likelihood classification of Sentinel 2 images; (2) extracting vegetation land cover categories (fruit trees, cropland and grassland) from the resulting maps; (3) calculating NDVI and SRVI vegetation indices from Sentinel 2 images of 2 March 2017 and 2 March 2018; (4) estimating CDS and net primary productivity (NPP) of vegetation categories in March 2017 and March 2018 based on the vegetation indices; and (5) analyzing CDS change detection between 2017 and 2018. The results indicate that the fruit trees sequestrate more CO_2 than cropland and grassland. The CDS of the three vegetation categories recorded a decrease between 2017 and 2018; about 20% for fruit trees dropping down from 3035 to 2420 t C, 12% for cropland, declining from 432 to 381 t C and about 35% for grassland decreasing from 211 to 137 t C. This behavior is driven by a significant rainfall decrease between both years.

Keywords

CO_2 sequestration • LULC • Remote sensing • GIS • Grombalia region

R. Mehdaoui (✉) · M. Anane
Wastewaters and Environment Laboratory, Water Research and Technologies Center, P.O. Box 273 8020 Soliman, Tunisia
e-mail: rim.mehdaoui@yahoo.com

M. Anane
e-mail: makram.anane@certe.rnrt.tn

1 Introduction

Global warming is one of the leading environmental problems of the twenty-first century. CO_2 is one of the most important greenhouse gases causing global warming. It has built up a blanket surrounding the earth which traps heat from the surface, increases temperature and subsequently causes climate change effects (Zhu et al., 2005). Therefore, the quantification of CO_2 sequestration is required in order to mitigate the earth warming.

Remote sensing could play a key role in estimating this sequestered amount. Boosted by the frequent temporal availability and low cost of multi-spectral satellite images, remote sensing is becoming a powerful tool in producing land use/land cover (LULC) maps, measuring and monitoring land surface parameters at large scale such as leaf area index (LAI), phenology and fraction of absorbed photosynthetic active radiation (fPAR) by vegetation, which is helpful to quantify and study the spatial distribution, seasonal and inter-annual change of NPP and mainly estimate the CO_2 sequestration (CDS) (Field et al., 1995; Los et al., 1994). The objectives of this research were to (i) map the LULC of Grombalia region for 2016/2017 and 2017/2018 agricultural seasons and (ii) estimate and monitor CDS of vegetation lands in the region based on GIS and remote sensing data.

2 Materials and Methods

2.1 LULC Classification

Grombalia region is located in the North-East of Tunisia between latitudes 36°75′–36°46′ North and longitudes 10° 72′–10°30′ East, covering an area of approximately 372 km^2. Mapping the LULC of Grombalia region was established in order to extract vegetation lands and calculate their areas. For this purpose, the available twelve cloud-free

A. Kallel et al. (eds.), *Selected Studies in Environmental Geosciences and Hydrogeosciences*, Advances in Science, Technology & Innovation, https://doi.org/10.1007/978-3-031-43803-5_7

Sentinel 2 images from October 2016 to June 2017 and from October 2017 to June 2018 were downloaded from Copernicus website (2019) corrected atmospherically using ESA's Sen2Cor, stacked to 10 m resolution and clipped to the study area. Then, supervised maximum likelihood classifications were carried out considering well-distributed 260 training parcels (12.7 km^2). Field visits were conducted in March 2017 and 2018 to identify the land covers types. The classifications were performed using the following combinations: "13 October 2016, 02 December 2016, 31 January 2017, 11 April 2017 and 20 June 2017" for the growing season 2016/2017 and "18 October 2017, 12 December 2017, 31 January 2018, 16 April 2018 and 05 June 2018" for 2017/2018 season. For each image, only ten bands (2–8, 8A, 11, 12) and normalized vegetation index (NDVI) were considered. The dates of the images of both combinations are almost similar and reflect the phenological stages of the main cultivation categories. The accuracy of the resulting classifications was carried out by overall accuracy and kappa index (Congalton, 1991) using 120 control parcels (7.4 km^2).

2.2 Estimation of NPP and CO_2 Sequestration

The CO_2 sequestration (CDS, kg CO_2) for a given vegetation category i is the product of the net primary productivity (NPP, gC m^{-2}) and the vegetation land area (A, ha) as shown in Eq. 1:

$$\mathrm{CDS}_i = A_i \times \mathrm{NPP}_i \tag{1}$$

NPP is the product of the actual light use efficiency (LUE) and the absorbed incident photosynthetically active radiation (APAR) as shown in Eq. 2:

$$\mathrm{NPP} = \mathrm{LUE} \times \mathrm{APAR}. \tag{2}$$

LUE (gC MJ^{-1}) is a function of the vegetation category. Based on literature review (Field et al., 1995; Running et al., 2000), it is assumed to be 0.255 gC MJ^{-1} for vines and citrus trees, 0.283 gC MJ^{-1} for olive trees, 0.242 gC MJ^{-1} for cropland and 0.229 gC $MJ^{-1}$for grassland.

APAR (MJ m^{-2}) is calculated using Eq. 3:

$$\mathrm{APAR} = \mathrm{SOL} \times \mathrm{FPAR} \times 0.5, \tag{3}$$

where SOL (MJ.m^{-2}) refers to the global solar radiation. In this study, the SOL provided by Beni Khalled meteorological station were 243.06 MJ m^{-2} in March 2017 and 230.51 MJ m^{-2} in March 2018; FPAR is the fraction of photosynthetically active radiation absorbed by green vegetation. The FPAR can be calculated from NDVI and simple ratio vegetation index (SRVI) RS indices using Eqs. 4, 5 and 6 (Field et al., 1995; Zhu et al., 2005):

$$\mathrm{FPAR}_{\mathrm{NDVI}} = \frac{(\mathrm{NDVI} - \mathrm{NDVI}_{\mathrm{i,min}})(\mathrm{FPAR}_{\max} - \mathrm{FPAR}_{\min})}{\mathrm{NDVI}_{\mathrm{i,max}} - \mathrm{NDVI}_{\mathrm{i,min}}} + \mathrm{FPAR}_{\min} \tag{4}$$

$$\mathrm{FPAR}_{\mathrm{SRVI}} = \frac{(\mathrm{SRVI} - \mathrm{SRVI}_{\mathrm{i,min}})(\mathrm{FPAR}_{\max} - \mathrm{FPAR}_{\min})}{\mathrm{SRVI}_{\mathrm{i,max}} - \mathrm{SRVI}_{\mathrm{i,min}}} + \mathrm{FPAR}_{\min} \tag{5}$$

$$\mathrm{NDVI} = \frac{\mathrm{PIR} + \mathrm{R}}{\mathrm{PIR} - \mathrm{R}} \text{ and SRVI } \frac{1 + \mathrm{NDVI}}{1 - \mathrm{NDVI}} \tag{6}$$

where for a given vegetation category i, $\mathrm{NDVI}_{i,\ \max}$ (or $\mathrm{SRVI}_{i,\ \max}$) and $\mathrm{NDVI}_{i,\ \min}$ (or $\mathrm{SRVI}_{i,\ \min}$) represent, respectively, 98% and 2% of the NDVI (or SRVI) values; $\mathrm{FPAR}_{\min}$ and $\mathrm{FPAR}_{\max}$ are independent of vegetation categories and assumed to be, respectively, 0.001 and 0.95; R is red band and PIR is near infrared band.

The literature review shows that NDVI/FPAR model (Eq. 4) overestimates the FPAR, but SRVI/FPAR (Eq. 5) underestimates the FPAR (Los et al., 1994). Therefore, an intermediate model, calculating the average FPAR from the NDVI/FPAR and SRVI/FPAR models (Eq. 7), was adopted:

$$\mathrm{FPAR} = \frac{\mathrm{FPAR}_{\mathrm{SRVI}} + \mathrm{FPAR}_{\mathrm{NDVI}}}{2}. \tag{7}$$

In this study, we calculated the CDS on 2 March because the vegetation biomass is at its maximum.

3 Results and Discussion

The overall accuracy for 2016/2017 classification is 74% and the 2017/2018 classification is 72%, and the Kappa index is 0.66 and 0.63, respectively, which demonstrates the good performance of the resulting LULC maps (Congalton, 1991). These maps (Fig. 1a, b) show six major land cover classes in the study area, namely fruit trees (olive trees, citrus trees and vine), cropland, grassland, sebkha, bare soil and urban areas. The main changes detected between both agricultural seasons are a 3.7 km^2 (9.3%) of cropland increase and 7.5 km^2 (4.5%) grassland and 4.8 km^2 (2.8%) bare soil decrease. The grassland is substituted by cropland. The fruit trees, sebkha, bare soil and urban areas remained approximately the same (change not exceeding 2%).

The NPP maps (Fig. 1c, d) show a significant spatial heterogeneity for different types of vegetation. For fruit trees, the NPP mean is 11.7 gC m^{-2} in March 2017 and 9.5 gC m^{-2} in March 2018. For cropland and grassland, the NPP means are, respectively, 13.5 and 8.3 gC m^{-2} in 2017 and 10.7 and 4.2 gC m^{-2} in 2018. The NPP means indicate a

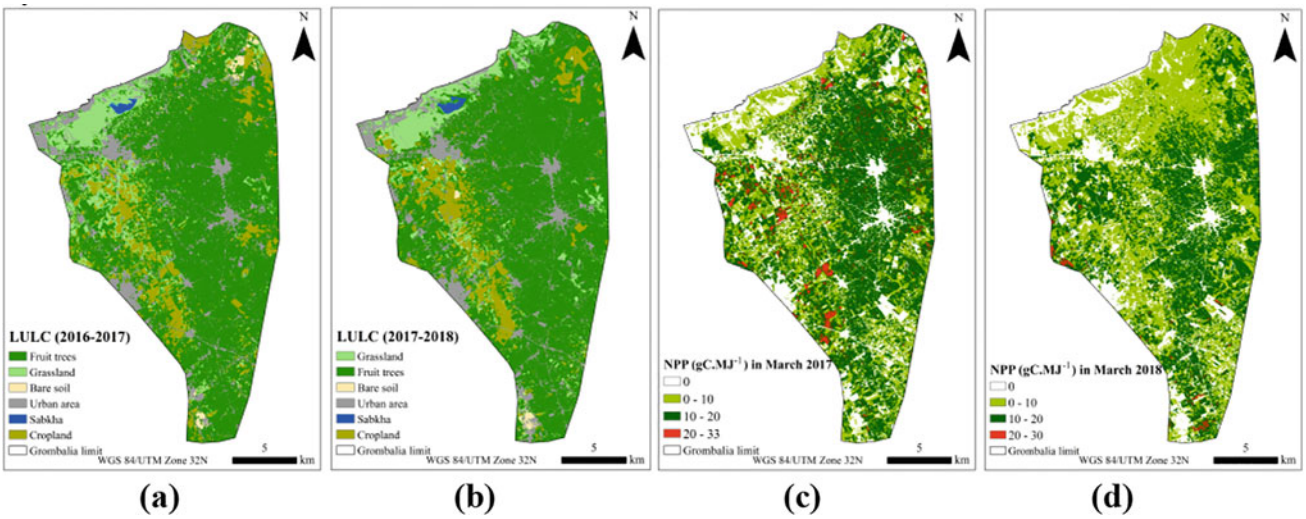

Fig. 1 Map of **a** LULC in 2016/2017; **b** LULC in 2017/2018; **c** NPP in March 2017 and **d** NPP in March 2018

decrease of 19, 21% and 49% for fruit trees, cropland and grassland, respectively. This can be explained by the effect by precipitation decrease and the amount of irrigated water provided to the farmers. NPP is proportionally related to rainfall.

The last result is consistent with that obtained by Jiao et al., (2018) who revealed that changes in precipitation played a key role in the NPP variation. However, the results are in discordance with (Yang et al., 2019) who found that air temperature was the main influencing climatic factor that controlled the inter-annual variability in NPP. The disagreement might result from environmental characteristics of the study area and the different analysis methods used.

The estimated CDS is 3035 t C in March 2017 and 2420 t C in March 2018 for fruit trees and showed a decrease of 20%. For cropland and grassland, the CDS is 432 and 210 t C in 2017 and 381 and 137 t C in 2018, respectively. Comparing the two years, CDS decreased by 12 and 35%, respectively, for cropland and grassland. CDS is proportionally related to NPP.

4 Conclusion

Remote sensing is a powerful tool to derive accurate and frequent information on LULC spatial distribution and changes detection and estimating CO_2 sequestration chronological changes inside the same vegetation category and between vegetation categories. These promising results could help decision makers to elaborate appropriate strategies management taking into account global warming issues. The adopted methodological approach is simple and easy to extend to other regions.

References

Congalton, R. G. (1991). A review of assessing the accuracy of classifications of remotely sensed data. *Remote Sensing of Environment, 46*(April), 35–46.

Copernicus website., https://scihub.copernicus.eu/.

Field, C. B., Randerson, J. T., & Malmström, C. M. (1995). Global net primary production: Combining ecology and remote sensing. *Remote Sensing of Environment, 51*, 74–88.

Jiao, Chen, W., Yli, W., Zhu, C., & Li, Z. (2018). Estimation of net primary productivity and its driving factors in the Ili River Valley, China. *Journal of Arid Land, 10*(5), 781–793.

Los, S. O., Justice, C. O., & Tucker, C. J. (1994). A global 1 by 1 NDVI dataset for climate studies derived from the GIMMS continential NDVI data. *International Journal of Remote Sensing, 15*, 3493–3518.

Running, S, W., Thornton, P. E., Nemani, R., &and Glassy, J. M. (2000). Global terrestrial gross and net primary productivity from the earth observing system. In O. Sala, R. Jackson & and H. Mooney (Eds.), *Methods in Ecosystem Science*, (pp. 44–57). Springer.

Yang, Y., Wang, J., Liu, P., Lu, G., & Li, Y. (2019). Climatic changes dominant interannual trend in net primary productivity of alpine vulnerable ecosystems. *Journal of Resources and Ecology, 10*(4), 379–388.

Zhu, W. Q., Pan, Y. Z., Long, Z. H., Chen, Y. H., Li, J., & Hu, H. B. (2005). Estimating net primary productivity of terrestrial vegetation based on GIS and RS: A case study in Inner Mongolia China. *Journal of Remote Sensing, 9*(3), 300–307.

Assessment of Acid Sulfate Soils' Physicochemical Properties for Oil Palm (*Elaeis guineensis* Jacq.) Cultivation in South-South Nigeria

Ajoke Adegaye, Segun Oladele, and Kehinde Erinle

Abstract

Besides aquaculture and rice farming which appear to be the common agricultural practices carried out on acid sulfate soils (ASS) in the mangrove swamp of Buguma Creek in Niger Delta, Rivers State, and in the Mbiabet Swamp of Ini Local government area, Akwa Ibom, respectively, little is known about the potentials of these soils for Oil palm production. Therefore, the present study aimed at expanding the use and management of ASS by assessing their physicochemical properties for Oil palm (*Elaeis guineensis* Jacq.) cultivation in South-South Nigeria. Soil samples were taken randomly from two sites (loamy sand (LS) and sandy loam (SL) soil types) each from both locations at 0–30 cm depth. Pregerminated Oil palm (cv. Tenera) seedlings were planted singly in nursery bags (38 × 50 cm) with equal volume of media. The greenhouse experiment was set up in a completely randomized design (CRD) with six replications per treatment. Treatments included Buguma SL; Buguma LS; Mbiabet SL; and Mbiabet LS. Significant differences ($p < 0.05$) were observed for plant height, stem girth, leaf area, and wet and oven-dry weights (55 °C) of roots and shoots at 3 and 8 months after sowing, with LS soils significantly recording the highest mean values for each parameter observed. This was likely due to increased chemical nutrients of LS soils compared with SL soils. Consequently, ASS with a higher percentage of silt and moderate chemical nutrients can be productively cropped with Oil palm in Nigeria following proper agronomical practices.

Keywords

Oil palm *(Elaeis guineensis* Jacq.) • Soil physicochemical properties • Acid sulfate soils • Soil types • South-South Nigeria

1 Introduction

Oil palm (*Elaeis guineensis* Jacq.) is one of the most profitable economic crops in the tropics (Mgbakor et al., 2013). The perennial crop is the most important member of the family *palmae,* subfamily *cocoideae* (Ibitoye et al., 2011; Opeke, 1987), and has quite an enormous importance which includes among others its use for cooking food, making soap and lubricants, brooms and roofing materials, cosmetics, sieve weaving, pond construction, margarine manufacturing, metal plating, glycerin, and livestock feed production (Mgbakor et al., 2013). The versatile tree crop has almost all its parts to be useful and of commercial value. The tapped sap is usually drunk as palm wine, while the spent fruit bunch and fiber serve as mulch materials, as manure and as fuel. The economic usefulness of the crop has made it one of the leading export crops in the world. Nigeria has once been the world's leading producer and exporter of palm oil in 1965. However, this position was lost to Malaysia over five decades ago (Atser, 2007), which marked the inception of oil boom in the early 1970s with an obvious decline in Nigeria's Oil palm production (Ibitoye et al., 2011; Mgbeje, 2004). Despite its usefulness, only very few Nigerians essentially engage in Oil palm cultivation and less effort has been made to resuscitate the situation.

The management and optimum use of acid sulfate soils (ASS) for the sustained production of crops have always been

A. Adegaye (✉) · S. Oladele
Federal University of Technology Akure, Ondo State, Nigeria
e-mail: acadegaye@futa.edu.ng

S. Oladele
e-mail: segun.oladele@aaua.edu.ng

S. Oladele
Department of Agronomy, Adekunle Ajasin University, Akungba, Akoko, Ondo State, Nigeria

K. Erinle
School of Agriculture, Food and Wine, University of Adelaide, Adelaide, Australia
e-mail: kehinde.erinle@adelaide.edu.au

A. Kallel et al. (eds.), *Selected Studies in Environmental Geosciences and Hydrogeosciences*, Advances in Science, Technology & Innovation, https://doi.org/10.1007/978-3-031-43803-5_8

challenging due to their characteristic low pH (less than 4) and the presence of sulfuric horizon, which is mostly due to pyrite (FeS_2) oxidation (Ubi & Osodeke, 2009). The low pH directly affects the growth of plants as a result of Al and/or Fe toxicity and indirectly decreases the availability of phosphorus and other plant available nutrients. Nevertheless, ASS have been extensively studied and managed successfully for the cultivation of several crops including Oil palm with good yields (Anda et al., 2009; Azura, 2012; Shamshuddin et al., 2014). Studies have also been conducted in the two most common acid sulfate soils in Nigeria (Dublin-Green et al., 2003; Ubi & Osodeke, 2009), both occurring at the south-southern part of the country. They include the mangrove swamp of Buguma Creek in Niger Delta, Rivers State, and the Mbiabet Swamp of Ini Local government area, Akwa Ibom. However, besides the usual aquaculture and rice farming which are the most common agricultural practices on such ASS in both areas, little is known about the potentials of these soils for Oil palm production. Oil palm is known to be moderately tolerant to Al and/or Fe toxicity (Shamshuddin et al., 2014). Furthermore, the shortage of agricultural land and long maturation period of the crop has made the reclamation of ASS vital for Oil palm cultivation. This study therefore aimed at expanding the use and management of ASS in the two areas by i. assessing their physicochemical suitability for Oil palm cultivation and ii. determining the soil type that best supports the growth and improves the physiological properties and biomass of Oil palm seedlings.

2 Materials and Methods

2.1 Experimental Site

The potted experiment was conducted in the greenhouse of the Department of Crop, Soil and Pest Management, Federal University of Technology, Akure (7°20 N, 5°30 E), Ondo, Nigeria, from April to December 2019 with air temperatures ranging from 24 to 36 °C. The physicochemical analyses of soil samples were carried out at the Soil Science Laboratory of the Department, FUTA. The mean annual rainfall in Buguma and Mbiabet swamps was recorded to be about 2, 010 mm and 2, 505 mm, respectively.

2.2 Soil Sampling and Analysis

Ten soil samples were collected randomly each from two sites (loamy sand (LS) and sandy loam (SL) soil types) in both Buguma and Mbiabet swamps at 0–30 cm depth. The samples were bulked and homogenized to form a representative sample of each soil type, making a total of 20 samples per location. Soil pH was determined in a 1:2.5 soil–H_2O suspension using an electronic pH meter; available P using the Bray-I method; organic matter using the wet oxidation method; total N content by the Kjeldahl digestion method; exchangeable cations and CEC using ammonium acetate method; sulfate-sulfur ions were extracted using KH_2PO_4 and determined by turbidimetric method; bulk density was determined using the core sampling method and particle size analysis by Bouyoucos hydrometer method. All physicochemical properties were analyzed following the detailed procedures of Mc-Keague (Mckeague, 1982).

2.3 Experimental Design and Procedure

The setup was in a completely randomized design (CRD) with six replications per treatment. Treatments included (1) Buguma, SL, (2) Buguma, LS, (3) Mbiabet, SL, and (4) Mbiabet, LS. Pregerminated Oil palm (cv. Tenera) seedlings were obtained from Nigeria Institute for Oil Palm Reserve (NIFOR) and planted out singly in single-stage nursery poly bags (38 cm × 50 cm) with equal volume of media. Watering was carried out twice daily, while weeding was done manually. There was no application of fertilizers in this research. The wet weight of roots and shoots was measured by harvesting 2 cm above the soil, while the roots were detached cautiously from the nursery bags. Dry weights were computed after oven-drying at 55 °C until constant weight was attained.

2.4 Data Collection and Analysis

Morphological (plant height, stem girth, and leaf area) and physiological (wet and oven-dry weights (55 °C) data were collected for roots and shoots of Oil palm seedlings at 3 and 8 weeks after sowing (WAS). Analysis of variance (ANOVA) of all collected data was performed using Minitab statistical software package version 17. Significant differences among treatment means were compared and separated using Tukey test at $p < 0.05$.

3 Results

Significant differences ($p < 0.05$) were shown to exist in the mean values of the physical and chemical data presented in Tables 1. The silt content and bulk density values of the soil were highest and lowest in Mbiabet LS and vice versa in Muguda SL, respectively. Mbiabet LS had the highest and significant ($p < 0.05$) mean values of 4.47, 4.67%, 0.39%, 3.39 mg kg^{-1}, and 1.36 cmol kg^{-1} for soil pH, organic matter (OM), total nitrogen (TN), available P, and potassium (K), respectively, while it recorded the least mean values of

11.48 and 0.72 cmol kg^{-1} for exchangeable acidity and magnesium (Mg), respectively. Muguda LS, on the other hand, recorded the highest significant ($p < 0.05$) mean value of 28.34 cmol kg^{-1} for CEC, while the least mean values of 3.28, 3.10%, and 1.19 mg kg^{-1} for pH, OM, and available P, respectively, were significantly ($p < 0.05$) observed for Muguda SL. The soil sulfate content ranged from 839 to 1344 mg kg^{-1}.

Table 2 shows the mean values of the analyzed physiological properties and biomass of Oil palm seedlings at 3 and 8 MAS. Generally, the highest mean values of each of the examined parameters significant at $p < 0.05$ were observed in LS soils of both study locations.

4 Discussion

Generally, LS soils gave better growth of Oil palm seedlings compared to their counterpart SL soils of both locations. The good growth in the physiological and morphological characteristics of Oil palm seedlings under study was observed in the order Mbiabet LS > Muguda LS > Mbiabet SL > Muguda SL (Table 2). The best growth obtained in Mbiabet LS was supported by a better capacity for soil nutrients, evident in the significantly highest values of soil pH, CEC, OM, and concentrations of basic cations except Mg^{2+} (Table 2). Also, the highest silt content (20%) and least bulk density (1.39 g cm^{-3}) values of Mbiabet LS (Table 1) must have assisted in better root growth and development, permitting easy penetration and accessibility to soil nutrients, and consequently a better plant biomass. The increased wet and dry weights of plant roots (Table 2) positively affected Oil palm growth and development in LS soils in both locations as it functions as the medium for water and nutrients uptake by the plant (Kurniasih & Wulandhany, 2009; Suryanto et al., 2015). Findings from this experiment were also corroborated by Rosenani et al. (Rosenani et al., 2016), who indicated that the physicochemical properties of a growing medium will directly impact the root development and, consequently, the growth of plants. The pH values obtained for all the treatments show the propensity of soils to become acidic upon air drying. However, the much lower pH values of SL soils might be indicative of the presence of high concentrations of aluminum (Al^{3+}) and iron (Fe^{3+}) which might have possibly bonded with phosphorus to form insoluble (Al- and Fe-phosphate) complexes in the soil, thereby making phosphorus unavailable for plant use. This must have probably accounted for the lower values of available P and other chemical nutrients obtained for SL soils in both locations, thereby impairing better development of Oil palm seedlings. Furthermore, poorer growth of Oil palm seedlings grown on Muguda SL, manifested by an overall decrease in physiological and the relative plant

Table 1 Mean ± standard deviation values of physicochemical properties of the two textural ASS from both study locations

Sample location	Tx	Sand	Silt	Clay	Bulk density	pH	OM	TN	Avail P.	SO_4-S	Exch. acidity	CEC	K	Ca	Mg
	%				($g\ cm^{-3}$)		%		mg kg^{-1}			cmol kg^{-}			
Muguda	SL	78.74 ±0.12a	10.74 ±0.03c	10.52 ±0.02a	1.57 ±0.03a	3.28 ±0.01d	3.10 ±0.04c	0.12 ±0.01c	1.19 ±0.03c	1344 ±5.48a	17.29 ±2.19a	18.74 ±1.04b	0.59 ±0.04ab	2.61 ±0.08b	6.38 ±1.06a
	LS	76.52 ±0.15b	15.06 ±0.07b	8.42 ±0.05b	1.45 ±0.08ab	4.33 ±0.04b	4.25 ±0.02b	0.24 ±0.02b	2.71 ±0.02b	839 ±2.87b	13.54 ±1.14b	28.34 ±0.72a	0.64 ±0.03ab	4.38 ±0.09a	4.51 ±0.15ab
Mbiabet	SL	74.79 ±1.18c	13.06 ±0.09b	12.15 ±0.03a	1.54 ±0.04a	3.60 ±0.01bc	3.62 ±0.06bc	0.10 ±0.02c	1.58 ±0.03b	1285 ±4.41a	15.66 ±1.96ab	15.00 ±1.00b	0.49 ±0.09b	2.96 ±0.10b	4.93 ±1.09ab
	LS	73.17 ±0.08c	20.39 ±0.04a	6.44 ±0.07b	1.39 ±0.05b	4.47 ±0.02a	4.67 ±0.02a	0.39 ±0.01a	3.39 ±0.01a	962 ±2.93b	11.48 ±1.82c	30.47 ±1.02a	1.36 ±0.08a	4.75 ±0.08a	3.81 ±0.11b

Tx = textural class; SL = sandy Loam; LS = loamy Sand; OM = organic matter; TN = total nitrogen; CEC = cation exchange capacity; K = potassium; Ca = calcium; Mg = magnesium. Mean values followed by the same letter in each column are not significantly different from one another according to Tukey's test at $p < 0.05$

Table 2 Mean ± standard deviation values of plant height, stem diameter, area of leave, and plant biomass of oil palm seedlings at 3 and 8 MAS

Sample location	Tx	Plant height (cm)	Stem girth (cm)	Leaf area (cm^2)	Wet shoot weight (g)	Dry shoot weight (g)	Wet root weight (g)	Dry root weight (g)
Muguda		AT 3 MAS						
	SL	18.06 ± 1.09bc	1.01 ± 0.08ab	91.35 ± 0.91 cd	63.88 ± 1.21b	16.80 ± 0.67b	8.70 ± 0.05b	3.42 ± 0.07b
	LS	24.65 ± 1.44ab	1.49 ± 0.07b	187.23 ± 1.50b	114.38 ± 1.93a	54.35 ± 0.92a	12.16 ± 0.63a	4.73 ± 0.09ab
Mbiabet	SL	17.65 ± 0.77bc	0.98 ± 0.14ab	99.42 ± 1.78c	75.60 ± 0.95b	19.925 ± 0.79b	8.85 ± 0.08b	4.43 ± 0.14ab
	LS	27.26 ± 1.27a	2.33 ± 0.24a	213.75 ± 2.41a	127.22 ± 1.01a	48.14 ± 0.55a	11.36 ± 0.44a	5.86 ± 0.12a
Muguda		AT 8 MAS						
	SL	57.07 ± 2.05c	4.21 ± 1.01ab	264.92 ± 2.11c	117.00 ± 0.88c	54.79 ± 0.42 cd	20.19 ± 0.85b	9.12 ± 0.03b
	LS	75.73 ± 2.83b	4.97 ± 1.52b	474.27 ± 2.04b	305.01 ± 1.82ab	144.93 ± 1.07a	28.43 ± 0.51a	12.61 ± 0.16a
Mbiabet	SL	48.16 ± 2.01d	3.53 ± 0.19c	257.11 ± 1.99c	148.27 ± 1.22c	69.13 ± 0.08c	20.60 ± 0.66b	11.80 ± 0.17ab
	LS	82.69 ± 2.04a	6.20 ± 0.22a	530.00 ± 2.05a	339.24 ± 1.07a	128.37 ± 0.97ab	27.29 ± 0.48a	15.63 ± 0.11a

Tx = textural class; MAS = months after sowing. Mean values followed by the same letter in each column are not significantly different from one another according to Tukey's test at $p < 0.05$

biomass, can be attributed to a higher concentration of soil acidity, evident in the significantly low pH and other chemical nutrients. This finding is in congruence with those of Shamshuddin et al. (2014); Poon, 1977), who reiterated that soil acidity tends to induce aluminum toxicity, resulting in reduced nutrients availability in soils, impaired root development, and with further consequent implications for the stunted growth of plants.

5 Conclusion

From this study, ASS with Loamy Sand gave better physiological and morphological growths of Oil palm seedlings compared to their Sandy Loam counterparts in both locations under study. Therefore, ASS with a higher percentage of silt and average chemical nutrients can be productively cropped for increased Oil palm cultivation in Nigeria following the proper agronomic practices, including an efficient water management practice. Further studies should therefore focus on improving the soil pH and fertility status, through the addition of Oil palm effluent waste, compost, or biochar for an envisioned better growth and yield of Oil palm seedlings.

References

Anda, M., Shamshuddin, J., Fauziah, C. I., & Syed Omar, S. R. (2009). Dissolution of ground basalt and its effects on an Oxisol chemical properties and Cocoa growth. *Soil Science*, *174*, 264–271.

Atser, G. (2007). Nigeria plans to reclaim its leading position as the world's largest producer of palm oil that it lost to Malaysia over three decades ago. The punch Publishing Co, October 2nd, (pp. 26).

Azura, A. E. (2012). Improving the fertility of an acid sulfate soil in Merbok, Kedah, Malaysia for Rice Cultivation, MS thesis, Universiti Putra Malaysia (unpublished).

Dublin-Green, C. O., Ayinla, A. O., & Ogori, T. K. (2003). Management of fish ponds built on acid sulfate soils in Buguma creek, Niger Delta, Nigeria. *Journal of Applied Sciences and Environmental Management, 7*(2), 39–43.

Ibitoye, O. O., Akinsorotan, A. O., Meludu, N. T., & Ibitoye, B. O. (2011). Factors affecting oil palm production in Ondo state of Nigeria. *Journal of Agriculture and Social Research, 11*(1), 97–105.

Kurniasih, B., & Wulandhany, F. (2009). Curl leaves, canopy and root growth of several varieties of upland rice in different water stress conditions. *Journal of Agricultural Science, 31*, 118–128.

Mckeague, J. A. (1982). Manual on soil sampling and methods of analysis. 3rd Edition. Canada soil survey committee. Subcommittee on methods of Analysis, Canadian Society of Soil Science, Ottawa (pp. 212).

Mgbakor, M. N., Ugwu, J. N., & Oghenemaro, F. (2013). Problems and prospects of oil palm production in isoko south local government area of delta state Nigeria. *American-Eurasian Journal of Agronomy, 6*(2), 40–45.

Mgbeje. (2004). Raw materials research and development council (RMRDC), Abuja. Report on Survey for Selected Agricultural Raw Materials in Nigeria. http://www.rmrdc.gov.ng

Opeke, L. K. (1987). *Tropical Tree Crops.* Published by Woye and Sons (Nig) Limited. Ilorin (pp. 252–266).

Poon, Y. C. (1977). The management of acid sulfate soils and its effects on the growth of oil palm (*Elaeis guineensis*). *Malaysian Agricultural Journal, 51*(2), 124–141.

Rosenani, A. B., Rovica, R., Cheah, P. M., & Lim, C. T. (2016). Growth performance and nutrient uptake of oil palm seedling in Prenursery stage as influenced by oil palm waste compost in growing media. *International Journal of Agronomy, Article ID, 6930735*, 1–8.

Shamshuddin, J., Azura, A. E., Shazana, M. A. R. S., Fauziah, C. I., Panhwar, Q. A., & Naher, U. A. (2014). Properties and management of acid sulfate soils in Southeast Asia for sustainable cultivation of rice, oil palm, and cocoa. Chapter 3. Advances in Agronomy, (Vol. 124). Elsevier Inc. ISSN 0065–2113. https://doi.org/10.1016/B978-0-12-800138-7.00003-6

Suryanto, T., Wachjar, A., & Supijatno. (2015). The growth of oil palm (*Elaeis guineensis* Jacq.) seedlings at various media and containers in double stage nursery. *Asian Journal of Applied Sciences*, *3*(5), 664–671.

Ubi, W., & Osodeke, V. E. (2009). Phosphate relationships in acid-sulphate soils of Mbiabet swamp rice farm, Akwa Ibom state Nigeria. *Global Journal of Agricultural Sciences, 8*(1), 61–65.

Forecasting Lower Tigris Basin Landscapes' Vegetation Response to Regional and Global Climate Variability

Ali Subhi Alhumaima and Sanjar Mutalovich Abdullaev

Abstract

Forecasting the response of wild and agricultural vegetation to climate variability, as well as assessing the quality of climate data, is an important part of ecological studies. Based on a random forest (RF) algorithm, we proposed a model to forecast the response of the Normalized Difference Vegetation Index (NDVI) of the Lower Tigris Basin (LTB) landscapes during the maximum biological productivity to regional and global climate variability. High-resolution NDVI dataset, monthly regional temperatures and precipitation data derived from five reanalysis datasets, and various global atmospheric indices over the period 2000 to 2020 were used to train and validate the model. Using the hypothesis developed in our previous works, we constructed a synthetic dataset. In which, temperatures and precipitation time series most correlated with the NDVI landscapes were chosen from the five datasets. The RF forecasting's results showed that the synthetic dataset-based climate factors hold the highest efficiency among the compared datasets. The model was able to explain 85.6% of spatiotemporal NDVI variability. This forecasting percentage has increased by about 2.6% when using the global circulation indices as additional predictors. This indicated that our proposed approach can successfully simulate the relationship between NDVI and climate. We also showed that the study area landscapes vegetation conditions can be forecasted (coefficient of determination, $R^2 = 0.981$) with 3–4 months lead time by training the algorithm based only on the data of global indices. The research presented here has valuable implications for regional environmental management in the context of climate change.

Keywords

NDVI • Climate variability • Landscapes • Ensemble climate • RF

1 Introduction

In this paper, we continued the works (Alhumaima & Abdullaev, 2019, 2020a) to study the impact of climate variability on the vegetation of the LTB landscapes. The following short introduction explains the interest in these studies. Climate variability is defined by the World Meteorological Organization as deviations from the mean state of the climate on temporal scales longer than the individual weather events. In practice, this means that we are looking at monthly and seasonal anomalies characterized by the climate system components against their 30-year average. In this work, we attempted to consider not only the variability of regional meteorological variables (e.g., precipitation, temperature), but also the topography, biosphere components, and global climate drivers (such as El-Nino-Southern Oscillation (ENSO)). The premise of this approach is that significant improvement in the performance of the neural network for modeling the vegetation conditions was obtained after incorporating the characteristics of the bioclimatic landscapes into the predictors, along with seasonal precipitation and temperatures (Alhumaima & Abdullaev, 2019). It was then shown in Alhumaima & Abdullaev, 2020a that: (i) regional meteorological data from different datasets, despite their inter-correlation, can lead to different types of Köppen–Trewartha bioclimatic landscapes; (ii) each landscape type has its own synthetic dataset that is more suitable to describe the NDVI variations; (iii) the overall interpretable scenario of the climate variability impact on the NDVI of the region is obtained when presenting the seasonal weather through an ensemble of normalized meteorological characteristics; iv) there is a different reaction of NDVI

A. S. Alhumaima (✉)
University of Diyala, Baqubah, Iraq
e-mail: alhumaimaali@uodiyala.edu.iq

S. M. Abdullaev
South Ural State University, Chelyabinsk, Russian Federation

A. Kallel et al. (eds.), *Selected Studies in Environmental Geosciences and Hydrogeosciences*,
Advances in Science, Technology & Innovation, https://doi.org/10.1007/978-3-031-43803-5_9

landscapes to the global state of the climate from unresponsive to strong correlation. In this study, we discussed these findings, in light of the possibility: (1) to interpret landscapes vegetation state by describing climate as an ensemble of weathers, and then (2) to a long-term forecast of NDVI landscapes using machine learning (ML) methods.

2 Data and Methodology

This study focused on the LTB ($\sim$251,400 km^2) which is distributed mainly among Iraq, Iran, and Turkey. It includes five main tributaries, these are Fesh Khabour, Greater Zab, Lesser Zab, Al-Adhaim, and Diyala. However, more description related to the regional environmental conditions, vegetation, and data used (March NDVI images; ASTER Global DEM; FAO GLC-SHARE; monthly precipitation and temperatures of five reanalysis datasets (ERA5, MERRA2, NCEP, JRA-55, and CFSR); and global circulation indices (Atlantic Multidecadal Oscillation (AMO), North Atlantic Oscillation (NAO), Dipole Mode Index (DMI), and ENSO)), can be found in Alhumaima & Abdullaev, 2020a; Alhumaima & Abdullaev, 2020b).

In (Alhumaima & Abdullaev, 2020a), we showed that the maximal biological productivity of the Tigris landscapes occurs during March–April, but its value depends on a combination of October–March precipitation and January-March temperatures. Because these combinations are dependent on the selected climate dataset, we offered an ensemble approach to describe climate variability. In which, cold and dry (CD), cold and wet (CW), warm and dry (WD), and warm and wet (WW) seasons were obtained by comparing a tuple of normalized precipitation and temperature from different datasets. The preliminary result of this approach, named in Alhumaima & Abdullaev, 2020b as ensemble climate in weather (ECW), showed that significant NDVI increase (decrease) were associated with WW (CD) events. Here we used the ECW potential to demonstrate that: (1) complex weather is the primary cause of NDVI variability; (2) to justify the express selection of the forecasting algorithm. Obviously, the choice of the optimal forecast method is a long-term procedure, including the choice of a machine learning algorithm and a set of input predictors. Since ECW analysis indicates that the decision tree (DT) algorithm could give a good result to the initial separation of the NDVI level, we decided to choose the RF algorithm, proposed in Breiman (2001). This choice is conditioned not only by the fact that the RF outperforms the single DT forecast, but also due to the RF stability to overfit and its capability to resolve nonlinear problems. This heuristic choice of the algorithm permitted us to focus on selecting predictors, including those indicated implicitly by the ECW analysis.

In (Alhumaima & Abdullaev, 2020a), we showed that there is no single optimal climate dataset for the entire basin, and it is typical for the region that the NDVI of certain types of plant landscapes responds well to variations in the time series generated by a certain dataset. In this work, landscapes have been classified based on altitude levels and land cover categories. In which, the landscapes of plains (P), foothills (F), and mountains (M) correspond to areas below 300 m, 300–900 m, and above 900 m, respectively. The types of vegetation were denoted as natural vegetation (NV) - grasslands, trees, shrubs, and herbaceous vegetation; agricultural rainfed (AR) and agricultural irrigated (AI) vegetation; and low vegetation (LV)—sparse vegetation and barren soil.

Therefore, it was expected that the RF can generate a specific synthetic dataset for a certain landscape and would lead to better forecasting results.

3 Results and Discussion

Anthropogenic causes of changes in mean values of the climate system components are almost unquestionable. The rise in global temperatures can almost be interpreted by greenhouse gas emissions. However, the causes of changes in hydrological regime and vegetation cover are less obvious. For example, in the case of the LTB, it was not known how to interpret the observed NDVI variability. Hence, using the ECW concept, we showed that this is due more to a combination of climatic anomalies, i.e., short-period climate variability. To do this, following the methods of Alhumaima & Abdullaev, 2020a; Alhumaima & Abdullaev, 2020b), we have calculated the four possible ECW categories for 21 winters (2000–2020) and sorted them according to the level of the basin average NDVI (Fig. 1). This simple procedure has linked the ECW to levels of relatively low, medium, and high biological productivity. It is clear that most cases of low (high) productivity correspond to CD (WW) winters. But there are also cases like winters of 2006 or 2001 when the weather was very different from the rest. Since the evaluation of anomalies raises questions about the choice of average values, for comparison, Fig. 1 shows the ECW categories determined according to the method proposed in L'Heureux et al. (2013). In this method, climate anomalies are calculated relative to their own climatic norm. We can see that some of the weather categories have changed in the direction of increasing the combination of dry and warm seasons. It is easy to notice that with this approach, the relationship with productivity becomes more complex. We also analyzed the relationship between de-trended NDVI anomalies and ECW seasons. As a result, we found that the explanation of the links has become even more difficult. Therefore, albeit tentatively, we concluded that our approach

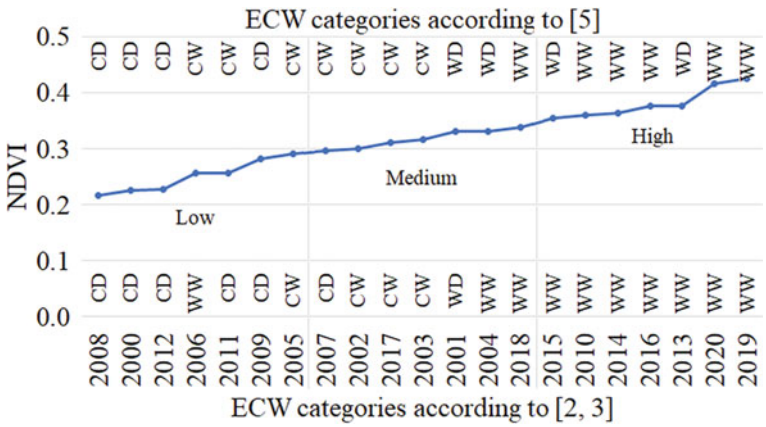

Fig. 1 Winter weather in the LTB and Its impact on NDVI

is more rational and suggests that fluctuations in the biological productivity are directly related to the variability of the climate combinations.

We associated the ECW categories and basin-averaged NDVI mainly with fluctuations in the global climate. In particular, we in Alhumaima & Abdullaev, 2020a; Alhumaima & Abdullaev, 2020b) have linked the most ferocious droughts to the cold phase of El Nino-Southern oscillation and found that regional and global effects are unevenly reflected in different groups of landscapes. Therefore, in the second part of the work, we investigated the NDVI predictability of individual landscapes with the inclusion of regional and global meteorological data. We assumed that the state of the global climate could complement regional data because it could indirectly reflect important climate "ingredients" such as wind, cloudiness, and humidity. For the purity of the experiments, we had to abandon the bioclimatic classification of landscapes that is based on using meteorological data. This explains the rigid method of landscape differentiation described in Sect. 2.

Using the data from 2000 to 2016 for calibration, and those from 2017 to 2020 for validation, in the first experiment, the RF predictors were information about the georeferencing of pixels (coordinates, range of heights, landscape type, and land cover categories) and temperatures and precipitation data derived from the five datasets in addition to the synthetic one (Alhumaima & Abdullaev, 2020a). As expected, the synthetic data showed the best results with overall predictability (R^2) of 0.856 compared to those of the ERA5 (0.796), MERRA2 (0.759), NCEP (0.808), JRA-55 (0.794), and CFSR (0.769). In addition, estimates were made also for all regional landscapes (Table 1). The best forecast quality estimates were observed for the least disturbed mountainous and foothill landscapes.

In the second experiment, the algorithm was trained on a sample that included a synthetic dataset to which the series of global climate indices (ENSO, AMO, NAO, and DMI) for late autumn (Alhumaima & Abdullaev, 2020a) were added. As we can see, the test results (Table 1) have been improved with an overall predictability of 0.879. Based on the RF model performance, it is clear that there is a close relationship between NDVI and climate in the LTB, and if regional climate factors can be realistically predicted, it would be possible to use such a model for monitoring the vegetation. However, in the third experiment when the algorithm was used to forecast landscapes' average vegetation, significant results (Table 1) have been achieved with an average $R^2 = 0.981$ and RMSE = 0.089. Despite this higher predictability, the resulting RMSEs were higher in agricultural landscapes than those of the natural vegetation.

Table 1 Performance of the experimental NDVI landscapes forecast during validation stages

Experiment	Measure	PNV	PAR	PAI	FNV	FAR	MNV	MAR
1	RMSR	0.131	0.188	0.143	0.086	0.162	0.073	0.070
	R^2	0.805	0.819	0.747	0.866	0.681	0.917	0.903
2	RMSR	0.114	0.184	0.124	0.085	0.149	0.076	0.074
	R^2	0.855	0.818	0.769	0.870	0.769	0.920	0.898
3	RMSR	0.082	0.161	0.124	0.073	0.092	0.042	0.049
	R^2	0.977	0.971	0.953	0.996	0.978	0.991	0.995

4 Conclusion

Utilizing the landscape approaches is essential to achieve climate change mitigation (Kaeslin et al., 2012). In this paper, using the concept of "ensemble climate in weather" we demonstrated that the random forest (RF) algorithm is adequate to predict the NDVI of Tigris basin landscapes. These landscapes were separated according to landforms and land cover patterns. This allowed us to focus on the experimental selection of climatic predictors, and in particular, use the idea of a synthetic climate dataset. In the first experiment, the synthetic data showed the highest efficiency in the validation period among all compared climate datasets. When global circulation indices (GCI) were used as additional predictors in the second experiment, the forecasting performance was improved only by 3%. However, in the third conclusive experiment, the RF was only trained on the GCI dataset, this has demonstrated that the maximal NDVI of landscapes can be forecasted ($R^2 = 0.98$) with 3 months leading time. Further research efforts should be made to optimize the present forecasting method.

References

Alhumaima, A. S., & Abdullaev, S. M. (2020a). Tigris basin landscapes: Sensitivity of vegetation index NDVI to climate variability derived from observational and reanalysis data. *Earth Interactions., 24*(7), 1–18.

Alhumaima, A. S., & Abdullaev, S. M. (2019). Landscape approach to normalized difference vegetation index forecast by artificial neural network: Example of Diyala River Basin. Bulletin of the South Ural State University. Series "Computer Technologies, Automatic Control & Radioelectronics", (Vol. 19(3), pp. 5–19).

Alhumaima, A. S., & Abdullaev, S. M. (2020). Influence of climate variability on the vegetation of the lower Tigris Basin landscapes: climate in weather and satellite vegetation indices. In Proceedings of 63rd All-Russian Scientific Conference, MFTI, Moscow (pp. 9–11).

Breiman, L. (2001). Random forests. *Machine Learning., 45*, 5–32.

Kaeslin, E., Redmond, I., & Dudley, N. (2012). Wildlife in a changing climate. Food and Agriculture Organization (FAO), Rome, Italy.

L'Heureux, M. L., Collins, D. C., & Hu, Z. Z. (2013). Linear trends in sea surface temperature of the tropical Pacific Ocean and implications for the El Niño-Southern Oscillation. *Climate Dynamics., 40*(5), 1223–1236.

Calibration and Evaluation of AquaCrop Model Under Different Irrigation Methods for Maize (Zea mays L.) in Central Region of Iraq

Diaa Hassan, Thamer Thamer, Rafal Mohammed, Ayad Almaeini, and Nadine Nassif

Abstract

AquaCrop simulation model is one of the most important models in the evaluation of irrigation management and the improvement of water use efficiency. This study aimed to test and simulate Aquacrop for maize with the Cropwat to calculate the evaporation under different irrigation methods. Experiments consisted in the use of furrow irrigation and drip irrigation surface (DI) and, sub-surface (SDI) for the depths (10, 20, and 30 cm). Three NPK treatments were used as subplots: 50N, 15P, 30 K kg ha^{-1}, 100N, 30P, 60 K kg ha^{-1}, 200N, 60P, 120 K kg ha^{-1}. Field observations were carried out in 2016 and 2017 seasons to evaluate AquaCrop performance in simulating dry yield, harvest index, biomass, canopy cover, and water productivity. Statistics for root mean square error (RMSE), coefficient of determination (R^2), index of agreement (d), coefficient of efficiency (E), mean bias error (MBE) suggest that the model prediction is good. The values of the (RMSE) statistics were (20.6%, 2.5%, 2.1%, 15.9%, and 18.4%) for biomass and (0.8%, 2.2%, 3.4%, 22.9%, and 1.6%) for dry yield and the harvest index (12.5%, 9.9%, 3.1%, 6.2%, and 9.2%) and for water productivity. The 2016 season results were higher than those of the 2017 season. The values were (29.4%, 5.6%, 34.5, 20%, and 68%). The canopy cover results ranged between (23. to 96.7) and (23.2 to 97.7) for 2016 and 2017, respectively. The crop coefficient Kc was calculated, and the results ranged between (0.25 to 1.42) for the 2016 season and (0.27 to 1.67) for the 2017 season, for the irrigation treatments and according to the plants growth stages. In central Iraq, AquaCrop can be used reliably to test the efficacy of the proposed irrigation management strategies for maize.

Keywords

AquaCrop model • Maize • Simulation • Water productivity • Canopy cover

1 Introduction

Maize (*Zea mays* L.) is the major irrigated summer cereal crop in Iraq. It is a very high consumer of the applied amounts of irrigation water. The seasonal water use is about 750–900 mm (Salih & Falih 2012; Ewaid, 2019), and therefore, accurate irrigation methods management and practices seem to be very important with this crop under irrigation water scarcity conditions.

Several models have been proposed to manage the irrigation process of field crops including maize in order to increase the water use efficiency and water productivity. These models differ in their simplicity and the validity of their use under different conditions of climate and management (Abd-El-Mooty, 2016; Bennis, 2015).

The increase the water use efficiency is a major goal of the irrigation process in arid and semiarid regions. Water use efficiency depends on many factors, including the genetics and management factors used with the crop, the irrigation

D. Hassan · A. Almaeini (✉)
College of Engineering, Al-Qasim Green University, Babylon, Iraq
e-mail: diaafliah@wrec.uoqasim.edu.iq

T. Thamer
Ecole Doctorale en Sciences et Technologie, Lebanese University, Beirut, Lebanon

Ministry of Water Resources, Baghdad, Iraq

R. Mohammed
College of Agriculture, Al-Qasim Green University, Babylon, Iraq
e-mail: rafalalshukiri@agre.uoqasim.edu.iq

A. Almaeini
College of Agricultural Engineering Sciences, Baghdad University, Baghdad, Iraq

N. Nassif
Faculty of Agronomy and Veterinary Sciences, Environment and Natural Resources Department, Lebanese University, Dekwaneh, Beirut, Lebanon

A. Kallel et al. (eds.), *Selected Studies in Environmental Geosciences and Hydrogeosciences*, Advances in Science, Technology & Innovation, https://doi.org/10.1007/978-3-031-43803-5_10

method, the provision of nutrients in quantity and quality, and the appropriate time to enhance the growth of roots (Lamm & Rogers, 2015). This is reflected in water and nutrient uptake from the soil to increase the vegetative growth and give a high economic yield.

The water requirement of a crop is the quantity of water, irrespective of its source, needed by a crop or a diversified crop pattern for its normal growth over a given period of time under field conditions, including evapotranspiration and other economically inevitable losses (Hammad et al., 2018; Tayel et al., 2019).

The aim of this study was to evaluate the performance of the AquaCrop model for maize at different irrigation methods and NPK levels under central Iraq weather conditions.

2 Materials and Methods

Field experiments were conducted in 2016–2017 growing season at the Yousifya region, 15 km southwest of Baghdad —Iraq (44° 18′ 75" E and 33° 07′ 84``N: 34.1 m above sea level). The soil texture of the field is silt clay. Climatic data were obtained from the meteorological station, which is 2 km away from the study area as shown in (Fig. 1). The Cropwat model relied upon the Penman–Monteith equation to calculate the evapotranspiration.

Treatments and Experimental Design:

The experiment was conducted according to a completely randomized complete block design (RCBD) in split block arrangement with three replications. The subplot area was 4 × 5 m. The irrigation treatments applied to the main blocks were: furrow irrigation (I_0), surface drip irrigation ($\mathbf{I}_1$), subsurface (emitter at 10 cm depth) ($\mathbf{I}_2$), subsurface (emitter at 20 cm depth) ($\mathbf{I}_3$), subsurface (emitter at 30 cm depth) ($\mathbf{I}_4$).

Three NPK treatments were also applied as subplots: 50N, 15P, 30 K kg ha^{-1} ($\mathbf{S_1}$), 100N, 30P, 60 K kg ha^{-1} ($\mathbf{S}_2$), 200N, 60P, 120 K kg ha^{-1} ($\mathbf{S}_3$).

Agronomic Practices and Irrigation Scheduling:

Maize seeds (Kalimeras hybrid F1) were planted on 7 August in the 2016 and 2017 seasons. The experimental plots were fertilized by adding on two equal meals the first at V_6 stage and the second at V_{12} stage. The growth stages were determined according to Muhammd Yasir et al. (2010). The drip irrigation system was manufactured by John Deere Company USA. Surface and subsurface drip irrigation treatments and measurements of soil moisture were applied using sensors system linked to data logger. The irrigation was scheduled when the depletion of 50% available water in the root zone had been exhausted, with a depth of 30 cm. For furrow irrigation according to equation**:** (Vermeriren & Jobling, 1980):

$$d = (\theta_{fc} - \theta_w)D \tag{1}$$

where θ_{fc} = Volumetric water content at field capacity (cm^3 cm^{-3}), d = depth of water applied (mm), θ_w = Volumetric water content before irrigation (cm^3 cm^{-3})

Crop coefficient was determined according to the following equation:

$$\boldsymbol{ET_a} = (\boldsymbol{k_c})(\boldsymbol{ET_o}) \tag{2}$$

where k_c = crop coefficient, ET_o = reference evapotranspiration (mm)

Harvest index (HI): It was calculated using the following Eq. (3):

$$\mathbf{HI}(\%) = \frac{\mathbf{GY}}{\mathbf{BY}} \times 100 \tag{3}$$

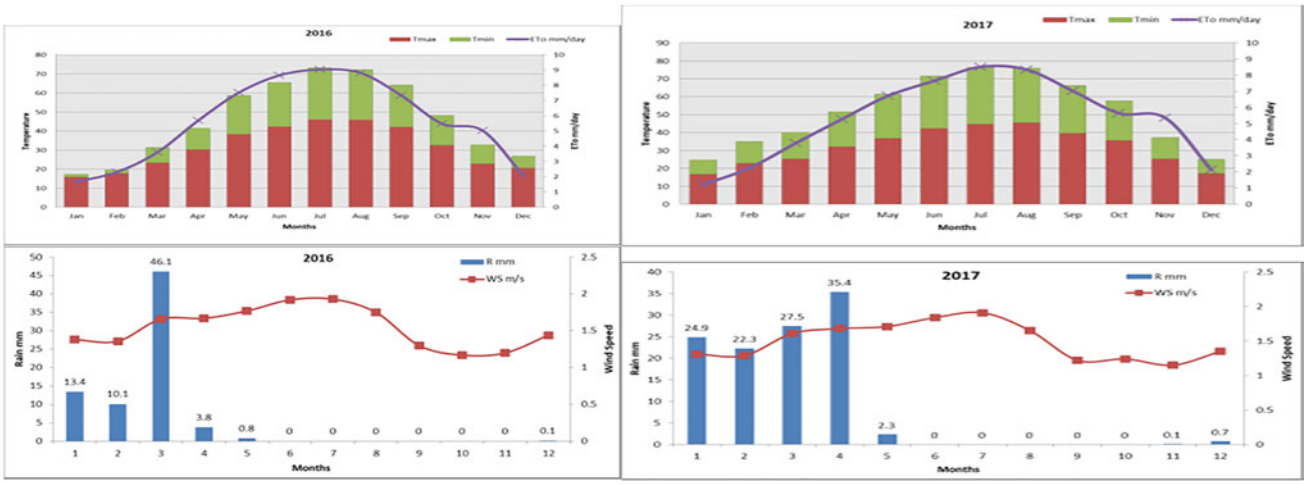

Fig. 1 Temperature, total evapotranspiration rain, and wind speed of Maize in 2016 and 2017

where BY: Biological yield includes all parts of the plant above the soil surface (t ha^{-1}).

LAI was converted to green canopy cover (CC) using Equation (Bennis et al., 2015):

$$\mathbf{CC} = \mathbf{1.005}\,[\mathbf{1} - \mathbf{exp}(-\mathbf{0.6}\,\mathbf{LAI})]^{\mathbf{1.2}} \quad (4)$$

Statistical comparison

Five statistical measures were applied to test the performance of the model and compare the simulated and measured results:

One is the root mean square error (RMSE):

$$RMSE = \sqrt{\frac{1}{n}\sum_{i=1}^{n}(Si - Mi)^2} \quad (5)$$

where *Si* and *Mi* are simulated and measured values, respectively, and *n* is the number of observations.

Two is the coefficient of determination (R^2):

$$R^2 = \frac{\sum Si\,Mi - \sum Si + \sum Mi}{\sqrt{\sum Si^2 - (\sum Si)^2 x}\sqrt{\sum Mi^2 - (\sum Mi)^2}} \quad (6)$$

Three is the mean bias error (MBE):

$$\mathrm{MBE} = \frac{1}{n}\sum_{i=1}^{n}(Si\,Mi) \quad (7)$$

Four is the index of agreement (d) of Willmott (1982):

$$d = 1 - \frac{\sum_{i=1}^{n}(Si - Mi)^2}{\sum_{i=1}^{n}\left(Si - \overline{M}\right| + Mi - \overline{M}|)^2} \quad (8)$$

where $\overline{M}$ is the mean of the n measured values. The value of d ranges from $-\infty$ to 1.0.

Five is the coefficient of efficiency (E)

$$E = 1 - \frac{\sum_{i=1}^{n}(Si - Mi)^2}{\sum_{i=1}^{n}\left(Mi - \overline{M}\right)^2} \quad (9)$$

3 Results and Discussion

AquaCrop model performance was assessed using statistical indices, root mean square error (RMSE), correlation coefficient (R^2), mean bias error (MBE), coefficient of efficiency (E), and the index of agreement (d). The model results for biomass, grain yield, harvest index, and water productivity for the experiment during two seasons 2016 and 2017 are presented in Table 1. From the AquaCrop results, it an be deduced that there is a strong agreement between the measured and simulated yield of grain with a relation coefficient R^2 (0.95 and 0.97) root mean square error (RMSE) (0.87 and 87), and a good agreement between measured and simulated value biomass for the mean bias error MBE (−0.38 and −0.47), coefficient of efficiency E (0.66 and 0.79), and the index of agreement d (0.92 and 0.94) for 2016 and 2017 seasons, respectively. The I_3S_3 treatment recorded the highest simulated and measured values for biomass 10 and 8.8, 10.6 and 9.3 (t ha^{-1}) grain yield 18.84 and 18.53, 21.09 and 19.95 (t ha^{-1}), harvest index 53 and 47.49, 50 and 46.62, and water productivity 1.8 and 2.8, 2.5 and 3.17 (kg m^{-3}) for 2016 and 2017 seasons, respectively.

AquaCrop model predictions for harvest index, grain yield, biomass, and water productivity R2 and d values approaching one corroborated with the observed results.

Figure 2a, b shows the different values of the crop coefficients Kc for the different growth stages of the maize and irrigation methods, which adopted the values of reference evapotranspiration (ET_0) and values of actual evapotranspiration (ETa). The highest value was at the flowering

Table 1 Statistical indices for biomass, grain yield, harvest index, and water productivity

Observation	R^2	RMSE	MBE	E	D
2016					
Biomass (t ha^{-1})	0.94	0.42	−0.38	0.66	0.92
Grain yield (t ha^{-1})	0.95	0.87	−0.85	0.03	0.78
Harvest index	0.79	4.00	−3.68	−0.50	0.69
Water productivity (kg m^3)	0.87	0.60	−0.40	−9.38	0.54
2017					
Biomass (t ha^{-1})	0.96	0.53	−0.47	0.66	0.92
Grain yield (t ha^{-1})	0.97	0.87	−0.83	0.03	0.78
Harvest index	0.88	3.50	−3.34	−0.50	0.69
Water productivity (kg m^3)	0.82	0.42	−0.13	−9.38	0.54

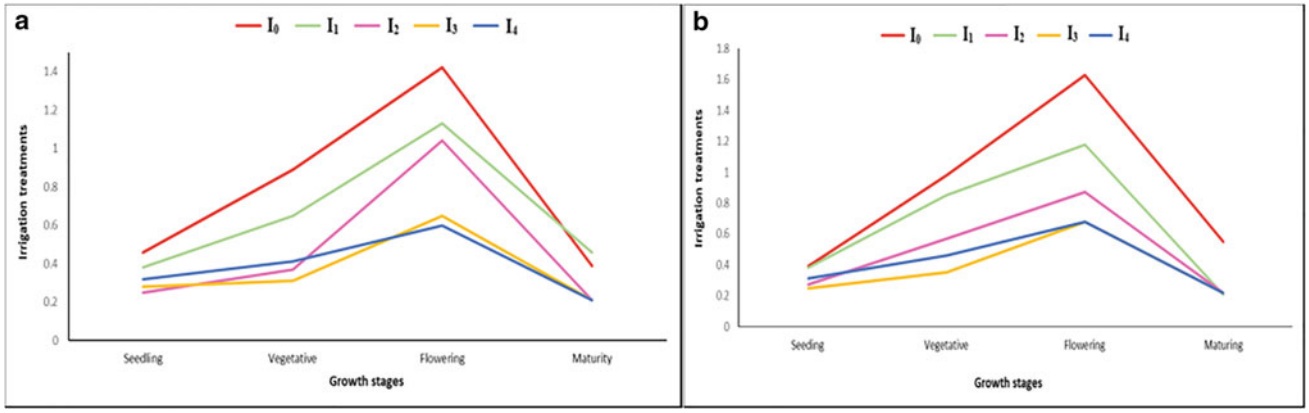

Fig. 2 **a** Crop coefficients Kc for irrigation methods season 2016 **b** Crop coefficients Kc for irrigation methods season 2017

stage due to the high water consumption of the plant at this stage (Salih & Falih 2012; Lamm, 2012), while the I_0 treatment recorded the highest value in all the stages due to the addition of more quantities of water than the other treatments for the 2016 and 2017 seasons.

Figures 3, 4, 5, 6, and 7 show the values of canopy cover for all irrigation treatments over the days of the stages of plant growth. The lowest value was at the beginning of plant growth while its highest was in the period between 70 and 90 days after germination (Greaves and Wang 2016; Hsiao,

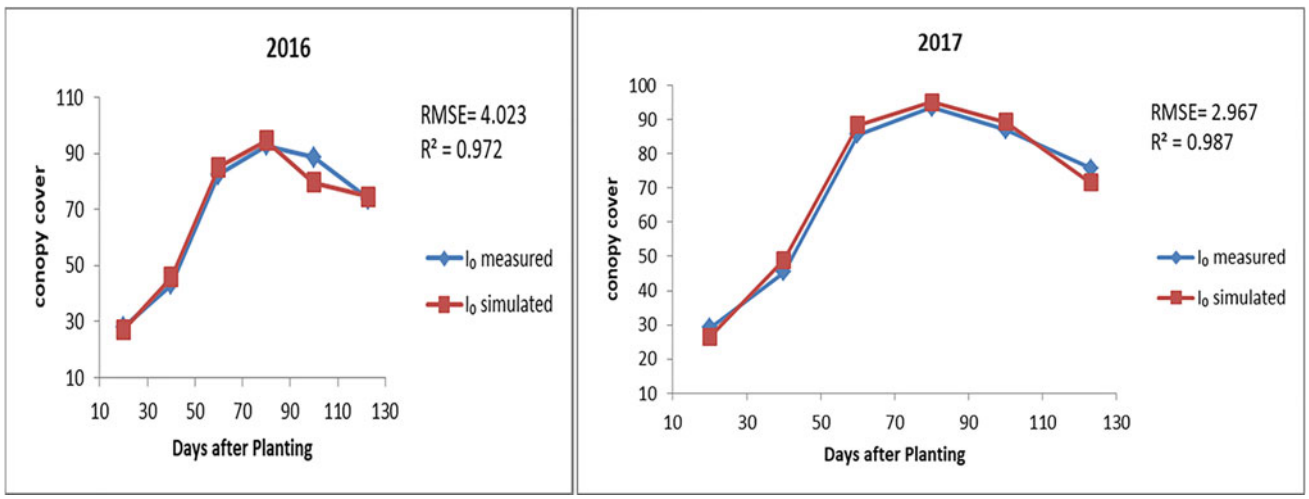

Fig. 3 Simulated and measured I_0 canopy cover for 2016 and 2017 seasons (Hassan et al., 2023)

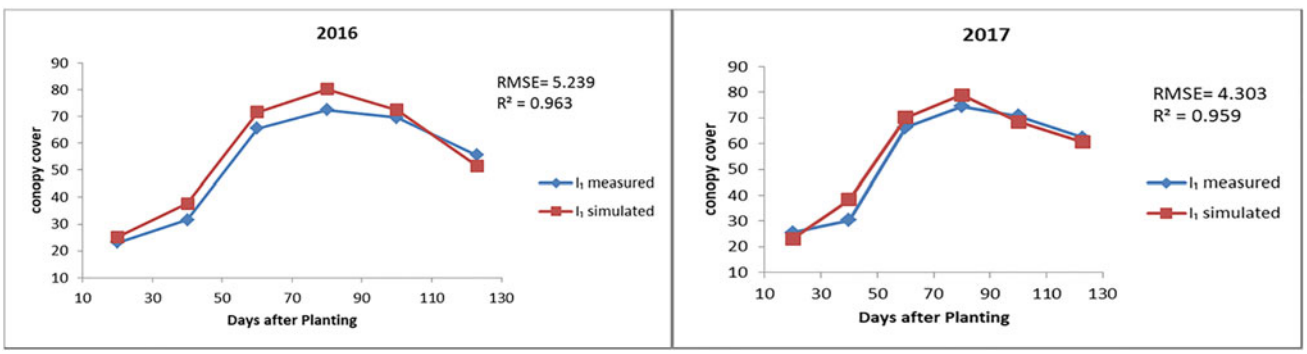

Fig. 4 Simulated and measured I_1 canopy cover for 2016 and 2017 seasons (Hassan et al., 2023)

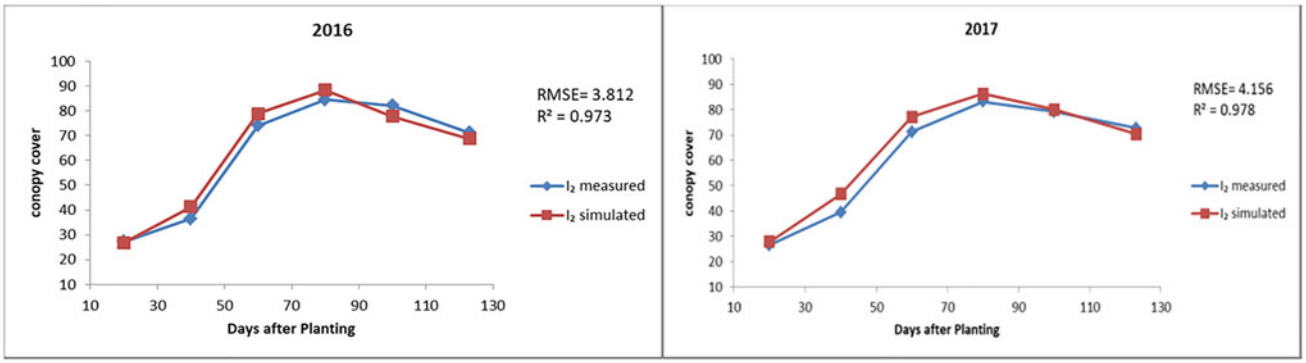

Fig. 5 Simulated and measured I_2 canopy cover for 2016 and 2017 seasons (Hassan et al., 2023)

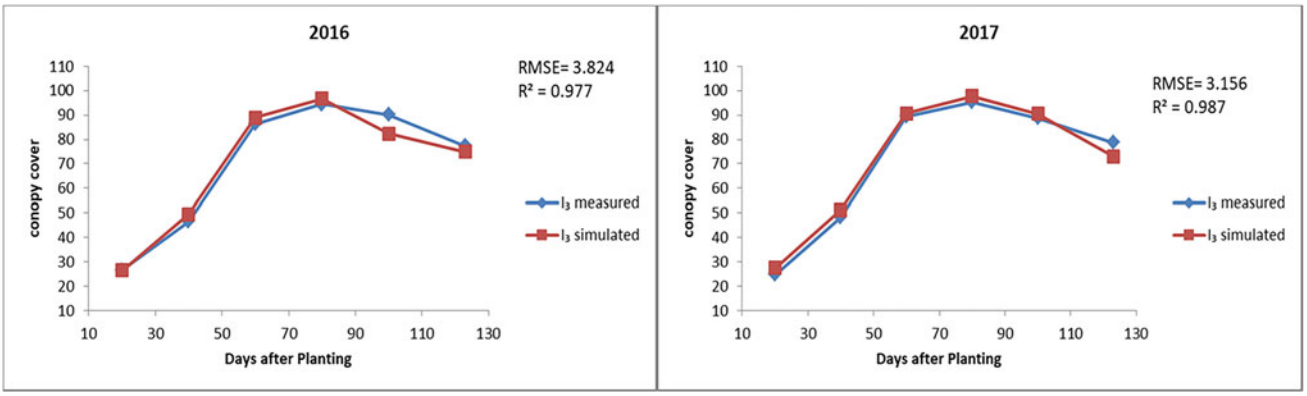

Fig. 6 Simulated and measured I_3 canopy cover for 2016 and 2017 seasons (Hassan et al., 2023)

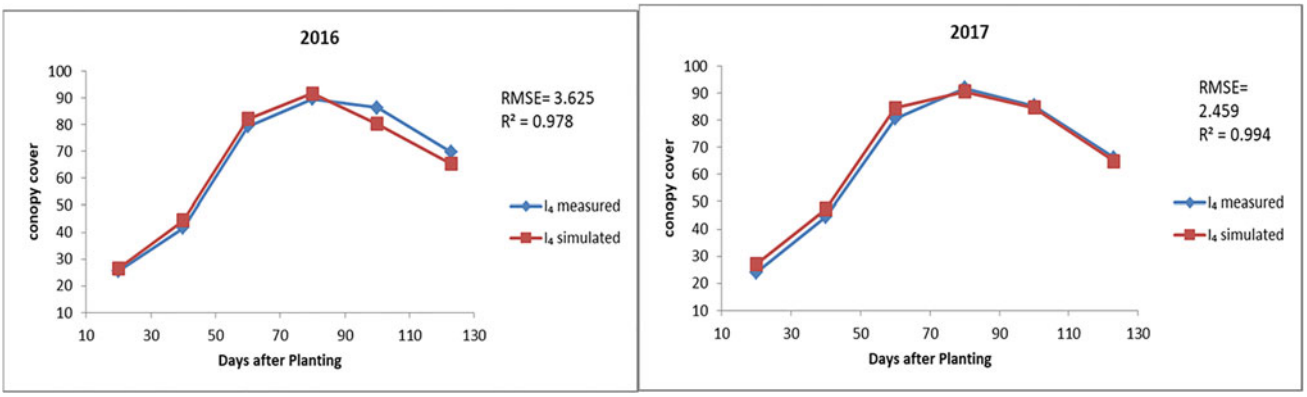

Fig. 7 Simulated and measured I_4 canopy cover for 2016 and 2017 seasons (Hassan et al., 2023)

2009). A high agreement between the measured and simulated values for the 2016 and 2016 seasons was noticed (Figs. 3, 4, 5, 6 and 7).

4 Conclusion

– AquaCrop model was able to simulate the biomass, dry yield, harvest index, and water productivity, where the values of the compatibility guide indicated a perfect compatibility between the measured and predicted values of all the above statistical criteria.

References

Abd-El-Mooty, M., Kansoh, R., & Abdulhadi, A. (2016). Challenges of water resources in Iraq. *Hydrology Current Research, 7*(4), 1–8.

Allen, R. G., Pereira, L. S., Raes, D., & Smith, M. (1998). Crop evapotranspiration. FAO Irrigation and Drainage. Paper 65, Rome.

Bennis, I., Fouchal, H., Zytoune, O., & Aboutajdine, D. (2015, September). Drip irrigation system using wireless sensor networks. In 2015 Federated Conference on Computer Science and Information Systems (FedCSIS) (pp. 1297–1302). IEEE.

Ewaid, S. H., Abed, S. A., & Al-Ansari, N. (2019). Crop water requirements and irrigation schedules for some major crops in Southern Iraq. *Water, 11*(4), 756.

Faleh, A. S. (2011). Estimation of water needs of maize crop based on incomplete irrigation and comparison with climate equations and evaporation measures. PhD thesis, Faculty of Agriculture, University of Baghdad, Iraq.

Greaves, G. E., & Wang, Y. M. (2016). Assessment of FAO AquaCrop model for simulating maize growth and productivity under deficit irrigation in a tropical environment. *Water, 8*(12), 557.

Hajim, A. Y., & Yassin, H. I. (1992). Engineering of field irrigation systems. Library of Books for Printing and Publishing. University of Al Mosul. Mosul. Iraq.

Hammad, H. M., Abbas, F., Saeed, S., Fahad, S., Cerdà, A., Farhad, W., & Bakhat, H. F. (2018). Offsetting land degradation through nitrogen and water management during maize cultivation under arid conditions. *Land Degradation & Development, 29*(5), 1366–1375.

Hassan, D. F., Ati, A. S., & Naima, A. S. (2023). Evaluation of the performance of the aquacrop model under diffrent irrigation and cultivation methods and thair effect on water consumption. *Iraqi Journal of Agricultural Sciences, 54*(2), 478–490.

Heng, L. K., Hsiao, T., Evett, S., Howell, T., & Steduto, P. (2009). Validating the FAO AquaCrop model for irrigated and water deficient field maize. *Agronomy Journal, 101*, 488–498.

Howell, T. A. (2003). Irrigation efficiency. Encyclopedia of Water Science, published by Marcel Dekker, New York. USA. V. 10. (pp. 467–472).

Hsiao, T. C., Heng, L., Steduto, P., Rojas-Lara, B., Raes, D., & Fereres, E. (2009). AquaCrop—the FAO crop model to simulate yield response to water: III. Parameterization and testing for maize. *Agronomy Journal, 101*(3), 448–459.

Lamm, F. R., & Rogers, D. H. (2015). The importance of irrigation scheduling for marginal capacity systems growing corn. *Applied Engineering in Agriculture, 31*(2), 261–265.

Lamm, F. R., Bordovsky, J. P., Schwankl, L. J., Grabow, G. L., Enciso-Medina, J., Peters, R. T., Colaizzi, P. D., Trooien, T. P., & Porter, D. O. (2012). Subsurface drip irrigation: Status of the technology in 2010. *Transactions of the ASABE, 55*, 483–491.

Muhammd Yasir, A., Khalil, S.A. Jan, M. T., & Khan, A. Z. (2010). Phonological, growth and grain yield of maize as influenced by folian applied urea at different growth stages of plant. *Nutrition, 33*, 71–79.

Salih, A. T., & Falih, A. S. (2012). Management of corn irrigation to increase water use efficiency in middle of Iraq. *Diyala Agricultural Sciences Journal, 4*(1).

Tayel, M. Y., Shaaban, S. M., & Mansour, H. A. (2019). Impact of seedbed preparation condition on aggregates stability, yield, water productivity and fertilizers use efficiency on maize (zea mays). *Plant Archives, 19*(Supplement 1), 706–710.

Vermeriren, I., & Jobling, G. A. (1980). Localized irrigation design, installation operation, evaluation. irrigation and drain. paper 36 FAO Rome.

Willmott, C. J. (1982). Some comments on the evaluation of model performance. *Bulletin of the American Meteorological Society, 63*, 1309–1313.

Pistachio Tree As a Source of Bioactive Molecules With Biological Properties

Manel Elakremi, Leyre Sillero, Lazher Ayed, Jalel Labidi, and Younes Moussaoui

Abstract

Recently, research on plants has increased in order to substitute synthetic products coming from non-renewable sources with products from biomass, particularly agricultural waste. The production of pistachio in Tunisia generates a large amount of potentially valuable waste such as leaves. The purpose of this work was to determine the total phenolics, flavonoids, and condensed tannins contents and evaluate the biological activity of the pistachio tree leaves. The chromatographic analysis was used in order to identify bioactive compounds of the extracts. There was significant difference in the amounts of phenolic compounds of male and female leaves and similar results in the amounts of flavonoids and condensed tannins. The extracts revealed good biological activities. The results highlighted the main identified compounds as Gallic acid (7.19%), Levoglucosan (43.38%), and Linolenic acid (7.57%). Finally, Pistachio tree leaves could be considered as a cheap source of bio-compounds with anti-radical potential and antimicrobial effect.

Keywords

Leaves of Pistachio tree • Flavonoids • Free radical scavenging activity • GC/MS analysis

1 Introduction

Pistachio tree (*Pistacia atlantica*) of the Anacardiaceae family is widely spread in the Mediterranean region (Doghbage et al., 2018). The pistachio crop production in Tunisia has increased in the last decades (Khedher et al., 2014), which resulted in the increase of the generated waste like leaves. This biomass can be used as a renewable resource of bio-compounds. The main used technique to extract biomolecules from biomass is conventional extraction, which is a solid–liquid extraction (Taghizadeh-Alisaraei et al., 2017).

In this work, maceration was carried out in order to extract bio-compounds from Pistachio tree leaves using ethanol as green solvent. The extract phytochemical composition was determined (total phenol content (TPC), total flavonoid content (TFC), and condensed tannins (CT). The anti-radical and antimicrobial activities (against both gram + and gram- strains) of the extract were evaluated. In addition, chromatographic techniques were used to identify the bioactive molecules in leaves extract.

2 Materials and Methods

2.1 Plant Material

Fresh leaves of the pistachio tree (male and female) were dried in an oven at 45 °C for 24 h. The dry leaves were manually grinded until obtaining a fine powder which was then stored in glass vials away from light and moisture.

M. Elakremi (✉) · Y. Moussaoui
Organic Chemistry Laboratory (LR17ES08), Faculty of Sciences of Sfax, Sfax, Tunisia
e-mail: manel.elakremi@yahoo.com

L. Sillero · J. Labidi
Department of Chemical and Environmental Engineering, Biorefinery Processes Research Group, University of the Basque Country, Bizkaia, Spain

M. Elakremi · Y. Moussaoui
Faculty of Sciences of Gafsa, University of Gafsa, Gafsa, Tunisia

L. Ayed
National School of Engineers of Gafsa, University of Gafsa, Gafsa, Tunisia

A. Kallel et al. (eds.), *Selected Studies in Environmental Geosciences and Hydrogeosciences*, Advances in Science, Technology & Innovation, https://doi.org/10.1007/978-3-031-43803-5_11

2.2 Extracts Preparation

The extraction method used was maceration using ethanol as extraction solvent. The extraction was performed according to the protocol described by Khedher et al. (Vázquez et al., 2014) with some modifications. Leaves (male and female) were extracted in ethanol for 24 h at room temperature with magnetic stirring. The extracts were filtered through Whatman filter paper and concentrated under vacuum at 50 °C, and the extraction yield was determined. The dried residues were stored at -4 °C until analysis.

2.3 Total Phenol Content

The total phenolic content (TPC) was performed by Folin–Ciocalteu method (Trabelsi et al., 2010). Gallic acid was used as referent standard. The TPC was expressed as mg of Gallic acid equivalents (GAE)/100 g of dry leaves.

2.4 Total Flavonoid Content

Total flavonoid content (TFC) was determined by an aluminum chloride colorimetric assay (Miliauskas et al., 2004). Quercetin was used as referent standard. The TFC was expressed as mg of quercetin equivalents (QE)/100 g of dry leaves.

2.5 Total Condensed Tannins Content

The condensed tannins assay was performed by the colorimetric method described by Hagerman (2002). Catechin was used as referent standard. The condensed tannins content (CTC) was expressed as mg of catechin equivalent/100 g of dry extract.

2.6 DPPH (2, 2'-Diphenyl-1-Picrylhydrazyl) Radical Scavenging Assay

The radical scavenging activity of leaves extracts was evaluated by the DPPH assay (Smeriglio et al., 2017). The method of the DPPH is widely used to evaluate the antioxidant activity. The radical DPPH (purple color) was reduced to diphenyl-picrylhydrazine (yellow color) in the presence of an antioxidant. The ascorbic acid was used as a referent standard. The scavenging effect of leaves extracts was compared to that of ascorbic acid.

The results were expressed as percent inhibition of the DPPH radical (IC_{50}).

2.7 Antimicrobial Efficacy

The samples antibacterial activity was evaluated by a disk diffusion method following the method of Trabelsi et al. (2012). Sterile disks were impregnated with 10 µL of extract. The plate was incubated for 24 h at 37 °C. The dimethyl sulfoxide (DMSO 10%) was used as a negative control and Gentamycin (10 µg / disk) served as a positive control.

2.8 Gas Chromatography–Mass Spectrometry (GC/MS) Analysis

A gas chromatograph coupled with an Agilent 5973 mass spectrometry detector (Agilent Technologies, In., USA) equipped with ionization voltage in the EI-mode (70 eV 166) was used for the identification of compounds from leaves extracts. The operating conditions were capillary column HP-5MS ((5% phenyl)—methylpolysiloxane, 60 m * 0.25 mm), and carrier gas, N2 (2 mL/min).

Abbreviations: total phenolic content (TPC), total flavonoid content (TFC), condensed tannins content (CTC), and 2, 2'-diphenyl-1-picrylhydrazyl (DPPH).

3 Results

3.1 Extraction Yield, TPC, TFC, and CTC

The amounts of total flavonoid and condensed tannins in both sample extracts have similar values. Nevertheless, the concentration of total phenolic of male leaves is higher than that of female leaves. The obtained results are summarized in Table 1.

Table 1 Effect of solvent on the extraction yield of pistachio leaves polyphenols, flavonoids, and tannins

	Yield (%)	TPC (mg GAE/100g)	TFC (mg QE/100g)	CTC (mg CE/100g)
Male leaves	3	214.00 ± 2.73	48.09 ± 3.62	108.78 ± 1.67
Female leaves	3.5	124.56 ± 1.95	44.42 ± 2.01	123.18 ± 1.44

3.2 Biological Activities

The leaves extracts have a high ability to reduce DPPH radicals. The IC50 values were 20 µg/mL for both extracts. Their inhibitory activity was stronger than that of ascorbic acid (IC50 = 30 µg/mL).

The evaluation of the antimicrobial activity showed that the extracts were active on *Staphylococcus aureus* (ATCC 29,213) and *Escherichia coli* (ATCC 25,922) with a growth of the inhibitory zone diameters of about 17 and 15 mm, respectively. Both extracts showed no antibacterial potential against Klebsiella pneumoniae (ATCC 13,883).

3.3 GC/MS Analysis

Identifying the bio-compounds is important to analyze the extract potential of Pistachio leaves as a functional food or therapeutic agent. The main compounds identified by GC/MS were: Gallic acid (7.19%), Levoglucosan (43.38%), Linolenic acid (7.57%), and Vitamin E (6.59%).

4 Discussion

Maceration is a simple extraction technique which is good for heat-sensitive compounds. We used a green solvent because it is nontoxic, environmentally safe, and inexpensive.

TPC, TFC, and CTC have been studied in many works for other biomass products. Lalegani et al. (2018) and Rajaei et al. (Camera et al., 2018) studied the TPC of green hull of pistachio extracts and found 28 mg and 48 mg GAE/g of sample. Another study reported the amount of phenolic in natural pistachios (359 mg GAE/100g) and roasted pistachios (225 mg GAE/100g) (Toul et al., 2016). Our results of condensed tannins were different compared to those reported by Toul et al. (2016) in the leaves of *Pistacia atlantica* (11.805 CE/g).

In this study, the leaves extracts have good biological activities. The antibacterial activity of pistachio leaves extract against the tested strains might be linked to the presence of phenolic compounds.

Different studies have proven the health benefits of the identified compounds by GC/MS. Tomas et al. (2000) reported that Gallic acid, which is adequately absorbed in the human body, exhibits positive effects against cancer cell under in vitro condition. Also, vitamin E has beneficial effects on human health such as cancer prevention and resistance against aging (Rustan et al., 1993).

5 Conclusion

The achieved results showed different levels of total polyphenol, total flavonoid, and condensed tannin contents in two samples. The study of the antioxidant activity (DPPH test) showed a significant value of the inhibitory concentration. Also, these extracts exhibited a moderate antimicrobial effect in ethanol particularly against Staphylococcus aureus and E. coli. The results also showed that the highest values were found in male leaves extracts.

This study demonstrated the preliminary chemical characterization of the pistachio leaves and their antioxidant and antimicrobial properties. Therefore, further phytochemical investigation is needed in order to isolate and identify bioactive compounds of these extracts. This study may serve as the basis of other works to investigate the activities of the identified compounds in the pistachio tree.

References

Doghbage, A., Boukerker, H., & Belhadj, S. (2018). Analyse éco-botanique comparative de deux populations du *Pistacia atlantica* en Algérie par le biais de marqueurs morphologiques foliaires. *Courrier Du Savoir, 25*, 119–126.

Hagerman, A. E. (2002). Vanillin assay. In The Tannin Handbook (pp. 1–4).

Khedher, O., Moussaoui, Y., Salem, B., & Ben, R. (2014). Solvent effects on phenolic contents and antioxidant activities of the *Echinops spinosus* and the *Limoniastrum monopetalum*. *Res J Pharm Biol Chem Sci*, *5*(2), 66–76.

Lalegani, S., Ahmadi Gavlighi, H., Azizi, M. H., & Amini Sarteshnizi, R. (2018). Inhibitory activity of phenolic-rich pistachio green hull extract-enriched pasta on key type 2 diabetes relevant enzymes and glycemic index. *Food Research International, 105*, 94–101.

La Camera, E., Bisignano, C., Crisafi, G., Smeriglio, A., Denaro, M., Trombetta, D., & Mandalari, G. (2018). Biochemical characterization of clinical strains of *Staphylococcus* spp. and their sensitivity to polyphenols-rich extracts from pistachio (*Pistacia vera* L.). *Pathogens, 7*(4), 82.

Miliauskas, G., Venskutonis, P. R., & Van Beek, T. A. (2004). Screening of radical scavenging activity of some medicinal and aromatic plant extracts. *Food Chemistry, 85*(2), 231–237.

Rustan, I., Damiano, M. A., Lergards, G., et al. (1993). Recherche d'antioxydants a usage alimentaire et applications. *Falsif Expert. Chim. Toxicol, 86*, 201–214.

Smeriglio, A., Denaro, M., Barreca, D., Calderaro, A., Bisignano, C., Ginestra, G., … & Trombetta, D.: In vitro evaluation of the antioxidant, cytoprotective, and antimicrobial properties of essential oil from *Pistacia vera* L. Variety Bronte Hull. *International Journal of Molecular Sciences, 18*(6) (2017).

Taghizadeh-Alisaraei, A., Assar, H. A., Ghobadian, B., & Motevali, A. (2017). Potential of biofuel production from pistachio waste in Iran. *Renew Sust Energ Rev, 72*, 510–522.

Tomas-Barberan, F., & Clifford, M. N. (2000). Dietary hydroxybenzoic acid derivatives–nature, occurrence and dietary burden. *Journal of the Science of Food and Agriculture, 80*, 1024–1032.

Toul, F., Belyagoubi-Benhammou, N., Zitouni, A., Ghembaza, N., & Atik-Bekkara, F. (2016). In-Vitro Antioxidant Effects of Tannin Extracts of *Pistacia atlantica*. *International Journal of Pharmaceutical Sciences and Research, 7*(1), 121–126.

Trabelsi, N., Megdiche, W., Ksouri, R., Falleh, H., Oueslati, S., Bourgou, S., Hajlaoui, H., & Abdelly, C. (2010). Solvent effects on phenolic contents and biological activities of the halophyte *Limoniastrum monopetalum* leaves. *LWT—Food Sci Technol, 43*, 632–639.

Trabelsi, N., Falleh, H., Jallali, I., Daly, A. Ben, Hajlaoui, H., Smaoui, A., & Ksouri, R. (2012). Variation of phenolic composition and biological activities in *Limoniastrum monopetalum* L. organs. *Acta Physiologiae Plantarum, 34*(1), 87–96.

Vázquez, M. F., Comini, L. R., Martini, R. E., Núñez, S. C., Bottini, S., & Cabrera, J. L. (2014). Comparisons between conventional, ultrasound-assisted and microwave-assisted methods for extraction of anthraquinones from *Heterophyllaea pustulata* Hook f. (Rubiaceae). *Ultrasonics Sonochemistry, 21*, 478–484.

In vitro Seed Germination of Some Wild Plants from Algeria: An Effective Means for Plant Biodiversity Preservation

Souad Mehalaine and Haroun Chenchouni

Abstract

For decades, the flora of Algeria has been experiencing immense degradation due to several environmental and socioeconomic constraints. Without adequate preservation and/or regeneration strategies, the Algerian flora would continue to degrade as already many taxa are threatened with extinction. In this context, this work was an attempt to regenerate two wild plants (*Datura stramonium* L. and *Peganum harmala* L.) via in vitro seed germination. These two species are very common in semiarid regions of Algeria and highly valued as therapeutic plants. The seed germination capacity of both plants was examined. The seed germination requirements were investigated through treatment using a phytohormone, gibberellic acid (GA_3) under two different phases: light and dark. The seed germination capacity test showed that *P. harmala* had the best germination rate (94%) while *D. stramonium* seeds showed no germination. The application of gibberellic acid had no significant effect on germination rates of both species. While *P. harmala* achieved very high germination rates (88–96%), those of *D. stramonium* were quite low (27–64%). Darkness improved significantly the germination of *D. stramonium* seeds ($P < 0.01$). Most of the germinated seeds of both plants developed into healthy and vigorous seedlings. Modeling the appropriate seed germination conditions is necessary for the regeneration and conservation of endangered plant species overused in traditional medicine and herbal industries.

Keywords

Algerian flora • *Datura stramonium* • *Peganum harmala* • Plant regeneration • Germination success • Germination conditions

1 Introduction

Datura stramonium L. and *Peganum harmala* L. are two plants rich in alkaloids, active ingredients with powerful pharmacological properties (Miraldi et al., 2001; Nenaah, 2010). Their richness in alkaloids gives them an important status in the world pharmacopeia (Iserin, 2007). *Datura stramonium* (Solanaceae) is widespread throughout Algeria, whereas *Peganum harmala* (Nitrariaceae) is common in Algerian steppe rangelands (Kouba et al., 2021; Quezel & Santa, 1963) and indicates a state of land degradation, especially due to grazing (Merdas et al., 2021; Neffar et al., 2018). Both herbs are highly valued in folk medicine of the Maghreb for their crucial therapeutic properties as they have several pharmacological uses (Boudjelal et al., 2013; Houmani et al., 1994). Wild populations of medicinal plants, including *D. stramonium* and *P. harmala*, are overexploited for various medicinal and industrial purposes, and these plants are wild harvested from natural ecosystems. In addition, they are not properly cultivated or domesticated. Consequently, they are experiencing severe decline and even threatened with extinction (Goel et al., 2009). Since wild species, including both *D. stramonium* and *P. harmala,* propagate spontaneously in nature, there is no information on the biological conditions and ecological requirements for a successful germination in their native habitat, in particular under semiarid conditions. To fill this scientific gap, this

S. Mehalaine (✉) · H. Chenchouni
Department of Natural and Life Sciences,
Faculty of Exact Sciences and Natural and Life Sciences,
Echahid Cheikh Larbi Tebessi University, 12002 Tebessa, Algeria
e-mail: souadmehalaine@yahoo.fr
souad.mehalaine@univ-tebessa.dz

H. Chenchouni
Higher National School of Forests, 40000 Khenchela, Algeria

Laboratory of Natural Resources and Management of Sensitive Environments 'RNAMS', University of Oum-El Bouaghi, 04000 Oum El Bouaghi, Algeria

A. Kallel et al. (eds.), *Selected Studies in Environmental Geosciences and Hydrogeosciences*,
Advances in Science, Technology & Innovation, https://doi.org/10.1007/978-3-031-43803-5_12

study aimed at (1) examining the germination potential of *D. stramonium* and *P. harmala* under standard controlled conditions; (2) testing the effect of the growth regulator responsible for breaking dormancy (GA_3) combined with the effect of light and darkness on seed germination and thereby deepen our understanding of propagation requirements of the two species via seed dispersal.

2 Materials and Methods

2.1 Seed Collection

The seeds of *D. stramonium* and *P. harmala* were collected at the maturation stage in September and November, respectively, from Ain Beida region in northeastern Algeria. The seeds were stored in paper bags at room temperature before being subjected to germination tests.

2.2 Seed Disinfection

The seeds were washed with tap water, then sterilized with ethanol (70%) for 1 min followed by immersion in mercury chloride solution (0.1% $HgCl_2$) for 2 min. Subsequently, the disinfected seeds were rinsed with sterile distilled water.

2.3 Seed Germination Capacity Test

The sterilized seeds of both plants were immersed in sterile distilled water for one hour at room temperature (~20 °C). Then, ten seeds were placed on sterile filter paper in sterile Petri dishes and incubated at laboratory ambient temperature. The seeds were moistened daily with sterile distilled water. The test was performed in five replications, and the germination rate was calculated using the following formula:

$$\text{Number of germinated seeds} / \text{Number of tested seeds} \times 100$$

2.3.1 Treatment of Seeds with Gibberellic Acid (GA_3), Light, and Darkness

The sterilized seeds were immersed in increasing doses of gibberellic acid (GA_3) (0, 125, 250, 500 mg/L) over two hours. Then the treated seeds of each species were placed on sterile Agar in sterile Petri dishes, ten seeds per plate incubated in continuous darkness and light independently at laboratory ambient temperature. The test was performed in five replications. The germination rate was calculated using the same above-mentioned formula.

2.4 Statistical Analysis

The results obtained from the germination capacity test were processed by a one-way analysis of variance (ANOVA) at a significance level of 5% to test the difference between the two plant species. The obtained results from the test of the effect of gibberellic acid (GA_3), light, darkness, and their interactions on germination were processed using two-way ANOVA at a significance level of 5% for each species independently.

3 Results

3.1 Seed Germination Capacity

The obtained results showed significant difference ($P < 0.001$) between the two plants where *Peganum harmala* showed the highest number of germinated seeds 9.4 ± 0.54 that is corresponding to germination rate of 94% while *Datura stramonium* exhibited no seed germination (Fig. 1).

3.2 Effect of Gibberellic Acid, Light, and Darkness on Germination Success

Unlike gibberellic acid (GA_3) and light which did not significantly affect the germination of *D. stramonium* seeds ($P > 0.05$), darkness had a significant effect ($P < 0.01$) on the number of germinated seeds with values between 3.2 ± 0.83 and 8.8 ± 0.83 at 0 mg/L and 500 mg/L GA_3

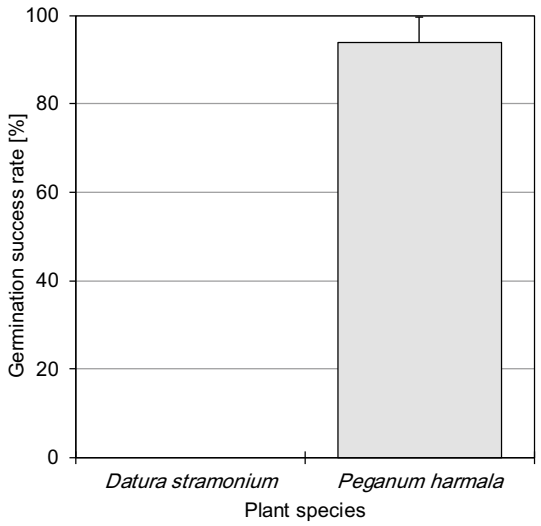

Fig. 1 Seed germination capacity test of *Datura stramonium* and *Peganum harmala*. Vertical bars represent the standard deviation (SD)

Table 1 ANOVA testing the effects of GA_3, light, darkness, and their interactions (GA_3 × Phase) on the variation of in vitro germinated seeds of *D. stramonium* and *P. harmala*

Source of variation	*df*	*MS*	*F*	*P*	Sig
Datura stramonium					
GA_3 doses	3	24.09	2.41	0.084	NS
Phase (Light/Dark)	1	93.02	9.32	0.004	**
GA_3 doses versus phase	3	6.15	0.61	0.608	NS
Peganum harmala					
GA_3 doses	3	1.09	0.65	0.587	NS
Phase (Light/Dark)	1	3.02	1.80	0.188	NS
GA_3 doses vs. Phase	3	0.62	0.37	0.772	NS

(*F*: *F*-statistics, *P*: *P*-value, *Sig*.: statistical significance, **: $P < 0.01$, NS: $P > 0.05$)

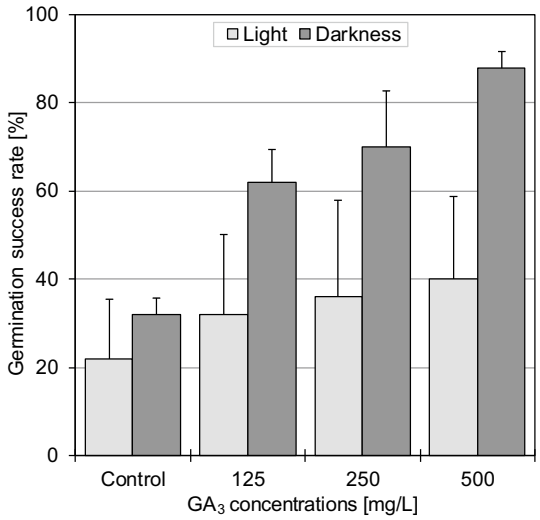

Fig. 2 Effect of different gibberellic acid (GA_3) levels, light, and darkness on seed germination of *Datura stramonium* under controlled conditions. Vertical bars are standard errors of the mean (SEM)

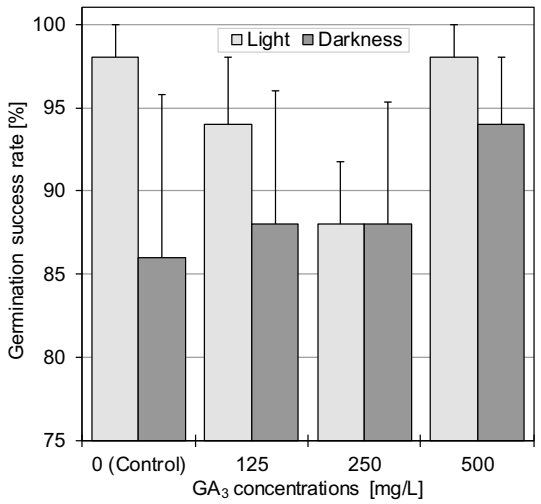

Fig. 3 Effect of different gibberellic acid (GA_3) concentrations, light, and darkness on seed germination of *Peganum harmala* under controlled conditions. Vertical bars are standard errors of the mean (SEM)

doses, corresponding to germination rates of 32% and 88%. In addition, the interactions GA_3 × light and GA_3 × darkness did not significantly influence the germination of *D. stramonium* seeds ($P > 0.05$) (Table 1; Fig. 2).

Gibberellic acid, light, darkness, and their interactions (GA_3 × light, GA_3 × darkness) did not record any significant effect ($P > 0.05$) on the germination of *P. harmala* seeds. The number of germinated seeds was high in all applied GA_3 doses in both phases; it ranged between 8.8 ± 0.83 and 9.8 ± 0.44 seeds in light and between 8.6 ± 2.19 and 9.4 ± 0.89 in darkness, which corresponds to germination rates of 88–98% and 86–94%, respectively (Table 1, Fig. 3).

4 Discussion

In the germination capacity test without pretreatment and after seed treatment with GA_3, light/darkness, *P. harmala* seeds showed high germination rates. This indicates that these seeds are viable and non-dormant, able to germinate under the applied conditions, without or with plant hormone treatment, light, darkness, and their interactions (*See* sects. 2.3, 2.4). Our findings disagree with previously-obtained data, as Goel et al. (2009) reported a lower germination rate (60%) compared to our results, and the germination constraints of *P. harmala* seeds is the very short duration of their viability. In addition, Saini and Jaiwal (2000) showed a very low germination rate (~8%) of untreated *P. harmala* seeds, whereas the treatment of seeds with GA_3 did not improve their germination rate, and this was attributed to viability loss by the storage and even the fresh seeds exhibited a relatively low germination rate (63%).

The germination capacity test showed that *D. stramonium* seeds did not germinate. The seeds were significantly affected by darkness where they exhibited the best germination rates. Light and GA_3 treatments had no significant effects. Benvenuti and Macchia (1997) reported that *D. stramonium* is characterized by a high photosensitivity. Hilhorst and Karssen

(1988) reported that light stimulates germination in the presence of exogenous gibberellins (GAs) in several plant species. However, Zhou et al. (2012) reported that darkness induced a high germination rate in *Magnolia officinalis*. Morsli et al. (2011) showed an important morphological diversity of Algerian *D. stramonium* collected from different bioclimatic regions and different habitats (woodlands or agricultural areas). So, the geographical provenance of seeds may be reflected in the capacity and requirements of seed germination of this species. Our previous study showed that the application of GA_3 did not necessarily increase the germination rates of non-dormant seeds, because the amount of endogenous GA_3 is sufficient to break dormancy. Moreover, the optimization of culture conditions—viz. seed sterilization, continuous imbibition, and ambient temperature—are favorable factors to induce the germination in non-dormant and non-demanding seeds like those of *Thymus algeriensis* (Mehalaine et al., 2017). However, various species require the so-called limiting factors for their seeds germination, such as light, moderate, or low temperature, exogenous GA_3, and chemical scarification (Conversa et al., 2010; Zhou et al., 2012).

5 Conclusion

The germination test revealed that the seeds of *D. stramonium* and *P. harmala* appeared to be non-dormant. *P. harmala* showed high germination capacity without or with gibberellic treatment, recording the best germination rates. Also, light and darkness had no significant effect on *P. harmala* germination. Darkness significantly improved the germination rate in *D. stramonium* while GA_3 and light did not significantly influence its germination. Further studies are needed to focus on other treatments and practices to improve the success of germination rates up to 100% and transfer the seedlings resulting from in vitro germination, to natural acclimatization conditions in order to induce normal morphological and physiological development of plantlets of the target species.

References

Benvenuti, S., & Macchia, M. (1997). Light environment, phytochrome and germination of *Datura stramonium* L. *Seeds. Environmental and Experimental Botany, 38*, 61–71. https://doi.org/10.1016/S0098-8472(96)01049-0

Boudjelal, A., Henchiri, C., Sari, M., et al. (2013). Herbalists and wild medicinal plants in M'Sila (North Algeria): An ethnopharmacology survey. *Journal of Ethnopharmacology, 148*(2), 395–402. https://doi.org/10.1016/j.jep.2013.03.082

Conversa, G., Lazzizera, C., & Elia, A. (2010). Effects of after-ripening, stratification and GA_3 on dormancy release and on germination of wild asparagus (*Asparagus acutifolius* L.) seeds. *Scientia Horticulturae, 125*, 196–202. https://doi.org/10.1016/j.scienta.2010.04.025

Goel, N., Singh, N., & Saini, R. (2009). Efficient *in vitro* multiplication of Syrian Rue (*Peganum harmala* L.) using 6-benzylaminopurine pre-conditioned seedling explants. *Nature and Science*, *7*(7), 1545–0740.

Hilhorst, H. W. M., & Karssen, C. M. (1988). Dual effect of light on the gibberellin- and nitrate-stimulated seed germination of *Sisymbrium officinale* and *Arabidopsis thaliana*. *Plant Physiology, 86*, 591–597. https://doi.org/10.1104/pp.86.2.591

Houmani, Z., Cosson, L., Corbineau, F., et al. (1994). Etude de la teneur en hyoscyamine et scopolamine d'une population sauvage de *Datura stramonium* L. *en Algérie, Acta Botanica Gallica*, *141*(1), 61–66. https://doi.org/10.1080/12538078.1994.10515135

Iserin, P. (2007). Larousse des plantes médicinales: Identification, préparation, soins. Ed Larousse, Paris.

Kouba, Y., Merdes, S., Mostephaoui, T., Saadali, B., & Chenchouni, H. (2021). Plant community composition and structure under short-term grazing exclusion in steppic arid rangelands. *Ecological Indicators, 120*, 106910. https://doi.org/10.1016/j.ecolind.2020.106910

Mehalaine, S., Menasria, T., Bouguessa, S., et al. (2017). *In vitro* seed germination of some Algerian medicinal plants and the effect of Gibberellic acid (GA_3) on breaking dormancy. *Journal of Materials and Environmental Science, 8*(6), 2034–2039.

Merdas, S., Kouba, Y., Mostephaoui, T., Farhi, Y., & Chenchouni, H. (2021). Livestock grazing-induced large-scale biotic homogenization in arid Mediterranean steppe rangelands. *Land Degradation and Development*. https://doi.org/10.1002/ldr.4095

Miraldi, E., Masti, A., Ferri, S., et al. (2001). Distribution of hyoscyamine and scopolamine in *Datura stramonium*. *Fitoterapia, 72*, 644–648. https://doi.org/10.1016/s0367-326x(01)00291-x

Morsli, A., Derridj, A., & Khelifi-Slaoui, M., et al. (2011). Diversité morphologique et teneur en hyoscyamine/scopolamine de douze provenances algériennes de *Datura stramonium* L. *Revue D Ecologie-La Terre Et La Vie, 66*, 291–302.

Neffar, S., Menasria, T., & Chenchouni, H. (2018) Diversity and functional traits of spontaneous plant species in Algerian rangelands rehabilitated with prickly pear (*Opuntia ficus-indica* L.) plantations. *Turkish Journal of Botany, 42*, 448–461. https://doi.org/10.3906/bot-1801-39

Nenaah, G. (2010). Antibacterial and antifungal activities of (beta)-carboline alkaloids of *Peganum harmala* (L) seeds and their combination effects. *Fitoterapia, 81*, 779–782. https://doi.org/10.1016/j.fitote.2010.04.004

Quezel, P., Santa, S. (1963). Nouvelle flore de l'Algérie et des régions désertiques méridionales. Tome 2, Ed. CNRS, Paris.

Saini, R., & Jaiwal, P. K. (2000). *In vitro* multiplication of *Peganum harmala*—An important medicinal plant. *Indian Journal of Experimental Biology, 38*, 499–503.

Zhou, J., Kulkarni, M. G., Huang, L. Q., et al. (2012). Effects of temperature, light, nutrients and smoke-water on seed germination and seedling growth of *Astragalus membranaceus*, *Panax notoginseng* and *Magnolia officinalis*: Highly traded Chinese medicinal plants. *South African Journal of Botany, 79*, 62–70. https://doi.org/10.1016/j.sajb.2011.11.004

Assessment of Moscow's New Territory for Biodiversity Conservation Using Remote Sensing

Anna M. Aleynikova, Elizaveta V. Karpukhina, Natalya V. Marsheva, and Elena A. Parakhina

Abstract

In recent years, the territory of Moscow has greatly increased in size, which led to a sharp decline in the biodiversity of many territories that were not part of Moscow before. Using remote sensing methods, the nature of vegetation and dynamics of land use in New Moscow for the 2014–2019 period were assessed in the article. Forests occupy about 42% of the territory of New Moscow, and cultural plantations account for about 28.5%. From 2014 to 2019, the area of residential sites increased by 8%, the area of meadows decreased by 7%, and that of forests—by 1%. The main areas for biodiversity conservation in New Moscow are specially protected natural areas (SPNAs). It is necessary to create an ecological frame of protected areas and monitor it by interpreting space images.

Keywords

Analysis of the dynamics • Vegetation cover • Satellite images • New Moscow • Biodiversity • Digital maps

1 Introduction

In recent years, Moscow has grown significantly in size due to the new territory located southwest of the city—New Moscow. In connection with the development of a new territory, there has been a noticeable reduction in the biodiversity of natural areas within the boundaries of New Moscow, the geo-ecological balance is disturbed. Conservation of biodiversity is possible practically only in the protected areas, which are also undergoing changes that can be monitored by remote research methods. Impact on protected areas is clearly displayed on satellite images; thus, it is possible to contribute to the conservation of biodiversity and fix illegal construction.

2 Research Methods

The main research methods were the analysis of literature data (Govin, 2013; Moscow City Government, 2015; Stanis et al., 2012, 2015, 2016), interpretation of space Landsat-8 multispectral images for the summer periods of 2014 and 2019 of the territory of New Moscow, creation of a map Normalized Difference Vegetation Index (NDVI) (Kavayas et al., 2011) and a map of the functional planning structure of the territory of New Moscow.

3 Results

The area under study—New Moscow (Troitsky and Novomoskovsky administrative districts)—is located in the zone of mixed coniferous-broad-leaved and broad-leaved forests. As a result of image interpretation, it can be seen that forests cover about 61,000 hectares, or 42.1% of the area. Indigenous broad-leaved communities account for only 1.8% (Fig. 1) and mixed communities with a predominance of primary forests—for 14.5%. The New Moscow area is dominated by mixed communities with a predominance of small-leaved forests (55.1%). Artificial phytocoenoses and cultural plantations account for 28.5%. All forest areas that entered the boundaries of the city of Moscow since 1 July 2012 were granted the status of specially protected green areas (Moscow City Government, 2015). Meadows in New Moscow have so far survived in limited areas and are mainly confined to river valleys and interfluve areas.

A. M. Aleynikova (✉) · E. V. Karpukhina · N. V. Marsheva · E. A. Parakhina
Faculty of Ecology, People's Friendship University of Russia, Moscow, Russia
e-mail: anshur@mail.ru

A. Kallel et al. (eds.), *Selected Studies in Environmental Geosciences and Hydrogeosciences*, Advances in Science, Technology & Innovation, https://doi.org/10.1007/978-3-031-43803-5_13

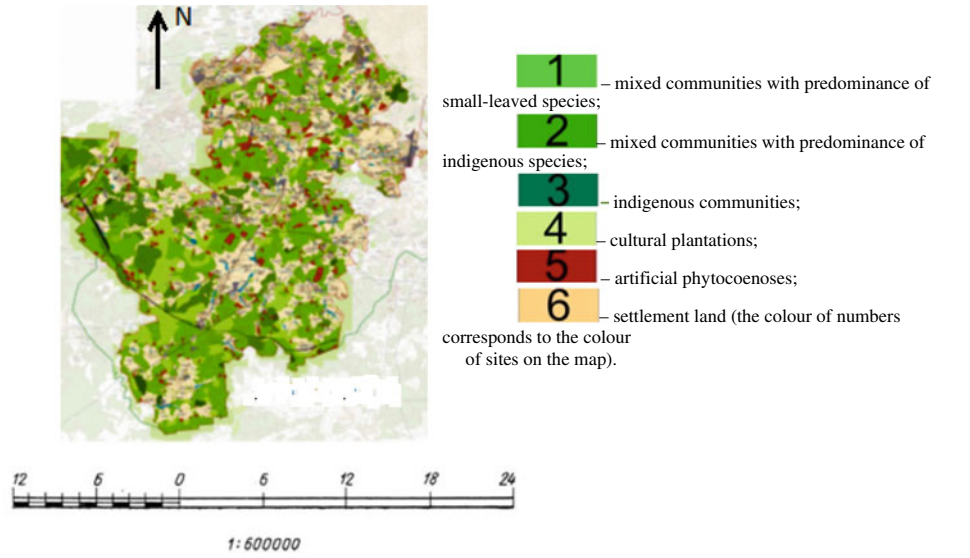

Fig. 1 Forest distribution in Troitsky and Novomoskovsky administrative districts

4 Discussion

The highest NDVI values apply to the outskirts of New Moscow and the territory of Troitsky Administrative Okrug. Within New Moscow, the total area of residential sites increased by 8% between 2014 and 2019, while the total area occupied by herbs and bushes and moderate vegetation decreased. As a result of space images interpretation, one can see the dynamics of land management for 2014–2019 (Fig. 2).

Most of the construction takes place primarily on meadow communities. This is due to the fact that legal tree felling requires a special permit, which is quite difficult to obtain (Fig. 3).

In general, the area of forests in the territory under study decreased by almost 1%, and that of meadows—by 7%. As a result of the reduction in the area of forests and meadows, 24 new construction projects started in this area.

The main areas for biodiversity conservation in New Moscow are SPNAs. The existing protected areas in Moscow represent almost the entire diversity of natural flora communities and about 90% of the species of animals and plants listed in the Red Book of the city. SPNAs can be elements of an ecological framework for the conservation of biodiversity and rare and endangered species.

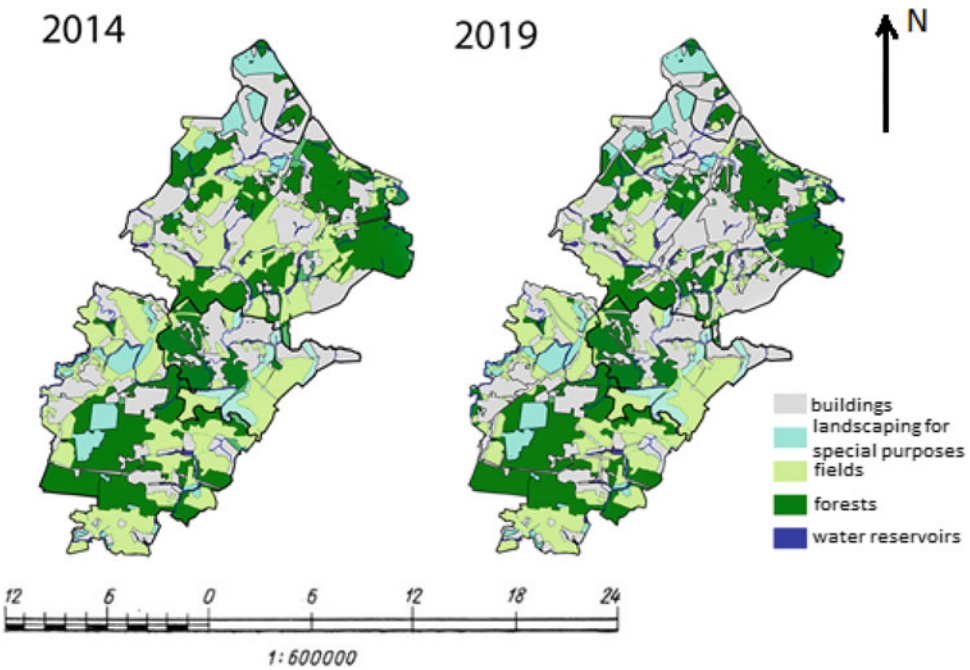

Fig. 2 Dynamics of land management in New Moscow in 2014 and 2019

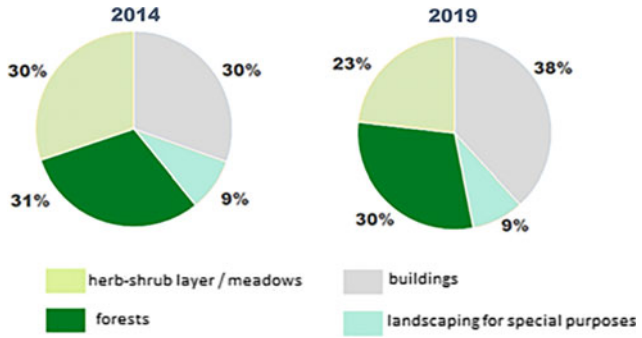

Fig. 3 Change in land use structure from 2014 to 2019

In New Moscow, there are territories where ecosystems have been almost completely preserved, mainly in territories 25 kms away from the Moscow Ring Road and further, in the valleys of the Pakhra and Mocha rivers. The preservation of natural biodiversity on the territory as the most important factor in maintaining a favourable environment should become a priority task of Moscow's environmental policy. However, a significant change in the territory in 2014–2019 and in the subsequent period occurs under the influence of development and road construction, increase in the accessibility of natural areas, which leads to the alienation of significant territories, their negative change, where it is still possible to preserve biodiversity and the existence of rare and endangered species.

5 Conclusion

According to the interpretation of the satellite images, forests occupy about 42% of the territory of New Moscow, and about 28.5% are cultural plantations. From 2014 to 2019, the area of residential sites increased by 8%, the area of meadows decreased by 7%, and that of forests—by 1%. Given constant dynamics of land use, the specially protected natural areas (SPNAs) are the main framework for biodiversity conservation in New Moscow. It is necessary to create an ecological frame of protected areas and monitor it by interpreting space images.

References

Govin, I. J., Stanis, E. V., & Parakhina, E. A.: Changes in the trophic state of Lake Valencia (Venezuela) from 2013 to 2019 according to remote sensing and modelling data atlantis highlights in material sciences and technology (AHMST). In volume 1 *International Symposium "Engineering and Earth Sciences: Applied and Fundamental Research"* (ISEES 2019) (conference proceedings) Published by Atlantis Press, (Vol. 1, pp. 288–592).

Kavayas, F., Ramos, Y., & Boye, A. (2011). Inventory and monitoring of urban green spaces using WorldView-2 data. Geomatika. No. 3 (pp. 67–73).

Moscow City Government, Department of Natural Resources Management and Environmental Protection of Moscow. Moscow, 2015 Report "On State of Environment in Moscow in 2014" (pp. 385).

Stanis, E. V., Karpukhina, E. A. et al. (2012). Natural Ecosystems of Moscow Region (pp. 94). Publishing and Analysis Centre Energia.

Stanis, E. V., Karpukhina, E. A., Makarova, M. G. (2015). Changes of new Moscow territory and preservation of natural heritage. In *Geology, geoecology, evolutionary geography: Collective monograph*. Volume 14, Saint Petersburg: Herzen University Publishing House, (pp. 258–262).

Stanis, E. V., Buldovich, N. S., Karpukhina, E. A., Makarova, M. G. (2016). Transformation of territorial structure of new territories of moscow and preservation of natural heritage. In *Natural and cultural heritage: Interdisciplinary research, preservation and development*, Saint Petersburg, Herzen University Publishing House, (pp. 563–566).

Smartest Countries, Happiest Countries: The World's Fight Against COVID-19 During the First Wave

Yasser Farhat and Wided Batita

Abstract

Recently (for 9 months), the world has lived an unprecedented pandemic known as coronavirus disease 2019 (COVID-19). This latter is caused by the severe acute respiratory syndrome coronavirus 2 (SARS-CoV-2), originating in Wuhan, China, in December 2019. As it is an unusual event, few studies have been conducted so far. For this reason, our statistical study in this paper is very important to help reveal how countries are facing this crisis and provide a scientific understanding of this pandemic during its first wave. Our data was gathered from the official websites of the World Health Organization and Our World Data of 21 countries: seven top ten happiest countries (Finland, Switzerland, Norway, Sweden, New Zealand, Austria, and Canada); six top ten smartest countries (UK, USA, France, Japan, Germany, and Singapore); three happiest and smartest countries (Netherlands, Denmark, and Iceland), UAE (the smartest Arabian country), Italy, Spain (the two most affected European countries), Tunisia and Nigeria (two poor African countries). The study showed that the happiest countries have more efficiently contained the pandemic than the smartest countries which have succeeded to bend their curves fast and performed the tests adequately. Tunisia, despite its poverty and lack of adequate tests, has a low number of cases and deaths. The UAE is the best in testing, leading to an excellent positive rate (0.4%), and the highest number of total COVID-19 tests per 1000 people (612.9) and total COVID-19 tests per 1000 people vs GDP capita. The significance of this research lies in its capacity to highlight the countries which overcame this crisis quickly. These countries could be taken as a model for other countries to overcome the crisis and to lessen as much as possible the economic and social impact of COVID-19.

Keywords

COVID-19 • Smartest country • Happiest country • Positive rate • Statistical study

1 Introduction

COVID-19 is an ongoing global pandemic of coronavirus disease 2019 caused by the severe acute respiratory syndrome coronavirus 2 (SARS-CoV-2), originating in Wuhan, China (Dhama et al., 2020). It is spreading fast around the world, causing deaths and major disruption to the global economy. So far, humanity has reached 25 million coronavirus cases and 850 thousand deaths (COVID-19 Coronavirus Pandemic, 2020) as of August 30, 2020; these numbers are changing every second, and no one knows when this pandemic will end and when people will be able to come back to their normal lives. The symptoms of coronavirus, though they may differ from one to another, are fever, dry cough, tiredness, aches and pains, sore throat, diarrhea, conjunctivitis, headache, loss of taste or smell, a rash on skin, or discoloration of fingers or toes, difficulty in breathing or shortness of breath, chest pain or pressure, loss of speech or movement (Dhama et al., 2020). Although 4.5 billion people were in quarantine after March 11, 2020, the virus has spread everywhere and at a high rate. This fact may be because of asymptomatic patients (The Daily Briefing, 2020). During the era of coronavirus, there are many measures: international global (directed by the World Health Organization (WHO), national, regional, or initiated by communities and individuals to slow down or stop the spread of COVID-19.

Y. Farhat
Abu Dhabi Polytechnic, 111499 Abu Dhabi, UAE
e-mail: Yasser.Farhat@adpoly.ac.ae

W. Batita (✉)
Sherbrooke University, 2500 Boulevard de l'Université, Sherbrooke, QC J1K 2R1, Canada
e-mail: widedbatita@gmail.com

A. Kallel et al. (eds.), *Selected Studies in Environmental Geosciences and Hydrogeosciences*, Advances in Science, Technology & Innovation, https://doi.org/10.1007/978-3-031-43803-5_14

2 Settings

This present statistical study was carried out on some countries within a defined period to see in close the response of these countries during the pandemic. This study started on March 11, 2020, when the COVID-19 was declared as a pandemic by the WHO and ended on August 17, 2020. This end date was decided by the authors to perform the statistical analyses and finalize the paper before the deadline. Twenty-one countries have been selected for this study for these reasons:

- The top ten happiest countries according to World Happiness Report (2020) (Helliwell et al., 2020): 1-Finland, 2-Denmark, 3-Switzerland, 4-Iceland, 5-Norway, 6-Netherlands, 7-Sweden, 8-New Zealand, 9-Austria, and 10-Canada. The UAE is ranked 21, and it is named the happiest Arab country. For this reason, it was selected in this study. The factors influencing happiness are mainly: subjective well-being, GDP per capita, social support, health life expectancy, freedom, generosity, level of crime, and corruption.
- Smartest cities according to a study done by IESE Business School (2020): 1-London (UK), 2-New York (USA), 3-Paris (France), 4-Tokyo (Japan), 5-Reykjavik (Iceland), 6-Copenhagen (Denmark), 7-Berlin (Germany), 8-Amsterdam (Netherlands), 9-Singapore, and 10-Hong Kong (China). China was not included in this study because when the pandemic was declared global, China had already flattened its curve. These smart and sustainable cities have been ranked according to nine dimensions: the economy, the environment, governance, human capital, international projection, mobility and transportation, social cohesion, technology, and urban planning.
- Italy and Spain: have been heavily affected by the COVID-19 outbreak.
- Tunisia and Nigeria are poor African countries, heavily indebted according to the latest statistics of the World Bank (2020). These countries were selected to find out how they were facing the crisis as poor countries.

Some countries are among top ten smartest and happiest countries at the same time which are Netherlands, Denmark, and Iceland. The data of this study were gathered mainly from official sites of the World Health Organization and (World Health Organization, 2020) Our World in Data (Our World Data, 2020). The data in the Annex, page 6 contains mainly: the COVID-19 total cases, total deaths, total recovered, active cases, total COVID-19 tests, and date of 1st cases in the 21 countries.

3 Results

3.1 Trajectories of Countries: COVID-19 Tests and Deaths

The trajectory for countries allows us to make comparisons of how quickly the number of confirmed cases has grown in different countries.

The blue lines in Fig. 1 mean that a country carries out many tests for each case it finds; the testing effort in these countries is adequate. These countries are the UAE, Canada, Norway, Finland, and New Zealand. The trajectories of the deaths (Fig. 2) show the impact of COVID-19 on different countries. The trajectories show the daily number of confirmed cases and deaths, and they become more meaningful if we interpret how much a country is testing (the USA was eliminated from Fig. 2 because the gap with the other countries is too big); the USA counts 173,485 deaths).

3.2 COVID-19 Testing

Testing is the only indicator to quantify the pandemic and shape its spread progression. Without testing, there is no data, and hence we have no idea how the countries are fighting this pandemic. In fact, it is very significant to see the portion of the tested population and analyze how countries are testing. The positive rate is a metric that allows us to see how the countries are testing and compute the spread of the virus (Fig. 3).

The countries that have a positive rate of less than 1% perform hundreds or thousands of tests to find one case.

The chart (Fig. 4) shows the extent of testing versus the scale of the outbreak in countries:

- Nigeria, Tunisia, Japan, and Italy are doing ten or hundred times fewer tests than other countries with a similar number of new confirmed cases.
- The UAE, Denmark, Iceland, Norway, Austria, Netherland, Switzerland, Sweden, New Zealand, and France find ten or a hundred times more cases than the others out of a similar number of tests.

Figure 5 shows a chart that describes the total COVID-19 tests per 1000 people. In Fig. 6, the chart plots the total COVID-19 tests per 1000 people vs GDP per capita shows that rich countries are doing more tests. Nigeria and Tunisia which are poor countries have done only a few tests per 1000 people, while the UAE, Denmark, and Iceland have done hundreds of tests per 1000 people. The testing policies have been planned differently.

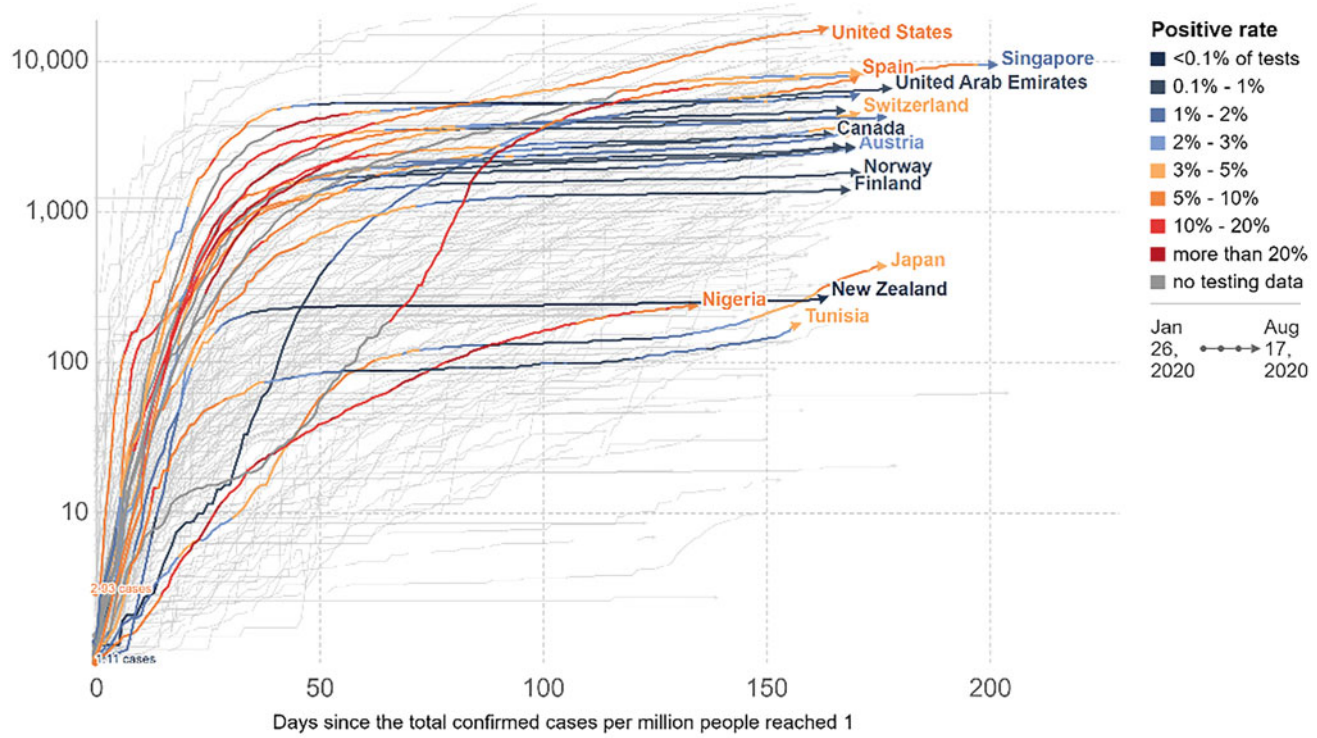

Fig. 1 Cumulative confirmed COVID-19 cases per million people

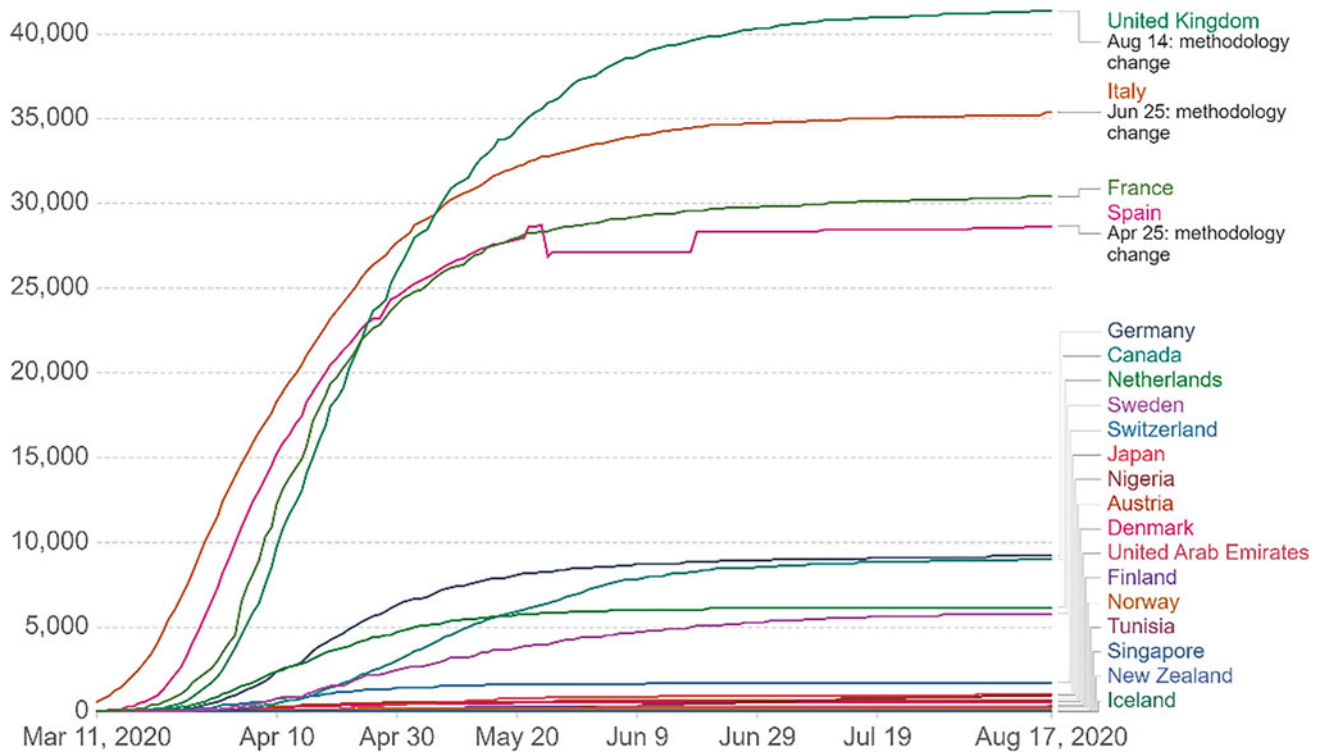

Fig. 2 Cumulative confirmed COVID-19 deaths without the USA

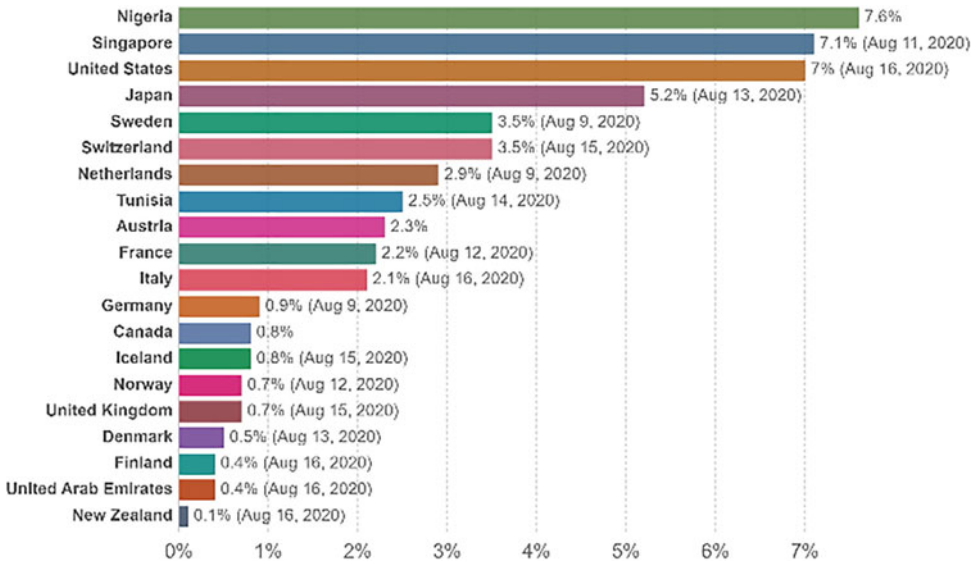

Fig. 3 Positive rate of August 17, 2020

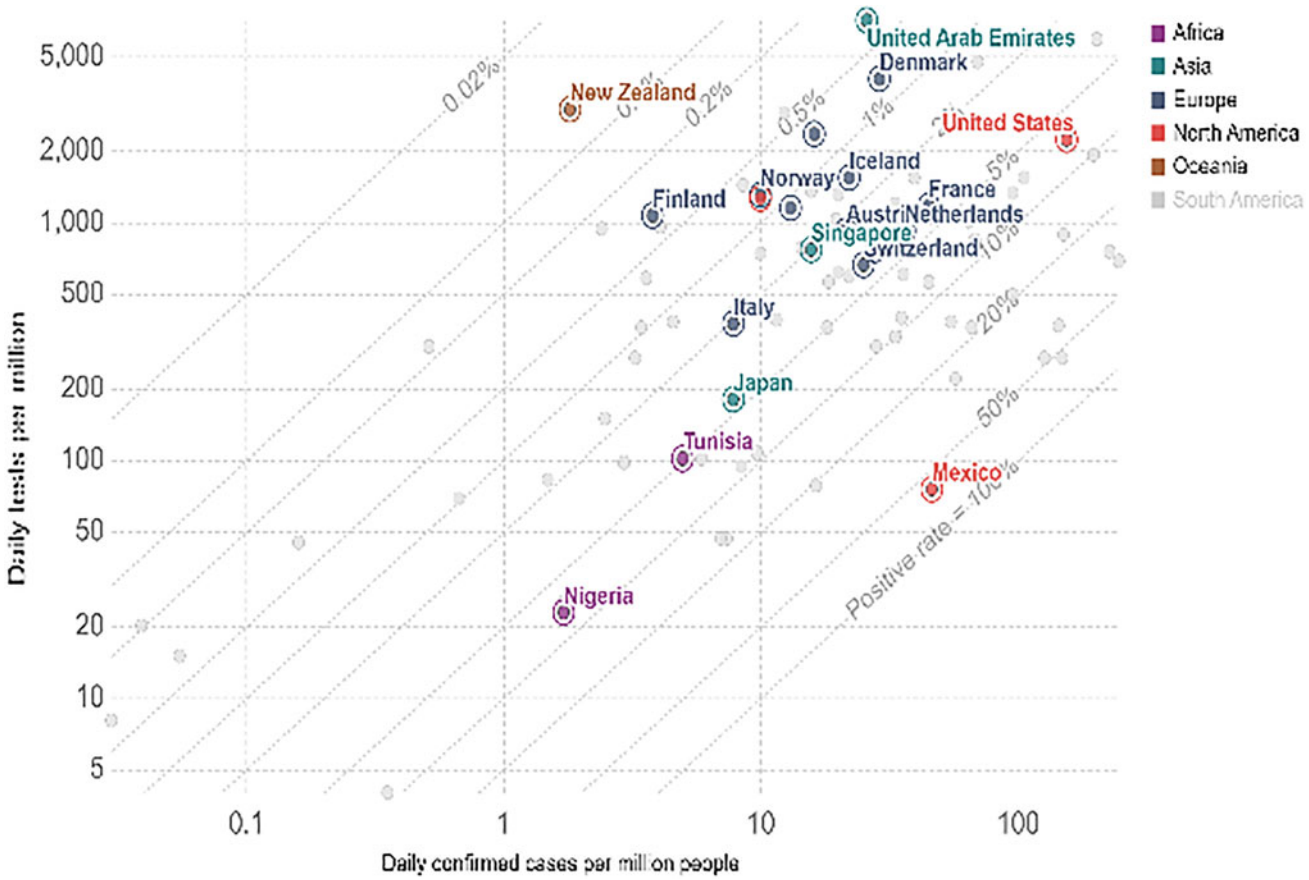

Fig. 4 Daily tests vs. daily new confirmed cases per million of August 17, 2020

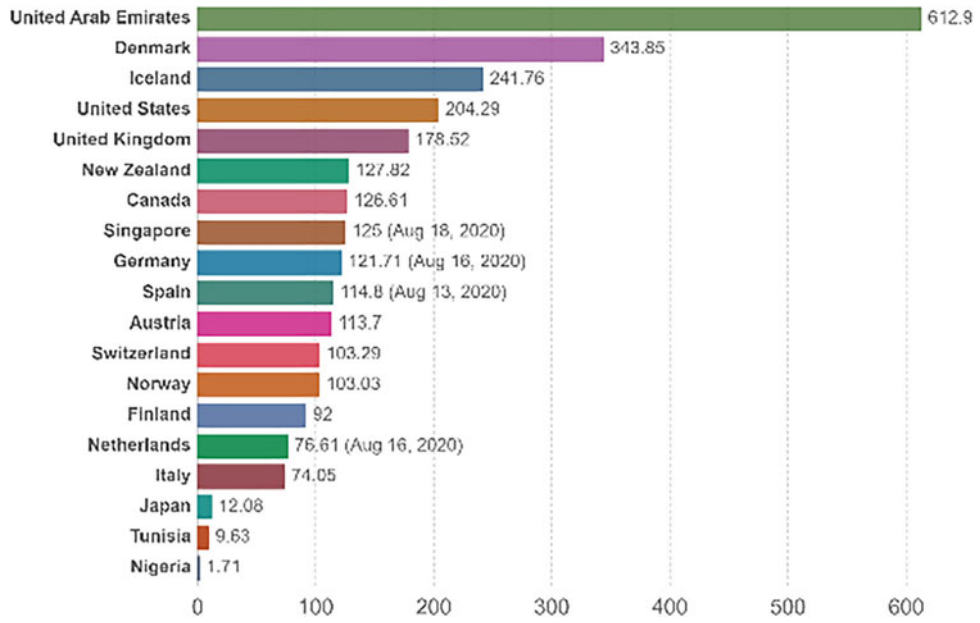

Fig. 5 Total COVID-19 tests per 1000 people, Aug 17, 2020

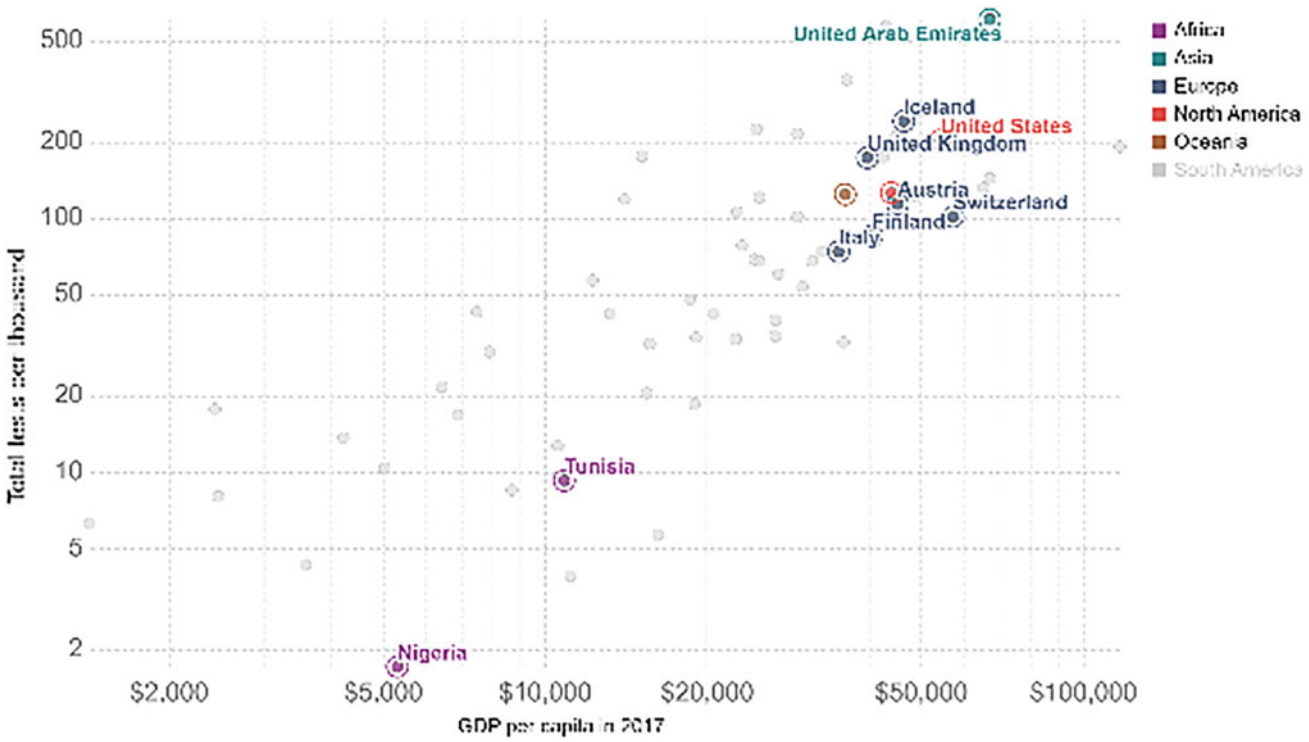

Fig. 6 Total COVID-19 tests per 1000 people versus GDP capita, Aug 17, 2020

4 Discussion

No country has brought its curve of confirmed cases down to zero. The curves of total COVID-19 confirmed cases in the USA, Spain, Singapore, Japan, and Nigeria are still going up. The USA was not able to contain the pandemic, the total number of deaths continues to rise, because it is the most populous country like India. However, the other countries succeeded to flatten their curves and brought the number of deaths down such as Italy, Germany, UK, France, and Canada. UAE, Iceland, New Zealand,

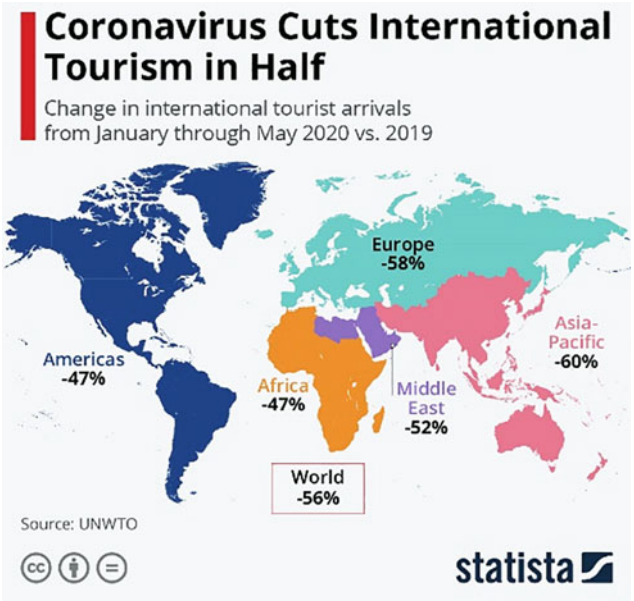

Fig. 7 Coronavirus cuts international tourism in half (Statista, 2020)

Singapore, Norway, Finland, Denmark, Austria, and Tunisia were able to minimize the pandemic and reduce the number of deaths quickly to lower rates. Despite its poverty, Tunisia has successfully managed the crisis presumably because the pandemic started late (March 2nd, 2020), and hence, it reacted fast as it saw the other countries heavily impacted (such as Italy and Spain). Bacille Calmette-Guérin vaccine could help to reduce the impact of COVID-19 as studies showed that countries that routinely used the vaccine in neonates had less reported cases of COVID-19 to date (WHO, 2020). Age is a crucial factor to get ill and the number of deaths increases. Indeed, as a person gets older, his/her risk for severe illness from COVID-19 increases. Warm weather could be a factor to lessen the COVID-19 impact. To understand better the pandemic, the positive rate was used. This metric shows clearly the countries which monitor and control the spread of the virus. In fact, the countries with positive rate of less than 5% are one indicator that the epidemic is under control in countries like New Zealand, the UAE, Finland, Denmark, UK, Norway, Iceland, Canada, Germany, Italy, France, Austria, Tunisia, Netherlands, Switzerland, and Sweden. Our results for the USA, Italy, and Spain are aligned with the results found in (Dehkordi et al., 2020). This study highlighted that the happiest countries have successfully contained the pandemic, better than the smartest countries.

Although this pandemic has severe negative impacts on the global economy, including the cuts on international tourism in half (Fig. 7), the happiest and smartest countries announced an emergency grant of millions of dollars to fund the COVID-19-affected companies.

This grant is devoted mainly to the health system to support increased testing, vaccine development, medical supplies, and for aid to households and firms.

5 Conclusion

In this paper, twenty-one countries were statistically examined in order to analyze their responses to the current crisis during the first wave. This study showed that the happiest countries have successfully contained the pandemic, better and faster than the smartest countries. This paper emphasized the importance of COVID-19 testing. It is crucial to help treat, isolate, or hospitalize people who are infected as well as collect relevant data in order to track progress.

The entire world is united around the same goal to bring cases and deaths of COVID-19 to zero. The WHO has presented two ways to outsmart COVID-19 as vaccines and specific medications are not yet available:

1. Governments: do as much as possible and adequately tests, isolate, treat patients with severe symptoms, trace and quarantine mild cases; inform, empower, listen to communities, and support them.
2. Individuals: keep physical distance, wear masks, wash hands regularly, cough safely, avoid crowding, no travelling, stay home, and go out for emergency.

Most of the studied countries have successfully slowed outbreaks by the end of August. However, by the beginning of fall, the second wave started and it will be worse according to media after reopening despite maintaining safe measures.

Annex: Data

Data contains: the COVID-19 total cases, total deaths, the percentage of deaths, total recovered, the percentage of active cases, total COVID-19 tests, the total COVID-19 tests per million population and date of appearance of first cases in the 21 countries. The cumulative numbers of August 17, 2020.

Country	Total cases	% Deaths	Total deaths	% Recovered	Total recovered	Active cases	Total COVID-19 tests	Total COVID tests-1M pop	Date of 1st case
USA	5,566,632	3	173,485	53	2,948,299	2,474,051	72,367,451	215,774	20-01-2020
UK	318,484	13	41,369				14,825,051	216,023	31-01-2020
France	218,536	14	30,429	38	83,848	104,752	6,000,000	219,029	24-01-2020
Singapore	55,838	0.04	27	94	52,350	3461	1,745,928	275,078	23-01-2020
Japan	54,714	2	1088	73	40,080	13,546	1,214,145	9312	16-01-2020
Germany	224,997	4	9296	90	202,900	14,421	9,265,361	110,541	27-01-2020
Netherlands	63,002	10	6172				1,312,787	69,749	27-02-2020
Iceland	2011	0,5	10	94	1888	116	183,283	536,659	28-02-2020
Denmark	15,617	4	621	86	13,417	1702	1,994,602	339,412	27-02-2020
Austria	23,370	3	729	89	20,795	2040	1,037,888	113,621	25-02-2020
Finland	7731	4	334	91	7050	368	500,021	84,864	29-01-2020
Norway	10,005	3	261	89	8857	917	564,549	102,578	26-02-2020
Switzerland	38,124	5	1991	87	33,300	2961	890,289	102,101	25-02-2020
Sweden	84,294	7	5787				917,036	90,730	24-01-2020
New Zealand	1631	1	22	94	1531	78	616,377	119,541	28-02-2020
Canada	122,087	7	9027	89	108,657	4592	4,880,172	126,465	22-01-2020
Tunisia	2107	3	56	65	1362	767	115,376	9631	02-03-2020
UAE	64,312	1	364	90	57,794	6383	6,121,609	611,978	29-01-2020
Spain	358,843	8	28,617				7,955,615	170,148	31-01-2020
Italy	254,235	14	35,400	80	203,986	14,867	7,642,059	125,526	31-01-2020
Nigeria	49,068	2	975	74	36,497	11,596	352,625	1681	27-02-2020

References

COVID-19 Coronavirus Pandemic. (2020). https://www.worldometers.info/coronavirus/. last accessed 2020/08/25.

Dehkordi, A. H., Alizadeh, M., Derakhshan, P., Babazadeh, P., & Jahandideh, A. (2020). Understanding epidemic data and statistics: A case study of COVID-19. *Journal of Medical Virology, 2020*, 1–15. https://doi.org/10.1002/jmv.25885

Dhama, K., Sharun, K., Tiwari, R., Sircar, S., Bhat, S., Malik, Y. S., Singh, K. P., Chaicumpa, W., Bonilla-Aldana, D. K., & Rodriguez-Morales, A. J. (2020). Coronavirus disease 2019—COVID-19. *Clinical Microbiology Reviews, 33*(4).

Helliwell, J. F., Richard, L., Jeffrey, S., & De Neve, J. E. (2020). *World happiness report 2020*. Sustainable Development Solutions Network.

IESE Business School. (2020). https://www.forbes.com/sites/iese/2020/07/08/these-are-the-10-smartest-cities-in-the-world-for-2020/#27ae721812af. Last accessed 2020/08/15.

Our World Data. (2020). https://ourworldindata.org/. Last accessed 2020/08/28.

Statista. (2020). https://www.weforum.org/agenda/2020/09/coronavirus-cuts-international-tourism-in-half/.

The Daily Briefing. (2020). https://www.advisory.com/daily-briefing/2020/08/10/asymptomatic#:~:text=Around%2030%25%20of%20patients%20who,asymptomatic%20transmission%20of%20the%20pathogen. Last accessed 2020/08/21.

WHO. (2020). Bacille Calmette-Guérin (BCG) vaccination and COVID-19. Scientific brief.

World Bank. (2020). https://data.worldbank.org/indicator/NY.GDP.MKTP.KD.ZG?locations=TN-NG-XE. Last accessed 2020/08/15.

World Health Organization. (2020). https://www.who.int/emergencies/diseases/novel-coronavirus-2019?gclid=Cj0KCQjw1qL6BRCmARIsADV9JtYfKigLyj4EYFNFCkIxUfsW9J3mmGZCpWnUEf8uyZ6U77aGe5yqPAaAjeKEALw_wcB. Last accessed 2020/08/26.

Environmental Earth Sciences and Geohazards

Assessment of Heavy Metal Contamination in Soil of El Eulma Area (Algeria)

K. Khemmoudj and S. Kissar

Abstract

This work assessed the level of soil pollution by heavy metals in the El Eulma area, Northeast (Algeria). The study area is characterized by various agricultural, commercial, and industrial activities. Twenty soil samples were collected and analyzed to measure cadmium, chromium, copper, iron, nickel, lead, and zinc contents. Geochemical indices including geoaccumulation index (Igeo), enrichment factor (EF), contamination factor (CF), pollution load index (PLI), and degree of contamination (CD) were used to appraise the concentrations and pollution status of these elements in soil. Results show the concentration of these heavy metals within the recommended national (Algeria) and global limits. The mean concentration of the metals in the soil of El Eulma area decreased in the following order Cd > Pb > Cr > Fe > Zn > Cu > Ni. The Igeo value for all metals ranged from -10.9 to 7.69. The enrichment factor (EF) > 50, the contamination factor (CF) ranged from 0.001 to 320.29, the pollution load index (PLI) ranged from 1.42 to 2.18, and the degree of contamination ranged from 11.64 to 320.29 for all metals.

Keywords

Geochemical indexing • Pollution • Heavy metals • Soil • El Eulma • Algeria

1 Introduction

Heavy metals are natural components of the Earth's crust and are present in all ecosystems, but their concentrations have increased many folds by anthropogenic activities (Kaddour et al., 2017). Various geochemical approaches, namely the geoaccumulation index (Igeo), enrichment factor (EF), contamination factor (CF), and pollution load index (PLI), have been used to appraise the heavy metal concentrations and pollution status in soil. Geochemical indexing approaches are extensively employed to appraise the degree of metal contamination in soil with their potential toxicity and distinguish between the natural and anthropogenic inputs of the contaminants. In the present study, conventional methods, such as Igeo, EF, CF, PLI, and Contaminant Degree (CD) (Muller, 1969; Singh et al., 2010; Hakanson, 1980), have been used to evaluate the existing contamination level in the soil of the El Eulma area.

2 Study Area

The study area is located in the Northeast of Algeria (Fig. 1). Most of its inhabitants are concentrated in the town of El Eulma with more than 160,000 inhabitants, working mainly in the production of cereals (barley, wheat). The climate is wet/semi-arid with annual precipitation of approximately 420mm. The rainy season extends from October to May with maximum rainfall during December and March of each year. The mean monthly temperature varies between 3 and 38 °C with an average of 15 °C. The vegetation is characterized by grasses and herbs. Soils are generally sandy to clayey, classified as arid soil, and are calcareous (Aliat et al., 2016). Mineralogically, most of the soils are dominated by kaolinite, illite, montmorillonite, muscovite, and biotite.

3 Materials and Methods

Surface soil (0–10 cm) samples were collected from 20 stations (March 2020) at El Eulma area (Fig. 2). At each station, the samples were collected by scraping the surface layer using a clean plastic spoon. Each sample was placed in

K. Khemmoudj (✉) · S. Kissar
Applied Zoological Laboratory and Animal Ecophysiology
University A/MIRA of Bejaia, 06000 Bejaia, Algeria
e-mail: Kaddour.Khemmoudj@univ-Bejaia.dz

A. Kallel et al. (eds.), *Selected Studies in Environmental Geosciences and Hydrogeosciences*,
Advances in Science, Technology & Innovation, https://doi.org/10.1007/978-3-031-43803-5_15

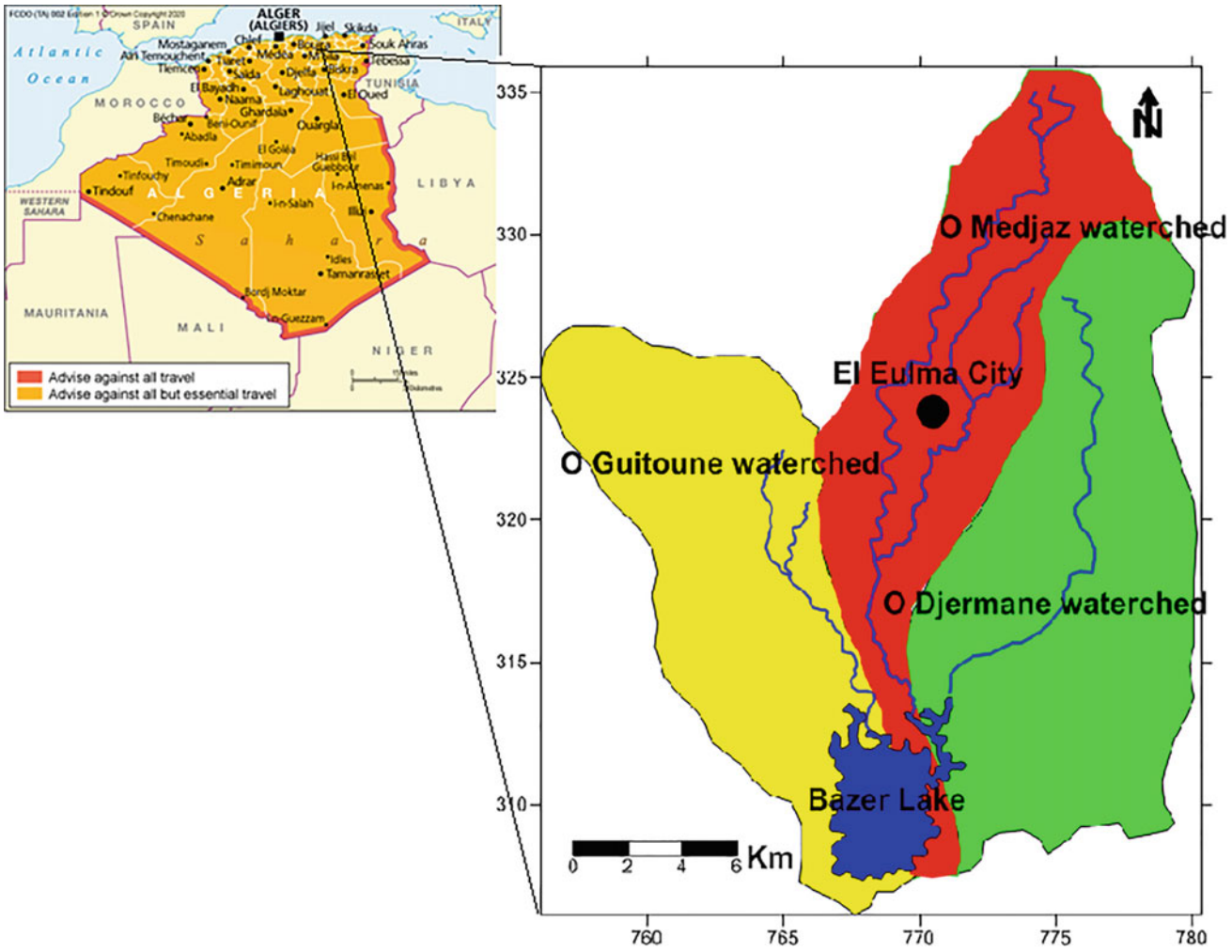

Fig. 1 Map study area

polyethylene plastic bags and was then kept in an icebox. In the laboratory, after air-drying the soil samples at room temperature, they were passed through a 2 mm nylon sieve. The fraction less than 2mm was ground in an agate mortar and passed through a 63 µm sieve to obtain silt and clay fractions. The total metals (Fe, Pb, Cu, Zn, Cd, Cr, and Ni) were digested using a mixture of (HNO_3 + HCl)-$HClO_4$ − HF in an open system as described in APHA (1989) and Hyacinthe and Van Cappellen (2004). The concentrations of the constituent elements were measured using atomic absorption spectrometry (AAS), using Perkin Elmer AAS 3300 with air–acetylene flame. The results obtained were subjected to analysis to determine the geoaccumulation index, enrichment factor, pollution load index, contamination factor, potential ecological risk index of the metals in the environment. The pollution load index (PLI) was calculated using the Tomlinson et al. (1980) approach. The PLI represents the number of times by which the metal content in the soil exceeds the average natural background concentration and gives a summative indication of the overall level of metal toxicity in a particular sample. The control samples were taken to represent the natural background. The PLI of the place is calculated by obtaining the n-CF that was obtained for all of the metals. The degree of contamination (CD) was defined as the sum of all contamination factors.

4 Results and Discussion

4.1 Metals Concentrations

Summary of the minimum, maximum, mean, and standard error (SE) concentrations of Fe, Cd, Cr, Pb, Zn, Cu, and Ni of20 samples are presented (Table 1). The elements were in this order: Fe > Pb > Zn > Cd > Cr > Ni > Cu. The range of concentration (mg/Kg) of metals in the studied area was Fe (0.00–3.56); Cd (0.00–0.08); Cr (0.00–0.07); Pb (0.01–0.76); Zn (0.00–0.14); Cu (0.00–0.03); Ni (0.00–0.07).

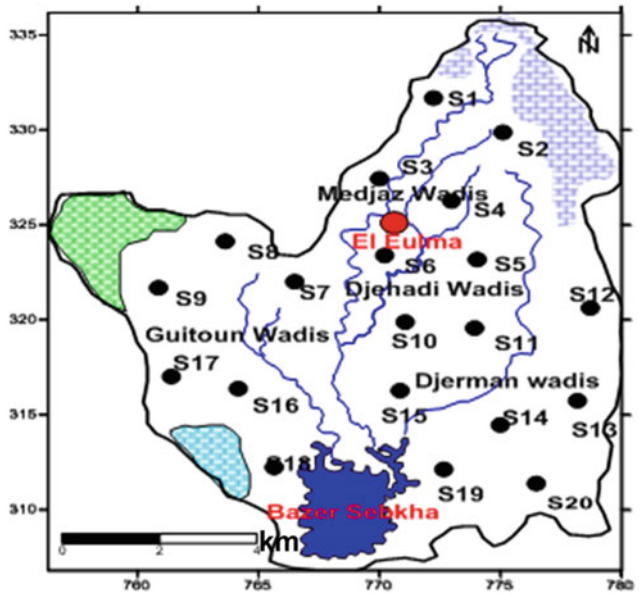

Fig. 2 Locations of soils samples carried out in the region of El Eulma, NE Algeria

4.2 Contamination Evaluation Based on Geoaccumulation Index

The Igeo was used to calculate metal contamination level in the soils (Table 2). Igeo values for all metals ranged from − 10.09 to 7.59.

4.3 Enrichment Factor Analysis

The enrichment factor is a suitable measure of geochemical trend and is used for making comparison between areas (Kaddour et al., 2017). Enrichment factor (EF) can be used to differentiate between the metals originating from anthropogenic activities and those natural sources. The EF value for all metals ranged from 0.01 to 9459 (Table 3).

4.4 Contamination Factor (CF), Pollution Load Index (PLI), Degree of Contamination (CD) and Mean Degree of Contamination (MCD)

The CF, PLI, CD, and mCD of all metals were calculated in the soil (Table 4). The value of all metals ranged as follows: CF (0.02–290), PLI (1.92–2.28), CD (143.38–320.29), mCD (20.57–45.75).

5 Discussion

The multi-approach calculation including geoaccumulation index, factor enrichment, contamination factor, pollution load index, and contamination degree in the soils of El Eulma area is affected by heavy metals due to the development of traffic roads, industrial and agricultural activities, etc. The heavy metals, Cd and Pb, contaminated the area. The soil of the study area was mainly derived from the upper cretaceous and Jurassic carbonates rocks. But the carbonate in general has a low concentration of lead.

Relatively, higher values of cadmium concentrations in the analyzed soil samples reflect anthropogenic effects due to the use of pesticides and industrial activity (Belabed et al., 2017; Bouaroudj et al., 2019).

6 Conclusions

The study revealed that the soil in the El Eulma area is predominantly composed of Cd > Pb > Cr > Fe > Zn > Cu > Ni. The Cr, Fe, Zn, Cu, and Ni levels are below 0,

Table 1 Basic statistical parameters for the distribution of heavy metal concentrations (mg/kg) at El Eulma area

HeahHeavy metametals	Fe	Cd	Cr	Pb	Zn	Cu	Ni
n	20	20	20	20	20	20	20
Min.	0.06	0.00	0.00	0.01	0.00	0.00	0.00
Max.	3.56	0.08	0.07	0.76	0.14	0.03	0.07
Mean	1.78	0.03	0.02	0.36	0.05	0.01	0.03
SE	1.09	0.02	0.01	0.25	0.04	0.01	0.01

Table 2 Geoaccumulation index of heavy metals in soil of El Eulma area

	Igeo Fe	Igeo Cd	Igeo Cr	Igeo Pb	Igeo Zn	Igeo Cu	Igeo Ni
n	20	20	20	20	20	20	20
Min.	− 10.09	3.47	− 8.28	− 1.32	− 8.5	− 9.55	− 7.22
Max.	− 4.27	7.59	− 1.25	4.68	− 1.44	− 0.58	− 0.56
Mean	− 7.21	5.97	− 5.62	2.38	− 3.99	− 5.20	− 3.82
SE	1.27	1.23	1.93	1.50	1.75	3.17	1.19

Table 3 Enrichment factors of heavy metals in the soil of El Eulma area

	EF Cd	EF Cr	EF Pb	EF Zn	EF Cu	EF Ni
n	20	20	20	20	20	20
Min.	3.00	0.80	7.50	0.51	0.11	0.01
Max.	64.00	22.50	9459.00	168.00	237.10	32.78
Mean	18.11	5.92	1178.32	27.93	24.28	9.77
SE	18.50	6.56	1977.12	46.01	58.51	8.02

Table 4 Contamination factor (CF), pollution load index (PLI), and degree of contamination (CD) of heavy metals in the soil of El Eulma area

	CF Pb	CF Zn	CF Cu	CF Ni	CF Fe	CF Cr	CF Cd	PLI	CD	mCD
n	20	20	20	20	20	20	20	20	20	20
Mean	13.88	0.17	0.19	0.24	0.02	130.83	0.09	1.92	143.38	20.57
Min.	0.60	0.00	0.00	0.01	0.00	11.11	0.00	1.42	11.64	1.66
Max.	38.50	0.55	0.70	1.14	0.07	290.00	0.62	2.28	320.29	45.75
SE	3.36	4.06	8.96	3.72	3.70	3.11	5.16	1.17	2.97	2.98

which demonstrates a background concentration. The distribution of metal concentrations in the study area has come about as a result of an anthropogenic influence, in particular the industrial, agricultural, and vehicular emissions.

References

Aliat, T., Kaabeche, M., Khomri, H., Nouri, L., Neffar, S., & Chenchouni, H. (2016). A pedological characterisation of some inland wetlands and Ramsar sites in Algeria. *Land Degradation & Development, 27*(3), 693–705. https://doi.org/10.1002/ldr.2467

APHA. (1989). *Standard methods for examination of water and wastewater* (17th Ed.). APHA.

Belabed, B. E., Meddour, A., Samraoui, B., & Chenchouni, H. (2017). Modeling seasonal and spatial contamination of surface waters and upper sediments with trace metal elements across industrialized urban areas of the Seybouse watershed in North Africa. *Environmental Monitoring and Assessment, 189*(6), 265. https://doi.org/10.1007/s10661-017-5968-5

Bouaroudj, S., Menad, A., Bounamous, A., Ali-Khodja, H., Gherib, A., Weigel, D. E., & Chenchouni, H. (2019). Assessment of water quality at the largest dam in Algeria (Beni Haroun Dam) and effects of irrigation on soil characteristics of agricultural lands. *Chemosphere, 219*, 76–88. https://doi.org/10.1016/j.chemosphere.2018.11.193

Hakanson, L. (1980). Ecological risks index for aquatic pollution control sediment logical approaches. *Water Research, 14*, 975–1001p.

Hyacinthe, C., & Van Cappellen, P. (2004). An authigenic iron phosphate phase in estuarine sediments: Composition, formation and chemical reactivity. *Marine Chemistry, 91*, 227–251.

Kaddour, K., Smail, M., Hocine, B., Bouzaza, A., & El Hacen, B. (2017). Assessment of heavy metal pollution due to the lead–zinc mine at the Ain Azel area (northeast of Algeria). *E3 Journal of Environmental Research and Management, 8*(1), 1–11. Available at http://www.e3journals.org. ISSN 2141-7466 © E3 Journals 2017. https://doi.org/10.18685/EJERM(8)1_EJERM-16-019

Muller, G. (1969). Index of geoaccumulation in sediments of the Rhine river. *Geochemical Journal, 2*, 108–118.

Singh, A., Sharma, R. K., Agrawal, M., & Marshall, F. M. (2010). Health risk assessment of heavy metals via dietary intake of foodstuffs from the wastewater irrigated site of a dry tropical area of India. *Food and Chemical Toxicology, 48*, 611–619. https://doi.org/10.1016/j.fct.2009.11.041

Tomlinson, D. L., Wilson, J. G., Harris, C. R., & Jeffrey, D. W. (1980). Problems in the assessment of heavy-metal levels in estuaries and the formation of a pollution index. *Helgoländer Meeresuntersuchungen, 33*, 566–575.

Naturally Occurring and Artificial Geochemical Barriers in Landfills of Northwestern Russia

Anatoly Belyi and Victor Shmakin

Abstract

Data from landfills in Northwestern Russia, varying both in size and type of construction, show minimal pollution of the underlying groundwater and significant pollution of groundwater within the landfills. Anaerobic, bluish, compacted, and impermeable (gleyed) layers were found underlying all of the landfills. These barriers appear being formed naturally by reactions between the leachate and the lower part of landfills, acting to suppress the contamination of groundwater beneath them.

Keywords

Colmation • Environmental protection • Geochemical barrier • Gleying • Groundwater • Landfill • Leachate • Pollution • Solid wastes • Surface water

1 Introduction

This research is focused on the pollution of groundwater within and beneath landfills in the Northwestern part of the Russian Federation. One of the first steps involves the development of mathematical models to predict the evolution of groundwater within and beneath the landfills and the progressive formation of geochemical shields, e.g., bluish-gray colmated layers formed at the base of the landfills with low permeabilities (Fortescue, 1985; Noble and Arnold, 1991). Methodologies for creating man-made leachate shields are also discussed (Islam et al., 2001; Viswanadham & Muthukumaran, 2007). Under these conditions, the leachate solutes are treated as being constant. The artificially natural processes (i.e., natural processes modulated by artificial exposures) likely attract less attention (Zhou et al., 2014).

2 Materials and Methods

We have analyzed both solid samples and groundwater leachates at 23 landfills in the North-West Federal District (NWFD) of Russia since 1993. 380 analyses were used, including from 6 to 24 components. As a common index for comparison of varying types of measurement, the hazard index "**R**" (Methodical Foundations for Assessment and Regulation of Anthropogenic Impact on Surface Water Quality, 1987) was utilized. It is symbolized by the formula:

$$R = \sum (\alpha_i/\zeta_i) / \sum \mathrm{MEL}_i \qquad (1)$$

where MEL is maximum exposure level, i varies from 1 to m, and m is the number of a given analyte in the calculation. Quantities under summation are the relative concentration of i analyte or (substance). In the denominator, there are summarized values of maximum exposure levels (MEL_i) for all considered substances. Other symbols are

$$\alpha_i = \mathrm{S}_i/\mathrm{S}; \quad \zeta i = \mathrm{MEL}_i \Big/ \sum \mathrm{MEL}_i, \qquad (2)$$

where $S = \sum S_i$ is the summarized concentration of all m considered substances in water, $\sum \mathrm{MEL}_i$ is the summarized value of MEL for all m substances (MEL_i).

As can be seen from (1), the value of R depends only on the composition of water but not on a grade of dilution. The limited value for R itself is not determined. So, a comparison by R is possible only inside homogeneous multitude, id, for analyses inside the one object. A comparison between different objects by R is meaningless.

In addition, for such correlation of analyses between objects, the Russian standards, as Conventional Complex Index of Water Pollution (CCIWP) (Methodical Foundations

A. Belyi · V. Shmakin (✉)
Vologda State University, 160000, 15, Lenin Str.,
Vologda, Russian Federation
e-mail: V_Shmakin@mail.ru

A. Kallel et al. (eds.), *Selected Studies in Environmental Geosciences and Hydrogeosciences*,
Advances in Science, Technology & Innovation, https://doi.org/10.1007/978-3-031-43803-5_16

for Assessment and Regulation of Anthropogenic Impact on Surface Water Quality, 1987), were used.

3 Results

Our detailed data are presented in (Belyi & Shmakin, 2017); here, we can only offer some examples.

The most representative region for all Russia by many indexes is the Vologda region. So, *Vologda*'s city center will serve as an example. The Old Vologda landfill is located on a lacustrine terrace. The first water confining bed (3–4 m) is a gray glacial-lacustrine clay with a permeability coefficient of about 9.3×10^{-8}m/s that meets the regulatory requirements for clay screens. In 1993, the landfill was equipped with four observation wells—in the center, up- and downstream of the underground flow. The observations in groundwater of the first aquifer (1.8–2.5 m) were conducted for 20 contaminants such as nitrogen group, heavy metals, biological, and chemical oxygen demand (BOD, COD) (Table 1).

As can be seen from the table, the major variations of *R* are associated with seasonal factors. The pollution of groundwater in summer time, without the influence of flooding, is high in the center and decreases to the periphery. But the significant difference between wells "below" and "above" is not observed.

The same results were obtained on the ***Cherepovets*** landfill although it is located on the lacustrine-alluvial terrace covered by **sands**, with filtration coefficients up to 2×10^{-5}m/s (!)—unlike Vologda, a natural clay screen under the waste body is missing.

On four unauthorized and unequipped dumps inside Vologda city, four country dumps of Vologda district, and five large fully equipped landfills in the vicinities of St.-Petersburg, similar levels of groundwater pollution below and above waste bodies were revealed. This depends neither on soil conditions nor on arrangement.

In many cases at the base of the waste bodies, **bluish-gray colmated layers soaked by the leachate** of 0.2–0.8 m thickness were revealed. Their filtration coefficients are about 1×10^{-8}…1×10^{-9} m/s, that is much less than the normative one.

The maximum value of the *R* index (186, which is much higher than even in the leachate) is dedicated to the samples of bottom sediments from the "Dead lake," where the leachate flows, near ***Kungolovo*** landfill (40 km from St. Petersburg).

In the center of the ***Kirovsk*** landfill, the stratified sampling revealed that the contamination is confined by the bluish-gray layer, outlined above. At the bottom of waste masses, it is distributed no deeper than the first 1…1.5 m regardless of ground composition. Deeper, the contamination does not exceed the allowed level (Fig. 1).

In ***St. Petersburg*** city and suburbs, the largest landfill is ¨Novosyolki." In the area of the landfill, the groundwater up to date remains virtually **clean**, obviously due to the underlying of the waste body by natural clay screen. On the contrary, the surface waters flowing from the landfill are polluted very intensively. Formally, they are "extremely dangerous" (even 2 km downstream CCIWP = 89!). Thus, once again, the most contaminated environment of the largest St. Petersburg landfill is surface waters.

4 Discussion

In general, our results indicate the presence of **natural phenomena, suppressing the migration** of contaminants in groundwater. The only reason for that may be the formation of **artificial–natural geochemical barriers** (Alekseenko & Alekseenko, 2003). Really, such barrier as colmated gleyed layer is visible at the bottom of every landfill. Its filtration coefficient ($\approx 10^{-9}$ m/s) is far below the normative values for artificial screens.

The bottom sediments, as shown in Kungolovo, obviously are of a considerable buffer capacity, so one can concede an adsorption barrier to contaminants too.

Some research of landfills in this direction has recently been conducted but without mentioning the concept of geochemical barriers. So, Spanish researchers (Regadío et al., 2012) had revealed the absorbing and insulating layers. They proved that rains and smectite–illite–carbonate clays act as a "reactor" that reduces pollution from leachate (Cuevas et al., 2012).

Under the studies of leachate migration in clay grounds in conditions of humid climate of SE China (Noble &

Table 1 Index of hazard (R) in groundwater in wells of Vologda landfill (25 samples)

Dates	22.07.99	14.10.999	14.06.00	02.11.00	14.06.01	31.10.01	10.12.07
282 (center)	8754	3341	18,988	3085	4206	3362	13.3
279 (above)	5541	3342	16.1	3272	3401	3481	–
283 (above)	3699	3345	10,071	2325	3495	3366	–
281a (below)	3972	3341	9723	1962	3457	3393	–

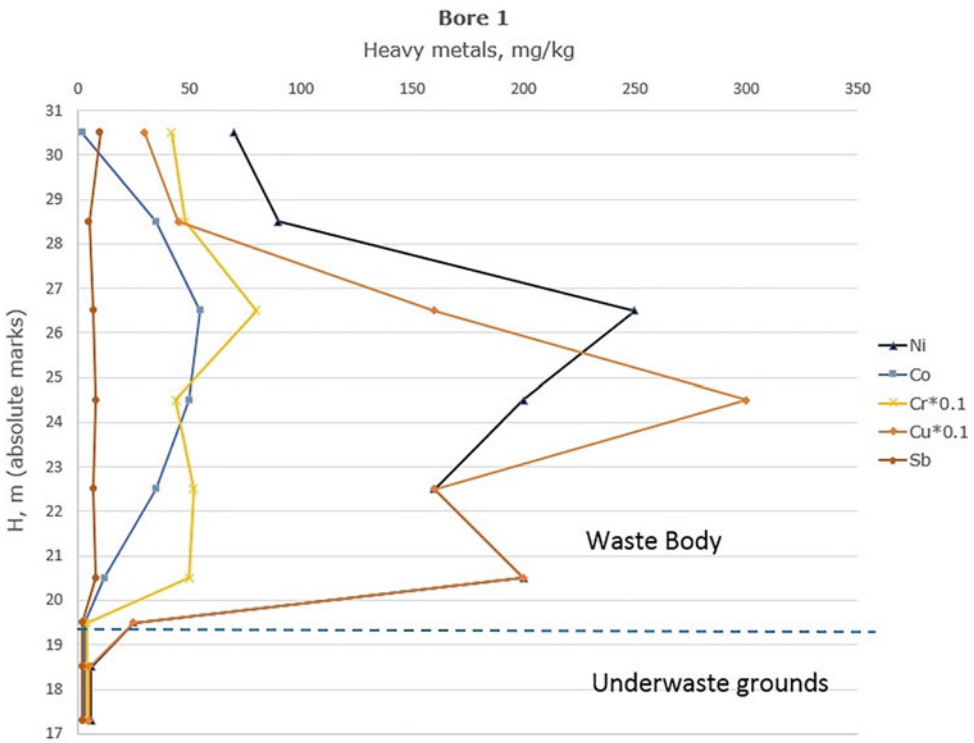

Fig. 1 Example of the distribution of heavy metals in soils in the central well of the Kirovsk dump (data of RGEC "Urangeo," plasma chromatography)

Arnold, 1991), the mechanical separation was revealed to be more important than molecular diffusion. The effectiveness of clay screens grows no more than 1 m (Zhou et al., 2014).

The term "gley," primarily arisen in soil science just in NWFD, means (Zaidelman, 1998) "more or less dense rock, gray with a greenish tinge, formed in conditions of prolonged waterlogging." In non-Russian literature the terms "gley," "gleying" are rare; in soil science, the closest microbiological processes may be named "redoximorphic" (Fortescue, 1985; Viswanadham & Muthukumaran, 2007).

According to (Zaidelman, 1998), all three simple factors for gleying such as waterlogging, the presence of organic substances capable of fermentation, and heterotrophic microflora on grounds, free from sulfates, are ubiquitous in base grounds of all landfills in NWFD and really the gleying is observed under all the studied landfills, regardless of the granulometry. Probably, this process with the colmation is of prime value in barriers.

5 Conclusions

The results allow suggesting the great importance of the assimilative capacity of the grounds under and near landfills. The effect of colmation and gleying processes which was proven under landfills in many different ground conditions is equivalent to the artificial succeeding of the normative filtration coefficient for landfills. This allows

(1) to achieve the desired rate of filtration coefficient for the underlying grounds within the storage site of a landfill, reducing the cost of construction of screens;
(2) to expand the spatial capabilities for a choice of sites for landfill displacement;
(3) to make easier and cheaper a recultivation for surroundings of closed landfills.

References

Alekseenko, V. A., & Alekseenko, L. P. (2003). *Geochemical barriers*. Logos. 144 pp. (in Russian).

Belyi, A. V., & Shmakin, V. B. (2017). Geochemical barriers in solid waste landfills of the Northwest Federal District in accordance with engineering survey results and monitoring data. *Engineering Survey, 6–7*, 78–92. (in Russian).

Cuevas, J., Ruiz, A. I., de Soto, I. S., Sevilla, T., Procopio, J. R., Da Silva, P., Jesús Gismera, M., Regadío, M., Jiménez, N. S., Rastrero, M. R., & Leguey, S. (2012). The performance of natural clay as a barrier to the diffusion of municipal solid waste landfill leachates. *Journal of Environmental Management, 95*(Supplement), 175–181.

Fortescue, G. (1985). *Geochemistry of the environment* (p. 360). Progress.

Islam, J., Singhal, N., & O'Sallivan, M. (2001). Modeling biogeochemical processes in leachate-contaminated soils: A review. In *Transport in porous media* (Vol. 43, pp. 407–440). Kluwer Academic Publishers.

Methodical Foundations for Assessment and Regulation of Anthropogenic Impact on Surface Water Quality. (1987). A. V. Karaushev (Ed.), 350 pp. Gidrometeoizdat (in Russian).

Noble, J. J., & Arnold, A. E. (1991). Experimental and mathematical modeling of moisture transport in landfills. *Chemical Engineering Communications, 100*, 95–111.

Regadío, M., Ruiz, A. I., de Soto, I. S., Rodriguez Rastrero, M., Sánchez, N., Gismera, M. J., Sevilla, M. T., da Silva, P., Rodríguez Procopio, J., & Cuevas, J. (2012). Pollution profiles and physicochemical parameters in old uncontrolled landfills. *Waste Management, 32*(3), 482–497.

Viswanadham, B., & Muthukumaran, A. (2007). Influence of geogrid layer on the integrity of compacted clay liners of landfills. *Soils and Foundations, 10*(3208), 517–532.

Zaidelman F. R. (1998). *The Gleyzation process and its role in soil formation*. Publishing house of Moscow University, 316 pp. (in Russian).

Zhou, D., Li, Y., Zhang, Y., Zhang, C., Li, X., Chen, Z., Huang, J., Li, X., Flores, G., & Kamon, M. (2014). Column test-based optimization of the permeable reactive barrier (PRB) technique for remediating groundwater contaminated by landfill leachates. *Journal of Contaminant Hydrology, 168*, 1–16.

Water Quality Influencing the Distribution of Benthic Macroinvertebrates at El Harrach River (North-Central Algeria)

Mouna Hafiane, Rania Maldji, Ghania Imekraz, Djaouida Bouchelouche, Imane Saal, Mohammed Mebarki, and Abdeslem Arab

Abstract

The site of study is wadi El Harrach (north-central Algeria), located in the capital of Algeria. The samples were tested by means of physicochemical analysis, carried out in situ and in the laboratory. This study aims to study the effect of water quality on the distribution of macroinvertebrates. According to SEQ-Water standards, we were able to highlight a spatial differentiation according to the different alterations in the physicochemical quality of the water. Thus, the river was divided into three sectors: Unpolluted sector: It has a biological capacity to harbor a strong taxonomic diversity in which the electrical conductivity values are around 529 µS cm^{-1} in H2. As for dissolved oxygen, it varies between 7 and 9 mg l^{-1}. In these stations, we have an important diversity of macroinvertebrates, mostly the pollution-sensitive taxon (Plecoptera). Moderately polluted sector: Their biological aptitude to harbor the macrofauna is weak compared to the first stations. The electrical conductivity reached 3560 µS cm^{-1} in H4. These values are explained by the releases from the thermal station in the Hammam Melouene village. Polluted sector: The degree of pollution is variable between these stations. In this sector, we have collected an abundance of the pollution-tolerant taxon as an example of the *Chironomus* genus. In this study, the degrees of mineralization and oxidizable materials are the most relevant alterations in the assessment of the water quality of the El Harrach River and the identification of the types of pollution.

Keywords

Disturbance • Macroinvertebrates • Water quality • Mineralization • Oxidizable materials

1 Introduction

Rivers are among the most complex and dynamic lotic ecosystems. They play essential roles in the conservation of biodiversity, in the functioning of organisms, and in the cycle of organic matter (Dynesius & Nilson, 1994). The physicochemical characterization of water bodies is essential for understanding the functioning of aquatic ecosystems, in particular the distribution of benthic macroinvertebrates and their responses to the natural and anthropogenic activities (Adandedjan et al., 2013; Mackintosh et al., 2015; Mebarki et al., 2017).

The goal of this work is to assemble the metrics needed to explain the distributions of benthic macroinvertebrates according to their sensitivity to environmental disturbances and mainly the physicochemical quality of the water.

2 Materials and Methods

The study was carried at El Harrach River in north-central Algeria. Ten stations (H1 to H10) are selected upstream, downstream, and at different tributaries, with respect to sources of pollution and discharges. All sampling stations are distributed between 220 and 15 m altitude. Monthly sampling was carried out from March 2015 to February 2016. Physicochemical parameters: dissolved oxygen (mg l^{-1}), electrical conductivity (µS cm^{-1}), and pH, were measured in situ at each of the sampling stations using a multiparameter analyzer (type WTW 340i). However, water samples were collected and returned to the laboratory to measure the concentrations of nitrites and phosphates.

M. Hafiane (✉) · R. Maldji · G. Imekraz · D. Bouchelouche · I. Saal · M. Mebarki · A. Arab
Laboratory of Dynamics and Biodiversity, Faculty of Biological Sciences, University of Sciences and Technology Houari Boumediene, BP 32 El Alia, Bab Ezzouar. Algiers, Algeria
e-mail: m.hafiane@usthb.dz

A. Kallel et al. (eds.), *Selected Studies in Environmental Geosciences and Hydrogeosciences*, Advances in Science, Technology & Innovation, https://doi.org/10.1007/978-3-031-43803-5_17

Macroinvertebrates were also sampled using a Surber net with a square frame (25 cm × 25 cm) and a 250 µm mesh and were identified at the family level in the laboratory.

3 Results

The result of the physicochemical analysis showed a different variation of values of parameters measured during the study period between upstream and downstream sampling stations (Table 1). The total number of macroinvertebrates is 30,403 individuals divided into 62 families.

4 Discussion

Depending on the types of organic and chemical pollution, the stations studied are divided into three sectors. These allowed the distribution of benthic macrofauna according to their characteristics.

The first sector is of good physicochemical quality, it combines the first three stations H1–H3 located in the upstream river between 220 and 170 m altitudes. Oxygen saturations were recorded at 9.86 mg l^{-1} in station H2 in the spring season, average mineralization 511 µS cm^{-1} in station H2, 627 µS cm^{-1} in station H3 in the spring and winter seasons, respectively. However, low nitrate levels of 0.04 mg l^{-1} were recorded at H1 and H3 in autumn. Indeed, these stations have the potential to harbor a large number of pollution-sensitive taxa such as the Plecoptera, as well as a significant taxonomic richness between 23 and 31 families, which are represented mainly by Ephemeroptera, Plecoptera, and Trichoptera (EPT). Huang et al. (2015) confirm our results, showing that these reference sites tended to have low concentrations of nutrients and low levels of disturbance. EPT taxa richness also decreased with increasing nutrient concentrations in a study conducted by Mackintosh et al. (2015). The families Capniidae, Perlidae, Heptageniidae, Leptophlebiidae, and Ecnomidae are present in these stations. These families prefer bright and clean environments. They are, therefore, pollution-sensitive to environmental disturbances since they disappear in the other stations located downstream. Leclercq et al. (1996) specify that the Perlidae are known to be very demanding in terms of oxygen.

The second sector includes stations H4, H5, and H6. Its physicochemical quality is average as the organic pollution is installed. This disturbance causes the disappearance of pollution-sensitive taxa and even reduces taxonomic diversity and richness. According to Mackintosh et al. (2015), the physicochemical constraints associated with urbanization can lead to a decrease in the richness of macroinvertebrates or a reduction of sensitive taxa, or both. These values occur, first of all, from the leaching of the soil loaded with fertilizers (nitrogen, phosphorus, and potassium) from agricultural fields located in the vicinity of the watercourse. 1.06 and 1.10 mg l^{-1} of phosphates in H4 and H6 stations, respectively, in the autumn season. According to Pesson (1976), the leaching of soils also enriches rivers with nitrates. The taxonomic richness of EPT also decreased with increasing nutrient concentrations (Macher et al., 2016).

The last sector located downstream includes stations from H7 to H10. It is of poor physicochemical quality where pollution has intensified in parallel with the increase in anthropization. This sector records extreme values, including the maximum phosphates values of 3.51 mg l^{-1} in the H10 station in the summer season, the values of electrical conductivity achieved 1652 µS cm^{-1} in the H9 station in the summer season. In parallel with these important values, an oxygen deficit is witnessed; 4.20 mg l^{-1} in the H8 station in

Table 1 Physicochemical variables (mean/standard deviation) measured at El Harrach River

Station	T (°C)	O_2 (mg l^{-1})	pH	EC (µS cm^{-1})	NO_3^- (mg l^-)	PO_4^{3-} (mg l^-)
H1	20.01 ± 6.66	6.95 ± 0.81	8.45 ± 0.30	1021.92 ± 171.66	0.06 ± 0.02	0.42 ± 0.47
H2	19.78 ± 6.16	7.37 ± 1.38	8.64 ± 0.22	550.33 ± 37.50	0.07 ± 0.03	0.42 ± 0.46
H3	20.21 ± 6.24	7.48 ± 1.21	8.61 ± 0.21	779.67 ± 86.31	0.09 ± 0.07	0.46 ± 0.56
H4	20.66 ± 6.66	7.58 ± 1.36	8.57 ± 0.23	1796.50 ± 938.26	0.08 ± 0.03	0.50 ± 0.56
H5	21 ± 6.91	7.60 ± 1.31	8.48 ± 0.19	1228.08 ± 372.03	0.08 ± 0.03	0.63 ± 0.45
H6	19.69 ± 6.46	8.14 ± 1.36	8.63 ± 0.21	1267.08 ± 470.51	0.08 ± 0.02	0.78 ± 0.79
H7	18.83 ± 6.09	6.77 ± 1.55	8.42 ± 0.34	1266.09 ± 493.32	0.08 ± 0.02	1.50 ± 0.97
H8	22.77 ± 6.29	7.84 ± 2.26	8.49 ± 0.15	1354.10 ± 386.23	0.08 ± 0.03	1.47 ± 0.52
H9	19.80 ± 6.94	6.45 ± 1.90	8.33 ± 0.36	1247.45 ± 362.18	0.09 ± 0.04	2.03 ± 1.23
H10	18.99 ± 5.53	2.98 ± 3.27	8.10 ± 0.35	1319.92 ± 288.88	0.08 ± 0.02	2.24 ± 1.20

Legend H1–H10: sampling stations, T: temperature of water, O_2: dissolved oxygen, pH: hydrogen potential, EC: electrical conductivity, NO_3^-: nitrate, PO_4^{3-}: phosphates

the winter season, 3.28 mg l^{-1} in the H9 station, and 0.24 mg l^{-1} in the H10 station in the summer season. This reflects a lethal condition for organisms. This deteriorated water quality eliminates pollution-sensitive taxa and promotes the establishment of pollution-tolerant taxa. According to Mackintosh et al. (2015), Chironomidae can tolerate a wide range of environmental conditions, including eutrophication and anoxia. In our sampling stations, they are the Baetidae, Caenidae, and the Hydropsychidae which supported disturbances, but with very low numbers: an individual of Hydropsychidae in stations H7 and H9. This deterioration in water quality highlights a stress gradient, in particular at stations H9 and H10, characterized by the abundance of Chironomidae, genus *Chironomus,* and Syrphidae. According to Adandedjan et al. (2013), stations where there were human activities and high levels of organic matter, also had a high abundance of pollution-tolerant taxa such as Chironomidae.

5 Conclusions

The metrics measured in the hydrographic network show that oxygen, mineralization, as well as mineral salts, are the relevant metrics influencing the physicochemical quality of water and disrupting the distribution of benthic macrofauna in the El Harrach River. The reduction of sensitive groups when quality deteriorates shows a gradient of stress or disturbance. This study allows describing the biotypology at El Harrach River; an unpolluted section, a moderately polluted section, and a polluted section. This depends on the physicochemical quality of the water and its biological aptitude to harbor a high, medium, or low taxonomic diversity and richness.

References

Adandedjan, D., Montcho, S. A., Chikou, A., Laleye, Ph., & Gourene, G. (2013). Caractérisation des peuplements de macroinvertébrés benthiques à l'aide de la carte auto-organisatrice (SOM). *Comptes Rendus Biologies, 336*, 244–248.

Dynesius, M., & Nilson, C. (1994). Fragmentation and flow regulation of river systems in the northeast third of the world. *Science, 266*, 753–762.

Huang, Q., Gao, J., Yin, H., Gao, Y., Zhao, J., Liu, L., & Huang, J. (2015). Development and application of benthic macroinvertebrate-based multimetric indices for the assessment of streams and rivers in the Taihu Basin, China. *Ecological Indicators, 48*, 649–659.

Leclercq, L., Rosillon, F., Vander Borght, P., Loncin, A., & El Mossaoui, M. (1996). Qualité chimique et biologique du bassin de la Semois (partie Belge). *Bulletin Français de la Pêche et de la Pisciculture, 341*(342), 81–108.

Macher, J. N., Salis, R. K., Blakemore, K. S., Tollrian, R., Matthaei, C. D., & Leese, F. (2016). Multiple-stressor effects on stream invertebrates: DNA barcoding reveals contrasting responses of cryptic mayfly species. *Ecological Indicators, 61*, 159–169.

Mackintosh, T. J., Davis, J. A., & Thompson, R. M. (2015). The influence of urbanization on macroinvertebrate biodiversity in constructed stormwater wetlands. *Science of the Total Environment, 536*, 527–537.

Mebarki, M., Taleb, M., & Arab, A. (2017). Environmental factors influencing the composition and distribution of mayfly larvae in northern Algerian wadis (regional scale). *Revue d'Ecologie (Terre et Vie), 72*, 303–313.

Pesson, P. (1976). La pollution des eaux continentales, incidence sur les biocénoses aquatiques. BORDAS, 285p.

Environmental Impact Assessment of the Algerian Cement Industry: A Case Study with Life Cycle Assessment Methodology

Ali Makhlouf, Ramdane Kardache, Raouf Chaabia, Abdelmadjid Drouiche, and Boualem Brahmi

Abstract

The purpose of this study is to assess the energy consumption and global warming of Portland cement production in Algeria. A cradle-to-gate Life Cycle Assessment (LCA) for the studied system was developed and conducted according to the LCA-ISO 14040 series. The results obtained were compared to that of a German production process extracted from the GEMIS 4.7 database. The results indicated that the energy requirement in the Algerian process, 5.716 MJ/FU, was higher than in the German process, 4.832 MJ/FU. However, the Green House Gas (GHG) from the Algerian process was less, 551.39 kg CO_2 eq/FU, compared with 882.36 obtained for the German process. These could be attributed to the difference in quality of fuels used in the two processes. While the Algerian process was exclusively based on natural gas, the German process was based on a mixture of fuels.

Keywords

Algeria • Clinker • GHG • Portland cement • Resources depletion

1 Introduction

Cement is a fundamental element for the civil engineering and habitat sectors. Driven by extensive urbanization, cement production and use have significantly increased. Between 2000 and 2010, world cement production went from 1.73 to 3.35 billion metric tons, and it is expected to reach 4.83 billion metric tons in 2030 (Statistica, 2017).

A. Makhlouf (✉) · R. Kardache · R. Chaabia · A. Drouiche · B. Brahmi
Department of Geological Sciences, Mouloud Mammeri University of Tizi-Ouzou, Tizi-Ouzou, Algeria
e-mail: almakhsme@gmail.com

The cement industry is characterized by its high consumption of energy and raw materials. In China, the world's biggest cement producer, energy needed for cement production represents 7% of the country's final energy consumption. Moreover, cement production is an important CO_2 precursor. In 2013, global CO_2 emissions from cement production were 3.6×10^9 t (Salas et al., 2016).

In Algeria, the cement production sector has grown from 11 million tons in 2011 to 12.5 million tons in 2015 and will reach 20 million tons yearly from 2020 (Global Cement, 2017).

This paper aims to conduct an LCA of cement production; "Société des Ciments de Hadjar Soud" (SCHS), which has two dry production lines with a total production capacity of 1×10^6 t/y and low energy efficiency. The results obtained were then compared with a fuel mix-based process (German process) extracted from the GEMIS 4.7 database, to determine how much the quality of the fuel used can influence the plant's carbon footprint.

2 Methodology

2.1 Life Cycle Assessment

LCA is a method for products and services environmental performance assessment. It is characterized by its ability to take into account the incoming and outgoing flows of the system and to report all this data to a Functional Unit (FU) (ISO, 2006a, 2006b).

2.2 Functional Unit

The goal of this study is to determine the environmental performances of a cement production plant by conducting a "cradle-to-gate" LCA study. The FU chosen for this study is the production of **one (1) ton** of Portland cement.

A. Kallel et al. (eds.), *Selected Studies in Environmental Geosciences and Hydrogeosciences*, Advances in Science, Technology & Innovation, https://doi.org/10.1007/978-3-031-43803-5_18

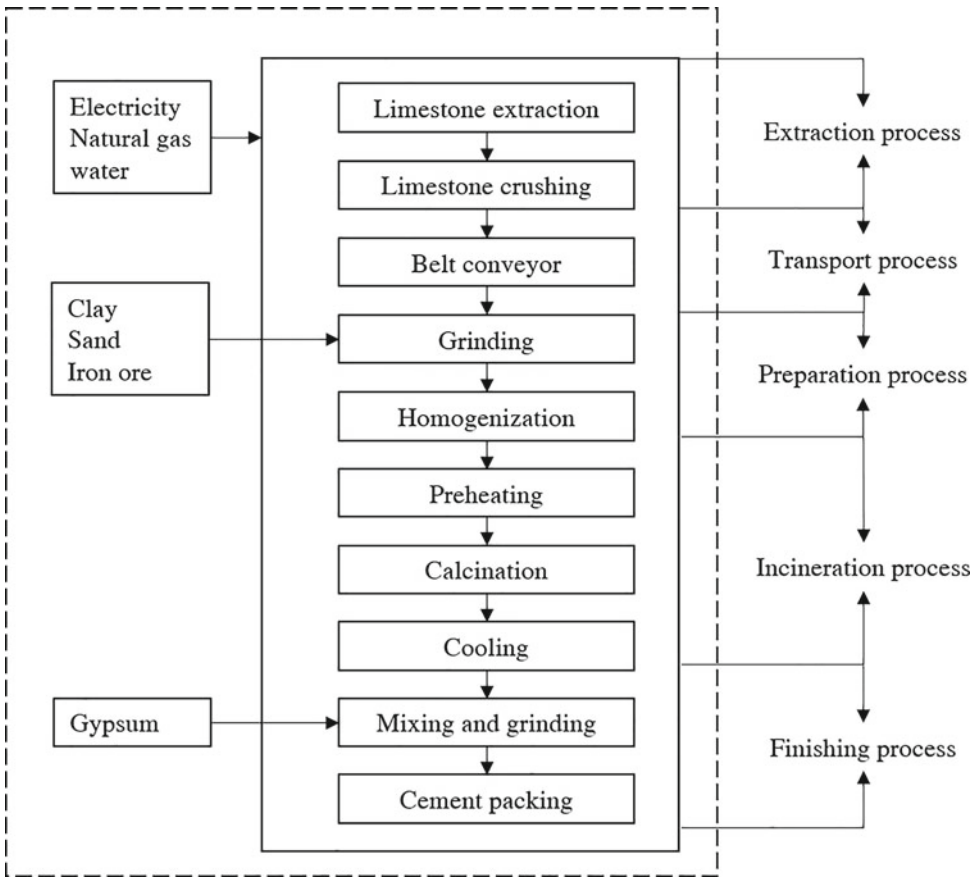

Fig. 1 System boundaries for cement manufacturing process

Two boundaries define the limits of the system (Fig. 1). They include all operations of cement production. They also cover the required materials and energy for cement production. The cumulative system boundary (broken line) presents inputs used in the system but delivered by processes located outside the studied system boundary. The second border (solid line) is the studied system boundary.

2.3 Life Cycle Inventory and Data Quality

Table 1 presents primary data collected directly from the SCHS factory; these data relate to a FU.

3 Results

3.1 Global Warming Mid-Point Impact

The quantity of GHGs emitted during the production of one ton of Portland cement is 882.36 kg CO_2 eq. The main gas related to global warming emitted in the studied system is carbon dioxide (CO_2) which represents more than 98% of total global warming impact, while other GHGs, like nitrous oxide (N_2O) and methane (CH_4), are emitted in very small quantities (1.43% and 0.5%, respectively).

The total amount emitted of carbon dioxide is 865 kg/FU. Clinker production is the main source of emission by

Table 1 Annual balance and material/energy input flows for a FU of Portland cement

Consumption	Units	Annual quantities	Quantity per FU
Natural gas	MJ	2.92×10^9	3437
Electricity		0.365×10^9	430
Limestone ($CaCO_3$)	Kg	1.253×10^9	1474.2
Clay (Al_2O_3)		0.334×10^9	393.12
Sand (SiO_2)		48.195×10^6	56.7
Iron (Fe_2O_3)		16.065×10^6	18.9

85.22%, of which 62.98% is due to the decarbonization of $CaCO_3$, and 22.34% to the combustion of fuel gas. Electricity generation is the second largest emission source by 12.48%, and finally, the crushing of the raw materials in the extraction phase by 1.87%.

3.2 Cumulative Energy Consumption

The production of a Portland cement FU in the Algerian plant requires 5716.38 MJ of energy (169.11 Nm^3). The Algerian process is characterized by an exclusive consumption of natural gas as fuel. Natural gas accounts for 95.31% of the total energy balance, followed by oil 4.49%, and finally, coal by 0.06% (coal and oil are used outside the studied system).

3.3 Comparison of Results

Comparing the results of the Algerian process to those of a German process extracted from the GEMIS database, we can notice that, the German process consumes less energy (4,832.8 MJ), despite that, its carbon footprint is higher than that of the Algerian process (951.36kg CO_2 eq) (Fig. 2).

As mentioned above, the Algerian process is based on the unique combustion of natural gas (non-renewable energy). For its part, the energy balance of the German process is based on a mixture of fossils (natural gas 3.29%, oil 16.6%, and coal 67.0%), nuclear energy (8.81%), and part of renewable energies (4.3%) (Fig. 3). This mixture should reduce CO_2 emissions, but the high ratio of coal in the energy balance causes an increase in the carbon footprint of the German process.

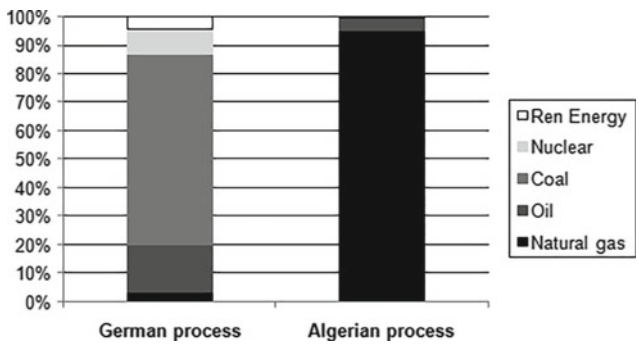

Fig. 2 Energy sources used in each process

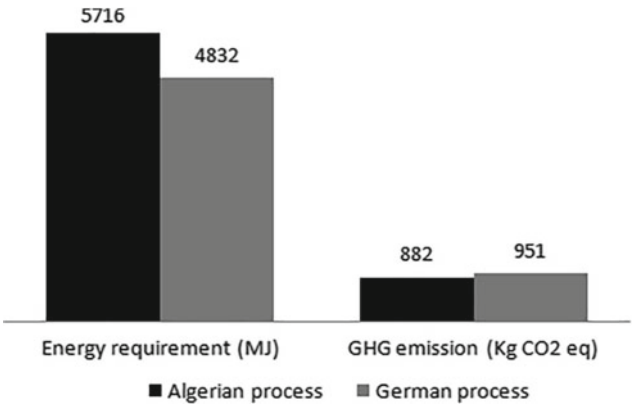

Fig. 3 Energy requirement and GHG emission in each process

4 Conclusion

This study was devoted to the environmental performance assessment of a cement plant with low energy efficiency. The results were compared with those of a plant with high-energy efficiency but based on the combustion of a mixture of fuels. By comparing the results of the study, we note that, although the demand for energy in the Algerian process is greater than the world average, its GHG emission is very low. This can be explained by the fact that the Algerian process is based on the combustion of natural gas only. While, worldwide, cement processes are based on a mixture of fossils (natural gas 3.29%, oil 16.6%, and coal 67.0%). The high ratio of coal in the energy balance causes an increase in the carbon footprint.

References

Global Cement. (2017). Two more Algerian plants. Retrieved February 10, 2018. http://www.globalcement.com/news/item/6805-two-more-algerian-plants

ISO. (2006a). ISO 14040. In *Environmental management—Life cycle assessment—Principles and framework*, 1–28.

ISO. (2006b). ISO 14044. In *Environmental management—Life cycle assessment—Requirements and guidelines* (7), pp. 652–668.

Salas, D. A., et al. (2016). Environmental impacts, life cycle assessment and potential improvement measures for cement production: A literature review. *Journal of Cleaner Production, 113*, 114–122.

Statistica. (2017). Major countries in worldwide cement production from 2012 to 2017 (in million metric tons). Retrieved February 10, 2018. https://www.statista.com/statistics/267364/world-cement-production-by-country/

Vulnerability of Beaches Nourished by Dunes: A Fight Between Waves, Winds, and Sediments. A Case Study of Mira Beach, Portugal

José Pinho, Ana Gomes, and Helena Granja

Abstract

The coastal stretch located south of Mira beach, Portugal, has been monitored since 2007 with the aim to register its morphological evolution. The monitoring program includes bathymetric and topographic surveys, analysis of sediments, and field observations. Dunes appear to be the predominant sedimentary source of these beaches. Although dunes present appreciable sedimentary reserves, the sediment size does not allow the beach to recover to previously observed morphologies. In fact, once a cliff is formed into the dune, generally, it is retreated by the action of the sea waves, wind, and precipitation. The size of the sediments (medium sands) favors low-slope beach profiles which will contribute to the retreat process. The reduced width of the new beaches does not facilitate the existence of a berm that could contribute to dune defense. This paper presents the monitoring results of this coastal sector and highlights the importance of sediment characteristics for the persistence of the erosion process. Dune retreats around 5 m/yr and an aggressive erosion process points to the high vulnerability of important sectors of this coastal stretch. These results highlight the high vulnerability of important sectors of the Portuguese coast, now fed almost exclusively by the sedimentary reserves. This opens up an opportunity for the development of solutions that are not limited to the preservation of the dunes systems but seek more effective alternatives.

Keywords

Coastal erosion • Sandy beaches • Sediments • Monitoring • Mira–Portugal

1 Introduction

Following the construction of an inland aquaculture unit located south of Mira beach, in Portugal, the coastal stretch adjacent to this unit has been monitored (Fig. 1), in order to follow its morphological evolution. It is intended to know and quantify the relative stability of this coastal stretch in order to acquire a consistent database that allows one to support future mitigation measures for the preservation of this coastal sector.

According to Dias (2005), in this sector, extending from south of Mira beach to Mondego cape, there were only, at that date, problems of coastal erosion over a few kilometers south of two coastal groins constructed for the protection of Mira beach and a camping park. It was also mentioned that the coastal dynamics forecast of the coastline pointed to the absence of significant erosion of the foredunes until 2020, along the coastal stretch between south of Mira beach and Mondego cape.

According to another study of coastal erosion risk (CEHIDRO, 1996), the sector under analysis was considered to be of low risk. The European Environment Agency (Lenôtre & Thierry, 2002) considered that the sector adjacent to the aquaculture facility was located in a stable area, with an almost imperceptible evolution on a human scale. This classification was used for sectors where it was not possible to objectively assess the recent trend of evolution. Other monitoring studies (e.g., Menezes, 2011; Pereira & Coelho, 2013) show results that point to accretion or temporary stability trend.

J. Pinho (✉) · A. Gomes
Department of Civil Engineering, University of Minho, CTAC, Braga, Portugal
e-mail: jpinho@civil.uminho.pt

H. Granja
Department of Earth Science, University of Minho, CIIMAR, Braga, Portugal

A. Kallel et al. (eds.), *Selected Studies in Environmental Geosciences and Hydrogeosciences*, Advances in Science, Technology & Innovation, https://doi.org/10.1007/978-3-031-43803-5_19

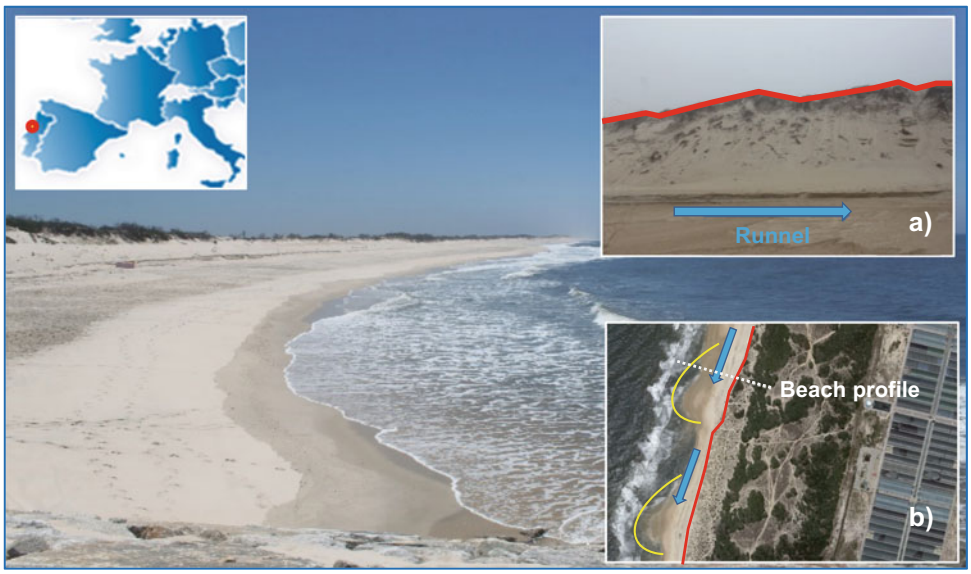

Fig. 1 Study area location. Dune cliff being eroded at the base by a runnel flow (**a**). Complex morphology of the beach with a sudden variation of beach width, rhythmic systems of runnels, micro-cliffs at the dune base, and local enlargements of the beach (**b**)

2 Methods

The monitoring program for this sector, in progress since 2007, includes bathymetric and topographic surveys, collection, analysis, and characterization of sediments and field observations (Bio et al., 2015). Nine beach profiles are regularly measured using a DGPS, five sediment samples were collected along each profile, and bathymetric data was obtained recurring to sonar techniques. Size sediments were characterized at laboratory and georeferenced data processed recurring to GIS.

3 Results

Figure 2a presents results related to the evolution registered between May 2008 and June 2016 in one of the beach profiles located in the central part of the coastal stretch that is being observed. A significant setback of the erosion cliff has been observed and verified by the measurements carried out which point to about 50 m in ten years.

Figure 2b synthesizes results obtained for sediment sizes and beach slopes. The majority of the sediments are medium sand which seems to be the major factor that is controlling the beach face slopes.

4 Discussion

Contrary to what was mentioned in the previously referred works, during the monitored period there was an erosive trend that progressed toward the south, having already reached the end of the section under observation (located circa 6 km from the southern groin of Mira beach). Between the two groins, there is relative stability induced by the action of these defense works. Immediately to the south of the groins, morphological variations are evident, having partially destroyed the southern groin (meanwhile repaired) due to the installed erosive process. Since the erosional process to the south took place, with the formation of an erosion cliff on the dune, no recovery in this sector has been observed to date. The dunes appear to be the predominant sedimentary source (as in other beaches in the world, Pilkey & Cooper, 2014) but, although it presents appreciable sedimentary reserves, its dimensional characteristics do not allow the beach to recover to previously observed morphology. In fact, once formed, the cliff continues, in general, to be eroded by the action of the waves (especially low and steep waves), offshore wind, and precipitation. The dimension of the sediments—medium sands—favoring low-slope profiles (e.g., McLean & Kirk, 1969), allied to a reduced width of the beach that doesn't promote the existence of berms, will contribute to process progression. Besides the storm action dominant in dune erosion, during fair weather conditions (swell waves) the base of the dunes is also submitted to erosion by the existence of occasional longitudinal runnels (coexisting with other beach features like micro-cliffs at the dune base and local beach enlargements that together form a pattern successively repeated along the coastal stretch, alternation of dissipative and intermediate beach states) (Fig. 1a, b).

5 Conclusion

The presented results highlight the high fragility of important sectors of the Portuguese coast since they are now fed almost exclusively by the sedimentary reserves of the dunes, providing sediments of smaller dimensions that imply new

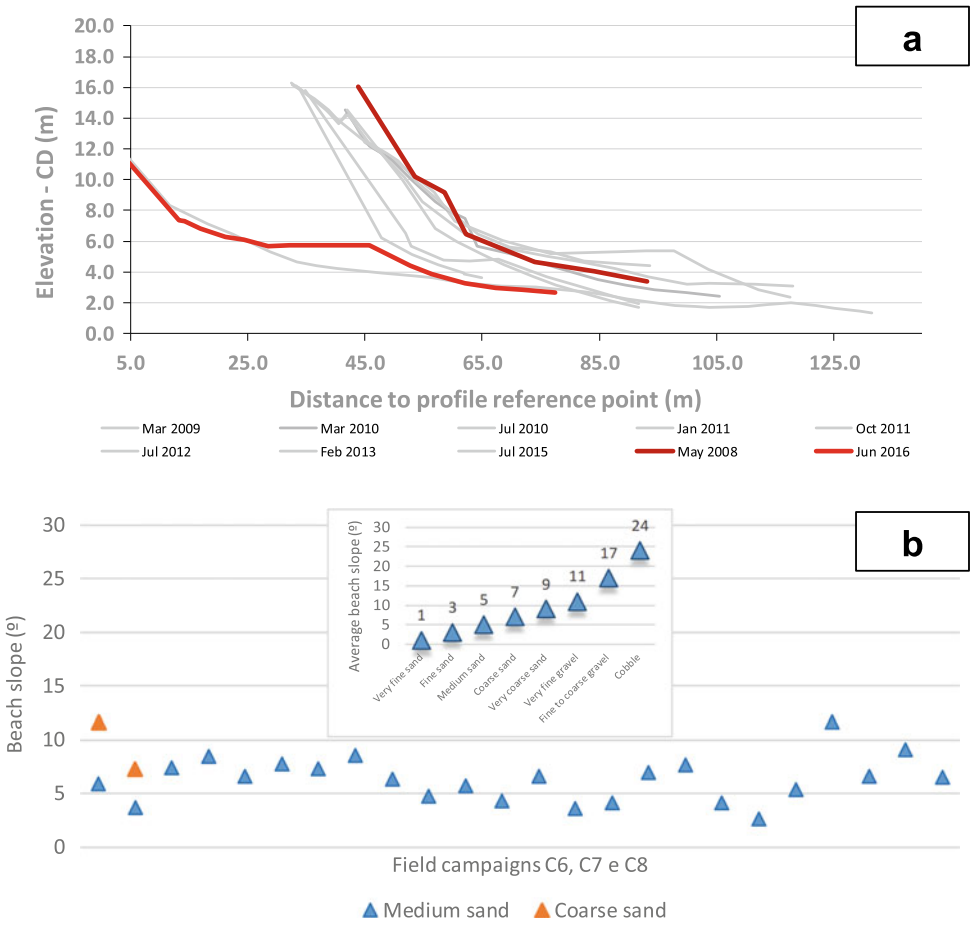

Fig. 2 Evolution of the beach profile located at the central part of the stretch that is being monitored (**a**). Beach face slopes and sediment sizes (**b**)

beach equilibria morphology fighting against low and steep waves for long periods. Solutions should therefore be considered. However, they should not be limited to the preservation of the dune on its surface (e.g., installation of dune fences) but seek more effective alternatives (underwater), so that they are not destroyed by the action of the sea.

References

Bio, A., Bastos, L., Granja, H., Pinho, J., Gonçalves, J., Henriques, R., Madeira, S., Magalhães, A., & Rodrigues, D. (2015). Methods for coastal monitoring and erosion risk assessment: Two Portuguese case studies. *Revista De Gestão Costeira Integrada Journal of Integrated Coastal Zone Management, 15*, 47–63.

Dias, J. M. A. (2005). Estudo Sintético de Diagnóstico da Geomorfologia e da Dinâmica Sedimentar dos Troços Costeiros entre Espinho e Nazaré. Edição electrónica: w3.ualg.pt/∼jdias/JAD/ebooks.

Lenôtre, N., & Thierry, P. (2002). Methodology to design the coastal erosion layer for EUROSION database. BRGM/PC-51916-FR, 35 p., 7 fig., 1 app.

McLean, R. F., & Kirk, R. M. (1969). Relationships between grain size, size-sorting, and foreshore slope on mixed sand-shingle beaches. *New Zealand Journal of Geology and Geophysics, 12*(1), 138–215.

Menezes, G. M. (2011). Estudo da evolução da linha de costa entre o cabo Mondego e Aveiro: (1958–2010). Dissertação de mestrado. Universidade de Coimbra.

Pereira, C., & Coelho, C. (2013). Mapas de risco das zonas costeiras por efeito da ação energética do mar. *Revista de Gestão Costeira Integrada-Journal of Integrated Coastal Zone Management, 13*(1).

Pilkey, H., & Cooper, J. A. (2014). *The last beach* (p. 236). Duke University Press.

Use of the BCG Henderson Matrix as a Tool for Differentiating Areas by the Cost of Housing, Depending on the Ecological State

Kamila Akhmedinova

Abstract

This article examines the impact of the environmental factor on the cost of residential real estate in the largest cities of Kazakhstan. For the representativeness of the analysis, B. Henderson's BCG diagram was used; the result of which was the determination that the importance of the environmental factor in assessing the cost of housing for the city of Nur-Sultan is reflected in 24% of the areas, against 40% for the city of Alma-Ata.

Keywords

BCG Henderson's matrix • Environmental assessment • Real estate market • Nur-Sultan • Alma-Ata

1 Introduction

Despite the close attention to the problems of environmental safety and sustainable development, to date, the assessment of the environmental factor in determining the value of residential real estate in the Republic of Kazakhstan is an insignificant factor. The concept of prestige is, first of all, embedded in the basis of cost estimation. The lack of such an assessment is one of the most pressing problems in the analysis of the value of residential real estate. Therefore, the author proposes his own developed methodology.

The aim of the work is to substantiate the use of the BCG matrix as a tool for assessing the impact of environmental factors on the formation of prices for residential real estate on the example of the largest cities of Kazakhstan: Nur-Sultan and Alma-Ata.

To achieve the goal, the following tasks were set:

- collection of factual data: official statistical and GIS information on the state of the environment in the studied cities;
- analysis of the real estate market for each capital;
- mapping of environmental characteristics and distribution of price indicators for the studied cities;
- analysis of tools for assessing the impact of environmental characteristics on the differentiation of prices for residential property;
- development of our own estimation algorithm and construction of an influence model using stochastic analysis by the method of pairwise comparison and correlation estimation using the BCG matrix.

2 Materials and Methods

For this, the Pearson correlation criterion and the differentiation of areas obtained by applying the method of hierarchy analysis (Akhmedinova, 2020) were used. According to this method, a pairwise comparison of all habitats is carried out by ecological factors: air pollution, hydrosphere pollution, soil pollution, noise pollution, radiation pollution, and landscaping of the territory. Based on the above-described methodology, maps were compiled for all factors, intermediate and integral, with the full environmental load (Figs. 1 and 2). After overlaying the map of the cost per square meter, which we obtained using open sources (Real Estate in Kazakhstan, 2020), the B. Henderson's BCG diagram (Pearce, 2000) was used to represent the analysis.

3 Results

As a result of using the BCG matrix, five categories were identified:

K. Akhmedinova (✉)
RUDN University, 117198 Moscow, Russia
e-mail: akhmedinovakamila@gmail.com

A. Kallel et al. (eds.), *Selected Studies in Environmental Geosciences and Hydrogeosciences*,
Advances in Science, Technology & Innovation, https://doi.org/10.1007/978-3-031-43803-5_20

Fig. 1 Location of the cities under study

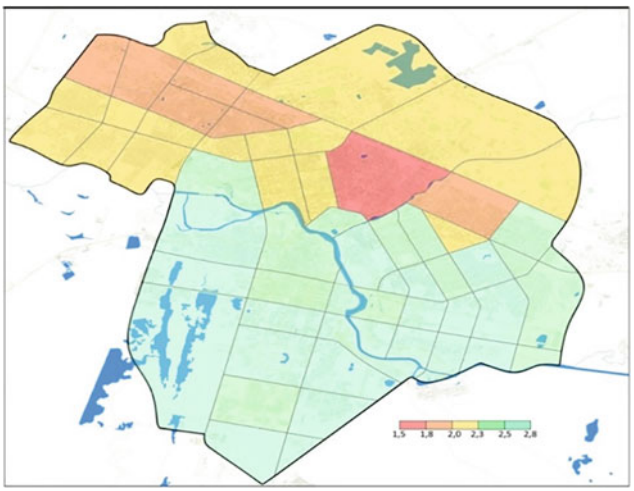

Fig. 2 Final assessment of the areas of Nur-Sultan

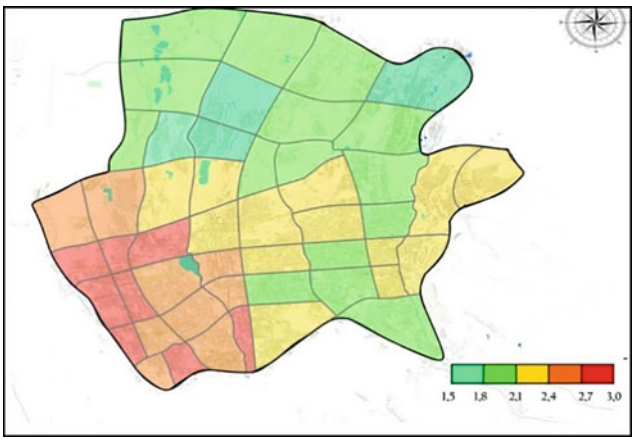

Fig. 3 Final assessment of the areas of Alma-Ata

- 1st category—This category is characterized by the highest values for the assessment of areas and the lowest values of the cost per square meter.
- 2nd category—This category is characterized by high values for the assessment of areas and the highest cost per square meter.
- 3d category—This category is characterized by the minimum values of the assessment of areas and the highest cost per square meter.
- 4th category—This category is characterized by the lowest values of the assessment of areas and the lowest cost per square meter.
- 5th category—This category is characterized by the average values of the assessment of areas and the cost per square meter (see Figs. 3, 4 and 5).

4 Discussion

Nur-Sultan city. The first category includes 8 areas of the city, which is 16%, the second includes 10 areas of the city, which is 20%, in the third category—1 area, which is 2%, in the fourth—2 areas, which is 4%, in the fifth category—29 areas of the city or 58%. Since 2 and 4 are significant categories for analysis, the importance of the environmental factor in assessing the cost of housing for the city of Nur-Sultan can be identified for 24% of the areas.

The city of Alma-Ata. 9 areas of the city fall into 1 category, 13 areas of the city (26%) fall into the second category, only 4 areas belong to the third category, 7 areas belong to the fourth category (14%), and 17 areas belong to the fifth category. Thus, the importance of the environmental

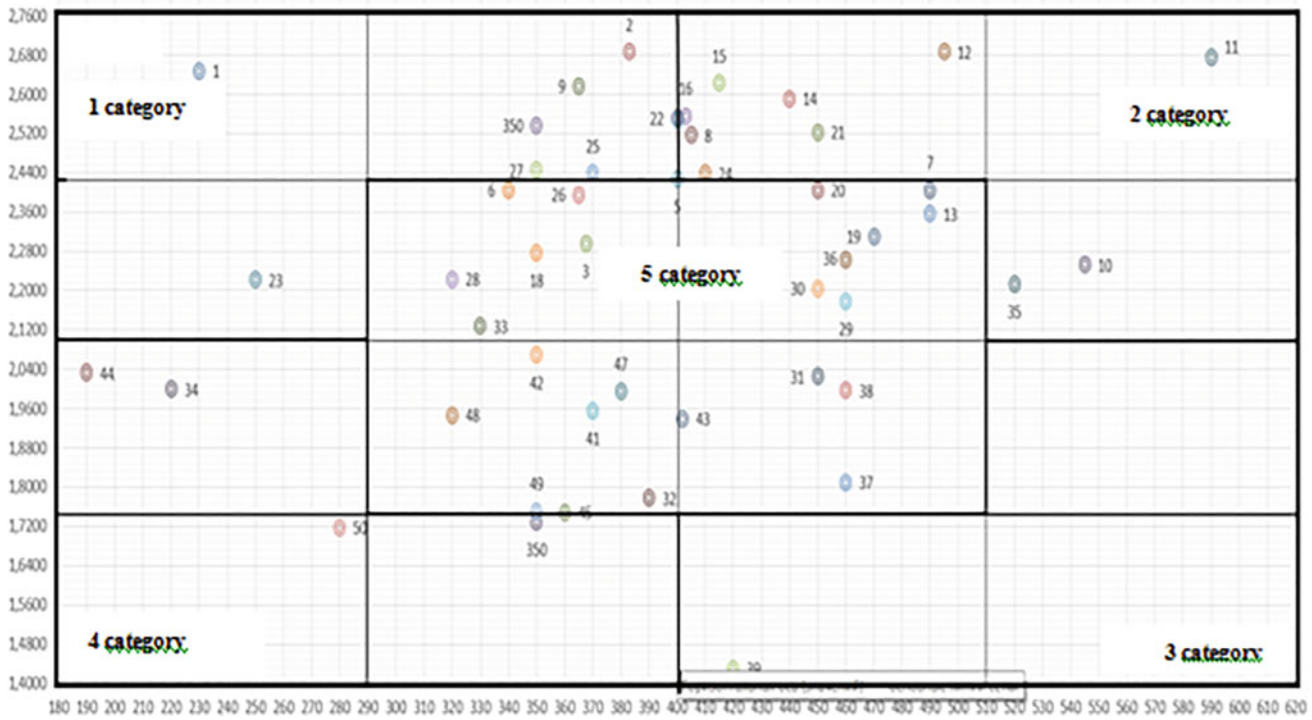

Fig. 4 Diagram of the relationship between the value of the ecological assessment of areas and the average cost per square meter in different micro-districts of Nur-Sultan

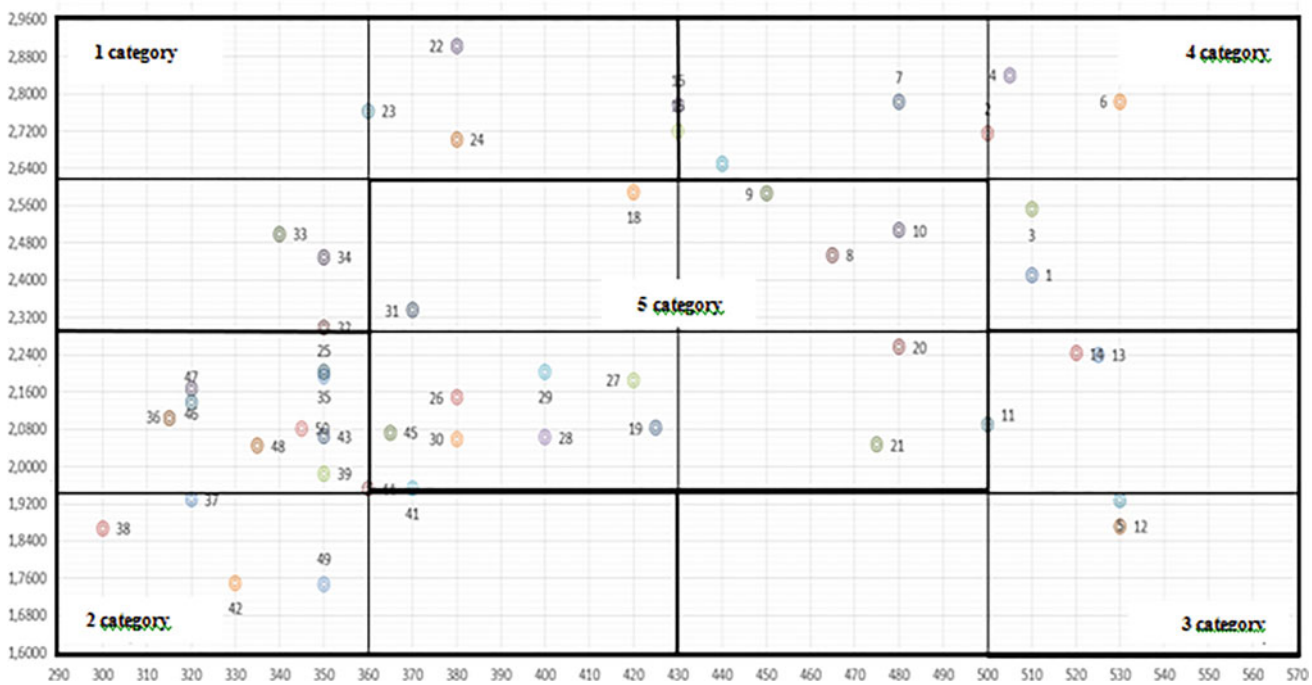

Fig. 5 Diagram of the relationship between the value of the ecological assessment of areas and the average cost per square meter in different micro-districts of Alma-Ata

factor in assessing the cost of housing for the city of Alma-Ata is reflected in 40% of the areas.

5 Conclusions

The Henderson Matrix is not limited to marketing. The use of the author's methodology proves that this tool can also be useful for a representative analysis of the dependences of economic and environmental characteristics. Thanks to the clarity of the matrix diagram, it was possible to establish the categories (2, 4), that is, the areas of the city, where the value of the environmental factor is reflected in housing prices. However, it should be noted that high attractiveness and prestige remain an important factor in the pricing of residential real estate in Kazakhstan. To change this situation, a prerequisite is the rebranding of the entire urban development.

References

Akhmedinova, K. (2020). Determining the environmental situation as a factor in the differentiation of housing prices in Nur-Sultan by using the analytic hierarchy process. *E3S Web of Conferences, 169*, 02017.

Pearce, J. A (2000). *Strategic management: Formulation, implementation, and control*. In J. A. Pearce II & R. B. Robinson, Jr. (Eds). Irwin/McGraw-Hill.

Real Estate in Kazakhstan. (2020). https://krisha.kz. Last accessed 2020/09/20

Mercury Exposure from Artisanal Small-Scale Gold Mining in Bunikasih, West Java, Indonesia

Idham Andri Kurniawan, Mirzam Abdurrachman, Masayuki Sakakibara, Kuang Xiaoxu, Irwan Meilano, Nurcahyo Indro Basuki, I. Gusti Bagus Eddy Sucipta, and Adzkia Noerma Arifa

Abstract

Artisanal small-scale gold mining (ASGM) is one of the major sources of mercury pollution in Indonesia. The village of Bunikasih, near Bandung, the capital city of West Java, is an ASGM operation that has developed since 1993. We investigated mercury exposure of soil and tea leaves from this village as dependent on the distance from the mining source and altitude using X-ray fluorescence and reducing-vaporization mercury analyzer, respectively. The results show that soil has much greater mercury contamination compared to tea leaves. The mercury concentration of the soil decreases with increasing distance from the source, while the mercury in tea leaves shows that mercury could spread 30 m in altitude. The mercury concentrations of soil samples exceeded critical toxicological limits.

Keywords

ASGM • Mercury • Soil • Tea leaves

1 Introduction

Mercury pollution is one of the major environmental problems facing Indonesia today with the proliferation of artisanal small-scale gold mining (ASGM) in various regions in Indonesia having a negative impact on the environment (Appleton et al., 2006; Basri et al., 2017; Bose-O'Reilly et al., 2016; Limbong et al., 2005; Prasetia et al., 2018; Tomiyasu et al., 2019, 2020). It is known that there are more than 2 million miners in more than 800 ASGM locations spread throughout Indonesia who produce 100 tonnes of gold every year. Mercury emissions generated from these activities constitute 58% of total national mercury emissions. Mercury pollution can have a clear impact up to around 10 km from the source (Prasetia et al., 2018) and can also accumulate along the food chain, e.g., in cattle (Basri et al., 2017), making it an important element to studying its polluting behavior.

Approximately 50 km south of the city of Bandung, in the village of Bunikasih, ASGM is found (Fig. 1), which has occurred from 1993 until now. This village is located amid tea plantations; as the communities surrounding Bunikasih village, in addition to carrying out tea and agricultural plantation activities, also conduct ASGM to support their livelihoods.

The previous study on mineralization in the Cibaliung section of the area (Subandrio & Basuki, 2010) reported anomalous gold related to veins trending northeast-southwest; additionally, milky quartz with dark gray to black manganese staining is found intermittently over a length of about 800 m. The veins range from one centimeter to a meter in size and the gold averages from 0.3 g per tonne ("g/t") to a high of 24.6 g/t (Subandrio & Basuki, 2010). On the basis of the abovementioned background, the aim of this study was to investigate the environmental pollution, especially of mercury, surrounding ASGM areas in this location.

2 Materials and Methods

We investigated whether mercury exposure of soil and tea leaves from Bunikasih village depended on the distance from the ASGM and altitude. In total, six samples of soil and five samples of tea leaves were collected. Surface soil

I. A. Kurniawan (✉) · M. Abdurrachman · N. I. Basuki · I. G. B. E. Sucipta · A. N. Arifa
Petrology, Volcanology and Geochemistry Research Group, Bandung Institute of Technology, Bandung, 40132, Indonesia
e-mail: idham@itb.ac.id

M. Sakakibara · K. Xiaoxu
Research Institute for Humanity and Nature, Kyoto, Japan

I. Meilano
Geodesy Research Group, Bandung Institute of Technology, Bandung, 40132, Indonesia

A. Kallel et al. (eds.), *Selected Studies in Environmental Geosciences and Hydrogeosciences*, Advances in Science, Technology & Innovation, https://doi.org/10.1007/978-3-031-43803-5_21

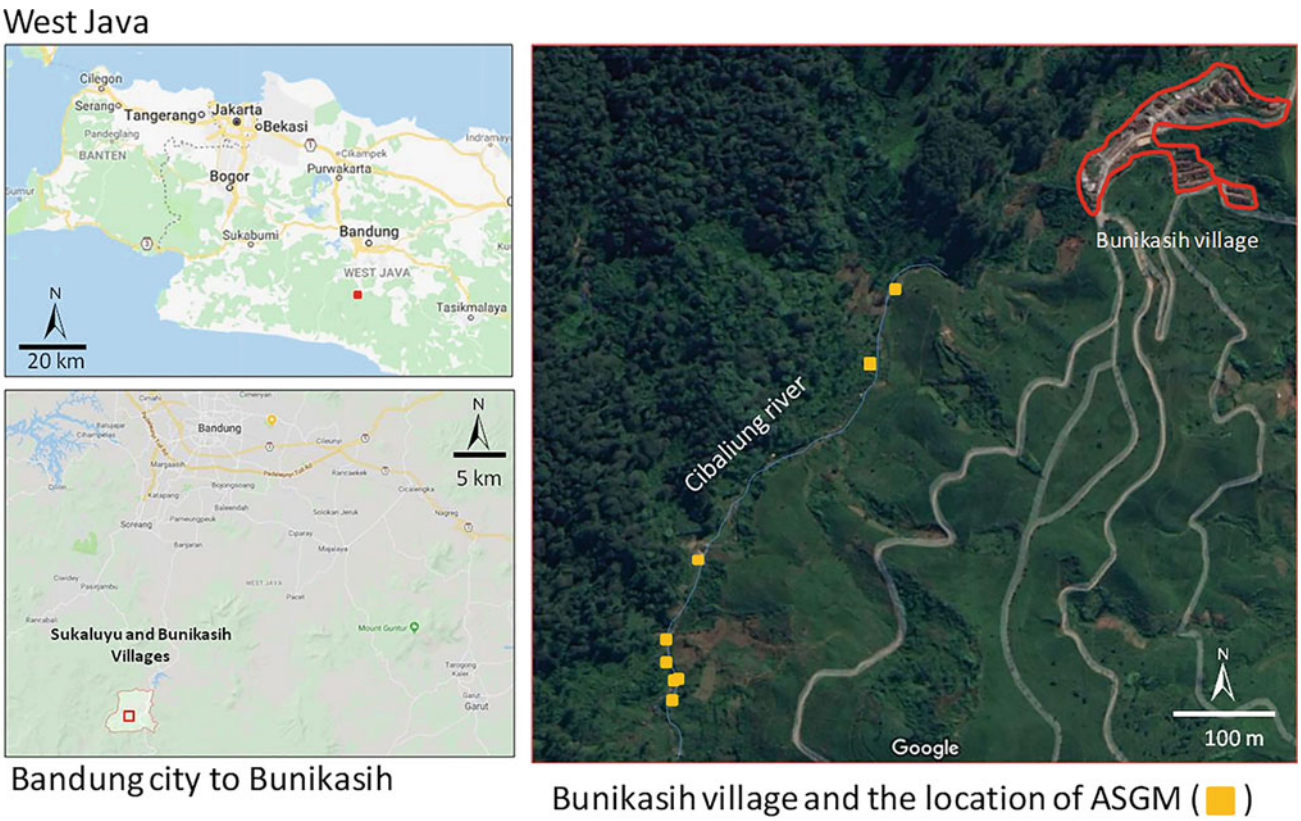

Fig. 1 Location of ASGM in Bunikasih village, West Java, Indonesia

samples were collected 50 to 100 cm from the river, except for one sample that was collected approximately 100 m away from the river. Tea leaves were mature leaves collected from 40 to 60 cm above ground level at different altitudes (1400–1430 m asl).

For soil samples, a total of 10 g was crushed to $\leq$ 50 m, and geochemistry measurements were performed using a Titan S1 handheld X-ray fluorescence (pXRF) spectrometer (Bruker, Berlin, Germany); the precision of this instrument is $\pm$ 0.5%. Tea leaf samples were analyzed using a reducing-vaporization mercury analyzer (RA-4300; Nippon Instruments, Tokyo, Japan).

3 Results

Figure 2 shows the decreasing mercury concentration in the soil with increasing distance from the mercury source area. The range of mercury concentrations was 185 to 446 mg kg^{-1}. Sample number 1 is not contaminated by mercury because of its location away from rivers.

The range of mercury concentrations in the tea leaves was much lower than the soils at 0.45 to 0.72 mg kg^{-1}. Figure 3 shows the decreasing mercury concentration of the leaves along with the increasing altitude and distance from the mercury source. The mercury exposure could spread until at least 30 m of difference in altitude (1400–1430 m asl).

4 Discussion

Soil samples showed very high mercury concentrations that were higher than other studies of soil mercury contamination in Java (e.g., < 57.4 mg kg^{-1} at Pongkor (Tomiyasu et al., 2020)) and other Indonesian islands (e.g., c. 5 mg kg^{-1} in North Sulawesi (Limbong et al., 2005))—this could be explained by the samples being collected close to the stream where mercury may be transported in suspended particulate matter that can have particularly high mercury concentrations (Appleton et al., 2006; Tomiyasu et al., 2019). However, it may also be due to the use of pXRF which analyzes the top few millimeters of the samples, and mercury concentrations are likely to be lower in deeper soil layers (Tomiyasu et al., 2020). Soil mercury concentrations at the Bunikasih area were greater than the Indonesian National Standard of 0.5 mg kg^{-1} and those of many other nations such as UK, USA, and The Netherlands (Appleton et al., 2006). The decline in mercury concentrations away from the ASGM source is as expected given the dilution in the running water which has already been seen in similar studies

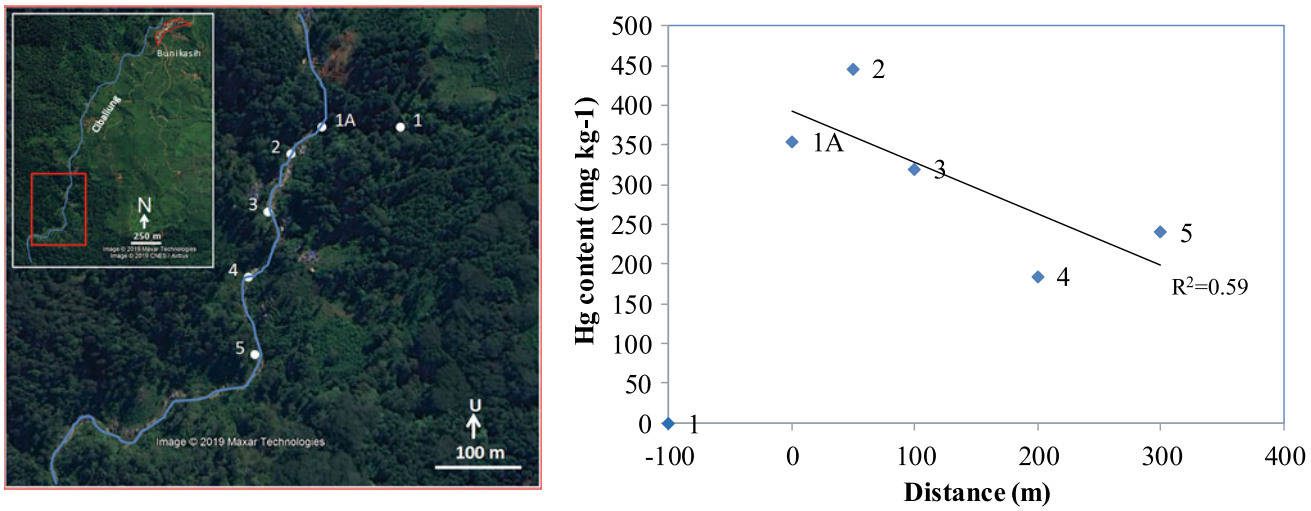

Fig. 2 Mercury concentration of soil samples related to the distance from the ASGM mercury source at Bunikasih village, West Java, Indonesia

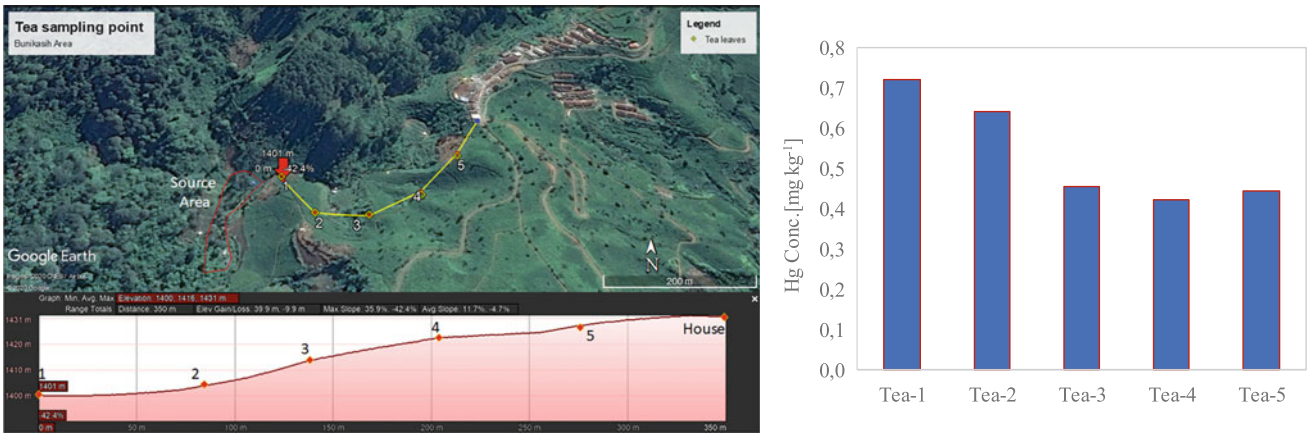

Fig. 3 Mercury concentration of tea leaves and the different altitudes (1400–1430 m asl) from the ASGM mercury source at Bunikasih village, West Java, Indonesia

(Barkdull et al., 2019; Tomiyasu et al., 2019). Mercury concentrations in the tea leaves were at much lower concentrations but with an order of magnitude greater than foliar mercury concentrations at greater distances from the point source of pollution (Obrist et al., 2011). Mercury in tea leaves, therefore, only presents a low–moderate hazard.

5 Conclusions

This study concludes that the area around Bunikasih village is contaminated by mercury. Soil has much greater contamination compared to the tea leaves but concentrations of mercury in both soils and leaves declined with distance from the ASGM source.

References

Appleton, J. D., Weeks, J. M., Calvez, J. P. S., & Beinhoff, C. (2006). Impacts of mercury contaminated mining waste on soil quality, crops, bivalves, and fish in the Naboc River area, Mindanao, Philippines. *Science of the Total EnVironment, 354*, 198–211.

Barkdull, N. M., Carling, G. T., Rey, K., & Yudiantoro, D. F. (2019). Comparison of mercury contamination in four Indonesian watersheds affected by artisanal and small-scale gold mining of varying scale. *Water, Air and Soil Pollution, 230*, 214.

Basri, Sakakibara M, Sera K and Kurniawan I A: Mercury contamination of cattle in artisanal and small-scale gold mining in Bombana, Southeast Sulawesi, Indonesia *Geosciences* 7: 133 (2017).

Bose-O'Reilly, S., Rudolf, S., Dennis, N., Uwe, S., Jossep, F. W., Fradico, T. O., & Yuyun, I. (2016). A preliminary study on health effects in villagers exposed to mercury in a small-scale artisanal gold mining area in Indonesia. *Environmental Research* 149: 274–281 (2016).

Limbong, D., Kumampung, J., Ayhuan, D., Arai, T., & Miyazaki, N. (2005). Mercury pollution related to artisanal gold mining in north Sulawesi Island, Indonesia. *Bulletin of Environmental Contamination and Toxicology, 75*, 989–996.

Obrist, D., Johnson, D. W., Lindberg, S. W., Luo, Y., Hararuk, O., Bracho, R., Battles, J., Dail, D. B., Edmonds, R. L., Monson, R. K., Ollinger, S. V., Pallardy, S. G., Pregitzer, K. S., & Todd, D. E. (2011). Mercury distribution across 14 U.S. forests. Part I: Spatial patterns of total Hg concentrations in biomass, litter, and soils. *Environmental Science and Technology, 45*, 3974–3981.

Prasetia, H., Sakakibara, M., Omori, K., Laird, J., Sera, K., & Kurniawan, I. A. (2018). *Mangifera indica* as bioindicator of mercury atmospheric contamination in an ASGM area in North Gorontalo Regency, Indonesia. *Geosciences, 8*, 31.

Subandrio, A. S., & Basuki, N. (2010). Alteration and vein textures associated with gold mineralization at the Bunikasih area, Pangalengan, West Java. *Jurnal Geologi Indonesia, 5*, 247–261.

Tomiyasu, T., Hamada, Y. K., Bransono, C., Kodamatani, H., Matsuyama, A., Imura, R., Hidayati, N., & Rahajoe, J. S. (2020). Mercury concentrations in paddy field soil and freshwater snails around a small-scale gold mining area, West Java, Indonesia. *Toxicology and Environmental Health Sciences, 12*, 23–29.

Tomiyasu, T., Hamada, Y. K., Kodamatani, H., Hidayati, N., & Rahajoe, J. S. (2019). Transport of mercury species by river from artisanal and small-scale gold mining in West Java, Indonesia. *Environmental Science and Pollution Research, 26*, 25262–25274.

Soil Mercury Along an Elevation Gradient in Northern Borneo

Francis Q. Brearley, Giacomo Sellan, David McKendry, Sukaibin Sumail, and Antony van der Ent

Abstract

The biogeochemical cycling of mercury (Hg) is an important topic of study due to the health implications of the release of this toxic element in the environment. Tropical ecosystems have been understudied, and examining elevational gradients can provide insights into mechanisms controlling soil Hg concentrations. The aim of this study was to determine soil Hg and its provenance along an elevation gradient (800–4100 m a.s.l.) on two mountains in Sabah, Malaysian Borneo. We took samples from soil profiles (5 depths) in minimally disturbed tropical forests from Mount Tambuyukon and Mount Kinabalu. The samples were acid-digested then analysed using a hydride generation ICP-OES technique. Mercury concentrations varied between 35.0 and 876 ng g^{-1} with a mean of 277 ng g^{-1} that was greater than many other 'undisturbed' forests. The highest Hg concentrations were found at mid-elevations where cloud cover was most persistent and Hg:Ti ratios suggested that a greater proportion of Hg at these elevations was from anthropogenic sources—particularly in surface soil horizons. If high Hg concentrations are common in this region, soil degradation in future could be an unanticipated source of future Hg release to the environment.

Keywords

Borneo • Mercury • Mountain • Soil

F. Q. Brearley (✉) · G. Sellan · D. McKendry
Manchester Metropolitan University, Manchester, M1 5GD, UK
e-mail: f.q.brearley@mmu.ac.uk

S. Sumail
Sabah Parks, Kota Kinabalu, 88806 Sabah, Malaysia

A. van der Ent
University of Queensland, St Lucia, Brisbane, QLD 4072, Australia

1 Introduction

Mercury (Hg) is a persistent and bio-accumulative environmental pollutant that is globally distributed; it is released to the atmosphere through industrial processes and, particularly, in tropical settings, artisanal gold mining processes. Soil plays a key role in the Hg cycle by acting as a sink for Hg via atmospheric deposition and litterfall, but also through releasing it to other environmental compartments with the potential for major impacts upon human health (O'Connor et al., 2019; Obrist et al., 2018). With the recent signing of the Minamata Convention, it is hoped that Hg emissions will be reduced but there will still be legacy pollution effects and Hg release from the soil for many years to come. Because of its environmental persistence, Hg can be transported long distances from its sources reaching remote areas with minimal disturbance, including many mountainous areas. Examining elevational patterns of soil Hg is important because it can provide clues to the relative importance of edaphic and climatic factors on Hg sequestration and determine which ecosystems are most at risk of Hg accumulation. We might expect Hg deposition to increase with elevation due to increased precipitation and lower temperatures slowing Hg release from soil (Tripathee et al., 2019), but case studies from different locations are not always in agreement. For example, Zhang et al. (2013) found a decline in soil Hg concentrations with elevation, whereas other authors found an increase (Blackwell & Driscoll, 2015; Tripathee et al., 2019) or contrasting patterns depending upon the location (Gong et al., 2014). Importantly, the elevation gradients studied above were often truncated (i.e., missed lower elevations). Additionally, there is surprisingly little data on soil Hg concentrations from tropical South-east Asia, and we, therefore, present the first elevation gradient to assess soil Hg concentrations in this region.

A. Kallel et al. (eds.), *Selected Studies in Environmental Geosciences and Hydrogeosciences*, Advances in Science, Technology & Innovation, https://doi.org/10.1007/978-3-031-43803-5_22

2 Materials and Methods

Soil samples were collected in 2014 from two mountains within Kinabalu Park, Sabah, Malaysian Borneo, where mean annual rainfall is 2300 mm $year^{-1}$ and the lapse rate is 0.55 °C 100 m^{-1} (Kitayama & Aiba, 2002). Mount Tambuyukon has mostly ultramafic geology, whereas Mount Kinabalu has a mixed geology including ultramafic, granite, and sedimentary rocks. A sampling station was established every ~100 m on Mount Tambuyukon from 800 to 2600 m a.s.l. and every ~200 m on Mount Kinabalu from 2000 to 4000 m a.s.l. where a soil pit was dug and samples were collected from 5, 15, 30, and 50 cm depth along with a litter layer sample. About 10 g of soil was collected from each depth and dried immediately in silica gel. The samples were homogenized, and 0.5 g was digested in HNO_3 and HCl in a CEM Mars Xpress microwave in sealed PTFE tubes. For quality control, Strawberry Leaves (LGC7162) and Soil (GBW 07,403) certified reference materials were analysed alongside the samples with recoveries of 102 ± s.d. 28% and 104 ± 13%, respectively. Digests were analysed on a Thermo Scientific iCAP6300 ICP-OES using a hydride generation technique. Titanium was analysed by ICP-OES in 'normal' running mode and the Hg:Ti ratio was calculated to suggest the provenance of Hg, i.e., anthropogenic or geogenic (Zhang et al., 2013).

We tested the influence of elevation and depth on soil Hg concentrations and Hg:Ti ratios using linear mixed models (*lme4* package version 1.1–2) (Bates et al., 2020). We chose the best model based on the lowest Akaike Information Criterion (AIC) among four models that included elevation, sampling depth, an additive, and a multiplicative interaction among these two as fixed effects; the mountain was included as a random effect. We calculated the conditional and marginal r^2 with the *r²_nakagawa()* function in the *performance* package (version 0.4.6) (Lüdecke et al., 2020). We further investigated the influence of elevation and depth on the Hg:Ti ratio separately for the two mountains using linear models with the same structure as above, but without random terms, and chose the best model based on the lowest AIC.

3 Results

Soil Hg concentrations across all 155 samples had a mean value of 277 ng g^{-1} but exhibited a broad range along the elevation and soil depth gradients from 35.0 to 876 ng g^{-1} (Fig. 1). Soil Hg concentrations were influenced by elevation but not soil depth (Table 1), showing a mid-elevation peak with the greatest concentrations between around 1500 to 2500 m a.s.l. (Fig. 1). The Hg:Ti ratios also showed a mid-elevation peak (Table 1), but this was at a lower elevation than where Hg concentrations were greatest (1000 to 1500 m). For the Hg:Ti ratios, there were indications of an interaction with soil depth as well on Mount Kinabalu, suggesting that a greater proportion of this Hg was from anthropogenic sources, particularly in upper soil layers at these elevations.

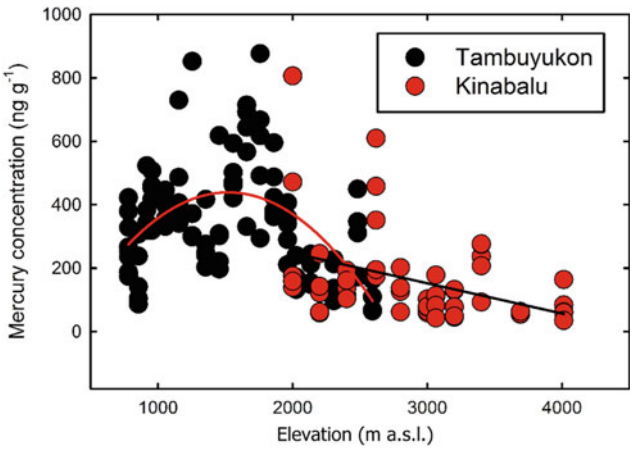

Fig. 1 Soil Hg concentrations on two mountains (Mount Kinabalu and Mount Tambuyukon) in Sabah, Malaysian Borneo. Samples were collected from five depths at each elevation, but this is not shown as there was no significant effect of depth on Hg concentrations

4 Discussion

We show here some clear patterns of soil Hg with a mean Hg concentration of 277 ng g^{-1} but with a broad range along the elevation gradient on these two mountains in Borneo. Nevertheless, our mean value was higher than many other studies of supposedly non-polluted sites from various sites around the world (Blackwell & Driscoll, 2015; Gómez-Armesto et al., 2020; Gong et al., 2014; Tripathee et al., 2019; Zhang et al., 2013) although some Amazonian locations had comparable soil Hg concentrations (Grimaldi et al., 2008), perhaps due to the increased concentrations of soil Fe that can form complexes with Hg (Gómez-Armesto et al., 2020; Grimaldi et al., 2008). It was somewhat surprising that there was no effect of sampling depth on Hg concentrations as Hg has a strong affinity for organic matter (Gómez-Armesto et al., 2020; Gong et al., 2014), which will be greater in the upper soil layers. However, the lack of a clear depth stratification suggests that much of the Hg must be geogenic although the anthropogenically derived Hg (i.e., greater Hg:Ti ratio) was more strongly associated with the upper soil layers and leaf litter on Mount Kinabalu. Nevertheless, Hg can be quite mobile in soil, particularly in illuviated soils (Lüdecke et al., 2020), so this could explain the reason for a minimal depth effect on Hg concentrations, and we do sometimes see high Hg:Ti ratios in deeper soil layers.

Table 1 Best-fitting linear mixed models (both mountains) and linear models (single mountains) explaining the difference in soil Hg concentration and soil Hg:Ti ratios for soils collected on two mountains (Mount Kinabalu and Mount Tambuyukon) in Sabah, Malaysian Borneo

	Mountain	Model	AIC	Conditional r^2	Marginal r^2	Adjusted r^2
Hg concentration	Both	Elevation	1978.5	0.24	0.16	NA
Hg:Ti ratio	Both	Elevation	1400.4	-	0.14	NA
Hg:Ti ratio	Tambuyukon	Elevation	931.8	NA	NA	0.08
Hg:Ti ratio	Kinabalu	Elevation × depth	407.7	NA	NA	0.16

AIC Akaike Information Criterion, *NA* Not applicable

The clear mid-elevation peak in Hg concentrations around 2000 m elevation can be explained by the prevalence of a cloud cap with the lower limit of cloud cover at around 2000 m on Mount Kinabalu (Kitayama, 1995) and slightly lower at about 1600 m on Mount Tambuyukon (AvdE, pers. obs.) and therefore increased wet deposition of Hg. Declining Hg concentrations above this mid-elevation peak are likely to result from a reduction in vegetation stature and thus reduced input via litterfall (Kitayama & Aiba, 2002) coupled with reduced soil organic matter concentrations. The reduced vegetation cover may also actually increase solar radiation and soil warming and thus Hg volatilization at higher elevations compared to lower elevations with a denser overstorey. Another explanation might be the suggested greater aridity towards the top of Mount Kinabalu (Kitayama, 1995; Kitayama et al., 2014) that would limit wet Hg deposition. Finally, the possibility of greater Hg deposition during the north-west monsoon with air masses coming from the Philippines and depositing more Hg on the exposed eastern slopes rather than the more sheltered southern slopes (our Mount Kinabalu transect) should be considered. Palawan in the southern Philippines has a former Hg mine (Samaniego et al., 2020) as well as artisanal gold mining activities, so it could be the source for much of the Hg deposited in northern Borneo.

5 Conclusions

There is surprisingly little data from South-east Asia from 'non-polluted' sites to compare our data with but, if such comparatively high concentrations are common in this region, soil degradation in future could be an unanticipated source of future Hg release. Overall, our results show potentially complex interactions between geogenic and anthropogenic influences on soil Hg in this tropical location, so future work will use Hg isotopes to unravel the origin of this Hg in greater detail, and we will expand our sampling across the island of Borneo to assess the generality of this pattern.

References

Bates, D., Maechler, M., Bolker, B., Walker, S., Christensen, R. H. B., Singmann, H., Dai, B., Scheipl, F., Groethendieck, G., Green, P., & Fox, J. (2020). Package 'lme4'. Linear Mixed-Effects Models using 'Eigen' and S4. Version 1.1–23. Retrieved from https://github.com/lme4/lme4/.

Blackwell, B. D., & Driscoll, C. T. (2015). Deposition of mercury in forests along a montane elevation gradient. *Environmental Science and Technology, 49*(9), 5363–5370.

Gómez-Armesto, A., Martínez-Cortizas, A., Ferro-Vázquez, C., Méndez-López, M., Arias-Estévez, M., & Nóvona-Muñoz, J. C. (2020). Modelling Hg mobility in podzols: Role of soil components and environmental implications. *Environmental Pollution, 260*, 114040.

Gong, P., Wang, X.-P., Xue, Y.-G., Xu, B.-Q., & Yao, T.-D. (2014). Mercury distribution in the foliage and soil profiles of the Tibetan forest: Processes and implications for regional cycling. *Environmental Pollution, 118*, 94–101.

Grimaldi, C., Grimaldi, M., & Guedron, S. (2008). Mercury distribution in tropical soil profiles related to origin of mercury and soil processes. *Science of the Total Environment, 401*(1–3), 121–129.

Kitayama, K. (1995). Biophysical conditions of the montane cloud forests of Mount Kinabalu, Sabah, Malaysia. In L. S. Hamilton, J. O. Juvik & F. N. Scatena (Eds.), *Tropical montane cloud forests* (pp. 183–197). New York, USA: Springer-Verlag.

Kitayama, K., Ando, S., Repin, R., & Nais, J. (2014). Vegetation and climate of the summit zone of Mount Kinabalu in relation to the Walker circulation. *Arctic, Antarctic Alpine Research*, *46*(4), 745–753.

Kitayama, K., & Aiba, S.-I. (2002). Ecosystem structure and productivity of tropical rain forests along altitudinal gradients with contrasting soil phosphorus pools on Mount Kinabalu Borneo. *Journal of Ecology, 90*(1), 37–51.

Lüdecke, D., Makowski, D., Waggoner, P., & Patil, I. (2020). Package 'performance'. Assessment of regression models performance. Version 0.4.6. Retrieved from https://easystats.github.io/performance/.

O'Connor, D., Hou, D., Ok, Y. S., Mulder, J., Duan, L., Wu, Q., Wang, S., Tack, F. M. G., & Rinklebbe, J. (2019). Mercury speciation, transformation, and transportation in soils, atmospheric flux, and implications for risk management: A critical review. *Environment International, 126*, 747–761.

Obrist, D., Kirk, J. L., Zhang, L., Sunderland, E. M., Jiskra, M., & Selin, N. E. (2018). A review of global environmental mercury processes in response to human and natural perturbations: Changes of emissions, climate, and land use. *Ambio, 47*(2), 116–140.

Samaniego, J., Gibaga, C. R., Tanciongco, A., & Rastrullo, R. (2020). Total mercury in soils and sediments in the vicinity of abandoned mercury mine area in Puerto Princesa city Philippines. *Applied Sciences, 10*(13), 4599.

Tripathee, L., Guo, J., Kang, S., Paudyal, R., Huang, J., Sharma, C. M., Zhang, Q., Rupakheti, D., Chen, P., Ghimire, P. S., & Gyawali, A. (2019). Concentration and risk assessment of mercury along the elevation gradient in soils of Langtang Himalayas Nepal. *Human and Ecological Risk Assessment, 25*(4), 1006–1017.

Zhang, H., Yin, R.-S., Feng, X.-B., Sommar, J., Anderson, C. W. N., Sapkota, A., Fu, X.-W., & Larssen, T. (2013). Atmospheric mercury inputs in montane soils increase with elevation: Evidence from mercury isotope signatures. *Scientific Reports, 3*, 3322.

Evaluation of Reliability, Resilience, and Vulnerability Application for Watershed Health Assessment—A Review

Kuswantoro Marko, Dwita Sutjiningsih, and Eko Kusratmoko

Abstract

Watershed monitoring and assessment efforts are essential to do to know the general health status of the watershed. One tool importantly used is the reliability–resilience–vulnerability (R–R–V) framework which is risk-based with the probabilistic statistical method. In principle, this approach looks at how the system fails when the watershed conditions do not comply with the established standards. This paper aimed to evaluate the application of the R–R–V framework due to the indicators and criteria selected through a review of the previous papers from 1982 to 2020. Based on the literature study, the long duration of time-series data is the main requirement for implementing the R–R–V framework. For this reason, the use of remote sensing data to identify landscape conditions in the form of natural land cover is better than relying on observational data. In addition to being a solution to data limitations, it has the ability to be applied to all areas in order to get a quick conclusion about a reliable health level of the watershed.

Keywords

Watershed health assessment • Reliability • Resilience • Vulnerability • Remote sensing

1 Introduction

In many water resource studies, the performance status of the system is expressed as satisfactory or unsatisfactory. Hashimoto et al. (Hashimoto et al., 1982) focused more on system failure analysis by analyzing three main indicators, namely reliability, resilience, and vulnerability (R–R–V) which were then applied to the performance of the reservoir system. This research is a development of previous research conducted by Holling (1973) and Fiering & Holling (1974). This framework was later adopted by Hoque et al. (2012) in the assessment of watershed health. The indicator used is water quality which is the result of reconstruction from limited observational data.

Watershed health assessment with the R–R–V framework is probabilistic (Hashimoto et al., 1982; Hoque et al., 2012; Sadeghi & Hazbavi, 2017) which refers to the frequency and severity of deviations from watershed health indicators against risk. Using risk-based parameters, one can measure the likelihood of deviations from the threshold set at various locations, the likelihood of natural recovery in the event of a threshold violation, and the damage incurred due to the duration spent on the offense (Hoque et al., 2012).

The objective of this paper is to identify the strength and weaknesses of the R–R–V framework in watershed health assessment so that researchers can apply it appropriately based on data availability.

2 Model Conceptual of Reliability, Resilience, and Vulnerability Framework

The first research applying R–R–V was conducted by Hashimoto et al. (1982) which aims to evaluate the performance of water resources systems with case studies on reservoirs, especially in certain conditions such as drought, extreme weather, and high water demand. System performance is evaluated by analyzing system failure, that is, if the

K. Marko (✉) · E. Kusratmoko
Department of Geography, FMIPA, Universitas Indonesia, Depok, 16424, Indonesia
e-mail: kuswantoro@sci.ui.ac.id

K. Marko · D. Sutjiningsih
Department of Civil Engineering, Faculty of Engineering, Universitas Indonesia, Depok, 16424, Indonesia
e-mail: dwita@eng.ui.ac.id

A. Kallel et al. (eds.), *Selected Studies in Environmental Geosciences and Hydrogeosciences*, Advances in Science, Technology & Innovation, https://doi.org/10.1007/978-3-031-43803-5_23

output value does not match the performance threshold. The three criteria are reliability, resilience, and vulnerability.

Reliability (Rel) is a system that can be described by the frequency or probability that a system is in a satisfactory condition:

$$\text{Rel} = \text{Prob}\left[S_{(t)} \in \text{NF}\right] \tag{1}$$

where $S_{(t)}$ is the system state at time t. Resiliency (Res) is how quickly the system returns to a satisfactory state after failure:

$$\text{Res} = \text{Prob}\{S_{(t+1)} \in \text{NF} | S_{(t)} \in \text{F}\}. \tag{2}$$

Vulnerability (Vul) is how severe the consequences of failure are.

$$\text{Vul} = \sum_{j \in F} e_{(j)} h_{(j)}, \tag{3}$$

where $h_{(j)}$ is the most damage that can occur during the *j*th failure event, while $e_{(j)}$ is the probability that $h_{(j)}$ is the greatest possible damage.

Then, Kjeldsen & Rosbjerg (2004) formulate a mathematical definition of reliability, resilience, and vulnerability in time-series data as follows:

$$\text{Rel} = 1 - \frac{\sum_{j=1}^{M} d_{(j)}}{T}, \tag{4}$$

where $d_{(j)}$ is the duration of the *j*th failure event, M is the) number of failure events, and T is the total number of time intervals.

$$\text{Res} = \left\{ \frac{1}{M} \sum_{j=1}^{M} d_{(j)} \right\}^{-1}. \tag{5}$$

For the mathematical formula of vulnerability, Kjeldsen and Rosbjerg (2004) refer to Jinno et al. (1995) which is based on a vulnerability measurement in the total water volume deficit, where v (j) is a deficit event.

$$\text{Vul} = \frac{1}{M} \sum_{j=1}^{M} v_{(j)}. \tag{6}$$

Hoque et al. (2012) clarify by simplifying the vulnerability formula written by Kjeldsen & Rosbjerg (2004), Eq. (6) as follows:

$$\text{Vul} = \frac{1}{M} \sum_{i=1}^{T} \left\{ \left[\frac{L_{\text{obs(i)}} - L_{\text{std(i)}}}{L_{\text{std(i)}}(i)} \right] \text{x } H\left[L_{\text{obs(i)}} - L_{\text{std(i)}} \right] \right\}, \tag{7}$$

where $L_{obs(i)}$ is the parameter load observed at time *i*, $L_{std(i)}$ is the specified threshold, and H[.] is the Heaviside function which ensures that only failed events are involved in the calculation of Vul in Eq. (7).

3 Results

The basic concept of R–R–V is based on the probability of watershed health conditions requiring long time-series data, as was done by Hashimoto et al. (1982). So that, the health assessment of the watershed is based on a few indicators only. Previous research using water quality indicators was conducted by Hoque et al. (2012, 2014a, b, 2016) in the Cedar Creek and Wildcat Creek USA watersheds, and Mallya et al. (2018) in the Mississippi, Ohio, whereas the Maumee USA watersheds do not have complete data. The criteria assessed are sediment, nutrients, and pesticides. Due to data limitations, a long daily data reconstruction was carried out. Hazbavi & Sadeghi (2017), Hazbavi et al. (2018a, b) conducted research in the Shazand watershed, Iran, by relying on monthly observational data of sediment and nutrients for more than ten years.

The hydrological indicators used consist of rainfall criteria and maximum and minimum river flow rates. The hydrological process in a watershed is strongly influenced by climatic factors; surface and subsurface characteristics such as topography, vegetation, and geology; and human activities such as water and land use (Kjeldsen & Rosbjerg, 2004). Rainfall criteria are widely used in research in Iran such as Sadeghi & Hazbavi (2017), Hazbavi & Sadeghi (2017), Hazbavi et al. (2018a, b). Rainfall is a factor that greatly affects the occurrence of erosion on a land, so it is a major concern for watershed conservation efforts (Hazbavi et al., 2019). Likewise with the flow rate which is a continuation of the process of falling rainwater will carry the load of eroded sediment. Both data are presented over a period of more than 30 years with monthly data collection.

Another indicator that is also used in assessing watershed health is the landscape, which consists of the normalized difference vegetation index (NDVI) criteria and the soil erosion index. These two indicators are strongly influenced by human activities in a watershed. NDVI informs the level of the greenness of the vegetation on the land. The green and broader vegetation indicate that the watershed is healthy. The erosion index shows how much soil erosion occurs due to the interaction between climate, topography, and land cover conditions of a watershed. In the context of changing times, the high erosion index indicates how easy it is for the soil to be eroded by rainwater due to the decrease in vegetation density and area in a watershed. Both indicators are used for the assessment of watershed health in Iran by Hazbavi et al. (2018c, 2019) and Sadeghi et al. (2019).

Table 1 List of reviewed R–R–V framework during the period 2012–2020 along with their applications

References	Indicator	Criteria	Threshold	Duration	Study Area
Hoque et al. (2012)	Water quality (daily data)	Atrazine	3 µg/L	6 years	Indiana, USA
		Alachlor	2 µg/L		
		Ammonia	1.94 mg/L		
		Total phosphorus	0.3 mg/L		
		Sediment	16.2 mg/L		
Hoque et al. (2014a)	Water quality (daily data)	Sediment	30 mg/L	14 years	Indiana, USA
		Kjeldahl nitrogen	0.591 mg/L		
		Nitrate nitrogen	0.633 mg/L		
		Nitrite nitrogen	1 mg/L		
		Total phosphorus	0.076 mg/L		
Hoque et al. (2014b)	Water quality (daily data)	Sediment	16.2 mg/L	13 tahun	Indiana, USA
		Total nitrogen	0.633 mg/L		
		Total phosphorus	0.076 mg/L		
Chanda et al. (2014)	Hydro-climatology (monthly data)	Permanent wilting point based on different soil type	1.6 m (alluvial)	50 years	India
			160 mm (black soil)		
			400 mm (red and laterite)		
			272 mm (de sert)		
Hoque et al. (2016)	Water quality (daily data)	Atrazine	3 µg/L	6 years	Indiana, USA
		Alachlor	2 µg/L		
		Ammonium	1.94 mg/L		
		Total phosphorus	0.3 mg/L		
		Total suspended solids	16.2 mg/L		
Hazbavi & Sadeghi, 2017)	Hydrology water quality (monthly data)	Standardized precipitation index	0.1	38 years	Markazi Province, Iran
		Low flow dis charges	0.16 m^3/s		
		High flow discharges	12.63 m^3/s		
		Suspended sediment concentration	25 mg/L/day		
Hazbavi & Sadeghi, 2017; Hazbavi et al. (2018a)	Hydro-climatology (monthly data)	Standardized precipitation index	+0.1	38 years, 32 years	Iran North Irlandia Portugal
			−0.1		
			−0.1		
Mallya et al. (2018)	Water quality (daily data)	Suspended sediment concentration	30 mg/L	30's years	Mississippi, Ohio, Maumee (USA)
Hazbavi et al. (2018b)	Hydro-climatology	Standardized precipitation index	+ 0.1, −0.1, −0.1	12 years	Iran, North Ireland, Portugal
	Hydrology	Low flow discharges	0.20, 0.01, 46.62 m^3/s		
		High flow discharges	7.50, 3.45, 67.99 m^3/s		
		Suspended sediment concentration	25 mg/L		
	Water quality (monthly data)	Total nitrogen	NA, 5.65, 5.65 mg/L		
		Total phosphate	NA, 0.09, 0.0035 mg/L		

(continued)

Table 1 (continued)

References	Indicator	Criteria	Threshold	Duration	Study Area
Hazbavi et al. (2018c)	Landscape (monthly data)	Normalized difference vegetation index (NDVI)	0.05	1 year	Markazi Province, Iran
Hazbavi et al. (2019)	Landscape (Monthly data)	Soil erosion	5 ton/ha/day	4 years	Markazi Province, Iran
Sadeghi et al. (2019)	Hydro-climatology Hydrology Landscape (monthly data)	Standardized precipitation index	+0.1	4 years	Markazi Province, Iran
		Low flow discharges	0.2 m^3/s		
		High flow discharges	7.5 m^3/s		
		Soil erosion	5 ton/ha/day		
		Normalized difference vegetation index (NDVI	0.05		
Zeng et al. (2020)	Hydro-climatology (monthly data)	Standard precipitation evapotranspiration index (SPEI)	−0.1, −0.5, −0.8 (dryness type)	30 years	China

4 Discussion

Based on the results of the literature review, the strengths and weaknesses can be identified. The strengths are (i) R–R–V framework is a quick assessment for watershed health, (ii) the selection of several indicators or criteria is the best solution in assessing watershed health with the R–R–V framework. The weaknesses are (i) the data required to carry out the analysis must have a long time series, (ii) it is too difficult to apply an integrated assessment of watershed health due to the lack of observational data. Therefore, the potential approach in applying R–R–V is (i) remote sensing approach can be a potential method in getting long-term time-series data either spatially or temporally, (ii) landscape and climatological indicators can be used as the key indicators for a quick assessment and monitoring of the watershed health, (iii) natural land cover conditions can be the main criteria in assessing watershed health, which is a driving factor in determining the hydrological characteristics and water quality of a water body which can also affect habitat and biological conditions (Table 1).

5 Conclusions

The application of the R–R–V framework in assessing watershed health has been carried out by many previous researchers. The long duration of time-series data is the main requirement for implementing the R–R–V framework. For this reason, the use of remote sensing data to identify landscape conditions in the form of natural land cover is better than relying on observational data. In addition to being a solution to data limitations, it has the ability to be applied to all areas and to get a quick conclusion about a reliable health level of the watershed.

Acknowledgements The authors would like to thank the Directorate of Research and Community Engagement (DPRM) University Indonesia for the research funding program Publikasi Terindeks Internasional (PUTI) Doktor in 2020 No. NKB-3359/UN2.RST/HKP.05.00/2020.

References

Chanda, K., Maity, R., Sharma, A., & Mehrotra, R. (2014). Spatiotemporal variation of long-term drought propensity through reliability-resilience-vulnerability based drought management index. *Water Resources Research*.

Fiering, M. B., & Holling, C. S. (1974). Management and standards for perturbed ecosystems. *Agro-Ecosystems, 1*, 301–321.

Hashimoto, T., Stedinger, J. R., & Loucks, D. P. (1982). Reliability, resiliency, and vulnerability criteria for water resource system performance evaluation. *Water Resources Research, 18*(1), 14–20.

Hazbavi, Z., Sadeghi, S. H., & Gholamalifard, M. (2019). Dynamic analysis of soil erosion-based watershed health. *Geography Environment Sustainability, 03*(12), 43–59.

Hazbavi, Z., Baartman, J. E. M., Nunes, J. P., Keesstra, S. D., & Sadeghi, S. H. (2018a). Changeability of reliability, resilience and vulnerability indicators with respect to drought patterns. *Ecological Indicators, 87*, 196–208.

Hazbavi, Z., Keesstra, S. D., Nunes, J. P., Baartman, J. E. M., Gholamalifard, M., & Sadeghi, S. H. (2018b). Health comparative comprehensive assessment of watersheds with different climates. *Ecological Indicators, 93*, 781–790.

Hazbavi, Z., & Sadeghi, S. H. R. (2017). Watershed health characterization using reliability–resilience–vulnerability conceptual framework based on hydrological responses. *Land Degradation and Development, 28*, 1528–1537.

Hazbavi, Z., Sadeghi, S. H., & Gholamalifard, M. (2018c). Landcover based in watershed health assessment. *AGROFOR International Journal, 3*(3), 47–55.

Holling, C. S. (1973). Resilience and stability of ecological systems. *Annual Review Ecology Systems, 4*, 1–23.

Hoque, Y. M., Tripathi, S., Hantush, M. M., & Govindaraju, R. S. (2016). Aggregate measures of watershed health from reconstructed water quality data with uncertainty. *Journal of Environmental Quality*.

Hoque, Y. M., Hantush, M. M., & Govindaraju, R. S. (2014a). On the scaling behavior of reliability-resilience-vulnerability indices in agricultural watersheds. *Ecological Indicators, 40*, 136–146.

Hoque, Y. M., Raj, C., Hantush, M. M., Chaubey, I., & Govindaraju, R. S. (2014b). How do land-use and climate change affect watershed health? a scenario-based analysis. *Water Quality, Exposure and Health, 6*, 19–33.

Hoque, Y. M., Tripathi, S., Hantush, M. M., & Govindaraju, R. S. (2012). Watershed reliability, resilience and vulnerability analysis under uncertainty using water quality data. *Journal of Environmental Management, 109*, 101–112.

Jinno, K., Zongxue, X., Kawamura, A., & Tajiri, K. (1995). Risk assessment of a water supply system during drought. *Water Resources Development, 11*(2), 185–204.

Kjeldsen, T. R., & Rosbjerg, D. (2004). Choice of reliability, resilience and vulnerability estimators for risk assessments of water resources systems. *Hydrological Sciences Journal., 49*(5), 755–767.

Mallya, G., Hantush, M., & Govindaraju, R. S. (2018). Composite measures of watershed health from a water quality perspective. *Journal of Environmental Management*.

Sadeghi, S. H., Hazbavi, Z., & Gholamalifard, M. (2019). Interactive impacts of climatic, hydrologic and anthropogenic activities on watershed health. *Science of the Total Environment*, *648*, 880–893

Sadeghi, S. H., & Hazbavi, Z. (2017). Spatiotemporal variation of watershed health propensity through reliability-resilience-vulnerability based drought index (case study: Shazand Watershed in Iran). *Science of the Total Environment, 587–588*, 168–176.

Zeng, P., Sun, F., Liu, Y., & Che, Y. (2020). Future river basin health assessment through reliability-resilience-vulnerability: Thresholds of multiple dryness conditions. *Science of the Total Environment*.

Iraq's Contemporary Environmental Problems, Their Causes, and Sustainability

Hassan Hassoon ALDelfi

Abstract

The area of the Middle East has been facing tragic and destructive disruption to its environmental, economic, and social aspects in the last one hundred years. These catastrophic issues started ever since the beginning of the twentieth century. Man-made environmental problems experienced in Iraq have inflected grave consequences on Iraq and the region. This article identifies certain environmental issues that have emerged as a result of the wars, conflicts, and extremism that ravaged Iraq which led to ecological destruction in all aspects of living and non-living eco-subsystems. An inductive approach for research has been considered to highlight some environmental issues, such as human loss, human suffering, human displacement, migration, infrastructure destruction, air pollution, water pollution, environmental degradation, soil pollution, and a serious threat to marine life. In this paper, the self-witnessed environmental problems and lately COVID-19 have been highlighted. The socioeconomic hardship affected children, women, and youth who revolted against traditions, identity, and moral values. The regional and international invasion, which followed in 2003, led the Iraqi society to corruption. The lack of a robust legal system in the country has influenced negatively the environmental reforms and basic infrastructure. In this paper, both short-range and long-range solutions to restore and solve environmental issues are presented. The expected outcomes of this research are to bring Iraq's environmental degradation to the attention of the decision-makers of the international community to rectify and safeguard Iraq's fragile ecosystems and degraded infrastructure.

Keywords

Iraqi environmental issues • Human displacements • Degradation • Migration • Infrastructure • Water pollution • Soil • Ecosystem

1 Introduction

The consequences of the wars on Iraq have resulted in irreversible non-curable environmental issues. Until now, there has been no clear assessment of the damages caused by those wars. During all of those wars, certain issues created many damages to Iraq and the region, which include.

- The huge quantities of toxic smoke produced by oil fires and the consequences of acid rains.
- A clear deterioration of medical, health care, and hospital systems.
- A worsening of environmental degradation caused by the continuous bombing campaign.
- The use of Depleted Uranium-enriched weapons represents a major threat to people and the ecosystem.
- An accumulation of pathogenic species on earth and water surface.
- A massive social damage due to human suffering and mass displacement.
- A massive environmental disruption which led to land and habitat destruction, which in turn caused wildlife degradations and extinction (Hassoon AL-Delphi).

1.1 Research Approach

In this work, an applied approach based on inductive reasoning and statistics was adopted. An investigation of specific cases of many governorates with rapid population

H. H. ALDelfi (✉)
Interior Design Department, Faculty of Engineering, Tishk International University TIU, 100 M Road, Erbil, Kurdistan, Iraq
e-mail: hassan.hassoon@tiu.edu.iq

A. Kallel et al. (eds.), *Selected Studies in Environmental Geosciences and Hydrogeosciences*, Advances in Science, Technology & Innovation, https://doi.org/10.1007/978-3-031-43803-5_24

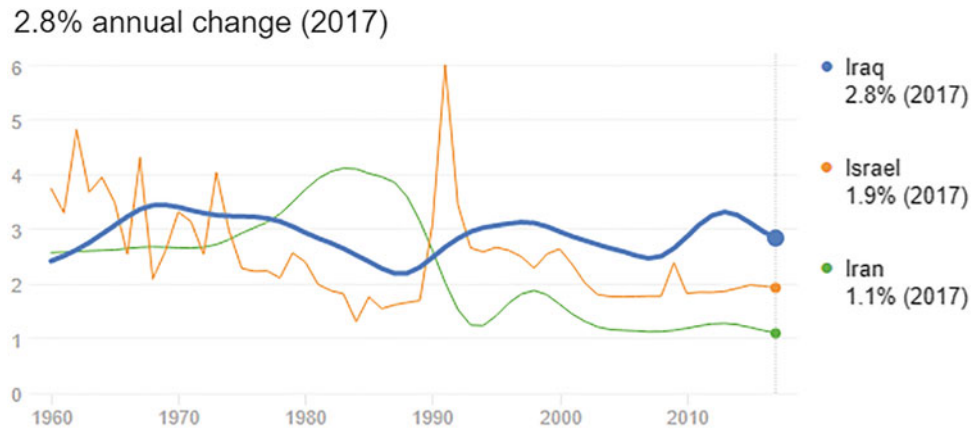

Fig. 1 Annual population change in Iraq up to the year 2017 compared with regional and international trends

growth has been documented by the UN in Iraq (https://iraq.unfpa.org/sites/default/files/pub-pdf/PSA%20English%202012.pdf), (Fig. 1). An annual change in population in the range of 2.8% is considered the highest in the Middle East, while the world average annual change in population is around 1.2% (https://www.google.com/search?q=iraq+population+growth+rate&amrlz=1C1GCEU_enIQ837IQ837&oq=iraq+population+rate&aqs=chrome.1.69i57j0l4., 19060 j1j8&sourceid=chrome&ie=UTF-8). Justified reasoning for the research approach a self-witnessed cases by the author that he experienced throughout the conflict periods.

The study area for the research analysis is based on inductive reasoning, of some cities like Mosul and Baghdad. The middle and southern regions of Iraq both showed considerable ecological degradation and demographic changes. They are considered as hot spot areas and require constant mitigation measures (https://reliefweb.int/sites/reliefweb.int/files/resources/pax-report-living-under-a-black-sky.pdf). The environmental and infrastructure damages are so severe that the author cannot hide emotive gestures, unfortunately. The expected outcomes of this research are to bring the attention of the decision-makers of the international community to rectify and safeguard the Iraqi fragile eco-system, demographic changes, and degraded infrastructure.

2 Results and Discussion

The resulting environmental problems can be categorized as follows:

2.1 Society and Wars

The results of the ever persistence of wars led to a massive emigration of Iraqis to the neighboring countries and the rest of the world. Statistics showed increased migrations of around 4 million following the First Gulf War, including a high percentage of highly qualified individuals, such as university professors, nuclear scientists, engineers, doctors, architects, and chemists. During the First and Second Gulf Wars, Iraq experienced dreadful sanctions from inside and outside. Many qualified individuals had to use depurate shortcuts to get out of the country. As a result, they left behind relatives who paid the consequences of such actions, including torture, imprisonment, and property confiscations. Some individuals' and families' illegal refuge approaches resulted in their loss of life in seas, oceans, and also some were interred in camps and so on. Some refugees were sent back against their will to Iraq after the 2003 invasions. As a result of such family separation miseries, one can say that Iraqi refugees have almost reached the extreme ends of the northern and southern hemispheres.

2.2 The Marshes and Wars

The marshlands of Mesopotamia (Al Ahwar, in Arabic), where civilizations of the Babylonians and Sumerians flourished, are today extremely fragile, despite the fact that some practical efforts have lately been made by the local authorities. The ecosystem forms part of the Tigris and Euphrates rivers' basins, which gives sustenance to Iraq, Turkey, and Syria. The heart of the wetlands lies in southern Iraq, near large cities like Basra along the border with Iran. The bordering areas with Iran are currently suffering from a profound humanitarian crisis, such as cuts of water supply by Turkey and Iran. Between 1973 and 2000, over 85% or 8000 km^2 of the Mesopotamian wetlands' freshwater was destroyed. Later, the United Nations called this catastrophe "one of worst humanity's engineered disasters". Over 80% of the marshes' endemic plants had been uprooted and destroyed to prevent the resistance from using it as a hiding place (https://www.academia.edu/843377/Marshland_of_Cities_Deltaic_Landscapes_and_the_Evolution_of_Early_Mesopotamian_Civilization).

Iraq's marshlands are home to millions of birds. Indeed, the marshes of what is modern-day Iraq are among the most important in the Middle East. As a regional oasis, these marshlands provided fertile land and clean water for millions of people and wildlife for centuries.

2.3 Oil and Wars in Iraq

Environmental pollution has no geographical or political boundaries to cross. Thus, the effect of wars and terrorism on oil was frequent for sabotage. Attacks on oil wells and oil pipelines led to serious consequences for the region since the Gulf War (1991) until now (https://www.hudson.org/research/11787-the-first-gulf-war-and-its-aftermath). Oil is free to access for sabotage whenever conflicts take place, deliberately burnt oil wells caused tremendous air pollution that affected the environment and human health for months.

2.4 Infrastructure and Wars

According to the World Bank, Iraq's human development indicators are among the lowest in the Middle East. Back in the 1970s and 1980s, Iraq led the Middle East in the development of infrastructure, social services, and health care. Yet, after years of successive wars and sanctions, many Iraqi people do not have access to basic staples like potable water and electricity, even today. A shortage of hospitals and healthcare facilities has added to their hardships. Current health statistics on Iraq are difficult to find, but a UNICEF report stated Iraq's mortality rate for children under five rose from 5% in 1990 to 12.5% in 2004. Iraq infant mortality rate was 23.82 in every 1000 for the year 2018. (https://knoema.com/atlas/Iraq/topics/Demographics/Mortality/Infant-mortality-rate).

2.5 Radioactive Toxic and Wars

The extremely dense Depleted Uranium (DU) shells easily penetrate steel armors and burn on impact. The fire releases microscopic, radioactive, and toxic dust particles of uranium oxide that travel with the wind and can be inhaled or ingested. The DU particles are of glassy color and size in the range of 1 μm, normally airborne. They also spread contamination by seeping into the land and water.

In the human body, DU may cause harm to the internal organs due to both its chemical toxicity as heavy metal and its release of radiation. (Hassoon, 2016) The cancer cases in Basra city as an environmental hot spot reached the rate of 320/100,000 of the population (Hassoon, 2016). Iraqi planning indicators and standards are very loose; houses are being built on plot areas less than 50 m^2, and individuals are confiscating pavements for building annexes (https://www.pinterest.com/pin/726698089852481192).

2.6 Corruption

Iraq is considered as one of the most corrupted countries in the world. Coalition forces were doing little to prevent the widespread looting, plundering, and destruction of Iraq's world-famous historical sites (https://www.theguardian.com/artanddesign/2004/aug/31/heritage.iraq). Corruption has spread over the various sectors of society where 500 billion dollars have been lost since 2003. Iraq is considered to be the 12th corrupted country in the world (https://www.kurdistan24.net/en/news/f08498e3-0697-40e9-8c83-4d35728ddcca). In the last two years, the GDP has plunged into the negative according to the World Bank's report. The GDP is an indicator of economic growth, mainly of oil extraction as shown in Fig. 2.

2.7 Absolute Freedom

For many centuries, Iraqi people never experienced freedom in all walks of life. It is therefore very difficult for the Iraqi people to appreciate such freedom. Freedom in Iraq is classified as (FALATAN) where people start to confiscate pavements and green areas for their own use. In addition, many thousands of random settlements have been built in green areas in cities.

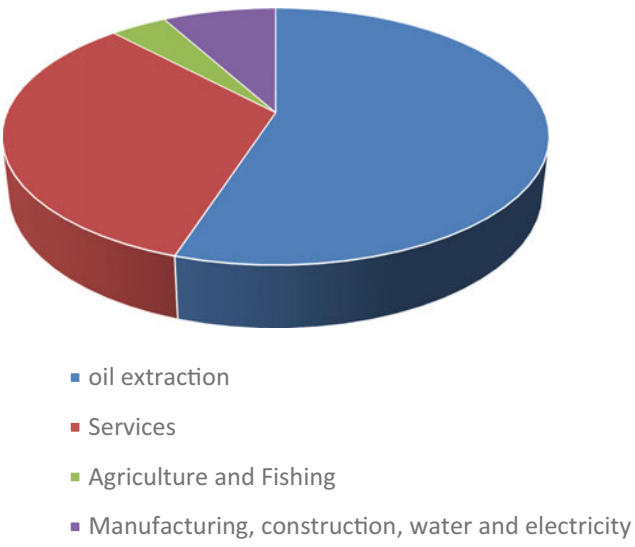

Fig. 2 Order of proportional percentages of Iraq current GDP

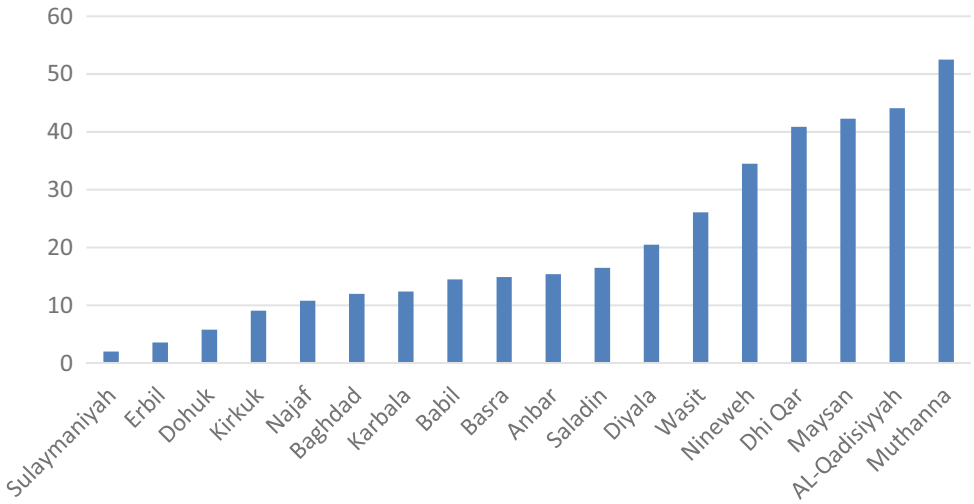

Fig. 3 Very recent poverty rate across Iraqi governorates

2.8 Poverty and Ignorance

Poor and low-income Iraqi families who live in rural areas very often cut trees for energy provision like heating and cooking which has led to drastic desertification. The poverty rate for the Iraqi governorates for the year 2019 (ALHurra Iraq TV) clearly shows the rise of poverty in the southern governorates (Fig. 3).

2.9 Loyalty

The invading powers brought many rebel groups (opposition to the Saddam regime) who have no loyalty to Iraq as a country. This of course led to much squandering and no economic growth.

2.10 Wars Mines and Booby Traps

Iraq is one of the world's most landmine-affected countries. The Iran–Iraq war of the 1980s and the First and Second Gulf Wars deeply affected shepherds and farmers who are exposed daily to booby traps and mines that have been left throughout the war zones of Iraq. More recently, with people keen to return to their homes following the end of the conflict, our teams in Nineveh governorate have begun clearing contaminated areas and working through the rubble of damaged or destroyed houses to remove explosive remnants of war and make it safe for the process of rebuilding to begin.

2.11 Deliberate Destruction of Fish Farms

The central and local administrations are too weak to prevent crimes. Millions of fish have been lost recently from unidentified causes. This action caused considerable damage to the food chain across Iraq. Massive fish death in Middle Euphrates has been experienced recently, as shown in Fig. 4 (Marwa, 2018); the cause of this catastrophic phenomenon has been announced unknown.

2.12 Deliberate Fires in Farms and Greeneries

Huge open land of grain fields was targeted by individuals who set fires to thousands of acres of grain farms across the country. The reasons are high-strength lenses found in the fields to set fires, neighboring countries' conflict of interest, and more conspiracy theories on that issue.

The causes behind the fires are as follows: 74 incidents were short-circuit electrical fires, 35 were fires deliberately started by farmers, 25 were caused by sparks from farming machinery, 22 incidents were caused by discarded lit cigarettes in fields… and the source of 84 fires remains unidentified, the statement reads (https://www.kurdistan24.net/en/news/d70e2b2e-6873-476a-97fe-ca65a0703fbb). Some of the farmers intentionally burned down their crops in hope of getting some financial compensation from the government

Fig. 4 Sample of massive fish death in Iraq Middle Euphrates

Fig. 5 Sample of Iraqi intentionally burned down crops

as some of their harvest and plots of land had been damaged by heavy rainfalls of March and April as shown in Fig. 5.

2.13 COVID-19 Coronavirus

Despite all the measures that have been taken to curb the disease, the coronavirus has been taking its toll within Iraq. The latest statistics of the disease spread during the last three months can be clearly indicated by the following Fig. 6 (https://www.google.com/search?sxsrf=ALeKk03mZ3HQhVSMvPZxnJbH22bVooEMfg%3A1591774494634&ei=Ho3gXqeaJumBjLsPloSb4Ac&q=latest+stats+on+coronavirus+in+the+world&oq=latest+stats+on+coronavirus+in+the+world&gs_lcp=CgZwc3ktYWIQAzoECAAQRzoECCMQJzoCCABQ6zdY8mZgw3NoAHABeACAAcIBiAHEEZIBBDAuMTOYAQCgAQGqAQdnd3Mtd2l6&sclient=psy-ab&ved=0ahUKEwinocKK3vbpAhXpAGMBHRbCBnwQ4dUDCAw&uact=5). The details of the status due to the COVID-19 coronavirus are given in Table 1. Iraq showed a 2.7% death rate compared to 5.7% worldwide, on the other hand, the Iraq COVID-19 recovery rate was 39.5% against no figure available worldwide.

Table 1 Updated confirmed cases in Iraq together with the recovered and death cases

Location	Confirmed	Recovered	Deaths
Baghdad governorate	2234	941	97
Sulaymaniyah governorate	811	246	23
Basra governorate	747	578	18
Najaf governorate	431	324	6
Erbil governorate	397	243	4
Karbala governorate	152	118	8
Al Muthanna governorate	117	95	4
Duhok governorate	102	26	0
Dhi Qar governorate	96	72	4
Kirkuk governorate	72	59	2
Wasit governorate	59	39	2
Maysan governorate	52	45	2
Babylon governorate	49	39	5
Diyala governorate	45	21	5
Halabja governorate	25	22	0
Al-Qadisyah governorate	15	11	1

Total confirmed = 14,268, Recovered = 5831, Deaths = 392

Fig. 6 Up to date COVID-19 cases confirmed across Iraq

2.14 Mitigation Measures

To enhance sustainable development, certain mitigation measures must be taken in the short term like restoring the damaged infrastructure in the hot spot areas. The long-term measures on the other hand are to spread environmental awareness throughout holy places, school education, or Nongovernment Organizations (NGOs). The Iraqi government should use the oil assets to invest in sustainable agriculture and sustainable industry. Water management is essential to prevent shortages in water due to climatic changes. The mitigation measures due to the COVID-19 pandemic are as suggested in the following:

The coronavirus is an environmental issue rather than just a public health issue. The design criteria to deal with sick building syndrome have to take two design and construction modes:

- **Mode A**: A 100% fresh air AC system must be introduced to make sure no virus accumulation and no dead spots or dead zones exist in any used space (i.e., fully opened windows and fresh air ducted system supply).
- **Mode B**: This mode is in parallel with mode A; ultraviolet exposure or generators are a must at lift entrances or classroom doors to kill any germs when entering into lifts or closed spaces.
- **Mode C**: The traditional model for air-conditioning closed spaces is no longer applicable. It is from my point of view is a germ-carrying system. Thus, it can be clearly stated that it is a risky approach to enhance sick building syndrome. Furthermore, this mode means in its best design and operational standard in its best is 20% fresh air only and 80% recirculated air.
- **Masks**: Masks that are being used are still not effective, if we were to consider the size of the coronavirus which is around 0.14 microns while the smoke of cigarettes peaks between 0.2 and 0.25 microns, I am sure everyone can smell the smokes that diffuse from any smokers nearby while wearing a mask.
- **Recommendations**: In order that the TIU take the initiative for securing a safe university environment, I recommend the urgent implementation of Mode A alongside Mode B. Onsite, I have noted that wearing an excess perfume will in no doubt enhance germ diffusion between individuals, unfortunately. To avoid any excessive human body sweating (vapor/germs carrier), it is recommended to meet thermal comfort conditions at 20 °C indoor dry-bulb temperature and 40% relative humidity (RH).

3 Conclusions

It is very clearly noted that in order to handle the consequences of the most complicated environmental problems, it is necessary to have capable and effective management. A selected, well-experienced team of engineers will be able to restore such a catastrophic situation using short- and long-term mitigation measures. The following conclusive remarks, in brief, can be drawn accordingly:

- An immediate action should be taken to restore the infrastructure in Iraqi cities.
- The invading forces should make available data for all the places which have been exposed to radiation. Additionally, immediate actions should be taken into consideration for the isolation of hazardous wastes of the wars.
- The current Iraqi government and the world nations should take immediate action to restore health services to an adequate level, to prevent life-threatening childhood diseases.
- An immediate action should be taken to rehabilitate the damaged ecosystem and landmines clearing.
- The immediate return of the displaced families to their homes in all parts of Iraq.
- Practical solutions to curb the side effects of COVID-19 have been recommended for implementation in crowded spaces like universities and so forth.

References

ALHurra Iraq TV Channel report, date 18–02–2020. Reconstructed histogram.

Hassoon, H. M. (2016). *Lectures notes for environmental engineering course*. Civil Engineering Dept., ISHIK University, Erbil, Iraq, Spring.

Hassoon AL-Delphi The Environmental problems in the Arab World Sustainability and Policy Making Dubai UAE, Retrived from http://ehealth.hbmeu.ae/Program/Presentation_The_Environmental_Problems_in_the_Arab_World.aspx, 8–9th April 2009

https://www.kurdistan24.net/en/news/f08498e3-0697-40e9-8c83-4d35728ddcca

https://www.hudson.org/research/11787-the-first-gulf-war-and-its-aftermath

https://www.google.com/search?sxsrf=ALeKk03mZ3HQhVSMvPZxnJbH22bVooEMfg%3A1591774494634&ei=Ho3gXqeaJumBjLsPloSb4Ac&q=latest+stats+on+coronavirus+in+the+world&oq=latest+stats+on+coronavirus+in+the+world&gs_lcp=CgZwc3ktYWIQAzoECAAQRzoECCMQJzoCCABQ6zdY8mZgw3NoAHABeACAAcIBiAHEEZIBBDAuMTOYAQCgAQGqAQdnd3Mtd2l6&sclient=psy-ab&ved=0ahUKEwinocKK3vbpAhXpAGMBHRbCBnwQ4dUDCAw&uact=5

https://www.google.com/search?q=iraq+population+growth+rate&rlz=1C1GCEU_enIQ837IQ837&oq=iraq+population+rate&aqs=chrome.1.69i57j0l4.19060j1j8&sourceid=chrome&ie=UTF-8

https://www.theguardian.com/artanddesign/2004/aug/31/heritage.iraq

https://reliefweb.int/sites/reliefweb.int/files/resources/pax-report-living-under-a-black-sky.pdf, pp. 24–30, June 2012

https://iraq.unfpa.org/sites/default/files/pub-pdf/PSA%20English%202012.pdf, pp. 22 November 2017

https://www.kurdistan24.net/en/news/d70e2b2e-6873-476a-97fe-ca65a0703fbb

https://www.pinterest.com/pin/726698089852481192, Baghdad 2019

https://www.academia.edu/843377/Marshland_of_Cities_Deltaic_Landscapes_and_the_Evolution_of_Early_Mesopotamian_Civilization

https://knoema.com/atlas/Iraq/topics/Demographics/Mortality/Infant-mortality-rate

Marwa, O. (2018). Iraq: Massive Fish Death in Middle Euphrates, American Herald Tribune.

Contributing Factors in Respirable Dust Lung Deposition in Underground Coal Mines: Short Review

Elham Rahimi, Younes Shekarian, Wei-Chung Su, and Pedram Roghanchi

Abstract

Exposure to respirable dust, particularly in underground mines, significantly affects the worker's health. During the last decades, respirable dust concentrations in surface and underground mines have been significantly reduced. However, the health data shows that the rate of mine workers with respiratory diseases is still high. Significant evidence suggests that respirable dust toxicity is related to particle characteristics, including mineralogy and morphology of the dust particles. This study discusses the respirable coal mine dust (RCMD) deposition in the human lung. Detailed investigation of RCMD particle characteristics, including size, shape, angularity, and composition, as well as bioaccessibility and wettability are required to better understand the RCMD lung deposition. Current mass-concentration-based sampling methods cannot provide sufficient information about the true dose of exposure. Therefore, lung deposition experiments are required to investigate the actual internal exposure dose among underground coal miners.

Keywords

Respirable coal mine dust • Lung deposition • Respiratory system • Dust characterization

1 Introduction

The term dust is used for suspended solid particles in the air within a 1–100 μm in diameter. Dust is an inherent byproduct of mining activities that increases notable health and safety concerns. In coal mines, concentrated coal dust is a hazard that can generate easily ignited explosive mixtures, and inhalation of smaller particles can negatively affect both internal and external organs, including the lung, kidney, and cardiovascular system. Inhalation and lung deposition of coal dust does not only depend on a particle's size but also its aerodynamic diameter. Respirable dust generally refers to particles having an aerodynamic diameter <10 μm and a median cut point (d_{50}) of 4 μm (World Health Organization, 1999).

Respirable coal mine dust (RCMD) is a mixture of more than 50 elements and their oxides. RCMD may contain pyrite, traces of other minerals, quartz, illite, kaolinite, and feldspars that can be found in the host rocks (Jing et al., 2010; Sarver et al., 2019). The main sources of respirable coal mine dust (RCMD) include coal seam and surrounded rock strata, intake air, diesel exhaust, mining operations, and rock dusting (National Academies of Sciences, 2018).

Current RCMD sampling methods rely on the total mass of the respirable coal dust and its quartz mass content. However, the efficacy of the mass-concentration-based monitoring system as an indicator of the actual dose of exposure is questionable. Therefore, RCMD lung deposition and its relationship with the RCMD particle characteristics should be comprehensively investigated in order to estimate the true exposure dose while working underground. This paper discusses the RCMD lung deposition mechanisms and the authors' attempt to understand the RCMD lung deposition through experimental studies.

E. Rahimi · Y. Shekarian · P. Roghanchi (✉)
Department of Mineral Engineering, New Mexico Institute of Mining and Technology, Socorro, NM, USA
e-mail: pedram.roghanchi@nmt.edu

W.-C. Su
Department of Epidemiology, Human Genetics, and Environmental Sciences in the School of Public Health, University of Texas Health Science Center at Houston, Houston, TX, USA

A. Kallel et al. (eds.), *Selected Studies in Environmental Geosciences and Hydrogeosciences*, Advances in Science, Technology & Innovation, https://doi.org/10.1007/978-3-031-43803-5_25

2 RCMD Lung Deposition

There are a variety of mechanisms for particle deposition in the respiratory system, some depending on size. These mechanisms include inertia impaction, gravitational sedimentation, and Brownian diffusion (Marin & Ostrowski, 2016). RCMD has a size of 10^{-3}–10 μm in diameter, which potentially deposits in different parts of a respiratory system. The dominant deposition mechanism of the coarse RCMD particles is inertia impaction due to their relatively large mass (Islam et al., 2020). In contrast, after being inhaled, the fine dust particle with a small particle mass can easily follow the inhaled air and deposit deep into the lung through the Brownian diffusion mechanism (Hofmann, 2011).

To illustrate lung deposition based on particle size, the human respiratory system is simplified into three regions: head region, tracheobronchial region (TB), and alveolar region (gas exchange region) (Fig. 1). Particles with an aerodynamic size of fewer than 10 μm could be inhaled through the nasal and oral cavities in the head region, which, based on the condition, may trap in different parts of the airways (International Commission on Radiological Protection: Human respiratory tract model for radiological protection, 1994). Since the smallest particles have little inertia, all move along with the air when inhaled and enter the respiratory tract. Most of these particles deposit with only a tiny percentage being breathed back out. Medium-sized particles also tend to move along with the air and are inhaled. However, the majority of them fail to deposit in the respiratory tract and are exhaled back out. Large particles may not follow air streamlines as the air turns to be inhaled; some of them will fail to be inhaled at all (Hinds, 1999; Saber & Heydari, 2012). Most of those inhaled deposits within the respiratory tract, but some will leave with the exhaled air. If a particle makes it deep into the lungs, there are alveolar macrophages that can gobble it up and then physically move up to the conducting bronchioles. However, very fine particles may find their way into the bloodstream with oxygen. At the blood-gas barrier, carbon dioxide diffuses out from the deoxygenated blood and into the air of the alveoli, which then gets breathed out, and with each breath in, oxygen enters the alveoli and freely diffuses into the blood (International Commission on Radiological Protection: Human respiratory tract model for radiological protection, 1994). In the case of an underground coal miner, that freshly oxygenated blood is prone to contain RCMD particles, which head off to the pulmonary veins, the heart, and then to the body tissues. Associated particles in the bloodstream potentially precipitate in different parts of a respiratory system or other organs incur a broad spectrum of health hazards (Hinds, 1999). These RCMD particles may include a considerable amount of fine or ultrafine particles according to technical mining factors used and the most damaging particles are probably those that are small enough to penetrate deep into the lungs. In light of this, diesel particulate matter (DPM) with a diameter of less than 1 μm is considered a concern for underground workers (National Academies of Sciences, 2018). Submicron particles are not cleared as efficiently as larger particles and have mobility within the respiratory system or beyond via translocation to blood (Ahookhosh et al., 2020).

Based on particle size, roughly 20% of the 10-nm (nm), 4% of the 300-nm, and nearly all of 10-μm (μm) particles end up depositing in the head region. Overall, deposition in the tracheobronchial region is relatively low, about 25% of 10 nm, less than 1% of 300 nm, and only about 1.5% of 10 μm particles will deposit. The deposition of particles larger than 3 μm and smaller than 10 nm can be higher if not already deposited in the head region. Approximately, 42% of the 10 nm, less than 6% of the 300 nm, and around 2% of 10 μm particles depositing in the alveolar region. The deposition of the 10 μm particles is negligible since very few of these particles reach the alveoli region. This shows that for equivalent masses, ultrafine particles (UFP) appear to result in a more severe lung response. (Heyder & Rudolf, 1984; Hinds, 1999; International Commission on Radiological Protection: Human respiratory tract model for radiological protection, 1994).

3 Discussion

Considerable research and analyses have been conducted to investigate the causes of rising lung diseases among coal miners despite the significant reduction in RCMD mass concentration in underground working areas (Blackley et al., 2014). In a recent study, a realistic estimate for respirable and thoracic fraction was provided based on experimental data and a mathematical model of oral and nasal inhalation concerning age, gender, activity, and smoking (Brown et al., 2002; Qian et al., 2016). Based on the defined thoracic and respirable fractions, the aerodynamic size of particles that can penetrate the respiratory tract might change by increasing the rate of activity with both nasal and oral inhalations. The remarkable results might help in the interpretation of health effect evidence and in designing experimental studies.

In the current experimental study at the New Mexico Tech with a partnership of UTHealth, the human airway system has been simplified using an innovative Mobile Aerosol Lung Deposition Apparatus (MALDA) to estimate RCMD lung deposition in a near-real situation. This system consists of head-airways, both realistic human nasal and oral cavities, a delicate and physiology-based human TB airway,

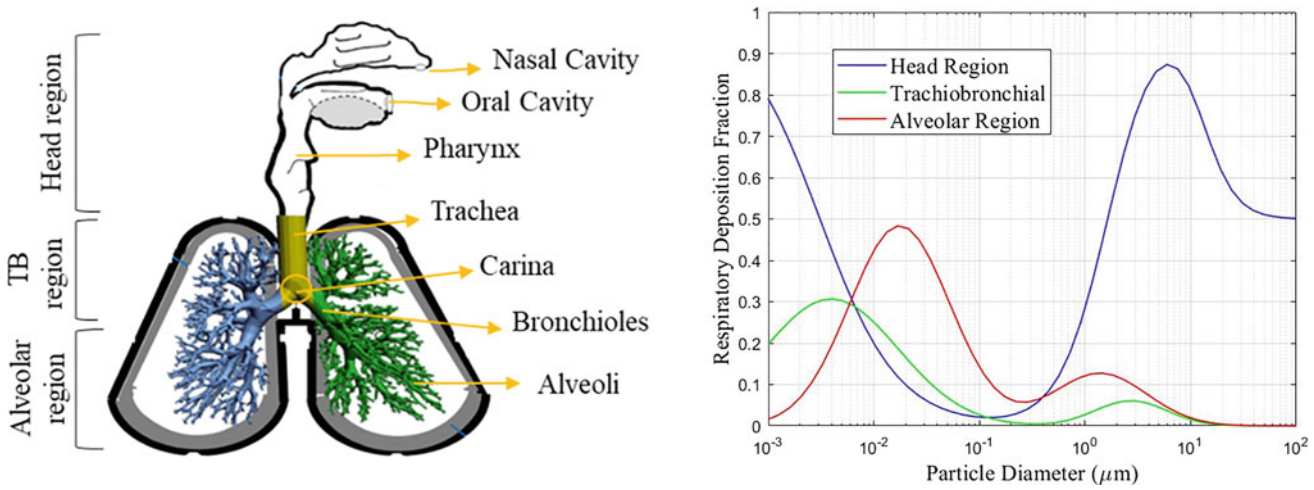

Fig. 1 Simplified human respiratory system included the main three regions (left) based on fractions of particle deposition (right)

the inner surface coated with silicon oil to mimic the sticky and wet nature of airways, and extended airways down to the 11th airway generation as a representative for the alveolar region. The flow rate distribution is adjustable by selecting conductive tubing with different inner diameters and the number of particles depositing is measured by a wide-range aerosol spectrometer (Rahimi, 2020; Su et al., 2019).

In a respiratory deposition of dust particles, in addition to the size of the particles, the shape, in other words, angularity and sphericality, will significantly affect the deposition. Specifically, non-spherical particles may easily halt in the path along the respiratory airways (Sellaro et al., 2015). Mass of particle can also affect the particle deposition, whether the mass is low and precipitates in diffusion mechanism of deposition, or when the mass of the particles is high and inertia is the dominant mechanism of deposition (Huang et al., 2005; Islam et al., 2020). Not all of the RCMD inhaled into a miner's respiratory tract will deposit in the lung to become the RCMD dose. A portion of the inhaled RCMD could be exhaled out of the respiratory tract during exhalation without deposition. This phenomenon is especially significant for nanosize dust particles or UFP (Brown et al., 2002; Su et al., 2019).

The true dose of environmental and internal exposure is necessary to be assessed and compared with the data from the mass-concentration-based sampling method. Currently, the mine health-related RCMD personal sampling is based on the mass concentration which may not correctly represent the true RCMD dose received by a coal miner, especially for RCMD less than 4 μm. Therefore, the total amount of RCMD inhaled may not be representative of the RCMD actual exposure dose. The number-concentration-based RCMD samples could be an alternative and ideal index for RCMD dose estimations (Rahimi, 2020; Shekarian, 2020).

4 Conclusions

A comprehensive investigation of RCMD characterization is essential to achieve a better understanding of the probable reasons for the rising RCMD exposure and lung diseases. It is also crucial to investigate the actual dose of exposure, both externally and internally, in order to understand the main causes of respiratory diseases. Therefore, the relationship between respirable dust particles characterizations and lung deposition is particularly needed to be understood. Furthermore, detailed studies of morphological properties, including particle size, angularity, mass, shape, and elemental composition as critical parameters, are essential to categorize dust particle deposition better. Other environmental factors may affect the process of particle lung deposition; hence, other detailed studies should be conducted to explore any involved factors contributing to particle deposition.

Acknowledgements This study is funded by the National Institute for Occupational Safety and Health (NIOSH) [75D30119C06390].

References

Ahookhosh, K., Pourmehran, O., Aminfara, H., Mohammadpourfard, M., Sarafraz, M. M., & Hamishehkar, H. (2020). Development of human respiratory airway models: a review. *European Journal Pharmaceutical Sciences* (145), 105233.

Blackley, D. J., Halldin, C. N., Wang, M. L., & Laney, A. S. (2014). Small mine size is associated with lung function abnormality and pneumoconiosis among underground coal miners in Kentucky, Virginia and West Virginia. *Occupational Environment Medicine, 71*, 690–694.

Brown, J. S., Zeman, K. L., & Bennett, W. D. (2002). Ultrafine particle deposition and clearance in the healthy and obstructed lung.

American Journal Respiratory Critical Care Medicine, 166, 1240–1247.

Heyder, J., & Rudolf, G. (1984). Mathematical models of particle deposition in the human respiratory tract. *Journal Aerosol Science, 15*(6), 697–707.

Hinds, W. (1999). Aerosol Technology: properties, behavior, and measurement of airborne particles. Chapter 11, University of Virginia Library, VA, USA.

Hofmann, W. (2011). Modelling inhaled particle deposition in the human lung-a review. *Journal Aerosol Science., 42*(10), 693–724.

Huang, X., Li, W., Attfield, M. D., Nadas, A., Frenkel, K., & Finkelman, R. B. (2005). Mapping and prediction of coal workers' pneumoconiosis with bioavailable iron content in the bituminous coals. *Environmental Health Perspectives, 113*(8), 964–968.

International Commission on Radiological Protection:. (1994). Human respiratory tract model for radiological protection. 24. ISN: 0146–6453.

Islam, M. S., Paul, G., Ong, H. X., Young, P. M., Gu, Y. T. & Saha, S. C. (2020). A review of respiratory anatomical development, air flow characterization and particle deposition. *International Journal Environmental Research Public Health*. 17, 380.

Jing, Y., Xiukun, W., Jianguang, G., & Gaiping, L. (2010). Surface characteristics and wetting mechanism of respirable coal dust. *Mining Science Technology, 20*, 0365–0371.

Marin, X. B., & Ostrowski, L. E. (2016). Cilia and Mucociliary Clearance. *Cold Spring Harbor Perspectives Biology* 9(4)

National Academies of Sciences. (2018). *Engineering and Medicine: Monitoring and sampling approaches to assess underground coal mine dust exposures* (pp. 1–150). The National Academies Press. Washington DC.

Qian, Q. Z., Cao, X. K., Shen, F. H., & Wang, Q. (2016). Correlations of smoking with cumulative total dust exposure and cumulative abnormal rate of pulmonary function in coal-mine workers. *Experimental Therapeutic Medicine, 12*(5), 2942–2948.

Rahimi, E. (2020). Investigation of Respirable Coal Mine Dust (RCMD) and Respirable Crystalline Silica (RCS) in the U.S. Underground and Surface Coal Mines. Order No. 28156748, New Mexico Institute of Mining and Technology. In PROQUESTMS ProQuest Dissertations & Theses A&I. Retrieved from http://libproxy.uoregon.edu/login?url=https://www.proquest.com/dissertations-theses/investigation-respirable-coal-mine-dust-rcmd/docview/2468128535/se-2?accountid=14698

Saber, E. M., & Heydari, G. (2012). Flow pattern sand deposition fraction of particles in the range of 0.1–10 mm at trachea and the first third generation sunder different breathing conditions. *Computers Biology Medicine* 42, 631–638.

Sarver, E., Kelesa, C., & Rezaee, M. (2019). Beyond conventional metrics: Comprehensive characterization of respirable coal mine dust. *International Journal Coal Geology, 207*, 84–95.

Sellaro, R., Sarver, E., & Baxter, D. (2015). A standard characterization methodology for respirable coal mine dust using SEM-EDX. *Resources, 4*(4), 939–957.

Shekarian, Y. (2020). An Investigation of the Effects of Mining Parameters on the Prevalence of Coal Worker's Pneumoconiosis (CWP) Risks among the US Coal Miners. Order No. 28156223, New Mexico Institute of Mining and Technology. In PROQUESTMS ProQuest Dissertations & Theses A&I. Retrieved from http://libproxy.uoregon.edu/login?url=https://www.proquest.com/dissertations-theses/investigation-effects-mining-parameters-on/docview/2467855260/se-2?accountid=14698. https://doi.org/10.13140/RG.2.2.22358.27205.

Su, W. C., Chen, Y., & Xi, J. (2019). A new approach to estimate ultrafine particle respiratory deposition. *Inhalation Toxicology, International Forum Respiratory Research, 1*(31), 1091–7691.

World Health Organization (1999). Hazard prevention and control in the work environment: Airborne dust. Occupational and environmental health, Department of the protection of the human environment, Geneva.

Impacts of CO and Air Quality-Related Emissions on the Urban Environment—A Case Study (Bhimavaram, India)

Pala Gireesh Kumar, Patnala Lekhana, and Musini Tejaswi

Abstract

The tremendous rise in the use of motorized vehicles by the public for multipurpose use (passenger/transport) was witnessed in the developing countries because of their flexibility and versatility with low initial cost. As per a recent study, one-fourth of the air pollution is caused by the traffic so vehicular pollution has been identified as a major factor that is more responsible for air pollution which has now become a serious threat to our society. This paper mainly focuses on the study of vehicular pollution and the factors that are affecting vehicle pollution. A prototype model, multi-gas sensor device, has been fabricated; it consists of an MQ7 sensor to detect CO, MQ135 sensor to detect various gases like NH3, NOx, alcohol, benzene, etc., in terms of air quality level. Arduino Mega 2560 board and LCD have been used as main parts, in order to detect and measure the pollutants like CO and air quality. A detailed explanation of the prototype model is clearly mentioned in this paper. A study area consisting of high traffic—namely Prakasam Chowk, J.P.Road, near a bus stop and a railway station, in Bhimavaram—was considered as a case study for this research. The maximum and the minimum values of CO were marked as 99 and 60 ppm in peak hours and non-peak hours, respectively, during weekdays and 90 and 61 ppm during weekends. This study concludes that air in the mentioned areas ranges from poor to moderate, and the proposed remedial measures can be followed in all other megacities in order to improve the air quality toward attaining a safe urban environment for better sustainability.

Keywords

Urban environment • NOx • CO • Vehicular pollution • Remedial measures • Sustainability

1 Introduction

Air quality has become a growing concern in the recent years. A combination of gases from industries, automobiles, and factories results in the introduction of pollutants into the environment. The transportation sector is a dominant integrant of the country's economy and a common tool used for the development of industries. As the development of transportation systems increases, the usage of individual motor vehicles also increases day by day which ultimately affects the environment. Generally, air pollution refers to the contamination of air due to gases, particulates, and various pollutants. Toxic pollutants released from motor vehicles cause many health problems to living beings. Particulate matter, which is also known as particle pollution or PM, is another main source of air pollution that is released especially from the transportation sector. Particulates are the most harmful form of air pollution because of their potentiality to pierce deep into the lungs, blood streams, and brain effectuating severe health problems. It can lead to cardiovascular effects and may damage the respiratory system. This paper mainly focuses on the effects of pollutants released from vehicles. A multi-gas sensor device has been fabricated in order to measure some of the pollutants released from the vehicles in traffic-congested areas. A questionnaire survey has been conducted to identify the perceptions of people regarding vehicular pollution, and the corresponding amount of CO_2 released from the vehicles has been calculated based on the quantity of fuel consumed by the vehicles.

P. G. Kumar · P. Lekhana (✉) · M. Tejaswi
Department of Civil Engineering, Shri Vishnu Engineering College for Women (Autonomous), Bhimavaram, Andhra Pradesh 534202, India
e-mail: lekhanapatnala46@gmail.com

A. Kallel et al. (eds.), *Selected Studies in Environmental Geosciences and Hydrogeosciences*, Advances in Science, Technology & Innovation, https://doi.org/10.1007/978-3-031-43803-5_26

2 Literature Review

Air pollution has become a growing problem in megacities and in large urban areas throughout the globe, and transportation is recognized as a major source of air pollution especially in developing countries (Goyal et al., 2006). An increase in the population leads to high usage of vehicles which results in the containment of GHG emissions in the atmosphere (Hari Bansha et al., 2011). Predicting the air pollution emissions which were released by the vehicles is necessary in order to control the consequences in the future (Marguerite et al., 2016). Monitoring the pollutants can be done through different sensors from anywhere using a computer or a mobile (Sai et al., 2019). The pollution released from the vehicles creates a lot of impacts not only on the atmosphere but also on human health and climate change (Elmar et al., 2010). The pollution from vehicles can be minimized by using new as well as innovative technologies, alternate fuels, and through government policies (Aditya & Sushanta, 2014). The past studies considered different models for measuring vehicular emissions which are expensive or overpriced; using those models to monitor the vehicular emissions in different places was accomplished. This current research not only focuses on finding the vehicular emissions in Bhimavaram city using a cost-effective device but also discusses some theoretical formulae in calculating the emissions released from the cars.

3 Multi-gas Sensor Device

A multi-gas sensor device has been fabricated in order to trap the pollutants like CO gas and the fumes discharged from the vehicles (Figs. 1, 2). Arduino Mega shown in Fig. 3 is used as a microcontroller board in this device and is connected to MQ7 and MQ135 sensors which were used to detect the CO gas and the air quality in the atmosphere. An liquid crystal display (LCD) is connected to the Arduino which helps in displaying the output detected by the sensors (Fig. 4).

The main purpose of this device (refer Fig. 5) is to measure the vehicular emissions which play a major role in polluting the environment. The survey has been performed in four traffic-dominated areas in Bhimavaram such as Prakasam Chowk, J.P.Road, near a bus stop and a railway station within a span of one month. The multi-gas sensor device has been tested for a week in each of the above-mentioned areas respectively during both forenoon and afternoon and measured the vehicular emissions.

Fig. 1 MQ7 sensor

Fig. 2. MQ135 sensor

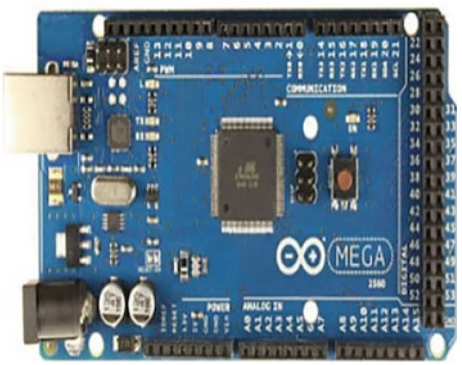

Fig. 3 Arduino mega 2560

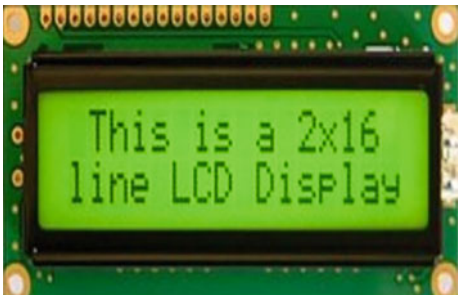

Fig. 4 LCD

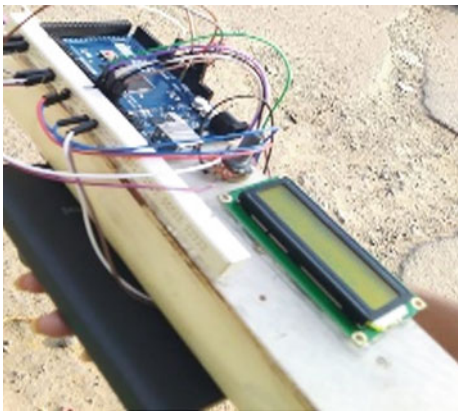

Fig. 5 Multi-gas sensor device

4 Results and Discussions

4.1 Calculation of CO_2 Emissions Based on the Fuel Consumption

A questionnaire survey was conducted from which the various quantities of fuel consumed by the vehicles per day were extracted, the corresponding CO_2 emissions were calculated, and the results were displayed in Table 1. In this survey, mostly 0–2 and 2–4 L were specified by the people as an average amount of fuel consumed by their vehicles per day, whereas the options consisting of 4–6 L and greater than 6 L were opted for by very few people. CO_2 emissions can be determined using the amount of fuel consumption. We know that around 8.8 kg of CO_2 (emissions) are produced for each gallon of fuel (1 gallon = 3.785 L).

4.2 Range Detection of CO and Air Quality

Multi-gas sensor device was used in four different places in Bhimavaram in order to measure the vehicular emissions and air quality levels. The maximum CO value was marked as 99 ppm, and the quality of air is mostly noted as medium throughout the survey in the peak hours; the minimum CO value was noted as 60 ppm and the quality of air is poor in the non-peak hours. The obtained results were given as input into MATLAB software in the form of a code, and the output graphs for each week were showcased from Figs. 6, 7, 8, 9, 10, 11, 12, and 13.

The results show that 79 and 83 ppm were obtained as average values of CO gas at Prakasam Chowk during both weekdays and weekends. Similarly, the average values at J. P.Road were determined as 81 and 76 ppm, at bus stop (four road junctions) as 85 and 81 ppm, and at railway station (four road junctions) as 83 and 89 ppm during both weekdays and weekends, respectively, which were detected by the MQ7 sensor. The air quality level was found to be medium in all areas.

5 Conclusions

A multi-gas sensor device using MQ7 and MQ135 sensors was developed which intends to measure the value of CO as well as the quality of air, respectively. From the obtained results, 79 and 83 ppm were found to be average values of CO gas at Prakasam Chowk during both weekdays and weekends. Similarly, the average values at J.P.Road were determined as 81 and 76 ppm, at bus stop (four road junctions) as 85 and 81 ppm, and at railway station (four road junctions) as 83 and 89 ppm during both weekdays and weekends, respectively. Results drawn from this survey concluded that the quality of air is medium at Prakasam Chowk, J.P.Road, near bus stop (four road junctions) and

Table 1 CO_2 Emissions corresponding to fuel consumption

Amount of fuel consumed (L)	CO_2 emissions (kg/L)	Amount of fuel consumed (L)	CO_2 emissions (kg/L)
0.5	1.16	3.5	8.12
1	2.32	4	9.28
1.5	3.48	4.5	10.44
2	4.84	5	11.6
2.5	5.8	5.5	12.76
3	6.96	6	13.92

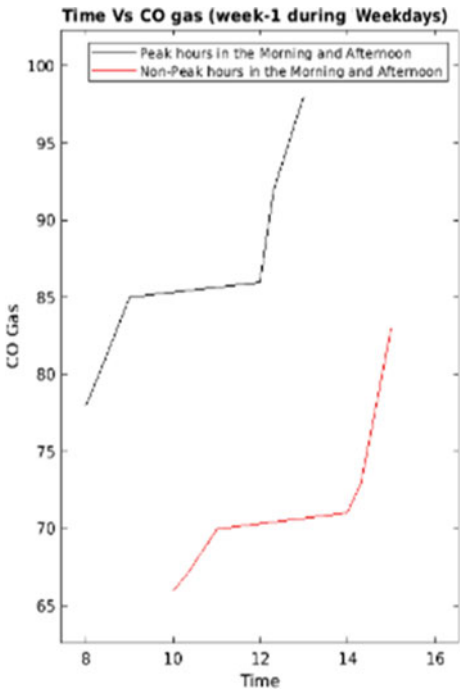

Fig. 6 Time versus CO graph at Prakasam Chowk @ weekdays

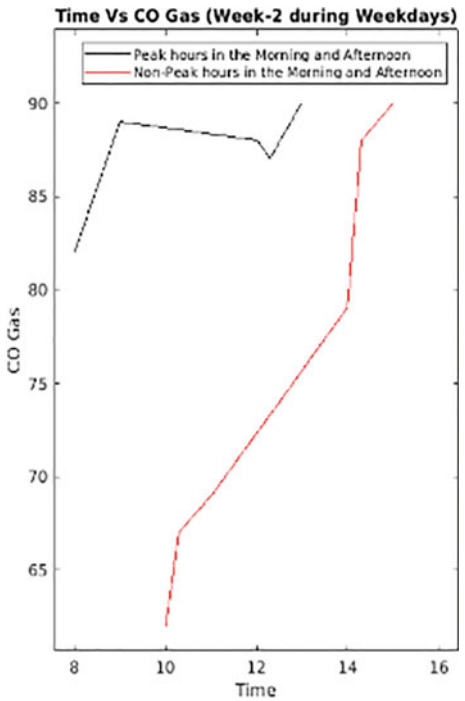

Fig. 8 Time versus CO graph at J.P.Road @ weekdays

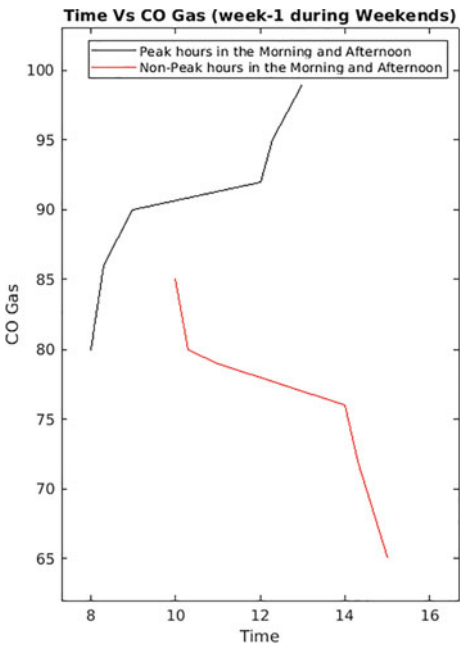

Fig. 7 Time versus CO graph at Prakasam Chowk @ weekends

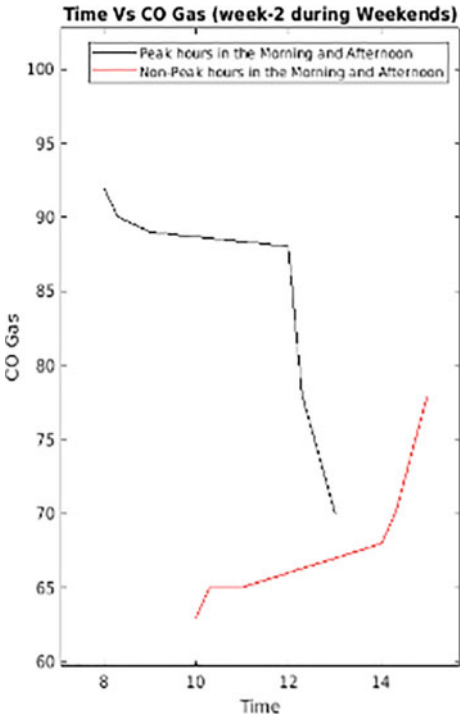

Fig. 9 Time versus CO graph at J.P.Road @ weekends

railway station (four road junctions) in Bhimavaram city. Graphs were plotted using MATLAB software with the obtained CO values for peak hour and non-peak hour in forenoon and afternoon during both weekdays and weekends. A questionnaire survey has been conducted to identify the perceptions of people regarding vehicular pollution. The amount of CO_2 released from the vehicles was calculated depending upon the amount of fuel consumed.

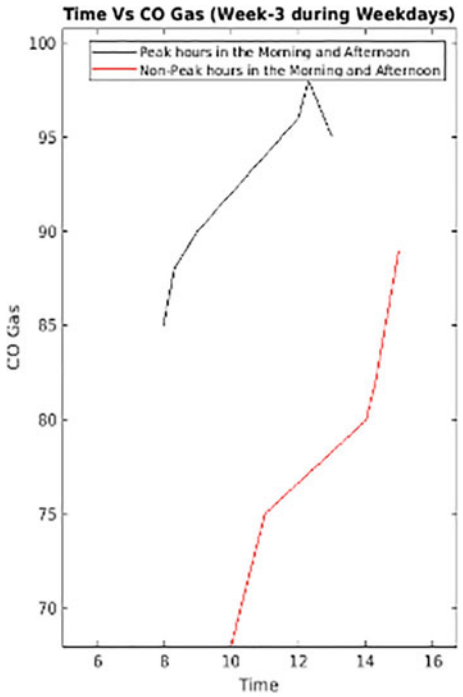

Fig. 10 Time versus CO graph near bus stop @ weekdays

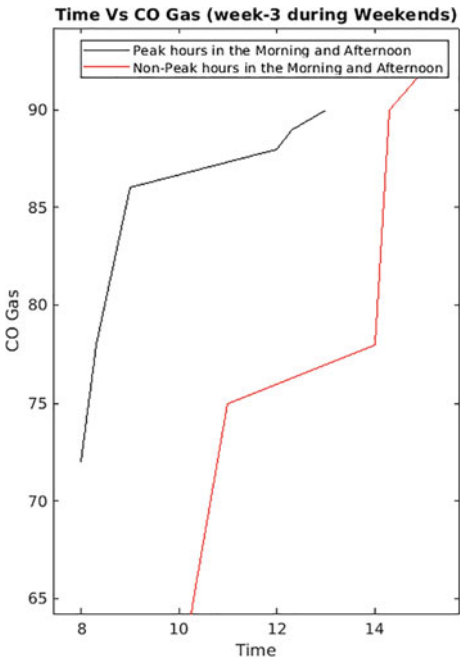

Fig. 11 Time versus CO graph near bus stop @ weekends

The study concludes that the quality of air is mostly noted as medium during the peak hours with a measured CO value of 99 ppm (maximum), whereas the quality of air is poor during non-peak hours with a minimum CO value of 60 ppm.

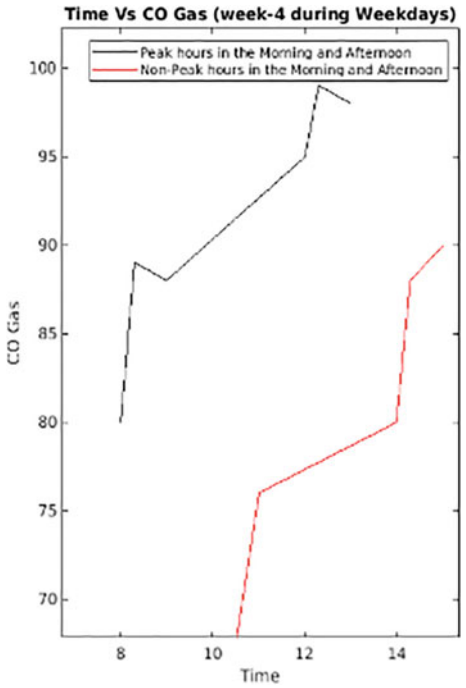

Fig. 12 Time versus CO graph near railway station @ weekdays

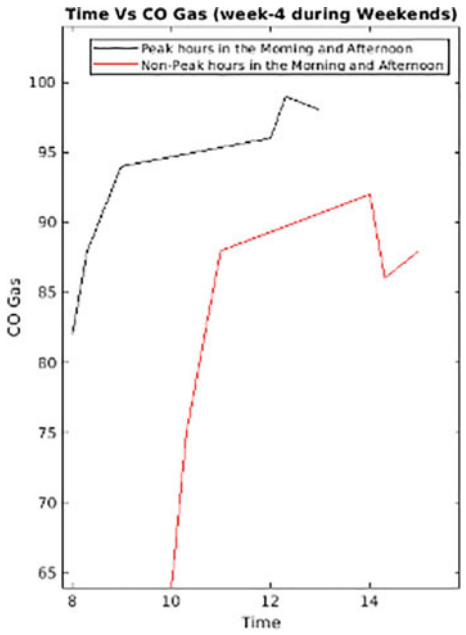

Fig. 13 Time versus CO graph near railway station @ weekends

References

Aditya, K., Sushanta, T. (2014). Study of vehicular pollution and its mitigation measures. In 3rd KIIT *international symposium on advances in automotive technologies* (pp. 49–56).

Elmar, U., Tomas, H., Jens Borken, K., Yves, B., Terje, B., Carlos, B., Michael, G., Peter, H., Katarzyna Juda, R., Jos, L., Dimitrios, M.,

Kristin, R., & Stephan, S. (2010). Transport impacts on atmosphere and climate: Land transport. *Atmospheric Environment* 44, 4772–4816.

.Goyal, S. K., Ghatge, S. V., Nema, P. S. M. T., & Tamhane, S. M. (2006). Understanding urban Vehicular problem vis - a - vis ambient air quality case study of a mega city, Delhi, India. *Environmental Monitoring Assessment*. 119, 557–569

Haimei, W., Jihu, Z., Tao, Y., Zhang, C., Peng, Z., & Xuefeng, L. (2020). Predicting the emissions characteristics of VOCs in a simulated vehicle cabin environment based on small-scale chamber tests: Parameter determination and Validation. *Environment International* 142.

Haiwan, W., Lixin, F., Xin, L., Yu, Z., & Jinchuan, C. (2008). A bottom-up methodology to estimate Vehicular Emissions for the Beijing urban area. *Science Total Environment, 407*(6), 1947–1953.

Hari Bansha, D., Hermit, B., & Charity, G. O. (2011). Climate change mitigation in the transport sector through Urban Planning. *Habitat International* 35, 494–500.

Marguerite, N., Stanislav, S., Chaogui, K., Prudence, R., Andrea, C., Michael, S., David, S., Zifeng, L., Rex, B., Steven, R. H. B., & Carlo, R. (2016). Predicting Vehicular Emissions in high spatial resolution using pervasively measured transportation data and microscopic emissions model. *Atmospheric Environment* 140, 352–363

Kinnera Bharath Kumar, S., Somula, R., & Ashish, K. R. (2019). Lumach. IOT based air quality monitoring system using MQ135 and MQ7 with machine learning analysis. *Scalable Computing* 20, 599–606.

Sociospatial Inequality Conceptual Space and Hexagonal Binning Technique: An Application in Albay Philippines

Ana Marie Rico Abante

Abstract

'Sociospatial inequality' as introduced in this study is defined as variations of unsafe, uncomfortable, and inaccessible space (hotspot area). The incapability to reject exposure holds cities or municipalities back from becoming resilient because they allow people to continue occupying risk hotspot areas. The hotspot information is regarded when greater than one quantity of risk is contrast with coldspot information calculated less than one risk quantity. Stability in this work is regarded as risk equal to one unit that is based on the risk reality triangle to examine the correlation of stability segment which parallels with the sociospatial inequality segment when risk is greater than one-unit z-score. The study aims to analyze the risk hotspot and coldspot z-score information that was stored and sorted in the tessellated hexagonal bins. To achieve this goal, we assess the case of Albay, Philippines. These bins were arranged equidistantly to each other which geographically symbolizes the sociospatial inequalities in every 100 ha of land. Although risk modeling is apt for macro-planning, the visualization of the risk hotspots and coldspots led to the question, where to start reducing sociospatial inequalities? The model answers how to carefully select suitable sites based on the following development control criteria: safe, comfortable, and accessible space for living. Undesirably, sprawl continues growing over time regardless of hazard events happening continuously. It was concluded that visualization of where to risk hotspots is a development control tool to control and eliminate if not reduce inequalities that are logical to unsuitable land utilization or improper selection of spaces for living and making a living.

Keywords

Sociospatial inequality • Uncomfortable space • Safe space • Risk hotspot • Exposure

1 Introduction

The Philippine Institute of Volcanology and Seismology (PHIVOLCS) is mandated to monitor volcanic-related events specifically on gullies and barrancas within the permanent danger zone.

Most of, if not all, the families that are from 90 to 99% significantly risk hotspots were already given housing units or have been resettled in safer locations (Abante, 2020a, b, 2021; Birkmann, 2006; Birkmann & Wisner, 2006; Getis & Getis, 1966; Ord & Getis, 1995). Meanwhile, those who were less than 90% at risk to randomly susceptible to volcanic-related hazards are constantly evacuated, adopting the Zero Casualty Strategy of the Provincial Government of Albay (Salceda, 2012). The people dwelling inside the permanent and extended danger zones are farmers tilling the rich soil of the Mayon foot slopes making it difficult to implement the Philippine Disaster Risk Reduction and Management Act of 2010 (Republic Act 10121), National Integrated Protected Areas System Act of 1992 (RA 7586), and the Expanded National Integrated Protected Areas System Act of 2018 (RA 11038). There is much to be learned from the 2018 Mayon Volcano Eruption, in which the existing evacuation protocols and evacuation practices are seemingly not appropriate for the situation (Abante & Balilo, 2018; Canon et al., 2018). Evacuees were brought to uncomfortable and unsafe temporary shelters exposing them to respiratory-related illnesses. The food and water were contaminated causing food and water poisoning (Abante & Balilo, 2018; Canon et al., 2018). Despite these threats, residential buildings, roads, and other socioeconomic support structures continue to increase within the 6-km

A. M. R. Abante (✉)
Bicol University, Legaspi, Philippines
e-mail: anamarie.abante@bicol-u-edu.ph

A. Kallel et al. (eds.), *Selected Studies in Environmental Geosciences and Hydrogeosciences*,
Advances in Science, Technology & Innovation, https://doi.org/10.1007/978-3-031-43803-5_27

permanent and 8-km extended danger zones marked by the institute. The evacuation-return behavior of residents within the no-build-zone, allowing barangay (smallest political unit) social and institutional facilities such as schools, barangay halls, and other developments, has contributed to uncontrolled sprawl within the danger zones. According to Panadero, an effective monitoring system for local government units in the Philippines must be instituted to harmonize the information demands objectively and effectively to meet the goals of the millennium declaration set by the World Health Organization (Panadero & City, 2004). However, according to Alexander (2001), land use planning and development control (zoning) have given different answers to the societal questions in which the function and enforcement of zoning restrict the production of the built environment (Abante, 2020a, b, 2021; Alexander, 2001; Soja, 2013). This paper introduces a way to visualize and analyze sociospatial inequality in the study area and a concept that can control undesired development.

This topic is useful to the environmental planners, engineers, researchers, and policymakers because it offers to visualize and analyze the undesired developments in terms of buildings along old railroads and rights-of-way near rivers that are prone to volcanic hazards such as lava, lahar, ashfall, as well as rain-induced landslides carrying lahar deposits, and critical landscape of the volcano. This paper put forward the locations of Open Street Maps' (OSM) buildings and roads that portray the main settlements of respective cities and municipalities around Mayon Volcano, located in the Philippines. The study applied the binning technique to assess the exposure defined as the location coincidence of OSM buildings and roads with geographic coordinates that are prone to topological conditions as hazard events recur within the Mayon 6-km permanent danger zone, extended to 8-km danger zone (Abante, 2020a, b, c, 2021; Abante & Abante, 2019; Abante & Balilo, 2018; Canon et al., 2018).

2 Framework

The 'sociospatial inequality conceptual space' is based on Gärdenfors' concept on space about the 'geometry of thought' and Soja's paper on seeking spatial justice where an area is assessed for its nearness to buildings and roads showing where social facilities are significantly located (Gärdenfors, 2004; Soja, 2013). The sociospatial inequality conceptual space is akin to the risk reality defined as risk hotspot areas that are characterized by the z-scores derived from the product of the three paired elements of risk; these are multiple hazards and preparedness; landscape vulnerability and competency; and passive exposure and coping capacity (Abante, 2018, 2020a, b, 2021; Abante & Abante, 2018, 2019). The sociospatial inequality conceptual space based on the golden ratio, triangle, spiral, and circle turned as measurable using hexagonal bins (Abante, 2020b). It outlines risk realities in terms of hotspots or coldspots information stored and sorted in honeycomb lattice-inspired cells that are geometrically and symmetrically arranged entails interdisciplinary thinking and remain reliant on the understanding of the spatial and aspatial data inputs, i.e., multiple hazards, landscape vulnerability, passive exposure, preparedness, competency, and coping capacity to measure receptiveness, responsiveness, and stability (Abante, 2018, 2020a, b, 2021; Abante & Abante, 2018, 2019; Birkmann, 2006; Birkmann & Wisner, 2006; Getis & Getis, 1966; Ord & Getis, 1995).

Figure 1 shows the sociospatial inequality based on the risk reality triangle ABC. Triangles ABC, ABD, or ACE (largest risk reality triangle) are composite isosceles triangles that mark the stability or instability segments regarded as risk reality reckoned from the geometric center, also regarded as sociospatial instability segment Phi σ. The smallest isosceles triangle area measures near zero risk quantity. The first ten series of risk reality triangles segments and areas are all below 1-unit risk quantity which implies resiliency quantities. The 11th isosceles triangle's base hints where the stable base has a risk quantity equal to 1-unit risk quantity. The series from the 12th to the 23rd isosceles triangles indicate where the potential risks are. The largest isosceles triangle comprises the base triangle ACE having the Phi φ equal to 125 units of risk together with the asymptotic segments CE and AE that represent the unreceptiveness and unresponsiveness to reduce disaster risk, respectively. These asymptotic segments represent the fuzzy risk reality having Phi φ greater than 125 units of risk. The 27 asymptomatic line segments proved that the receptiveness and responsiveness segments are all pivoting the 25 vertices of resiliency as well as orbiting the spiral curve until the 27th segment (connected to Vertex 25) whirl back to Vertex 23. The risk reality inflection was reckoned as where the spiral Phi φ equal to 47.74 risk quantity. The risk reality hotspot z-scores equal to or greater than 64 risk units with 95–99% hotspot level of confidence hint at a catastrophe, environmental damages, or economic activity disruption (Abante, 2020a, b, 2021; Birkmann, 2006; Birkmann & Wisner, 2006; Getis & Getis, 1966; Ord & Getis, 1995).

The middle circle as shown in Fig. 1 interconnects the longest asymptotic segments and the longest baseline. The third circle shows the DRRM cycle was reckoned at the Geocenter (0,0) of the spiral and series of isosceles triangles that mark where the stability, vertices of resiliency, and asymptotic segments, which express the risk reality in terms of unreceptiveand unresponsive risk reduction programs and actions of the government. The unreceptive–unresponsive risk reduction hints at sociospatial inequalities because of improper land utilization and allowing people to continue

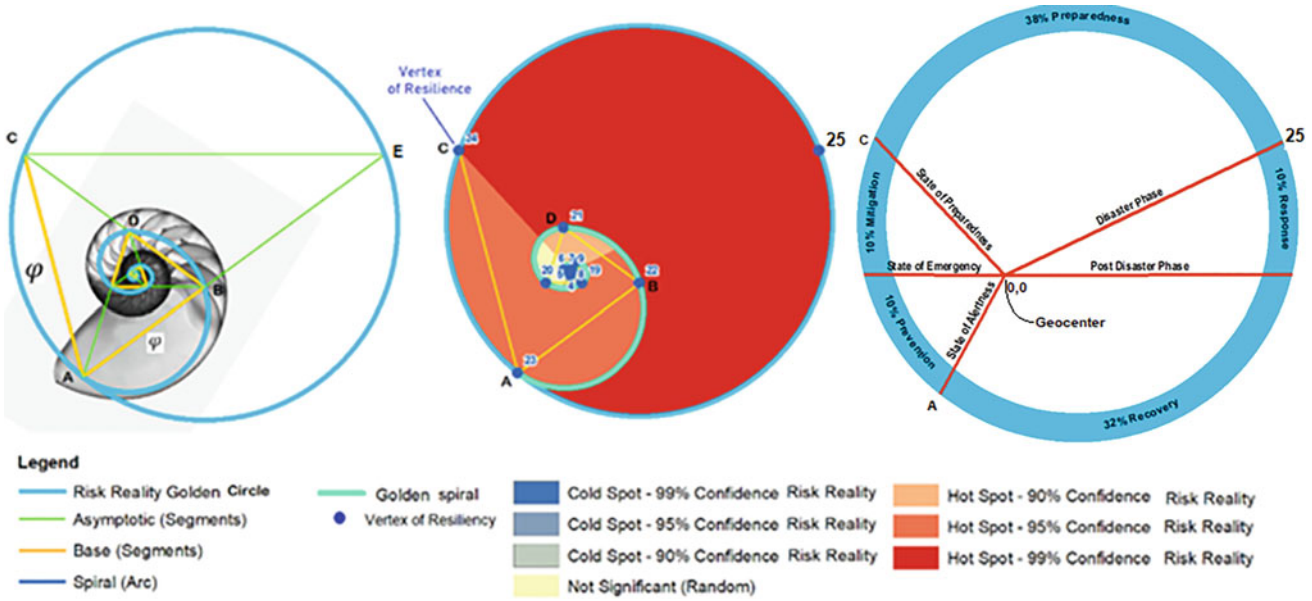

Fig. 1 Sociospatial inequality sociospatial conceptual space based on risk reality spiral and circle (Abante, 2020b)

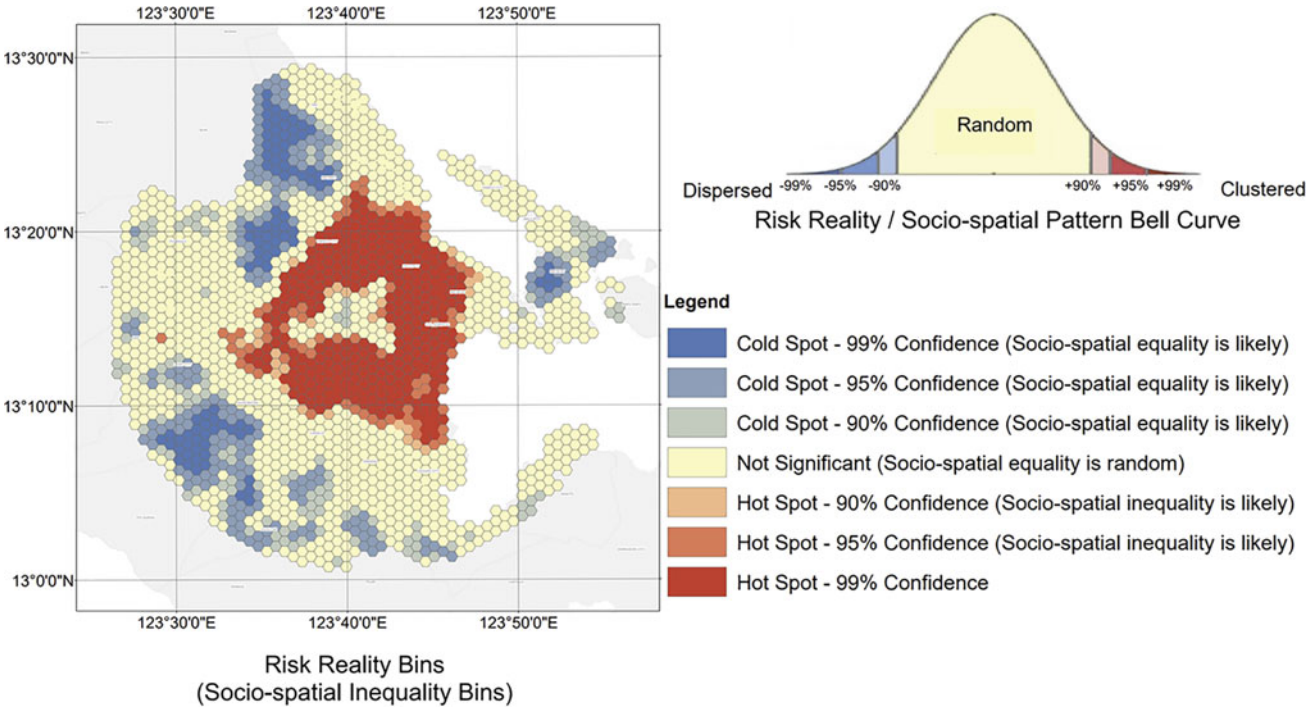

Fig. 2 Risk reality in ArcGIS platform (Abante, 2020b)

living unsafe and uncomfortable in risk hotspot areas likely impacted repetitively by multiple hazard events (Abante, 2020b, 2021). The asymptotic line segments AC and BC represent unreceptiveness and unreceptiveness having an angle of 36° and opposite line segment AB attributed to sociospatial fuzzy reality when risk measurement reaches 125 risk quantity (highest value). Segments CE and AE are the longest unreceptiveness and unreceptiveness segments, respectively (Abante, 2020b, 2021). Segment AC is the longest instability length. On the contrary, the stability (state of balance) is a constant (one unit of risk) that is orbiting within the golden circle based on the Fibonacci golden ratio and Schoen golden triangle. All the 25 vertices of resiliencies take an angle kappa equal to 36° in which the

asymptotic segments take an angle beta β equal to 72 °. Vertex E is the pinnacle of the 23rd risk reality triangle as the last triangle orbiting within the golden circle based on the Fibonacci golden ratio and Schoen golden triangle (Abante, 2020a, b, 2021). The x-ray of a nautilus shell cross-section (credits to the photograph owned by Mike Hill) as shown in Fig. 1 was used for better visualization of the risk reality and fuzzy risk reality that are correlated to instability, unreceptive, and unresponsive risk reduction. The 3rd circle implies a 10% prevention, 10% mitigation, 38% preparedness, 10% response, and 32% recovery to keep stability in DRRM or hints at sociospatial equality (Abante, 2018, 2020b, 2021; Abante & Abante, 2018, 2019). Stability and sociospatial equality are alike in this study because the unreceptive risk reduction hinted at the lack of spatial quality (improper land utilization), while the unresponsive risk reduction hinted at social injustice (allowing people to continue living unsafe and uncomfortable in risk hotspot areas likely impacted repetitively by multiple hazard events (Abante, 2020a, b, 2021; Birkmann, 2006; Birkmann & Wisner, 2006; Getis & Getis, 1966; Ord & Getis, 1995).

3 Methods

The approach is to demonstrate how the hexagonal bins that were arranged equidistantly locate and visualize the risk hotspots and coldspots within the 25-km radial distance from the crater of Mayon Volcano in Albay Province (Abante, 2020a, b, 2021; Abante & Balilo, 2018; Birkmann, 2006; Birkmann & Wisner, 2006; Canon et al., 2018; Getis & Getis, 1966; Ord & Getis, 1995). The risk hotspots were influenced by types of hazard and/or proximity to the critical condition of the landscapes or seascapes that are highly prone or regularly impacted by hazards. The risk hotspot binned the spatial patterns information to represent the geographical aspects of the risk reality quantities or sociospatial inequality conceptual space in Albay (Abante, 2020a, b, 2021; Birkmann, 2006; Birkmann & Wisner, 2006; Getis & Getis, 1966; Ord & Getis, 1995).

The exposures are regarded as the building and/or road objects' coincidence with the hexagonal bins. As multiple hazard events naturally re-emerge, the land morphology relatively implies physical and environmental modifications, making people vulnerable to environmental changes and discovered to be dangerous. Undesired developments inside the permanent danger zone as well as uncontrolled construction of OSM buildings along the existing OSM roads, old railroads, and rights-of-way, near rivers prone to flash floods carrying lahar deposits were analyzed in the ArcGIS platform (Fig. 2). Figure 3 shows the OSM roads and building footprints of the present time shaped the urban sprawl that was measured approximately 100 m within the recommended six (6) kilometer permanent danger zone up to the (8) km extended danger zone (Abante, 2020a, b, 2021).

The characterization of landscape vulnerability and passive exposure of buildings and roads in the context of sociospatial instability complicates the unsafe utilization of

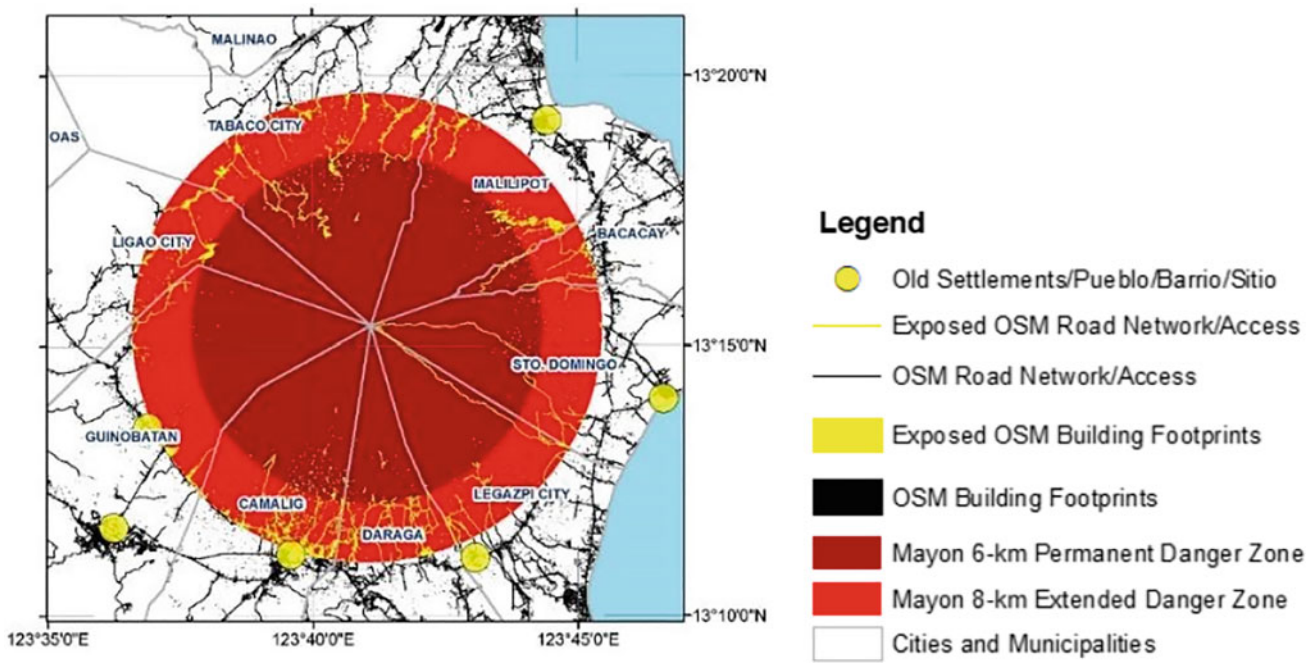

Fig. 3 Exposure happenstance information (exposed OSM buildings and roads)

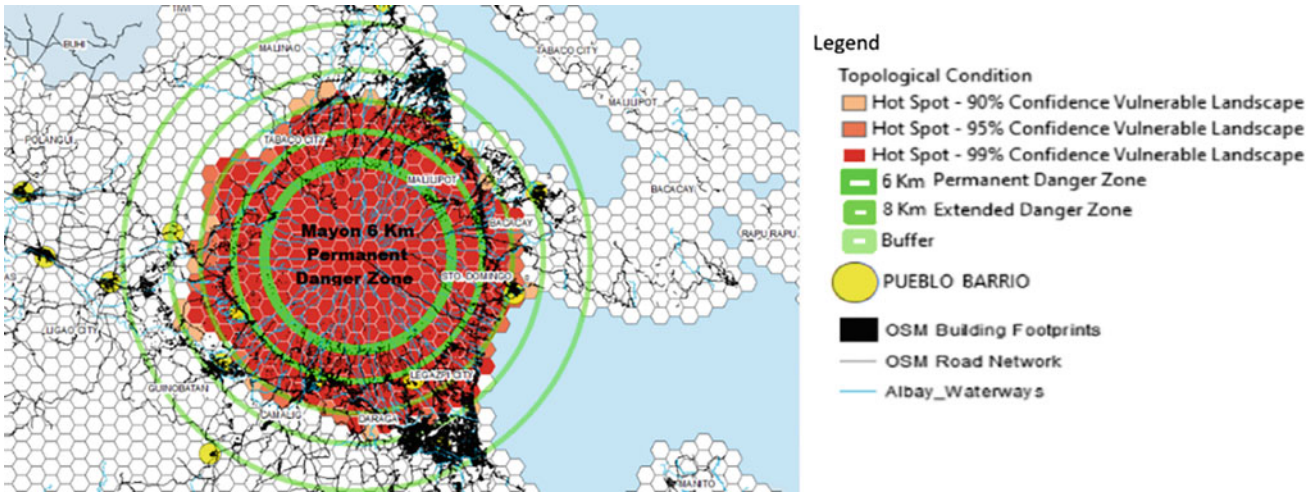

Fig. 4 Topological conditions information stored in hexagonal bins

lands and land improvements that are prone to topological condition physical changes due to hazard events happening again and again (Abante, 2020a, b, 2021; Soja, 2013). Fig. 4 discloses that all the hexagonal bins within the 6 km permanent danger zone and 8 km extended danger zone store land condition hotspots information with 99% confidence level vulnerable landscape (Abante, 2020a, b, c, 2021; Abante & Abante, 2019). However, the GIS model reveals that 91.6% of the land covering the 8–10 km range reckoned from the crater of Mayon Volcano are hotspots with a 99% confidence level signifying these areas are prone to geomorphological and topological changes that will occur naturally. Similarly, there are at least 1.58 and 6.82% prone to topological changes with 90 and 95% levels of confidence (Abante, 2020a, b, c, 2021; Abante & Abante, 2019; Abante & Balilo, 2018; Birkmann, 2006; Birkmann & Wisner, 2006; Canon et al., 2018; Getis & Getis, 1966; Ord & Getis, 1995).

4 Results

The study revealed that there are about 29,400 ha in Albay which are significant risk hotspots, with a 99% level of confidence. Also, at least 7100 ha of land are significant risk hotspots, with a 95% level of confidence, and 3100 ha are significant risk hotspots with a 90% level of confidence. The total number of moderately to highly exposed buildings is 8537. The building exposure incidence within the 6-km radius permanent danger zones is 1080 buildings, while the extended buffer zone has a building frequency of 7457. In terms of road accessibility within the permanent danger zone, an approximate 16 km distance of pathways, 12 km track distance, less than 2 km of footpath, service, and residential routes, and almost 9 km of tertiary (city road) were mapped encroaching the 6-km permanent danger zone. The proposed extended danger zone reckoned from 6 to 8 km buffer from the crater of the volcano covers the following OSM road classes: primary (national roads) with 5.56 km, secondary (provincial road) with 0.40 km, tertiary (city or municipality) 15.71 km, residential (private subdivisions), and combined distance of 85.13 km for path, service, track, trunk, and unclassified. Tabaco City has the highest exposure within the permanent danger zone with 379 mostly residential houses, followed by Camalig with 71 residential buildings in most cases. The lowest is Guinobatan with 9 residential houses of farmers (Abante, 2020a, b, 2021).

5 Discussion

The disaster risk reduction entails interdisciplinary thinking to determine where the natural and man-made hazards, landscape vulnerable, and passive and active exposure hotspots or coldspots exist as a result of sprawl and realization of the tri-nodal spatial developments now trending in Legazpi City, Tabaco City, and Ligao City that are geographically located at the foot of Mayon Volcano (Abante, 2020a, b, c, 2021; Abante & Balilo, 2018; Birkmann, 2006; Birkmann & Wisner, 2006; Canon et al., 2018; Getis & Getis, 1966; Ord & Getis, 1995). The geospatial information modeling enables visualization of risk quantities to start thinking on solutions to overcome the challenges to eliminate if not reduce risk by correctly solving the spatial inequalities logical to uncertainties resulting from improper site selection or land use planning (Abante, 2018, 2020b, 2021; Abante & Abante, 2018, 2019). The risk and the state of being at risk, wherein the state of actuality or the existing situation is objectively lucid in the spatial environment, are contained in a hexagonal-shaped area with segments at an

Table 1 Sociospatial inequality conceptual space in Mayon danger zones

Danger zone (buffer)	Risk hotspots	Level of confidence	Exposure				
			Unsafe and uncomfortable location (social aspect)	Access (spatial aspect) in km			
			Buildings	Earth road/tracks footpath	Tertiary road	Secondary road	Primary road
6-km (permanent)	29,400	99%	1080	30	9	0	0
6 to 8-km (extended)			7457	85.13	15.71	0.40	5.56

equidistance of 500 m. The risk quantity equal to one-unit risk constitutes stability (state of balance), and any value greater than one unit represents risk hotspot contained in hexagonal bins mimicking the geographical aspects of the risk realness triggering sociospatial inequalities (Abante, 2020a, b, 2021; Soja, 2013). However, the risk quantity that is less than one unit of risk hints at spatial equality, and the risk coldspot spatial information hints at a resilience state. Although the author acknowledges the limitations of the spatial data modeling only accurate for 1:50000 scale input maps suitable for macro-planning and rapid risk assessment, this study infers that the more detailed information and smaller hexagonal bins can lead to greater variations of risk and its elements. Furthermore, the hexagonal binning technique determines where the sociospatial inequalities exist (Abante, 2020a, b, 2021; Soja, 2013).

Relatively, Tabaco City has the longest open access within the permanent danger zone creating 8.46 km of tertiary (city) roads mixed with 5.45 km path and unclassified road access. The longest tertiary road hints at the route to Mayon Skyline Tourist Spot. The second highest is Sto. Domingo with 8.35 km path and Legazpi City with 5.91 km path. In most cases, paths are utilized as farm-to-market roads. Similarly, Tabaco City has the highest exposure within the extended danger zone with 2163 buildings utilized for mixed residential, commercial, and/or industrial uses, again followed by Camalig with 1661 mostly residential houses and shanties of farmers tilling the land. The lowest exposed houses within the buffer area are the City of Legazpi. Again, Tabaco City has the longest tertiary (city) road within the proposed extended danger zone with 15.17 km. However, in terms of farm-to-market roads, Daraga has the longest path or unidentified routes with 25.76 km followed by Legazpi City and Tabaco City with 15.20 and 15.17 km, respectively. Camalig is also highly exposed to open access within the proposed extended danger zone.

The sociospatial instability based on Abante (2021) concept on DRRM partitions answers how to analyze risk measurements that uphold the information that can disclose where the risk hotspots are. Understanding risk reality phenomena can hint at sociospatial stability when land use development rejects exposure and relocates people to safe, comfortable, and accessible sites. The sprawl (undesired developments) through the expanded road network within the vulnerable landscape of Mayon Volcano is an indicator of poor environmental planning based on the risk hotspot information that was stored in the hexagonal bins (Abante, 2020a, b, 2021; Abante & Balilo, 2018; Birkmann, 2006; Birkmann & Wisner, 2006; Canon et al., 2018; Getis & Getis, 1966; Ord & Getis, 1995). The increasing exposure entails more problems in DRRM because of the constructed public roads accessible to farmers, residents, and tourists (Abante, 2020a, b, 2021; Birkmann, 2006; Birkmann & Wisner, 2006; Getis & Getis, 1966; Ord & Getis, 1995). Residential buildings, roads, and critical infrastructures within the context of exposure as shown in Table 1 demonstrate how difficult it could be to reduce risk or control sprawl. Mitigation to reduce disaster risk seems doubtful—and if not it is costly—when residual risks from previous hazard events andtopological changes that repetitively happened (Abante, 2018, 2020a, b, c, 2021; Abante & Abante, 2018, 2019; Salceda, 2012; Soja, 2013).

6 Conclusions

Binned risk hotspot information proved useful to assess or reassess the DRRM impractical practices such as repetitive evacuation or allowing people to continuously dwell near or within the danger zones or environmental critical areas such as riverbanks or natural waterways. The researcher concluded that the geoinformation-based disaster risk assessment binning tool was proven to be useful to assess the sociospatial instability of residents who are exposed to volcanic hazards and critical landforms or unsuitable landscapes for living. Furthermore, the sociospatial instability concept model based on DRRM-Circumspectial Isometric Stages can be used as development control to start eliminating if not reducing inequalities that are logical to unsuitable land utilization or improper selection of spaces for dwelling. It was concluded that visualization of where to risk hotspots is a development control tool to control and eliminate if not reduce inequalities that are logical to

unsuitable land utilization or improper selection of spaces for living and making a living. Additionally, what the DRRM-Circumspectial Isometric Stages offers can be applied to further analyze the five partitions of the DRR cycle to restore sociospatial equality toward a stable and sustainable development.

References

Abante, A. M. R., & Abante, C. G. R. (2018). Sensitive land use planning, Malinao, Albay, Philippines. In *IOP conference series: earth and environmental science* (vol. 123, No. 1, p. 012001). IOP Publishing

Abante, A. M. R. (2018). Understanding Preparedness Insufficiency in the Context of DRRM: A Case Study in Malinao, Albay, Philippines. In *Recent advances in geo-environmental engineering, geomechanics and geotechnics, and geohazards* (pp. 497–501). Springer, Cham.

Abante, A. M. R. & Abante, C. G. R. (2019). Topophilia-exposure central space concept model. *International Architecture Photogrammae Remote Sensing Spatial Infromation Science, XLII-4/W19*, 1–8.

Abante, C. G. R. (2020). Mayon volcano cultural heritage as a source of place identity in Guinobatan, Albay, Philippines. *R & D Journal*, *23*(1).

Abante, A. M. R. (2021). Geophilosophical realness of risk: A case study in national housing authority resettlement sites in Albay, Philippines. *SN Applied Sciences*, *3*(4), 1–32.

Abante, A. M. R. (2020a). Risk hotspot conceptual space characterized by hexagonal data binning technique: an application in Albay, Philippines. *International Journal of Computing Sciences Research, 5*(1), 550–567.

Abante, A. M. R. (2020b). *Unpublished dissertation entitled "Geophilosophical perspective on socio-spatial fuzzy reality phenomenon."* Bicol University.

Abante, A. M. R., & Balilo, B. B., Jr. (2018). Resource location-intelligence model conceptualized for Mayon volcano danger zones in Albay, Philippines. *International Journal of Computing Sciences Research, 2*(2), 55–67.

Alexander, E. R. (2001). A transaction-cost theory of land use planning and development control: towards the institutional analysis of public planning. *The Town Planning Review*, 45–75.

Birkmann, J., & Wisner, B. (2006). Measuring the unmeasurable: the challenge of vulnerability. UNU-EHS.

Birkmann, J. (2006). Measuring vulnerability to promote disaster-resilient societies: Conceptual frameworks and definitions. *Measuring Vulnerability to Natural Hazards: Towards Disaster Resilient Societies, 1*, 9–54.

Canon, M. J., Sy, C., & Austero, L. (2018). Discovering themes from online news articles on the 2018 Mt. Mayon Eruption. In *2018 International Symposium on Computer, Consumer and Control (IS3C)* (pp. 242–245). IEEE.

Gärdenfors, P. (2004). Conceptual spaces: The geometry of thought. MIT press.

Getis, A., & Getis, J. (1966). Christaller's central place theory. *Journal of Geography, 65*(5), 220–226.

Ord, J. K., & Getis, A. (1995). Local spatial autocorrelation statistics: Distributional issues and an application. *Geographical Analysis, 27* (4), 286–306.

Panadero, A. A., & City, M. S. Q. (2004, October). Local Government Monitoring Tools for the Millennium Development Goals (MDGs). 9th National Convention on Statistics (NCS), Philippines.

Salceda, J. S. (2012). Adapting to climate change: strategies of Albay, Philippines. *Agriculture and Development Notes on Climate Change Adaptation*, *2*.

Soja, E. W. (2013). Seeking spatial justice (Vol. 16). U of Minnesota Press.

Multi-source Earth Observation Derived Data for Delineating the 2011 High Flood Line in the Okavango Delta (Botswana) for Flood Risk Mitigation and Management

Kelebogile Botseo Mfundisi, Stella Gachoki, Elfatih Abdel-Rahman, Tobias Landmann, and Alex M. Mudabeti

Abstract

Globally, climate-related extremes, particularly floods and droughts, affect freshwater ecosystems and related human systems. The seasonal, annual, and decadal inundated extent of the Okavango Delta in north-west Botswana is highly variable. In 2011, an extreme regional flooding event occurred in the Cubango-Okavango River Basin because of a relatively high rainfall event at its upstream area in the highlands of Angola. This resulted in flood hazards to natural resources in the Okavango Delta wetland system and flood risks to communities living in the Basin. Substantial damages to property and infrastructure occurred in Namibia along the Kavango River and within the Okavango Delta and its proximity in Botswana. The effect of the high flood pulse was felt in downstream areas, particularly in the town of Maun. Therefore, we aim to develop an integrated wetland flood mapping method for populated areas in the Cubango-Okavango River Basin. The objectives of our study were to integrate high spatial resolution Earth observation data to delineate high flood waterline in the Okavango Delta, identify floodplain areas and vegetation cover types that are susceptible to flooding, and develop flood risk mitigation and management strategies. RapidEye data were used to calculate normalized difference water index (NDWI), while Sentinel-2 imagery and shuttle radar topographic mission (SRTM) digital elevation model (DEM) were used to derive recent baseline vegetation cover types. Expert knowledge on the area, existing topographic maps, review of documentation by local land management authorities on the flood event, and ground surveys were used for validation of the results. Preliminary results reveal that flood recession farms on the eastern part of the Okavango Delta Panhandle are susceptible to flooding. Additionally, Shashe River floodplains in the town of Maun are susceptible to flooding; hence, the allocation of land parcels along the area should be circumvented. The results of our study contribute to the development of large-scale flood risk map products for populated areas around the Delta. Also, the study provides recent baseline maps on vegetation cover types in the Okavango Delta system at a landscape scale for wetland monitoring. These are essential elements of integrated wetland flood mapping.

Keywords

Flood risk mitigation • Wetland flood mapping • Earth observation • Cubango-Okavango River Basin

1 Introduction

The seasonal, annual, and decadal inundated extent of the Okavango Delta in north-west Botswana is highly variable. In 2011, an extreme regional flooding event occurred in the Cubango-Okavango River Basin because of a relatively high rainfall event at its upstream area in the highlands of Angola. This resulted in flood hazards to natural resources in the Okavango Delta wetland system and flood risks to communities living in the basin. Substantial damages to property and infrastructure occurred in Namibia along the Kavango River and within the Okavango Delta and its proximity in Botswana. The effect of the high flood pulse was felt in

K. B. Mfundisi (✉)
University of Botswana, Maun, Botswana
e-mail: kmfundisi@ub.ac.bw

S. Gachoki · E. Abdel-Rahman
International Centre of Insect Physiology and Ecology, Nairobi, Kenya

E. Abdel-Rahman
University of Khartoum, Khartoum, Sudan

T. Landmann
Remote Sensing Solutions GMBH, Munich, Germany

A. M. Mudabeti
Namibia Statistics Agency, Windhoek, Namibia

A. Kallel et al. (eds.), *Selected Studies in Environmental Geosciences and Hydrogeosciences*, Advances in Science, Technology & Innovation, https://doi.org/10.1007/978-3-031-43803-5_28

downstream areas, particularly in the town of Maun. The abundance of low-cost remote sensing data has proven to be an effective means of mapping wetlands, which can be particularly difficult to access. Both active and passive remote sensing data have been used in attempts to map the inundation extent of the Okavango Delta over the years with varying results. Due to the scale of focus, but perhaps also constrained by lack of access to higher resolution data, recent flood mapping and forecasting studies in this region have used medium resolution products that allowed such work to be done with reasonable accuracy using Landsat, MODIS, and NOAA AVHRR imagery products. Therefore, there is a need for large-scale, higher-precision flood map products that can inform decision-makers involved in disaster risk mitigation and sustainable land management. Therefore, we aim to develop an integrated wetland flood mapping method for populated areas in the Cubango-Okavango River Basin. The objectives of our study are to integrate high spatial resolution Earth observation data to delineate high flood waterline in the Okavango Delta; identify floodplain areas and vegetation cover types that are susceptible to flooding; and develop flood risk mitigation and management strategies.

2 Materials and Methods

The study was carried out in the Okavango Delta, which occurs in a semi-arid climatic region. It has a high species diversity with 1300 plants, 71 fish, 33 amphibians, 64 reptiles, 444 birds, and 122 mammals (Ramberg et al. 2006). RapidEye data were used to calculate normalized difference water index (NDWI), while Sentinel-2 imagery and shuttle radar topographic mission (SRTM) digital elevation model (DEM) were used to derive recent baseline vegetation cover types. Expert knowledge on the area, existing topographic maps, review of documentation by local land management authorities on the flood event, and ground surveys were used for validation of the results.

3 Results

3.1 Spatial and Temporal Vegetation Cover Dynamics in the Okavango Delta from Sentinel-2 Imagery

Recent baseline vegetation cover types derived from Sentinel-2 imagery are presented in Figs. 1, 2, 3, and 4.

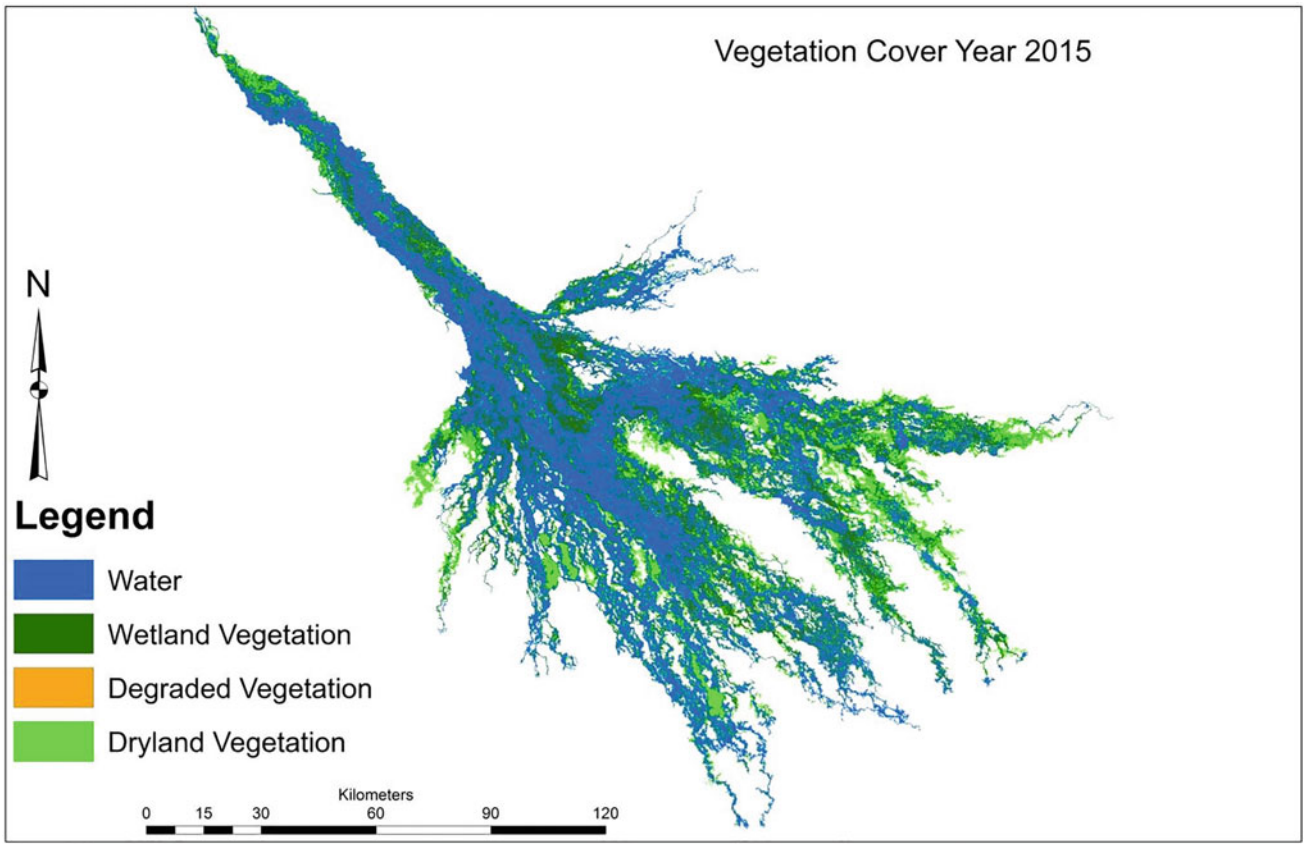

Fig. 1 Vegetation cover dynamics for the year 2015

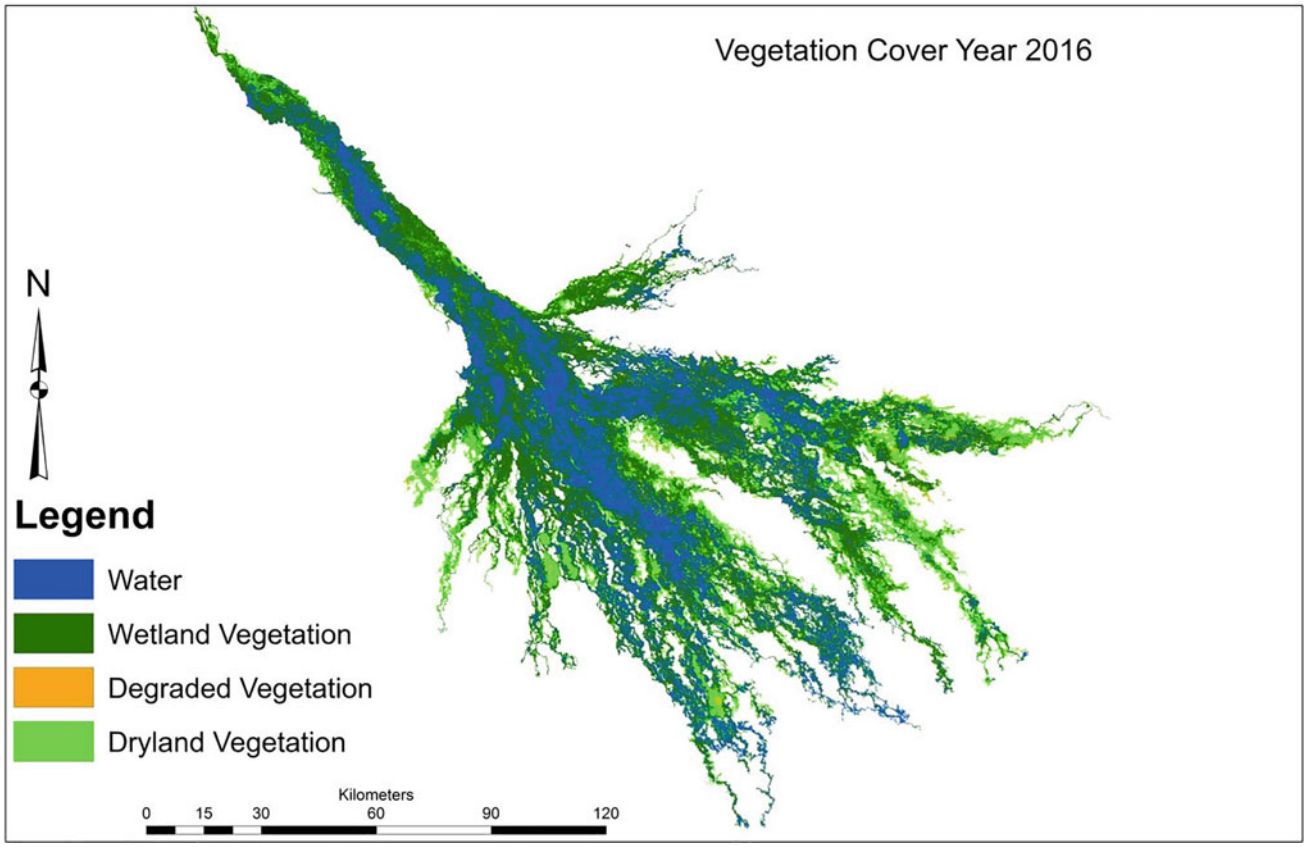

Fig. 2 Vegetation cover dynamics for the year 2016

These provide spatial and temporal vegetation cover dynamics as baseline information to be used for assessing the impacts of flood variability on vegetation types in our study area. The results reveal that there is an inverse relationship between the amount of wetland vegetation cover and inundation extent until a tipping point is reached. It was discovered that at relatively high inundation extent (Fig. 1 and Fig. 3), there is a reduction in the amount of area covered by wetland vegetation, whereas at relatively low inundation extent (Fig. 2 and Fig. 4), there is an increase in the amount of area covered by wetland vegetation. However, a reduction in inundation extent from about 5000 km^2 in 2015 to below 3000 km^2 in 2016 caused an increase in vegetation degradation. We discovered that the amount of dryland vegetation increases manifold when a low tipping point in inundation extent is reached at below 2000 km^2. This was followed by a severe drought in the Cubango-Okavango region over the 2018/2019 rainfall season.

3.2 Normalized Difference Water Index (NDWI) Pre-test

The pre-test results on NDWI calculations indicate that flood recession farms in the eastern part of the panhandle are susceptible to flooding. Information from land management authorities and local knowledge on Maun reveal that Shashe River floodplains are susceptible to flooding.

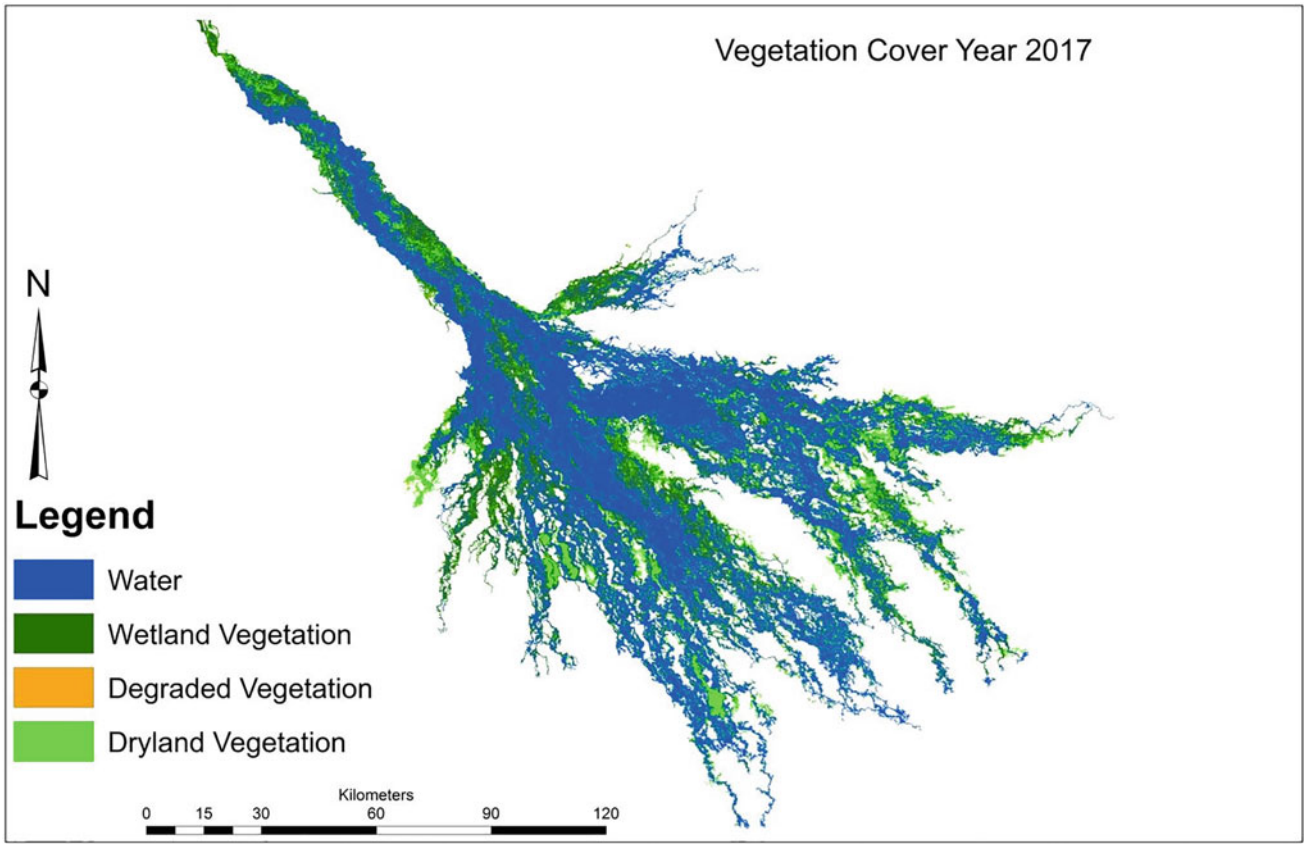

Fig. 3 Vegetation cover dynamics for the year 2017

4 Discussion

Our preliminary results provide conclusive information on high spatial resolution recent baseline maps on vegetation cover dynamics in the Okavango Delta system at a landscape scale, which will be used as a basis to assess the impact of the 2011 high flood on natural resources using RapidEye. Attempts by Bartsch et al. (2009) to map inundated areas in the Okavango Delta using the ENVISAT SAR sensor could only produce inconclusive results. Local communities living in floodplain areas remain at risk of flooding during high inundation extent. Therefore, sustainable land management strategies should be developed based on the scientific evidence provided by this study. Allocation of land parcels on floodplains should be circumvented.

5 Conclusions

The recent vegetation cover types derived from Sentinel-2 imagery provide comprehensive and more accurate baseline information compared to previous studies done in the area. Our future work will use this solid baseline to further assess

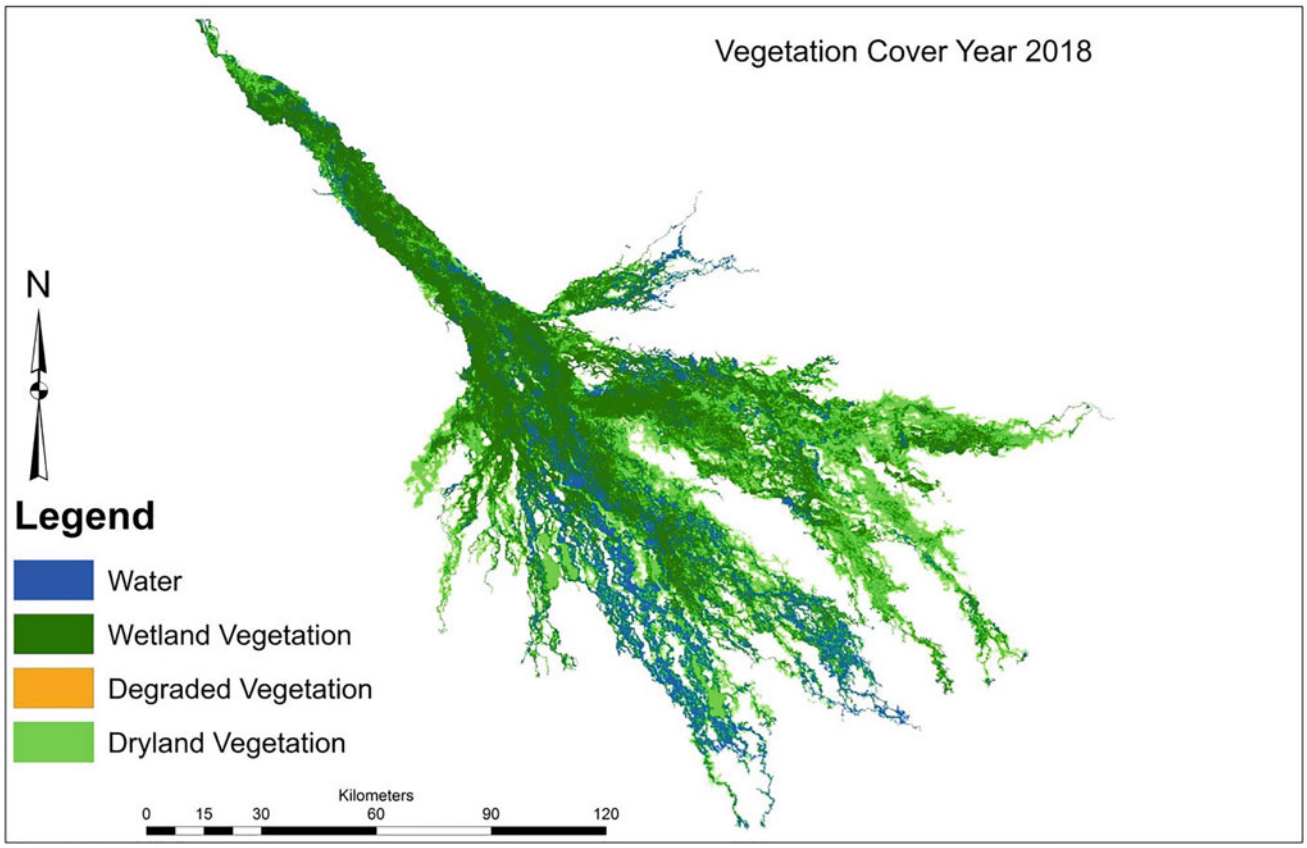

Fig. 4 Vegetation cover dynamics for the year 2018

the effects of the 2011 high flood and for wetland monitoring subsequent to the 2019 drought.

References

Bartsch, A., Wagner, W., Scipal, K., Pathe, C., Sabel, D., & Wolski, P. (2009). Global monitoring of wetlands—the value of ENVISAT ASAR global mode. *Journal of Environmental Management, 90*, 2226–2233.

Ramberg, L., Hancock, P., Lindholm, M., Meyer, T., Ringrose, S., Sliva, J., Van As, J., & VanderPost, C. (2006). Species diversity of the Okavango Delta. *Botswana. Aquatic Sciences, 68*, 310–337.

Overview of Research on the Behavior of Mines to Climate Change

Sabrina Zitouni

Abstract

The infiltration of rainwater into underground mines and groundwater fluctuations cause flooding of mines and make them more vulnerable. The aim of this paper is to highlight the potential impact of climate change on underground mines taking account of new scientific information and research data despite the uncertainties in rainfall patterns due to climate change and geotechnical hazards in underground quarries. This article summarizes the following findings: (1) mechanisms of water impact on the behavior of underground structure; (2) temperature and hygrometry of the rock mass and gallery air, interstitial pressure, level of the physicochemical parameters of the water in the galleries, deformation of the pillars; (3) other effects: microbiological metabolism and transfer of CO_2; (4) models estalished to study the impact of the fluctuation of the water table on the evolution of the deformations in the mines. This review concludes with a critical analysis of the described methods and models, and a discussion on their applicability is also presented.

Keywords

Climate change • Mines • Pillar • Groundwater • Deformation

1 Introduction

Many researchers have focused on a possible impact of climate forcing on hydroclimatic conditions in the underground mines by the observation of an increase in the number of incidents following heavy rainfall at several sites. Heavy rainfall reaches cavities by infiltration, by rising or capillarity water tables.

In France, the results of climate modeling work show a change in the pattern of extreme precipitation events (Ducharne et al., 2009). Modeling carried out by Météo--France highlights the evolution of cumulative rainfall during future extreme events. The increase could reach 16%, even though with significant regional disparities. MétéoFrance (2018), confirms an important impact of climate change on the cost of insurance against natural disasters in 2050.

Several territories in France suffer the consequences and the considerable economic stakes related to the costs of rehabilitation and development of disaster areas linked to the existence of underground quarries (Mathon et al., 2014). According to the annual report of the IGC Paris (2016), the flood at the beginning of June 2016 caused a very rapid rise in the level of the Seine River, which reached 6.10 m, corresponding to a ten-year flood exceeding that of the last great centennial flood of 1910. Water inflows into the underground quarries by infiltration of heavy rains and by the rising of the water table were observed and caused several localized collapses and subsidence in Paris and the suburbs.

2 Sensitivity of Cavities to Climate Change Variations

Temperature

The temperature rise is among the most widespread predictions of global warming (IPCC, 2001). Climate change in quarries cannot be perceived on a human time scale because of the inertia in the quarries explaining the decades-long lags in the warming of the cavity system (Badino, 2004). Most caves have an almost constant temperature over the year (Moore and Sullivan 1978, Smithson 1991 in Mammola et al., 2018), with an annual variability of a few tenths of a degree (Badino 2010). The average temperature of the rainwater that

S. Zitouni (✉)
Paris 7 Diderot University, Paris, France
e-mail: sabzitouni@yahoo.fr

A. Kallel et al. (eds.), *Selected Studies in Environmental Geosciences and Hydrogeosciences*,
Advances in Science, Technology & Innovation, https://doi.org/10.1007/978-3-031-43803-5_29

infiltrates the surrounding banks can balance the temperature of the rock surrounding the cavity (Badino, 2010). Other researchers go so far as to estimate a delay of almost 20 years in the warming of the cavity in relation to its environment (Domìnguez-Villar et al., 2015, In Mammola, 2018).

– Sensitivity of Cavities to Hydrogeological Variations

Many researchers have confirmed the adverse effects of water on the strength and deformability of several sedimentary rocks (Thierry et al., 2009; Zhang, 2012a, b; Didier et al., 2010; Al Heib et al., 2015; Zhou et al., 2015; Gombert et al., 2018; Meng et al., 2018) and long-term stagnant groundwater or runoff compromises the stability of underground cavities (Sadeghiamirshahidi and Vitton, 2018).

– Climate Change and Rainfall Erosivity

Greenhouse gas emissions influence precipitation properties (regime, intensity, frequency, seasonality, quality). The erosivity of rain R is generally defined in the universal soil loss equation A = R*K*LS*C*P where A represents the potential long-term average annual soil loss, K is the erodibility factor, and R is the rainfall and runoff factor. In the absence of data, researchers have established a relationship between K (erodibility factor) and daily, monthly, annual, and interannual rainfall (Choukri et al., 2016). The purpose of this method is to set the period of intense erosivity of the rains in the study site.

The dilution of atmospheric CO_2 in the water of the raindrops reduces its PH. Acid rain can accelerate the dissolution rate of carbonate and increase CO_2 emissions (Lan, 1997; Yu et al., 2012) in (Zhou et al., 2012). The results of simulation experiments indicate that the rate of carbonate dissolution under the effect of acid rain is ten times faster than dissolution under normal PH rain.

– Climate Change and CO_2 in Cavities

The atmospheric CO_2 can reach a ventilated cavity; hence, another source of CO_2 that is not to be underestimated is the CO_2 in the ground above the cavities. The production of this CO_2 increases with the increase in temperature and humidity when the soil reaches the saturation value.

– Ambient Hygrometry

Water can reach underground mines by fringe capillarity during a low water period (Gombert et al., 2018). It affects structural and textural changes in geomaterials (Sorgi and Germmaro, 2011). Pillar's evolution can be impacted by the ambient hygrometry of a mine when the water level shows a decreasing trend. This is observed in gypsum mines and in chalk mines (Auvray et al.., 2004). The continual degradation of these pillars leads to their inability to support the entire quarry. This aging mechanism, which varies over time, is due to the action of water contained within the mine atmosphere (Auvray et al., 2008).

– Groundwater Fluctuations

Climate change has a potential impact on groundwater quantity and quality (Bear and Cheng, 1999). Annual groundwater recharge cycles result in winter high water tables and summer low water tables. However, the highest amplitude cycles can occur at multi-year scales and cause flooding or dewatering of shallow underground mines (Gombert et al., 2013). The recharge process is complicated by human activities such as pumping. The presence of frozen soil causes limited infiltration, and the vegetative cover can change the magnitude and timing of infiltration and exfiltration by evapotranspiration (Green et al., 2011). In France, groundwater is not subject to climatic variations in a homogenous way; fluctuations in the piezometric level of groundwater that interact more with the surface are the most sensitive to infiltration, evapotranspiratory recoveries, and human solicitations. Heavy rainfall is expected in winter and a probable drought in summer. The shallow groundwater tables, thus recharged, may have a higher piezometric level in winter and a lower level in summer (Didier et al., 2010).

The increase in temperature will increase evapotranspiration from the soil and shallow groundwater (Eckhardt & Ubricht 2003). A consequence of summer drought is the over-consumption of groundwater.

Water containing CO_2 is more aggressive because its dissolution potential has increased (1). The presence of calcite in a wet environment in the presence of CO_2 gives rise to an acid: carbonic acid (H_2CO_3).

$$CaCO_3 + CO_2 + H_2O \Leftrightarrow Ca + 2 + 2HCO- \qquad (1)$$

Zhou et al. studied the effects of climate change on the dissolution of carbonates (Calcite and Dolomite). For them, the increase in temperature increases the reaction between CO_2 and carbonates; thus, the dissolution rate of carbonates increases.

The Weight of Rainfall

During heavy and persistent rainfall, the weight of the ground increases. The load on the pillars will increase during rainy periods and decrease during dry periods. This phenomenon is often referred to in the case of underground mines with little overburden. A direct correlation, without a shift in time, is observed between the rainy days and those with high deformation rates (Auvray, 2008).

3 Estimating of Stability of Underground Mines in a Climate Change Context

In order to anticipate the consequences of climate change on underground mines, scholars use laboratory tests, instrumentation in situ, and the response of rock depending on groundwater levels (Auvray, 2004, Auvray, 2008, 2016, Gombert et al., 2018).

Multi-annual Water Levels.

Researchers reproduce a characterization of the previous water state (climatic state, hydrologic state, hydrogeological state) of the study area at the time of the collapse. The evolution of multi-annual trends and multi-decennial trends is used in the modeling of hydric system operation. Underground mines were instrumented in order to follow the development of piezometric and physicochemical parameters (Gombert et al., 2018).

Geomechanical Parameters.

The monitoring of the geomechanical parameters of the pillar concerns its horizontal deformation and vertical deformation (Gombert et al., 2018). Observations carried out in situ show that the deformation of the pillars tends to increase at the same time at the piezometric level and, therefore, the degree of water saturation of the chalk. The 3D model has been developed to simulate the elasto-visco-plastic behavior of a chalk pillar, taking into account its short and long-term behavior. The chalk behavior has been described by combining a creep law associated with an elasto-plastic law with a failure criterion. Al Heib et al. (2015) evaluated the stability of the quarry by analyzing the resistance of the pillars. They used the tributary table method. The parameters used were: the geometry of the galleries and pillars, the depth of mining, and the weight of the overburden. The pillars are essential to ensure the stability of the quarry and to support the overlying layers to the surface. The safety factor is related to the strength of the pillar, and the average of the stresses exerted FOS = S/σp. Feedback on stability studies carried out in underground chalk quarries shows that the estimated coefficient of security often comes up against the choice of values: resistance to be retained, the characteristics to be taken into account to reproduce the behavior of this material in the presence of water.

The impact of moisture on the behavior of materials that make up the roofs, pillars, and floors of underground quarries has been analyzed in several studies (Gombert et al., 2013; Auvray et al., 2008; Gombert et al., 2018). The methods used are laboratory observations, field measurements of strain rate, modelling, environmental scanning electron microscope, temperature, and relative humidity.

4 Discussion

Little research on the impact of climate change on underground mines and some studies show very site-study-specific results. Even though the incidents coincide with heavy rains, the authors remain skeptical about the assertion of the correlation between current and future climate changes and aging in underground mines (Gombert, 2018). The difficulty is to focus on this impact by isolating it from other anthropogenic impacts, such as pumping, and to predict a scenario of the state of the quarries in the short, medium, and long term (Badino, 2010). The absence of data or the existence of gaps in long piezometric series makes the task more complex and the results uncertain. However, previous scholars only focused on the applicability of the uniaxial fracture criterion. Research on the fracture criterion under confining pressure is still lacking (Meng, 2018). The geomechanical behavior of the pillar and model does not correctly reproduce the range of their annual oscillations. Therefore, this model must be improved before it can be applied in the long term. They argue that the long-term effects of climate change have not been adequately integrated (most methodologies focused on multi-hazard assessment without considering changes in space or time).

5 Conclusion

The complex relationships between the outdoor atmosphere, the soil/rock, and the underground atmosphere comprise a multi-component system. The analysis of climate change impact on underground mines requires knowledge of basically two variables: climate change and underground mines. The complexity and uncertainties related to these two fields (the geological context, the geodynamics and hydrogeologyof the quarries, and the context of climate change) make the task difficult. Climate variability cannot be anticipated because of scientific and technical uncertainty as well as uncertainties related to socioeconomic choices. The predictions about precipitation or temperature need precision with regard to their scale of application, and correlation must be with data of climatic variables at the interval of daily time for the finest forecasts. Researchers are modeling the behavior of the pillars.

References

Al Heib, M., Duval, C., Theoleyre, F., Watelet, J. M., & Gombert, P. (2015). Analysis of the historical collapse of an abandoned underground chalk mine in 1961 in Clamart (Paris, France). *Bulletin of Engineering Geology Environment, 74*, 1001–1018.

Auvray, C. et al. (2004). The aging of gypsum in underground. *Engineering Geology, 74*, 183–196

Auvray, C. et al. (2008). The influence of relative humidity on the rate of convergence in an underground gypsummine. *Internatinal Journal of Rock Mechanics and Mining Sciences, 45*, 1454–1468.

Badino, G. (2004). Cave temperatures and global climatic change. *International Journal of Speleology, 33*, 103–113.

Badino, G. (2010) Underground meteorology—what's the weather underground? *ACTA Carsologica, 39/3*:427–448, POSTOJNA.

Bear, J., Cheng, H.-D. (1999). *Seawater intrusion in coastal aquifers-concepts, methods and practices* (625 p). Dordrecht, Boston, London: Kluwer Academic Publisher

Didier, C. (2010). Impact of climate change on the stability of underground shallow cavities. The case of a tragedy inFrance in relation with the Seine flooding in 1910. In *ISRM International Symposium 2010 and 6. Asian RockMachanics Symposium "Advances in Rock Engineering"*.

Ducharme, A., Théry, S., Viennot, P., Ledoux, E., Gomez, E., & Déqué, M. (2009) *Rapport de fin de contrat : impact du changement climatique sur les ressources en eau et les extrêmes hydrologiques dans les bassins de la Seine et de la Somme. Programme GICC.* Paris : Ministère de l'Écologie, de l'Énergie, du Développement durable et de la Mer

Domìnguez-Villar, D. et al. (2010). The effect of visitors in a touristic cave and the resulting constraints on natural thermalconditions for paleoclimate studies (Eagle cave, central Spain). *Acta Carsologica, 39*(3), 491–502

Eckhardt, K., Ulbrich, U. (2003). Potential impacts of climate change on groudwater recharge and streamflow in acentral European low mountain range. *Journal of Hydrology, 284* (1–4), 244–252.

Fatiha, C., Mohamed, C., Mustapha, N., Damien, R., Yannick, P. (2016). Impact du changement climatique sur l'évolution de l'érosivité des pluies dans le Rif Occidental (Nord du Maroc). *European Scientific Journal European Scientific Institute*, *12*(32), 79–93. https://doi.org/10.19044/esj.2016.v12n32p79ff. ffhal-02634046f

Gombert, P., Auvray, C., & Al Heib, M. (2013). In-situ and laboratory tests to evaluate the impact of water table fluctuations on stability of underground chalk mines. *Proc Earth Planet Sci, 7*, 304–308.

Gombert, P., Thoraval, A., Watelet, J.-M. (2018). Geomechanical response of an abandoned chalk mine to multi-annualwater table fluctuations. *Bulletin of Engineering Geology and the Environment*. https://doi.org/10.1007/s10064-018-1321-7

Green, T. et al. (2011). Beneath the surface of global change: Impacts of climate change on groundwater. *Journal of Hydrology, 405* (2011), 532–560.

IPCC (2001). Climate change 2001: The scientific basis. Contribution of working group I to the third assessment report of the Intergovernmental panel on climate change. In J. T. Houghton, et al. (Eds.), (pp. 944). Cambridge, United Kingdom, and New York, NY, USA: Cambridge University Press.

Lan, J. (1997). Research on the erosion of simulated acid rain on limestone. *Journal of Guilin Institution and Technology, 17*(2), 164–169.

Mammola, S. et al. (2018). Climate change may drive cave spiders to extinction. *A Journal of Space and the Time in Ecology*.

Mathon, V. (2014). *Caractérisation du pergélisol en vue de la réfection et de l'adaptation aux changementsclimatiques de l'aéroport d'Iqaluit, Nunavut Mémoire (M. Sc.)–Université Laval.*

Mavrommatis, E. et al. (2019). Towards a comprehensive framework for climate change multi-rist assessment inthe mining industry. *Infrastructure, 4*(3), 38.

Meng, T. et al. (2018). Study of th deformation characteristics and fracture criterion of the mixed mode fracturetoughness of gypsum interlayers from Yunying salt cavern under a confining pressure. *Journal of Natural GasScience and Engineering, 58*, 1–14

Moore, G.-W., Sullivan, G.-N. (1978.) *Speleology: the study of caves*. Zephyrus, Teaneck, 150p

Sadeghiamirshahidi, M., & Vitton, S. J. (2018). Analysis of drying and saturating natural gypsum samples for mechanical testing. *Journal Rock Mechanics Geotechnical Engineering*

Sorgi, C., & De Gennaro, V. (2011). Water-Rock Interaction Mechanisms and Ageing Processes in Chalk. *Advances Data Methods Models Applications Geoscience*.

Thierry, P., Prunier-Leparmentier, A. M., Lembezat, C., Vanoudheusden, E., & Vernoux, J. F. (2009). 3D geological modelling at urban scale and mapping of ground movement susceptibility from gypsum dissolution: The Paris example (France). *Engineering Geology*, *105*.

Yu, S. et al. (2012). Carbonate rock acid rain dissolution capacity and surface dissolution micromorphology. *Journal of Guilin University and Technology, 32*(1), 48–54.

Zhang, Y., Hernandez, M., Anson, E., Nearing, M., Wei, H., Stone, J., & Heilman, P. (2012a). Modeling climate change effects on runoff and soil erosion in southeastern Arizona rangelands and implications for mitigation with conservation practices. *Journal Soil Water Conservation, 67*, 390–405.

Zhang, Y., Hernandez, M., Anson, E., Nearing, M., Wei, H., Stone, J., & Heilman, P. (2012b). Modeling climate change effects on runoff and soil erosion in southeastern Arizona rangelands and implications for mitigation with conservation practices. *Journal Soil Water Conservation, 67*, 390–405.

Zhou, G. et al. (2015). Overview of 30 years of research on solubility trapping in Chinese karst. *Earth-Science Reviews, 146*, 183–194.

Zhou, Q., Mikkelsen, P. S., Halsnæs, K., & Arnbjerg-Nielsen, K. (2012). Framework for economic pluvial flood risk assessment considering climate change effects and adaptation benefits. *Journal Hydrology, 414–415*, 539–549.

Cemented Surface Paste Disposal as a Mine Tailings Management Scenario: In Situ Long-Term Hydro-Geochemical Behavior Using Field Experiments

Abdellatif Elghali, Mostafa Benzaazoua, and Abdelkabir Maqsoud

Abstract

Ore treatment and processing generate large quantities of finely milled mine tailings. They are generally stored as conventional slurry in surface impoundments. Several problems could occur during tailings deposition such as: (i) risks of physical instability of dams, (ii) chemical instability due to sulfide oxidation, and (iii) environmental footprint due to land use and wasted water. Exposition of tailings to atmospheric water and oxygen accelerates sulfide oxidation, and consequent carbonate dissolution can lead to acid mine drainage formation. The objectives of this study were to evaluate the effectiveness of surface paste disposal combined with the use of cementitious amendments to solidify/stabilize acid-generating tailings. The studied tailings were characterized for their physical, chemical, and mineralogical properties. Two field cells (cemented cell and uncemented reference cell) were constructed at the operating LaRonde mine (Quebec, Canada) to investigate the long-term hydro-geochemical effectiveness of cemented surface paste disposal to limit tailings' reactivity. The cells, which were inverted truncated pyramids (up to 800 m^3), were equipped with suction and water content probes. The chemical and mineralogical composition of the mine tailings revealed high sulfide content, mainly as pyrite, of about 29 wt%. Carbonates (acidity buffers) occurred at low content (around 0.1 wt%). The addition of cement within surface paste disposal reduces water infiltration and consequently contact surface and time between reactive tailings and water. Moreover, the geochemical behavior of cemented and uncemented cells was relatively similar at the beginning of the tests. pH values were circumneutral around 7 and electrical conductivity ranged between 1 and 8 ms/cm. Considering metal(oid)s, uncemented cells showed higher release for Al, As, Fe, Cd, Co, Ni, S, and Zn. This means promising results of using cemented surface paste disposal to limit contamination from these sulfidic tailings when runoff is integrated into the concept. However, pH values dropped down at the fifth year of the hydro-geochemical monitoring, but the metal(oid)s stabilization was successfully achieved. The main mechanisms responsible for metal(oid)s attenuation were precipitation of secondary phases such as iron oxy-hydroxides and/or contaminant physical trapping.

Keywords

Cemented surface paste • Tailings disposal • Sulfides • Field cells • Geochemical behavior

1 Introduction

Mining industries generate a large volume of finely crushed tailings that are generally deposited in saturated surface impoundments. Conventional disposal of tailings can result in several serious issues related to the geotechnical stability of dams, the release of contaminants into the environment, and the storage capacity of impoundments (Tuylu et al., 2019). Cemented surface paste disposal (CSPD) of tailings is a promising technique that consists of reducing the tailings water content to limit sulfide reactivity and adding cemented layers to improve the mechanical properties of tailings (e.g. UCS) (Benzaazoua et al., 2004). Cement addition allows acidity buffering and matrix hardening; pH values are kept near circumneutral values. Consequently, the risk of acid

A. Elghali (✉)
Geology and Sustainable Mining Institute, Mohammed VI Polytechnic University, 43150 Ben Guerir, Morocco
e-mail: abdellatif.elghali@um6p.ma

A. Elghali · M. Benzaazoua · A. Maqsoud
Université du Québec en Abitibi-Témiscamingue 445, Boul. de L'Université, Rouyn-Noranda (Québec), J9X 5E4, Canada

M. Benzaazoua
Mining Environment and Circular Economy, Mohammed VI Polytechnic University, 43150 Ben Guerir, Morocco

A. Kallel et al. (eds.), *Selected Studies in Environmental Geosciences and Hydrogeosciences*, Advances in Science, Technology & Innovation, https://doi.org/10.1007/978-3-031-43803-5_30

mine drainage (AMD) formation is reduced. Moreover, in a neutral and alkaline environment, the mobility of heavy metals is limited (Cravotta, 2008; Elghali et al., 2019). The main mechanisms responsible for metal(oid)s stabilization are: (i) chemical precipitation at circumneutral pH values, (ii) physical trapping of contaminants, and (iii) decrease of water infiltration rate which reduces time and surface contact between oxidizing agents and sulfide.

2 Materials and Methods

2.1 Materials

Tailings used in this study were sampled at the Laronde mine site located in Quebec (Canada). The specific gravity (Gs) of the tailings was about 3.4, and their specific surface area (SSA) was about 2.6 m^2/g. The chemical characterization showed that the tailings are enriched in sulfur (18.4 wt %) and iron (23.15 wt%). The mineralogical composition performed by XRD confirmed the results of chemical characterization. Indeed, pyrite (acidifying mineral) content was around 29 wt%, and carbonate content was lower than the detection limit of XRD. The main identified neutralizing minerals were silicates such as paragonite (6.5 wt%), muscovite (5 wt%), and chlorite (4.7 wt%). However, silicate minerals are characterized by low solubility. Consequently, Laronde tailings are acid-generating.

The cement used in this study was Portland cement GU10. Its Gs and SSA were 3.15 and 1.6 m^2/g, respectively. The major oxides (wt.%) were about 65.76 of CaO, 19.51 of SiO_2, 19.51% of SiO_2, 4.86% of Al_2O_3, and 2.44% of Fe_2O_3.

2.2 Field Cells Description, Construction and Instrumentation

The field cells are considered as the most representative kinetic tests for the assessment of the geochemical behavior of solid materials. They are performed on a large sample's mass in realistic conditions in terms of temperature, precipitation, humidity, and bacterial activity. The field cells were constructed in 2010 and have the geometry of the inverted pyramid (Fig. 1). The surface areas of the base and top of each cell were about 118.5 m^2 and 16.2 m^2, respectively. The cells were equipped with probes for water content and suction monitoring, but the results are not presented here. The leachates were collected in a storage barrel after a rain event. The leachates were analyzed for their pH, electrical conductivity (EC) using pH/EC meters, and their chemical composition using ICP-AES on filtered ($\leq$ 0.45 µm) acidified samples (2% v/v HNO_3).

3 Results

Mine tailings contained high sulfide content mainly as pyrite and trace amounts of calcite, which confirms their acid-generating behavior. However, pH monitoring (Fig. 2a) showed that acidity is generated after a lag time which corresponds to the first year. The lag time is due to acidity buffering by carbonate and silicate dissolution. However, after one year, the pH dropped down for the cemented and the uncemented cells to attain acidic values (pH $\sim$ 2.8); the pH of the leachates from the cemented cell was higher than that observed for the uncemented cell. Then, the pH values stabilized between 2.6 and 6.5. The average electrical

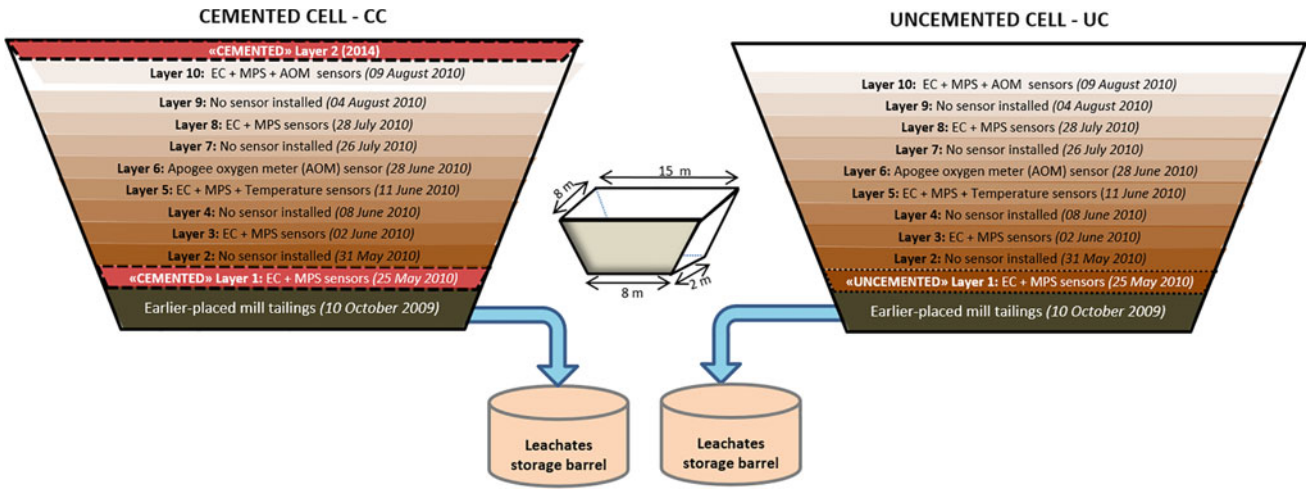

Fig. 1 Schematic illustration of filed cells constructed at Laronde mine (Quebec)

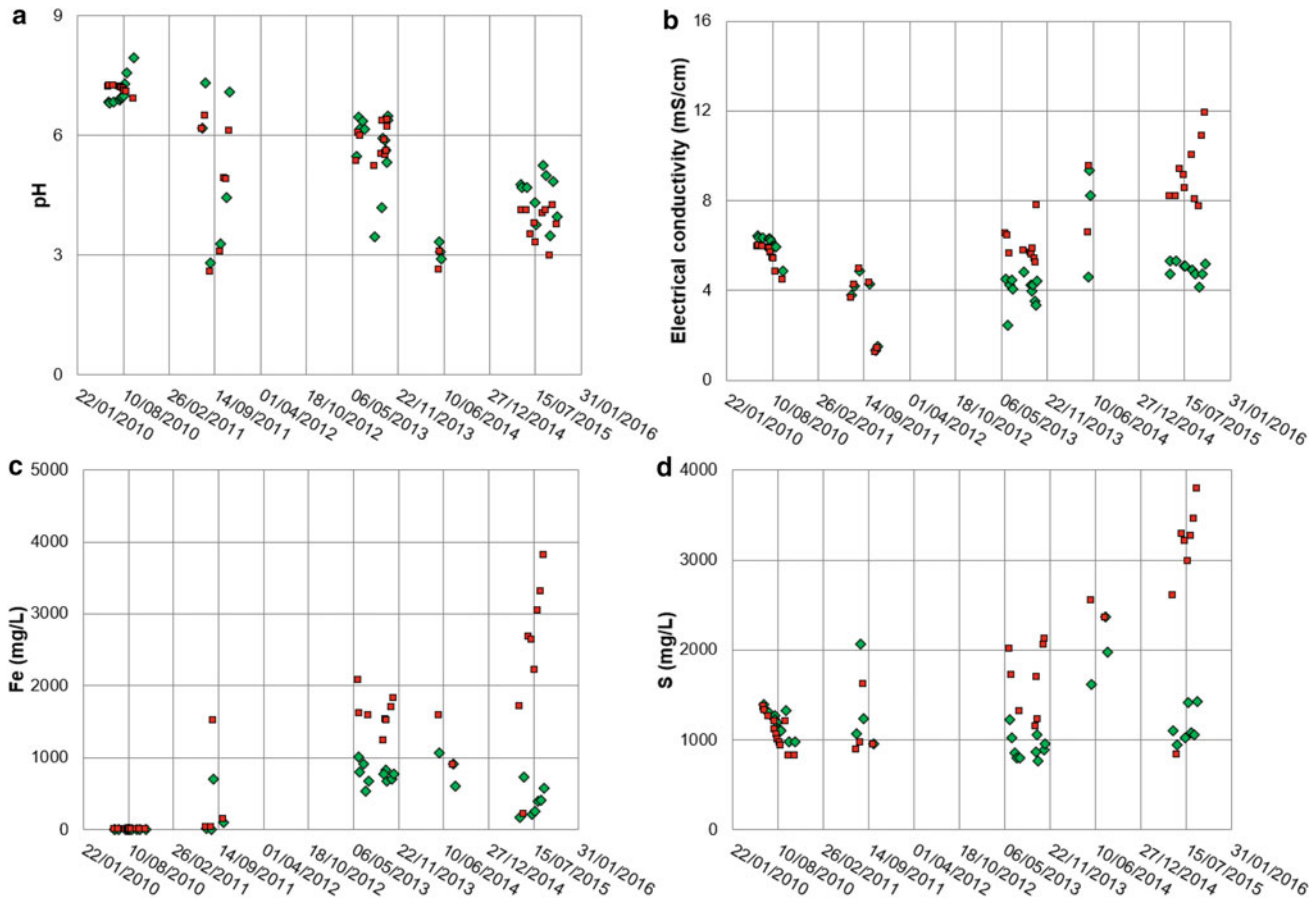

Fig. 2 Evolution of pH (**a**), electrical conductivity (**b**), Fe (**c**), and S (**d**) within the leachates from uncemented cell (red square) and cemented cell (green rhombus)

conductivity (EC) (Fig. 2b) is 4.88 and 6.40 mS/cm for cemented and uncemented cells, respectively. Iron leaching (Fig. 2c) was higher within the uncemented cell compared to the cemented cell. Indeed, average iron leaching was about 551 and 1024 mg/L for cemented and uncemented cell, respectively. The same tendency was observed for sulfate leaching, which indicates pyrite oxidation. Indeed, the average sulfate leaching was about 3542 and 6270 mg/L for cemented and uncemented cells, respectively. Other chemical species such as Al, As, Cd, Co, Ni, and Zn were more released within the uncemented cell compared to the cemented cell.

Results of water content and the suction within layer 5 (Fig. 1), which are not presented here, showed that tailings saturation degree remained high compared to the uncemented layer; high saturation degree decreases sulfide reactivity and, thus, prevents acid mine drainage formation. Actually, during the first stages of cementation, the water infiltrates to saturate deeper layers. However, after cementation of the top layer, water vertical infiltration and evaporation became limited, which allows keeping deeper layers saturated.

4 Discussion

Field tests performed in this study to evaluate the effectiveness of cemented surface paste disposal to prevent contamination by acid mine drainage and increase tailings impoundments life cycle showed promising results. The addition of cement provides additional neutralization potential which explains high pH values within the cemented cell compared to the uncemented cell. Moreover, contaminants' release was highly reduced. Indeed, contaminants reduction factors (R = Ci-cc/Ci-uc, where Ci-cc is the concentration of the element i within a cemented cell and Ci-uc is the concentration of the element i within an uncemented cell) for Al, Co, Fe, Ni, Pb, S, Sb, and Zn were about 0.04, 0.26, 0.15, 0.17, 0.12, 0.38, 0.2, and 0.09, respectively. Contaminants immobilization is ensured due to chemical and physical mechanisms: (i) cement dissolution increases pH of pore waters which enhances metals precipitation in alkaline conditions, (ii) contaminants physical trapping within the cementitious matrix, (iii) reduction of water vertical infiltration which reduces time and surface contact between

reactive tailings and oxidizing agents (e.g. water, oxygen), and iv) increase of tailings saturation degree which reduces their reactivity. Moreover, field observations showed that the crack intensity factor (CIF) which is an indicator of surface degradation was higher for the uncemented cell compared to the cemented cell. This means that water will infiltrate easily within the uncemented cell.

5 Conclusions

Five years of field tests monitoring showed that cemented surface paste disposal is a promising alternative for conventional disposal of tailings. Adding cementitious layers prohibited and decreased metal(oid)s mobility. However, the acidic behavior of tailings was not successfully buffered due to the high sulfide content (28 wt% pyrite). However, the industrial use of such technique needs an economic feasibility study to estimate costs related to cement use.

References

Benzaazoua, M., et al. (2004). A laboratory study of the behaviour of surface paste disposal. In *Proceedings of the 8th International Symposium on Mining with Backfill, The Nonferrous Metals Society of China, Beijing*.

Cravotta III, C. A. (2008). Dissolved metals and associated constituents in abandoned coal-mine discharges, Pennsylvania, USA. Part 2: Geochemical controls on constituent concentrations. *Applied Geochemistry, 23*(2), 203–226.

Elghali, A., et al. (2019). In Situ effectiveness of alkaline and cementitious amendments to stabilize oxidized acid-generating tailings. *Minerals, 9*(5), 314.

Tuylu, S., Bascetin, A., & Adiguzel, D. (2019). The effects of cement on some physical and chemical behavior for surface paste disposal method. *Journal of Environmental Management, 231*, 33–40.

Statistical Study of Rainfall and Sediment Transport in the North-West of Algeria

Faiza Hallouz, Mohamed Meddi, Gil Mahé, Salah Eddine Ali Rahmani, and Fateh Chebana

Abstract

The study area is in the Ghrib–Cheliff sub-watershed, extending over ~1380 km^2 and is located ~100 km South-West of Alger. The proposed model was tested using monthly data, total rainfall (R), peak discharge (Qmax), and suspended sediment load (SSL). Data is obtained from Ghrib stations (hydrometric and rainfall) located on the Cheliff wadi. Twenty years of available data were subjected to bivariate copulas. Results from the statistical analysis show that events reasonably fit with the Log-Normal type 2 for the pair SSL and Qmax and generalized logistic (GL) for the pair SSL and R (AIC and BIC Criteria). In addition, the dependence of these events was tested using bivariate copulas, the results of which show that Clayton and Gumbel's copulas are most suitable.

Keywords

Ghrib–Cheliff • Rainfall • Peak discharge • SSL • Copulas

F. Hallouz (✉)
Djilali BOUNAAMA University of Khemis Miliana, Ain Defla, Algeria
e-mail: F.Hallouz@univ-dbkm.dz

F. Hallouz · M. Meddi
National Higher School of Hydraulics (ENSH), Water and Environmental Engineering Laboratory, ENSH, Blida, Algeria

G. Mahé
Hydrosciences Montpellier, University Montpellier, CNRS, IRD, IMT Alès, Montpellier, France

S. E. A. Rahmani
Faculty of Earth Sciences, Geography and Territory Planning, Geo-Environment Laboratory (LGE), University of Sciences and Technology Houari BOUMEDIENE (USTHB), Bab Ezzouar, Algiers, Algeria

F. Chebana
Eau Terre Environnement Research Centre, INRS, Québec, Canada

1 Introduction

The region's water resources are scarce (average of about 450 mm.y^{-1}). Hence, there is a necessity to preserve and enhance the storage capacity of dams within the region. This capacity is under increasing threat from siltation, which consistently grows year after year. Unfortunately, the absence of models and tools hampers our ability to monitor the spatial and temporal evolution of solid transport. Indeed, the study area is the sub-watershed of the Ghrib–Cheliff wadi, with an area of approximately 1380 km^2. It is located about 100 km South-West of Algiers (Fig. 1). This basin has been chosen as a basin of application of our work for the range of the available data and, therefore, the near-total absence of studies on this basin (only one or two studies are administered like Mokhtari (2017).

This work, the first of its kind, analyzes the influence of the temporality of the transport of suspended sediment load (SSL), corresponding rainfall (R), and peak discharge (Qmax). It also studies the distribution of these events. Additionally, we aim to model dependencies between (SSL, Qmax) and (SSL, R), and we will achieve this through the development of various bivariate copulas (Kao & Govindaraju, 2008; Renard & Lang, 2006).

2 Method

2.1 Data

The data for the SSL, rainfall, and discharge come from the National Agency for Water Resources (ANRH). These data were recorded by two stations: a hydrometric station (011407) that gives us maximum monthly peak discharges (Qmax) and monthly suspended sediment load (SSL), and the rainfall station (011407) that records total monthly rainfall ®. They are recorded at the two stations for the period from 1976 to 1996 (20 years).

A. Kallel et al. (eds.), *Selected Studies in Environmental Geosciences and Hydrogeosciences*, Advances in Science, Technology & Innovation, https://doi.org/10.1007/978-3-031-43803-5_31

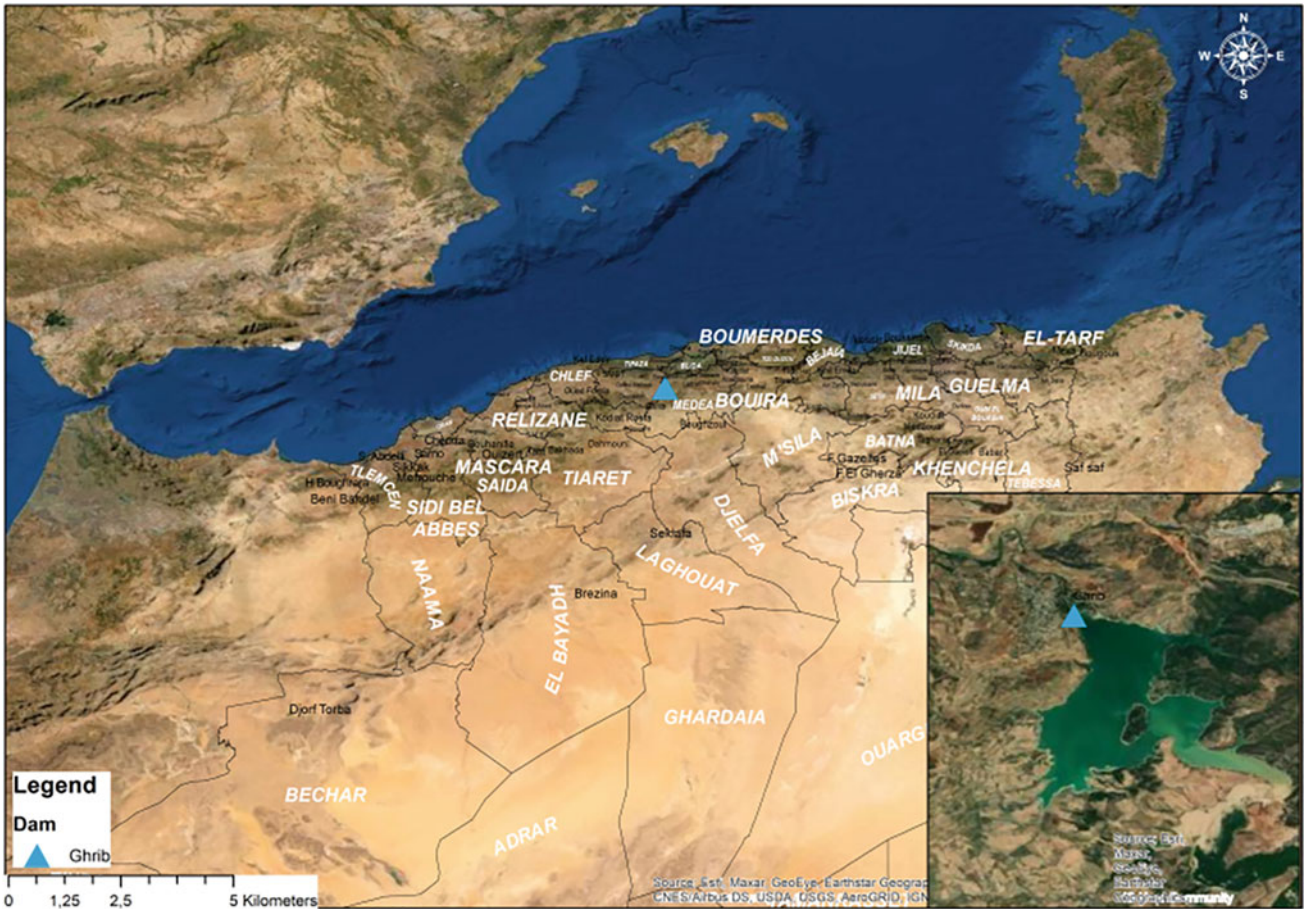

Fig. 1 Cheliff–Ghrib sub-watershed situation

2.2 Distributions and Statistical Testing

The generalized extreme value (GEV), the generalized logistic function (GL), the Log Pearson (LP), Log-Normal (LN), Weibull (W), Gumbel (G), and Gamma (GAM) were tested. The Kolmogorov–Smirnov test (ks) is used to determine and verify the reliability of the adjustment of these characteristics with five proposed distributions (Bezak et al., 2017; Hosking & Wallis, 1997). Adjustments are made for each of the distributions via the HYFRAN-PLUS software (Adlouni & Bobée, 2014).

2.3 Copulas

To model the dependencies between two variables, many bivariate copulas have been built. Among these copulas, the Archimedean (Clayton, Frank, Gumbel et Ali-Mihail-Haq), Elliptical copulas (Gaussian and Student), and Plackett, and Farlie–Gumbel–Mordenstrern are some of the most widely used copula families, owing to its flexibilities in capturing a wide range of modeling the statistical dependencies of hydro-pluviometry extremes (Bezak et al., 2017; Kao & Govindaraju, 2008; Mingzhong et al., 2019; Renard & Lang, 2006). The corresponding copulas were tested using the R program (Lmomco Package: Program R., 2017).

2.4 Goodness-Of-Fit Test for Copula

Several goodness-of-fit tests (GOF) have been proposed. Considering the availability of excessive copula functions, some criteria (the Akaike information criterion (AIC) and Bayesian information criterion (BIC)) are widely used to select the appropriate copulas as well as other multidimensional models by estimating their fitting biases (Bezak et al., 2017).

3 Results

3.1 Copulas and Comparison of Marginal Fitting

Figures 2 and 3 show the K-plot for the different Archimedean copulas, as well as the empirical one. Indeed, bivariate copulas were used to model the pair dependency of

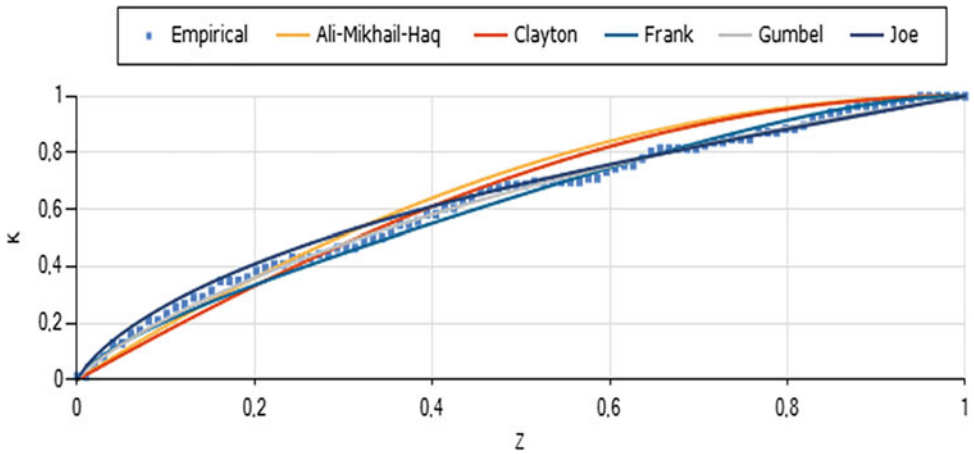

Fig. 2 Kendall plot for SSL and Qmax at Ghrib station

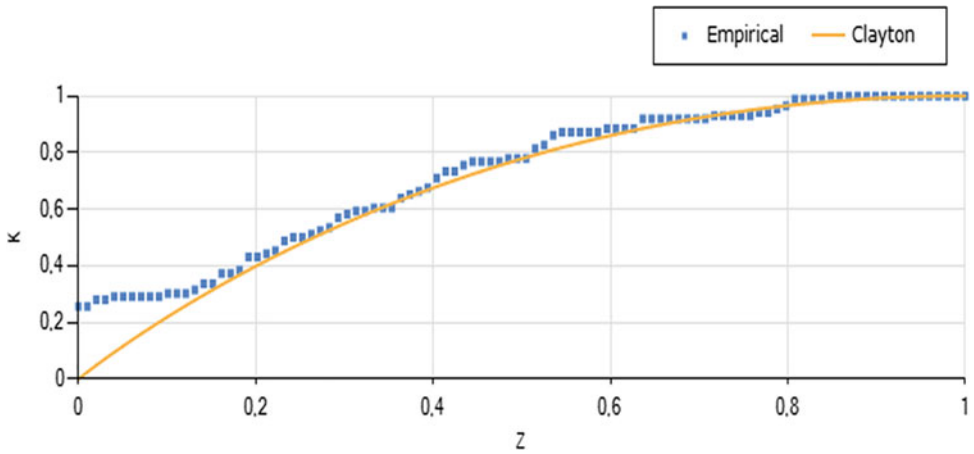

Fig. 3 Kendall plot for SSL and R at Ghrib station

suspended sediment load (SSL), rainfall (R), suspended sediment load (SSL), and discharge (Qmax).

The comparison of marginal fitting is in Table 1 for the pair SSL versus Qmax and in for the pair SSL versus R in Table 2.

According to the previous analysis (SSL and Qmax), the best marginal distributions are Log Pearson and Log-Normal type 2 (Table 1), and the best copula is Gumbel (Fig. 2).

According to the previous analysis (SSL and R), the best marginal distributions are Log-Normal type 2 (Table 2) and generalized logistic and the best copula is Clayton (Fig. 3).

4 Discussion

Our work consists of conducting a study of the statistical distribution of suspended sediment load (SSL) events based on corresponding rainfall and discharge in the Ghrib–Cheliff sub-basin. It shows that the best marginal distributions are Log Pearson and Log-Normal type 2 for the pair SSL and Qmax, and Log-Normal type 2 for the pair SSL and R. The application of the criteria BIC and AIC information has just confirmed this choice.

Table 1 Descriptive statistics for Qmax at Ghrib station

Distribution	Nb. parameters	X(T)	BIC	AIC
GEV LM	3	243.34	775.61	768.24
Generalized logistic LM	3	241.18	776.80	769.44
Log Pearson DMM	3	234.01	774.59	767.23
Log Pearson SAM	3	244.65	765.09	757.73
Log-Normal type 2 ML	2	275.77	760.79	755.88

Table 2 Descriptive statistics for SSL at Ghrib station

Distribution	Nb. parameters	X(T)	BIC	AIC
Generalized logistic LM	3	172,909.90	1843.53	1836.17
Log-Normal type 2 ML	2	664,695.50	1705.09	1700.18

The study of copulas showed that Clayton and Gumbel's copulas perform better in modeling the pair dependency of solid matter (Qs, rainfall ®, and flood (Qmax), respectively.

Finally, it has been observed that an increase in rainfall intensity and a decrease in rainy days would increase the sedimentation rate of the dam reservoir. The change of climatic conditions leads to a rise of erosion, consequently, the sediments' transport increases.

5 Conclusions

This study was carried out with data on the transport of suspended sediment load (SSL), corresponding rainfall, and peak discharge in the Ghrib–Cheliff sub-basin, in a semi-arid climate.

At the top of this work, we recommend that it is necessary to seek out effective solutions and to place systems capable of preserving this resource and, therefore, the protection of storage structures (reservoirs). Indeed, risk reduction can happen at the extent of a modernization project and prevention procedures, including solutions with a reserved and active protection requiring intervention or supervision of the operator. Effective solutions to risk reduction should be implemented.

Acknowledgements We want to thank ANRH for the hydrological and rainfall data. This work was done in the framework of Young Teams Associated with the IRD of ENSH Blida (Jeunes Équipes Associées à l'IRD).

References

Bezak, N., Rusjan, S., Kramar Fijavž, M., Mikoš, M., & Šraj, M. (2017). Estimation of suspended sediment loads using copula functions. *Water, 9*, 628. https://doi.org/10.3390/w9080628

El Adlouni, S., & Bobée, B. (2014). Analyse Fréquentielle avec le logiciel HYFRAN-PLUS. Guide d'utilisateur disponible avec la version Démo. http://www.wrpllc.com/books/HyfranPlus/indexhyfranplus3.html

Hosking, J. R. M., & Wallis, J. R. (1997). *Regional frequency analysis: An approach based on L-moments*. Cambridge University Press.

Kao, S. C., & Govindaraju, R. S. (2008). Trivariate statistical analysis of extreme rainfall events via the Plackett family of copulas. *Water Resources Research, 44*, W02415.

Lmomco Package: Program R. Available online: https://cran.r-project.org/web/pacages/lmomco/lmomco.pdf. Accessed on July 15, 2017.

Mingzhong, X., Zhongbo, Y., & Yuelong, Z. (2019). Copula-based frequency analysis of drought with identified 6 characteristics in space and time: a case study in Huai River basin, China. *Theoretical and Applied Climatology*. https://doi.org/10.1007/s00704-019-02788-x

Mokhtari, E.H. (2017). Impact de l'érosionhydrique sur l'envasement du barrage Ghrib. These Doctorat En Sciences, Universite de Chlef, p. 272, Mars 2017.

Renard, B., & Lang, A. (2006). Use of a Gaussian copula for multivariate extreme value analysis: Some case studies in hydrology. *Advances in Water Resources, 30*, 897–912.

The Effects of Landfill Leachate Irrigation on Soil Properties

Soukayna Rhouat, Mohammed Salaheddine El Youbi, and Fouad Dimane

Abstract

The reuse of treated leachate in irrigation or green spaces watering can be considered as an alternative solution for facing water deficit. However, it represents a risk of environmental contamination by the accumulation of hazardous elements in the soil layers and plant tissues, which reduce the crop yields and its performance. This article will assess the irrigation suitability of different types of leachates by measuring their impacts on soil quality. The experimental test has been done using Meknes municipal landfill leachate. We have irrigated ten plots of corn with clean water (witness plot) and three types of effluent: (1) raw leachate (RL), (2) leachate treated by membrane bioreactor (MBRL), and (3) leachate treated by membrane bioreactor and reverse osmosis (MBRROL). In this investigation, soil parameters have been analyzed before and after irrigation to follow up the quality degradation of this one. The initial values of the studied soil were: pH = 8.31, the salinity = 0.36 mS/cm, the permeability = 0.53 cm/h. The results obtained show that MBRL can be used in irrigation with continuous control to avoid soil salinity (EC) after irrigation had increased up to 2.89 mS/cm). As for the MBRROL, it is respecting the recommended standards and can be judged suitable for irrigation. Contrary to RL which is strictly banned for irrigation because of the high pollution loads that had increased the soil pH (8.65) and salinity (6.22 mS/cm) and had reduced the permeability rate (0.13 cm/h).

Keywords

Irrigation • Landfill leachate • Salinity • Soil quality • Suitability

1 Introduction

The demographic growth is inducing great pressure on water supplies; the agriculture practice is the most consuming sector by 70% of the total consumption (Hamoda, 2004). This shows that it is important to manage the available water resources and to look forward to non-conventional water resources for their reuse in irrigation; it will help to save water (river, groundwater, dams) for drinking uses only.

The household landfill leachate is a source of pollution in many countries, but it can be non-conventional water that can be reused for irrigation. It is very rich in organic and mineral loads that make it a source of water and nutrients and can be used as a secondary raw material to produce a rich fertilizer (Romero et al., 2013). Those elements are beneficial for the growth and development of plants (Singh & Agrawal, 2010). Zupanc and Justin (2010) had confirmed the fertilization properties of landfill leachate; they had shown a positive effect on the growth of P deltoids and the increase of the biomass production after irrigation essay. Cheng and Chu (2011) and Justin and Zupančič (2009) had also affirmed that the irrigation reuse of landfill leachate had contributed to fast growth and well-nourished plants. The plant grown in leachate-irrigated soil indicated a positive response by increasing the shoot length, root length, number of leaves, and harvest index (Singh et al., 2017).

However, the high rate of salinity, minerals, and suspended matter of landfill leachate can have a negative effect on plants and physicochemical soil properties. For this reason, we must assess the suitability of these effluents to be reused in irrigation.

S. Rhouat (✉) · M. S. El Youbi
Laboratory of Electrochemistry, Materials and Environment, Faculty of Science, IBN Tofail, Kenitra, Morocco
e-mail: soukayna.rhouat@gmail.com

F. Dimane
National School of Applied Sciences, Al Hoceima, Morocco

A. Kallel et al. (eds.), *Selected Studies in Environmental Geosciences and Hydrogeosciences*, Advances in Science, Technology & Innovation, https://doi.org/10.1007/978-3-031-43803-5_32

Recently, different research works were conducted on the reuse of charged effluents in irrigation after their treatment (Bedbabis et al., 2014; Heidarpour et al., 2007). Membrane bioreactor and reverse osmosis had shown their efficiency to reach the optimum quality of irrigation water (Falizi et al., 2018).

The objective of this study is to assess and determine the impact of irrigation by three different landfill leachate treatments on soil parameters.

2 Materials and Methods

The experimentation was carried out from May to September 2017, in a Corn (Zea mays) culture near Meknes municipal landfill, Morocco (33.931743, −5.574957). The soil plots were irrigated by four different types of effluents, raw leachate (RW), leachate treated by a bioreactor membrane (MBR) composed by a nitrification basin, ultrafiltration as membrane treatment (MBRL), leachate treated by the same MBR treatment followed by reverse osmosis (MBRROL), and clean water (CW) as a sample witness (Fig. 1).

The leachate used in the study was collected from the municipal landfill of Meknes city in Morocco, which receives only household waste, with 71.3% of the biodegradable fraction. The samples were regularly analyzed all along the experimental period, according to the standard method for the examination of water and wastewater (American Publishing Health Association (APHA), American Water Works Association (AWWA), Water Environment Federation (WEF), 2005). The results of the analyzed parameters are summarized in Table 1.

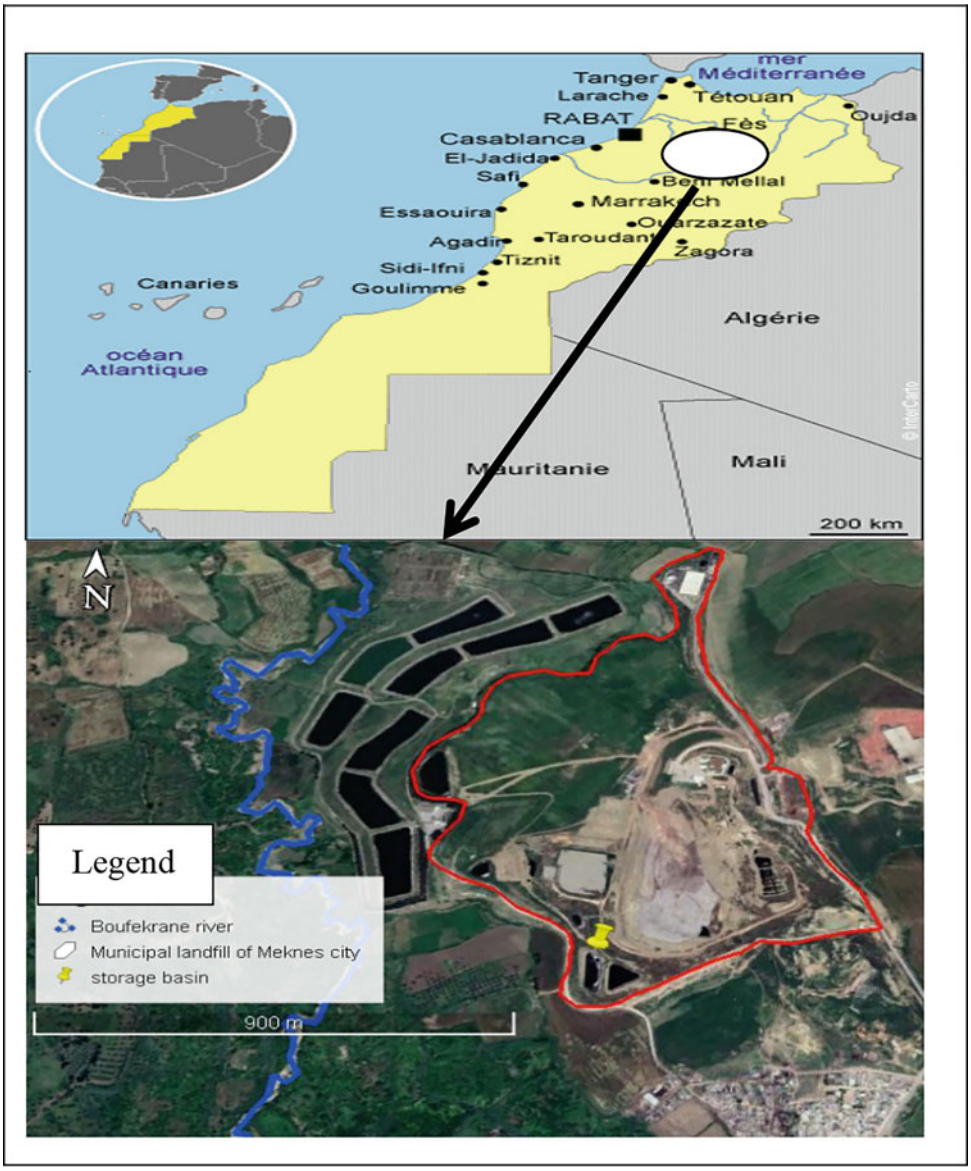

Fig. 1 Study location maps (Rhouat et al., 2019)

Table 1 Composition of the leachate used in the irrigation test

	RL	MBRL	MBRROL	Limit value (International standards) (Recommended Limits for Constituents in Reclaimed Water for Irrigation & United States Environmental Protection Agency, 2004)	Limit value (Moroccan standards) (SEEE, 2007)
pH	8.26	7.52	6.83	6–9	6–8.5
Conductivity mS/cm	27.9	12.70	1.25	3	12
Suspended matter (SM) mg/l	2100.76	8	< 2	100	350 if sprinkler irrigation 5 if surface irrigation
Na (mg/l)	1684	1202.8	54.78	69	None
HCO_3 (mg/l)	13.087	446.66	84.6	500	518

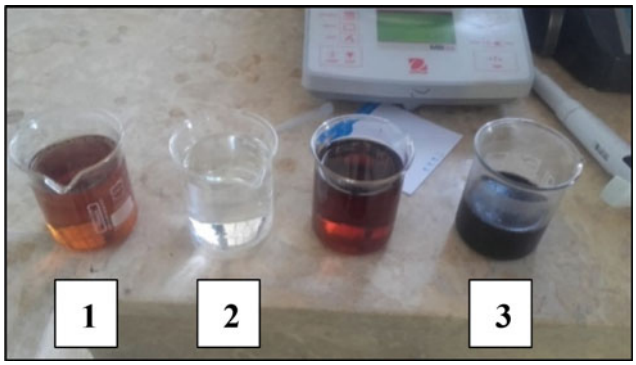

Fig. 2 Different effluents used during the irrigation test. (1) MBRL, (2) MBRROL, (3) RL

The type of studied soil (SS) is clay with 61.8% of clay particles, 22.7% of silt particles, and 15.6% for sand particles. The initial characterization had shown that it is moderately alkaline soil (initial pH = 8.1) and had a moderate rate of infiltration (0.13 cm/h). The soil does not represent any problem of salinity since the EC is around 0.36 mS/cm (Fig. 2).

All the soil analyses were carried out according to the internationally recommended methods (Sparks et al., 1996). Soil samples were analyzed before and after the irrigation period from the different soil plots. The soil samples were dried and gently crushed before being analyzed.

3 Results

From Fig. 3, we can identify the changes that come out through the irrigation with the different types of leachates. The results indicate a significant variation in parameters that are in correlation with the irrigation water composition. We had observed a high alteration of soil quality by the most charged effluent, which is raw leachate.

It had been noticed that the pH increases in the soil irrigated by RL (SIRL) and decreases for the one irrigated by

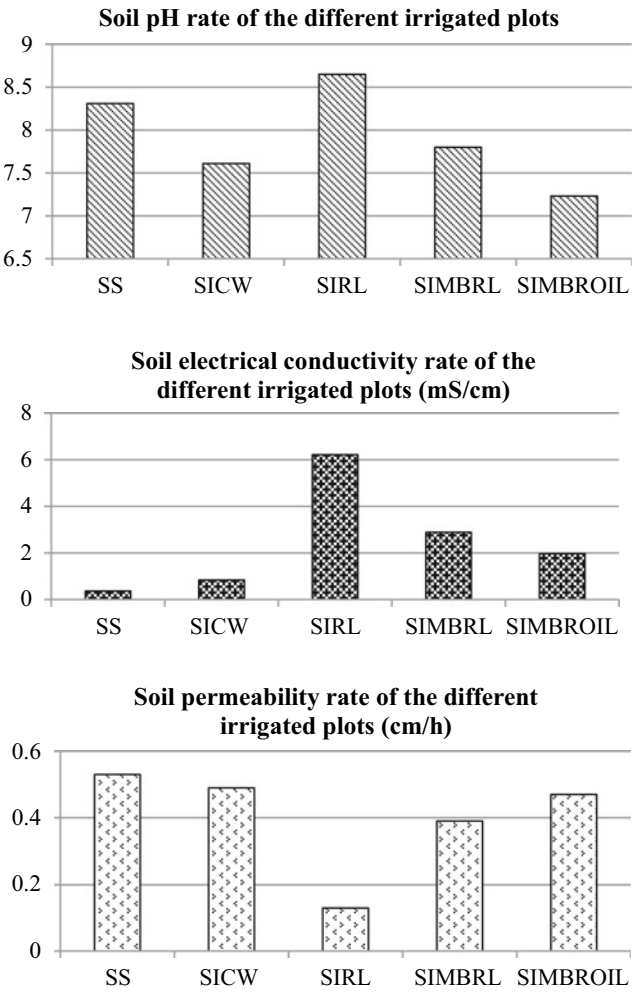

Fig. 3 Soil quality before and after the irrigation test

MBROIL (SIMBROIL). It shows a slight fall for the one irrigated by MBRL (SIMBRL).

The initial salinity does not represent any high levels, but after irrigation, we had generally observed an increase in soil EC. The SIRL shows a drastic rise when SIMBRL and SI

show a moderate increase compared to the plots irrigated by clean water.

For the permeability, a high value was recorded in SIRL, contrary to SIMBRL and SIMBROIL, which are slightly affected by the quality of the irrigation effluent.

4 Discussion

Figure 3 shows that the pH of SIRL is increasing contrary to the other irrigated soils. This increase can be due to the high values of bicarbonates contained in raw leachate or the high contents of sodium, calcium, and magnesium (Tarchouna et al., 2010). For the other treatments, the pH level decreases to reach neutrality; this can be explained by the small rate of bicarbonates contained in MBRL and MBRROL and also by the leaching of the initial total calcareous through repeated irrigation (Solis et al., 2005). The increase of the soil pH can cause hazardous problems by blocking the plants from taking up the micronutrients from the soil, which results in decreasing their growth (Al Mansouri & Alhendawi, 2014). This was also confirmed by Lucena (2000) who found that the ferric reductase activity of plant roots is reduced sharply when in high levels of pH, which is the main reason for an iron deficiency in soil and plants.

The soil's EC represents, in general, an increase in all the plots. SIRL and SIMBRL indicate the higher amount, but the SIMBRL is still be under 4 dS/m as a non-saline soil (Qadir et al., 2000). This rise of the "EC" is a result of the high values of the salts contained in the effluents and also because of the fine-textured soil which makes the accumulation of salts easier (Douaoui & Hartani, 2007). Singh et al. (2017) and Justin et al. (2009) had also shown that despite the high concentration of trace elements contained in leachate, the irrigation by pre-treated leachate or diluted leachate had not revealed any excessive accumulation of salts, heavy metals, or nutrients that could negatively affect soil properties and plant growth. The trace element concentrations in the soil after irrigation were below the permissible limit in force (Singh et al., 2017). Alghobar and Suresha (2017) had also confirmed that the EC of the soil irrigated by treated wastewater increased compared to the soil irrigated by fresh water. This salinity rise is going to alter the soil structure (SSSA, 1997), perturb the plants' growth, reduce the plants' ability to absorb water and nutrients, and lastly increase the pathogens' populations which boost the development of crop disease (Besri, 1981).

Soil permeability is an important factor to determine the water and air circulation in the soil. The SIRL permeability was highly affected by the irrigation water quality, and the decrease observed in SIRL can be due to: (i) the pores clogging by the high amount of SM, (ii) the deflocculating and the dispersion of soil particles by the high concentration of sodium (Bouma et al., 1972). The MBRL characterization represents a high concentration of sodium and a low rate of SM, but the soil permeability after irrigation does not show a high decrease compared to the witness sample plot, while the SIMBRROL, which does not have any high values of Na + or MS, showed approximately the same value of permeability when compared with the SICW. From what was mentioned before, we can deduce that The MBRL and MBRLO do not affect the soil structure in the short term, but the sodium dispersion can affect the soil structure in the long term after yearly repeated irrigation. The permeability decrease means a restriction of air and water in the soil which affects the nutrients' availability and, as a result, plant growth and decreased yield of crops.

5 Conclusions

From the results above, we can conclude that the RL cannot be used in irrigation without prior treatment. It has represented a high value of salinity, MS, and bicarbonates which will affect the plants' development and the soil structure. This was confirmed by the drastic increase of the pH and the salinity of the irrigated soil, and also, a sharp fall of the permeability was observed a sharp fall after the irrigation due to the pores clogging.

The MBR treatment had removed a large portion of the pollutants contained in the RL, but still represented high values of these. On the other hand, after the irrigation, the effluent had not induced great soil salinity and kept the EC soil under 4 µS/cm. The permeability and the pH did not show a large difference compared to the values of the witness plots. This effluent seems to be a good alternative for irrigation reuse but will need continuous monitoring, regular soil leaching, and a good choice of soil type.

As for the MBRROL, the results indicate that it is suitable for irrigation. The parameter values after irrigation did not show any huge difference compared to the witness plot, which means that we are not going to face problems of soil desegregation or alteration that can affect the plants' growth or the soil quality.

References

Al Mansouri, H. M., & Alhendawi, A. M. R. (2014). Effect of increasing concentration of bicarbonate on plant growth and nutrient uptake by Maize plants. *American-Eurasian Journal of Agriculture and Environmental Science, 14*(1), 01–06.

Alghobar, A., & Suresha, S. (2017). Evaluation of metal accumulation in soil and in tomatoes irrigated with sewage water from Mysore city, Karnataka, India. *Journal of the Saudi Society of Agricultural Sciences, 16*, 49–59.

American Publishing Health Association (APHA), American Water Works Association (AWWA), & Water Environment Federation (WEF). (2005). *Standard methods for the examination of water and wastewater, 21 edition*. Washington DC, USA.

Bedbabis, S., Ben Rouina, B., Boukhris, M., & Ferrara, G. (2014). Effect of irrigation with treated wastewater on soil chemical properties and infiltration rate. *Journal of Environmental Management, 133*, 45–50.

Besri, M. (1981). Influence de la salinité du sol et des eaux d'irrigation sur la population de Fusarium oxysporum (Schl.) f.sp. lycopersici (Sacc.) Snyd. et Hans. *Phytopathologia Mediterranea,* **20**(2, 3), 101–106.

Bouma, J., Ziebell, W. A., Olcott, P. G., Mc Coyle, E., & Hole, F. D. (1972). Soil absorption of septic tank effluent. *University of Wisconsin, Extention-Geological and Natural History Survey, 20*, 2–55.

Cheng, C. Y., & Chu, L. M. (2011). Fate and distribution of nitrogen in soil and plants irrigated with landfill leachate. *Waste Management, 31*, 1239–1249 (2011).

Douaoui, A., & Hartani, T. (2007). Impact de l'irrigation par les eaux souterraines sur la dégradation des sols de la plaine du Bas-Chéliff. In 3rd Regional workshop of Sirma project atelier, pp. 1–5. Nabeul, Tunisie.

Falizi, N. J., Hacıfazlıoğlua, M. C., Parlara, I., Kabaya, N., Ö. Pekc, T., & Yüksela, M. (2018). Evaluation of MBR treated industrial wastewater quality before and after desalination by NF and RO processes for agricultural reuse. *Journal of Water Process Engineering, 22*, 103–108.

Hamoda, M. F. (2004). Water strategies and potential of water reuse in the south Mediterranean countries. *Desalination, 165*, 31–41.

Heidarpour, M., Mostafazadeh-Fard, B., Abedi Koupai, J., & Malekian, R. (2007). The effects of treated wastewater on soil chemical properties using subsurface and surface irrigation methods. *Agricultural Water Management, 90*, 87–94.

Justin, M. Z., & Zupančič, M. (2009). Combined purification and reuse of landfill leachate by constructed wetland and irrigation of grass and willows. *Desalination, 24*, 157–168.

Lucena, J. J. (2000). Effects of bicarbonate, nitrate and other environmental factors on iron deficiency chlorosis: A review. *Journal of Plant Nutrition, 23*, 1591–1606.

Qadir, M., Ghaffoor, A., & Murtaza, G. (2000). Amelioration strategies for saline soils: A review. *Land Degrad, 11*, 501–521.

Recommended Limits for Constituents in Reclaimed Water for Irrigation, United States Environmental Protection Agency, Tables 2–7 (2004).

Rhouat, S., El Youbi, M. S., & Dimane, F. (2019). Physico-chemical characterization of Meknes municipal landfill leachate and assessment of the seasonal effects using PCA. *Environmental Engineering and Management Journal, 18*(11).

Romero, C., Ramos, P., Costa, C., & Márquez, M. C. (2013). Raw and digested municipal waste compost leachate as potential fertilizer: Comparison with a commercial fertilizer. *Journal of Cleaner Production, 59*, 73–78.

SEEE (2007). *Water quality guidelines for irrigation in Morocco*. State Secretariat at the Ministry of Energy, Mines, Water and Environment, in charge of Water and Environment.

Singh, S., Janardhana Raju, N., & RamaKrishna, Ch. (2017). Assessment of the effect of landfill leachate irrigation of different doses on wheat plant growth and harvest index: A laboratory simulation study. *Environmental Nanotechnology, Monitoring & Management, 8*, 150–156.

Singh, R. P., & Agrawal, M. (2010). Variations in heavy metal accumulation, growth and yield of rice plants grown at different sewage sludge amendment rates. *Ecotoxicology and Environmental Safety, 73*(4), 632–664.

Solis, C., Andrade, E., Mireles, A., Reyes-Solis, I. E., Garcia-Calderon, N., Lagunas-Solar, M. C., Pina, C. U., & Flocchini, R. G. (2005). Distribution of heavy metals in plants cultivated with wastewater irrigated soils during different periods of time. *Nuclear Instruments and Methods in Physics Research, 241*, 351–355.

Sparks, D. L., Page, A. L., Helmek, P. A., Loeppert, R. H., Soltanpour, P. N., Tabatabai, M. A., Johnston, C. T., & Sumner, M. E. (1996). *Methods of soil analysis, Part 3, chemical methods*. ASA, CSSA, SSSA.

SSSA. (1997). *Glossary of soil science terms*. Soil Science Society of America.

Tarchouna, L. G., Merdy, P., Raynaud, M., Pfeifer, H., & Lucas, Y. (2010). Effects of long-term irrigation with treated wastewater. Part I: Evolution of soil physico-chemical properties. *Applied Geochemistry, 25*, 1703–1710.

Zupanc, V., & Justin, M. Z. (2010). Changes in soil characteristics during landfill leachate irrigation of *Populus deltoids*. *Waste Management, 30*, 2130–2136.

Cavitant Flow Characterization Through the Opening of a Flat Valve in a Rectangular Channel

Wahiba Mokrane and Amina Messaoudi

Abstract

Hydraulic equipment vulnerability to pressure drops, due to flow velocity change, and poses real operating and management complications. Thus, a risk of material degradation and performance arises. Hence, flow control is an imperative action to manage this risk. The present work focused on a controlling study of consequences due to a non-forced flow contraction and through a rectangular channel. For this purpose, we carried out experimental work, using a vertical valve, to induce a flow section reduction. Two series of tests were carried out. In the first one, we have considered an opening of two centimeters and for the second an opening of four centimeters. Water height was measured at different positions and for various values of flow rates in order to obtain the pressure profile. We have also calculated the pressure coefficient, the cavitation parameter, and the Reynolds number. On the other hand, we followed the development of an additional phase to the liquid which is composed of air. As result, we have detected a turbulent flow character, mostly cavitant with air bubbles attached to the valve wall. These bubbles are susceptible to induce wall erosion, and air entrainment is also observed upstream of the flat valve.

Keywords

Valve • Contraction • Pressure • Cavitation • Bubbles

1 Introduction

An obstacle, intercepting a flow, generates important hydraulic parameters change until its rupture. This is seen as a gaseous phase development, due to flow germs as mentioned by some researchers (Lecoffre, 1988), in other words, the cavitation phenomenon, defined by Osborne Reynolds in 1894 (Braun & Hannon, 2013). Several studies were widely carried out, in this background and in a pressurized flow domain (Mokrane & Kettab, 2019). The free surface flow was poorly investigated against penstocks and hydraulic machines flow, despite the serious consequences for spillways (Chanson, 1989; Hager, 2009; Muyzen & Chanson, 2009) and bottom valves. In this work, we aim to determine the parameters which allow flow controlling through a flat valve opening. We study flow rate influence on both cavitation and turbulence dimensionless numbers. On the other hand, we follow the air entrainment accompanying the hydraulic jump created downstream of the valve.

2 Materials and Methods

Our experimental tests were carried out on the setup shown in the Fig. 1. It is composed of a rectangular channel, a flat valve, and a control panel.

The flat valve is able to move in the vertical direction and constitutes the flow obstacle. This permits controlling the flow section contraction. The flow rate adjustment is done by means of the control panel related to an electromagnetic flowmeter. To eliminate any external substance, we begin by cleaning the channel, and then, we start on the installation and adjust the horizontality of the channel.

Firstly, we open the valve at 0.02 m. We measure the water height at the valve upstream and downstream, the water temperature, and the air zone length for five flow rate values. Secondly, we open the valve at 0.04 m and repeat the previous operations.

W. Mokrane (✉)
Research Laboratory of Water Sciences, National Polytechnic School, Algiers, Algeria
e-mail: mokranewah@yahoo.fr; o.mokrane@ensh.dz

W. Mokrane · A. Messaoudi
Department of Urban Hydraulic, MVRE Research Laboratory, High National School of Hydraulics, Blida, Algeria

A. Kallel et al. (eds.), *Selected Studies in Environmental Geosciences and Hydrogeosciences*, Advances in Science, Technology & Innovation, https://doi.org/10.1007/978-3-031-43803-5_33

Fig. 1 Experimental setup

3 Results

Pressure variations through the measuring section are presented, for the two cases of the valve opening, in Figs. 2 and 3.

Pressure coefficient, cavitation parameter 'Thomas number', and Reynolds number vary depending on the flow rate. This is illustrated in the Figs. 4 and 5.

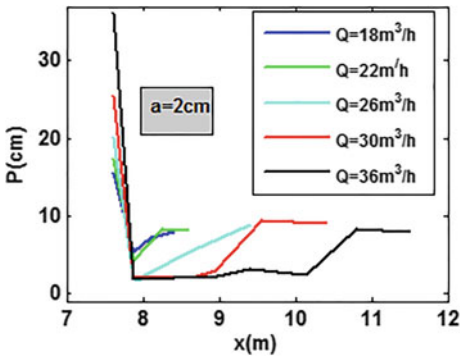

Fig. 2 Pressure profile for the valve opening of 0.02 m

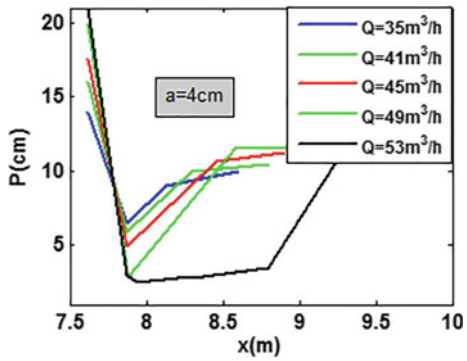

Fig. 3 Pressure profile for the valve opening of 0.04 m

4 Discussion

Results of Fig. 2 show a brusque and regular drop of pressure at the valve upstream. The weakest values of pressure are detected at the position 7.87 m, counted from the upstream of the rectangular channel. In the case of 0.02 m valve opening and for flow rates comprised between 18 and 24 m^3/h, pressure values increase and then stabilize at about 784.8 Pa

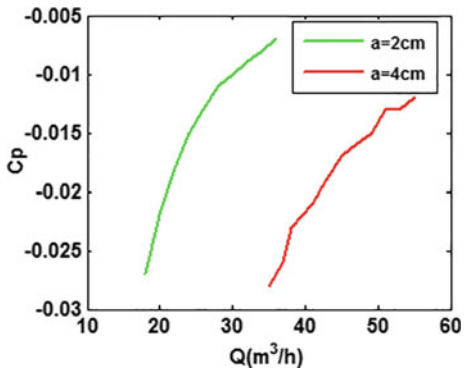

Fig. 4 Pressure coefficient variation with the flow rates

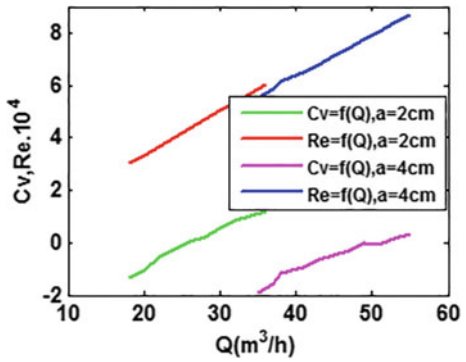

Fig. 5 Cavitation number and Reynolds number variation with the flow rates

from the position of 8.25 m. For flow rates' values exceeding 24 m^3/h, pressure increases until a value of 932 Pa.

For a valve opening of 0.04 m, Fig. 3 shows that pressure values increase and stabilize at about 981 Pa, from the position of 8.25 m, for flow rates of 35–43 m^3/h. For values higher than 43 m^3/h, pressure increases until a value of 1177 Pa, for which the profile stabilizes. Figure 4 reveals that the cavitation number 'Cv' decreases when the valve opening value increases. For an opening of 0.02 m, Cv changes from −1.35 to 1.2. It is less than zero, for flow rates' values comprised between 18 and 24 m^3/h. This reveals a cavitant flow character. Cavitation phenomenon happens for values less than 0.2 (Hager, 2009). So, we characterize the flow as cavitant for flow rate values less than 26m^3/h in this case. Reynolds number values show a turbulent character for the previous case.

When the valve is opened at 0.04 m, 'Cv' is between −1.89 and 0.32. It is negative for flow rates included between 35 and 51 m^3/h. This indicates the cavitant character of flow. Also, in this case, Reynolds number values show a turbulent character.

In the two cases, flow changes from subcritical, in the valve upstream, to supercritical in its downstream and ended by a subcritical regime. A hydraulic jump is generated entraining the air bubbles generated by cavitation. For a flow rate of 18 m^3/h and a valve opening, air bubbles are observed with different sizes. Small ones remain attached to the valve wall, while other bubbles rise to the surface and implode.

5 Conclusions

Two series of experimental tests were carried out in order to characterize the flow through a flat valve opening. In the first one, an opening of 0.02 m was considered, and in the second one, 0.04 m was considered. The obtained results have revealed a turbulent character that accentuates from the upstream to the downstream of the obstacle and a, mostly, cavitant flow at the contraction section. Also, a hydraulic jump was created entraining air bubbles generated by cavitation. Part of these bubbles develops and vanishes, but others remain attached to the valve wall and will induce its damage.

Hence, the flow through a bottom valve, installed on a rectangular and horizontal channel, is turbulent and cavitant with a hydraulic jump entraining air bubbles.

References

Braun, M. J., & Hannon, W. M. (2013). *Cavitation formation and modeling. Encyclopedia of tribology*. Springer.

Chanson, H. (1989). Etude des phénomènes d'entrainement d'air, Application aux évacuateurs de crue. *Houille Blanche, 6*, 443–462.

Hager, W., & Schleiss, A. (2009). *Constructions hydrauliques* (2nd ed.). Presses Polytechniques et Universitaires Romandes.

Lecoffre, Y. (1988). Germes et cavitation Effets-Techniques de contrôle. *Houille Blanche, 2*, 135–147.

Mokrane, W., & Kettab, A. (2019). Flow behaviour analysis through a venture designed for industrial and environmental processes. *Euro-Mediterranean Journal for Environmental Integration, 1*(4), 01–08.

Muyzen, F., & Chanson, H. (2009). Two phase flow measurements in turbulent hydraulic jumps. *Chemical Engineering Research and Design, 87*(6), 789–797.

Determination of Pesticide Residue in Soil and Groundwater of Gezira Scheme (Sudan)

Ahmed Hammad, Rowida Yousif, Azhari Abdelbagi, Abd Elaziz Ishag, Amna Mohamed, Jang-Hyun Hur, and Mark Laing

Abstract

The present study is to investigate the level of pesticide residues in soil and water samples from the Gezira Scheme. The results revealed the presence of OCs (lindane, *o-p'* DDT, endrin, aldrin, dieldrin, α-endosulfan), OPs (profenofos, malathion, chlorpyrifos), and the plant growth regulator (ethephon) in soil and water samples. Lindane, *o-p'* DDT, and profenofos were detected in all soil samples, while the rest of the pesticides were in some samples. The pesticide residues detected were higher in north Gezira, except for α-endosulfan, which was detected highest in the south Gezira Scheme. The levels of endrin, malathion, and chlorpyrifos were relatively low in soil samples. Violative levels of lindane and o-p' DDT were detected in all water samples (100%), followed by profenofos (80%) and ethephon (20%). The levels of endrin, aldrin, dieldrin, α-endosulfan, profenofos, and malathion in the water samples were observed under the detection limits. The concentrations in soil and water samples greatly exceeded the maximum residues limit set by Codex, USA, and EU, except for lindane and *o-p'* DDT in water samples.

Keywords

Gezira Scheme • Organochlorines • Pesticide residues • Soil and water samples

1 Introduction

The Gezira Scheme is the largest irrigated Scheme occupying 25% of the irrigated area in Sudan. The main crops produced in this Scheme are cotton, wheat, sorghum, groundnut, and vegetables, which are generally attacked by pests and diseases such as aphis, whitefly, Jassid or leafhopper, mealy bug, African bollworm, fungal, bacterial, viruses, nematodes, parasitic plants, and weeds. The use of pesticides in Sudan started in 1949 with the application of DDT for the control of cotton jassid (*Jacobiasca lubica* deberg). Early in the sixties, organophosphates became a reliable partner to the organochlorines for chewing and sucking insect pests. The increased use of pesticides coupled with the drastic change in the cotton pest complex led to the introduction of synthetic pyrethroids and neonicotinoids in order to replace DDT (Abdelbagi et al., 2000, 2003). The persistent application of pesticides for a long time period may lead to the accumulation of their residues in foodstuff, water, soil, and the associated environment (Nesser et al., 2016). The determination of the pesticides residues in various components of the environment is very crucial for healthy food and human safety (Elbashir et al., 2015; Nesser et al., 2016). Therefore, the main objective of this study is to estimate the pesticide residues in soil and water samples from the Gezira Scheme.

A. Hammad (✉) · A. Abdelbagi · A. E. Ishag
Department of Crop Protection, University of Khartoum, Khartoum, Sudan
e-mail: ahmed7399@yahoo.com

R. Yousif
Plant Protection Directorate, Ministry of Agriculture, Khartoum, Sudan

A. Mohamed
Department of Crop Protection, University of Kordofan, Kordofan, Sudan

A. E. Ishag · J.-H. Hur
Department of Biological Environment, Kangwon National University, Chuncheon, Republic of Korea

M. Laing
School of Agricultural, Earth and Environmental Sciences, University of Kwazulu-Natal, Natal, South Africa

A. Kallel et al. (eds.), *Selected Studies in Environmental Geosciences and Hydrogeosciences*, Advances in Science, Technology & Innovation, https://doi.org/10.1007/978-3-031-43803-5_34

2 Materials and Methods

2.1 Reagents, Sample Collection, and Extraction

The analytical standard (99% pure) of lindane, aldrin, dieldrin, endrin, endosulfan (α and ß), *o-p'* DDT, chlorpyrifos, profenofos, ethephon, and malathion was obtained from PPD, Sudan. The solvents (99.8%) such as acetone, dichloromethane, methanol, n-hexane, anhydrous sodium sulfate, and sodium chloride were purchased from Lab Line Co., Sudan. Soil samples (18) were randomly collected (0–30 cm depth) from different sites in the Gezira Scheme and mixed thoroughly to make composite samples (1 kg each). Three samples were taken from each location and kept separately in polyethylene bags. The groundwater samples were collected from nine wells in the area, kept separately in polyethylene bottles, and sent to the pesticides monitoring laboratory, University of Khartoum. The soils and water samples were extracted and cleaned up following the Association of Official Agricultural Chemists AOAC method (AOAC-International: Association of Official Analytical Chemists, 1996).

2.2 GC Analysis

The samples were analyzed using gas chromatography (GC; Shimadzu, Japan, 2010) equipped with FID and a DB-5 capillary column (30 ml length and 0.25 mm internal diameter). Nitrogen gas was used as a carrier and make-up gas at a flow rate of 6.8 ml/min and 30.0 ml/min, respectively. The split mode of injection was used during sample analysis. The airflow rate in the instrument was fixed at 400 ml/min, and the temperature of the injector and detector was 280 °C and 300 °C, respectively. Triplicate injections (1 µl) of different concentrations of pesticide standards were injected into the GC, and the response was used for the construction of the standard curves. The triplicate injections (2 µl each) of each sample were analyzed under similar conditions. Pesticides were identified by retention times, and concentrations (mg/kg) were determined from the standard curve. The limit of detection (LOD) ranged from 0.001 to 0.266 to the tested pesticides. It was calculated according to the following equation:

$$\mathrm{LOD} = 3.3\ \sigma/S.$$

σ = Standard deviation of intercepts of calibration curves.
S = Mean of slopes of the calibration curves.

3 Results

3.1 Pesticide Residues in Soil Samples

The soil samples from north Gezira were found to be more contaminated than the south and middle Gezira Scheme (Fig. 1). The cotton soil indicated a relatively higher frequency of detection (80% (cotton soil) vs. 60% (tomato soil), respectively) and residue load as compared to the tomato soils (Table 1). The lindane, o-p' DDT, endrin, aldrin, dieldrin, profenofos, and malathion were observed from the cotton soil, while lindane, *o-p'* DDT, α-endosulfan, profenofos, and malathion in tomato soil (Table 1). The highest residue level was associated with profenofos, while the lowest was with *o-p*' DDT. The levels of ethephon and chlorpyrifos were found to be below the detection limit. Violative samples in cotton soil (80%) were greater than those in tomato soil (70%) (Table 1).

3.2 Pesticide Residues in Water Samples

The results obtained from the water samples' analyses indicated that the pesticide residues in all the samples as well as the profenofos, lindane, o-p' DDT, and ethephon were higher than the limit prescribed by Codex MRLs (Table 1). The concentration of ethephon was the highest (104 mg L^{-1}), while the lindane was the lowest (0.024 mg L^{-1}). The pesticide residue in the water samples collected from north Gezira indicated a higher concentration as compared to that of middle and south Gezira (Fig. 1).

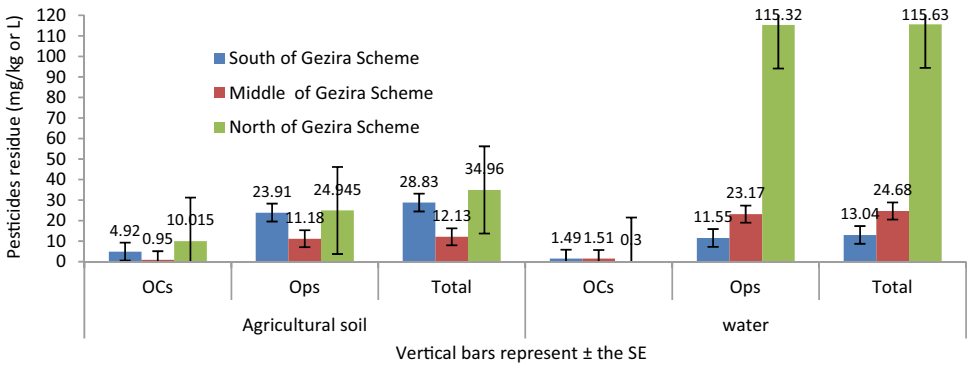

Fig. 1 Total pesticide residues load (mg kg^{-1}) in soil and water samples from Gezira Scheme OCs ≡ Organochlorines; OPs ≡ Organophosphates

Table 1 Pesticide residues in soil and water samples from Gezira Scheme

Area	Crop	Location	Sample analyzed	Insecticides	Mean	SE ±	Median	Range	+ ve Sample %
Agricultural Soil	Cotton	South	3	Profenofos	23.78	0.86	23.78	ND–14.13	66
				Lindane	2.496	0.081	0.292	0.152–3.0	100
				Endrin	0.930	0.188	0.93	ND–1.26	33
				o-p' DDT	1.498	0.187	0.49	0.187–2.433	100
				Malathion	0.13	0.014	0.13	0.059–0.20	33
		Middle	3	Profenofos	11.18	1.6	11.18	8.41–13.96	100
				Lindane	0.498	0.93	0.498	0.337–0.659	100
				o-p' DDT	0.449	0.08	0.449	0.309–0.589	100
		North	3	Profenofos	24.522	1.85	24.522	21.30–27.73	100
				Lindane	2.049	0.32	2.049	1.49–2.604	100
				o-p' DDT	1.228	0.316	1.228	0.68–1.274	100
				Malathion	0.423	0.09	0.423	0.265–0.58	100
				Aldrin	0.076	0.022	0.076	0.038–0.114	66
				Dieldrin	0.062	0.015	0.062	0.035–0.089	66
	Tomato	South	3	Lindane	0.445	0.121	0.445	0.235–0.655	100
				o-p' DDT	0.345	0.072	0.34	0.221–0.469	100
				Profenofos	12.04	1.20	12.04	9.96–14.13	100
		Middle	3	Lindane	0.04	0.024	0.03	0.022–0.07	100
				o-p' DDT	0.34	0.072	0.406	0.199–0.415	100
				Profenofos	6.0	1.23	6.0	2.20–10.03	100
		North	3	Lindane	1.163	0.194	1.163	0.827–1.499	100
				o-p' DDT	0.722	0.171	0.722	0.425–1.019	100
				Malathion	0.377	0.0774	0.377	0.243–0.511	100
				α-endosulfan	6.6	1.20	6.6	4.52–8.69	100
				Profenofos	12.0	1.08	12	10.12–13.87	100
Water	South		3	Profenofos	11.549	0.9	11.549	9.914–13.184	100
				Lindane	0.244	0.052	0.244	0.153–0.335	100
				o-p' DDT	1.247	0.338	1.247	0.663–1.831	100
	Central		3	Profenofos	23.173	2.031	23.173	19.645–26.69	100
				Lindane	0.548	0.148	0.552	0.296–0.808	100
				o-p' DDT	0.963	0.257	0.963	0.519–1.407	100
	North		3	Profenofos	11.324	0.973	11.324	9.639–13.009	100
				o-p' DDT	0.301	0.077	0.301	99.30–108.70	100
				Ethephon	104.0	2.71	104.0	99.30–108.70	100

4 Discussion

The cotton soil showed a higher frequency of detection and residue load as compared to the tomato soils, which may be due to the fact that cotton is the main cash crop and requires more pesticides to prevent damage by serious pests as compared to the tomato crop (Abdelbagi et al., 2000, 2003). The detected OCs were used for almost three decades in the Gezira Scheme against cotton pests complex before their severe restriction and ban (Abdelbagi et al., 2000, 2003). The levels of ethephon and chlorpyrifos were below the detection limit, and this can be explained by their conversion in the environment (Matsumura, 1985). Violative samples were more from the cotton soil, while less from the tomato soil and associated with most of the detected pesticides, which may be due to long environmental persistence as well as recent misuses (Tomlin, 2003). The soil samples collected from north Gezira revealed more contamination, followed by south and middle Gezira that may be owing to the

differences in the use pattern and awareness level among farmers in these areas. Generally, the level of organophosphate was observed relatively higher than OCs; this may be explained by their ongoing use in the area as compared to OCs, which were severely restricted and banned (Abdelbagi et al., 2000, 2003). The residues of profenofos, lindane, *o-p'* DDT, and ethephon were detected in all water samples at levels exceeding the Codex MRLs (FAOSTAT, 2020) that may be due to close locations of the sampled wells with the spraying aircraft, airports as well as the pesticide stores.

5 Conclusion

Pesticide residues were detected in all groundwater and soil samples, with cotton soil showing a higher residue load and violations as compared to the tomato soil. Violations were associated with most of the detected pesticides. The soil of north Gezira has been found to be more contaminated than that of the south and middle Gezira, while groundwater residues (all violative) followed a different order. The study suggests regular monitoring of the pesticides in soil and water sources of the Gezira Scheme.

References

Abdelbagi, A., Elmahi, A., & Osman, G. (2000). Chlorinated hydrocarbon insecticides residues in the Sudanese soil of limited or pesticide use. *Arab Journal of Plant Protection, 18*, 35–39.

Abdelbagi, O., Elmahi, A., & Osman, G. (2003). Organochlorine insecticides residues in Sudanese soil of intensive pesticide use and in surface soil of Qurashi pesticide store. *U. of K. Journal of Agricultural Science, 11*, 59–68.

AOAC-International: Association of Official Analytical Chemists. (1996). *Official methods of analysis of the ed*. Anonymous, Washington, USA.

Elbashir, A., Abdelbagi, A., Hammad, A., Elzorgani, G., Laing, D.: Levels of organochlorine pesticides in the blood of people living in areas of intensive pesticide use in Sudan. *Environmental Monitoring and Assessment, 187*(3).

FAOSTAT: crops [Internet]. Rome: The Food and Agriculture Organization of the United Nations. 1961—[updated 2017; cited 2020 Jan 22]. Available from: http://www.fao.org/faostat/en/#data/QC

Matsumura, F. (1985). Toxicology of insecticides, p. 406. Plenum Press.

Nesser, G., Abdelbagi, A., Hammad, A., Tagelseed, M., & Laing, D. (2016). Levels of pesticides residues in the White Nile water in the Sudan. *Environmental Monitoring and Assessment, 188*, 374. https://doi.org/10.1007/s10661-016-5367-3

Tomlin, S. (2003). *The pesticide manual* (12th ed.). University of London.

Morphological Features of Soils in the Low-Mountain Relief of the Southeastern Crimea (The Area of Karadag Nature Reserve)

Polina Drygval, Anna Drygval, Elena Stanis, Yaroslav Lebedev, and Roman Gorbunov

Abstract

Low-mountainous landscapes' soils of the southeastern part of the Crimean Peninsula were studied on the territory of Karadag Nature Reserve. The reserve includes the Besh-Tash Ridge, on whose slopes the research was conducted in 2019–2020. For mountain soils of the studied territory by the rate of moisture, there are different conditions of formation: automorphic, trans-accumulative, and accumulative. The study aims to investigate the morphological and physicochemical properties and the granulometric composition of soils in the Karadag Nature Reserve. Soils of the studied territory were formed on different lithological differences of mother rock eluvium, which are strongly differentiated by mineralogical composition, degree of disturbance, and particle size distribution. On the test sites, there is a change of vegetation cover of elementary landscapes. Six soil cuts are studied. As a result of field and laboratory studies, it was established that in the investigated territory, the soil cover consists of brown soils (Cambisols Chromic (CMcr)), brown mountain forest soil (Calcisols Haplic (CLha)), and mountain meadow-steppe chernozemic soil (Leptosols Mollic (LPmo)). Soil cuts are represented by different numbers of genetic horizons. In terms of particle size distribution, soils are light and medium loamy. Down in the relief, the thickness of the soil profile increases. Based on soil texture, all soils have skeletal structures. Acidity changes from neutral to slightly alkaline.

Keywords

Mountain soils • Morphological features of soils • Soil profile • Genetic horizon

1 Introduction

Soils of low-mountain landscapes in the southeast of Crimea are of great interest because they have rarely been studied. Though the study of Crimean soils started in the first half of the twentieth century (Dragan, 1995; Kochkin, 1967), there are few modern studies. The soil cover of the nature reserves is one of the components of protected landscapes and represents a system of reference and rare soils. This is their high scientific value.

Soils are the most important element in ecological systems and affect their biodiversity, including the possibility of the existence of certain biogeocenoses. The study and monitoring of soils in protected intact areas are an important and relevant scientific direction (Taghizadeh-Mehrjardi et al., 2019).

The peculiarity of the research object within the mountain system of the Crimean Peninsula is connected with the fact that it is situated in the Karadag Nature Reserve, which is presented as a mountain massif (the highest point is 577 m). It is situated between Otuzskaya valley and Koktebelskaya area on the Black Sea coast (Kostenko et al., 2011). In the Karadag Nature Reserve, soil studies were carried out locally, with a single soil profile cut within Mount Svyataya. No work has been carried out on the geochemical or morphological assessment of soils of the whole reserve.

The aim of this work is to study mountain soils of the southeastern part of Crimea and to reveal regularities of their structure change by height gradient on the example of soils of the Karadag Nature Reserve.

P. Drygval (✉) · E. Stanis
Peoples' Friendship, University of Russia, RUDN University, Moscow, Russia
e-mail: any-poly@mail.ru

A. Drygval · Y. Lebedev
Moscow Representative Office A.O. Kovalevsky Institute of Biology of the Southern Seas of RAS, Moscow, Russia

R. Gorbunov
A.O. Kovalevsky Institute of Biology of the Southern Seas of RAS, Sevastopol, Russia

A. Kallel et al. (eds.), *Selected Studies in Environmental Geosciences and Hydrogeosciences*, Advances in Science, Technology & Innovation, https://doi.org/10.1007/978-3-031-43803-5_35

2 Materials and Methods

Field and laboratory studies are conducted to study morphological characteristics of low-mountain soils in the southeastern Crimea (Fig. 1). The object of the study is slope soils of Besh-Tash ridge located in the western part of the Karadag Nature Reserve.

Six test sites were laid on the slope of the ridge at different altitudes down the slope in the direction from the top of the Besh-Tash ridge to the bottom of the Karadag gully where the description of vegetation cover and soil profile cuts were laid. Test site No. 1 is located in automorphic landscape conditions, and sites Nos. 2–6 forms a soil catena (trans-accumulative and accumulative landscape conditions). The landscape of the territory is a typical low-mountain landscape of the southeastern Crimea.

The territory of the Karadag Nature Reserve has a complex geological structure. Bedrock is represented by rocks of fractured terrigenous flysch formation (argillites, siltstones, sandstones) of Triassic–Jurassic age, limestones, sandstones, conglomerates, clay slates, mainly of Jurassic and Cretaceous ages. In addition, the multi-phase geological history of the Karadag has resulted in a heterogeneous composition of rocks in a relatively small area. For example, according to the geological map (Dyakonova-Savelyeva & Levinson-Lessing, 1925), the Magnitnyj Ridge in the profile area is composed of tuffs and tuff breccias, flows of spilites, keratospilites, andesite, and basalt of the Upper Bajocian Age. Absolute heights of the test sites vary from 100 to 227 m. At the sites of soil profiles, the vegetation cover was studied; it is represented by different vegetation formations: from steppe to forest communities.

The climate of the reserve can be defined as transitional from the sub-Mediterranean climate, typical of the western part of the South Coast of Crimea, to a moderately continental and moderately hot dry climate typical of the steppe part of the peninsula (Kostenko et al., 2011).

Soil samples for morphological analysis were taken from all genetic horizons. Soils are classified according to WRB and (IUSS Working Group – FAO, 2014) soil classification (Egorov et al., 1977).

3 Results

As a result of field studies in accordance with the conditions of soil formation, the following are identified: brown soils (Cambisols Chromic (CMcr)), brown mountain forest soils (Calcisols Haplic (CLha)), and mountain meadow-steppe chernozem soils (most corresponding to Leptosols Mollic (LPmo)). Their mechanical composition and active soil acidity are determined. Also, vegetation communities are described on the test sites. A brief description of soils is given in Table 1.

Thus, a total of six soil profile cuts are described. According to conditions of formation at the site №. 4, the soils were formed in trans-accumulative conditions (sites 2, 3, 4, 5). At the same time, by mechanical composition, they are predominantly medium-loam, and one of them (test site №. 5) belongs to Cambisols Chromic (CMcr), one (test site

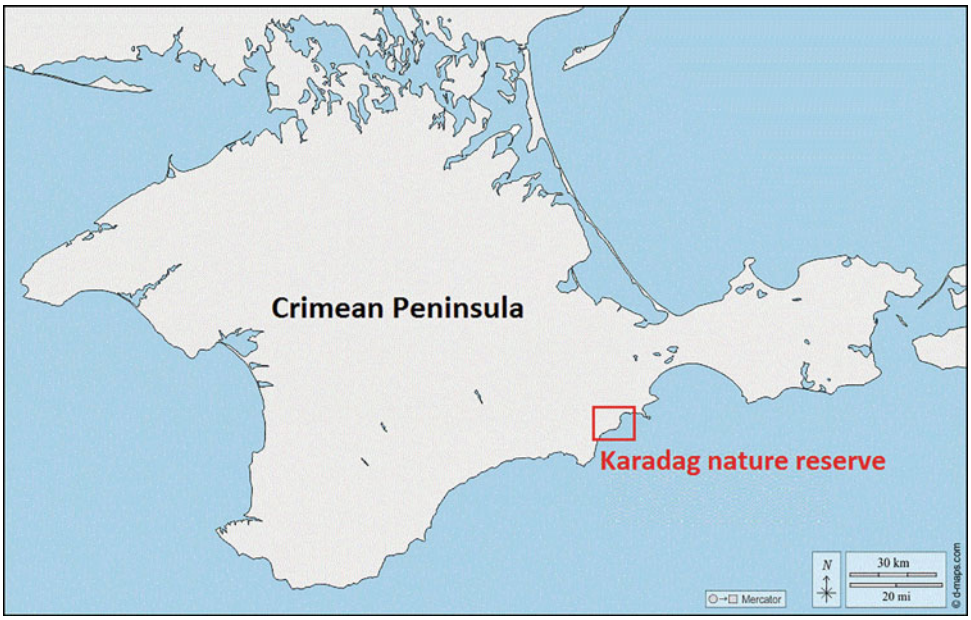

Fig. 1 Study area (Karadag Nature Reserve)

Table 1 Characteristics of soils on the test sites

No. (sea level)	Soil type	Landscape conditions	Genetic horizons	Texture	Vegetation	Bedrocks' deposits
1. (219 m)	Brown soil/Cambisols Chromic (CMcr)	Automorphic	A0-Ad-A-Bm-Cg	Light-loamy	Steppe grass with the dominance of gramineous plants	Eluvium of limestone, pudding rock, and malmrock
2. (227 m)	Mountain meadow-steppe chernozemic soil/Leptosols Mollic (LPmo)	Trans-accumulative	A0-Ad-A-BC	Medium-loamy	Steppe grass with the dominance of gramineous plants	Diluvium of limestone, pudding rock, and malmrock
3. (171 m)	Brown mountain forest soil/Calcisols Haplic (CLha)	Trans-accumulative	A0-Ad-B-BC	Light and medium loamy	Pubescent oak forest with hornbeam	Diluvium of limestone, pudding rock, and malmrock
4. (156 m)	Brown mountain forest soil/Calcisols Haplic (CLha)	Trans-accumulative	A0-A-AB-B1-B2-BC	Medium-loamy	Pubescent oak forest with hornbeam	Diluvium of limestone, pudding rock and malmrock
5. (108 m)	Brown soil/Cambisols Chromic (CMcr)	Trans-accumulative	A0-Ad-A-Bm-BC	Medium-loamy	Steppe grass	Diluvium of flysch
6. (100 m)	Mountain meadow-steppe chernozemic soil/Leptosols Mollic (LPmo)	Accumulative	A0-A-B- A^{-}(buried)-A^{-}(buried)-BC^{-}(buried)	Medium-loamy	Ash forest	Proluvium and diluvium of flysch

No. 2) to Leptosols Mollic (LPmo), and two (test sites No. 3 and No. 4) to Calcisols Haplic (CLha). At test site No. 1, the soil of Cambisols Chromic (CMcr) with a light loamy composition was formed in automorphic conditions. At site No. 6, light loamy Leptosols Mollic (LPmo) soil was formed under accumulative conditions. All soils' types are skeletal and were formed on different colluviums.

Active soil acidity is determined for all soils types, and its values for different horizons vary from 6.1 to 7.8, i.e., the reaction from slightly acidic to slightly alkaline.

Genetic horizons are determined and described for all soils, and their thickness is estimated. The results are presented in Fig. 2.

In the vegetation cover of three sites, there is noted steppe (at sites: Nos. 1, 2, and 5) and various types of tree vegetation at other test sites (Nos. 3, 4, and 6) (Table 1).

4 Discussion

Despite the dry climate of the southeast part of the Crimean Peninsula, with decreasing relief, there is a change of automorphic conditions of formation (site 1) to accumulative (test site 6). This process is due to a sharp decrease in the angle of slope of the surface at the site №6, increased humidity, and increased density and change of vegetation cover. As a result, the soil type changes down the relief, and different genetic soil horizons are formed. The decrease in total soil thickness at site №6, compared to site №3, can be explained as follows. During the rainy period, surface water runoff sharply increases. Flow rates on steep slopes (inclination angle about 20 degrees) are high. Water is concentrated in the lowering of the terrain, which leads to the washout and moving part of the soil toward the flow area.

Brown soil		
	Site №1	Thickness, cm
Horizon	A0	2
	Ad	6
	A	36
	Bm	18
	Cg	35

Mountain meadow steppe chernozemic soil		
	Site №2	Thickness, cm
Horizon	A0	2
	Ad	5
	A	6
	BC	26

Brown mountain forest soil		
	Site №3	Thickness, cm
Horizon	A0	4
	Ad	3
	B	22
	BC	24

Brown mountain forest soil		
	Site №4	Thickness, cm
Horizon	A0	3
	A	8
	AB	19
	B1	11
	B2	19
	BC	13

Brown soil		
	Site №5	Thickness, cm
Horizon	A0	1
	Ad	3
	A	10
	Bm	15
	BC	18

Mountain meadow steppe chernozemic soil		
	Site №6	Thickness, cm
Horizon	A0	2
	A	11
	B	6
	A¯	4
	B¯	11
	BC¯	10

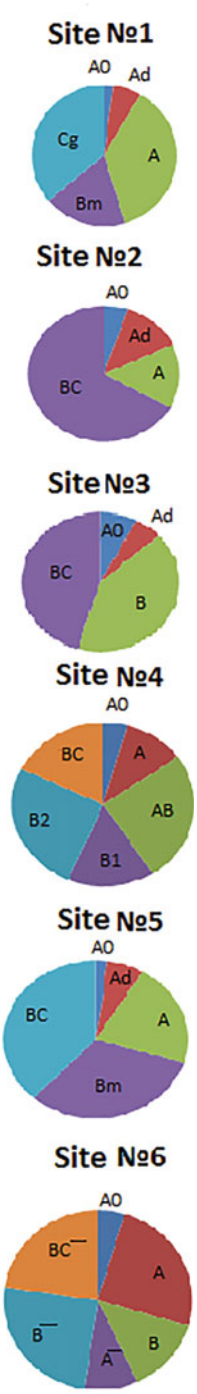

Fig. 2 Genetic horizons of soils and their thickness

Some unevenness of soil thickness on slopes can be explained by local relief irregularities and different thicknesses of the vegetation cover. Thus, the greatest thickness of a soil cross-section is noted in the area of automorphic soils that are formed on eluvium of bedrocks, instead of on poorly fixed deposits of a slope series (colluvium).

5 Conclusions

As a result of the conducted study, it was revealed that under conditions of low-mountain landscapes spreading in the southeastern part of the Crimean Peninsula, soils that belong to different taxonomic groups are formed. In automorphic conditions, brown soils are formed. In transient trans-accumulative conditions—depending on the mother substrate, the degree of moisture, and relief—a mountain meadow-steppe chernozemic soil, brown mountain forest soil, and brown soil can form. Under accumulative conditions, the mountain meadow-steppe chernozemic soil forms. As a result of different studies, the new data on the diversity of mountain soils of the Crimea are obtained, which can be used in monitoring studies of the natural environment of low-mountainous areas and zones located on the border of temperate and subtropical zones.

Acknowledgements The work was carried out within the framework of research work of A.O Kovalevsky Institute of Biology of the Southern Seas of RAS—«Study of the spatial and temporal organization of water and land ecosystems in order to develop an operational monitoring system based on remote sensing data and GIS technologies» registration number: 121040100327-3.This paper has been supported by the RUDN University Strategic Academic Leadership Program.

References

Dragan, N. A. (1995). Geography of natural and anthropogenic processes in soils of Crimea. In: *Materials of the international regional conference on "Problems of ecology and recreation in the Azov-Black Sea region"*. Tavrida, Simferopol.

Dyakonova-Savelyeva, E. N., & Levinson-Lessing, F. Yu. (1925–1926). *Petrographic map of Karadag*.

Egorov, V. V., Friland, V. M., & Ivanova, E. I. (1977). *Classification and diagnostics of soils of the USSR*. Kolos.

IUSS Working Group—FAO. (2014). WRB-World Reference Base for soil resources 2014. *World Soil Resources Report No. 106*. FAO.

Kochkin, M. A. (1967). *Soils, forests and climate of the mountainous Crimea and ways of their rational use*. Kolos.

Kostenko, N. S., Kukushkin, O. V., & Zuev, A.V. (2011). Climate. In: *Reserve Karadag: Popular science essays*, pp. 29–39. N. Oriadna, Simferopol.

Taghizadeh-Mehrjardi, R., Bawa, A., Kumar, S., Zeraatpisheh, M., Amirian-Chakan, A., & Akbarzadeh, A. (2019). Soil erosion spatial prediction using digital soil mapping and RUSLE methods for Big Sioux River watershed. *Soil Systems, 3*(3), 43.

Cinnamon Wood as a Low-Cost Adsorbent for the Removal of Methylene Blue from Aqueous Effluents

Dilendra Wijesekara and Chandani Udawatte

Abstract

This study investigated the removal of methylene blue (MB) by non-modified (NMSD) and alkaline-modified (MSD) sawdust from cinnamon (*Cinnamomum verum*) wood. Characterization via SEM and FT-IR suggested that changes in surface morphology and functional groups may account for the increase in adsorption capacity of MSD, which is considerably higher than NMSD. The highest adsorption capacity observed for NMSD and MSD was found to be 44.4 and 119.6 mg g^{-1}, respectively. The adsorption data for NMSD fit best with the Toth model, and there was insignificant variance with pH. The best fit for the pseudo-first-order model indicates that physisorption is dominant over chemisorption. Redlich–Peterson isotherm and the pseudo-second-order kinetic model fit best for MSD, with correlation coefficients greater than 0.99. Kinetic data suggest the possibility of the involvement of Liquid-Film diffusion and intra-particle diffusion models for adsorption in NMSD and MSD. The results demonstrate that cinnamon wood sawdust can be used as a low-cost adsorbent for MB from aqueous effluents.

Keywords

Adsorption isotherms • Adsorption kinetics • Low-cost adsorbent • Methylene blue

1 Introduction

At present, a large number of industrial dyes used mainly in the textile industry are released untreated to streams and waterways, causing water and soil pollution and irreparable damage to the environment. Therefore, low-cost adsorbents for industrial dyes are a burning need (Yagub et al., 2014). Cinnamon (*Cinnamomum verum* also known as *Cinnamomum zeylanicum*) is native to Sri Lanka, and cinnamon wood, unlike the bark, is used as firewood or discarded. Its sawdust can be obtained easily and is inexpensive. The objective of this study was to demonstrate the potential use of cinnamon wood sawdust as a low-cost adsorbent, both in its raw state and after a cost-effective modification. To our knowledge, this is the first study that uses cinnamon wood as an adsorbent for the removal of industrial dyes from aqueous solutions.

2 Methodology

MB was obtained from Sisco Research Laboratories Pvt. Ltd. and cinnamon wood from Ratnapura, Sri Lanka. Cinnamon wood sawdust was separated into a range of particle sizes by passing through USA standard testing sieves with pore sizes of 2000, 1700, 600, 500, and 150 µm. Surface morphology images of sawdust particles were obtained by scanning electron microscopy (SEM) (EVO 18 Research, Carl-Zeiss). The base modification for cinnamon sawdust was carried out according to the method of Djilali and Elandaloussi (2012). About 2.50 g of cinnamon sawdust obtained in different particle sizes was incubated in 25 mL of 20% (wt.) NaOH solution in 50 mL centrifuge tubes and mixed in a shaker overnight at room temperature. The suspension was filtered using cheesecloth and washed with deionized water until the pH was neutral. The neutral suspension was finally washed with acetone and dried in an oven at 60 °C overnight. Fourier transform infrared (FT-IR)

D. Wijesekara (✉) · C. Udawatte
College of Chemical Sciences, Institute of Chemistry Ceylon, Rajagiriya, 10100, CO, Sri Lanka
e-mail: dilendrawijesekara@ichemc.edu.lk

A. Kallel et al. (eds.), *Selected Studies in Environmental Geosciences and Hydrogeosciences*, Advances in Science, Technology & Innovation, https://doi.org/10.1007/978-3-031-43803-5_36

spectroscopy was carried out at 400–4000 cm^{-1} to determine chemical changes in sawdust after alkali modification.

Binding studies were carried out at 200 rpm in 50 mL centrifuge tubes at room temperature using a digital precise shaking water bath (Maxturdy-30, Daihan Scientific Co. Ltd.). Absorbance was measured at λmax of 663.1 nm. The binding capacity of MB to cinnamon wood sawdust was calculated by the following formula:

$$q = \frac{(\mathrm{Co} - \mathrm{Ce})V}{W}, \quad (1)$$

where q is the binding capacity (mg g^{-1}), Co is the initial concentration of MB solution (mg L^{-1}), Ce is the equilibrium concentration of MB in solution (mg L^{-1}), V is the volume of MB solution (mL), and W is the weight of the cinnamon sawdust adsorbent (g). Batch adsorption experiments were carried out separately for the NMSD and MSD to study the effect of several physical parameters. All experiments were carried out at room temperature in triplicate, along with a control that did not contain sawdust. For further analysis of the sorption mechanism and the rate-controlling steps, kinetic models such as pseudo-first-order, pseudo-second-order, intra-particle diffusion (IPD), and Liquid-Film diffusion (LFD) were used (Qiu et al., 2009). Isotherms were constructed to determine the highest amount of adsorbate adsorbed by a given mass of adsorbent, and the fit for each model was evaluated by nonlinear regression analysis.

3 Results

3.1 Characterization Study

FT-IR images revealed the absence of the peak at 1732 cm^{-1} for MSD, possibly due to the conversion of esters or carboxylic acid to carboxylate upon alkali treatment. This peak is visible in NMSD (Fig. 1).

SEM images of NMSD (Fig. 2a) reveal low porosity and irregular surface structure, and MSD (Fig. 2b) depicts large pores leading to a macroporous surface.

3.2 Effect of Particle Size, pH, and Time of Exposure

Results show that as particle size increased from 150 to 2000 µm, the amount of MB adsorbed decreased significantly. The smallest particle size (less than 150 µm) had the highest adsorption capacity. Even though pH did not have a significant influence on the NMSD, the highest adsorption capacity of 44.4 mg g^{-1} was obtained at pH 6. The highest adsorption capacity by MSD, 119.6 mg g^{-1}, was at pH 4 and was similar to the adsorption at pH 6 and pH 8, which were 97.1 and 102 mg g^{-1}, respectively. The adsorption for NMSD was rapid within the first 90 min, possibly due to the high availability of vacant sites. The adsorption continued but at a slower rate up to 180 min, and there was no measurable increase in adsorption beyond 300 min. Thus, the minimum time for the adsorption to attain equilibrium was 90 m for NMSD. In the case of MSD, the rate of adsorption increased rapidly from 5 to 120 min, beyond which the increase in the rate of adsorption was slow, indicating that it had reached equilibrium. Thus, the time to reach equilibration is similar for NMSD and MSD.

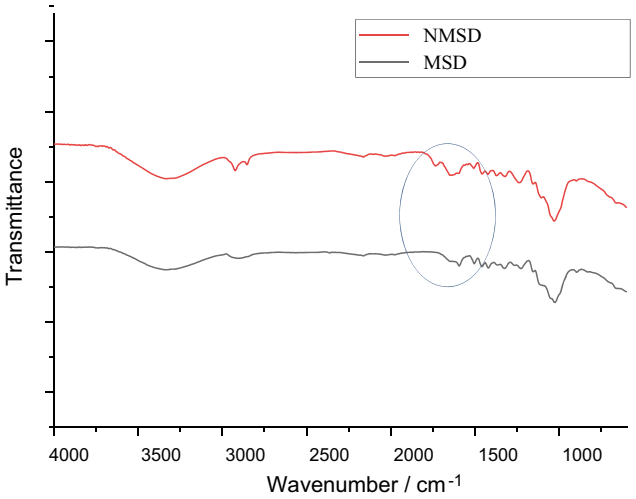

Fig. 1 FT-IR spectra of NMSD and MSD

3.3 Adsorption Kinetics, Diffusion Models, and Isotherm Study

The linear plots of pseudo-first-order and pseudo-second-order for NMSD and MSD are depicted in Figs. 3 and 4. The pseudo-first-order model fits best for NMSD, while the pseudo-second-order model fits best with MSD when considering R^2 values. According to kinetic data for the IPD and LFD models, both sets of plots for NMSD and MSD were linear with high R^2 values, suggesting the applicability of both these models for the adsorption process. Langmuir, Freundlich, Sips, Redlich–Peterson, Toth, and Temkin adsorption isotherms were used to analyze the equilibrium data (Figs. 5 and 6). The adsorption data for NMSD fit best with the Toth model, and the Redlich–Peterson model was the best fit for MSD.

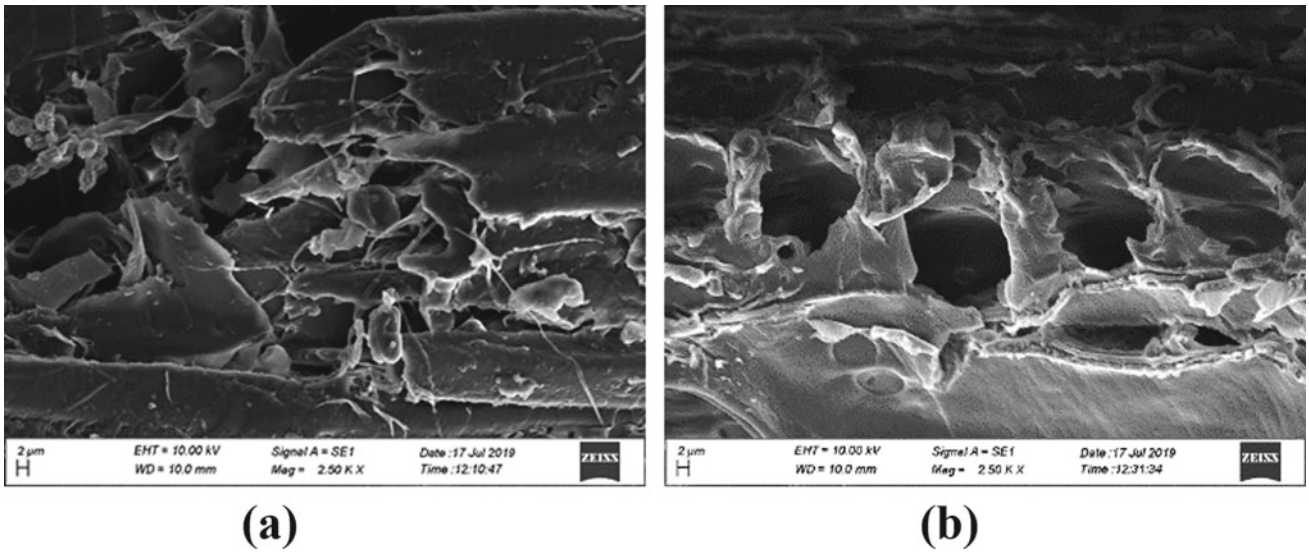

Fig. 2 SEM images of **a** NMSD and **b** MSD at 2500× magnification

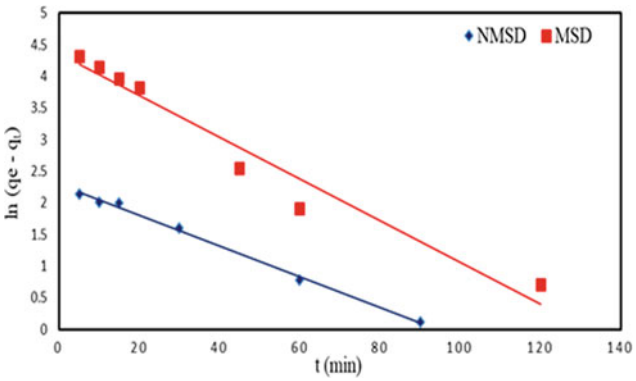

Fig. 3 Pseudo-first-order kinetic model

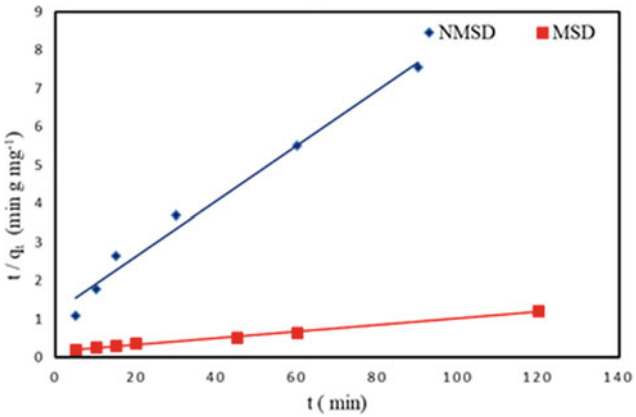

Fig. 4 Pseudo-second-order kinetic model

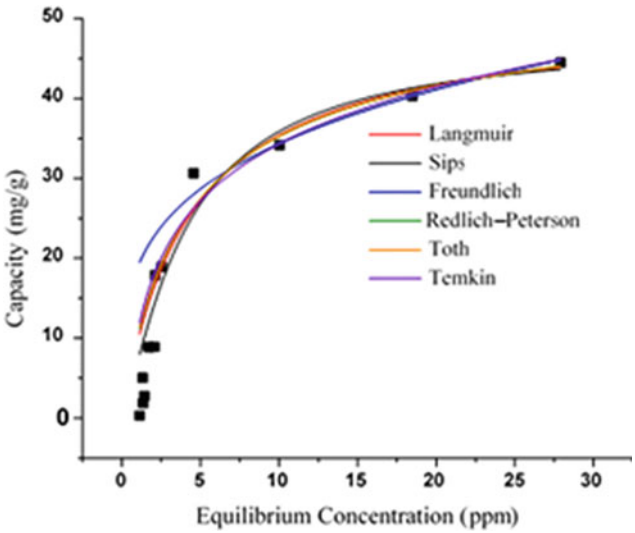

Fig. 5 Isotherms for NMSD

4 Discussion

Insignificant variance with pH and best fit to pseudo-first-order model indicate physisorption to be dominant over chemisorption for NMSD. The highest adsorption capacity for MSD was observed at pH 4, probably due to the cationic form of MB interacting with the available functional groups on the surface via hydrogen bonding. Even though the adsorption capacities of MSD and NMSD were expected to

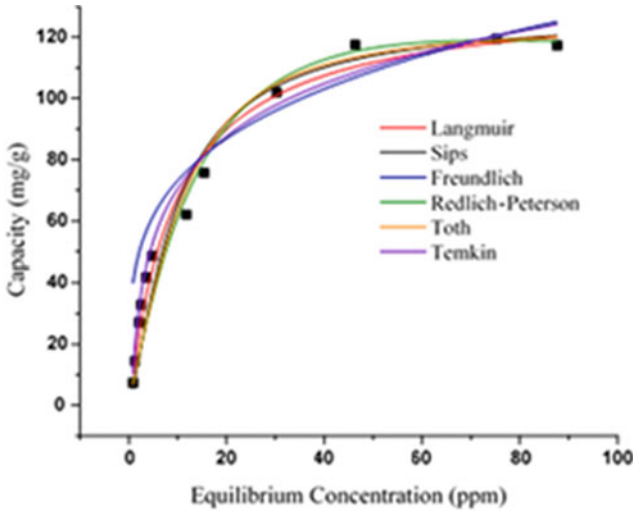

Fig. 6 Isotherms for MSD

increase at pH above 6, the MB molecules may have been restricted by the blocking of adsorption sites with the increase in the concentration of hydroxyl ions. According to adsorption kinetic models, kinetic data for MSD fit best to the pseudo-second-order model suggesting adsorption are primarily a chemisorption process. The IPD and LFD models were used to assess the mode of MB adsorption onto NMSD and MSD. In the present research, the plot for IPD presents two linear portions and does not pass through the origin, indicating that intra-particle diffusion is not the sole rate-determining step (Pholosi et al., 2020; Sen Gupta & Bhattacharyya, 2011). However, the plot for the LFD model for both NMSD and MSD was very close to passing through the origin and linear, with R^2 values of 0.983 and 0.996, respectively. Therefore, LFD could not be ruled out in the adsorption process. Toth isotherm best described the adsorption data for NMSD with a correlation coefficient R^2 of 1, indicating a multilayer adsorption system, while the value for the Toth parameter suggested that the surface heterogeneity is not very high. The Redlich–Peterson isotherm showed the highest R^2 value for MSD, suggesting that the mechanism of adsorption is not necessarily ideal monolayer adsorption.

5 Conclusions

This study revealed that the alkaline modification improved the adsorption capacity of cinnamon wood sawdust. This could be due to the extraction of lignin and hemicellulose and the conversion of surface residues to give a negatively charged cellulose surface. This would favor the binding of the cationic dye, MB via electrostatic interactions due to the new-found abundance of negatively charged sites in the MSD. Removal of MB by both NMSD and MSD was influenced by particle size and contact time and by pH for MSD only. The adsorption mechanism was jointly controlled by both LFD and IPD. The calculated maximum adsorption capacities for MB by NMSD and MSD were 44.4 and 119.6 mg g^{-1}, respectively, which are good for a low-cost adsorbent. Results demonstrated the potential use of cinnamon wood sawdust with an economical yet simple modification to be used in the adsorption of MB as a low-cost adsorbent for the treatment of industrial wastewater.

References

Djilali, Y., & Elandaloussi, E. H. (2012). Alkaline treatment of timber sawdust: A straightforward route toward effective low-cost adsorbent for the enhanced removal of basic dyes from aqueous solutions. *Journal of Saudi Chemistry*.

Pholosi, A., Naidoo, E. B., & Ofomaja, A. E. (2020). Intraparticle diffusion of Cr(VI) through biomass and magnetite coated biomass: A comparative kinetic and diffusion study. *South African Journal of Chemical Engineering, 32*(2019), 39–55.

Qiu, H., Lv, L., Pan, B., Zhang, Q., Zhang, W., & Zhang, Q. (2009). Critical review in adsorption. *Kinetic Models, 10*(5), 716–724.

Sen Gupta, S., & Bhattacharyya, K. G. (2011). Kinetics of adsorption of metal ions on inorganic materials: A review. *Advances in Colloid and Interface Science, 162*(1–2), 39–58.

Yagub, M. T., Sen, T. K., Afroze, S., & Ang, H. M. (2014). Dye and its removal from aqueous solution by adsorption: A review. *Advances in Colloid and Interface Science, 209*, 172–184.

The Structures and the Vibrational Frequencies of Organic Cd Complexes with Forced Symmetry

Yang Zhao, Yongbing Li, Qi Cheng, Jianming Liu, and Yaolin Shi

Abstract

The structures and the vibrational frequencies of complexes are basic parameters, and Cd (cadmium) is a crucial transition metal element in nature and their organic complexes are important for Cd transportation in organism systems. Here, we use the Gaussian 09 with forced symmetry to calculate the structures and the vibrational frequencies of selected Cd complexes. Our calculated results show that for Cd organic complexes, the calculated bond lengths of these complexes by the two methods (with and without forced symmetry) are almost the same, and though there exists a very small difference between the frequencies calculated by these two methods, the frequency difference of Cd isotope ^{110}Cd and ^{114}Cd is almost the same. Overall, with and without forced symmetry can be used to calculate these parameters of Cd complexes, but without using forced symmetry in the calculation is able to reduce the CPU time consumption and improve computational efficiency, especially for Cd organic complexes with more atoms.

Keywords

Isotope fractionation • Forced symmetry • Density functional theory

Y. Zhao · Q. Cheng
College of Earth and Planetary Sciences, University of Chinese Academy of Sciences, Beijing, 100049, China

Y. Li (✉) · Y. Shi
Key Laboratory of Computational Geodynamics, Chinese Academy of Sciences, University of Chinese Academy of Sciences, Beijing, 100049, China
e-mail: yongbingli@ucas.ac.cn

J. Liu
Key Laboratory of Mineral Resources, Institute of Geology and Geophysics, Chinese Academy of Sciences, Beijing, 100029, China

1 Introduction

Cadmium (Cd) is a ubiquitous transition metal element in terrestrial and aquatic environments. Cd can be transported and taken up as Cd complexes by living organisms due to their mobile ability. It can impair the organisms themselves and by long-term consumption of foods containing high concentrations of Cd transport and accumulate in animals and humans (Wiggenhauser et al., 2016). Cd isotope fractionation may be a useful tool to understand the fate of Cd in organism systems. Thus, exploring the structures and vibrational frequencies of Cd complexes which are the basis in establishing Cd isotope fractionation by theoretical calculation is essential.

There are two ways to study the structures and vibrational frequencies of complexes: experiment and theoretical calculation (Bertoli et al., 2015; Delalande et al., 2010; Yang et al., 2015). Here, we aimed to explore the structures and vibrational frequencies of selected Cd hydrate and organic complexes (Tables 1, 2) which are important in the terrestrial, aquatic environments, and other organism systems using the Gaussian 09 with forced symmetry.

2 Theory and Methods

Density functional theory (DFT) can be used to calculate the structures and the vibrational frequencies of Cd organic complexes. Here, the Gaussian 09 (Dennington et al., 2009; Frisch et al., 2009) was used to calculate the geometries optimization and vibrational frequencies of Cd hydrate complexes and organic complexes. Becke-style 3-parameter (B3) with the Lee–Yang–Parr (LYP) correlation functional (Becke, 1993a, 1993b; Lee et al., 1988) was used. In this study, we choose the def2-TZVP basis set (Andrae et al., 1991; Weigend & Ahlrichs, 2005) for Cd and the 6–311 + G (d, p) basis set (Francl et al., 1982; Krishnan et al., 1980; McLean & Chandler, 1980; Spitznagel et al., 1987) for all

A. Kallel et al. (eds.), *Selected Studies in Environmental Geosciences and Hydrogeosciences*, Advances in Science, Technology & Innovation, https://doi.org/10.1007/978-3-031-43803-5_37

Table 1 Optimized bond lengths (Å) of the Cd hydrate complexes and citrate complexes

	$Cd(H_2O)_4^{2+}$	$Cd(H_2O)_6^{2+}$	$Cd(cit)_2^{4-}$	$Cd(Hcit)(H_2cit)^-$	$CdH(cit)(H_2O)_4$	$Cd(cit)(H_2O)_3^-$
Cd–O	2.23 (2.23)	2.33 (2.33)	2.22 (2.22)	2.19, 2.12, 2.13, 2.41 (2.19, 2.12, 2.13, 2.41)	2.25, 2.31,2.31, 2.39, 2.34, 2.41 (2.25, 2.31, 2.31, 2.39, 2.34, 2. 41)	2.26, 2.29, 2.28, 2.46, 2.44,2.35 (2.26, 2.29, 2.28, 2.46, 2.44, 2.35)
	2.24[a]	2.33[a]	2.34–2.37[b]			

Data in the brackets are calculated without forced symmetry. [a]Yang et al., 2015; [b]Bertoli et al., 2015

Table 2 Optimized bond lengths (Å) of the organic Cd complexes

	CdEDTA	$Cd(his)_2H_2O$	$Cd(DMPS)_2^{4-}$	$Cd(DMPS)(H_2O)_2^-$	$Cd(cys)(H_2O)_3^{2+}$	$Cd(GS)_2(H_2O)_2^{2-}$
Cd–O	2.25,2.39 (2.25,2.39)	2.28(2.28)		2.39,3.50 (2.39,3.50)	2.31,2.32, 2.34 (2.31,2.32,2.34)	2.40,2.65 (2.40,2.64)
	2.24,2.40[a]	2.48[b]		2.39[c]		
Cd–N	2.47 (2.47)	2.38,2.39, 2.42,2.48 (2.38,2.39, 2.42,2.48)				
	2.46[a]	2.287,2.29[b]				
Cd-S			2.63,2.64, 2.66,2.67 (2.63,2.64,2.66,2.67)	2.40,2.47 (2.40,2.47)	2.42(2.42)	2.44,2.47 (2.44,2.47)
			2.57[c]	2.48[c]		

Data in the brackets are calculated without forced symmetry. [a]Kovács et al., 2010; [b]Colaneri et al., 2013; [c]Zeini Jahromi et al., 2014

other elements; the "ultrafine" numerical integration grid was used. In addition, we compared the results with forced symmetry by this study with our previous calculation without forced symmetry.

3 Results

Tables 1, 2 and 3 list calculated bond lengths and frequencies by this calculation. For comparison, previous computational results and other studies data are also listed. It can be seen that the bond lengths of optimized structures and the vibrational frequencies of the selected Cd complexes with the forced symmetry are consistent with the experimental data and those with no symmetry.

4 Discussion

Calculating molecules with forced symmetry is able to rotate different coordinate systems to the standard orientation in molecules and without any forced symmetry make computations to be performed in the input orientation. These two methods may cause the deviation of the optimized structures and vibrational frequencies from the experimental data, and it is necessary to test which method can lead to a smaller deviation.

Tables 1 and 2 show that the calculated bond lengths of these Cd complexes are almost the same, so for these Cd complexes, the bond lengths calculated by these two methods are almost the same and each method can be used to optimize their structures. Table 3 shows that the frequency

Table 3 Comparison of experimental vibrational frequencies with calculated results for $Cd(Hcit)(H_2cit)^-$

w/cm^{-1}	Vibrational modes	$Cd(Hcit)(H_2cit)^-$		
		EXP[a]	^{114}w	^{110}w
w_1	$\tau(HCH) + \nu(CO)$	1027.05	1041.616 (1041.4752)	1041.6164 (1041.4756)
w_2	$\rho(HCH) + \nu(CC)$	1078.98	1082.246 (1082.4186)	1082.2459 (1082.4188)
w_3	$\omega(HCH) + \delta(OH)$	1280.53	1287.107 (1287.133)	1287.1072 (1287.1331)
w_4	ν_s	1391.44	1387.82 (1387.8086)	1387.82 (1387.8087)
w_5	ν_{as} (COO^-)	1638.7	1696.119 (1696.108)	1696.1197 (1696.109)

Data in the brackets are calculated without forced symmetry. δ: scissoring vibration; ρ: rocking vibration; ω: wagging vibration; τ: twisting vibration; ν_s: symmetrical stretching vibration; ν_{as}: asymmetrical stretching vibration. [a]Experimental data obtained for Cd (not Cd isotope specific) by Bertoli et al. (2015)

values of the same Cd isotope calculated by the different two methods are very close, and the frequency difference of ^{110}Cd and ^{114}Cd by the same method is also almost the same. Thus, for Cd complexes, these two methods can be used to calculate their structures and frequencies, and the results by them are almost the same.

For the CPU time consumption, the organic Cd complexes are more sensitive to the two calculation methods. Without using forced symmetry can save the CPU time consumption for most organic Cd complexes with more atoms, but the effect is not obvious for inorganic Cd complexes.

5 Conclusions

Our calculated results show that for Cd hydrate and organic complexes, the bond lengths of these complexes calculated by the two methods (with and without forced symmetry) are almost the same, and though there exists a very small difference between the frequencies calculated by the two methods, the frequency difference of ^{110}Cd and ^{114}Cd is almost the same. However, without using forced symmetry is more capable of saving the CPU time consumption, especially for the organic Cd complexes with more atoms. Therefore, with and without forced symmetry can be used to calculate these parameters of selected Cd complexes, and without the forced symmetry is able to improve the calculation efficiency.

References

Andrae, D., Häußermann, U., Dolg, M., Stoll, H., & Preuß, H. (1991). Energy-adjustedab initio pseudopotentials for the second and third row transition elements: Molecular test for M2 (M=Ag, Au) and MH (M=Ru, Os). *Theoretica Chimica Acta, 78*, 247–266.

Becke, A. D. (1993b). A new mixing of Hartree-Fock and local density functional theories. *The Journal of Chemical Physics, 98*, 1372–1377.

Becke, A. D. (1993a). Density-functional thermochemistry III. The role of exact exchange. *Journal of Chemistry and Physics, 98*, 5648–5652.

Bertoli, A. C., Carvalho, R., & Freitas, M. P., et al. (2015). Theoretical spectroscopic studies and identification of metal-citrate (Cd and Pb) complexes by ESI-MS in aqueous solution. *Spectrochim Acta Part A: Molecular Biomolecular Spectroscopy, 137*, 271–280.

Colaneri, M. J., Vitali, J., & Kirschbaum, K. (2013). Electron paramagnetic resonance spectroscopic study of copper hopping in doped bis(l-histidinato) cadmium dihydrate. *Journal of Physical Chemistry A, 117*, 3414–3427.

Delalande, O., Desvaux, H., & Godat, E., et al. (2010). Cadmium—glutathione solution structures provide new insights into heavy metal detoxification. *FEBS Journal, 277*, 5086–5096.

Dennington, R., Keith, T., & Millam, J. (2009). GaussView, Version 5.0.8. Semichem Inc., Shawnee Mission, KS.

Francl, M. M., Pietro, W. J., Hehre, W. J., et al. (1982). Self-consistent molecular orbital methods. XXIII. A polarization-type basis set for second-row elements. *Journal of Chemistry and Physics, 77*, 3654–3665.

Frisch, M. J., Trucks, G. W., Schlegel, H. B., et al. (2009). Gaussian 09, Revision A.01. Gaussian, Inc.

Kovács, A., Nemcsok, D. S., & Kocsis, T. (2010). Bonding interactions in EDTA complexes. *Journal of Molecular Structure THEOCHEM, 950*, 93–97.

Krishnan, R., Binkley, J. S., Seeger, R., & Pople, J. A. (1980). Self-consistent molecular orbital methods. XX. A basis set for correlated wave functions. *Journal of Chemistry and Physics, 72*, 650–654 (1980).

Lee, C., Yang, W., & Parr, R. G. (1988). Development of the Colle-Salvetti correlation-energy formula into a functional of the electron density. *Physical Review B, 37*, 785–789.

McLean, A. D., & Chandler, G. S. (1980). Contracted Gaussian basis sets for molecular calculations. I. Second row atoms, Z=11–18. *Journal of Chemistry and Physics, 72*, 5639–5648.

Spitznagel, G. W., Clark, T., von Ragué Schleyer, P., & Hehre, W. J. (1987). An evaluation of the performance of diffuse function-augmented basis sets for second row elements, Na-Cl. *Journal of Computational Chemistry, 8*, 1109–1116.

Weigend, F., & Ahlrichs, R. (2005). Balanced basis sets of Split valence, triple zeta valence and quadruple zeta valence quality for H to Rn: Design and assessment of accuracy. *Physical Chemistry Chemical Physics: PCCP, 7*, 3297–3305.

Wiggenhauser, M., Bigalke, M., Imseng, M., et al. (2016). Cadmium isotope fractionation in soil–wheat systems. *Environmental Science and Technology, 50*, 9223–9231.

Yang, J., Li, Y., Liu, S., et al. (2015). Theoretical calculations of Cd isotope fractionation in hydrothermal fluids. *Chemical Geology, 391*, 74–82.

Zeini Jahromi, E., Gailer, J., Pickering, I. J., & George, G. N. (2014). Structural characterization of Cd^{2+} complexes in solution with DMSA and DMPS. *Journal of Inorganic Biochemistry, 136*, 99–106.

Hydrology, Hydrochemistry, Hydrogeology

Water Balance and Streamflow Modelling Using the Soil and Water Assessment Tool (SWAT): A Case of Gaojiaping Watershed in South China

Hamza Jakada and Abdulazeez Rotimi

Abstract

Models help in the derivation of qualitative and quantitative information that aid decision-making. In hydrology, models attempt to describe water transport systems in a given catchment in order to evaluate and protect water resources for sustainable use. The soil and water assessment tool (SWAT) is one of the most widely used hydrological models. In this study, SWAT was used to model the water balance and streamflow discharge of Gaojiaping watershed located in the Xiangxi River Basin, South China, using an ensemble of global-scale DEM, soil, and land use as well as meteorological data. Local daily time step streamflow data from 2014 to 2016 were used to model the streamflow discharge with the first two years (2014/2015) used for calibration and the last year (2016) for validation. The water balance model showed that 31.7% of total precipitation is evapotranspiration, 17.4% is surface runoff, 43.9% is lateral flow, and 7% percolates to shallow and deep aquifers. For the streamflow discharge, the average R^2 and NSE solutions for the calibration periods are 0.85 and 0.7, respectively, while for the validation period, the R^2 and NSE solutions are 0.8 and 0.7, respectively. In addition, global sensitivity analysis highlighted the initial depth of water in shallow aquifer (SHALLST), over-land Manning's roughness (OV_N), and average slope steepness (HRU_SLP) as the most sensitive parameters to the model solution. Overall, the model performance was found to simulate the streamflow hydrodynamics well, whereas the degree of variance in magnitude between observed and simulated discharges is weak. Enhanced results in future modelling efforts will rely on the availability of large observation data to ensure a more robust model calibration.

Keywords

Water balance • Streamflow • Modelling • SWAT • Watershed • GIS

1 Introduction

The SWAT is a continuous process-based semi-distributed model that can operate on a sub-daily time step and is designed to predict the impact of land use and management on water, sediment, and agricultural chemical yields in watersheds (Gadissa et al., 2019). The model primarily utilizes digital elevation data (DEM) to define flow directions in order to delineate a watershed and further subdivide the watershed into multiple sub-watersheds. These are then further subdivided into Hydrologic Response Units (HRUs) that consist of homogeneous land use, management, topographical, and soil characteristics (Arnold et al., 2012). In this work, SWAT was used to model streamflow and water balance components. The paper investigated the case of Gaojiaping watershed in South China.

2 Materials and Methods

2.1 Climate and Environmental Setting of Study Area

Gaojiaping watershed is a sub-basin of Gaolan River Basin located in Yichang city, western Hubei province in the People's Republic of China (Fig. 1). It is characterized by a subtropical monsoon climate with abundant rainfall that averages 900–1200 mm annually. The watershed has about 75% of its entire catchment underlain by an igneous rock, while 15 and 10% are metamorphic and carbonate rocks, respectively (Jakada et al., 2019).

H. Jakada (✉) · A. Rotimi
Department of Civil Engineering, Faculty of Engineering, Baze University, Abuja, Nigeria
e-mail: jakadahamza@gmail.com

A. Kallel et al. (eds.), *Selected Studies in Environmental Geosciences and Hydrogeosciences*, Advances in Science, Technology & Innovation, https://doi.org/10.1007/978-3-031-43803-5_38

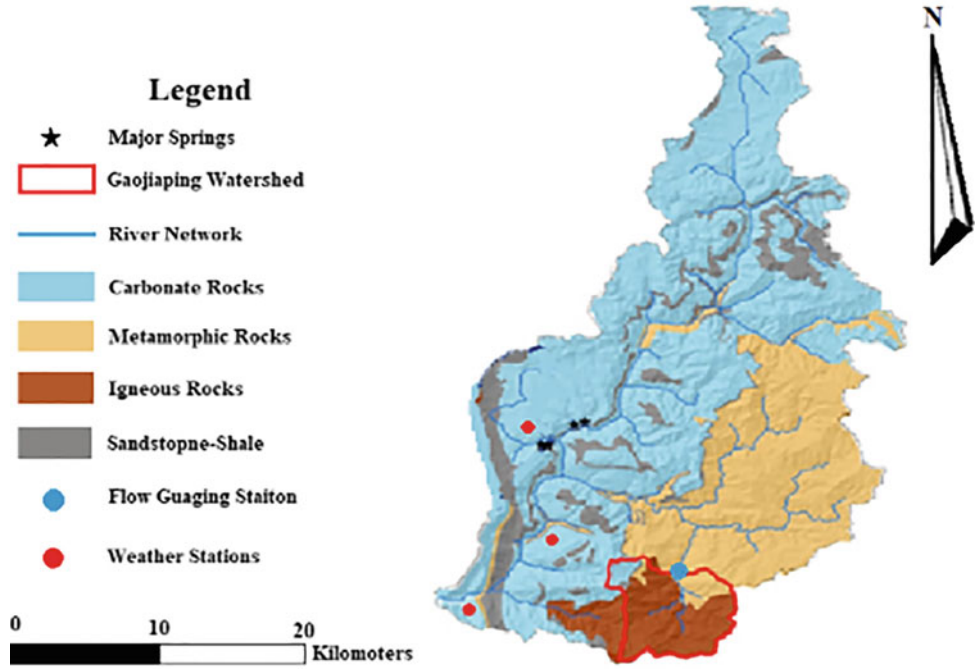

Fig. 1 Study area

2.2 SWAT Model Setup

The model requires four main data input, topographic data (DEM), land cover, soil, and meteorological data. The first three have to be converted to raster format in order for the model to process them.

2.2.1 Topographic, Land Cover, and Soil Data

Based on SRTM DEM (3-ARC, 90 m), the relief of Gaojiaping is between 762 and 1974 m above mean sea level. The European Union Global Environmental Monitoring land use/land cover datasets (HTML: EU-GEM, 2000) show that evergreen forest is most dominant covering about 74% of the entire watershed. Other land cover in the area is agriculture and shrub land both at 8.6% and then Mosaic Forest at 2.1% (Fig. 2). The United Nation Food and Agriculture Organization (HTML: FAO-AGL, 2003) shows Loam (Cambisol) as the dominant soil cover.

2.2.2 Weather and Streamflow Data

Meteorological data required to run the SWAT model include precipitation, wind, solar radiation, minimum and

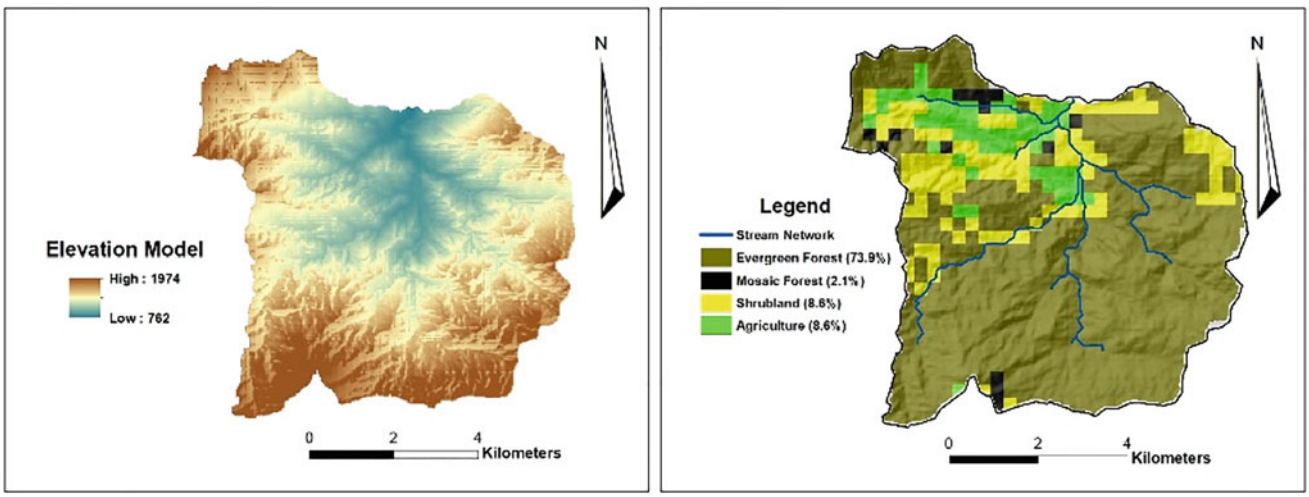

Fig. 2 Digital elevation model (level) and land cover (right) of Gaojiaping watershed

Table 1 Results' summary showing water balance components of Gaojiaping watershed

S/No	Water balance component	Value (mm)
1	Precipitation	1294.9
2	Evapotranspiration	410.9 (31.7% precipitation)
3	Surface runoff	225.38 (17.4% precipitation)
4	Lateral flow	569.72 (43.9% precipitation)
5	Percolation to shallow aquifer	93.93 (7% precipitation)
6	Return flow	74.09 (78.8% perc. to shallow aquifer)
7	Recharge to deep aquifer	4.7 (5% perc. to shallow aquifer)
8	Revap from shallow aquifer	17.82 (18.9% perc. to shallow aquifer)

Table 2 Results' summary showing the model efficiency

Calibration	R^2	NSE	RMSE
Event 1 (2014)	0.9	0.8	0.4
Event 2 (2015)	0.8	0.6	0.3
Validation			
Event	0.8	0.7	0.8

maximum temperatures, and relative humidity. These were all collected on a daily time step from the Hydrology and Water Resources Bureau of Yichang for the period of 16 years (2001–2016) where the first 6 years were used as warm-up period. Online automatic ultrasonic water level gauge (CJ 800) installed at the outlet of Gaojiaping watershed was used to collect streamflow data from January 2014 to December 2016 (Jakada et al., 2019).

2.2.3 Model Efficiency Evaluation, Calibration, and Validation

The calibration and validation in this study were carried out using the Coefficient of Determination (R^2) and Nash–Sutcliffe Efficiency index (NSE). The Sequential Uncertainty Fitting (SUFI) software was used for calibration and global sensitivity analysis.

3 Results

3.1 Water Balance and Streamflow Models

The water balance model showed that 31.7% of total precipitation is evapotranspiration, 17.4% is surface runoff, 43.9% is lateral flow, and 7% percolates to shallow and deep

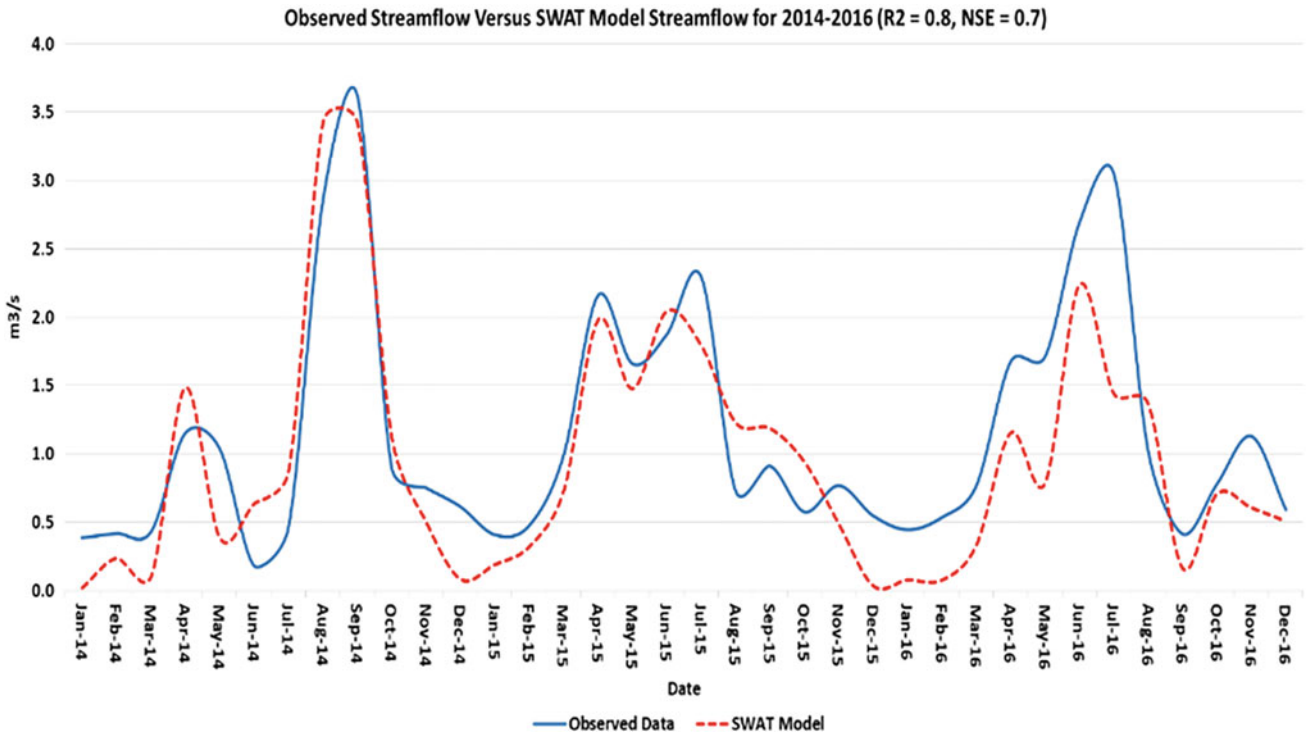

Fig. 3 Observed streamflow against simulation estimates for Gaojiaping (2014–2016)

aquifers. For the streamflow discharge, the average R^2 and NSE solutions for the calibration periods are 0.85 and 0.7, respectively, while for the validation period, the R^2 and NSE solutions are 0.8 and 0.7, respectively (Tables 1 and 2; Fig. 3).

4 Discussion and Conclusion

The sensitivity analysis highlighted the initial depth of water in a shallow aquifer (SHALLST), over-land Manning's roughness (OV_N), and average slope steepness (HRU_SLP) as the most sensitive parameters to the model solution. Overall, the model performance was found to simulate the streamflow hydrodynamics well, whereas the degree of variance in magnitude between observed and simulated discharges is weak. Enhanced results in future modelling efforts will rely on the availability of large observation data to ensure a more robust model calibration.

References

Arnold, J. G., Moriasi, D. N., Gassman, P. W., Abbaspour, K. C., White, M. J., Srinivasan, R., Santhi, C., Harmel, R. D., van Griensven, A., van Liew, M. W., Kannan, N., & Jha, M. K. (2012). SWAT: Model use, calibration, and validation. *Transactions of the ASABE, 55*, 1491–1508.

European Union Global Environmental Monitoring (EU-GEM). (2000). https://ec.europa.eu/jrc/en/scientific-tool/global-land-cover. Accessed March 20, 2020.

FAO-AGL, United Nation Food and Agriculture Organization. (2003). http://www.fao.org/ag/agl/agll/wrb/soilres.stm#down. Accessed June 15, 2016)

Gadissa, T.; Nyadawa, M.; Behulu, F.; Mutua, B. (2019). Assessment of Catchment Water Resources Availability under Projected Climate Change Scenarios and Increased Demand in Central Rift Valley Basin. In Extreme Hydrology and Climate Variability: Monitoring, Modelling, Adaptation and Mitigation; Melesse, A.M., Abtew, W., Senay, G., Eds.; in press

Jakada, H., Chen, Z., Luo, M., Zhou, H., Wang, Z., & Habib, M. (2019). Watershed characterization and hydrograph recession analysis: a comparative look at a karst vs. non-karst watershed and implications for groundwater resources in Gaolan River Basin, Southern China. *Water, 11*, 743. https://doi.org/10.3390/w11040743

Good Data Handling in Hydrogeology

Broder Merkel

Abstract

Good handling of data begins with fieldwork and sampling and ends with data quality control, statistics, assessment, and modeling. Designing a research project and writing up a good scientific paper are important, but this is not the topic of this presentation. In the very beginning, some comments about fieldwork are given (sampling, reading of field parameters). The next point addressed is the treatment, which is done by many scientists and researchers in medicine, chemistry, physics, geoscience, biology, engineering sciences, and social sciences. Some examples from hydrogeology are presented. Nowadays, complex software and powerful computers are available. However, software and computers do not guarantee proper handling of the data obtained from fieldwork or experiments. Unfortunately, even peer-reviewed papers sometimes contain absurd statements, e.g., a correlation coefficient has to be $>|0.7|$ to be significant. But, the correct use of the statistical procedures or complex ones such as random forest cluster analysis or artificial neural networks or a Bayes' approach is not science by itself. These procedures are only tools for revealing the causal reasons behind a process in the given context. In many cases, analytical or numerical models are needed. However, the data used in a model have certain uncertainties and can be a bias. Thus, results from models suffer from uncertainties and risks concerning predictive power. Some hints are given on how uncertainties and limitations of methods can be minimized. Finally, ethical aspects of scientific work in general and aspects regarding the field of psychology and phenomena such as the illusion of overconfidence of experts which is important for stakeholders, politicians, and some scientists are addressed.

B. Merkel (✉)
Technische Universität Bergakademie Freiberg, Freiberg, Germany
e-mail: Merkel@geo.tu-freiberg.de

Keywords

Dos and don'ts • Sampling • Statistics • Bayes' theorem • Deep learning • Modeling • Scientific ethics

1 Introduction

The design of a research (area, methods, and parameters), scientific hypothesis, and aims are very important issues at the very beginning of any research, because a poor concept may be the reason for failure and poor or even meaningless results. In the very end, writing up the scientific paper itself is important as well. However, both aspects are not the topic of this contribution. But, dos and don'ts during fieldwork, sampling, analytical treatment in the laboratory, data handling, quality control, statistical treatment, modeling, and causal assessment are addressed and illustrated with some practical examples. The scientific discussion has to include uncertainties of both data and results. In particular, stakeholders and politicians and in some cases as well scientists do not have sufficient knowledge about ethical aspects of science and the illusion of overconfidence of scientific experts. This is especially important in long-term predictions regarding complex and multidisciplinary research projects.

2 Fieldwork, Sampling, and Laboratory Work

Fieldwork requires careful planning and good documentation. One missing part (e.g., a battery or a missing calibration solution) can ruin the entire campaign or part of it. Planning also includes considering enough time and suitable weather conditions. Take-home message: a poor sampling and poor fieldwork cannot be healed later by excellent work in the laboratory. In the following, some pieces of advice are

A. Kallel et al. (eds.), *Selected Studies in Environmental Geosciences and Hydrogeosciences*, Advances in Science, Technology & Innovation, https://doi.org/10.1007/978-3-031-43803-5_39

given which are not valid for special investigation such as species and isotope analytics.

Water temperature, pH, oxygen reduction potential (ORP), oxygen content (O_2 in mg/L and %), and electric conductivity (EC) have to be read with handheld devices. Details about calibration, check and automatic temperature standardization have to be documented. In case a pH probe cannot be calibrated, one can read the mV and calculate the pH after calibration in the lab. If possible, temperature should be read directly in the groundwater. Probes for reading pH, ORP, O_2, and EC should be placed in a flow-through cell to avoid contamination with ambient air. Samples should be taken after pH, O_2, and EC have stabilized at constant values (protocol!). Suitable containers (e.g., pretreated glass bottles for organic traces analytics), proper filtration with 0.2 µm pore size (e.g., for trace element investigations), and conservation (e.g., acidification with ultra-pure HNO_3) and cooling of samples during transport should be considered. Details have to be checked prior to sampling with the respective analytical laboratory. Using a sampling pump or a built-in groundwater pump is a prerequisite. Bailer samples are not adequate and may be used only in extreme cases as ultima ratio. Labeling the samples with waterproof stickers with an unambiguous ident (no., name, date, [time], and [targets]) is the last step before storing the samples in a cooler ($\sim$4 °C).

Documentation of sampling includes weather conditions, GPS-coordinates of sampling points, names of the sampling team, and any incidents during the sampling campaign. Additionally, certain parameters can be measured in the field. This is often the titration of K_S and $K_{B,}$ although taking a bottle to determine total inorganic carbon (TIC) and dissolved organic carbon (DOC) would be the better option. However, in particular for water with low ORP and low O_2, determining sulfide (H_2S), Fe(II), nitrite, and ammonia, e.g., by means of photometry is advisable.

Samples should be handed over to the laboratory as soon as possible together with a sampling list containing the sample-ident and the field parameters pH, ORP, O_2, and EC. Standard methods in water chemistry are nowadays ion chromatography (IC) and Inductively Coupled Plasma–Mass Spectroscopy (ICP-MS), HPLC, and GC-MS. Other methods exist but will not be mentioned here. One last point has to be mentioned here: ORP is not the redox potential (eH), which is the Standard potential to the Hydrogen Electrode (SHE). Therefore, readings from the field have to be standardized with respect to the temperature measurements from the field and the used ORP probe to obtain eH values with respect to 25 °C. Only in very rare cases, do ORP devices perform this standardization automatically. On the contrary, most devices do this automatically for pH and EC. If pH and/or EC is not wanted as a standardized value with respect to 25 °C, most devices offer the option to disable this function. But changing this automatism may be critical for other users if the option is not enabled afterward. Another option is to re-calculate pH and EC by means of the field temperature.

3 Data Handling, Quality, and Statistics

Data handling means merging field and laboratory data including the management of missing values and the "less than detection limit" problem. For the latter, it is recommended to use "<value" with value being the detection limit, which may vary even within one bundle of sample due to using different dilution factors. When it comes to quality checks and statistics, it might be worth thinking about replacing missing values and "less than" values. The simplest method to replace missing values is to use the mean or median, and more sophisticated is multiple linear (or non-linear) regression. "Less than" values can be replaced, e.g., by multiplying the detection limit with 0.3 or another value between 0 and 1. In any case, the original data have to be kept together with the raw data (field and lab).

Quality control of chemical analysis is comparatively easy for the major inorganic constituents. By definition, the sum of all cations and anions has to be zero and can be used to calculate a simple percent error value. Nowadays it is recommended to do this not by a manual calculation but by means of computer programs such as PHREEQC (Parkhurst & Appelo, 2013) because these computer codes consider all elements and calculate the species. Assuming that calcium in water is at 100% Ca^{2+} is wrong and it may reach only 70% in some cases. A common rule is that the relative balance error should be in the range of −5 to +5%. Another option is to compare pairs of data: If the O_2 content of water was determined with 0.5 mg/L and the nitrate concentration with 100 mg/L, then a huge discrepancy becomes obvious, because it is not plausible that water with very low O_2-concentration contains a rather high concentration of the oxidizes species of the element nitrogen. Whenever such discrepancies occur or the balance between anions and cations is too large, it is time for error search together with the laboratory. For inorganic, organics' trace elements and isotopes, quality control is more sophisticated and would go beyond the scope of this contribution.

The laboratory should by the way always deliver information about detection limit and reproducibility and accuracy of the methods used. This is a very important point for the further treatment of the data and the interpretation as well. Let us assume a certain lab device that delivers a concentration of 11.50345 mg/L and has a reproducibility of ±5%. Then, this means that the concentration is between 10.928 and 12.079 mg. As a consequence, it does not make any sense to present this value with 5 decimals because the

last 4 decimals are completely meaningless. Instead, 11.5 mg/L would be a meaningful value for further utilization and discussion.

Statistics can be used for analysis, interpretation, condensing, and presentation of data. Mathematics is often rather simple and can be done partly with a simple calculator. However, nowadays computer software offers convenient operations. But users have to know certain snares they may be trapped in by using the wrong tools. Statistical procedures are often based on the distribution of data, and many procedures are suited only for normal distributed data (e.g., the well-known and very common Pearson correlation and many other tests). In natural science and geoscience, often data are not normal distributed. In such cases, one has to use a rank-correlation (e.g., Spearman or Kendall) or rank (non-parametric) test (e.g., non-parametric ANOVA analysis). For all non-parametric procedures, the first step is ranking the data (convert your data in grades) which is done nowadays automatically by the software. The second step is, then, to perform the non-parametric statistical test/procedure.

Another trap might be the scale of measure (Table 1). Pearson correlation is for example only useful for data on either interval or ratio level, while non-parametric tests like Kendall or Spearman correlation may be used for all levels. Statistical procedures with alpha variables (e.g., stratigraphically named) are not addressed here, but they can easily be transformed into logical ordered numbers.

The next critical point comes with the interpretation, and once again, we can use the correlation analysis as example. The correlation coefficient r is a number from −1 to +1. One of the most stupid errors is a statement like this: "$|r|$ must be at least 0.7 to be statistically important or meaningful". Other statements are, that a certain r-value is low or high or the correlation is strong or weak or whatever. Fact is that (1) the r-value is nonlinear depending on the number of observations (n) and (2) the correlation is normally a test to check if a correlation between two variables (e.g., the concentration of Ca and F in water) is significant. In such a case, we have the null hypothesis stating that no correlation exists. The criterion to decide is not the r-value but the p-value (probability). If the p-value is smaller than your defined threshold value, you can reject the null hypothesis. A common threshold value for p is 0.01 meaning that if your p is ≤ 0.01, you accept the hypothesis that the two variables are correlated. This is then true with an error probability of 1%.

Another common mistake is confusing principal component analysis (PCA) and factor analysis (FA). As a matter of fact, PCA generates "components" and FA "factors". PCA is a mathematical procedure to reduce the number of variables creating uncorrelated components that contain most of the information of the original data. The goal of the PCA is to reduce the number of variables and account for as much of the variability of the data as possible on the first component. Thus, it is rather unlikely that the components are interpretable regarding the variables used in the PCA. FA is often based on PCA as the first step. But, in a second step, the remaining degree of freedom is used to rotate the components and explore a latent structure of the components and thus create factors, which are often interpretable by means of the original variables. Common rotations are VARIMAX, EQUAMAX, and QUARTIMAX.

Bayes' theorem was basically ignored for decades by many scientists but actually is a powerful tool for estimating both the probability of occurrence of an event or plotting spatial distribution of data (Deutsch et al., 2020). It is based on prior knowledge in the form of an a priori probability distribution of the unknown parameter. Artificial intelligence (AI) algorithms can use Bayes' theorem based on uncertain knowledge.

Deep learning, machine learning (Lary et al., 2016), and artificial or deep neural networks (ANN, DNN) are fashionable terms these days, but not necessarily better than common techniques. In a way, these methods are a kind of unsupervised cluster analysis and pattern recognition algorithms based on massive data for training algorithms and creating results. With regard to hydrogeology, high-resolution satellite images and uncertainty quantification are challenging examples. Disadvantages of these new methods are besides time and resources, the need for massive data of good quality, high error susceptibility, and the difficulty of interpretation of the results leading to the next point.

Statistical tests and procedures deliver certain results, e.g., that certain variables are significantly correlated with each other. But this is no more no less a hint and it is the task of the scientists to present a causal reason based on experience, physico-chemical knowledge, and physical and/or geochemical processes. Finding causal reasons might not be possible in any case and is then another example of the whim of fate (random correlation). Not looking for causal reasons and processes is one of the worst shortcomings of a scientific manuscript.

Table 1 Scale of measure

Levels	Measurable properties	Examples
Nominal	Frequency (abundance)	Zip-codes
Ordinal	Frequency, rank	Grades (at school)
Interval	Frequency, rank, distance	Temperature (Celsius)
Ratio	Frequency, rank, distance, natural zero point	Temperature (Kelvin)

4 Models

Models are utilized for very different purposes. Examples are regulation of processes (e.g., pumping rate with respect to daily water demand), estimating river runoff with respect to rainfall occurrence, groundwater flow and transport of contaminants, or optimizing clean-up of contaminated sites. Depending on the demand and the aim, a certain type of model may be suitable and recommended. A general rule is that data are needed and that the quantity and quality of the data provided induce the quality of the results and it uncertainties. Additionally, the conceptual model is the key for a successful one (Betancur et al., 2012).

Empirical (statistical) models such as linear or nonlinear regression, multiple linear or nonlinear regression equations can be useful; but the disadvantage is their empirical nature and in consequence the fact that they are site-specific and not transferrable to other sites and areas. Even more important is that they do not improve the scientific knowledge. One example for this kind of meaningless models is the concept of retardation of inorganic trace elements on solids (*kd*-values). For organic traces and contaminants, these kind of models might be acceptable, if better approaches are not available.

Analytical models (closed solutions of a differential equation) have the advantage to deliver the solution very fast and that results are true. The disadvantage is that they can be developed only for simple and generalized boundary conditions and uniform parameters in the region of interest (e.g., equations estimating the aquifer permeability from pumping test data). As a consequence, the results are neither true nor correct for the area of interest. Nowadays, numerical models are very often used for interpretation and assessment of data. Numerical models are based on discretization in space (and time) and offer the utilization of complex boundary conditions and spatial and time-wise distributed parameters. Disadvantages are high costs in terms of computational time, the need for calibration with measured data, and the general problem of verification of the results, which is basically impossible from the mathematical point. Thus, checking the plausibility and sensitivity and assessing the uncertainties of the results in particular in the case of prognosis are a very important task for any kind of numerical models.

Critical are all kind of models which combine statistical models with analytical and numerical ones (e.g., climate models), because the verification and checking of plausibility is difficult and sometimes impossible.

5 Interpretation

The scientific discussion about the research including the methods applied, the findings, and their importance is the most important part of any research project and has to consider uncertainties of both used data and results. Stakeholders and politicians and in some cases scientists as well do not have sufficient knowledge about the ethical aspects of science and the illusion of overconfidence in scientific expertise This is especially important in the case of long-term predictions regarding complex and multidisciplinary research projects. Falsifying, suppressing uncertainties, and intentionally misrepresenting research data are critical aspects which may be considered as criminal acts.

References

Betancur, T., Palacio, C. A., & Escobar M. J. F. (2012). Conceptual models in hydrogeology, methodology and results. In *Hydrogeology—A global perspective* (No. February, 2012).

Deutsch, C., Deutsch, J., & Objec, L. (2020). An application of Bayes theorem to geostatistcal mapping (pp. 1–9).

Lary, D. J., Alavi, A. H., Gandomi, A. H., & Walker, A. L. (2016). Machine learning in geosciences and remote sensing. *Geoscience Frontiers, 7*(1), 3–10.

Parkhurst, D. L., & Appelo, C. A. J. (2013). Description of input and examples for PHREEQC version 3—A computer program for speciation, batch-reaction, one-dimensional transport, and inverse geochemical calculations. In *U.S. Geological survey techniques and methods, book 6, chapter A43* (497 p.).

Hydrogeochemical and Groundwater Flow Studies in El Oued Region (Southeast Algeria)

Mohammed Ouarekh, Boualem Bouselsal, Mohamed Salah Belksier, and Maha Kharroubi

Abstract

Over the last few years, considerable resources have been used and increased the number of wells due to intense irrigation and high population growth. This, in turn, has led to a drop in the water level and deterioration of water quality. A sum of 22 water samples collected from bore wells and analyzed for physico-chemical parameters. The results revealed that the contents of major elements (calcium, potassium, sodium, magnesium, sulfate, and chloride) exceeded the WHO and Algerian standards. According to the Water Quality Index (WQI), all the groundwater samples (100%) belong to the very poor category. According to the Sodium adsorption ratio (SAR), Richard diagram, Wilcox diagram, electrical conductivity (EC), permeability index (PI), and magnesium risk (MR), the groundwater is unsuitable for irrigation. The hydrogeochemical study revealed that the groundwater chemistry is controlled mainly by the evaporite dissolution (halite and gypsum) necessary to control the groundwater contamination.

Keywords

Oued Souf • Groundwater • Piezometric level • Hydrogeochemical study • GIS

1 Introduction

Following the water quality deterioration of Oued Souf superficial aquifer from the eighties, the recent drilling focused on the exploitation of the terminal complex aquifer (Bouselsal & Kherici, 2014). This aquifer, considered as fossil (OSS, 2003), is rapidly becoming overexploited in the entire Oued Souf region, resulting in the rapid deterioration of the water quality and significantly dropping in piezometric level.

The objective of the present paper was to evaluate groundwater both quantitatively and qualitatively and its suitability for drinking and irrigation purposes around the Oued Souf.

2 Materials and Methods

Oued Souf area is located in the southeast Algeria (Fig. 1), and it covers an area of 11,738 km^2 and with a population of about 4,69,129 inhabitants. It is bounded by the following Lambert coordinates: X = 2,75,200/3,22,000 E and Y = 3,665,000/3,743,000 N (Bouselsal & Kherici, 2014). The El Oued aquifer system is distinguished by the superposition of three aquifer layers. These are the continental intercalated aquifer (IC) at the base, the complex terminal aquifer (CT), and the phreatic aquifer (UNESCO, 1972).

The piezometric level of the CT aquifer was measured by the piezometric sonde in two periods (April 2010 and March 2017) to determine the annual variation of the aquifer, caused by overexploitation. A sum of 22 water samples were collected in polyethylene bottles after filtration and acidification for analysis in the laboratory (Rodier et al., 1996). The geographic base map of the region and the sampling location points have been prepared using Arc-GIS. The DIAGRAM software was used to establish the Piper diagram and make binary diagrams between the different hydrochemical parameters in order to specify the probable origin of water mineralization (Schoeller, 1962) in the terminal complex aquifer.

M. Ouarekh (✉) · B. Bouselsal · M. S. Belksier · M. Kharroubi
Laboratory of Underground Oil, Gas and Aquifer Reservoirs, Department of Earth and Universe Sciences, University of Kasdi Merbah, Route de Ghardaia, BP 511 30000 Ouargla, Algeria
e-mail: ouarekh.mohammed@univ-ouargla.dz

A. Kallel et al. (eds.), *Selected Studies in Environmental Geosciences and Hydrogeosciences*, Advances in Science, Technology & Innovation, https://doi.org/10.1007/978-3-031-43803-5_40

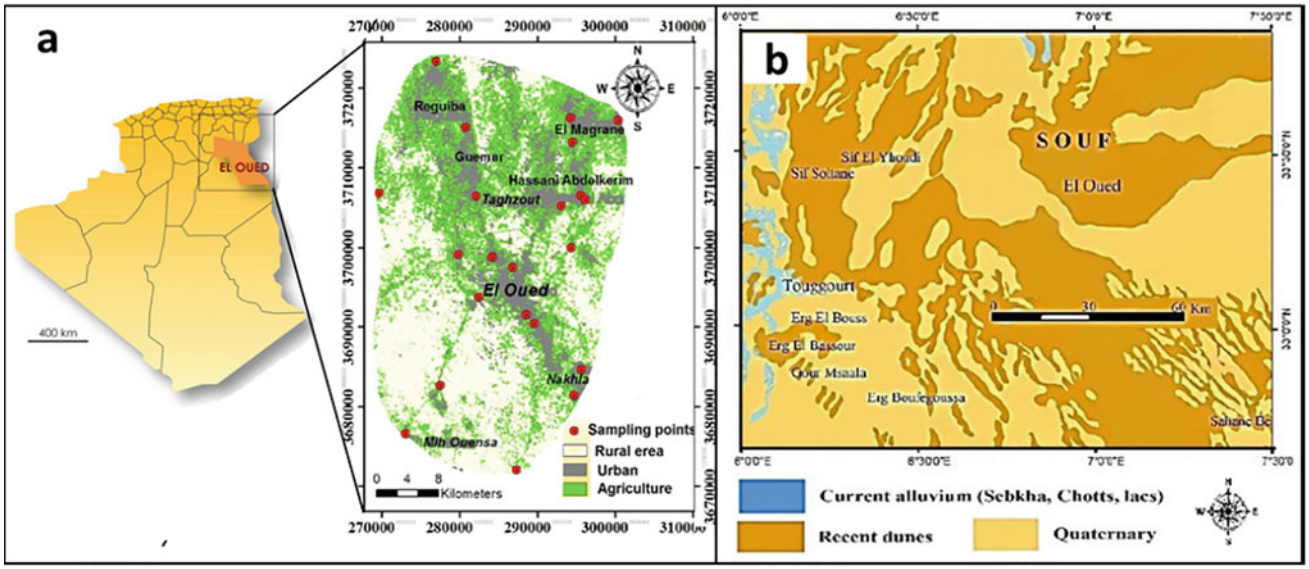

Fig. 1 Location map of the study area (**a**). Geological map of Oued Souf (M.G. Betier 1952, modified) (**b**)

3 Results and Discussion

3.1 Piezometry of the Terminal Complex Aquifer

The comparison between the two piezometric maps (2010 and 2017) (Fig. 2) shows a general decrease in the piezometric level throughout the study area ranging from 7.5 to 17.5 m. The water flow direction is in a general southwest to northeast. It can be seen that the number of boreholes for water supply and irrigation has increased. The two piezometric depressions observed from the maps were due to the overexploitation of the aquifer for the irrigation of cultivated areas, allocated to market gardening, cereals, and potatoes.

3.2 Geochemical Characterization of the Groundwater

The representation of the results on a Piper diagram (1944) (Fig. 3a) prove the dominance of: Na–Ca–SO_4, Na–Cl hydrochemical facies.

The concentrations of major elements exceeded the WHO (OMS, 2004) and Algerian standards. The Water Quality Index (WQI) (Narsimha et al., 2013; Simsek & Gunduz, 2007) calculated for the terminal complex aquifer waters range from 212.54 to 267.71, which indicates that all samples (22) are of very poor quality (Fig. 3b). The sodium percentage (% Na^+) in the study area varies between 54% and 62.47%. A 68.19% of the samples were classified as admissible and 31.81% of the samples were considered as doubtful for irrigation (Wilcox, 1948). According to the Richards diagram (US Salinity Laboratory, 1954), all the sample points are in fields C_4-S_2 and C_4-S_3 indicating a risk of high salinity and medium to high alkalinity. In this study, the permeability index (PI) of Doneen (1964) varies from 45.04 to 54.92, indicating moderate water quality for irrigation. The magnesium risk ratio that Raghunath (1987) calculated in the study area was greater than 50%, indicating that the CT aquifer waters are unsuitable for irrigation.

3.3 Multivariate Statistical Analysis

The correlation matrix (Table 1) shows several very highly significant correlations, between (EC) and Cl^- (r = 0. 92), (EC) and Na^+ (r = 0.90), (EC) and SO_4^{-2} (r = 0.84), Na^+ and Cl^- (r = 0.85), Na^+ and SO_4^{-2} (r = 0.71). This indicates that the groundwater mineralization is mainly related to sulfates and chlorides as well as other elements. This mineralization is acquired through the dissolution of evaporitic minerals (Schoeller, 1962) such as halite (NaCl) and gypsum ($CaSO_4$, $2H_2O$). The presence of evaporites is supported by the high correlation between sodium and chloride ions (r = 0.85), magnesium and sulfates (r = 0.823), and calcium and sulfates (r = 0.52).

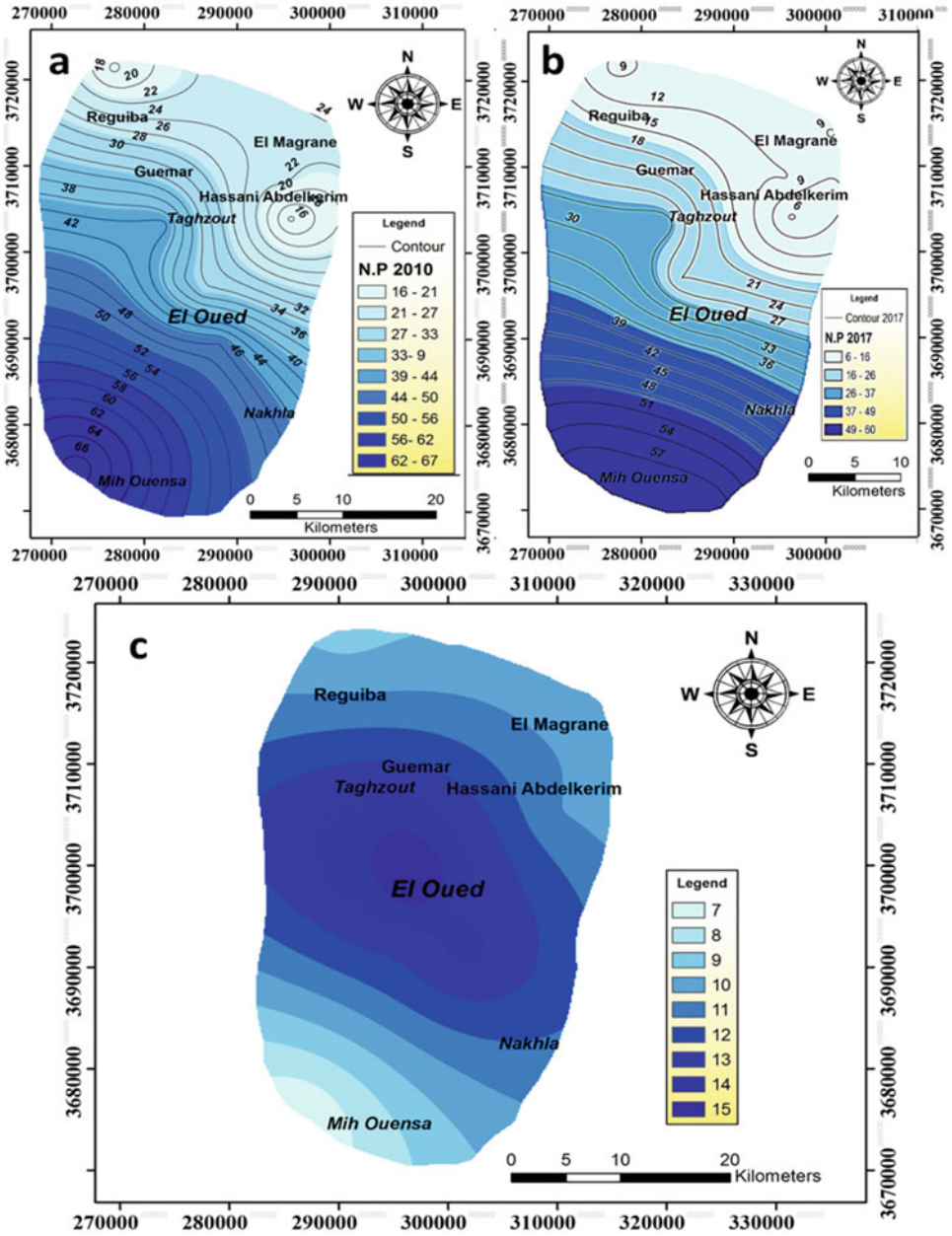

Fig. 2 Piezometric map of terminal complex aquifer. **a** April 2010, **b** March 2017, **c** map of the piezometric variation between 2010 and 2017

4 Conclusion

The study of the complex terminal aquifer of El Oued (South East Algeria) shows a decrease in the piezometric level between the period of 2010 and 2017 that varies between 7.5 and 17.5 m, and generally caused by overexploitation.

The major hydrogeochemical facies fall in the field of Na–Ca–SO_4, facies followed by Na-Cl facies. The groundwater chemistry of the complex terminal aquifer showed that water mineralization is consistent with the dissolution of the evaporites (gypsum and halite) and the silicate weathering. The concentrations of major elements exceeded the WHO and Algerian standards. The Water Quality Index (WQI) values calculated for the waters range from 212.54 to 267.71 indicated very poor quality for consumption.

The samples fall in doubtful and doubtful to unsuitable categories for irrigation use.

Groundwater management plans are urgently needed to control the development of groundwater resources and prevent further deterioration of the groundwater quality.

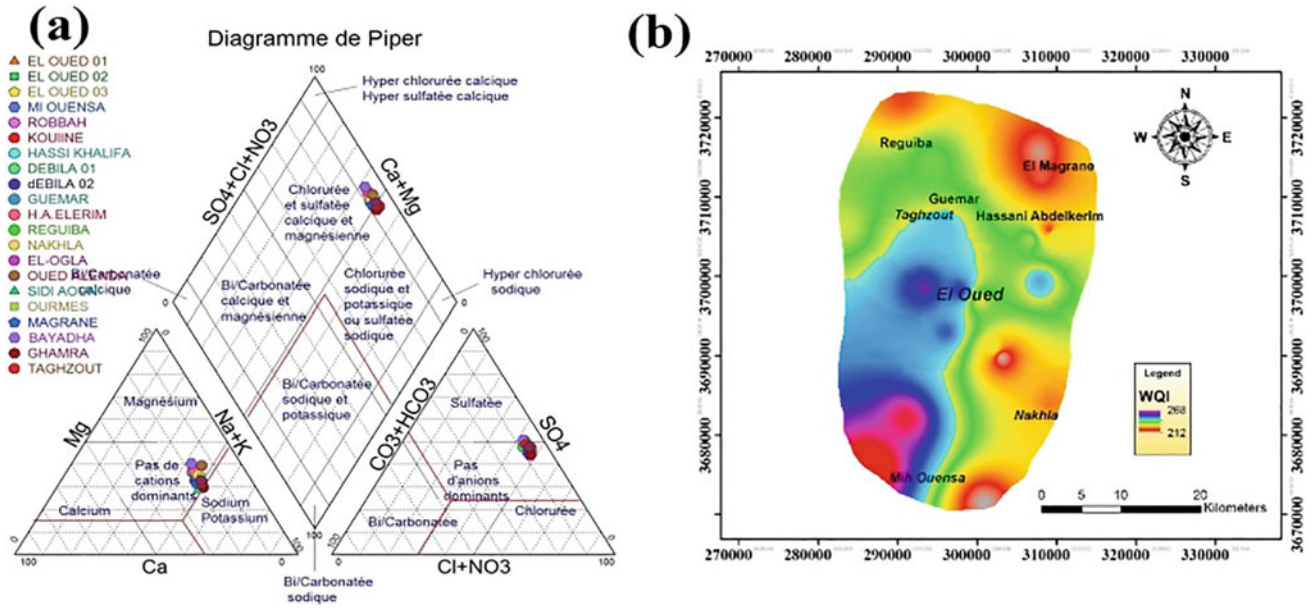

Fig. 3 **a** Piper trilinear diagram for hydrogeochemical facies, **b** Spatial distribution map of WQI for drinking

Table 1 Correlation matrix analysis result of the groundwater quality parameters

	Ca^{+2}	Mg^{+2}	Na^{+}	K^{+}	HCO_3^{-}	SO_4^{-2}	Cl^{-}	NO_3^{-}	C.E
Ca^{+2}	1								
Mg^{+2}	0.007	1							
Na^{+}	0.483	0.369	1						
K^{+}	0.288	−0.101	0.531	1					
HCO_3^{-}	0.114	−0.033	0.027	0.017	1				
SO_4^{-2}	0.518	0.727	0.712	0.069	0.024	1			
Cl^{-}	0.252	0.608	0.845	0.368	0.161	0.674	1		
NO_3^{-}	−0.181	0.233	0.390	0.130	−0.123	0.094	0.463	1	
C.E	0.396	0.597	0.902	0.293	0.116	0.836	0.918	0.334	1

References

Bouselsal, B., & et Kherici**.** N. (2014). Effets de la remontée des eaux de la nappe phréatique sur l'homme et l'environnement : cas de la région d'El-Oued (Sud-Est Algérie). *Afrique Science*, *10*(3).

Doneen, L. D. (1964). *Water quality for agriculture* (p. 48). University of Calfornia.

Narsimha, A., Sudarshan, V., & Swathi, P. (2013). Groundwater and its assessment for irrigation purpose in Hanmakonda area, Warangal District, Andhra Pradesh, India. *International Journal of Research in Chemistry and Environment, 3*(2), 196–200.

OMS (Organisation Mondiale de la Santé). (1999). Directives pour la qualité de l'eau de boisson, Vol 1 Recommendations (3ème edition), OMS (Author, F., Author, S., Author, T.: Book title. 2nd edn. Publisher, Location)

OSS (Observatoire Sahara et Sahel). (2003). Système aquifère du Sahara septentrional: gestion commune d'un bassin transfrontière. *Rapport de synthese* (322 p). OSS.

Piper, A. M. (1944). Graphical interpretation of water analysis. *Transactions of the American Geophysical Union, 25*, 914–923.

Raghunath, H. M. (1987). *Groundwater*. Wiley.

Rodier, J., Brazin, C., Broutin, J.P., Chambon, P., Champsaur, H, Rodi, L. (1996). *L'analyse de l'eau* (8ème edition). DUNOD

Schoeller, H. (1962). *Les eaux souterraines: Hydrologie dynamique et chimique. Recherche, exploitation et évaluation des ressources* (642 p). Masson et Cie. Editions

Simsek, C., & Gunduz, O. (2007). IWQ index: A GIS-integrated technique to assess irrigation water quality. *Environmental Monitoring and Assessment, 128*, 227–300.

UNESCO. (1972). *Etude des Ressources en Eau de Sahara Septentrional*. UNESCO

US Salinity Laboratory. (1954). *Diagnosis and Improvement of Saline and Alkaline Soils. Handbook* (No. 60). US Department of Agriculture

Wilcox, L. V. (1948). The quality of water for irrigation use (No.1488-2016-124600).

Comparison of Water Quality Parameters in Two Regions (Northern Cameroon, Central Africa) Based on Statistical Tools

Estelle Gaëlle Dammi Djimi, Placide Désiré Belibi Belibi, Patrice Takam Soh, Andrew Ako Ako, Godwin Tabi Agbor, Rachel Nkwaju Yanou, Julius Ghogomu Numbonui, and Joseph Ketcha Mbadcam

Abstract

Access to good quality water remains a challenge in developing countries. In ecologically risk areas such as Northern Cameroon, with a high livestock and poor sanitation practice, the water quality state is still questionable. This work investigated the microbial and physico-chemical quality of waters from North and Adamawa Regions to assess their suitability for human use. To this end, 74 water samples were collected from September to October 2017 (rainy season) and analysed for 26 water quality parameters. Data were analysed using inferential and descriptive statistics. Heterotrophic Aerobic and Mesophilic Bacteria (HAMB), total coliforms (TC), faecal coliform (FC), faecal streptococci (FS), *Salmonella* and *V. cholerae* median counts in both, North and Adamawa Regions were, respectively, 39 000 and 50 250 CFU/100 mL, 37 000 and 39 500 CFU/100 mL, 2750 and 1750 CFU/100 mL, 1220 and 790 CFU/100 mL, 1205 and 520 CFU/100 mL, 310 and 205 CFU/100 mL. The microbial counts in over 75% of the sampling sites exceeded the Cameroon Drinking Water Quality Standards (CDWS) and WHO recommended values. No statistically significant difference ($p > 0.05$) was observed in the prevalence of the microbial parameters between the two regions. In contrast, physico-chemical parameters like NO_3^- (67.20–0.64 mg/L), F^- (0.76–0.00 mg/L), turbidity (53.40–0.09 NTU), electrical conductivity (EC) (1230–10 µS/Cm) and Fe^{2+} (23.20–0.05 mg/L) in the North Region were within the recommended limits for human consumption, except for a few locations; these were, however, higher compared to Adamawa Region. In both regions, the most affected water sources were boreholes and unprotected wells. This study revealed that drinking water is most polluted in the North Region than in the Adamawa Region. The high level of faecal and bacterial contamination in both regions could be attributed to anthropogenic sources which make the water unhealthy to drink.

Keywords

Water quality • Northern Cameroon • Rural area • Microbiological parameters • Physico-chemical parameters • Public health

1 Introduction

Water quality is central to human, animal and ecosystem health (Ogwueleka & Christopher, 2020). However, access to clean water remains a big problem in developing countries. In Cameroon, 53% of rural areas have no access to clean water (Ako Ako et al., 2010). This situation is exacerbated in fragile areas like Northern Cameroon where most of the population is analphabetic and lack toilets and other waste management facilities (Ebot et al., 2008). Also, Northern Cameroon, especially Adamawa Region, is the largest cattle rearing area in the country (Kouamo & Pa-ana, 2017). Although (Abai et al., 2014) and (Yossa et al., 2014) investigated the state of few water sources in the Adamawa

E. G. D. Djimi (✉) · P. D. Belibi Belibi · G. T. Agbor · J. K. Mbadcam
Department of Inorganic Chemistry, University of Yaounde I, P.O. Box 812 Yaounde, Cameroon
e-mail: estelledammi@gmail.com

P. T. Soh
Department of Mathematics, University of Yaounde I, P.O. Box 812 Yaounde, Cameroon

A. Ako Ako
Hydrological Research Centre Yaounde, MINRESI, P.O. Box 4110 Yaounde, Cameroon

R. N. Yanou
Local Materials Promotion Authority, MINRESI, P.O. Box 2396 Yaounde, Cameroon

J. G. Numbonui
Department of Chemistry, University of Dschang, P.O. Box 067 Dschang, Cameroon

A. Kallel et al. (eds.), *Selected Studies in Environmental Geosciences and Hydrogeosciences*, Advances in Science, Technology & Innovation, https://doi.org/10.1007/978-3-031-43803-5_41

and North Regions, respectively, these studies have not studied how the water quality in rural areas is affected during the rainy season and how this influences the prevalence of waterborne diseases in Northern Cameroon.

This paper applied statistical analyses (descriptive and inferential statistics) to compare water quality parameters of new data in North and Adamawa Regions, in order to target the most polluted regions during the rainy season. The data from this study also provided additional information that can be used by decision makers for proper water management to improved health conditions.

2 Materials and Methods

The study area is located in the North and Adamawa Regions of Cameroon which have similar geological setting (Precambrian basement). The two regions differ greatly in terms of yearly rainfall, altitudes, land use, landscape, soils, as well as hydrological settings.

The samples were collected from the boreholes, unprotected wells, protected wells, spring and surface waters (river, stream, pond and oasis (locally called Mayos)), and analysed using standard methods. The results obtained from the physico-chemical and bacteriological analyses were statistically evaluated using the SPSS software version 16.0 to compare the variation of water quality parameters in the two regions. Using the Shapiro–Wilk test, the data were not normally distributed. Descriptive statistics was computed to generate median values, range and interquartile (IQR) (Oumar & Mbonigaba, 2017). Mann–Whitney U test was used to test for any difference in water quality parameters between the North and Adamawa Regions. Boxplots were used to investigate the spatial variation of water quality parameters based on the type of water sources.

3 Results

3.1 Variation of Water Quality Parameters in the Study Area

The variations in the water quality parameters investigated in the current study are given in Table 1. Overall, between regions, there was no significant difference for K^+, NO_3^-, NH_4^+, Mn^{2+}, *V. cholerae*, *Salmonella*, FS, HAMB, TC and FC. However, temperature, EC, turbidity, pH, TDS, TH, Mg^{2+}, Ca^{2+}, TAC, SO_4^{2-}, Cl^-, NO_2^-, PO_4^{3-}, Fe^{2+}, Al^{3+} and F^- differed significantly between the regions.

3.2 Variation of Water Quality with Respect to the Different Water Sources

In the North Region, 50% of boreholes had IQR of *V. cholerae* (1473 CFU/100 mL) higher compared to 50% of 19 boreholes in the Adamawa Region with an IQR of *V. cholerae* (490 CFU/100 mL).

Also, 50% (2) of the four unprotected wells in the North Region had the highest IQR of FC (53 200 CFU/100 mL) higher than the IQR of FC (6500 CFU/100 mL) in 50% of 11 unprotected wells in the Adamawa Region.

Table 1 Median and range (Maximum–Minimum) values of some high priority parameters during the rainy season based on land use

Physico-chemical parameters	Median (Range)		*p*-value	CDWS (2012)	WHO (2011)
	North region (n = 40)	Adamawa region (n = 34)			
EC	35.00 (1230–10)	10.00 (130–0)	<0.001*	1000	/
pH	7.48 (8.09–6.99)	8.24 (8.64–6.83)	<0.001*	6.5–9	6.5–8.5
NO_3^-	2.02 (67.20–0.64)	2.70 (21.60–1.36)	0.127	≤ 50	50
NO_2^-	0.03 (0.07–0.00)	0.01 (0.08–0.00)	<0.001*	≤ 0.1	3
NH_4^+	0.00 (0.29–0.00)	0.02 (0.81–0.00)	0.051	≤ 0.5	35
PO_4^{3-}	0.10 (1.30–0.00)	0.00 (1.20–0.00)	<0.001*	0.4	/
F^-	0.01 (0.76–0.00)	0.00 (0.32–0.00)	0.004*	≤ 0.7/1	1.5
Bacteriological parameters	North region (n = 40)	Adamawa region (n = 34)	*p*-value		
V. cholerae	310 (10 600–0)	205 (3500–10)	0.329	0	0
Salmonella	1205 (10 200–0)	520 (7250–10)	0.326	0	0
FS	1220 (18 000–0)	790 (18 000–20)	0.498	0	0
HAMB	39 000 (1 380 000–2500)	50 250 (408 000–1000)	0.471	/	0
TC	37 000 (432 000–500)	39 500 (480 000–500)	0.660	0	0
FC	2750 (135 000–0)	1750 (240 000–0)	0.284	0	0

4 Discussion

Compared to the Adamawa Region, the median degree of bacterial and faecal contamination in the North Region did not differ (Mann–Whitney U test, $p > 0.05$). This suggests that these regions have almost the same concern about the amount of faeces transported by runoff during rain events. FC/FS values vary between 0.7 and 4, and this indicates that the contamination in these waters could be of an undetermined origin (Pourcher, 1991). The presence of the coliform group of bacteria is indicative that other kinds of microorganisms capable of causing diseases may also be present, and that the water is unsafe for drinking (Gerba & Pepper, 2019). The pH varies from slightly acidic to alkaline in the two regions which is a conduisive environment for *V. cholerae* to thrive.

Regarding all the sampled waters, boreholes in the North Region contain highest concentration of NO_3^- (67.20 mg/L, outlier), Fe^{2+} (23.20 mg/L, outlier) and F^- (0.76 mg/L, suspected outlier). The highest value of NO_3^- exceeding the CDWS and WHO limits (50 mg/L). This excess of NO_3^- in a borehole at Mayo Ndjarendji could reflect a permeable soil vulnerable to anthropogenic activities as observed by Njitchoua and Ngounou (1997). In the meantime, the highest Fe^{2+} is above the acceptable CDWS (≤ 0.2 mg/L) and WHO (0.3 mg/L), which could be attributed to the erosion of natural deposits in the North Region of Cameroon. The maximum value of F^- (Hoy village in Poli) is within a few units above the CDWS limit (0.7 mg/L), which is probably due to the higher alkalinity recorded in the borehole in the North Region which is attributed to fluoride dissolution according to Fantong, et al. (2010). There are more risks of faecal contamination in unprotected wells in the North than in Adamawa Regions. Despite the small sample sizes in other water sources, we might say that, compared to the standards, boreholes and unprotected wells are unsuitable for domestic and irrigation purposes in both regions.

5 Conclusion

This study showed that at least 75% of water samples had the bacteriological parameters with above the CDWS and WHO standards. As for the physico-chemical parameters only, the values of NO_3^-, Fe^{2+}, $Mg^{2+}$and F^- ions were higher than the guideline in the North Region and Al^{3+}, K^+, $NH4^+$ in Adamawa region. The abundance of the bacteriological parameters followed the order: *V. Cholerae* < *Salmonella* < FS < FC < TC < HAMB.

The results of the present study indicate that drinking water sources in the North and Adamawa Regions of Cameroon are polluted by the lack of adequate sanitation facilities, high population density and intensive animal husbandry. Water quality might be improved in the two regions by regular disinfection, and in the long term through combining the above solutions with adsorption of NO_3^-, Fe^{2+} and F^- ions by local adsorbent like clays or recycled agricultural wastes. This situation can also be remedied by prohibiting the practice of open defecation and promoting the proper design and construction of boreholes and wells.

References

Abai, E. A., Ombolo, A., Ngassoum, M. B., & Mbawala, A. (2014). Suivi de la qualité physico- chimique et bactériologique des eaux des cours d' eau de Ngaoundéré, au Cameroun. *Afrique Science, 10*(4), 135–145.

Ako Ako, A., Shimada, J., Eyong, G. E. T., & Fantong, W. Y. (2010). Access to potable water and sanitation in Cameroon within the context of Millennium Development Goals (MDGS). *Water Science and Technology, 61*(5), 1317–1339.

Ebot, V., Tening, O., & Read, A. D. (2008). Waste management in Cameroon: A new policy perspective? *Resources Conservation & Recycling, 52*, 592–600.

Fantong, W. Y., et al. Geochemical provenance and spatial distribution of fluoride in groundwater of Mayo Tsanaga River Basin, Far North Region, Cameroon: Implications for incidence of fluorosis and optimal consumption dose. *Environmental Geochemistry Health 2009*

Gerba, C. P., & Pepper, I. L. (2019). Chapter 13—Microbial contaminants. In *Environmental and Pollution Science* (3rd ed., pp. 191–217). Elsevier, Inc.

Kouamo, J., & Pa-ana, P. (2017). Typology of cattle farms in the northern regions of Cameroon. *Revue d'elevage et de Médicine vétérinaire des pays Topicaux, 70*(3), 73–80.

Njitchoua, R., & Ngounou, B. (1997). Hydrogeochemistry and environmental isotope iinvestigations of the North Diamak Plain, northern Cameroon. *Journal of African Earth Sciences, 5382*(97).

Ogwueleka, T. C., & Christopher, I. E. (2020). Hydrochemical interfaces and spatial assessment of Usuma River water quality in North-Central Nigeria. *Scientific African, 8*, e00371.

Oumar, S. B., & Mbonigaba, J. (2017). The disposition of water supply and demand in Cameroon: What potential for what standard of living conditions? *Journal of Economics and Management, 28*(2), 40–56.

Pourcher, A.-M. (1991). *Contribution à l'Etude de l'Origine (Humaine ou Animale) de la Contamination Fécale des Eaux de Surface*. Université des Sciences et Techniques de Lille Flandres Artois.

Yossa, R. C. K., Fadil-Djenabou, S., Ndjigui, P.-D., Bayiga, E. C., & Bitchong, A. M. (2014). Variabilité des paramètres physico-chimiques (pH et Eh) dans deux composantes (sol et eau) du bassin versant de Ngaye, Nord-Cameroun. *Science, Tehnologies et Développement, 15*(1965), 78–86.

Mineralization Mechanisms and Water Quality of the Complex Terminal Aquifer in Algerian Desert (Ouargla)

Maha Kharroubi, Boualem Bouselsal, Samia Hadj Said, Aziez Zeddouri, and Mohammed Ouarekh

Abstract

The Complex Terminal (CT) is one of the main aquifers of the Algerian Sahara and has become widely exploited due to the high mineralization of the shallow aquifer. This research interpreted and examined the mineralization mechanisms of the Complex Terminal waters (Mio-pliocene) characterizing their drinking water quality and suitability for agricultural use. Chemical analyses were carried out on 40 sampled boreholes during February 2015. The chemical interpretation of the waters reveals the dominance of evaporitic facies: Mg^{2+}–Cl^{-}, Na^{+}–Cl^{-}, Mg^{2+}–SO_4^{2-} and Na^{+}–SO_4^{2-}. The natural mechanisms of mineralization and salinization of the CT waters were found to be linked with the dissolution evaporated minerals and ion exchange reactions. The water quality of the CT is found to be unsuitable for drinking and irrigation purposes; yet, it might be used for irrigation in permeable soil and salt tolerant plants.

Keywords

Ion change • Mineralization • Mechanism • Complex terminal • Water quality

1 Introduction

Groundwater is considered as a major source of drinking water and irrigation in hyper-arid areas. The underground water resources of the Algerian Sahara are represented by two large superimposed reservoirs, namely the Continental Intercalary (CI) and the Complex Terminal (CT) characterized by mineralized waters estimated around 5 g/l in the basin of Ouargla (OSS, 2003). The Complex Terminal has an area of 350,000 km^2 extending from Algeria to Tunisia. Due to high pollution and increased mineralization of the phreatic aquifer, the Complex Terminal has been extensively exploited. This research work identified and highlighted the mineralization mechanisms of the Complex Terminal waters (Mio-pliocene), and evaluated the chemical quality related to drinking and irrigation purposes.

M. Kharroubi (✉) · B. Bouselsal · S. H. Said · A. Zeddouri · M. Ouarekh
Underground Oil, Gas and Aquifer Reservoirs Laboratory, University of Kasdi Merbah Ouargla, BP 511 30000 Ouargla, Algeria
e-mail: kharroubimahamaha@gmail.com

2 Materials and Methods

2.1 Study Site

The city of Ouargla is located in the southeast of Algeria, 800 km from the capital, covering an area of 163,323 km^2 between the coordinates, UTM: X = 710,000/7,30,000 N and Y = 3,530,000/3,60,000 E (Bouselsal et al., 2015). The study area is characterized by a population of approximately 297,696 inhabitants in 2018, distributed on five municipalities, among which we can cite N'goussa and Sidi Khouiled. The climate of the region is hot and dry in summer and mild in winter. The surface waters are generally missing, the annual average precipitation is approximately 40.44 mm/year, and the monthly average temperature is around 35.98 °C (2007–2018). The aquifer system of Ouargla (Fig. 1) contains three main aquifers from top to bottom: the phreatic aquifer, the Complex Terminal, and the Continental Intercalary. The reservoir Complex Terminal consists of two successive permeable layers: the Mio-pliocene (sand and clay sand) and the Senono-eocene (limestone) (OSS, 2003).

2.2 Analytical Methods

Chemical analyses of 40 samples were carried out according to standard techniques at the laboratory of underground oil, gas, and aquifer reservoirs (Rodier, 1996). Nitrate, sulfate,

A. Kallel et al. (eds.), *Selected Studies in Environmental Geosciences and Hydrogeosciences*, Advances in Science, Technology & Innovation, https://doi.org/10.1007/978-3-031-43803-5_42

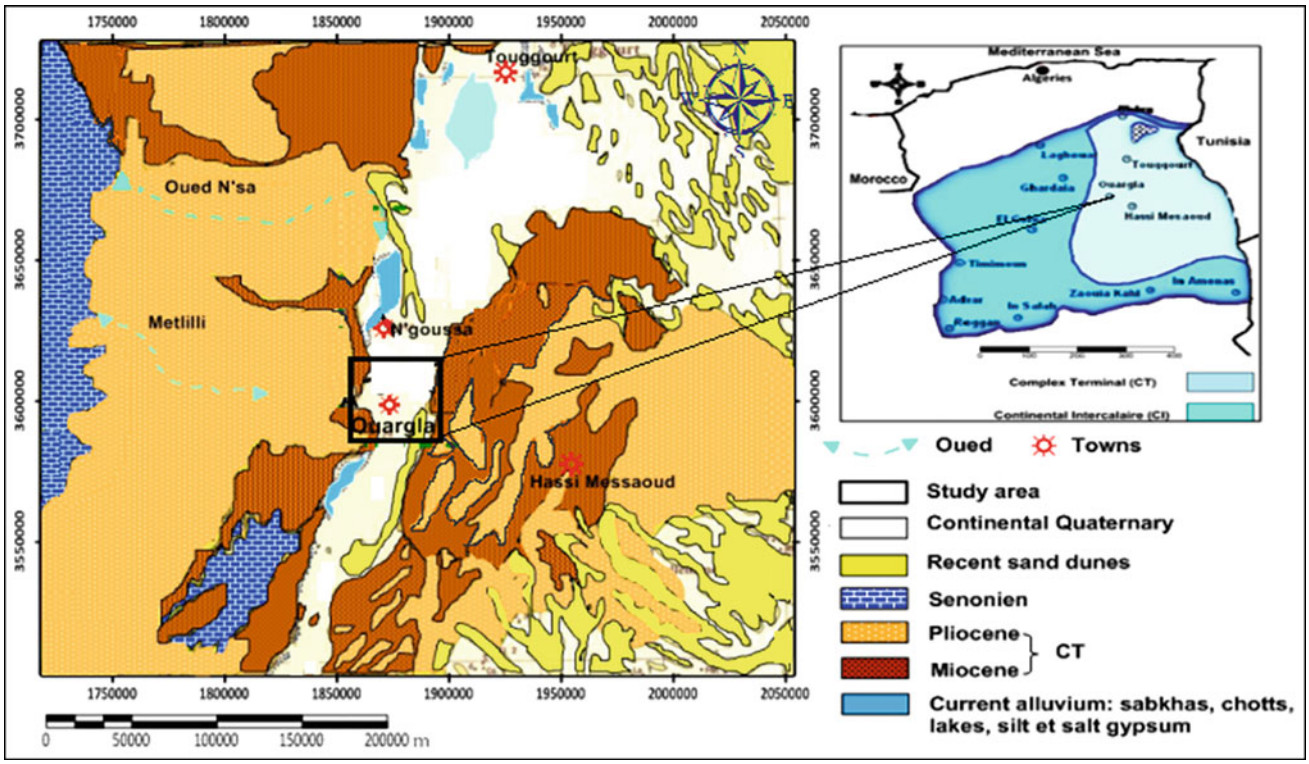

Fig. 1 Geological map of the study area (Zeddouri, 2008)

and chloride were analyzed using a spectrophotometer type DR2000. Calcium, sodium, and potassium were studied using flame photometry (410 CORNING). Magnesium was deduced from the difference Mg^{2+} = TH-Ca^{2+}, and pH was measured using a pH meter. The ionic equilibrium error calculation was evaluated by taking the relationship between total cations and total anions for each water sample. The anion–cation balance was less than 5% (Domenico & Schwartz, 1997).

3 Results and Discussion

3.1 Chemical Facies and Groundwater Quality

The sample analysis indicated that pH values (Table 1) ranged from 7 to 8, which indicated that the CT water was neutral to slightly alkaline. The total dissolved solids and EC values range from 1367 to 7344 mg/L (avg. 1467.24 mg/L) and 2040 to 10,961 µs/cm (avg. 2189.91 µs/cm), respectively. The decreasing order of cationic abundance is found to be $Na^+ > Ca^{2+} > Mg^{2+} > K^+$ (meq/L), whereas the anionic as $SO4^{2-} > Cl^- > HCO_3^- > NO_3^-$ (meq/L). The concentration of SO_4^{2-} in the CT water is observed from 600 to 1872.1 mg/L, which is high and may be due to the presence of gypsum formations in the CT aquifer, as well as anthropogenic activities. The nitrate concentration in 12 of the samples exceeded the maximum level of 50 mg/l prescribed by WHO. But the concentrations of 28 samples were observed to be greater than 25 mg/l due to leaching or runoff anthropogenic contamination. The highest values of Na^+ and K^+ were mainly due to its release from the weathering and dissolution of the evaporate minerals and anthropogenic activities (Gaury et al., 2018). The piper diagram indicated

Table 1 Statistical summary of physico-chemical parameters in the Complex Terminal water

	pH	Ca^{2+}	Mg^{2+}	Na^+	K^+	Cl^-	SO_4^{2-}	HCO_3^-	NO_3^-	EC (µs/cm)	TDS
Minimum	7	44	33.36	200	10	305	600	79	0	2040	1367
Maximum	8	352.4	257.5	2246.9	27	2724.2	1872.1	479.4	69	10,961	7344
Moyenne	7.9	200.3	154.8	627.6	16.3	909.8	1001.7	177.5	24.9	4363.5	2923.6
Ecart type	0.3	78.3	50.5	465.4	4.64	610.4	355.9	90.8	14.3	2190	1467.2
WHO	**6.5–8.5**	**75**	**50**	**200**	**12**	**250**	**250**	**240**	**50**	**1000**	**1500**

Bold value indicates importance of elements in the table

various hydrochemical facies Mg^{2+}–Cl^{-}, Na^{+}–Cl^{-}, Mg^{2+}–SO_4^{2-} and Na^{+}–SO_4^{2-} (Fig. 2). Most samples belong to Na^{+}–Cl^{-} (45%) water type, followed by Na^{+}- SO_4^{2-} (27%), and Mg^{2+}–SO_4^{2-} (15%), which are often due to leaching of gypsum levels Mg^{2+}–Cl^{-} (13%). The TH (total hardness) of all the samples exceeded 300 mg/l, and the groundwater of Mio-pliocene (CT) is hard. The interpretation of the major elements reveals that all the parameters exceeded the recommended standards by WHO, indicating that CT waters are not suitable for drinking water. The Richards diagram (Fig. 2) illustrates two classes (Richards, 1954): (1) poor waters (C_4S_2) these are more loaded with salts, that may be suitable for irrigation of salt-tolerant plants and on well drained and leached soils. (2) bad water (C_5S_3) which is unsuitable for irrigation; yet, it might be used in very permeable soil salt tolerant with good leaching for salt-tolerant plants.

3.2 Hydrochemical Processes

The major elements that correlate well (Fig. 3) with TDS are Na^{+}. Cl^{-}, and SO_4^{2-}, Additionally, most of Na^{+} versus Cl^{-} (Fig. 4a) shows that most of the samples were along the line meaning that Na^{+} and Cl^{-} are originally derived from halite dissolution.

Most samples (Fig. 4b) are above the line showing excess of Ca^{2+} relative to SO_4^{2-}, which indicates another origin of Ca^{2+} which is probably the cation exchange process by which Na^{+} is absorbed by the clay minerals against the release of Ca^{2+} according to the following reaction: (½ Ca^{2+} − clay + Na^{+} → ½ Ca + Na^{+} − clay) (Gaury et al., 2018). The graph Ca^{2+} and Mg^{2+} as a function of Cl^{-} (Fig. 4c) shows a significant contribution of these cations to the salinization of groundwater relative to the solution of evaporation minerals ($MgCl_2$. $CaCl_2$). Then, the graph Ca^{2+} and Mg^{2+} as a function

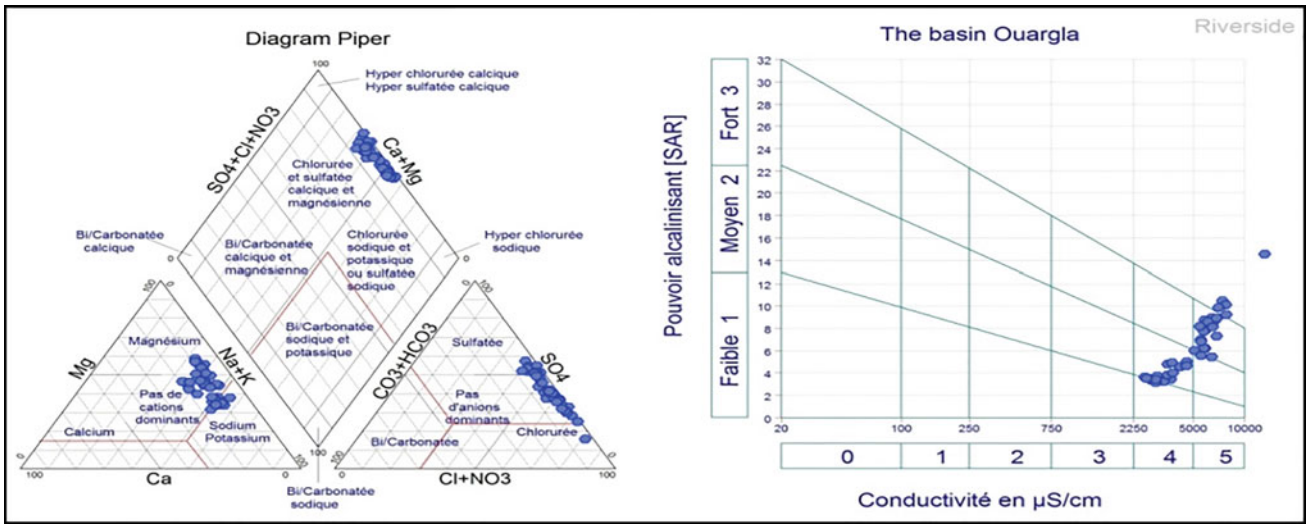

Fig. 2 Piper and Richard's diagrams

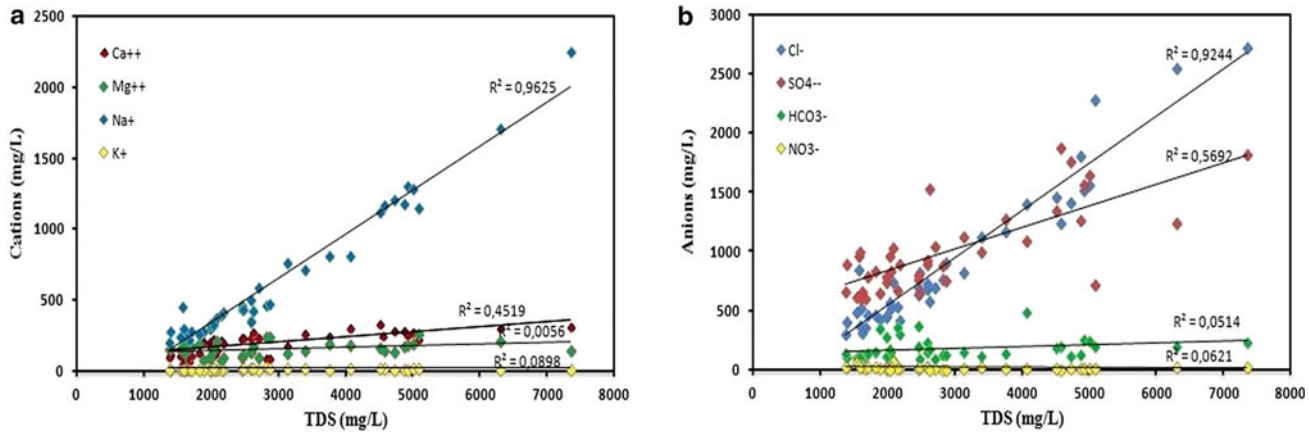

Fig. 3 Relationship among **a** cations and **b** anions versus TDS where R^2 indicates the regression coefficient

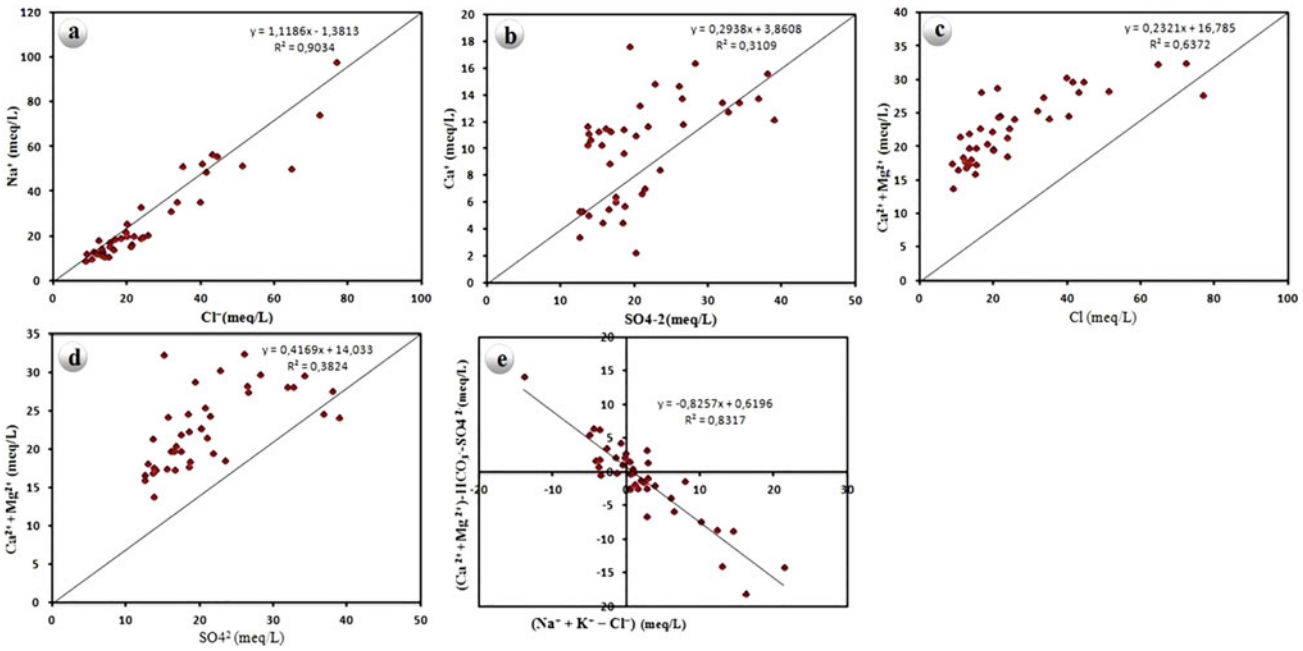

Fig. 4 Relationship between major elements: **a** Na/Cl, **b** $Ca^{2+}/SO4^{2-}$, **c** Ca^{2+} Mg^{2+}/Cl, **d** $[(Ca^{2+} + Mg^{2+})- (HCO_3^- - SO_4^{2-})]/(Na^+ + K^+) - Cl^-$)

of SO_4 (Fig. 4d) shows a dominance of carbonate rocks precisely magnesium. This means the participation of Ca^{2+} and Mg^{2+} in the mineralization of the waters of the CT, compared to $MgSO_4$ magnesium sulfate solution and gypsum minerals ($CaSO_4.2H_2O$). However, according to figure (Fig. 4e), the samples align on and near the line. It was found that these exchanges are performed toward the fixation of Ca^{2+} of water versus the release of Na^+ which is affected by cation exchange (Pawan et al., 2019).

4 Conclusion

The geochemical analysis is highlighted on the control mechanisms of mineralization of the Complex Terminal (Mio-pliocene) waters. The distribution of water samples reveals that most waters are characterized by a water type Na^+–Cl^- and are followed by Na^+–SO_4^{2-}, Mg^{2+}–SO_4^{2-}, and Mg^{2+}–Cl^-. The results indicate that water mineralization is controlled by natural mechanisms whose water–rock interaction, such as the dissolution of evaporites ($MgCl_2$, $CaCl_2$, $CaSO_4 \cdot 2H_2O$), as well as the cation exchange reaction is caused by the interaction of clay minerals. The waters of the Complex Terminal aquifer are not suitable for human consumption, according to the recommended standards of the World Health Organization (WHO). Additionally, the waters of the Complex Terminal are qualitatively classified according to Richard's diagram into three categories: admissible, mediocre, and bad for agricultural use.

References

Bouselsal, B., Zeddouri, A., Belksier, M. S., & Fenazi, B. (2015). Contribution de la Méthode de Vulnérabilité Intrinsèque GOD à l'Etude de la Pollution de la Nappe Libre d'Ouargla (SE Algérie). *International Journal for Environment & Global Climate Change, 3* (4), 92–99.

Domenico, P. A., & Schwartz, S. (1997). *Physical and chemical hydrogeology*. Wiley.

Gaury, P. K, Meena, N. K., & Mahajan, A. K. (2018). Hydrochemistry and water quality of Rewalsar Lake of Lesser Himalaya, Himachal Pradesh. *Environmental Monitoring and Assessment, 190*(2). https://doi.org/10.1007/s10661-017-6451-z (India)

OSS. (2003). Système Aquifère du Sahara Septentrional. *Modèle Mathématique. Projet SASS* (2nd ed.) Observatoire du Sahara et du Sahel,

Pawan, K, Ambrish, K. M, & Anil, K. (2019). Groundwater geochemical facie: implications of rock-water interaction at the Chamba city (HP), northwest Himalayas. *Environmental Science and Pollution Research*, *27*(9). https://doi.org/10.1007/s11356-019-07078-7 (India)

Richards, L. A. (1954). *Diagnosis and improvement of saline alkali soils*. US Department of Agriculture, Handbook No. 60.

Rodier, J. (1996). *Water analysis, natural water, wastewater, seawater* (8th ed.). Denod.

Zeddouri, A. (2008). *Hydrogeological and hydrochemical characterization of the aquifer Complex Terminal of the Ouargla region* (Doctoral thesis). University of Annaba.

Geology and Geochemistry of Geothermal Water in Northwestern Algeria, Bouhanifia Area

Mohammed Abdel Illah Benamar, Azzaz Habib, Maarten W. Saaltink, Albert Folch, and Khaldi Abdel Kader

Abstract

The present study indicated the hydrodynamics and the characteristics geothermal systems of Bouhanifia and Saida by means of hydrochemistry and isotopic data collected from different springs. Because of the lack of data (relying only on regional studies), our work defined the local geology and hydrogeochemistry behavior, following a small scale of investigation. These hot springs were produced by the ascent of thermal water in quaternary age faults marked by the Travertine formations created by the discharge of this groundwater. The geostatistical techniques used to characterize the geochemistry assert that the main contributors of mineralization are Na^+, Cl^-, Ca^{2+}, and HCO_3^-, confirming various origins of the chemical elements, from the carbonate formations and interaction with saline shallower water shown through the excess of Na^+ and Cl^-. The isotopic results confirm the low enthalpy of geothermal water and refute a magmatic origin from calc-alkaline volcanism activity during the Neogene.

Keywords

Bouhanifia area • Geothermal water • Geology • Hydrogeochemistry

1 Introduction

In recent years, geothermal systems have gained importance for tourism and energy production. North Africa, especially the Maghreb, has more than 238 hot springs (Mimi et al., 1998). In this region, the geothermal system in the north of Algeria has been studied thoroughly (Belhai et al., 2014, 2016; Ouali, 2007). However, the northwestern part of Algeria has received little attention, particularly, the Bouhanifia region, situated 25 km to the southwest of the city of Mascara. In this area, geothermal water with a temperature between 39 and 67 °C discharges to the surface. It has been classified as hyper-thermal with a flow rate of 23 L/s (Ouali, 2007). Earlier studies identified the Saida Mountain, situated 80 km to the south of Bouhanifia, as the recharge area for these thermal waters (Dalloni, 1925).

The objective of this work was to define the local hydrogeochemistry and the geothermal behavior of the groundwater system in Bouhanifia, using hydrochemical and geostatistical methods as well as environmental isotopic data.

2 Geological Setting

The west of Algeria consists of two major tectonic elements, the West African Precambrian Craton, and surrounding mobile belts (Saibi, 2009). The study site is a part of the Alpine-Maghrebines belt (Belhai et al., 2014) with a significant tectonic activity resulting in fractured and/or pleated geological formations following faults in NEE–SWW direction. According to the regional geological context, the

M. A. I. Benamar (✉) · K. A. Kader
Mustapha Stambouli University, Biological Systems and Geomatics Laboratory (LRSBG), Faculty of Nature and Life Sciences, 29000 Mascara, Algeria
e-mail: abdelillah.benamar@univ-mascara.dz

A. Habib
Mustapha Stambouli University, Laboratory of Water Science and Technology (LSTE), Faculty of Science and Technology, 29000 Mascara, Algeria

M. W. Saaltink · A. Folch
Department of Civil and Environmental Engineering, Universitat Politécnica de Catalunya, Jordi Girona 1-3, 08034 Barcelona, Spain

Associated Unit, Hydrogeology Group (UPC-CSIC), Barcelona, Spain

A. Kallel et al. (eds.), *Selected Studies in Environmental Geosciences and Hydrogeosciences*, Advances in Science, Technology & Innovation, https://doi.org/10.1007/978-3-031-43803-5_43

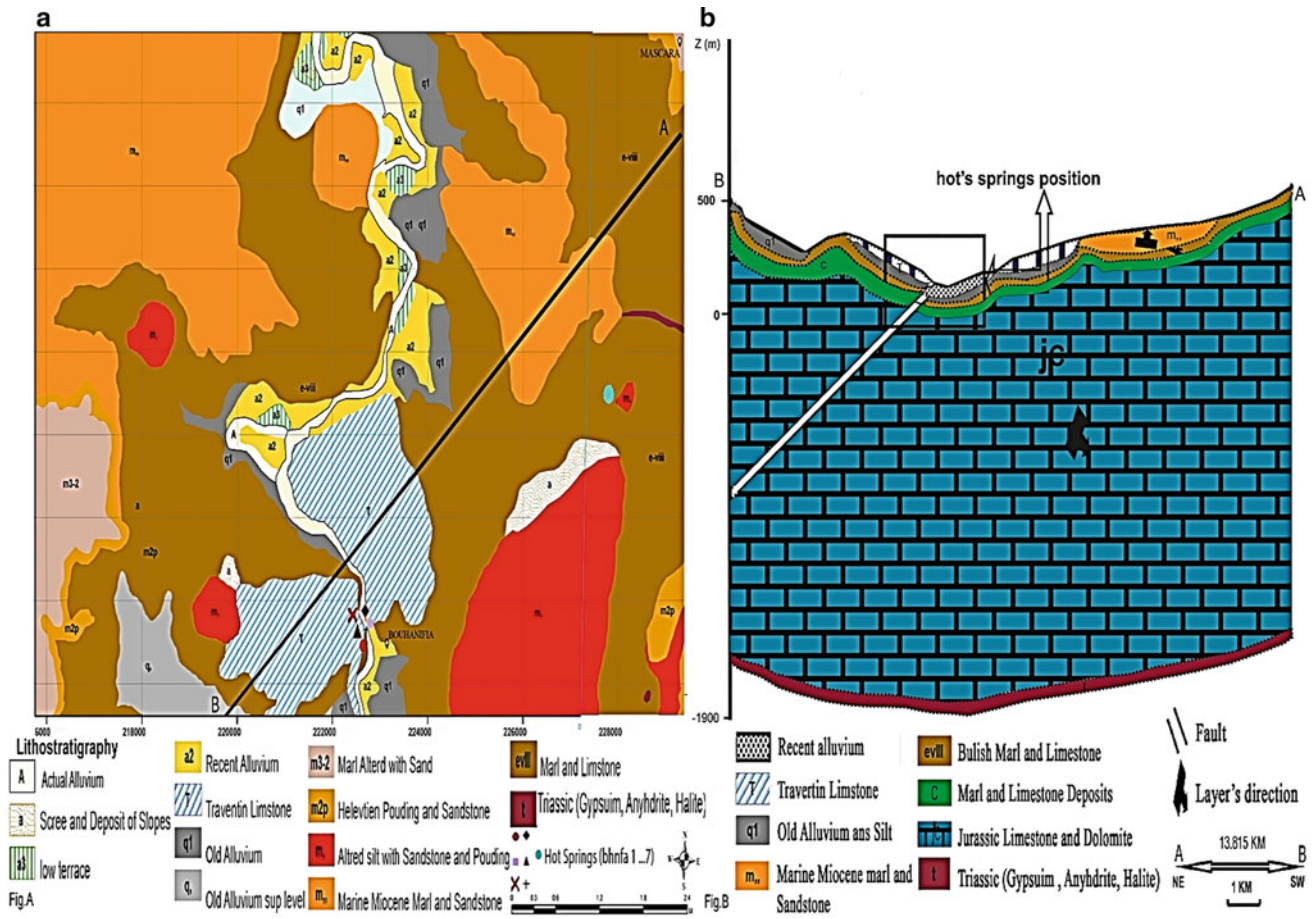

Fig. 1 **a** Local geological map of Mascara N°212 (After, Dalloni, 1925). **b** Geological cross section of profile A–B

study area belongs to the extended zone of the Tell Atlas, which in the surroundings of Mascara is overlain by a Quaternary formation consisting of recent alluvial formations of coarse material and older formations of Conglomerate. The Silt Hot springs outcrop above the Quaternary formation. Further, there is Eocene Limestone of bluish marls reaching a depth of 100 m, approximately (Fig. 1a). In the north east of the geothermal area, there are outcrops of the marine Pliocene Tripoli formation, mainly composed of sandstone.

The Miocene formation is heterogeneous and consists mainly of marine facies (Fig. 1a). The main cement is marl and sandstone with a thickness of around 100 m. The Upper Miocene also contains evaporites deposited during the closure of Mediterranean Sea, known as the Messinian Salinity Crisis (MSC). Eocene is the dominant outcropping formation within the thermal zone and is deposited on cretaceous of marl and limestone deposits with a thickness of approximately 100 m (Fig. 1a). This formation outcrops in the Benichougran Mountains in the north of the geothermal area. The Jurassic formation of fractured limestone and dolomite is defined as the host rock of the thermal water. It has a thickness of more than 1500 m, and its transmissivity is estimated between 10^4 and 10^{-2} m^2/s (Bekoussa, 2009). It is underlain by a Triassic layer of gypsum and halite (Fig. 1a).

Structurally, the study area is characterized by NE-SW faults and echelon folds that caused the collision of the Iberian and European plates during the Mio-Pliocene (Aifa et al., 2003).

3 Hydrochemistry

In order to compare the geothermal zones, samples from nine springs were collected in October 2017, i.e., seven samples from the Bouhanifia region (bhnfa1, 2, 3, 4, 5, 6, and 7) and two from the Saida region (Said 1 and 2). The piper diagram (Fig. 2a) classified the Bouhanifia water as Na^+–Ca^{2+}–Cl^-–HCO_3^- and the Saida water as Na^+–SO_4^{2-}–Cl^-; showing the effect of carbonated formations from fractured Jurassic of limestone and dolomite, and mixing with shallow water for Bouhanifia hot springs.

To better understand the chemical behavior of the thermal waters, the principal components analysis (PCA) method was

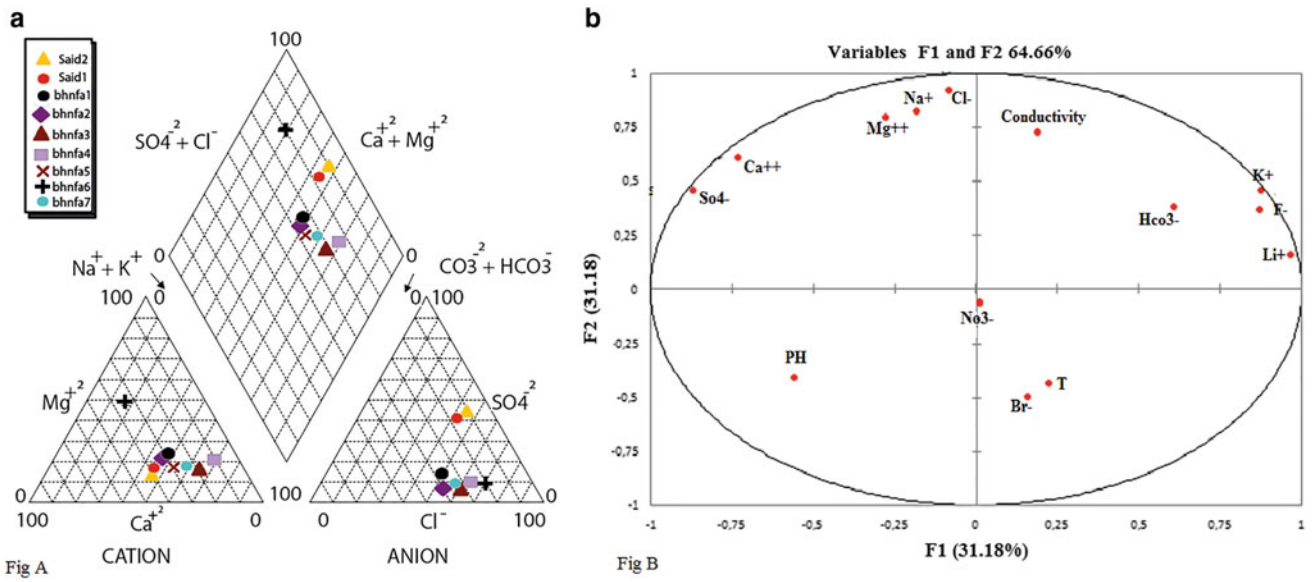

Fig. 2 **a** Piper diagram of the Bouhanifia and Saida thermal water. **b** Variation of hydrochemical elements as a function of F1 and F2

used. The Mg^{2+}, Na^{+}, and Cl^{-} are correlated to the conductivity and F2 (Fig. 2b), indicating the interaction with the Jurassic formations rich in dolomite, and mixing with deeper evaporitic formations. The negative correlation of NO_3^{-} with F1 and F2 confirms the natural origin of mineralization. On the other hand, the strong correlation between SO_4^{2-} and Ca^{2+} affirms the same origin of these elements and suggests the dissolution of gypsum (probably from Triassic or Messinian formations). Binary diagrams of Na^{+}/Cl^{-} and Ca^{2+}/SO_4^{2-} (Fig. 3) confirm the dissolution of halite and gypsum or anhydrite. Considering the geological context, the geothermal water is influenced by carbonate dissolution and mixing with either shallow water from evaporitic Messinian formation rich in halite or Pliocene Marine formations of Tripoli (Belhai et al., 2016) or deep water from Triassic formations of halite, anhydrite, and gypsum.

4 Isotopes' Geochemistry

The isotopic approach was used to further identify the origin and exchange of the Bouhanifia geothermal water. The measured isotopic values of 18O and 2D lie between − 6.53 to −8.41 and −45.1 to −45.1‰, respectively (Fig. 4). Additionally, the alignment of the points on the Global Meteoric Water Line indicates the thermal water's meteoric origin. The shift toward less negative values of δ18O and δ2D of the bhnfa1 sample is probably due to mixing with shallower evaporated cold water (Belhai et al., 2016). The difference between the samples of Saida and Bouhanifia is probably related to the difference in the recharged zone altitude of the Saida and Benichougran Mountains, around 1200 m and 800 m, respectively.

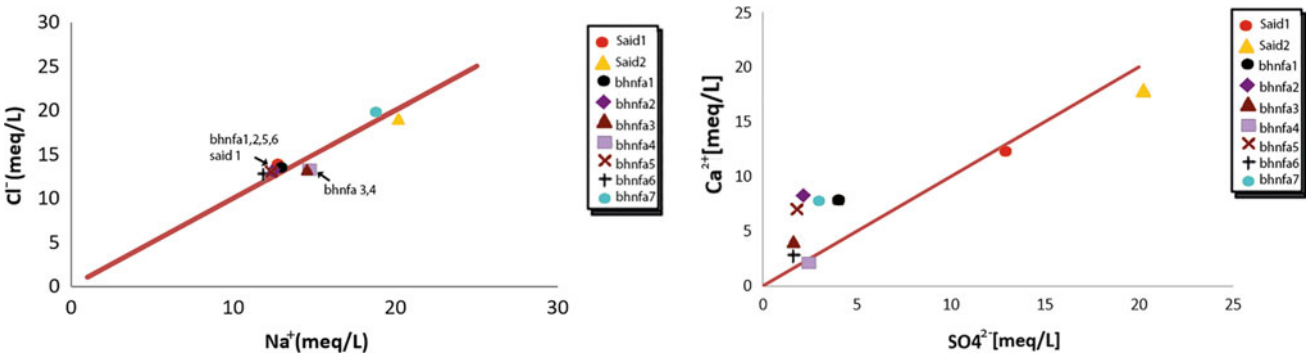

Fig. 3 Binary diagrams for Na^{+}/Cl^{-} and Ca^{2+}/SO_4^{2-} of the Bouhanifia and Saida geothermal waters

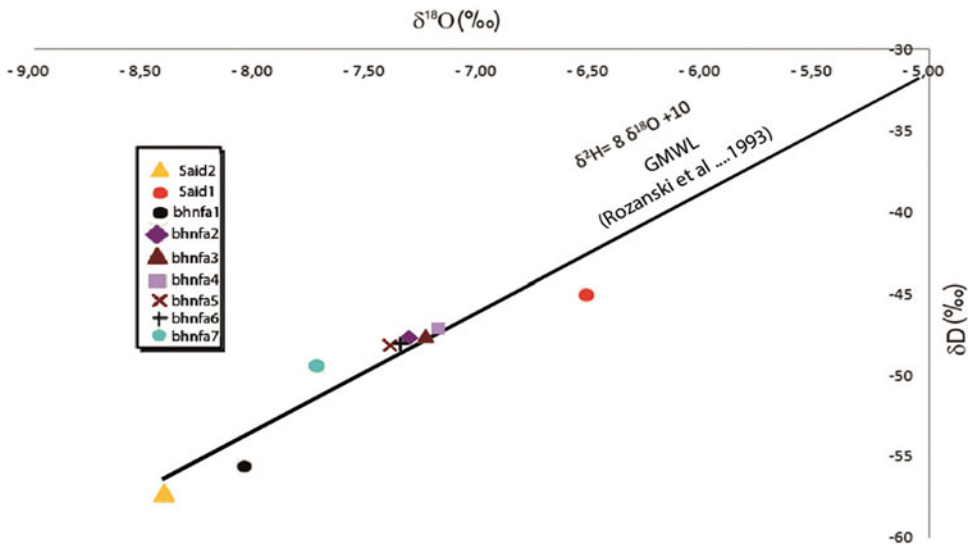

Fig. 4 Plot of δ18O versus δ2D showing the position of hot springs on the Global Meteoric World Line (GMWL; Rozanski et al., 1993)

5 Conclusion

The type of water for the springs of Bouhanifia was found to be Na^+–Ca^{2+}–Cl^-–HCO_3^-, while the springs of Saida were as Na^+–SO_4^{2-}–Cl^-. The strong correlation between conductivity and Na^+, Cl^-, and Mg^{2+} indicates that the chemical behavior depends on Jurassic formations of limestone and dolomite, mixing with shallow water from evaporitic Messinian formations or Pliocene formation of Tripoli or deep water from Triassic formations. The application of stable water isotopes 18O and 2D confirmed the meteoric origin of the thermal waters. The shifting of points from Saida highlighted the possibility that the thermal system of Bouhanifia is influenced by Benichougran recharged area including a strong connection with Saida water.

Acknowledgements We would like to thank the Algerian Center of Nuclear Research for isotopic and chemical analysis, especially Chorfi Hadjer and Abdelouhab Rachid. The first author would also like to thank the Polytechnic University of Cataluna for the reception especially hydrogeology group (UPC-CSIC). Also, the PNE scholarship allocated by the Algerian Ministry of Higher Education and Scientific Research is highly appreciated. We thank Dr. Hamed Younes and the International Association of Water Resources in the Southern Mediterranean Basin, Tunisia, for his help and support during the work.

References

Aifa, T., Feinberg, H., Derder, M. E., & Merabet, N. E. (2003). Contraintes magnéto stratigraphiques concernant la durée de l'interruption des communications marines en Méditerranée occidentale pendant le Messénien supérieur. *Geodiversitas, 25*, 617–631.

Bekoussa, B. (2009). *Modélisation du transfert et de la propagation des nitrates dans les eaux souterraines de la plaine de Ghriss*. Université des Sciences et de Technologie d'Oran.

Belhai, M., Fujimitsu, Y., Bouchareb-Haouchine, F. Z., Iwanaga, T., & Noto, M. (2014). Geochemistry of the North Western Algerian geothermal system. In *Proceedings, Thirty-Ninth Workshop on Geothermal Reservoir Engineering Stanford University, Stanford, California, SGP-TR-202*.

Belhai, M., Fujimitsu, Y., & Bouchareb-Haouchine, F. Z., et al. (2016). Hydrogeochemical and isotope geochemical study Of northwestern Algerian thermal. *Arabian Journal* of *Geosci*ences *9,* 169

Dalloni, M. (1925). Notice explicative de la carte géologique de Mascara N°212.

Mimi, A. L., Dhia, H. B., Bouri, S., Lahrach, A., Abidate, L. B., & Bouchareb-Haouchim, F. Z. (1998). Application of chemical geothermometers to thermal springs of the Maghreb, North Africa

Ouali, S. (2007). *Les sources Thermales en Algérie*. Division Energie Solaire Thermique et Géothermie.

Rozanski, K., Araguás-Araguás, L., Gonfiantini, R. (1993). Isotopic patters in modern global precipitation. In: Swart, P.K., et al. (Eds.), *Climate Change in Continental Isotopic Records.* American Geophysical Union Monogr. Ser. *78*, Washington, DC, USA, pp. 1–36.

Saibi, H. (2009). Geothermal resources in Algeria. *Renewable and Sustainable Energy Reviews, 13*, 2544–2552.

Identifying the Potential Geothermal Zones Based on Probability Mapping of Radon Gas Concentration, Lineaments Density, Geochemistry, and Alteration Data

Mohamad Nur Heriawan, Maisyita Azizah Oetomo, Arie Naftali Hawu Hede, Taiki Kubo, Yohei Tada, Koki Kashiwaya, and Katsuaki Koike

Abstract

The issue of global warming must be immediately responded to by reducing carbon emissions. However, in Indonesia, the main energy needs are still met by using fossil fuels which produce quite large carbon emissions. The solution to this problem is to use a clean alternative energy such as geothermal energy. Indonesia's potential geothermal resource is very large, which is around 27,500 MWe or about 30–40% of the world's geothermal potential. Wayang Windu geothermal field in West Java is one of the areas that show a large geothermal potential in Indonesia. Further study was carried out to extend the geothermal potential area by identifying and modeling the permeability zone from the results of Rn gas concentration, lineament density, geochemistry, and alteration data using geostatistical methods. The probability map of Rn gas concentrations, trace elements of alkali metal, pH, temperature, and alteration index are generated using sequential Gaussian simulation (SGS). Meanwhile, for the lineament density data, the spatial distribution of lineament was extracted based on digital terrain model (DTM) using segment tracing algorithm (STA). After that, the probability map was modeled using SGS as well. The result of this study was a spatial distribution of geothermal potential zones based on the permeability index.

Keywords

Geothermal potency • Rn gas concentration • Lineament density • Geochemistry • Alteration index

1 Introduction

Fossil fuels are experiencing a decline in production and price volatility, so that in Indonesia, energy needs from new and renewable energy need to be increased according to the National Energy Council (DEN) target until 2050. The target of reducing petroleum consumption from 46% in 2015 reaches 20% by 2050. New and renewable energy from 5% in 2015 is targeted to increase to be 31% by 2050 (National Energy Council (DEN), 2015).

The existence of geothermal manifestations as an indication of geothermal potential is always related to the permeability parameter. A permeable zone is a fluid pass zone that allows the formation of fluid circulation as a manifestation pathway appearing on the surface of a reservoir. This research is indispensable to map the distribution of permeable zones, so that the geothermal potential zones could be identified. In this study, the determination of the permeable zone was based on several parameters, including radon concentration, lineament density, geochemistry, and alteration index. Wayang Windu geothermal field (WWGF) located at West Java, Indonesia, was used as a case study. The other active geothermal fields around the study site are Patuha, Darajat, and Kamojang (see Fig. 1).

2 Material and Methods

Radon gas (Rn) concentration, alteration index, geochemistry, temperature, and pH data were obtained from field samples in WWGF which were then simulated using sequential Gaussian simulation (SGS) method. Lineament

M. N. Heriawan (✉) · A. N. H. Hede
Faculty of Mining and Petroleum Engineering, Research Group of Earth Resources Exploration, Bandung Institute of Technology, Bandung, Indonesia
e-mail: heriawan@mining.itb.ac.id

M. A. Oetomo
Graduate Program of Mining Engineering, Faculty of Mining and Petroleum Engineering, Bandung Institute of Technology, Bandung, Indonesia

T. Kubo · Y. Tada · K. Kashiwaya · K. Koike
Department of Urban Management, Graduate School of Engineering, Kyoto University, Kyoto, Japan

A. Kallel et al. (eds.), *Selected Studies in Environmental Geosciences and Hydrogeosciences*, Advances in Science, Technology & Innovation, https://doi.org/10.1007/978-3-031-43803-5_44

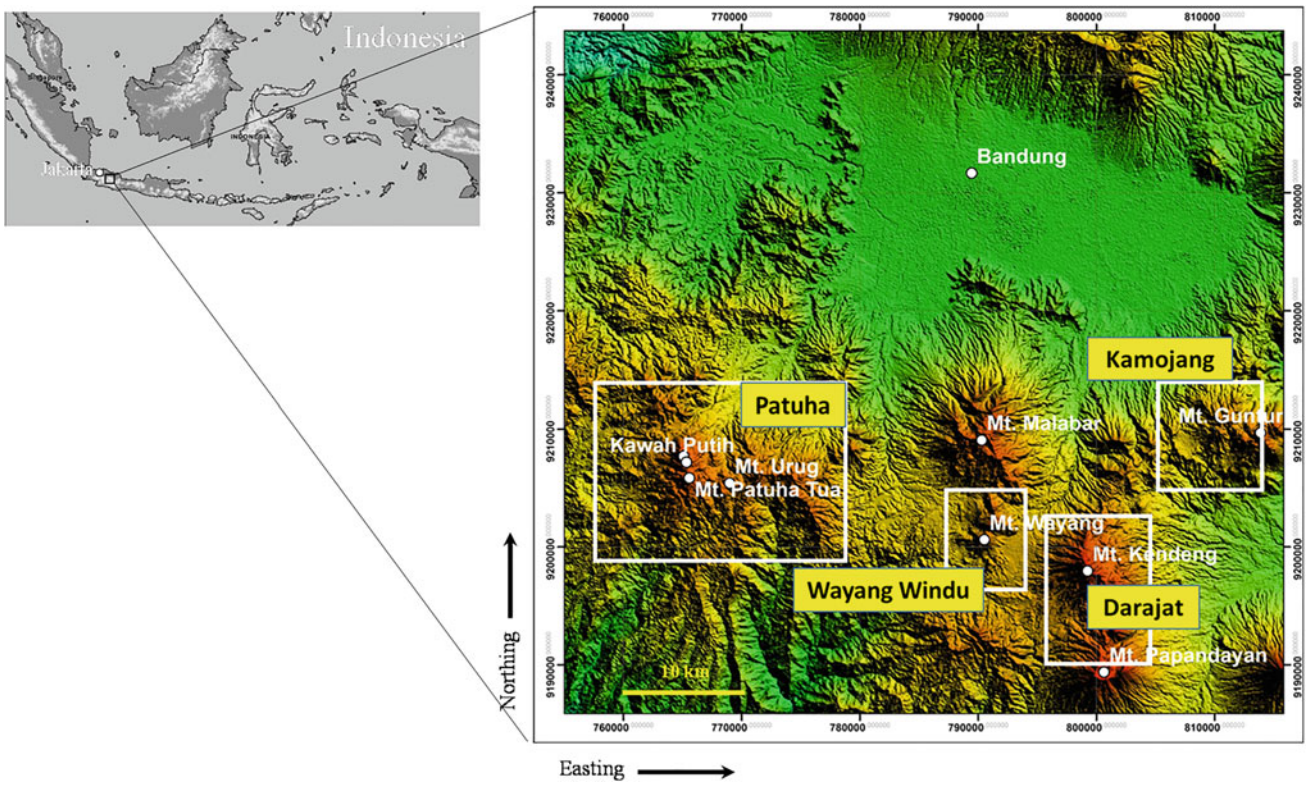

Fig. 1 Wayang Windu geothermal field (WWGF) as a study site around three others active geothermal fields located at West Java, Indonesia

density data was obtained from the digital terrain model (DTM) map of WWGF area from the DEMNAS website (DEMNAS, 2020). DEMNAS is a digital elevation model produced by the National Mapping Agency of Indonesia. The lineament was extracted from DTM data using segment tracing algorithm (STA) method to produce the density of lineament number, length, and intersection. The density result is then simulated using SGS method. The statistical parameters for all data are given in Table 1. The probability of all data that has been calculated from SGS method is used to generate the potential map using "OR" function to identify the area that has the highest probability.

Trace elements and rare alkali metals were used as geochemical data, namely Cl, B, Li, Rb, and Cs. Rare alkaline metals such as Li, Rb, and Cs are good high-temperature indicators of hydrothermal fluids (Goguel, 1983). Cl and B are highly mobile during rock–water interaction in the fluid pathway and are also good indicators of rock leaching at depth, and B tends to correlate with Cl because of its volatile behavior at depth (Nicholson, 1993). Rare alkali metals Li, Rb, and Cs which are reactive in the deep parts of the reservoir beyond drilling depths, have highly positive correlations with Cl, suggesting that they are considerably mobile and are the

Table 1 Statistical summary of all dataset

Parameters	Rn (Bq m^{-3})	Alteration index	Density of lineament number (count/m^2)	Density of lineament length (km/km^2)	Density of lineament intersection (count/m^2)	Li (µg/L)	Rb (µg/L)	Cs (µg/L)	Cl (mg/L)	*B* (µg/L)
Mean	8264	47	0.25	0.04	0.13	10.46	19.79	2.26	529	*3203*
Variance	3.4×10^7	424	0.01	0.00	0.02	569	1938	32	8.26×10^6	*8.38×10^7*
Minimum	2100	14	0	0	0	0	0	0	0.19	*0.00*
Q1	4927	32	0.18	0.02	0	0.00	0.00	0.00	0.94	*0.05*
Median	6887	45	0.25	0.04	0.06	0.00	0.00	0.00	2.42	*1.58*
Q3	9625	61	0.31	0.05	0.18	0.06	0.11	0.02	13	*97*
Maximum	31,267	100	0.68	0.11	1	72.08	161.48	21.63	16,016	*36,183*

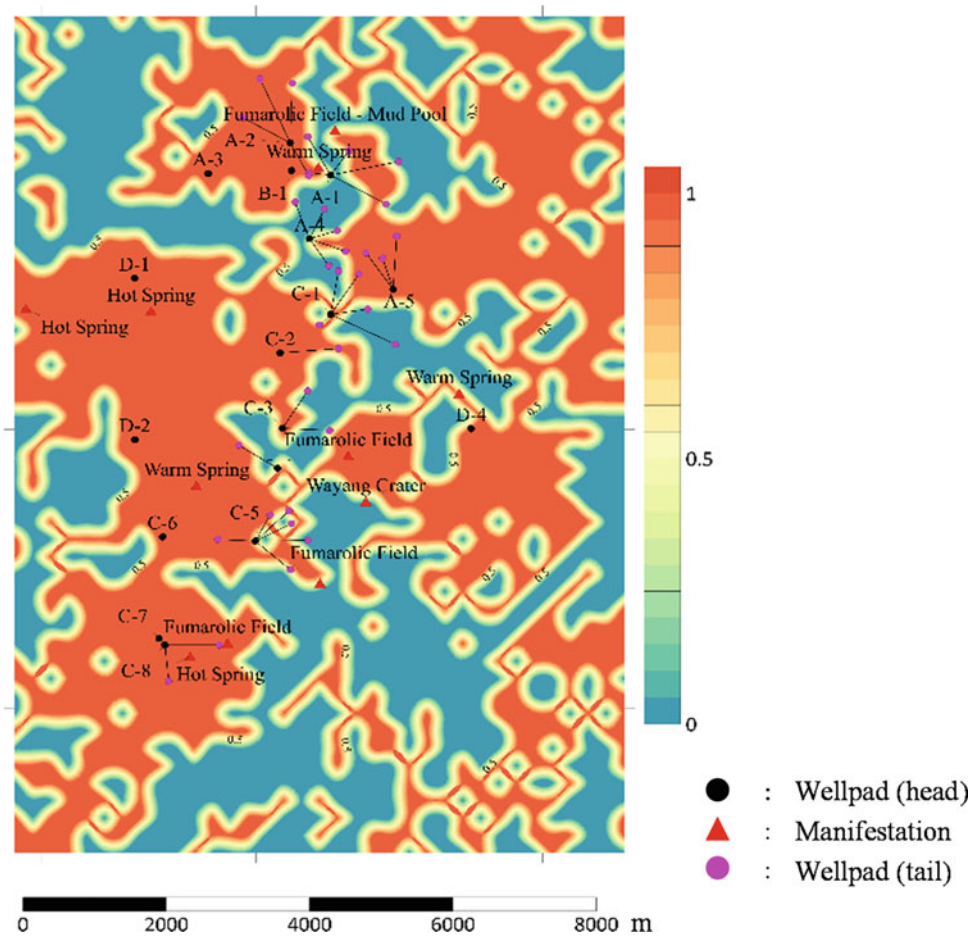

Fig. 2 Potential map of all data combined (Rn concentration, lineament density, geochemistry, temperature, pH, and alteration index) using "OR" function at WWGF

least affected by relatively shallow processes (Angcoy & Arnórsson, 2015).

SGS is a process for creating an array value that has the same statistical and spatial characteristics as its true grade (Remy et al., 2009). By using the SGS, we could produce some realization in each simulated cell or grid while considering the local variability. From these realizations, we could calculate the probability of existing parameter in cell or grid above a certain threshold. This method is an alternative for other methods, such as fuzzy logic which is usually used to produce the potential map in GIS. Meanwhile, STA is a computerized automatic lineament extraction by considering a continuous straight valley in satellite imagery with a non-filtering approach (Koike et al., 1995). All data were processed using SGS method to generate the probability map and then continued to generate the potential map using "OR" function to identify the area that has highest probability of permeable zone. By using this "OR" function, at least one parameter could solely define the potential zone.

3 Results and Discussion

The simulated potential map of all data that has been generated using "OR" operator is shown in Fig. 2. "OR" function of each factor used the third quartile threshold of each parameter, except for pH. The threshold for pH is <5. The closest probability index to one means that the area is most likely to be a potential permeable zone. Distribution of the area that showing index 1 (red color) looks quite widespread. Most of the distribution of geothermal manifestations and production wells is in areas with an index ranging from 0.5 to 1. This shows that the combination of Rn concentration data, lineament density, geochemical data, and alteration index simulated by SGS and generated by "OR" function shows a fairly good correlation with geothermal manifestations and production well which are associated with up-flow and outflow zones at WWGF.

The use of STA method in lineament density extraction is a simple, fast, and economical method of lineament

extraction. It can be easy and economically efficient in identifying permeable zones by correlating lineament density with one or two other field data. This study used quite a lot of supporting data such as Rn concentration, geochemistry data, and alteration index, so that it produced fairly accurate results.

4 Conclusion

The combination of Rn concentration, lineament density, geochemistry data, and alteration index to generate probability map using the SGS method and "OR" function has been successfully applied to determine the spread of high permeable zones, which were mostly associated to the location of geothermal manifestations and production wells at WWGF. The Rn concentration and lineament density were the two parameters which are the most directly related to the existence of permeability zones in geothermal fields. But, by adding the geochemistry an alteration index, we could obtain more confident results in mapping the potential zones.

References

Angcoy, E. C. Jr., & Arnórsson, S. (2015). Systematics of rare alkalis and halogens in the high-temperature Mahanagdong geothermal field, Leyte, Philippines. In *Proceedings World Geothermal Congress 2015*, Melbourne

DEMNAS. (2020). Homepage, http://tides.big.go.id/DEMNAS/. Last accessed August 30, 2020.

Goguel, R. (1983). The rare alkalies in hydrothermal alteration at Wairakei and Broadlands, geothermal fields, N.Z. *Geochimica et Cosmochimica Acta, 47*.

Koike, K., Nagano, S., & Ohmi, M. (1995). Lineament analysis of satellite images using a Segment Tracing Algorithm (STA). *Computers & Geosciences, 21*(9), 1091–1104.

National Energy Council (DEN). (2015). Energy Mix. Available only in Bahasa Indonesia.

Nicholson, K. (1993). *Geothermal fluids: chemistry and exploration techniques*. Springer.

Remy, N., Boucher, A., & Wu, J. (2009). *Applied geostatistics with SGeMS* (264 p). Cambridge University Press

Operating Principle of the M'Chaki Spring-Jijel (North-East Algeria)

Tekkouk Mustapha and Benzaid Riad

Abstract

The M'Chaki intermittent spring situated in Lâayoune in Selma Benziada is located about 20 km south-east of the village of Ziama Mansouriah and about 50 km south-west the town of Jijel (North-eastern Algeria). Well known for its current and historical appeal, the M'Chaki karst spring is distinguished by its magical site and its functioning which has always aroused the curiosity of those, laymen or scientists, who have visited it. Discovered more than ten centuries ago, the M'Chaki spring continues to pour out its waters and amazes its visitors with its secrets it has very jealously kept. M'Chaki spring deserves special attention because, so far, all the attempts or studies undertaken to attribute it to a conceptual diagram of its device, explain its operation mechanism, and clarify the reasons for its intermittence have remained little or not at all convincing. The origin of the M'Chaki spring waters and the reservoirs that feed it continues to be unknown. We are faced with hydrogeological problem: the intermittence of a brackish water spring in mountainous karst area where the average rainfall clearly exceeds 1400 mm annually. The M'Chaki spring's operation is well explained in this work by the diagram which was proposed by A. Mangin to Fontestorbes spring and that we have modified and applied for our spring. Using the different phases of observation and monitoring of M'Chaki spring's behavior during an intermittent period, the average discharge rate and the variation of the Air/water rate were calculated. We, therefore, hope to be able to demystify the enigma of M'Chaki spring's functioning.

Keywords

M'Chaki spring • Karst • Intermittent • Hydrogeology • North-East Algeria • Jijel

1 Geographical Location of the M'Chaki

The spring is located in the middle of the mountains, about thirty kilometers south-west of Jijel, in Beni Foughal at a place called El Aioune in the municipality of Selma Benziada (Fig. 1). M'Chaki spring continues to awaken the desire and curiosity of people to understand the mysteries surrounding its operation and the reasons for its intermittence (El-Bekri, 1040–1094).

With its waters flowing all year round to be discharged into the course of the Wadi Djendjen, M'Chaki spring coordinates are:

Longitude 36°36′18.95″N–Latitude 5°39′37.27″E.

2 Geology of the M'Chaki Spring Sight

The cross section shown in Fig. 2 allows locating and placing M'Chaki spring in its natural geological context (Leikine, 1971).

3 Hydrogeology

Before explaining the intermittence mechanism of the M'Chaki spring, it is important to note that it is, as Ehrman (1926) so well described, "both perennial and intermittent". Indeed, at the main outlet of the spring, at the lowest level, toward the coast 549.5 m, four (4) points located approximately at the same height, flow continuously and thus discharge their water throughout the year. Taken together, these water points form what we will call the perennial spring

T. Mustapha (✉) · B. Riad
Geological Engineering Laboratory (LGG),
University of Jijel, Jijel, Algeria
e-mail: mustapha.tekkouk@univ-jijel.dz

A. Kallel et al. (eds.), *Selected Studies in Environmental Geosciences and Hydrogeosciences*,
Advances in Science, Technology & Innovation, https://doi.org/10.1007/978-3-031-43803-5_45

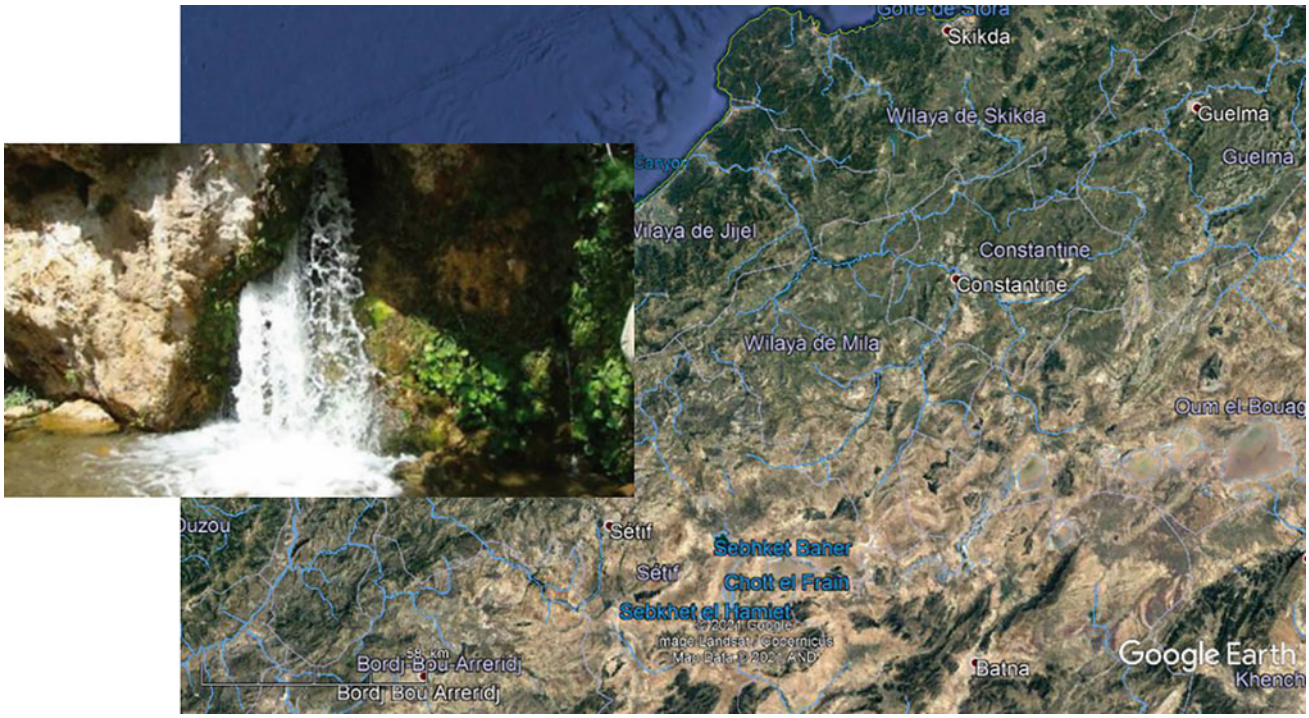

Fig. 1 Geographical location and photo of M'Chaki spring

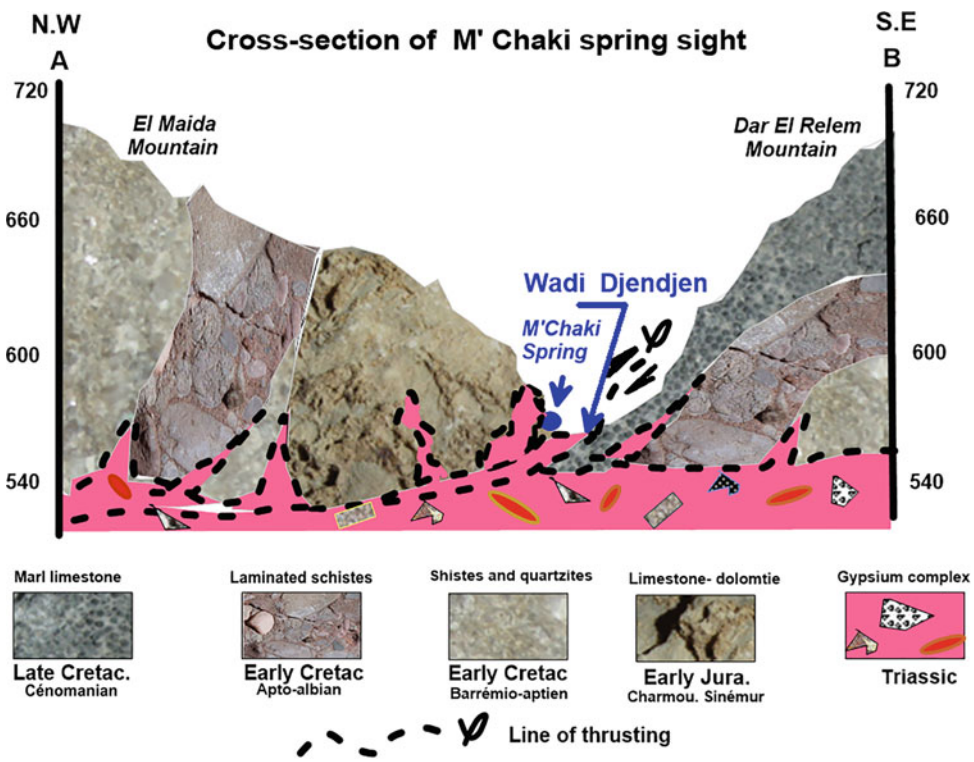

Fig. 2 Cross section of M'Chaki spring sight

"SP." Higher, at the approximate coast level 550 m from the main outlet, and over a length of two (2) meters, the intermittent spring—theme of our paper—continues to amaze visitors with its mysterious behavior.

3.1 Hydrogeological System of the M'Chaki Spring

Taking advantage of the intense karstification of the limestone mountains of the region, the reservoir (RSI) serving to supply the intermittent part of the M'Chaki spring is placed within the geological formations (Tekkouk, 2005) (Fig. 3a, b).

3.2 "Air–Water" Flow Mechanism and Monitoring During an Intermittency Period

The diagram proposed by Mangin (1973) to explain the operation of Fontestorbes spring that we modified and adapted to M'Chaki spring (Fig. 3b) perfectly explains the intermittence of this water source.

Varying from one intermittent period to another (Nicod, 2009), the rate and duration of discharge could not be definitively fixed because, even if the shape of the curves is the same for all the periods, each of these periods differs from the others by its own curve.

From our different phases of observations and monitoring of the behavior of the spring, we opted for the determination of the average discharge rate that we represent in Fig. 4a, b and which can be read in the following order:

1. Beginning of the period corresponding to point "A" (Fig. 4a) at time $t = 0$. At the start, only the air circulates at the outlet, there is no water, the spring is dry it is at "rest." The air, by its volume, occupies the entire extent of the outlet.
2. Initiation and acceleration corresponding to section "A-B" (Fig. 4a) lasting 4 min. When the first drops of water appear at the outlet (Fig. 4a), rumblings of air coming from inside the mountain begin to be heard; the space occupied by the air begins to decrease and is replaced by water which flow increases more and more at the outlet. The acceleration is marked by the mixing of the two volumes (air and water). It is characterized by a rapid increase in the discharge water flow and, by an equally rapid loss of air volume and its rumblings.
3. Level corresponding to points "B–C" (Fig. 4a) lasting 2mn 30s: The acceleration quickly reaches its peak, and the water flow is at its maximum. The air volume at the outlet is zero and so is the rumbling. The water in the main tank (RSI) reaches point B of the air duct, where it is flooded. The air duct is completely disconnected from the drain duct. Only the water appears at the outlet, and it is strongly drained during about 4 min as shown by the level of the blue curve given in Picture 5.
4. De-priming corresponding to points "C–D" (Fig. 4a) lasting 28 min: This step begins at the end of the plateau having marked the maximum flow rate of the source. The water flow starts to decrease at the outlet; the loss in

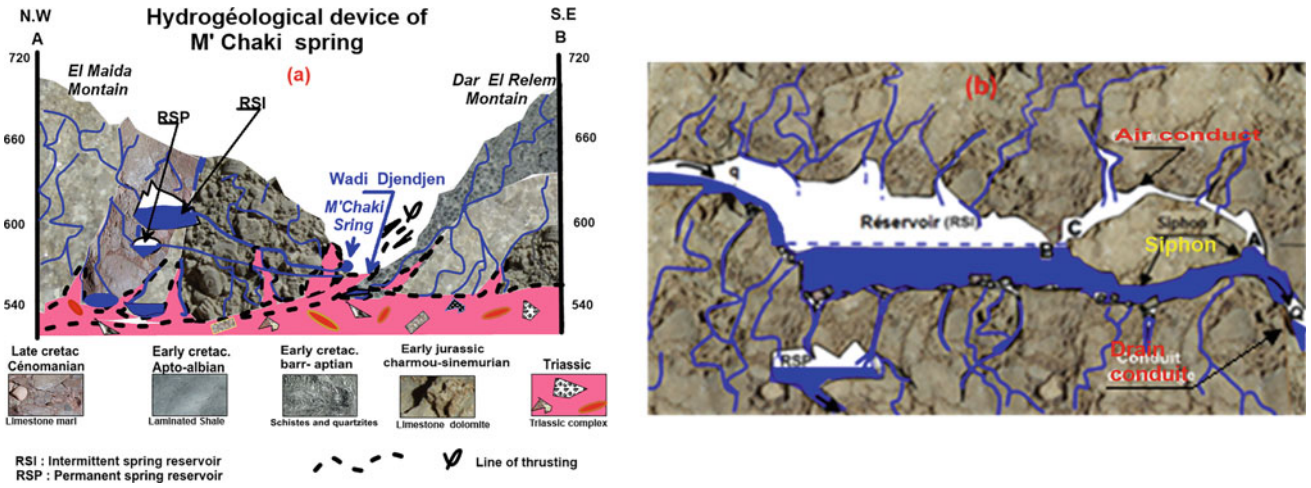

Fig. 3 **a** Hydrogeological device of M'Chaki spring. **b** Diagram of Mangin's intermittence mechanism modified and applied to M'Chaki spring. **With**: For Fig. 3a, b: RSI: supply tank for the intermittent spring and RSP: supply tank for the perennial spring. For Picture (b): q: supply flow, Q = drain flow, Gallery AB: drain pipe (siphon), Gallery AC: air intake pipe. **N.B**: The perennial spring (RSP) was intentionally ignored in this paper

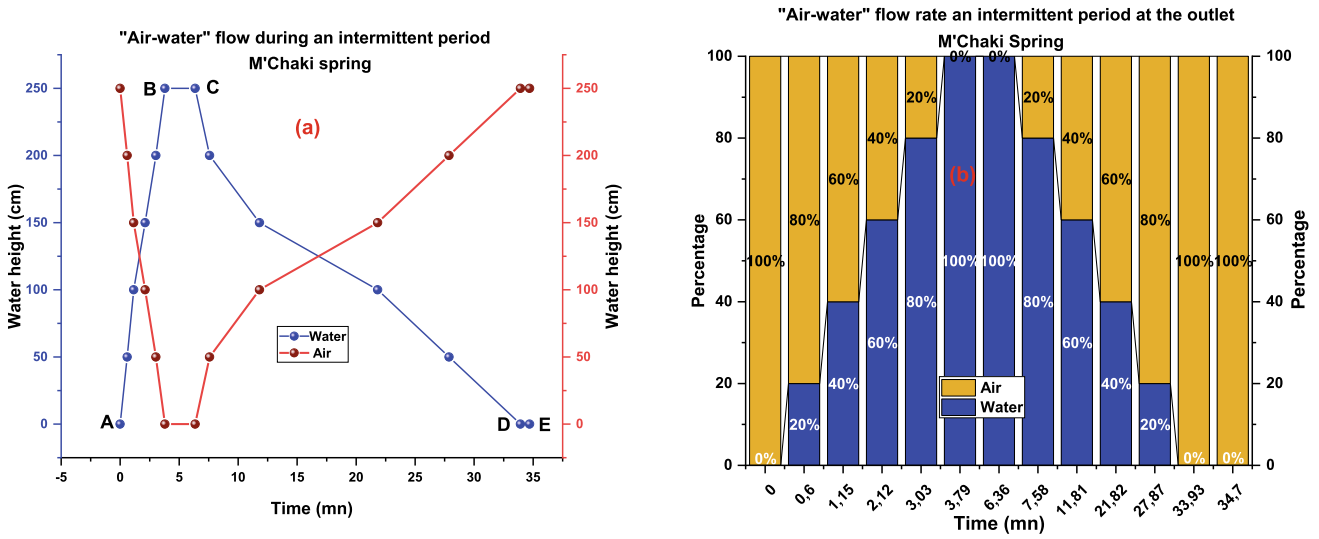

Fig. 4 **a** Variations in "Air–water" flow during an intermittency period at M'Chaki spring. **b** Percentage "Air–water" mixture delivered during an intermittency period at M'Chaki spring

water volume is immediately replaced by air; the pipe connected to the siphon is operational again.

5. Drying-up corresponding to points "DE" (Fig. 4a) extending until the start of the following intermittence: The water is no longer discharged; the outlet no longer receives water; only the air ""happy because no longer rumbling" occupies all the space; the dead time (rest) sets in and lasts until the start of the next intermittence.

Intermittency mechanism can simply be explained by the water level's variation of the reservoir between points B and C (Fig. 4b).

4 Conclusion

Finally, we hope to have demystified the M'Chaki spring once and for all. So far, all the attempts to explain the intermittent behavior of the spring and its functioning have, in our view, remained superficial. The Mangin's device offers the Fontestorbes spring, which we have slightly modified, and fits perfectly with M'Chaki spring. The role of the siphon, the time, and the different stages of an average intermittent cycle are clearly illustrated by the evolution curves and the rate of the "air–water" flow. M'Chaki can also be considered according to Meinzer as belonging to the family of intermittent sustainable springs.

References

El-Bekri, A-O. (1040–1094): Description de l'Afrique Septentrionale. Traduit par Mac Guckin de Slane (1965) Imprimerie Imperiale.

Ehrman, F. (1926). Carte géologique de Ziama au 1/50.000.

Nicod, J. (2009). Acta carsologica 37/1 2008. In: Karstologia: revue de karstologie et de spéléologie physique, n°54, 2e semestre 2009. La grotte de Kanaan (Liban) et Géomorphosites karstiques. p. 61.

Leikine, M. (1971). Géologie des Babors occidentaux. Thèse de Doctorat. Faculté des Sciences, Université de Paris, France, 550 p.

Mangin A. (1973). Sur les transferts d'eau au niveau du karst noyé à partir de travaux sur la source de Fontestorbes. Ann. *Spéléologie, 28*(1):21–40.

Tekkouk, M. (2005). Étude de la pollution par les sulfates des eaux du bassin versant de l'Oued Djendjen, Jijel-Algérie – Mémoire de Magister en Hydrogéologie (260 p). Université des frères Mentouri-Constantine, Algérie.

Diagnosis of Shallow Aquifer Dynamics and Problem of Groundwater Rising in Ouargla City (Algeria)

Fadila Hafsi, Samia Hadj-Said, and Aziez Zeddouri

Abstract

Algerian desert contains a very important groundwater reserve. However, the mismanagement and the quality of these waters, which are often too mineralized and salty, present the source of major problems in certain regions of the Sahara, including phenomenon of water table rise. One of the areas that suffer from this problem is Ouargla city. This rising groundwater level in shallow aquifers is mainly due to the overexploitation of deep aquifers for irrigation and drinking purposes. Irrigation and (waste)-water return flow into shallow aquifers. Natural constraints, such as the almost flat topography (4 per 1000) and the absence of an effective natural outlet disadvantage the natural drainage of the aquifer and thus contribute to accentuate this problem. To fight this rise of shallow groundwater, many studies and projects have been carried out, and a major project was launched by the Algerian government since 2009 followed by recent operations. The present work aims to study and monitor the evolution of the level of the water table by analyzing various piezometric maps established in Ouargla region since 1968 in order to determine the groundwater dynamic conditions. This analysis, coupled with previous studies' results, makes it possible to have a diagnosis of the phenomenon to propose a solution in terms of improving the drainage system on one side and the management of the groundwater resource on the other. The main purpose is to contribute to solving this problem which caused a serious environmental and economic impact, and which threatens public health in the region. The results of the study concerning the spatio-temporal evolution of the groundwater level and its salinity carried out in terms of profiles show an increase in the level of the water table in 2018 compared to 2003. The depth of the water table drops from 2.56 m in 2003 to 1.300 m in 2018 at the profile located in the North-East of the city. Electrical conductivity measurements show a decrease in groundwater mineralization for most profiles between the two periods. The EC values dropped from 230,000 µS/cm in 2003 to 151,700 µS/cm in 2018.

Keywords

Groundwater table rise problem • Shallow aquifer • Piezometric level • Arid zone • Mineralization

1 Introduction

Water resources face the risk of converging natural and anthropogenic factors that affect their quality. In this context, salinization is one of the main causes of the degradation of groundwater quality. This salinization is increasingly accentuated in arid and semi-arid regions where freshwater resources are limited (Mondal & Singh, 2011).

The groundwater rising phenomena has been studied throughout the world. At Aswan in Egypt, an increase in the level of a dozen meters was observed between 1971 and 2014, which led to deterioration in infrastructure and deterioration of the water quality (Sayed et al., 2014). At Nouakchott in Mauritania, the growth of population and the lack of a sanitation network were the cause of a 2 m-rise in the water table for 40 years (Ahmed-Salem et al., 2017).

Groundwater is the main water resource in the Algerian Sahara, the subsoil contains significant reserves but is mostly salty and has a poor quality. The northern Sahara Aquifer System (SASS) occupies an area of more than one million km^2 in the western part of North Africa, including about 700,000 km^2 in Algeria. The system has two deep aquifers:

F. Hafsi (✉) · S. Hadj-Said · A. Zeddouri
Laboratory of Underground Reservoirs: Petroleum, Gaz and Aquifers, Université Kasdi Merbah-Ouargla, Ouargla, Algeria
e-mail: hdila22@yahoo.fr

A. Kallel et al. (eds.), *Selected Studies in Environmental Geosciences and Hydrogeosciences*, Advances in Science, Technology & Innovation, https://doi.org/10.1007/978-3-031-43803-5_46

The Continental Intercalaire (CI) at the base and the Complex Terminal (CT) and topped by the shallow aquifer. This aquifer system (CI and CT) contains significant reserves estimated at 30,000 × 10^9 m^3 (Ould Baba, 2005). The overexploitation of the SASS for irrigation has caused a significant drawdown of the two deep aquifers which led to the decrease in artesian. On the surface, the flat topography favors the stagnation of this irrigation water and accentuates the rise in the water table level.

The soils of the Ouargla region are affected by salts. This salinity is due to multiple factors among them: the climate aridity, the importance of evapotranspiration, and the rise of the water table, which requires good irrigation management and improvement of the drainage system. In order to achieve this objective, the present work aims to realize a diagnosis of the dynamic and hydrochemical state of the water table by studying the spatio-temporal evolution of its level and its mineralization.

2 Presentation of the Study Area

Ouargla region is located in the North-East of the great Algerian Sahara, precisely, 850 km South of the capital Algiers (Fig. 1). It occupies an area of 361,980 km^2 with an estimated population of about 633,967 inhabitants in 2016. The city of Ouargla is located in a depression limited by Sebkhet Safioune to the North, the ergs of Touil and Arifdji to the East, the dunes of Sedrata to the South, and the eastern slope of the M'Zab ridge to the West.

2.1 Geological and Hydrogeological Characteristics of the Region

Concerning the Geology, only the Mio-Pliocene formations crop out, they are covered by quaternary deposits of small thickness in the form of ergs and dunes. Ouargla depression is dug in the continental formations of the Mio-Pliocene. These are composed of red sands and soft sandstones with intersecting stratification accompanied with limestone nodules interspersed with limestone or gypsum levels which outcrop on the East and West edges of the basin.

The studied region contains a deep hydrogeological system surmounted by a shallow aquifer. The northern Sahara Aquifer System "SASS" (EREES, 1972; OSS, 2015) extends over a vast area whose boundaries are located in Algeria, Tunisia, and Libya. This basin contains a series of aquifers which have been grouped into two reservoirs called the Continental Intercalaire (CI) and the Complexe Terminal (CT).

In the Ouargla region, the (CI) aquifer is located more than 1000 m deep. It is contained in detrital layers which are deposited in the lower Mesozoic, between two marine cycles. The Terminal Complex (CT) brings together several aquifers that are located in different geological formations as these layers are part of the same hydraulic unit.

The shallow aquifer is contained in the permeable sand-gypsum formations of the Quaternary. It is based on a waterproof impermeable substrate with more than 20 m thickness, which prevents any communication between the upper aquifer and the underlying Mio-Pliocene aquifer

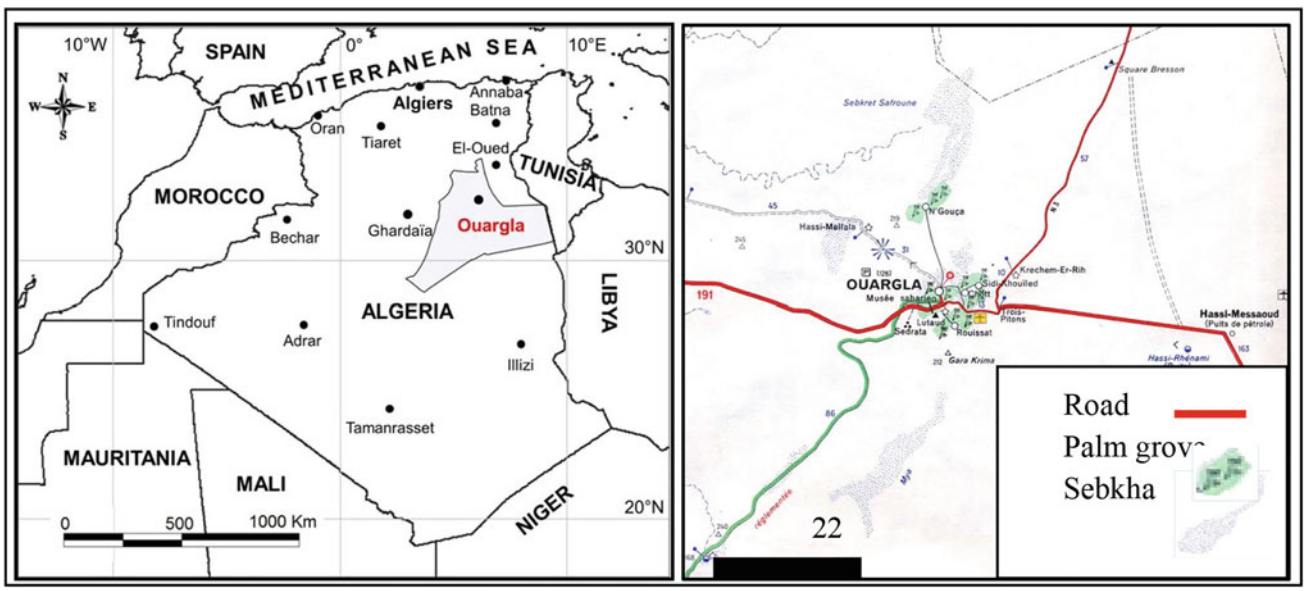

Fig. 1 Location map of study area

(Bonnard et Gardel, 2004). This groundwater is mainly supplied by irrigation and urban water.

3 Materials and Methods

Collection and Processing of Piezometric Data

To highlight the variation in the piezometric level of the water table, old piezometric data were collected from the ANRH (National Agency for Hydraulic Resources) of Ouargla and from reports of old works carried out in the region. Database may include campaigns for measuring piezometric levels since 1968 until 2018. These data were used to establish piezometric maps using the software SURFER. Further, a map of water table fluctuation between the years 2012 and 2015, as well as a follow-up of the inter-annual evolution of piezometric level, was carried out. In addition, the evolution of level and salinity of the water table were monitored between 2003 and 2018 following five profiles.

4 Results and Discussions

4.1 Water Balance of the Shallow Aquifer

The studied region is characterized by an arid climate which is marked by the scarcity and irregularity of precipitation that does not exceed 50 mm/year, very high temperatures with an annual average of 24 °C, and an evaporation rate of around 3000 mm/year. The components of the water balance in the region are mainly, for inputs, the infiltration of water of anthropogenic origin: irrigation water and leaks in the drinking water supply and sanitation networks. It is evaporation which represents the major factor of outputs in the region and which occurs from free water surfaces and wetlands, from the drainage system and through the exit to the northern outlet at Sebkhet Safioune.

4.2 State of the Water Table Dynamics

The observation of the piezometric map of 2012 (Fig. 2) shows a general flow from South to North toward Sebkhet Safioune which is located 40 km from the city with a hydraulic gradient of 10^{-3}. Moreover, we note that the highest point is of 138.01 m, which was measured with the P413 piezometer, located to the South of the city of Ouargla. Whereas, the lowest level of 101.58 m was measured with the P23 piezometer located to the North-East at Sebkhet Safioune. According to the piezometric map of the 2015 campaign, we notice that the piezometric level goes from 139.95 m in the South of the city to 103.23 m at P23, following the slope of the valley. The hydraulic gradient of the water table towards Sebkhat Sefioune is about 9.2 10^{-4}.

A water table fluctuation map was established for the period 2012–2015. Generally, there is a rise in the level of the water table which reaches a maximum of 1.72 m at P23. In addition, a rise in the level of 1.9 m is observed in the North-East of the city which is linked to irrigation.

For the study of the inter-annual piezometric evolution, three piezometers, namely P6, P7, and P12, were used. The piezometers show the same trend. An increase in the level is observed in 2003 which reached 116.23 m at P12 then a decrease to 112.5 m in 2009 at P6. An increase was observed in 2012 and continued until 2015 to reach a maximum of around 116 m at P12.

4.3 Evolution of Groundwater Salinity

Shallow groundwater is highly mineralized. Results of chemical analyses of samples taken in March 2018 showed that sodium was the most dominant cation with grades ranging from 2000 mg/l to 39,000 mg/l. Chloride is the most dominant anion with contents varying from 4500 mg/l to 60,000 mg/l, and sulfate concentrations vary between 2700 mg/l to 19,000 mg/l. The chemical facies of the groundwater is sodium-chloride or sodium-sulfate for most of the samples.

The spatio-temporal evolution of the water table level and salinity of groundwater according to three profiles show an increase in 2018 compared to 2003 except for the one profile where we have noticed a decrease in the time as well as in space from the palm grove to the drain. As for the salinity of the water table, the values of the electrical conductivity reveal a drop for most of the profiles between the two periods. The maximum measured value at the first profile was 200,000 in 2013 which decreased to 148,000 µS/cm in 2018, from 230,000 to 151,700 µS/cm for the second profile, and from 193,000 to 161,300 µS/cm for the third profile.

5 Conclusion

The shallow aquifer is contained in the dune sands and alluvium of the old Oued (Oued Mya). It is, on average, of 2 m deep from the ground. The water table forms a dome under the city of Ouargla and its flow is from South to North toward Sebkhet Safioune. The piezometric measurements of the water table show that it reached 138.01 m in 2012 and 139.95 m in 2015, which indicates a rise in the water table. The study of the inter-annual piezometric evolution reveals a decrease in the level in 2009; then, an increase was observed in 2012 and in 2015. Concerning water mineralization, the values of the electrical conductivity increased for most of the

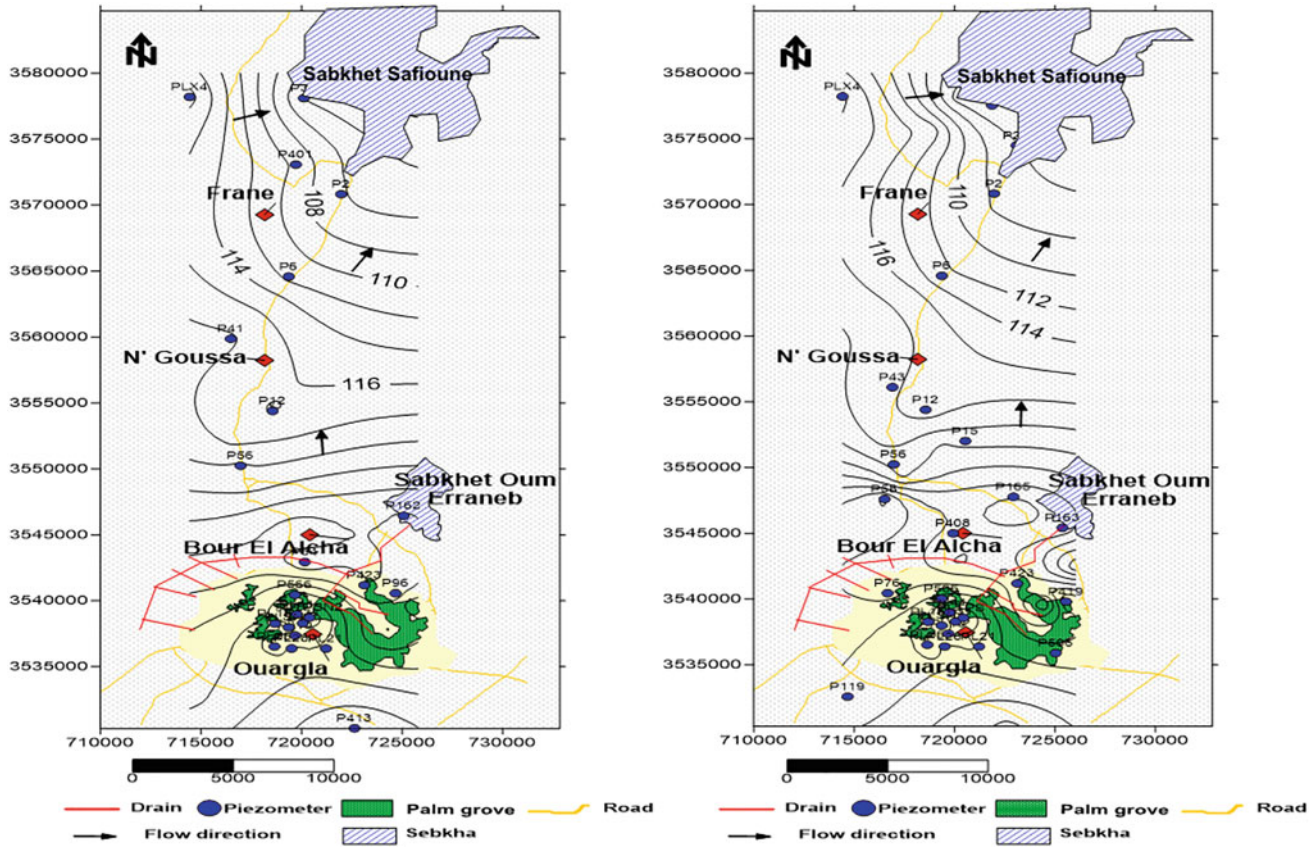

Fig. 2 Piezometric map of the Ouargla water table 2012 and 2015

profiles from 2003 to 2018. To fight against this water rising problem, the drainage network must be renewed, more efficient irrigation systems must be implemented, and re-use of treated water for irrigation in order to preserve deep aquifers should be applied.

References

Ahmed-Salem, M., Christian, L., Christelle, M., Oumar, W., & Sidi Cheikhe, M. A. (2017). Impacts of climate change and anthropization on groundwater resources in the Nouakchott urban area (coastal Mauritania).

Bonnard et Gardel. (2004). Etudes d'assainissement des eaux résiduaires, pluviales et d'irrigation. Mesures complémentaires de lutte contre la remontée de la nappe phréatique. Mission II: rapport final investigations, essais de pompage et bilans d'eau, établissement des cartes piézométriques, diagnostic des captages d'eau et mesures de réhabilitation, de protection des ressources en eau, Ouargla.

EREES. (1972). Etude de ressources en eau dans le Sahara Septentrional, UNESCO rapport final, Paris.

Mondal, N. C., & Singh, V. P. (2011). Hydrochemical analysis of salinization for a tannery belt in Southern India. *Journal of Hydrology, 405*(2–3), 235–247.

OSS. (2015). Pour une meilleure valorisation de l'eau d'irrigation dans le bassin du SASS Diagnostic et recommandations, ISBN: 978-9973-856-84-5.

Ould Baba, S. Y. M. (2005). Recharge et paléorecharge du système aquifère du Sahara septentrional. Thèse de Doctorat en Géologie, Université de Tunis El Manar, Tunisie.

Sayed, A., Selim, A., & Hamdan, M. (2014). Groundwater rising as environmental problem, causes and solutions: case study from Aswan City, Upper Egypt.

Conceptual and Numerical Hydrogeological Modeling of the Shallow Aquifer of Sidi Bouzid: Discussion of the Different Hypothesis

Asma Gharbi, Zouhaira IbnAli, Mouna Abidi, Amal Kammoun, and Moncef Zairi

Abstract

The Sidi Bouzid region is one of the main centers of agricultural production in Tunisia, based on groundwater. Therefore, a numerical regional hydrogeological model of the shallow aquifer of Sidi Bouzid was developed to estimate the regional impact of current and future groundwater use. A numerical flow model using a finite difference method and the Processing Modflow code version 5.3 was built for the steady state in the year 1989 and the transient conditions for the period 1989–2015. The developed numerical model was used to estimate the regional impact of current and future groundwater use. The addressed aspects, based on many hypotheses, consisted of natural recharge estimation, quantification of water budget, as well as the assessment of the impacts of overexploitation on the decrease of groundwater levels. A sensitivity analysis was also conducted in order to identify the most sensitive parameters in determining the aquifer behavior. The model parameters calibration was performed under steady-state flow conditions, and the simulations of groundwater flow were then performed under the stress conditions for the period 1989–2015. The simulations' results showed a high decline of the piezometric levels from 1989 to 2015 that can be related to the weak and irregularity of precipitation in the study region as well as the groundwater overexploitation. This work has shown that the study area is now in a situation of water stress. It suffers from overexploitation conditions throughout the whole study area. Consequently, the Sidi Bouzid aquifer requires urgent action through good management, which consists of implementing a priority control plan for the pumping system. In the meantime, measures must be taken to reach an integrated management plan for the Sidi Bouzid aquifer.

Keywords

Shallow aquifer • Conceptual model • Groundwater modeling • Management

1 Introduction

In Central Tunisia, the groundwater abstractions have been recently increasing due to the rapid increase in the number of private wells for irrigation and drinking purposes. Excessive pumping of groundwater from these wells is causing a gradual decline in water table as well as the groundwater quality (Lachaal et al., 2013). Hence, the most serious groundwater challenge facing the country presently is not only the development of groundwater, but also the sustainable management. The main objectives of this work are to develop the regional groundwater flow and give quantitative estimates of the hydrodynamic parameters to help improving the understanding of the present hydrogeological conditions of the Sidi Bouzid shallow aquifer by means of numerical simulation.

2 Materials and Methods

2.1 Settings

Located in the western part of central Tunisia, the study area is characterized by an arid climate, marked by irregularity in time and space, with an average precipitation estimated at 220 mm/year. The average annual temperature is 19 °C and the mean annual potential evapotranspiration is estimated to be 2370 mm/year (CRDA-Sidi Bouzid, 2014).

A. Gharbi (✉) · Z. IbnAli · M. Abidi · A. Kammoun · M. Zairi
Laboratory 3E, Sfax National School of Engineers,
Univ. of Sfax, PB 1173, 3038 Sfax, Tunisia
e-mail: asma.gharbi1185@gmail.com

A. Gharbi
Higher School of Technological Studies of Sidi Bouzid,
PB 377, 9100 Sidi Bouzid, Tunisia

A. Kallel et al. (eds.), *Selected Studies in Environmental Geosciences and Hydrogeosciences*,
Advances in Science, Technology & Innovation, https://doi.org/10.1007/978-3-031-43803-5_47

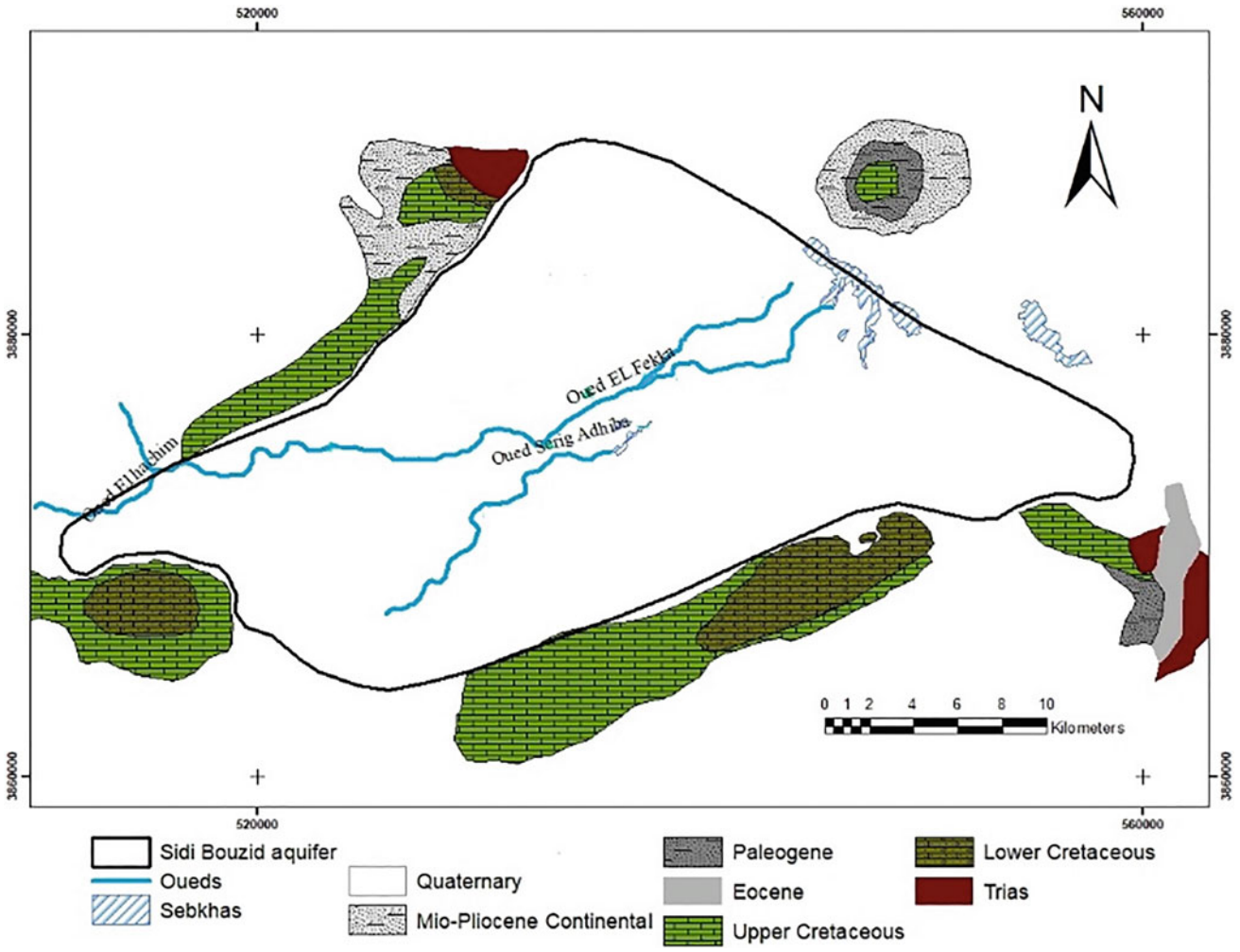

Fig. 1 Location map showing surface outcrops and streams

Sidi Bouzid aquifer is considered as lenticular and multilayered system (Yangui et al., 2011; Khazri and Gabtni, 2018). The aquifer shallow levels reach 100 m in depth. The permeability of the aquifer ranges between 10–4 and 10–8 m/s. The water table of Sidi Bouzid aquifer is influenced by infiltration of Oued El Fekka stream water with an annual average flow of 36.3 $\times$ 10^6 m^3 (Smida, 2008; Yangui et al., 2011; Amouri, 1994; Simonot, 1995; Aydi, et al., 2013). Figure 1 shows that groundwater flows from the South-West down to the North-East converging toward Oued El Fekkastream.

2.2 Conceptual Model

The objective of a conceptual model is to synthesize the information retrieved from the analysis of hydrogeological data. This type of summary of results and observations is a crucial step before building a numerical model. A numerical model built according to a conceptual model will be conditioned by the quantity and nature of the assumptions that have been made for the development of the conceptual model.

The latter identifies the inputs and outputs of water, as well as the limits of the aquifer which are then transposed in terms of boundary conditions and the distribution of hydraulic parameters in a numerical model. The main geometric, structural, and hydrogeological characteristics of the Sidi Bouzid aquifer were determined on the basis of previous studies (Amouri, 1994; Bédir et al., 1996; Simonot, 1995; Smida, 2008; Khazri et al., 2018).

The reservoir model domain was mainly chosen to cover the detrital filling of the Mio-Plio-Quaternary of Sidi Bouzid in central Tunisia. Otherwise, adequate boundary conditions will be used within the boundary of the study area to demonstrate the connection between this compartment and other areas of the study region.

Starting with a regional-scale conceptual study, the complete stratigraphic stack of the study area was coupled with numerical modeling of flows on a finite difference mesh surface using Processing Modflow software.

3 Results and Discussions

3.1 Numerical Flow Model Calibration

The steady-state calibration was carried out for the year 1989, because of the low rate of exploitation and the fluctuations of the water table during this period are generally constant. For the transient state, the boundary conditions were based on the annual average values of rainfall, extraction rates, and water table fluctuations. Average groundwater measurements were used for 5 observation wells.

The approach taken in the numerical model calibration is a trial and error approach. It was performed until the simulated and measured piezometric levels approached.

In order to assess the impact of concentrated recharge on calibrated hydraulic conductivities, three models will be tested with concentrated recharge rates of 15, 20, and 30%.

The diffuse recharge of about 4% of precipitation seems to correspond best to the simulation of the water table of Sidi Bouzid in each sub-model. Flux and well boundary conditions were assigned on finite difference nodes.

The optimized distribution of the hydraulic conductivity of the study area was obtained after setting the model for a recharge rate of 30% for concentrated recharge. It is recalled that this distribution will be used in the simulations in transient regime.

Figure 2 presents the measured and simulated values of the hydraulic head with the relative piezometric map. This model partially reproduces the general trend of observed hydraulic loads.

A 26-year time series exists in the project area to allow calibration of transient states.

The calibration of the storage coefficient in transient regime was carried out for an equivalent homogeneous storage coefficient for the whole of the aquifer.

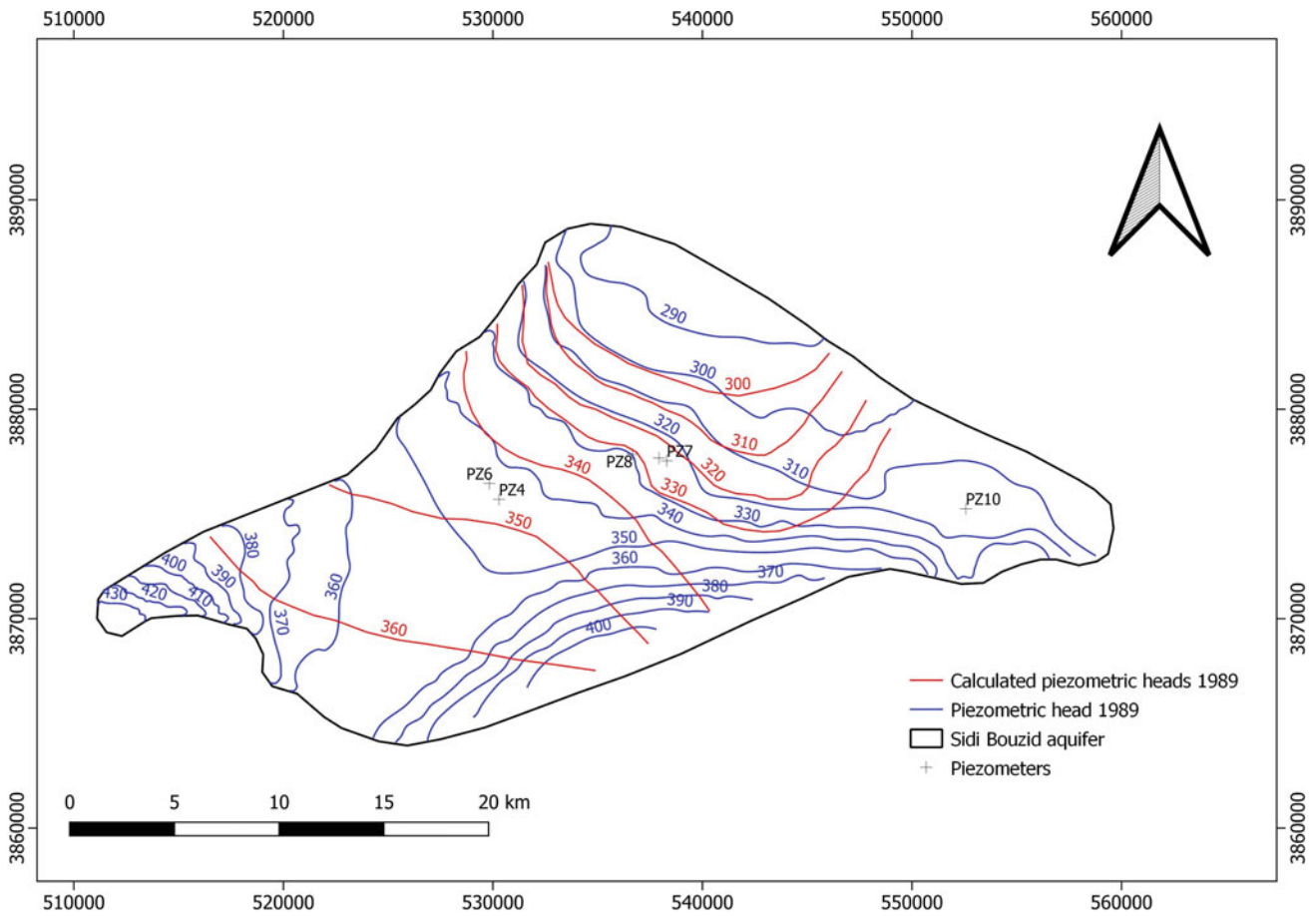

Fig. 2 Calibrated piezometric map at steady state for the year 1989

The transient model was satisfactorily calibrated on the basis of relative affinity between the calculated and observed hydraulic heads from 1989 to 2015.

3.2 Numerical Simulation Scenarios

In order to assess the evolution of groundwater in the water table of Sidi Bouzid, the numerical flow model developed is used to simulate several scenarios for a period of 35 years until 2050. The starting point of the simulations of the different scenarios was the end of the model adjustment to the transient regime, corresponding to the distribution of hydraulic loads for the year 2015.

The first scenario tested the future evolution of the piezometry without any change in the extraction rates and groundwater recharge. The results indicate that if the current groundwater exploitation and recharge conditions continue, the water table will decrease by 2050 with an average drawdown of 25 m. In this scenario, we assume that the 2015 exploitation is increased by 50%; all the boundary conditions of the reference model remain the same. The drawdown in piezometric levels presented in Fig. 3 showed that there is an important decrease in the Sidi Bouzid water table that ranges between 30 and 40 m.

4 Conclusions

The aim of this chapter is to reproduce a numerical model of the same general trend as the real system. The model quantitatively estimates the different components of groundwater dynamics and their interactions. This represents the first step toward a strategy for the management and conservation of the region's groundwater resources.

The numerical model was calibrated against the piezometric levels of the water table during the stationary and transient regimes. The groundwater flow model successfully simulates the overall dynamics of the aquifer such as recharge, exploitation, and their impacts on hydraulic loads. The results of the calibration of the model, whether at stationary or transient conditions, show a reasonable agreement between the measured piezometry and that calculated.

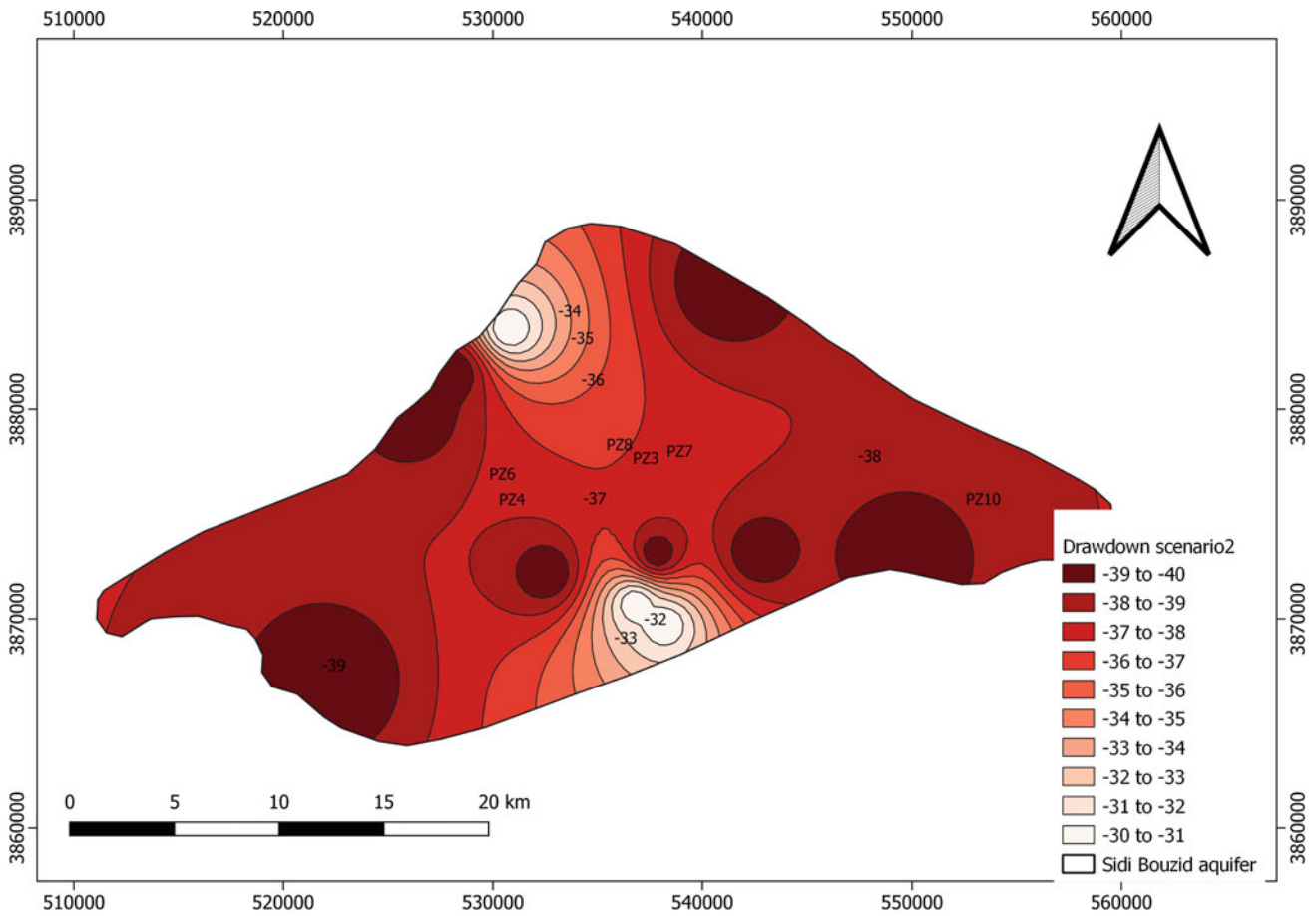

Fig. 3 Piezometric iso-variation map for the second scenario (2015–2050)

The development of this regional digital model made it possible to better understand the components of the water balance and the impacts of the exploitation of groundwater on its storage. It is considered to be a tool for evaluating better management options for a sustainable use of groundwater.

The results can provide basic information to water resources' managers, researchers, and planners for the establishment of local and regional management plans for the monitoring of piezometric levels on the one hand, and share for the economic development of the region on the other. Thus, corrective actions are necessary to improve the management of groundwater resources in the Sidi Bouzid region.

References

Amouri, M. (1994). Etude hydrogéologique du système aquifère de Sidi Bouzid. Rapport de Direction Générale des Ressources en Eau (DGRE).

Aydi, W., Saidi, S., Chalbaoui, M., Chaibi, S., & Ben Dhia, H. (2013). Evaluation of the groundwater vulnerability to pollution using an intrinsic and a specific method in a GIS environment: application to the plain of Sidi Bouzid (Central Tunisia). *Arabian Journal for Science and Engineering, 38*, 1815–1831. https://doi.org/10.1007/s13369-012-0417-9

Bédir, M., Tlig, S., Bobier, C., Zargouni, F., & Aïssaoui, N. (1996). Sequence stratigraphy, basin dynamics and petroleum geology of Miocene from the eastern Tunisia. *Am Assoc Pet Geol Bull, 80*(1), 63–81. In *9th International proceedings on proceedings* (pp. 1–2).

CRDA (Commissariat régional du développement agricole de Sidi Bouzid) (2014). Données pluviométriques gouvernorat de Sidi Bouzid (unpubl.).

Khazri, D., & Gabtni, H. (2018). Geophysical methods integration for deep aquifer reservoir characterization and modeling (Sidi Bouzid basin, central Tunisia). *Journal of African Earth Sciences, 138*, 289–308. https://doi.org/10.1016/j.jafrearsci.2017.11.024

Lachaal, F., Mlayah, A., Anane, M., Bédir, M., Tarhouni, J., & Leduc, C. (2013). Comprehension and hydrogeological conceptualization of aquifer in arid and semi-arid regions using integrated hydrogeological information system: Case of the deep aquifer of Zéramdine-Béni Hassen (east-central Tunisia). *Arabian Journal of Geosciences, 6*, 2655–2671. https://doi.org/10.1007/s12517-011-0498-x

Simonot, M. (1995). Plaine de Sidi Bouzid: Etude de l'impact de l'épandage des crues sur le recharge de la nappe phréatique. Rapport DGRE.

Smida, H. (2008). *Apports des Systèmes d'Informations Géographiques (SIG) pour une approche intégrée dans l'étude et la gestion des ressources en eau des systèmes aquifères de la région de Sidi Bouzid (Tunisie centrale)*. Thèse Troisième Cycle, Univ.

Yangui, H., Zouari, K., Trabelsi, R., & Rozanski, K. (2011). Recharge mode and mineralization of groundwater in a semi-arid region: Sidi Bouzid plain (central Tunisia). *Environmental Earth Sciences, 63*, 969–979. https://doi.org/10.1007/s12665-010-0771-4

Delineation of the Groundwater Potential Zones of Upper Tigris Diyarbakır Sub-basin in Turkey Using GIS and Analytical Hierarchical Process (AHP) Techniques

Recep Çelik

Abstract

With its water resources and agricultural activities, the Diyarbakir basin is considered as an important field not only in Turkey but also in the Middle East. Since the irrigation project has not been completed yet, there is a wide use of groundwater for irrigation. For this reason, the determination of groundwater potential should be evaluated properly. Instead of determining the Groundwater potential of the region with observation wells, which is an expensive method, this study opted for evaluating the groundwater potential of the basin by the GIS-based Multi-Criteria Decision Making (MCDM) method by means of essential factors affecting groundwater formation. For the delineation of the groundwater potential zones of Upper Tigris Basin, the AHP method and ArcGIS 10.2.1 program were used. 8 key criteria were properly taken into consideration; Geomorphology, Geology, Line Density, Drainage Density, Slope, Land use, Rainfall, and Soil Type. Weights of all criteria were assessed via the AHP technique. Finally, considering the weights of all the parameters through the Overlay Weighted Sum method, the Groundwater Potential Index (GWPI) was obtained. The potential was classified into five stages for the sub-basin as 1447 km^2 (13.8%) portion of the basin is very poor potential, 3758 km^2 (35.8%) portion of the basin is poor potential, 3267 km^2 (31.1%) portion of the basin is moderate potential, 1443 km^2 (13.7%) portion of the basin is good potential, 585 km^2 (5.6%) portion of the basin is very good potential.

Keywords

Groundwater potential • Multi-criteria decision making (MCDM) • GIS • AHP method • Diyarbakır basin

1 Introduction

The Upper Tigris's Diyarbakır sub-basin is known for its rich surface water potential. Since the irrigation projects of the GAP project have not been completed yet in the basin, agricultural activities along the riverbank are based on surface water and in other places, water is generated from the groundwater through wells Çelik (n.d.). Thus, it is necessary to figure out the quality and amount of potential in this region. The determination of all fields of groundwater potentials by wells is not always possible, neither is it economical. It is preferable to rely on another way for determining the possible parameters groundwater supplies depend on and their impacts. In this respect, the GIS and MCDM methods have been widely and successfully used throughout the World (Çelik, 2019; Feizizadeh et al., n.d.; Greene et al., 2011; Haghizadeh et al., 2017; Mukherjee & Singh, 2020).

This study aimed to determine the groundwater potential zones of the upper Tigris Basin through the appropriate use of the GIS-based MCDM method. There are eight key criteria that were properly taken into consideration: Geomorphology, Geology, Line Density, Drainage Density, Slope, Land use, Rainfall, and Soil Type. Weights of all criteria were assessed via the AHP technique. The ultimate results were compared with 61 wells previously recorded in the chosen field. According to this validation, the results were found to be positively consistent at 84%.

R. Çelik (✉)
Faculty of Civil Engineering Department, Dicle University Engineering, 20180 Diyarbakır, Turkey
e-mail: recep.celik@dicle.edu.tr

A. Kallel et al. (eds.), *Selected Studies in Environmental Geosciences and Hydrogeosciences*, Advances in Science, Technology & Innovation, https://doi.org/10.1007/978-3-031-43803-5_48

2 Materials and Methods

2.1 Study Area

Diyarbakır sub-basin is located between eastern longitudes at 40–44° and northern latitudes at 37–55°, around the Diyarbakır province. The northern part of this basin is surrounded by mountains. The Tigris River flows through this basin.

Materials

Eight parameters were taken into consideration: Geomorphology (GM), Land Use (LU), Geology (G), Line Density (LD), Drainage Density (DD), Slope (S), Rainfall (R), and Soil Type (ST). The weight of each parameter was assessed via the AHP technique. Table 1 describes how all these parameters were obtained.

2.2 Method

The AHP is a common method of the multi-criteria decision analysis. The method is based on three principles: decomposition, relative decision, and combining the preferences (Saaty, 2000). The AHP consists of four stages.

In the first stage: the objective, criteria, and alternatives of the problem are determined. The hierarchical structure is formed.

In the second stage: The comparison of the criteria and alternatives is made. The comparison shows which criterion is more significant. The comparisons are conducted according to the 1–9 scale determined by Saaty (1980).

In the third stage: The vector of the weights (W) is determined through the priority vectors and comparison matrices (Table 2). The normalization is determined via division of all a^{ij} matrix elements by the column total.

$$\text{Weight calculation; } Wi = \sum_{i=1}^{n} a^{ij} \Big/ \text{n} \qquad (1)$$

In the fourth stage: The calculation of consistency ratio and the CR coefficient are performed after the consistency index (CI). In the paired comparison of decision matrices, it is accepted as consistent if CR is lower than 10%. The coherence ratio of precedence matrix can be feasible with the aid of this technique.

Table 1 Data source and processing mode of each potential recharge parameter

Parameter	Data source	Processing mode
Slope (S)	Topographic maps (M44,M45,M46 layouts): 1/100,000), DEM	Digitalization/3D analyst ArcGIS
Lineament density, geology	Geological map from www.mta.gov.tr online maps	Analysis and classification/line calculation/validation
Geomorphology	DEM maps, topographic maps	Digitalization/3D analyst ArcGIS/classification
Land use (LU)	Landsat and imagery	Classification in ENVI
Soil type	(https://www.tarim.gov.tr)	Digitalization/classification in ArcGIS
Rainfall (R)	Turkish State Meteorological Service (https://mgm.gov.tr)	Interpolation/classification
Drainage density	DEM maps, topographic maps	Stream generation with arc hydro tools/density line calculation/validation

Table 2 AHP normalized matrix and significance weighting values of the used parameters

	S	LD	G	GM	LU	ST	R	DD	Weight
Slope (S)	0.17	0.16	0.16	0.16	0.16	0.16	0.16	0.16	0.16
Lineament dens (LD)	0.09	0.09	0.09	0.09	0.09	0.09	0.09	0.09	0.12
Geology (G)	0.13	0.12	0.12	0.12	0.12	0.12	0.12	0.12	0.11
Geomorphology (GM)	0.15	0.14	0.14	0.14	0.14	0.14	0.14	0.14	0.13
Land use (LU)	0.09	0.10	0.10	0.10	0.10	0.10	0.10	0.10	0.12
Soil type (ST)	0.13	0.12	0.12	0.12	0.12	0.12	0.12	0.12	0.11
Rainfall (R)	0.15	0.16	0.16	0.16	0.16	0.16	0.16	0.16	0.14
Drainage dens (DD)	0.08	0.12	0.12	0.12	0.12	0.12	0.12	0.12	0.13

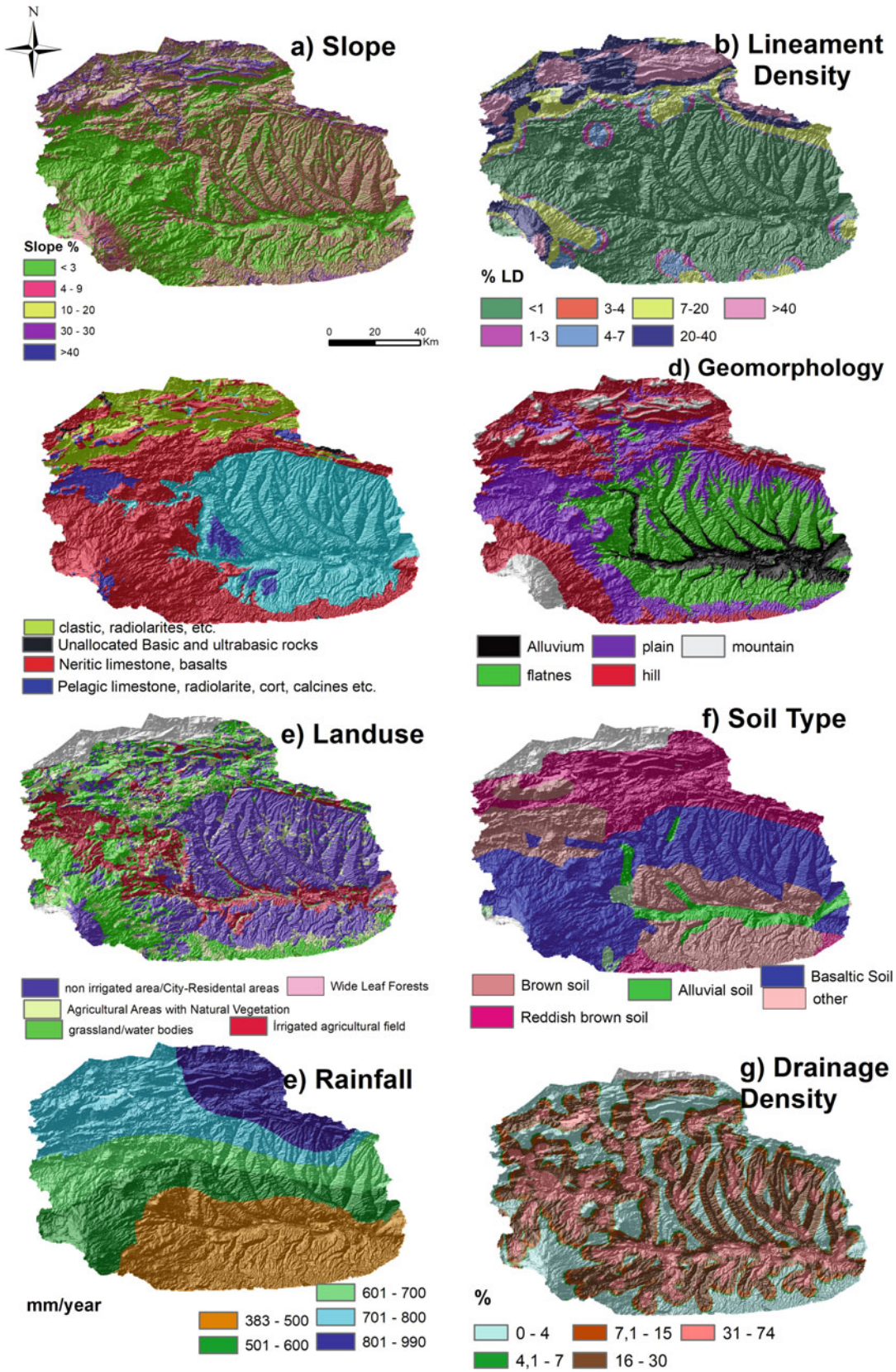

Fig. 1 Main criteria affecting the GWPI reclassified raster maps

3 Results

In order to determine the potential groundwater recharge zones in the study area, the main parameters are mapped in Fig. 1: Slope (SL), Lineament Density (LD), Geology (G), Geomorphology (GM), Land Use (LU), Soil Type, Rainfall®, and they are summarized and finally, Groundwater Potential Zones were mapped in Fig. 2.

3.1 Groundwater Potential Index (GWPI) and Groundwater Potential Zones

The GWPI represents a dimensionless magnitude, which proves the groundwater potential in a region. It is obtained through the weights of the various parameters. Therefore, it gives information about groundwater potential in various locations (Rahmati et al., 2015; Shekhar et al., 2015) (Fig. 2).

It is calculated according to the AHP method as indicated below;

$$\begin{aligned} GWPI = & Sr.Sw + LDr.LDw + Gr.Gw + GMr.GMw + LUr.LUw \\ & + STr.STw + Rr.Rw + DDr.DDw \end{aligned} \quad (2)$$

where; GWPI is the Groundwater Potential Index, S is the Slope, LD is the Lineament Density, G is Geology, GM is Geomorphology, LU represents the Land Use, ST is the Soil Type, R is the Rainfall, and DD is the Drainage Density. In addition, the subscripts "r" and "w" which refer to the rating and weight of the parameter, respectively.

The Groundwater Potential Zones (GWPZ) are obtained from the reclassification of GWPI index and revealed in Fig. 2.

4 Discussion

The groundwater potential map is a significant means that can be useful in basin-based hydrological studies and possible groundwater well diggings and operations in the future. This study is additionally a macro-level study performed over an expanded area. For micro planning, a more reliable assessment can be conducted with the help of similar criteria and lower-scale maps. Especially, the geological factors, slope, geomorphological factors, and the potential effects of the land use should be taken into consideration. On the other hand, aquifer region risk and pollution analyses due to agricultural and other anthropological activities should be carried out regularly and sustainable groundwater management should be properly provided.

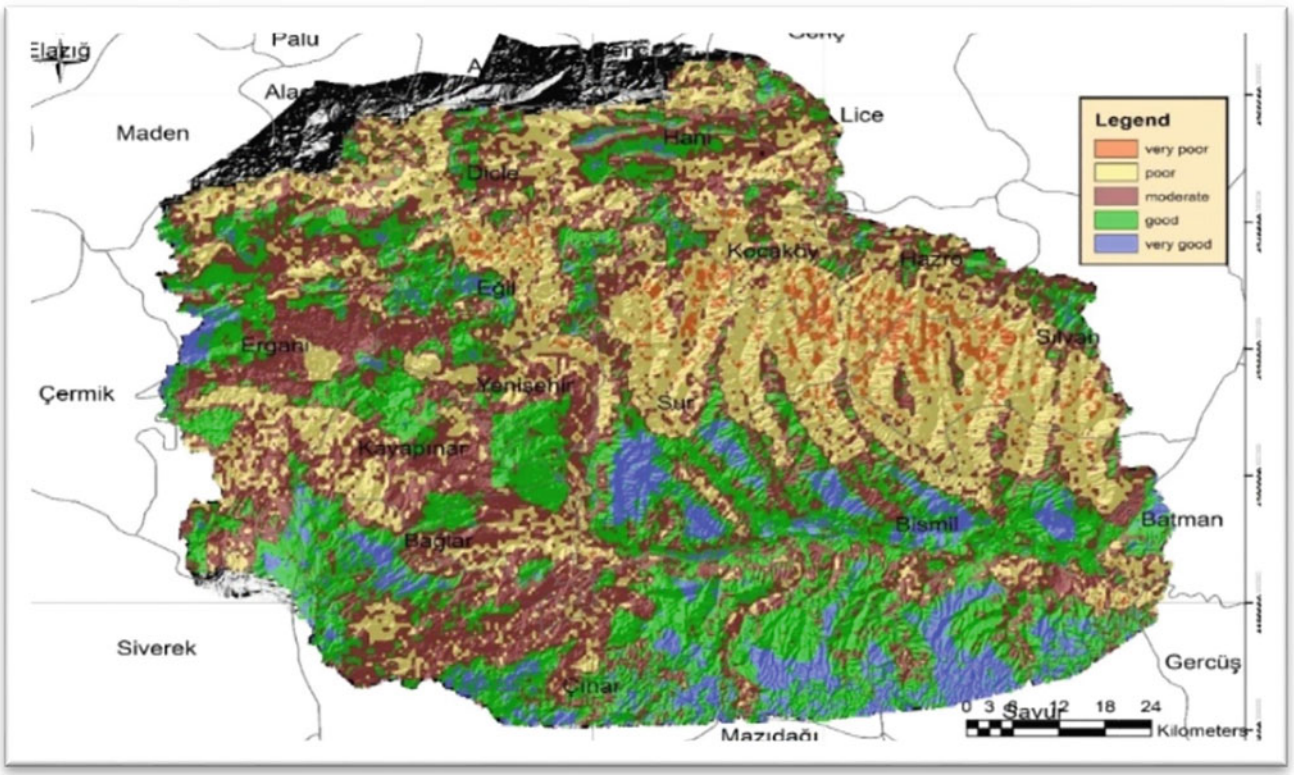

Fig. 2 Upper Tigris basin groundwater potential recharge map

5 Conclusion

The Analytical Hierarchical Process (AHP) integrated with Geospatial technology represents an immensely practical method in determining the groundwater potential of a region. The groundwater potential map was obtained with an accuracy of 84% in the North Tigris Basin relying on this method. As a result of the study, it was determined that 13.8% of the basin area has very poor potential, 35.8% has poor potential, 31.1% has moderate potential, 13.7% has good potential, and 5.6% of the basin area shows very good potential characteristics.

References

Çelik, R. (2019). Evaluation of groundwater potential by GIS-based multicriteria decision making as a spatial prediction tool: case study in the Tigris River Batman-Hasankeyf Sub-Basin, Turkey. *Water, 11*(12), 2630.

Çelik, R. (n.d.). Temporal changes in the groundwater level in the Upper Tigris Basin, Turkey, determined by a GIS technique. *Journal of African Earth Sciences*, *107*, 134–143.

Feizizadeh, B., Jankowski, P., & Blaschke, T. (n.d.). A GIS based spatially-explicit sensitivity and uncertainty analysis approach formula multi-criteria decision analysis. *Computers Geosciences*, *64*, 81–95.

Greene, R., Devillers, R., Luther, J. E., & Eddy, B. G. (2011). GIS-based multiple-criteria decision analysis. *Geography Compass, 5*(6), 412–432.

Haghizadeh, A., Moghaddam, D. D., & Pourghasemi, H. R. (2017). GIS-based bivariate statistical techniques for groundwater potential analysis (an example of Iran). *Journal of Earth System Science, 126* (8), 109.

Mukherjee, I., & Singh, U. K. (2020). Delineation of groundwater potential zones in a drought-prone semi-arid region of east India using GIS and analytical hierarchical process techniques. CATENA *194*, 104681.

Rahmati, O., Samani, A. N., Mahdavi, M., Pourghasemi, H. R., & Zeinivand, H. (2015). Groundwater potential mapping at Kurdistan region of Iran using analytic hierarchy process and GIS. *Arabian Journal of Geoscience, 8*(9), 7059–7707.

Saaty, T. L. (2000). *Fundamentals of decision making and priority theory*. RWS.

Saaty, T. L. (1980). *The analytic hierarchy process*. McGraw-Hill.

Shekhar, S., & Pandey, A. C.: Delineation of groundwater potential zone in hard rock terrain of India using remote sensing, geographical information system (GIS) and analytic hierarchy process (AHP) techniques. *Geocarto International*, *30*(4), 402–421

Geological, Geophysical and Geochemical Characterization of the Salinization of the Plio-Quaternary Coastal Aquifer in the Chiba Downstream Basin, Eastern Cap-Bon Tunisia

Farah Nefzaoui, Haifa Boussiga, Trabelsi Emna, Mohamed Fethi Ben Hamouda, and Jamila Tarhouni

Abstract

The present work seeks to characterize the water resources of the overexploited aquifer of Oued Chiba watershed, thus identifying the geochemical process controlling the mineralization. Physico-chemical analyses (T°C, pH, electrical conductivity and major elements) were carried out during two sampling campaigns. The piezometric study showed depressions at Tafelloune, Gsar Saad and Diar Hajjej, which were caused by the overexploitation of the aquifer. The results showed high values of total dissolved solids (TDS) and salinity, due to contamination by seawater intrusion; this is confirmed by negative values of piezometry and high concentration of chloride. The interpretation of the Piper diagram revealed that the water facies of the Chiba plain are chloride-sodium and mixed chloride and mixed sulphate. Subsequently, to understand the mechanisms governing the water quality of the region, we used the statistical tool especially the principal components analysis which showed that the two factors F1 (water mineralization) and F2 (anthropogenic activities) account for 65% of the total variance in groundwater quality.

Keywords

Cap-Bon • Geochemistry • Geophysics • Overexploitation • Salinization

1 Introduction

Groundwater resources in arid, semi-arid and coastal regions are weakly renewable and largely solicited to meet the needs of agriculture, industry, tourism and to a lesser extent drinking water supply.

In recent decades, these resources have been subjected to an increased exploitation such as the plio-quaternary aquifer on the eastern coast of the Cap-Bon peninsula.

The main objective of this work was to study the plio-quaternary aquifer of Oued Chiba. Being an agricultural area where the water table has a drawdown below zero sea level due to overexploitation. The excessive use has degraded the groundwater quality and increased the salinity level. Several methods have been developed to study the salinization of this aquifer, detect the intrusion of the salt level, delimit the contaminated area and get an idea about the spatial distribution of salinity.

In addition to the geochemistry classical methods, other techniques can be applied. Among these, we cite the geophysical method by electrical prospecting and the analysis of logs (Gamma Ray and resistivity).

2 Materials and Methods

Two geophysical approaches were used to delineate the aquifers and their water quality; they consist of 26 vertical electrical sounding points and the 12 well logs data.

Moreover, to assess the water chemical quality, two sampling campaigns were organized during which pH, T°C and electrical conductivity (EC) were measured in-situ using a multi-parameter testing portable kit. During the first sampling campaign (July 2018), 29 samples were collected involving 2 samples from surface waters of Oued Chiba and 27 from wells along the coastal zone.

Then, the water samples were analyzed in laboratory for major elements such as Ca^{2}, Mg^{2+}, Cl^{-} and HCO_3^{-} using

F. Nefzaoui (✉) · T. Emna · M. F. Ben Hamouda · J. Tarhouni
Carthage University, 2036 Tunis, Tunisia
e-mail: farah.nefzaoui@fst.utm.tn

H. Boussiga
Tunis El Manar University, 1068 Tunis, Tunisia

A. Kallel et al. (eds.), *Selected Studies in Environmental Geosciences and Hydrogeosciences*,
Advances in Science, Technology & Innovation, https://doi.org/10.1007/978-3-031-43803-5_49

titrimetric method, K^+ and Na^+ using the flame spectrometry and SO_4^{2-} using the spectrophotometer.

Furthermore, to study the contamination by the nitrates, three samples were collected from the surface waters of Oued Chiba, 42 from wells along Oued Chiba and 1 from Chiba dam in October 2018.

Finally, the PCA was carried out to understand the mechanisms governing the region's waters quality. The intermediate the correlation matrices, the coefficients of correlation between the variables and the two axes F1 and F2 and the projection of the variables in the space of the F1 and F2 axes were obtained using the XLSTAT software.

3 Results and Discussion

3.1 Geophysical Results

The plio-quaternary aquifer is mainly formed by two principal geological units (Ben Hamouda et al., 2009).

It consists of the sandy Pliocene and the Quaternary deposits (Failed, 1992). The second unit is formed by the lower and the middle Miocene. Well correlation showed that the study area is characterized by lithological heterogeneity on both sides of Oued Chiba (Fig. 1). In addition to its opening onto the Mediterranean, Oued Chiba plain is characterized by the dominance of permeable and porous rocks such as sandstones and sands, which make it more vulnerable to all forms of salinization, in particular marine intrusion.

The salinization of the plio-quaternary aquifer is due to an intrusion of a salty wedge, especially noted in Diar Hajjej

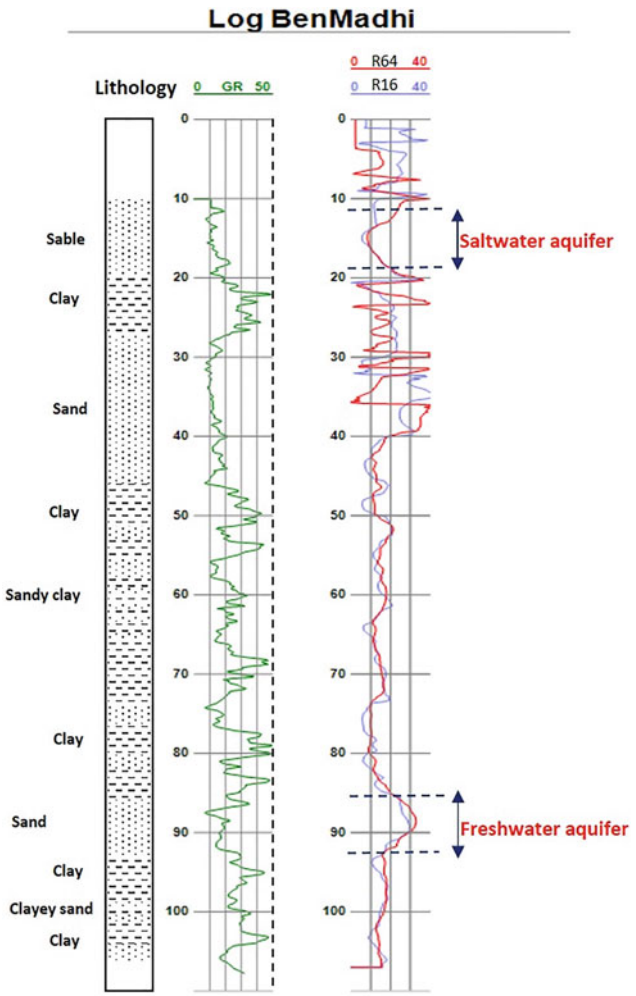

Fig. 2 Well log Ben Madhi

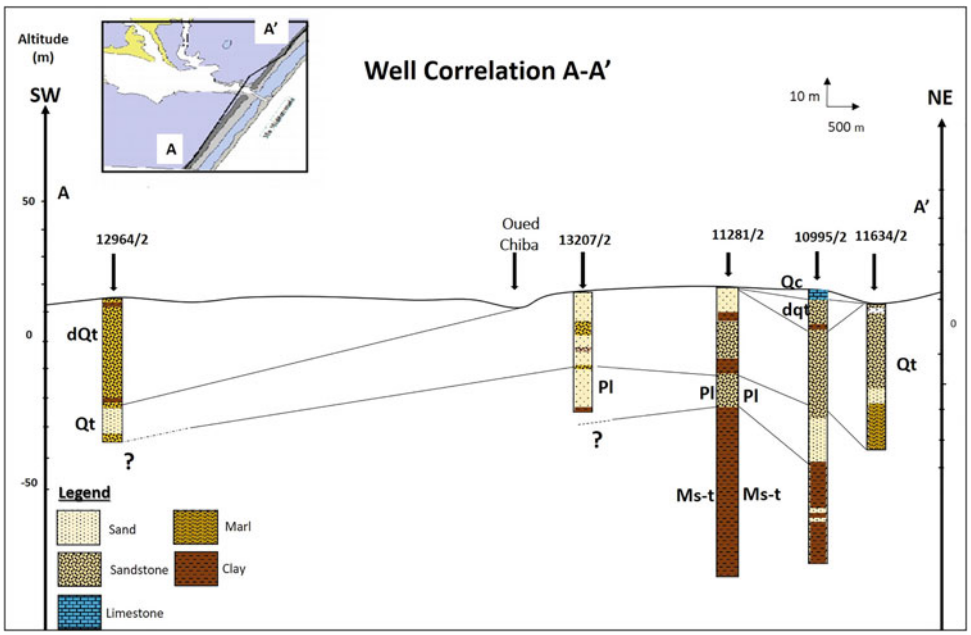

Fig. 1 Well correlation A-A' along Oued Chiba plain

region. In fact, in Ben Madhi log (Fig. 2), a first aquifer at 10 m depth shows low resistivity values, indicating sand with salty water. A second freshwater deep aquifer is underlain between 84 and 92 m.

VES 13 at Diar Hajjej (Fig. 3) reveals low values of resistivity in sand and sandstone (8773/2 well; Fig. 4), highlighting the presence of salty waters.

3.2 Geochemical Results

The Piper diagram (Fig. 5) shows that the majority of the groundwater is classified under a chloride-sodium and mixed chloride and mixed sulphate chemical facies.

The piezometric map (Fig. 6) shows a wide variation between 2 and 12 m below sea level. We noticed that the flows are directed towards the piezometric depressions. The decrease in piezometric levels along the coast indicates that the aquifer is strongly lowered by pumping due to overexploitation for agriculture needs, especially in the region of Taffeloune, Diar Hajjaj and Gsar Saad.

In addition, chloride and sodium are characterized by very high concentrations between 426–3400 mg/l and 140–1364 mg/l, respectively. The samples from Oued Chiba are characterized by concentrations of 10 mg/l for Cl and 5200–6200 mg/l for Na^+. The highest groundwater Cl^- and Na^+ values are recorded in areas with significant decrease in piezometry and low electrical resistivity values, e.g. Diar Hajjej, Garaat Sassi and Tafelloune regions. These high values are due to contamination by seawater (Kouzana et al., 2009) (Fig. 7).

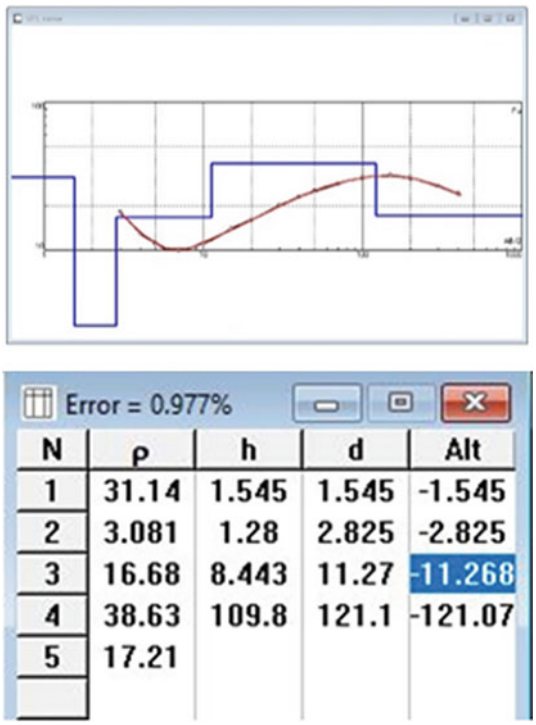

Fig. 3 Interpreted vertical electrical sounding 13 at Diar al Hajjaj locality

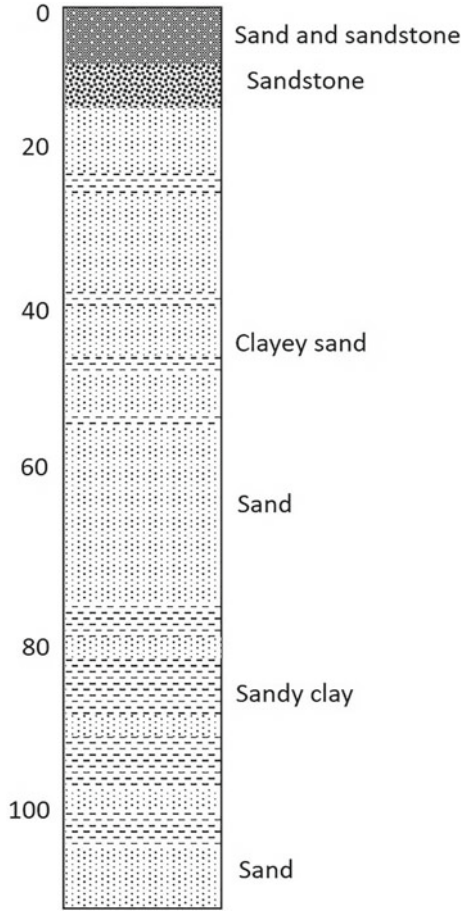

Fig. 4 Lithological log well 8733/2 at Diar Hajjej Region

The correlation matrix reveals the presence of a set of well correlated variables directly related to salinity, EC with Cl^-, Na^+, SO_4^{2-}, Ca^{2+} and Mg^{2+}, expressed by a relatively high correlation coefficient 0.89, 0.85, 0.74, 0.685 and 0.64. This strong correlation confirms that the water salinity depends mainly on these elements. Most of the samples indicated higher nitrate levels than the permissible limit prescribed by WHO (50 mg/l) and the Tunisian standards (45 mg/l). The surface waters of Oued Chiba do not have nitrate contents, which can be explained by the dilution of these waters by the rain (Fig. 8).

4 Conclusion

The strong development of agricultural and industrial activities along this plain is degrading the groundwater quality. The compilation of geophysical (VES and logs) and

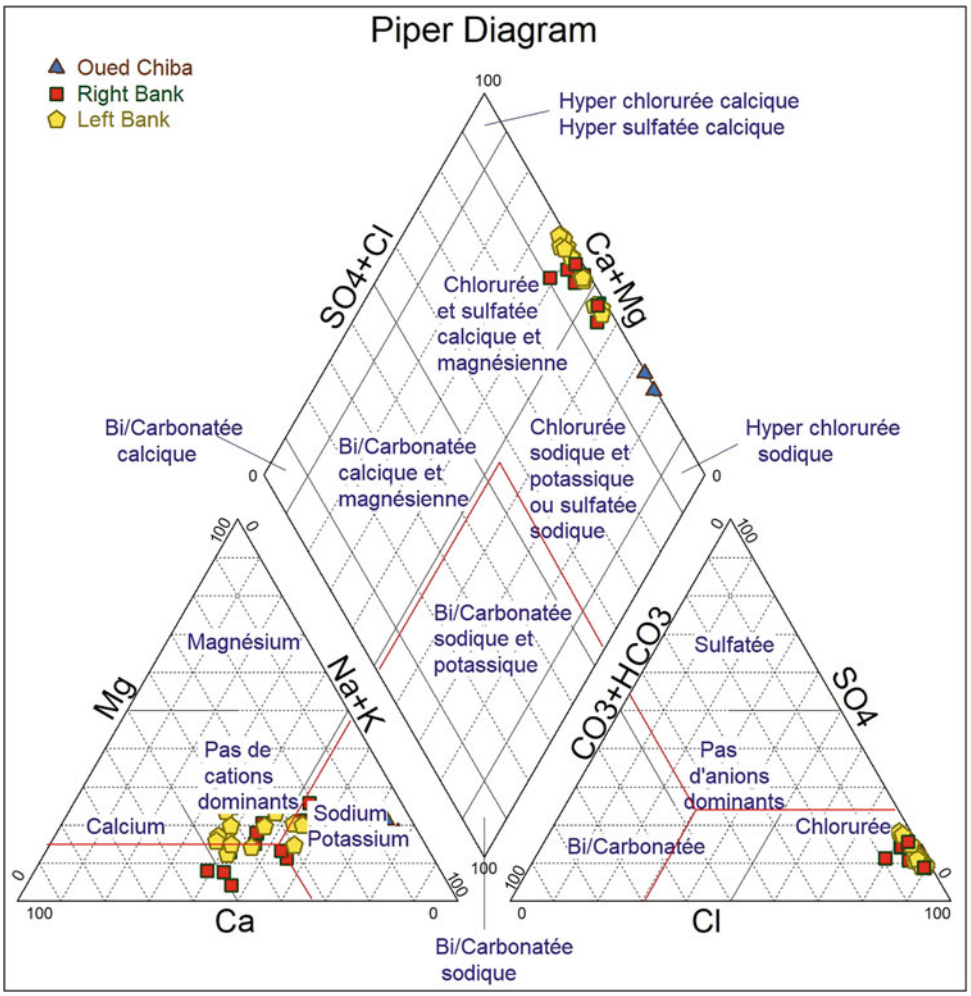

Fig. 5 Piper diagram of Oued Chiba plio-quaternary aquifer (July 2018)

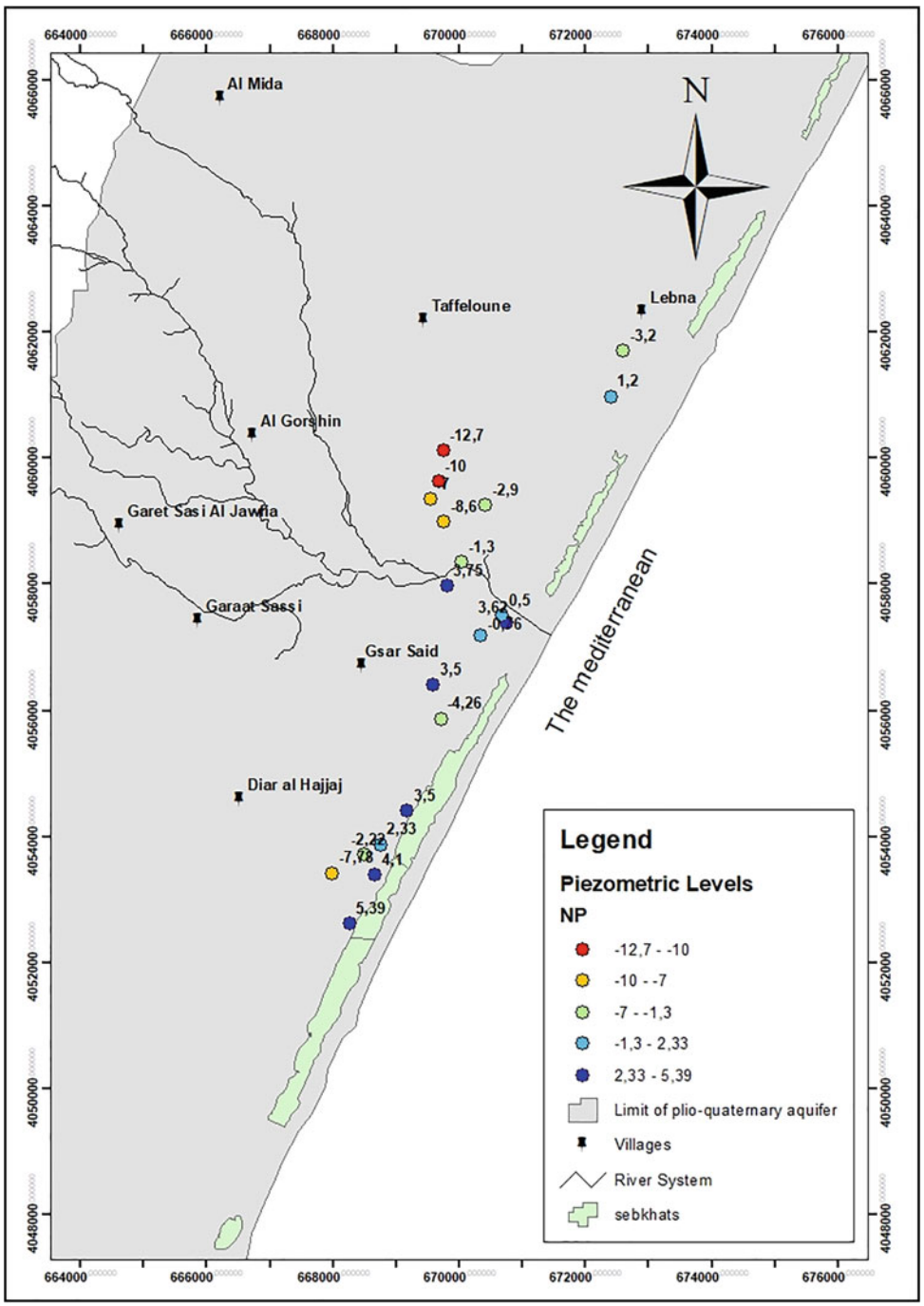

Fig. 6 Piezometric map of Oued Chiba plio-quaternary aquifer (July 2018)

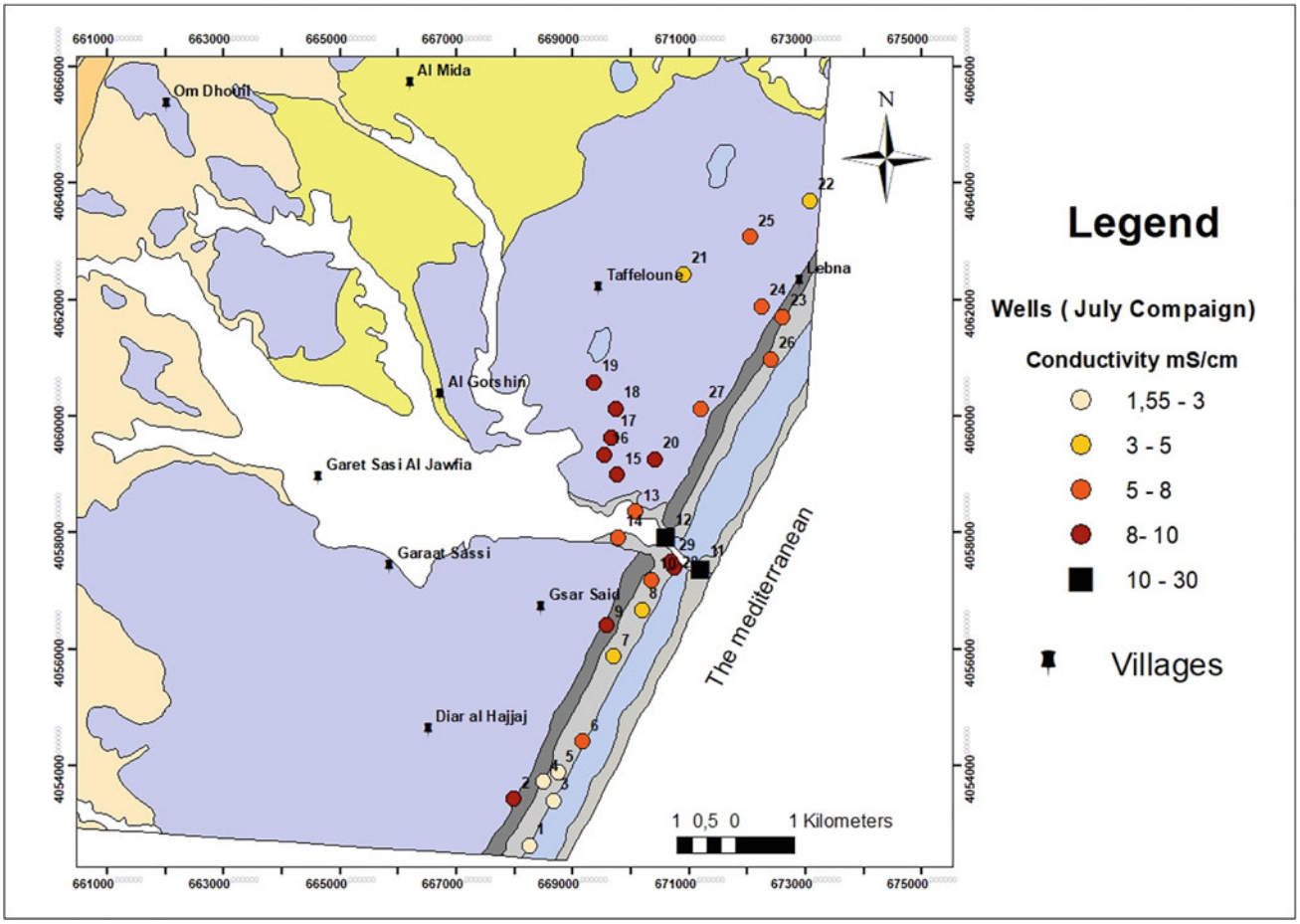

Fig. 7 Spatial distribution map of electrical conductivity along Oued Chiba plain (July 2018)

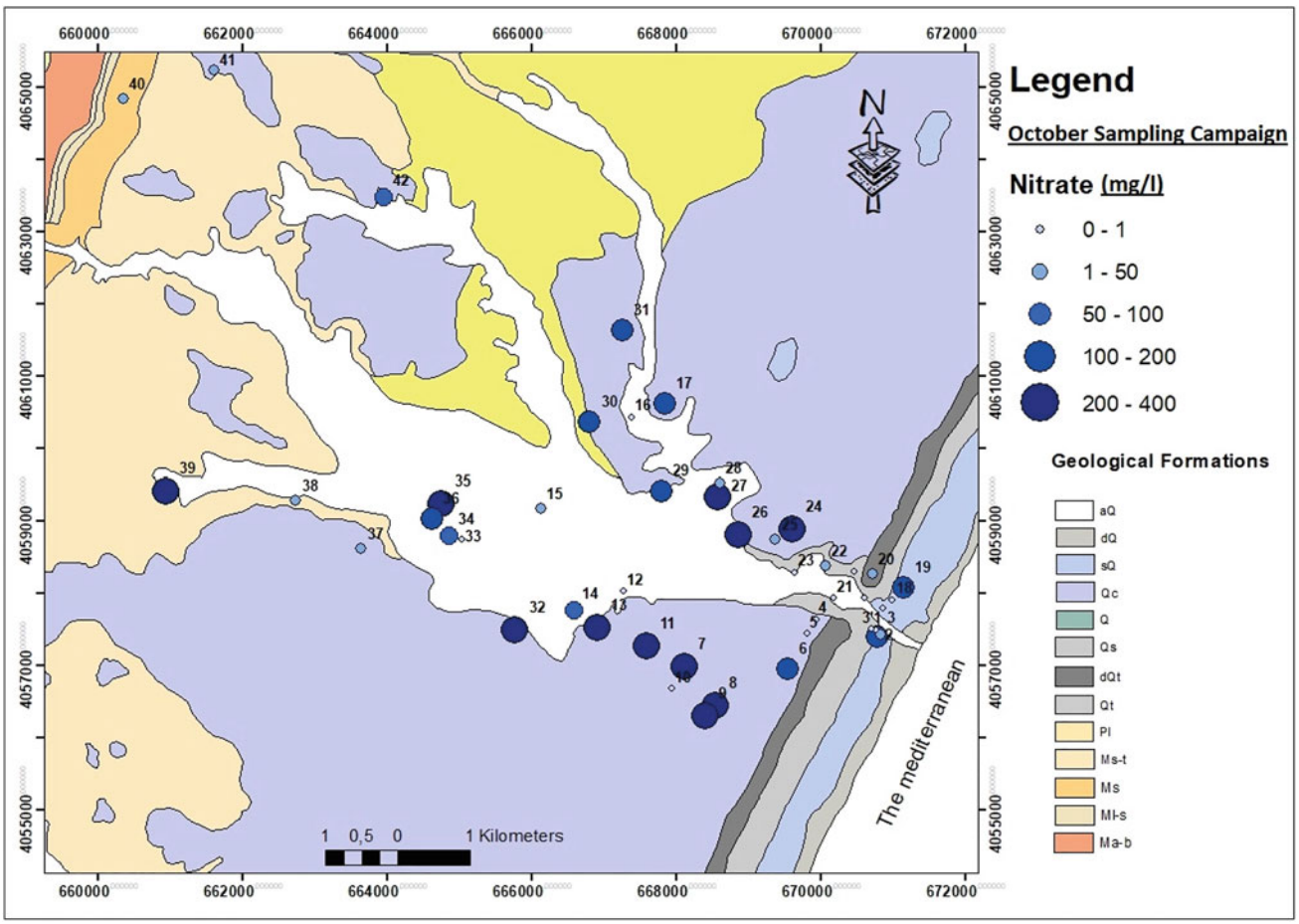

Fig. 8 Distribution of nitrate concentrations in Oued Chiba watershed (October 2018)

geochemical results showed the existence of a marine intrusion that invaded the region of Diar Hajjej, Garaat Sassi and Tafelloune combined with nitrate pollution.

References

Ben Hamouda, M. F., et al. (2009). Origine de la minéralisation dans l'aquifère plio-quaternaire de la côte orientale du cap Bon (Tunisie). *Science Et Changements Planétaires/sécheresse, 20*(1), 78–86.

Ben Salem, H. (1992). Contribution à la connaissance de la géologie du Cap Bon: stratigraphie, tectonique et sédimentologie. Unpublished Ph. D. Thesis, University of Tunis.

Kouzana, L., Mammou, A. B., & Felfoul M. S. (2009). Seawater intrusion and associated processes: case of the Korba aquifer (Cap-Bon, Tunisia). *Comptes Rendus Geoscience*, *341*(1), 21–35.

Irrigation Strategies and Crops Selection as a Sustainable Water-Resource Management in Water Limited Environments: Tunisian Case Study

Hacib El Amami, Abdelaziz Zaïri, and Insaf Mekki

Abstract

Combined with the simultaneous effects of climate change and the increasing rate of groundwater depletion, current agricultural practices can no longer be sustained in water-scarce regions. In this context, the use of water for agricultural production requires innovative and sustainable strategies to increase its efficiency as well as the crops' productivity. Undertaken at Sidi Bouzid area, located in the arid center parts of Tunisia, this paper discusses some of these aspects, mainly relative to on-farm irrigation management and appropriate crops selection. A two-stage simulation/mathematical programming model was developed to analyze farm level irrigation management and crops selection under conditions of limited water availability. Research results showed that deficit irrigation strategy and crops selection were successful in increasing water productivity at the farm level without causing severe economic reduction. Even though such adaptation leads to a reduction in the farmer's income in the short term, it allows sustaining it, however, in the medium term. Therefore, it can be suggested among strong adjustments that can be recommended for water-scarce areas.

Keywords

Water • Scarcity • Crops • Selection • Deficit irrigation

1 Introduction

In the central parts of Tunisia, where rainfall and surface water are both scarce and random, groundwater is falling quickly, reaching 1.5 m per year in some zones (DGRE, 2014); thus, threatening the sustainability of irrigated agriculture. Combined with the increasing impact of climate change, current agricultural practices can no longer be sustained in these water-scarce regions. In this context, the use of water for agricultural production requires innovative and sustainable strategies to increase its efficiency as well as the crops' productivity. Several possible approaches were suggested. Deficit irrigation is widely investigated as a valuable strategy where water is the limiting factor in crop cultivation such as dry regions (English, 1990). Deficit irrigation is defined as an optimizing strategy under which the crops are deliberately allowed to sustain some degree of water deficit, resulting in yield reduction in order to achieve maximum profit per unit of water (English and Raja, 1996).

While the intention is to economically optimize production for each unit of water, different crops respond much differently to water deficit. There is a need to closely assess the deficit irrigation as several trees and crops respond differently to water stress (Reddy, 2016). Crops' selection is also indicated as possible mitigation actions and measures aiming to minimize water scarcity in agriculture and its impacts. However, according to farmers, the choice of crops is not done only on the basis of water requirements and water availability but also on the basis of expected net economic benefits.

The objectives of this study were to ascertain whether deficit irrigation and crops choices can be an economically viable option in the center parts of Tunisia.

2 Methodology

An integrated economic and biophysical approach modeling was developed for this study. The modeling framework includes two principal components: **(a)** an economic model and **(b)** a biophysical model to simulate how crops' yields would respond to varying levels of water irrigation applications. The economic model uses mathematical programming

H. El Amami (✉) · A. Zaïri · I. Mekki
Carthage University, 1054 Tunis, Tunisia
e-mail: hacib.amami@gmail.com

A. Kallel et al. (eds.), *Selected Studies in Environmental Geosciences and Hydrogeosciences*,
Advances in Science, Technology & Innovation, https://doi.org/10.1007/978-3-031-43803-5_50

techniques to simulate the potential effect of optimum crops' choices and irrigation strategies on sustainability of groundwater management under the decline of wells' yield and the increasing pumping lift in water limited areas, so as to maximize net return from agricultural production. The integrated model predicts whether the adoption of water-efficient cropping strategies and crops selection would contribute to maintaining groundwater use and save farmers' incomes in water shortage areas. The implications of these adjustment practices were also derived from the model's results. This integrated economic and biophysical approach was constructed for a representative farm in the Sidi Bouzid area, located in the center of Tunisia.

3 Results

Results were reported for three scenarios of water availability and agricultural practices. In scenario I, called baseline scenario, it was assumed that water is available in sufficient quantity and farmers continue to adopt the current technology practices, with no new modification in cropping pattern and water irrigation strategies. Scenario II evaluated the case where there is water shortage and increasing pumping lift, but there are no changes in crops' selection and irrigation water strategies. Various scenarios of increasing pumping lift were simulated based upon the average annual depletion observed in the past years. Scenario III considered the case of water shortage and increasing pumping lift, but there are several alternatives of water irrigation strategies and crops selection.

3.1 Baseline Scenario (Scenario I)

As indicated by Table 1, the optimal solution in scenario I (baseline scenario) proposes to plant, in succession onion, potato and olive tree.

All crops were suggested under full irrigation regime as this water regime provides maximum yields, and as a consequence, the maximum of net economic return. The total gross margin (net return) is defined as total gross value of production minus total cost of production. The net return corresponding to the baseline scenario was 60,000 TND. The gross margin per unit of cultivated area (ha) and per unit of water diverted (m^3) were 8141 TND and 2.1 TND, respectively.

3.2 Water Shortage and Increasing Pumping Depth Scenarios

Due to this decline in water table's depth, the farmers have to deepen their wells, thus regularly increasing the energy requirement to lift one cubic meter, which has an additional impact on pumping costs. Table 2 compares, at different levels of pumping water lift, the gross margin per hectare and per cubic meter between the two simulated scenarios: water shortage and increasing pumping depth without agricultural practices' adjustments (scenario II) and water shortage with adjustments (scenario III). The evolution of these indicators, relative to the baseline scenario (scenario I), was also shown. Results revealed that, at each level of pumping depth, the difference between the expected gross margin per ha and per cubic meter for scenario III and those obtained in the baseline scenario is low. However, this difference is high for scenario II without adjustments; and this difference becomes more much higher when pumping depth increases.

For example, at depth level simulation of 40 m, farmers don't adopt coping strategies that could obtain only 50% of gross margin per ha obtained in the baseline scenario, and only 56% of the gross margin per ha obtained by farmers adopting adaptive strategies.

4 Discussion

The reduction of economic indicators under adaptive scenario (III) is much lower than the one under the scenario where farmers don't make adjustments (scenario II).

Coping strategies help to mitigate groundwater shortage impacts and the increase of its pumping costs by introducing flexibility in resources' allocation. Even though such adaptation leads to a reduction in economic return in the short term, it allows sustaining it in the medium term and therefore sustaining the economic viability of existing irrigated farming systems in these areas. While effective, it is clear that these strategies alone cannot mitigate all the negative impacts of further groundwater depletion in the future. To

Table 1 Agronomic and economic indicators in the baseline scenario (scenario I)

Indicators	Copped area (ha)	Pumped water (m3)	Total income (TND*)	Gross margin/ha (TND)	Gross margin/m^3 (TND)
Level of indicators	5	48,900	60,000	8141	2.1

*TND = Tunisian Dinar ≈ 0.36 USD in 2021

Table 2 Evolution of gross margin (G.M) per ha and gross margin (G.M) per cubic meter relative to the various scenarios

Well level depth (m)	Scenario II: Without adjustment				Scenario III: With adjustment			
			Change relative to baseline (%)				Change relative to baseline (%)	
	G.M/ha	G.M/m^3	G.M/ha	G.M/m^3	G.M/ha	G.M/m^3	G.M/ha	G.M/m3
30	11,500	1.42	− 0.44	− 0.23	19,800	1.78	− 0.03	− 0.04
35	10,900	1.38	− 0.47	− 0.25	19,000	1.86	− 0.07	0.01
40	10,200	1.25	− 0.50	− 0.32	18,260	1.95	− 0.11	0.05
45	9550	1.17	− 0.53	− 0.37	17,500	2.03	− 0.15	0.10
50	8870	1.08	− 0.57	− 0.42	16,800	2.115	− 0.18	0.14
55	8300	0.99	− 0.60	− 0.46	16,000	2.2	− 0.22	0.19

support farmer's adaptive strategies, there is an urgent need to implement, in parallel, significant policy reforms to control groundwater withdrawal in order to sustain the production system in these areas. Among robust policies, this study suggests the involvement of local users, with the assistance of Regional Department of Agriculture (CRDA), to ensure effective control on groundwater withdrawal.

5 Conclusions

This study aimed to ascertain whether deficit irrigation and crops' choices can be an economically viable option in the context of water shortage and increasing pumping depth in the Center of Tunisia. Research results showed that this strategy is successful in increasing water productivity at the farm level without causing severe economic reductions, compared to the scenario where there are no adjustments made. Even though such adaptation leads to a reduction in the farmer's income in the short term, it allows sustaining it in the medium term. Therefore, it can be among strong adjustments that can be recommended for water-scarce area.

References

DGRE. (2014). Annuaire piézomètrique de la Tunisie. Ministère de l'Agriculture et des Ressources hydrauliques (p. 329).

English, M. (1990). Deficit irrigation. I: Analytical framework. *Journal of Irrigation and Drainage Engineering*, *116*(3), 399–412. https://doi.org/10.1061/(ASCE)0733-9437(1990)116:3(399)

English, M., & Raja, S. N. (1996). Perspectives on deficit irrigation. *Agricultural Water Management, 32*(1), 1–14. https://doi.org/10.1016/S0378-3774(96)01255-3

Evans, R. G., & Sadler, E. J. (2008). Methods and technologies to improve efficiency of water use. *Water Resources Research*, *44*, W00E04. https://doi.org/10.1029/2007WR006200

Reddy, P. P. (2016). *Sustainable intensification of crop production* (p. 404). Springer Nature Singapore Pte, Ltd.

A Decision Support Tool for the Dynamic Groundwater Management of Coastal Aquifers Under Uncertainty

Chefi Triki, Mohammad Mahdi Rajabi, Ali Al-Maktoumi, and Slim Zekri

Abstract

In this paper, we described a computationally efficient simulation–optimization (S/O) framework for coastal groundwater management (CGM), based on the combined application of numerical modeling, artificial neural networks, and genetic algorithm. The objective was to analyze the 'trade-off' between optimality and risk in deriving CGM strategies and to show that reformulating the problem using a mean–variance bi-criterion objective function can be a valuable tool in minimizing the risk of non-optimality. As a case study for our analysis, we studied the optimal design of an aquifer storage and recovery (ASR) system in the Muscat metropolitan area in Oman. S/O was applied to find the optimal constant daily abstraction and injection rates that maximize the net present value (NPV) of the ASR system. The results show that the choice of the decision variables significantly affects the risk of non-optimality, and reducing this risk comes at the cost of a decrease in the expected NPV.

Keywords

Robust optimization • Uncertainty quantification • Artificial neural network • Coastal aquifer

C. Triki (✉)
College of Sciences and Engineering, Hamad Bin Khalifa University, Ar-Rayyan, Qatar
e-mail: ctriki@hbku.edu.qa

M. M. Rajabi
Civil and Environmental Engineering Faculty, Tarbiat Modares University, Tehran, Iran

A. Al-Maktoumi · S. Zekri
College of Agricultural and Marine Sciences, Sultan Qaboos University, Seeb, Oman

1 Introduction

An effective approach to developing sustainable coastal groundwater management (CGM) strategies is to combine groundwater numerical models with optimization algorithms that systematically search for improved management alternatives based on model outputs. The objective of such simulation–optimization (S/O) procedures is often two-fold: first to increase fresh groundwater extraction, and second, to reduce seawater intrusion. Previous applications of S/O in the context of CGM mostly ignore predictive uncertainty and rely on deterministic models. However, this ignorance of uncertainty can be problematic because a management strategy that is considered optimal using a deterministic model may become non-optimal when uncertainty in the model outputs is considered (Rajabi and Ketabchi, 2017). Therefore, in recent years, the classic deterministic S/O approach has been extended by e.g., Lal and Datta (2019) and Triki et al. (2020) to account for uncertainty in key model parameters. In these and other similar studies, multiple-realization methods are used and the objective is often to optimize the mean or expected value of the probability distribution of the objective function. This is called 'mean-based' optimization. Despite being a very common approach, the mean-based S/O approach does not take into account the fact that each combination of the decision variables may result in a different level of uncertainty in the objective function. Hence in the presence of uncertainty in the model parameters and external forcing terms, an optimal solution in mean-based S/O may carry a bigger risk of non-optimality compared to a sub-optimal robust solution. This issue has been addressed in previous studies on optimization of oil reservoir production (in e.g., Capolei et al., 2015; Mohammadi et al., 2020) or geothermal reservoir utilization (e.g., Serafino et al., 2020). But to the authors' knowledge, it has never been studied in the context of CGM. Hence the objective of this study was to analyze the 'trade-off' between optimality and risk in deriving coastal

A. Kallel et al. (eds.), *Selected Studies in Environmental Geosciences and Hydrogeosciences*, Advances in Science, Technology & Innovation, https://doi.org/10.1007/978-3-031-43803-5_51

aquifer management strategies and to show that reformulating the coastal management problem using a mean–variance bi-criterion objective function can be a valuable tool in minimizing the risks associated with uncertainty.

2 Methodology

As a case study of our analysis, we investigated the optimal design of an aquifer storage and recovery (ASR) system in Al-Khoud coastal aquifer located in the Muscat metropolitan area in the Sultanate of Oman. The aquifer is being considered as a natural reservoir for the storage of seasonal excess desalinated water. In order to simulate the groundwater dynamics of Al-Khoud aquifer, a three-dimensional MODFLOW numerical model was used. Details about the aquifer and its numerical model can be found in Triki et al. (2017). In our study, the python package 'FloPy' was used to automate the model simulations. Due to the nature of the prevailing arid climate in the study area, we assumed that natural recharge rate (R_N) is the key uncertain parameter affecting prediction of aquifer response to ASR. We characterized uncertainty in R_N with a bimodal normal distribution pertaining to wet and very dry years. A total of 195 triple-purpose abstraction/injection/monitoring wells were defined in the ASR scheme. Our aim was to find the optimal constant daily abstraction and injection rates (Abs and Inj respectively) that maximize the net present value (NPV) of the ASR system, while controlling the aquifer hydraulic head to prevent seawater intrusion. This notion can be presented as follows:

$$\mathrm{NPV} = \sum_{t=1}^{n} \frac{CI_t - CO_t}{(1+r)^t} - C_0 - P_e(H_0 - H_t) \qquad (1)$$

where n is the number of years in the planning period ($= 20$ years); r is the annual discount rate ($= 0.07$); C_0 is the initial investment ($= 1,5 \times 10^6$ \$), H_0 and H_t are the average hydraulic head in the observation wells at the start of the planning period and at the end of each year respectively, and P_e is a penalty coefficient which is zero if $H_0 \leq H_t$ and increases in a stepwise manner as $H_0 - H_t$ increases. $CI_t = 2.36 d_{\mathrm{abs}}$ Abs is the yearly revenue (in \$) from water sales, and $CO_t = 1.04 d_{\mathrm{inj}}$Inj (in \$) is the yearly cost of ASR. d_{abs} is the number of days in the high demand interval of each year ($= 245$ days), and d_{inj} is the number of days in the low demand interval of each year when the aquifer is used for storage of excess desalinated water ($= 120$ days) (see Triki et al., 2020). We referred to Monte Carlo simulation (MCS) to estimate NPVs in the presence of uncertainty in R_N. Based on this set and within a risk-aware framework, the objective function is defined as:

$$\text{Maximize } c\mu(\mathrm{NPV}) - (1-c)\sigma(\mathrm{NPV}) \qquad (2)$$

where $\mu(\mathrm{NPV})$ is the expected value of NPV and is related to maximizing return, while the term $\sigma(\mathrm{NPV})$ characterizes the standard deviation in NPV and is related to minimizing risk, and c defines the relative weight. The trade-off between risk and return can be assessed by analyzing different values of c. In this study, the optimization phase was carried out using genetic algorithm by employing the python 'geneticalgorithm' library. To overcome the computational burden of S/O, artificial neural networks (ANNs) were used as a surrogate model. The inputs to the ANN meta-models are the initial heads in the 195 observation wells at the start of each one year period, plus the abstraction, injection, and natural recharge rates during that year. The ANN model then simulates the state transition and predicts hydraulic head in each observation well after a one year period. The training dataset consists of 4,700 input–output pairs generated using the calibrated MODFLOW model, and 300 other pairs were reserved for model evaluation. The python 'TensorFlow' library was used to build the neural network.

3 Results and Discussion

The choice of the ANN model architecture was achieved using trial and error, and a feed-forward neural network consisting of an input layer with 198 neurons, two hidden layers each having 150 neurons, and an output layer with 195 neurons was used as the meta-model. The transfer function was chosen to be hyperbolic tangent for the input and hidden layers, and linear for the output layer. As one measure of accuracy, the scatter plot of numerical model vs. ANN meta-model outputs is shown in Fig. 1. The diagonal bisector shows a perfect match, and the points in Fig. 1 form two disjoint clouds, one for observation wells closer to the shoreline and the other for wells farther from the sea. Both clouds are close to the 1:1 line, indicating that the developed ANN model is sufficiently accurate. Figure 2 shows the coefficient of variation CV(NPV) ($= \sigma/\mu$) as standardized measure of uncertainty in NPV estimations, for different combinations of the decision variables Abs and Inj. As demonstrated, the choice of the decision variables significantly affects the NPV uncertainty, and the highest level of uncertainty pertains to low values of Abs and high values of Inj. . This shows the importance of considering the risk of non-optimality in S/O for CGM. Based on this fact, we used the bi-criterion objective function (Eq. 2) for S/O of the ASR system. The suitable GA parameters were found based on the convergence rate of the objective function as follows: population size = 100, maximum number of generations = 130, mutation and crossover probabilities = 0.2 and

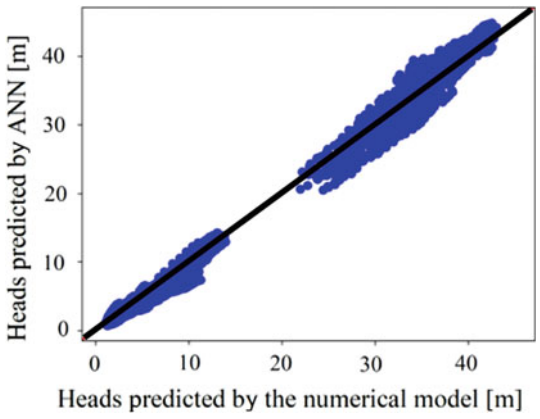

Fig. 1 Pairwise comparison of simulated heads of the MODFLOW model and the associated ANN outputs

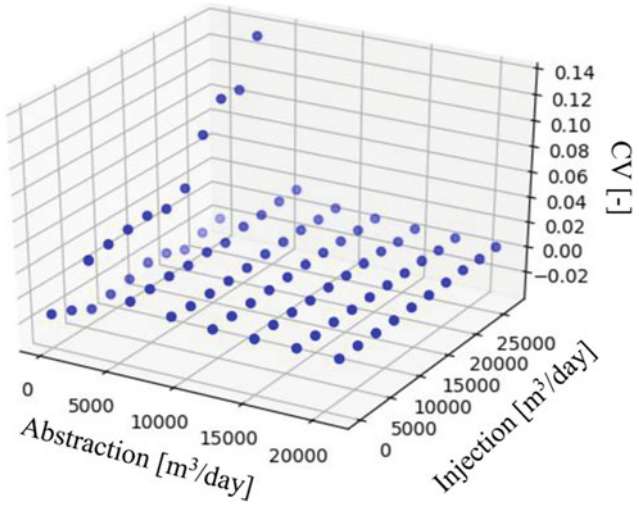

Fig. 2 Coefficient of variation (CV) as a function of the two decision variables (abstraction and injection rates)

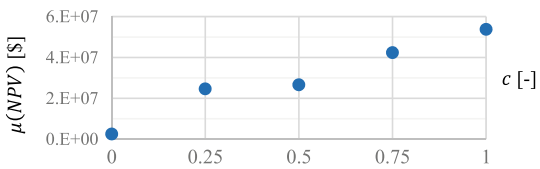

Fig. 3 Expected NPV versus the mean–variance trade-off parameter c

0.9 respectively, and elite ration = 0.01. The S/O problem is solved for various values of the mean–variance trade-off parameter, c, and the results are presented in Fig. 3. The figure shows that reducing the risk of non-optimality (by decreasing c) comes at the price of decreasing the expected NPV, and there is a non-monotonous relationship between $\mu(\text{NPV})$ and c.

4 Conclusion

In this paper, we described a computationally efficient S/O framework for CGM, based on the combined application of numerical modeling, ANNs and genetic algorithm were used together with a mean–variance bi-criterion objective function within this framework. An ASR system for a coastal aquifer was used as a case study. We demonstrated that the choice of the decision variables significantly affects the risk of non-optimality as presented by the standard deviation of NPV estimates, and reducing this risk comes at the cost of decreasing the expected NPV. In the future, we aim to compare the proposed bi-criterion with the conditional-value-at-risk method (see Musmanno et al., 2010).

Acknowledgements The authors would like to acknowledge the financial support of the NPRP grant # [NPRP13S-0129-200198] from the Qatar National Research Fund (a member of Qatar Foundation).

References

Capolei, A., Suwartadi, E., Foss, B., & Jørgensen, J. B. (2015). A mean–variance objective for robust production optimization in uncertain geological scenarios. *Journal of Petroleum Science and Engineering, 125*, 23–37.

Lal, A., & Datta, B. (2019). Multi-objective groundwater management strategy under uncertainties for sustainable control of saltwater intrusion: Solution for an island country in the South Pacific. *Journal of Environmental Management, 234*, 115–130.

Mohammadi, M., Ahmadi, M., & Kazemi, A. (2020). Comparative study of different risk measures for robust optimization of oil production under the market uncertainty: a regret-based insight. *Computational Geosciences*, 1–19

Musmanno, R., Scordino, N., Triki, C., & Violi, A. (2010). A multistage formulation for GENCOs in a multi-auction electricity market. *IMA Journal of Management Mathematics, 21*(2), 165–181.

Rajabi, M. M., & Ketabchi, H. (2017). Uncertainty-based simulation-optimization using Gaussian process emulation: application to coastal groundwater management. *Journal of Hydrology*, *555*, 518–534

Serafino, A., Obert, B., Vergé, L., & Cinnella, P. (2020). Robust optimization of an organic Rankine cycle for geothermal application. *Renewable Energy, 161*, 1120–1129.

Triki, C., Zekri, S., Al-Maktoumi, A., & Bazargan-Lari, M. R. (2020). Optimal location of wells for storage and recovery of surplus desalinated water in coastal aquifers. *Groundwater, 58*(5), 831–841.

Triki, C., Zekri, S., Al-Maktoumi, A., & Fallahnia, M. (2017). An artificial intelligence approach for the stochastic management of coastal aquifers. *Water Resources Management, 31*(15), 4925–4939.

Policy Interventions to Improve Groundwater Management: Case of a Depleted Aquifer in Mahdia (Tunisia)

Rania Soula, Ali Chebil, Rajouene Majdoub, Daniel Crespo, Taher kahil, and José Albiac

Abstract

Water supply in the Mahdia region of Tunisia originates mainly from groundwater sources. As a common pool resource, these aquifers are highly susceptible to overexploitation, resulting in the classical tragedy of the commons. In this study, a hydro-economic optimization model was developed to determine the most efficient allocation of groundwater resources between farmers in the present and also by considering the needs of future generations. An economic analysis was performed with the model to find efficient policies that contribute to decrease aquifer overuse in normal and drought years and improve its sustainability. Financial analysis of returns and costs of producing irrigated crops were determined in the Mahdia-Ksour Essef aquifer, in which the benefits of drip, flood, and sprinkler irrigation were compared for each crop. The efficiency of alternative scenarios (baseline scenario "no policies undertaken" and water policy scenarios) were compared. Data for the analysis were obtained from multiple sources. Results show the importance of cooperation between farmers. The consideration of pumping costs along time in the farmers' benefit equation allows the recovery of the water table level over the next two decades. This study assessed the importance of policy interventions to maximize social benefits for sustainable groundwater management. This paper introduced a case application of a dynamic model for managing an aquifer of the Mahdia region in Tunisia. This overused coastal aquifer requires the urgent application of the proposed water policies to maintain groundwater's natural level and prevent the propagation of saltwater intrusion.

Keywords

Common pool resource • Dynamic modeling • Hydro-economic modeling • Mahdia aquifer • Sustainability • Water policies

1 Introduction

Groundwater is mainly used for irrigation in the semi-arid region "Mahdia". Over the past decades, groundwater extraction rate has exceeded the recharge (CRDA, 2018). In this case, the resource would be mined over time until supplies were exhausted. A marginal pumping cost was associated with mining groundwater reflecting the opportunity cost associated with the availability in the future of each amount of water used in the present (MacEwan et al., 2017). This study analyzed three groundwater management regimes: the free market regime, the partial cooperation regime, and the full cooperation regime. In the partial cooperation regime, only the costs of water extractions (the pumping cost externality) were considered. In the full cooperation model, the social costs of environmental damages were also included in the model.

2 Materials and Methods

The studied aquifer "Mahdia-Ksour Essef" is located in the *central eastern part* of Tunisia where irrigated agriculture represents an important source of income (Fig. 1).

R. Soula (✉) · R. Majdoub
High Agronomic Institute of Chott Mariem, University of Sousse, Sousse, Tunisia
e-mail: raniaso1@hotmail.fr

A. Chebil
National Research Institute for Rural Engineering, Water and Forestry (INRGREF), Tunis, Tunisia

D. Crespo
School of Public Policy, University of California, Riverside, USA

T. kahil · J. Albiac
International Institute for Applied Systems Analysis (IIASA), Laxenburg, Austria

J. Albiac
Agrifood Research and Technology Center, Government of Aragon, Zaragoza, Spain

A. Kallel et al. (eds.), *Selected Studies in Environmental Geosciences and Hydrogeosciences*, Advances in Science, Technology & Innovation, https://doi.org/10.1007/978-3-031-43803-5_52

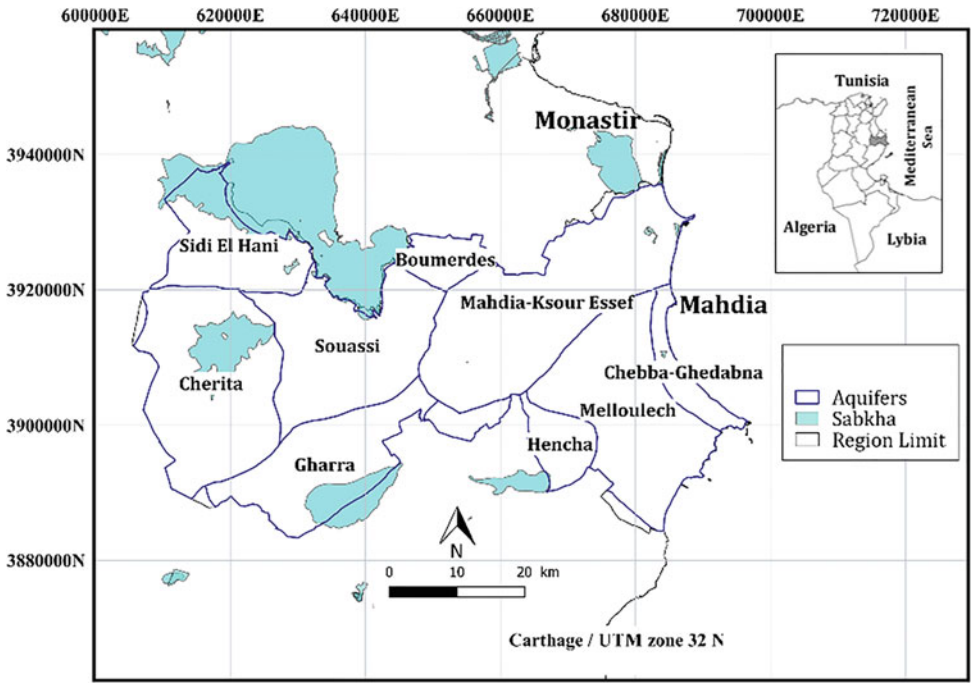

Fig. 1 Location of Mahdia-Ksour Essef aquifer in Mahdia

Three groundwater management regimes were analyzed in this study. The first regime is called free market (myopic pumping by agents). Agents ignore the future pumping extraction cost and the environmental damages of aquifer depletion. Farmers maximize their private benefits in the current period, because the water they do not extract would be extracted by others. The second regime is called "partial cooperation". Agents consider the full stream of benefits in the planning period, accounting for the future aquifer extraction costs and the wellbeing of future generations (Social opportunity costs) (Afshar et al., 2020; Gisser & Sánchez, 1980). An additional cost "the externality cost" (i.e., environmental damages, cost of saline intrusion, drought buffer, etc.) is considered in the third regime "full cooperation" (Esteban & Albiac, 2011; Expósito et al., 2020). These regimes were set up with five types of farmers that produce cereals (c), vegetables (v), fruit trees (ft), olive trees (o), and fodders (fd). These crops were irrigated by different irrigation systems, which influence the return flow coefficients (Table 1).

The private profits of farmers are given by the following expression:

$$T_{AG}(t) = \sum_i \sum_j \text{Net income}_{i,j}(t)^* \text{Land}_{i,j}(t) \qquad (1)$$

where $\text{Land}_{i,j}(t)$ is the surface for each crop (i), irrigated by the irrigation system (j) in the year (t).

The extraction costs of water from the aquifer are given by:

$$C_{pw}(t) = \sum_i \sum_j (\boldsymbol{C}_0 + \boldsymbol{C}_1 * (\boldsymbol{S}_I - H_t))^* \, \mathrm{w}_{i,j}^* \, \text{Land}_{i,j}(\mathrm{t}) \qquad (2)$$

The change of the water table level is given by the equation:

$$H_t - H_{t-1} = \frac{R - \sum_i \sum_j (1-\alpha) * w_{i,j} * \text{land}_{i,j}(t)}{A * s} \qquad (3)$$

where A the area of the aquifer, and s is the storativity coefficient.

The costs of ecosystem damage are given by:

$$\mathrm{D}\,[H(t)] = \beta * (\sum_i \sum_j (1-\alpha) * w_{i,j} * \text{land}_{i,j}(t) - R) \qquad (4)$$

The expression for the collective private profits under the partial cooperation regime is given by:

$$T_{AG}(t) - C_{pw}(t) \qquad (5)$$

The expression of the full cooperation regime is given by:

$$\text{Max} \;\; e^{-rt} \sum_{t=1}^{n} T_{AG}(\mathrm{t}) - C_{pw}(t) - \; \mathrm{D}\,[H(t)] \qquad (6)$$

Subject to

$$H_t - H_{t-1} = \frac{R - \sum_i \sum_j (1-\alpha) * w_{i,j} * \text{land}_{i,j}(t)}{A * s} \qquad (7)$$
$$\text{with}\, H_0(0) = H_0$$

Table 1 Hydrologic and economic parameters of the Mahdia-ksour Essef Aquifer *(relative to the base year 2015)*

Parameters	Description	Value
$w_{C,\text{surf}}$	Water use by cereals and surface irrigation system	2475 (m^3/ha)
$w_{o,\text{drip}}$	Water use by olive trees and drip irrigation system	1531 (m^3/ha)
$w_{o,\text{surf}}$	Water use by olive trees and surface irrigation system	2300 (m^3/ha)
$w_{ft,\text{drip}}$	Water use by fruit trees, drip irrigation	918 (m^3/ha)
$w_{ft,\text{surf}}$	Water use by fruit trees, surface irrigation	1378(m^3/ha)
$w_{fd,\text{surf}}$	Water use by fodders and surface irrigation	14,033 (m^3/ha)
$w_{vg,\text{drip}}$	Water use by vegetables and drip irrigation	10,904 (m^3/ha)
$w_{vg,\text{surf}}$	Water use by vegetables and surface irrigation	16,365 (m^3/ha)
C_0	Pumping cost intercept	0.07 (TND/m^3.ha)
C_1	Pumping cost coefficient	0.005 (TND/mm^3.ha)
α_j	Return flow coefficient by irrigation system	(10% drip, 20% sprinkler, 40% surface irrigation)
H_0	Water table current elevation	25 m above the sea level
R	Recharge	2.9 mm^3
A	Area of the aquifer	611 Km^2
s	Storativity coefficient	0.05
S_l	Elevation of the aquifer surface	40 m above the sea level
Net income_c	Net income of cereals	110 (TND/ha)
Net income_o	Net income of olive trees	2100 (TND/ha)
Net income_{ft}	Net income of fruit trees	1830 (TND/ha)
Net income_{fd}	Net income of fodders	550 (TND/ha)
Net income_{vg}	Net income of vegetables	4900 (TND/ha)
β	Environmental damages of depletion	0.7 (TND/m^3)

$$\sum_i \sum_j \text{land}_{i,j}(t) \leq \text{Land}_{\text{tot}}(t) \quad (8)$$

where $\text{land}_{\text{tot}}(t)$ is the total irrigated area in the year t and r is the discount rate.

The software general algebraic modeling system GAMS was used to run the calculations (Grossmann, 2021). The model was calibrated using positive programing, following the procedure of Dagnino and Ward (2012).

3 Results

The groundwater modeling presented in the previous section was used to compare the three regimes of aquifer management. Under "free market" management, farmers maximize their private benefits in the current period, causing the progressive fall of the water table (Fig. 2).

Under the scenario of "partial cooperation", the consideration of current and future pumping costs in the farmers benefit equation allows the water table level to slightly increase over two decades (Fig. 2).

Under the full cooperation scenario, cereals and fodders production under surface irrigation are abandoned, while the natural table level is rapidly recovered over two decades (Fig. 2).

4 Discussion

The results show clearly the importance of cooperation management that improves the sustainability of the aquifer. By considering only the pumping cost externality, the water table level rises but cannot be recovered to its natural level. During the last few years, despite the attempts of collective actions in the studied aquifer (GDA: farmers association), farmers did not cooperate (Frija et al., 2015; Soula et al., 2021). Therefore, the pumping competition behavior between agents in the irrigated perimeters led to the water table progressive lowering. Collective action implemented in the region should be revised; moreover, other water policies should be applied to move toward recovering the natural groundwater level.

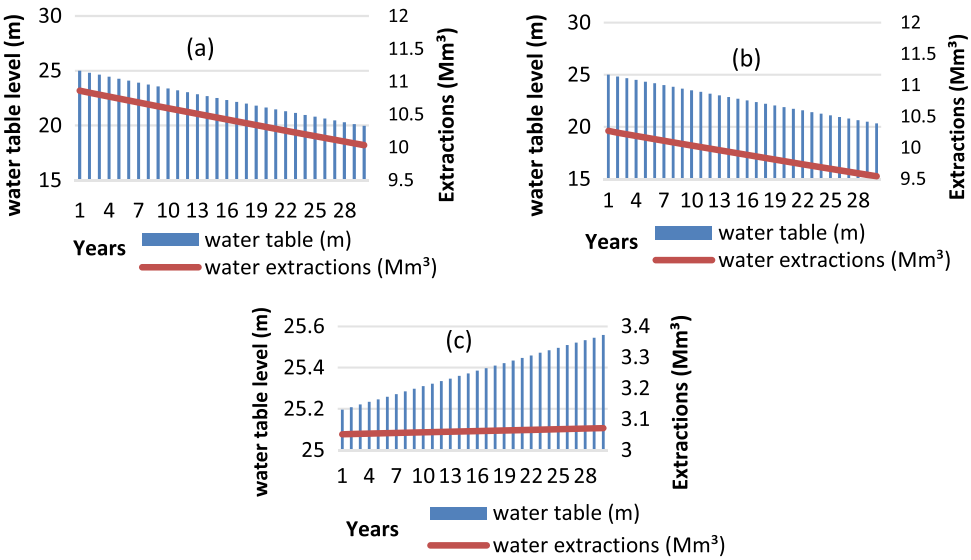

Fig. 2 Water table and extractions under three regimes: free market **a**, partial cooperation **b**, and full cooperation **c**

5 Conclusion

This study shows that under the free market regime, the depletion of the aquifer will continue over the next two decades. However, under the partial cooperation regime, the water table rises but cannot reach its natural level. Compared to the policies applied in the past, these results indicate that the GDA (the farmers' association to induce collective action) has failed to manage the aquifer toward sustainability in recent decades. Therefore, new policies and institutional and economic instruments are required to ensure the sustainability of Mahdia-ksour Essef aquifer.

References

Afshar, A., Tavakoli, M. A., & Khodagholi, A. (2020). Multi-objective hydro-economic modeling for sustainable groundwater management. *Water Resources Management, 34*(6), 1855–1869.

CRDA. (2018). *Water resources in Mahdia* (pp. 1–20). CRDA Mahdia, Tunisia.

Dagnino, M., & Ward, F. A. (2012). Economics of agricultural water conservation: empirical analysis and policy implications. *International Journal of Water Resources Development, 28*(4), 577–600.

Esteban, E., & Albiac, J. (2011). Groundwater and ecosystems damages: Questioning the Gisser-Sánchez effect. *Ecological Economics, 70*(11), 2062–2069.

Expósito, A., Beier, F., & Berbel, J. (2020). Hydro-economic modelling for water-policy assessment under climate change at a river basin scale. *Water, 12*(6), 1559.

Frija, A., Dhehibi, B., Chebil, A., & Villholth, K. (2015). Performance evaluation of groundwater management instruments: The case of irrigation sector in Tunisia. *Groundwater for Sustainable Development., 1*, 23–32.

Gisser, M., & Sánchez, D. A. (1980). Competition versus optimal control in groundwater pumping. *Water Resources Research, 31*, 638–642.

Grossmann, I. (2021). *Advanced optimization for process systems engineering*. Cambridge University Press.

MacEwan, D., Cayar, M., Taghavi, A., Mitchell, D., Hatchett, S., & Howitt, R. (2017). Hydroeconomic modeling of sustainable groundwater management. *Water Resources Research, 53*(3), 2384–2403.

Soula, R., Chebil, A., McCann, L., & Majdoub, R. (2021). Water scarcity in the Mahdia region of Tunisia: Are improved water policies needed? *Groundwater for Sustainable Development, 12*, 100–510.

Understanding the Value of Water—a Comparison Between Policy and Public Attitudes in Saudi Arabia and Ireland

Omar K. M. Ouda and Stephen J. McIlwaine

Abstract

With annual average rainfalls of 59 mm and 1180 mm respectively, the difference in renewable water availability between Saudi Arabia and Ireland is stark. For both countries, until recently, the price of water for domestic consumers has been zero or almost zero. Per capita water usage was high, and the cost of providing the supply was heavily subsidised by the government. To recover some of the supply costs and address the financial shortfall suffered by water utilities, a new tariff for household water was introduced in Ireland in 2014 and in Saudi Arabia in 2015. In both countries, the public was unprepared for the price increases, which led to significant public opposition, revealing a lack of appreciation of the value of water and the cost of supply. This paper examines the history around low domestic water prices in Saudi Arabia and Ireland, and the public responses to the recent price increases. It highlights warnings from economic theory that when water is undervalued, both its allocation and its use will be inefficient. It argues that a more comprehensive public understanding of the value of water must be developed to ensure that consumers are willing to pay to cover the cost of supply. The experience of water pricing from water-stressed countries such as Saudi Arabia, is helpful for less water-stressed countries facing new situations of climate-change-induced scarcity, and higher costs of supply.

Keywords

Water tariff • Socio-economic impact • Public attitudes • Public water resources • Saudi Arabia • Ireland

O. K. M. Ouda
National Centre for Water Research and Studies, Ministry of Environment, Water and Agriculture, Riyadh, Saudi Arabia

S. J. McIlwaine (✉)
School of the Natural and Built Environment, Queen's University, Belfast, UK
e-mail: s.mcilwaine@qub.ac.uk

1 Introduction

With an average annual rainfall of around 59 mm per year, Saudi Arabia has one of the lowest rates of renewable water availability in the world. Its total renewable resource is estimated at 6.2 billion m^3/year (Ministry of Environment, n.d.), which for a population of 34.2 million people, amounts to 181 m^3 per person per year. At the other extreme, with an average annual rainfall of around 1180 mm, Ireland has one of the world's highest rates of renewable water availability, estimated at around 13,000 m^3 per person per year (World Resources Institute, n.d.).

For both countries, the price of domestic water has historically been very low. To reduce subsidies yet ensure sufficient revenue to the water utility, both countries recently introduced significant increases in the water price. In each case, this attracted public criticism, forcing each Government to revise plans for the price increase.

Using a qualitative approach, this paper examined the public response to the price rises in these two countries and explained the importance of pricing water at an appropriate level to encourage efficient usage while also ensuring the financial sustainability of the water utility. The paper emphasised the importance of public education for the value of water to ensure consumer acceptability of the prices needed to cover the costs of the service.

2 Water Pricing in Saudi Arabia

Domestic water pricing was first introduced in Saudi Arabia in 1994. Price levels were very low and provided a revenue which contributed to only around 7% of the cost of the service (Ouda, 2013). This was financially unsustainable and put significant pressure on the country's public finances. In 2015, in response to a new Government initiative to reduce subsidies to public services, a new tariff structure for domestic water was introduced. This significantly increased

A. Kallel et al. (eds.), *Selected Studies in Environmental Geosciences and Hydrogeosciences*, Advances in Science, Technology & Innovation, https://doi.org/10.1007/978-3-031-43803-5_53

most household water bills, with the bill for a typical household usage rising 16-fold for usage of 50 m^3/month, and 29-fold for monthly usage of 100 m^3. The new tariff was estimated to recover around 30% of the cost of supply (McIlwaine et al., 2020).

There was significant public unease at these new prices, unprecedented in the Kingdom, with consumers complaining vocally that the new prices were unfair and were introduced without warning. The Government moved quickly; the minister of water and electricity and the chief executive officer of the National Water Company were replaced, and an announcement was made that a new publicly acceptable tariff would be developed, (5). Water price regulation was transferred to the Electricity and Cogeneration Regulatory Authority. Although the new tariff has been retained in the interim, a study has been commissioned into developing a new tariff regime which would be publicly acceptable while still achieving the aim of recovering costs from consumers (McIlwaine et al., 2020).

3 Water Pricing in Ireland

Between 1977 and 1983, Ireland had no domestic water charge. A tariff was introduced in 1983 and abolished in 1997, and the service became fully subsidised (Zhao et al., 2012). Domestic water charges were reintroduced in 2015 as part of wider reforms of the water sector (Brady & Gray, 2017). One impetus for this was the need to address public sector funding constraints following the financial crash of 2008 and the resulting EU/IMF bailout.

Even early proposals on the reintroduction of a domestic water charge were unpopular and politically contentious. The public was concerned that charges would disproportionally impact low-income households, and would lead to privatisation of the service (Zhao et al., 2012). Mass protests were held in November 2014 in anticipation of the announcement of new charges and repeated again in January 2016. The water protests were 'the single largest protest the country has experienced in recent history' (Brady & Gray, 2017). Following such vocal resistance, the charges were first suspended and then cancelled. A new proposal has been published whereby domestic customers will be billed only for excess household usage, from 2022 onwards (Irish Water, 2020).

4 Discussion

4.1 Understanding the Public Response

The opposition to new water charges can be explained by examining the concept of willingness to pay (WTP) against the background of historically low prices. Without monthly water bills, consumers do not appreciate the costs of supply of a good perceived to be free. In Saudi Arabia, consumers had come to expect Government services to be provided at no cost (Jawadi & Ftiti, 2019). For Ireland, 'water charges have historically been viewed as politically unpalatable and there has been a general lack of both public and political will for their introduction' (Brady & Gray, 2017). Where consumers have no understanding of the value of water, their WTP is low, and, when a new tariff that exceeds WTP is introduced, consumers will resist paying it. WTP in both countries must therefore be increased if the new tariffs are to become acceptable.

4.2 The Importance of Charging for Water

Water utilities in both countries need to recover more of the cost of supply in order to finance new investments in the water systems. For Saudi Arabia, the fall in oil prices in 2015 saw the public deficit rising to 16% (Jawadi & Ftiti, 2019) and this is currently growing due to the ongoing global coronavirus pandemic. To address this, the Government needs to reduce public service subsidies and recover more the costs of supply from consumers. The stark imbalance between renewable supply and increasing demand has also led to the development of expensive sources such as deep groundwater and desalinated seawater, which increases the operating costs (Ministry of Environment, n.d.). For its part, Ireland has seen historic underinvestment in the water service (Brady & Gray, 2017; Murray, 2012). In 2011, an estimated several billion euros was needed to meet the full costs of upgrading the water and wastewater services to comply with EU requirements (Brady & Gray, 2017). The reforms of 2014 were designed to address this funding gap and encourage new investment. Irish Water's new business plan sees € 5.5 Billion needed to bring the system and service to an acceptable level (Irish Water, 2021).

A second crucial benefit to charging for water is that its price affects usage. Economic theory suggests that demand for a good decreases as the price rises. For domestic water supply, this is true at higher levels of usage, but is known to be less so at lower levels of consumption, since a minimum amount of water is necessary for survival. For moderate levels of household usage, when water is cheap or free, demand is unconstrained and consumers use more than they need (McIlwaine et al., 2020).

So where the price of water has been low—e.g. in Saudi Arabia and Ireland—consumers do not appreciate the costs which go into its production, distribution, and supply. The breaking of the link between the service and the payment means that consumers are less likely to be aware of water

conservation or efficiency, and less likely to address excess demand (Murray, 2012). With low water prices, consumers are less likely to care about water conservation, which suggests that the introduction of metered water charges is a necessary component to encouraging water efficiency. In fact, the use of high water tariffs to reduce demand is one of the most common tools used in the EU (Lu et al., 2019).

5 Conclusion

Raising the price of domestic water to levels approaching the socio-economic costs of supply is necessary to help moderate excessive demand, and reduce subsidies. However, in both water-stressed and water-abundant countries, consumers used to low prices for water, need to be engaged within an open and honest way, and provided with clear arguments on the costs of supply, while also addressing affordability for low-income users, and ensuring a quality service.

Both Saudi Arabia and Ireland have taken steps to address public opposition to sudden price rises, by moderating their original proposals. Both countries have recognised that better public communication is needed to explain the cost of providing a quality service. New prices need to be explained and justified, and experience of other countries which have already adjusted their tariffs can inform policymakers.

References

Arabian Business, New Saudi minister to set 'affordable' water tariff, May 17, (2016). https://www.arabianbusiness.com/new-saudi-minister-set-affordable-water-tariff-631981.html. Accessed October 30 2020.

Brady, J., & Gray, N. F. (2017). Reform of the Irish water sector: opportunities and challenges. In *Proceedings of the institution of civil engineers, water management* (Vol. 170, pp. 165–174).

Irish Water. (2020). https://www.water.ie/conservation/household-conservation/. Accessed October 30 2020.

Irish Water. Irish water business plan: transforming water services in Ireland to 2021. https://www.water.ie/docs/Irish-Water-Business-Plan.pdf. Accessed October 30 2020.

Jawadi, F., & Ftiti, Z. (2019). Oil price collapse and challenges to economic transformation of Saudi Arabia: A time-series analysis. *Energy Economics, 80*, 12–19.

Lu, L., Deller, D., & Hviid, M. (2019). Price and behavioral signals to encourage household water conservation: Implications for the UK. *Water Resources Management, 33*, 475–491.

McIlwaine, S. J., & Ouda, O. K. M. (2020). Drivers and challenges to water tariff reform in Saudi Arabia. *International Journal of Water Resources Development*.

Ministry of Environment, Water and Agriculture, Saudi National Water Strategy (2030).

Murray, K. (2012). The water funding gap in Ireland. *Proceedings of the Institution of Civil Engineers, Management, Procurement and Law, 165*, 173–179.

Ouda, O. K. M. (2013). Review of Saudi Arabia municipal water tariff. *Journal of World Environment*, *3*(2), 66–70.

World Resources Institute, World Resources 2005—The wealth of the poor: Managing ecosystems to fight poverty, (2005).

Zhao, Y. Q., & Crosbie, D.: Water pricing in Ireland: a techno-economic and political assessment. *International Journal of Environmental Studies*, *69*(3), 427–442.

Rainwater Conservation and Its Viability in the Semi-Arid City: A Case of Ahmedabad, India

Mona Khakhar and Keshvi Ahir

Abstract

In arid and semi-arid regions, the availability of adequate water of appropriate quality has always remained a challenge in different parts of the world. With less water available per person in such areas, it is of utmost importance that rainwater harvesting (RWH) practices are adopted. Further, with water resources under tremendous pressure due to the growing population and the effect of climate change, RWH is an important measure to reduce the load on the central water supply system and satisfy the majority of the water requirements at the decentralized location. The present research involves some residential projects such as individual houses (bungalows) and row houses with RWH and rainwater recharging practices. The study assessed the potential of the RWH or recharging system to meet occupants' water requirements for various activities. The research showed that 61–80% of the total water requirement for bungalows and 5–7% for the row houses could be met if full potential of the terrace catchment in the residential premises to harvest rainwater was considered. The study demonstrated that the annual drinking and cooking water requirement can be fully satisfied by the harvested rainwater for all the studied residential units. Lastly, the study inferred that per person catchment/terrace, an area of 86.26m^2 is required to meet the total water demand. In contrast, it is 3.19 m^2 for drinking and cooking water demand.

Keywords

Rainwater harvesting • RWH • Rooftop • Recharging • Residential • India

1 Introduction

In arid and semi-arid regions across the world, the availability of a sufficient quantity and quality of water has always been a challenge. Nevertheless, this trend is expected across the world due to the increased use of resources and the rising population. As per World Water Development Report (2018), 3.6 billion people worldwide are already living in potential water-scarce areas at least one month per year and this could increase to some 4.8–5.7 billion in 2050. About 73% of the affected people live in Asia (69% by 2050). With this scenario, it is of utmost importance that alternative water sources are thought out and created. Rainwater Harvesting (RWH) is one of the promising ways to address the issue of water scarcity and the looming effects of climate change (Sendanayake, 2016). Evidence of the use of RWH techniques is found in many countries around the world, such as India, Jordan, Palestine, Syria, Tunisia, and Iraq (Agarwal and Narain, 1997; CGWB, 2011; Al-Adamat, 2008).

Ahmedabad is the largest city in the Gujarat state and the seventh-largest city in the country, with a population of 7.2 million in a semi-arid region (District Ahmedabad, 2020). The city has many ancient examples of RWH practices in the old city area, indicating the existence of such practices since olden times, which has helped the community to reduce reliance on the centralized water distribution systems.

The average annual rainfall in the Ahmedabad district is 714 mm as per (GSDMA, 2018). Besides, at the annual scale, the maximum number of dry days is between 306.2 and 319 days as per the Indian Meteorological Department (2020). With this climate and population conditions, the city of Ahmedabad happens to be the most appropriate case for such a study. Further, very few studies related to the RWH/recharging other than the old city have been reported. This research intended to study various modes of RWH/recharging practices in different housing types in Ahmedabad. This is the most crucial aspect since the

M. Khakhar (✉) · K. Ahir
CEPT University, Ahmedabad, Gujarat, India
e-mail: mona.khakhar@gmail.com

A. Kallel et al. (eds.), *Selected Studies in Environmental Geosciences and Hydrogeosciences*,
Advances in Science, Technology & Innovation, https://doi.org/10.1007/978-3-031-43803-5_54

installation of RWH systems in the individual housing units depends on the awareness, attitude, and/or perception of the user/occupant as noted by (Ward et al., 2008; Islam et al., 2011; Barthwal et al., 2014). The present research focused on the four case studies involving individual houses (bungalows) and rows of houses out of the total eight cases achieved as a part of the research.

2 Methodology

The cases for this research include the residential buildings with the RWH systems for the last 20 years and the more recently achieved to give a spectrum of the system functioning and the user/occupant perspective on maintaining the system. The residential buildings with at least two samples of the same type and scale were selected to draw some comparable conclusions. The method involves site visits and a questionnaire to study the quantitative aspect of onsite conditions and the qualitative aspect of user awareness and attitude (Barthwal et al., 2014; Dutta, 2005). The site visit involved measurements of the premises with individual types of catchment areas and the type of water harvesting/recharging practice, storage sizing/capacity, type of end-use, and the period of water availability for various activities. The study also involved a questionnaire to understand the various types of activities and water demand of the harvested rainwater, maintenance schedule and cost, capital expenditure, and the attitude and experience of using the RWH system by the user/occupants. The data regarding these water practices were compiled to analyze and determine the reliability of these systems from the user/occupant perspective.

3 Results

3.1 Quantitative Aspects

The study included the two bungalow units and two row house units as cases in western Ahmedabad. The individual bungalow No. 1 has been harvesting rainwater since 2015, while bungalow No. 2 has harvested rainwater since 2006. The row house no. 1 has harvested rainwater since 2001 while the row house no. 2 has harvested rainwater since 2003. The schematic rainwater harvesting system in the residential units is as shown in the Fig. 1.

To derive the results in Table 1, the annual average rainfall for Ahmedabad was considered to be 714 mm (GSDMA, 2018), and the runoff coefficient for different surfaces was adopted as recommended by CPCB (2016). The total domestic demand of 135 lphd was adopted as per NBC (2016). The drinking and cooking water demand was assumed to be 5 lphd based on a survey of the residents of the case study. As indicated by the results in the table, it may be noted that if the residential unit made use of the full potential of their premises to conserve rainwater such that all the possible rainwater falling in their property is either recharged or harvested, then 86–118% of the total water requirement would be satisfied for the individual bungalow units. In comparison, due to the small footprint, the row houses can make up to 6–8%. However, if the full potential of rooftop rainwater was executed, the bungalow units would be capable to meet 61–80% of their total water demand compared to row houses that could meet 5–7% of its total water demand. For the present study, as per the actual provision of the storage tank for rooftop rainwater, it is seen that the rooftop rainwater meets 61 and 9% of the total water demand for bungalow no. 1 and bungalow no. 2 respectively. The occupants of the bungalow no. 2 had consciously made provision for storage of rooftop rainwater required only for drinking and cooking purposes. The actual storage for rooftop rainwater in row houses was able to cater to 4% of the total water demand as compared to the bungalows. This was attributed to the smaller terrace catchment area and the smaller storage capacity.

Further, it is observed that 100% of the water required for drinking and cooking for the entire year is satisfied for all the cases with the actual provision of storage for the rooftop rainwater. For bungalows, it is 1643–2160%, while for row houses, it is 131–176% of drinking and cooking water requirement. Besides, for bungalow no. 1, the excess rainwater generated from the premises is discharged into the municipal drainage system while for bungalow no. 2 and both of the row houses the excess runoff from the premises recharges the common recharge well of the housing society. Thus, considering the runoff contribution from the premises toward recharge in the common society bore well, it can be said that for bungalow no. 2 and both row houses, 100% of the water conservation is possible. In contrast, for bungalow no. 1, it is just 52%.

Additionally, considering 135 lphd demand for domestic water as per NBC (2016), it was deduced that a catchment area of 86.26 m^2 is required per person to meet the total water demand for the entire year in Ahmedabad. Besides, the area required per person per year for drinking and cooking water demand is 3.19 m^2 for this city. Validating this information for all the case studies, it was observed that 69m^2 terrace catchment area is available per person for bungalow no. 1 while 52.5 m^2 for bungalow no. 2. In contrast, for row houses no. 1 and no. 2, it is 4.3 m^2 and 5.6 m^2, respectively. It can be inferred that a 100% demand for water will not be met from the rooftop rainwater harvesting for any of the cases. In contrast, all will quickly meet the drinking and cooking requirements for the year.

Table 1 Observations and estimations for the RWH for various residential units

Criteria	Bungalow no. 1	Bungalow no. 2	Row house no. 1	Row house no. 2
Number of residents	5	8	6	4
Total site area (m^2)	960	1140	40.2	34.5
Terrace area (m^2)	345	420	25.2	22.5
The volume of rainwater that can be captured from the terrace (m3) (*a*)	197.06	239.90	14.39	12.85
Paved surface area (m^2)	150.00	120.00	8.00	12.00
The volume of rainwater that can be captured from the paved area (m^3) (*b*)	42.84	34.27	2.28	3.43
Unpaved surface area (m^2)	465.00	600.00	7.00	0.00
Volume of rainwater that can be captured from unpaved area (m^3) (*c*)	49.80	64.26	0.75	0.00
Total volume of potential rainwater that can be captured from the whole site (m3) ($a + b + c$)	289.71	338.44	17.43	16.28
Drinking/cooking water requirement for the year (m^3)	9.13	14.60	10.95	7.30
Total water requirement for the year (m^3)	246.38	394.20	295.65	197.10
% of water demand that can be satisfied by potential rainwater that can be conserved from the entire site	118%	86%	6%	8%
% of water demand that can be met by potential roof rainwater	80%	61%	5%	7%
% of cooking/drinking water demand that is met by harvested potential rainwater from the terrace	2160%	1643%	131%	176%
The actual volume of rainwater harvested (m^3)	150.00	36.00	13.00	7.00
The volume of rainwater recharged (m^3)		302.44	4.43	9.28
% of water demand that can be met by actually stored/conserved roof rainwater	61%	9%	4%	4%
% of cooking/drinking water demand that is met by actually stored/conserved roof rainwater	1644%	247%	119%	96%
The total volume of rainwater conserved (m^3)	150.80	338.44	17.43	16.28
% of potential exploited	52%	100%	100%	100%

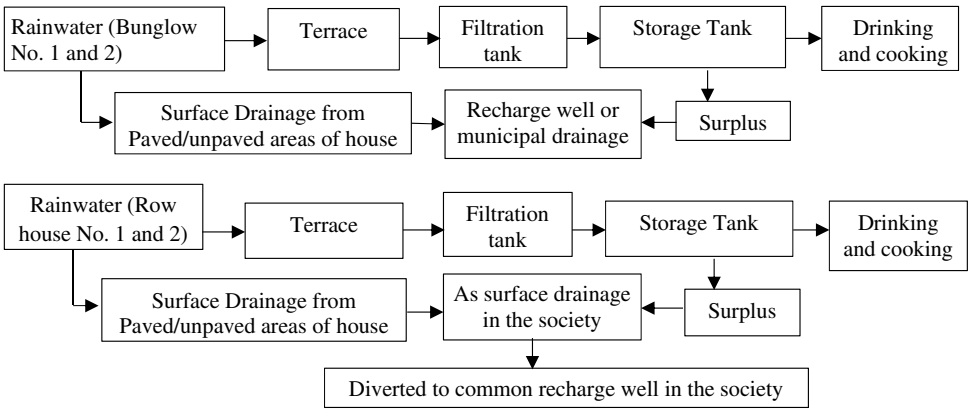

Fig. 1 Schematic rainwater harvesting/recharging system in residential units

3.1.1 Cost

The installation cost for the RWH system is one of the essential governing criteria that will determine the user's decision for investment in such a system. The study has made an effort to present the actual installation and maintenance costs for the RWH systems. The range of costs for the various case studies highlights that such a system may not be an economic burden with the increase in the number of years after installation and the benefit of the quantity and quality of water it provides. The Table 1 below shows the installation and maintenance costs for all the studied cases. The maintenance of this system includes cleaning the

Table 2 Cost of installation and maintenance

Criteria	Bungalow no. 1	Bungalow no. 2	Row house no. 1	Row house no. 2
Conserving rainwater since	2015	2006	2001	2003
Installation cost for the rainwater harvesting/recharging system (₹)	1,60,000	1,80,000	12,500	1300
Construction cost of reinforced cement concrete (RCC) storage tank	15,00,000	2,88,000	91,000	49,000
The actual volume of rainwater harvested (m^3)	150.00	36.00	13.00	7.00
Total water harvested for a life span of 40 years (m^3)	6000	1440	520	280
Total installation cost (including RCC storage tank) per liter	0.28	0.33	0.20	0.18
Annual Maintenance cost (₹)	1500	1500	500	200
Annual Maintenance cost per liter (₹)	0.010	0.042	0.038	0.029
Installation and maintenance cost per liter (₹)	0.287	0.367	0.238	0.208

filtration tank and media, replacement of filter media if needed, cleaning the terrace area, minor repairs, and clearing the choked pipes.

From the above table, the maximum installation and maintenance cost per liter is ₹0.4, while the minimum is ₹0.2, which is very nominal and affordable. This indicates that the perception and/or awareness are the important factors that need to be addressed more predominantly so that a greater number of households adopt RWH practices.

3.2 Qualitative Aspects

As a part of the study, effort was made to understand the attitude and perception of the users with respect to rainwater harvesting system. It was found that occupants in all the cases were able to harvest sufficient water for drinking and cooking from the rooftop. The harvested water required only Ultra Violet (UV) treatment before use. One of the respondents of the row house no. 2 also shared the reduction in cooking time as compared to groundwater which they previously used. It may be noted that municipal water supply in the city of Ahmedabad is from surface water. However, it is not enough to meet the water demands. The citizens, therefore, use private bore wells at greater depths. The water from such depths has high total dissolved solids (TDS) and is sometimes brackish (Khakhar et al., 2017; Gupte, 2011). This water has high TDS of the order of 2000 mg/l or more (Khakhar et al., 2017) and requires reverse osmosis treatment. The occupants did not perceive and experience any problem concerning maintaining the RWH system as they valued the harvested water quantity and quality. The users appreciated the harvested water quality as compared to the groundwater with high TDS from the bore well. All the residents opined to have a compulsory RWH system. The occupant from row house no. 1 shared a critical observation about the need for some incentives/measures from the Government that may help citizens to implement and maintain the RWH system actively. Such incentives would especially encourage all those who do not understand the merits of rainwater harvesting and hence are unwilling to invest in it.

4 Discussion

There are ample benefits of water conservation through the RWH system that range from good quality and quantity of water to suffice the year-round drinking and cooking needs as experienced by all the occupants studied in this research. Besides, it also helps in recharging the aquifers during monsoon season, which can be later used during the dry period of the year. As shared by the respondents from the row house society, the people were required to deepen the society bore well since the groundwater levels had gone deeper. After the installation of the common society recharge well, the need for further deepening of the bore well in the later years did not arise.

Despite positive experience by people, RWH/recharging is not widely implemented in most of the residential projects, including the more recent ones. The stake-holders are not willing to invest in such systems for various reasons that may be attributed to the capital and maintenance costs, awareness and willingness to have such facilities on their premises and the perception of maintenance to be a botheration/burden (Dutta, 2005; Domenech and Sauri, 2011; Barthwal et al. 2014). The study reveals the need for more similar studies that may formally bring forward the tangible and intangible benefits of RWH and the relative investment and maintenance cost of such systems. This will contribute to bringing awareness in the masses and help to positively influence the investment for the RWH in residences.

5 Conclusion

The study deduced that generally the drinking and cooking water requirement for the whole year could be availed from the harvested rainwater for the residential case studies undertaken in this research. Further, it was found that a substantial amount of annual water demand was met from the harvested rainwater for the individual bungalow units as compared to the row houses for the semi-arid city of Ahmedabad. The smaller amount of annual water availability for row houses is attributed to the smaller size of the unit, terrace catchment, and the smaller space to build the rainwater storage tank. Thus, it is deduced that for more compact developments such as row houses, the common recharging/harvesting systems at a larger scale of the society may be more beneficial. In addition, the contribution of runoff from all row house units to a common recharging system adequately increases the groundwater level. This subsequently helps in reducing the expenditure to fetch water from deeper aquifers through bore wells as observed in one of the cases.

The calculated estimations indicate that the installation and maintenance cost per liter of harvested rainwater varies in the range of ₹0.2–₹0.4. Despite the reduced costs, the RWH/recharging is not much adopted in most of the projects including the more recent ones due to either lack of awareness or perception of investment and maintenance as an additional burden. Additionally, most people consider the expenditure for such systems with respect to their personal economic benefit and fail to connect with the resource issues experienced by the society/region at large. Therefore, many building owners/builders are not willing to implement RWH/recharging. In conclusion, there is a need for more concrete and scientific demonstrations and documentation of successful RWH/recharging practices and the measured benefits of all aspects so that it appeals to a greater number of the masses to implement such systems. Besides, the policy should mandate the adoption measures with such incentives that would attract more people to implement these measures.

Acknowledgements The authors of the research would like to thank CEPT University for the support and the stipend to the student Ms. Keshvi Ahir, to carry out this research. We are also grateful to all the residents of the units who allowed us to study the buildings and cooperated for providing the information required from them.

References

Agarwal, A., & Narain, S. (1997). *Dying wisdom: rise, fall and potential of India's traditional water harvesting systems.* Centre for Science and Environment (CSE).

Al-Adamat, R. (2008). GIS as a decision support system for siting water harvesting ponds in the Basalt Aquifer/NE Jordan. *Journal of Environmental Assessment Policy and Management, 10*(02), 189–206.

Barthwal, S., Chandola-Barthwal, S., Goyal, H., Nirmani, B., & Awasthi, B. (2014). Socio-economic acceptance of rooftop rainwater harvesting–A case study. *Urban Water Journal, 11*(3), 231–239.

Bureau of Indian Standards. (2016). *National Building Code of India.* BIS.

CGWB. (2011). Select case studies: rain water harvesting and artificial recharge. Ministry of Water Resources.

CPCB. (2016). *Rainwater harvesting in India—An appraisal*. Central Pollution Control Board, Ministry of Environment, Forests and Climate Change.

District Administration Ahmedabad, D. a. (2020, April 24). District Ahmedabad. Retrieved from Administration Ahmedabad. https://ahmedabad.nic.in/demography/

Dome`nech, L., & Saurı´, D. (2011). A comparative appraisal of the use of rainwater harvesting in single and multi- family buildings of the Metropolitan Area of Barcelona (Spain): social experience, drinking water savings and economic costs. *Journal of Cleaner Production*, *19*, 598–608.

Dutta, V. (2005). Public support for water supply reforms in unplanned sector: empirical evidence from an urban water utility. Mimeo, Centre for Regulatory and Policy Research, India Habitat Centre.

GSDMA. (2018). *Rainfall Report.* State Emergency Operation Centre, Revenue Department, Gandhinagar.

Gupte, P.R. (2011). Ahmedabad–Gandhinagar Twin City, Gujarat. In *Central Ground Water Board, Ground water scenario in major cities of India* (pp. 7–17). Central Ground Water Board, Ministry of Water Resources, Government of India, Faridabad.

IMD. (2020). Observed rainfall variability and changes over Gujarat State. India Meteorological Department, Ministry of Earth Sciences.

Islam, M. M., Chou, F. N. F., & Kabir, M. R. (2011). Feasibility and acceptability study of rainwater use to the acute water shortage areas in Dhaka City, Bangladesh. *Natural Hazards, 56*, 93–111.

Khakhar, M., Ruparelia, J. P., Ruparelia, & Vyas, A. (2017). Assessing groundwater vulnerability using GIS-based DRASTIC model for Ahmedabad district, India. *Environmental Earth Sciences*, *76*(12), 440.

Sendanayake, S. (2016). Rainwater harvesting for urban living. South Asian Institute of Technology and Medicine.

UN World Water Assessment Programme The United Nations World Water Development Report 2018: Nature-based Solutions for Water UNESCO, Paris (2018), p. 139.

Ward, S., Butler, D., & Memon, F.A. (2008). A pilot study into attitudes towards and perceptions of rainwater harvesting in the UK. In *10th British hydrological society national hydrology symposium* (pp. 366–372). University of Exeter, 15–17 September 2008.

A Qualitative Assessment of a Hydrometric Network for Monitoring an Integrated Hydropower and Water Supply System

J. Kibiiy and J. Kihamba

Abstract

Timely access to accurate hydro-meteorological information is required for an efficient management of any water project. It is for this reason that water projects have hydrometric networks incorporated in their design. The Thika Dam–Ng'ethu Water Treatment Plant System is an integrated water supply and hydropower project forming part of the water works of the City of Nairobi. It is an inter-basin water collection and transfer system comprising a reservoir and tunnels interlinking four rivers that serve simultaneously as water sources and transmission channels. The hydrometric installations for monitoring the system include water level and flow measuring structures. The main objective of this study was to assess the network for fitness against the stated project objectives and expectations of integrated water resources management (IWRM). The analysis was performed based on operation rules and field observations. The results show that five out of eleven (45%) of the installed flow monitoring stations were in an unsatisfactory condition: three were non-operational for want of maintenance while two did not seem to conform to theoretical principles of flow measurement. Further, it was found that seven out of fifteen (47%) inflow/outflow elements of the system were left out of the monitoring scheme. It was concluded that lack of maintenance and shortcomings in design make the entire network ineffectual and incapable of supporting management based on IWRM. It is recommended that the network be upgraded and installation of an intelligent water allocation and management system be considered.

Keywords

Hydrometric networks • Inter-basin water transfer • Flow measurement

1 Introduction

Fresh water on earth is limited and unevenly distributed. Great efforts and resources must be expended to get it to points of use in adequate amounts. When water is abstracted from a source and conveyed through a conduit for specified end purposes, it acquires additional economic value, becomes finite and must be distributed according to the set objectives. Hydrometric measurements thus become necessary in any water resource system to determine availability, abstraction, transmission and distribution and to provide data and information necessary for an effective management (Stewart, 2015). In many jurisdictions world-over, water rights operate on a permit system in which the right to water use is granted for a specified amount of water to be abstracted from a source. Ecological flows are also catered for in most jurisdictions and must be taken into consideration. Flow measurement is thus crucial in meeting regulatory requirements, allocating water to competing uses and in resolution of disputes. Efficient management of water projects is based on timely access to reliable and accurate information to support decision-making (Basri et al., 2019). It is for these reasons that water projects have hydrometric networks incorporated in their design. The layout of a hydrometric network depends on the objectives set for the project (WMO, 2008). However, a more elaborate design may be needed for optimal network layouts.

The Thika Dam–Ng'ethu Water Treatment Plant System is an integrated water supply and hydropower project forming part of the water works of the city of Nairobi in Kenya. It is an inter-basin water transfer system that taps water from the headwaters of R. Tana and takes it across the

J. Kibiiy (✉)
Department of Civil and Structural Engineering,
Moi University, P. O. Box 3900-30100 Eldoret, Kenya
e-mail: kibiiy@mu.ac.ke

J. Kihamba
Thika Dam, Nairobi City Water and Sanitation Company,
P.O. Box 26-01013 Gatura, Kenya

A. Kallel et al. (eds.), *Selected Studies in Environmental Geosciences and Hydrogeosciences*,
Advances in Science, Technology & Innovation, https://doi.org/10.1007/978-3-031-43803-5_55

water divide into R. Athi basin. It is a water collection and transfer system comprising a dam reservoir and two tunnels interlinking four rivers (Thika, Kiama, Kimakia and Chania) that serve as water sources. A schematic layout of the system is illustrated in Fig. 1. One of the rivers (R. Kiama) also serves simultaneously as a transmission channel linking the two tunnels. It is a fairly complex integrated project for harnessing and conveying water connecting four rivers. Thika Dam is connected to Ng'ethu Water Treatment Plant (WTP) through two tunnels running in series. Water is drawn off the reservoir through a powerhouse into a 960-m tunnel discharging into a tributary of R. Kiama (AWSB, 2018). The hydropower station is not operational at the moment. The water then flows downstream for about 450 m where a weir on the river diverts the water into a second tunnel. Additional water is abstracted from the river. The tunnel runs 3370 m and discharges into R. Chania. The tunnel passes below R. Kimakia. A weir on R. Kimakia diverts water into the tunnel through an intake shaft. The water flows along the Chania up to Mwagu Weir where it is abstracted into Ng'ethu WTP.

The main objective of this study was to assess the operational level of the installed hydrometric network against the project objectives and the ideals of integrated water resources management (IWRM) (UNWWAP et al., 2009) and to subsequently suggest ways of improving operations. This assessment is essentially a health audit of the system and is very important in view of many similar water supplies across the country and world-over.

2 Methodology

Field observations, project materials and information from staff provided an insight into the operations and management of the System. An assessment was conducted for the ability of the network and its individual installations to meet the project objectives and the network's ability to address IWRM expectations. The hydrometric stations were rated as satisfactory or unsatisfactory based on their operational status. The rating 'satisfactory' was given to stations deemed to be serving the intended purpose and 'unsatisfactory' to those that were not operational or not generating useful data. The network was checked for its ability to address the needs of other stakeholders by accounting for all inflows and outflows of the System.

2.1 Assessment Criteria and Approach

The assessment was conducted for the ability of the network and its individual installations to meet the stated project objective.

A set of three criteria was used: first, project objectives; second, operation rules; and third, theoretical aspects in flow measurement. For each criterion, a hydrometric station was rated as satisfactory or unsatisfactory based on the adjudged status. The rating 'satisfactory' was given to stations found to be generating useful data while 'unsatisfactory' was given to those that were not operational or defective in design and

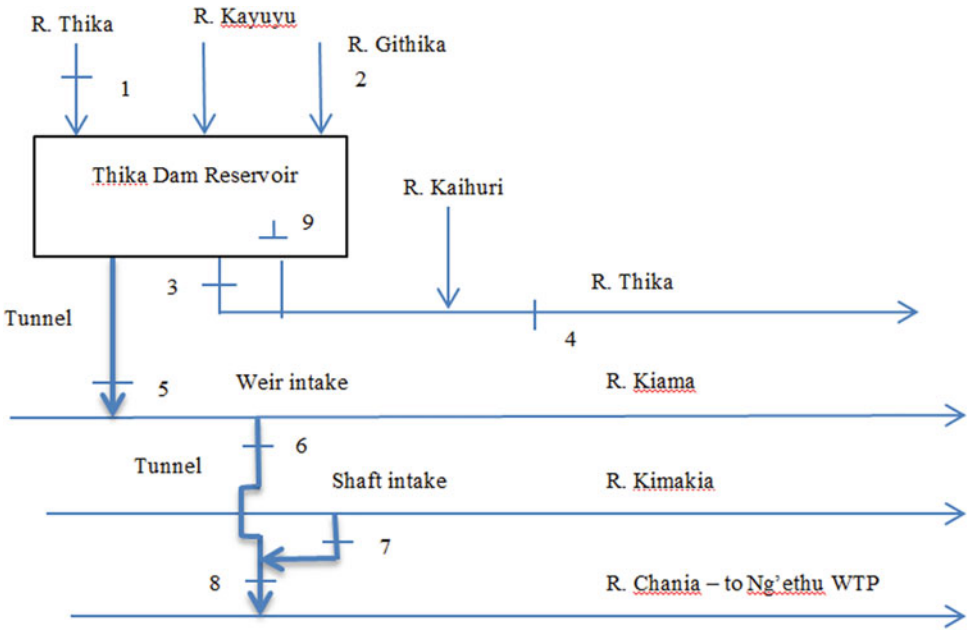

Fig. 1 Thika Dam–Nge'thu WTP System (No. 1–8 are the existing flow measuring stations; No. 9 is water level gauging)

thus generating data of questionable integrity. Because of the multiple criteria, it was necessary to ensure that the final analysis outcome for each station was mutually exclusive and collectively exhaustive, a concept borrowed from logic and probability theory (Guerrero, 2019). The outcomes are mutually exclusive because a station can belong to only one of the two categories, either satisfactory or unsatisfactory. If a station returns 'unsatisfactory' in one criterion, it will have an overall result 'unsatisfactory' irrespective of the returns of the other two criteria. The overall outcome of a station is considered collectively exhaustive because it captures the result of the combined criteria in all the possible outcomes (only two in this case), namely satisfactory or unsatisfactory.

2.2 System Analysis

For ease of analysis, the Thika Dam-Ng'ethu WTP System was represented as a system consisting of storage elements and transfer elements. This is depicted in Fig. 2. The circles represent storage elements while the lines represent the transfer elements. The storage elements are places that receive inflows and from where water is abstracted into the System. The storage elements are the Thika Dam Reservoir and those points on R. Kiama and R. Kimakia from where water is abstracted into the System. The transfer elements are transmission channels connecting the storage elements. These include inflows into Thika Dam Reservoir, the two tunnels and all the rivers upstream and downstream of intakes. The system has fifteen transfer elements; eight elements are monitored (flow measurement stations) numbered 1–8 in Fig. 2 and seven (flows) elements are unmonitored marked by letters *a*–*g*.

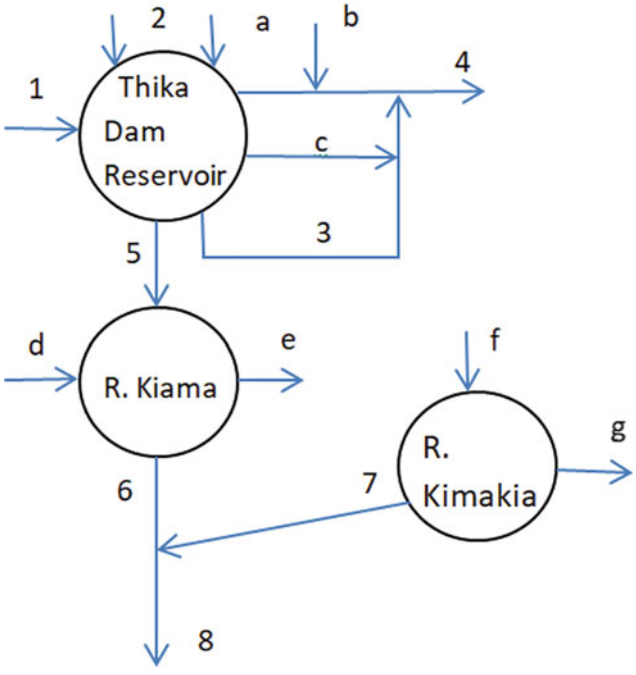

Fig. 2 Flow monitoring points (No. 1–8) and unmonitored points (a–g) on Thika Dam–Ng'ethu WTP System

3 Results and Discussion

The assessment flagged out incomplete monitoring due to omission of potential stations in the network; unscientific flow measurement in some stations due to non-conforming design and construction; and maintenance challenges.

It was found that approximately 56% of all the existing hydrometric stations (five of nine) were in an unsatisfactory condition because they were either in a state of disrepair or were incapable of scientific measurement of flow. Considering flow measurement in particular, four of the eight existing flow measuring stations (50%) were found to be unsatisfactory because they were in a state of disrepair and three of the five existing telemetric flow measuring installations (60%) were not functional. The stations in the network appeared not to have benefited from any maintenance attention for a long time. Rusting was a common problem affecting staff gauges and steel gates at the weirs. Further, it was found that the hydrometric network was inadequate because some streams flowing into and out of the system were not being monitored because they were not included in the monitoring plan. Seven of the fifteen inflow/outflow elements in the system (Fig. 2) constituting ≅ 47% were not included in the monitoring network. This omission may be attributed to the rather narrow project objective which sets out to have 100% water demand of Ng'ethu WTP met without taking into consideration the requirements of other water users downstream. The state of the network is typical of many in developing countries where the status of hydrological services is characterized by a fragmented policy environment, insufficient budget, inadequate maintenance and lack of qualified personnel (World Bank, 2018). An ideal network should meet minimum national and international standards (WMO, 2008; Mishra and Coulibaly, 2009).

The system is an intra-basin water transfer system within the upper Tana basin and at the same time an inter-basin water transfer system from the Tana to the Athi basin. Given that the flow gauging stations in the system are not functioning effectively, the Mwagu Weir is the only point at which the project objective of getting 100% demand for Ng'ethu WTP is monitored. Considering that the system is a complex one consisting of numerous hydrometric stations and comprising both intra- and inter-basin water transfers and a potential hydropower station, the installation of an

intelligent water allocation and management system should be considered. An upgraded hydrometric network would collect and transmit data in real time and allow water to be distributed according to the determined allocations intra- and inter-basin.

4 Conclusion and Recommendations

Assessment of the hydrometric network for the Thika Dam —Ng'ethu WTP System was made to determine its effectiveness based on a set of three criteria. The identified gaps can be attributed to shortfalls in project design and to lack of effective maintenance.

It is recommended to retrofit and calibrate all stations to operate on sound theoretical basis and best practice. The network should be enhanced so that it can monitor all inflows and outflows in the System. This would enable a management based on integrated water resources management (IWRM) principles. A feasible repair and maintenance programme is necessary to ensure uninterrupted timely monitoring and flow of hydrometric data and information. This assessment was limited to the state of the hydrometric installations in the Thika Dam–Ng'ethu WTP System.

References

Athi water Services Board (AWSB). (2018). Operation rules of Thika Dam. Feasibility study and master plan for developing new water sources for Nairobi and satellite towns, Ministry of water and Irrigation.

Basri, H., Mohd Sidek, L., Abdul Razad, A. Z., Mohd Salleh, S. R., Kamarulzaman, M. S., & Pokhrel, P. (2020). Performance of operational inflow forecasting system for hydropower reservoir. In: L. Mohd Sidek, G. Salih, & M. Boosroh (Eds.) *ICDSME 2019. Water resources development and management*. Springer. https://doi.org/10.1007/978-981-15-1971-0_14

Guerrero, H. (2019). *Excel data analysis. Modelling and simulation* (2nd ed.). Springer Nature Switzerland.

Mishra, A., & Coulibaly, P. (2009). Developments in hydrometric network design: a review. *Reviews of Geophysics*, *47*, RG2001. https://doi.org/10.1029/2007RG000243

Stewart, B. (2015). Measuring what we manage—the importance of hydrological data to water resources management. In *Proceedings of the 11th Kovacs Colloquium* (Vol. 366). IAHS Publ. https://doi.org/10.5194/piahs-366-80-2015

United Nations World Water Assessment Programme, DHI Water Policy, UNEP-DHI Centre for Water and Environment. Integrated Water Resources Management in Action (2009).

World Meteorological Organization (WMO). (2008). *Guide to hydrological practices hydrology—from measurement to hydrological information* (Vol. 1, No. 168, 6th ed.). World Meteorological Organization.

World Bank. (2018). *Assessment of the state of hydrological services in developing countries*.

Estimation of Peak Discharge by Slope-Area Method for a Channel Reach Encompassing a Bridge

Joel Kibiiy and Wangai Ndirangu

Abstract

The slope-area method is used in estimating flood peak discharge at un-gauged sites or when flows exceed the maximum stage at a gauged site. The method is based on the concept of uniform flow and requires a channel reach which is fairly straight and uniform, free from falls or any features that could generate non-uniform flow patterns. However, it is not always possible to find a suitable channel reach. In this study, a flood peak discharge is estimated using a channel reach encompassing a bridge that was overtopped in the flood. A review of the literature shows that for flows under a bridge, the effect of the constriction by the bridge piers on the flow extends for distances between one and two times the bridge opening before uniform flow is re-established. No reference was found for situations when the bridge has been submerged. It was surmised that its effect was to contribute to increased flow resistance and reflected in a new steeper slope of the water line. Field measurements and an existing flow rating curve were used to calculate the peak discharge. Uncertainty in the calculated discharge was estimated at 22% by performing a first-order analysis of variance on Manning's equation with discharge as the principle variable, thus yielding a discharge of 7076 $\pm$ 1557 m^3/s. Studies are recommended to verify the estimated discharge and to establish the impact of riverine structures such as bridges on flow patterns and on the slope-area method.

Keywords

Slope-area method • Channel reach encompassing a bridge

1 Introduction

The slope-area method is used for the estimation of flood peak discharge at un-gauged points on a river (French, 1988; Patra, 2011) or when flows exceed the maximum stage at a gauged site. The use of this method requires a channel reach that is fairly straight and uniform—free from constrictions, expansions, jutes, or falls—in order to facilitate accurate measurement of the slope (Dalrymple and Benson, 1976). These requirements refer to natural channel conditions and do not envisage the presence of a structure such as a culvert or bridge that introduces constrictions and flow patterns undesirable for the slope-area method. In this paper, the slope-area method was used to estimate flood peak discharge on a channel reach encompassing a bridge that was overtopped and submerged—a situation that was not foreseen in the development of the method, and probably also, unprecedented in its application.

The aim of this study was to estimate the magnitude of the peak discharge of an extremely high flood that occurred on 24th of April 2018 in Athi River, Kenya, using the slope-area method on a channel reach encompassing the Kiaoni Bridge which was submerged. The site was the best option under prevailing circumstances.

2 Literature Review

The slope-area method is based on the concept of uniform flow. It assumes that the change in stage of the flood hydrograph is so gradual that the friction slope is the result of boundary friction alone (French, 1988; Chow, 1959). This

J. Kibiiy (✉)
Department of Civil and Structural Engineering, Moi University, P. O. Box 3900-30100 Eldoret, Kenya
e-mail: kibiiy@mu.ac.ke

W. Ndirangu
Department of Civil, Construction and Environmental Engineering, Jomo Kenyatta University of Agriculture and Technology, P.O. Box 62000-00200 Nairobi, Kenya

A. Kallel et al. (eds.), *Selected Studies in Environmental Geosciences and Hydrogeosciences*, Advances in Science, Technology & Innovation, https://doi.org/10.1007/978-3-031-43803-5_56

assumption is justified for this study given the large size of the catchment (20,216 km^2), and that the discharge is the response of the river system to the gradual input by precipitation in the catchment, as opposed to a dam break. The slope-area method is an approximate method for estimating peak discharge after the event.

The magnitude of a flood is estimated from the extent of inundation (Ackers, 1991). It uses the observed slope of the waterline and a flow resistance equation such as the Chezy or Manning equation to estimate the discharge. When a flood recedes, it leaves behind the remains of vegetative matter such as grass, straw, or leaves at the extremities of its extent on the flood plain. These form the high water marks of the flood (Benson & Dalrymple, 1976) that are used to determine the slope of the flood water.

The piers of a multi-span bridge have the effect of reducing the channel cross section, thus forming constrictions. Near a constriction, starting at a distance between one and two times the opening width upstream from the centre of the opening (Chow, 1959), the central body of water begins to accelerate while deceleration takes place along the outer boundaries. As the water passes through the contraction, the stream reaches a minimum depth at the piers similar to the *vena contracta* in orifice flow. It then expands gradually until a uniform flow is again re-established on the full width of the channel. The energy loss over the extent encompassing the constriction is the same as that of the uniform flow (Chow, 1959). No reference was found for situations when the bridge has been submerged. However, it may be surmised that when floods overtop and submerge a bridge, the overall energy loss around the bridge will be the same as that of uniform flow. If the bridge is well submerged, its impact is an increase in flow resistance, which will reflect on the slope of the waterline.

A flooded river constitutes a compound channel with a main channel at the centre and the flood plains on either side of the main channel. Estimates of peak discharge using the slope-area method can be calculated from resistance equations. Manning's equation for discharge (French, 1988; Patra, 2011) is given as

$$Q = \frac{1}{n} A R^{\frac{2}{3}} s^{\frac{1}{2}}, \tag{1}$$

where n is Manning's roughness coefficient, A is the flow area in m^2, R is the hydraulic radius in m, and s is the channel slope. The hydraulic radius (R) is computed as

$$R = \frac{A}{P}. \tag{2}$$

The channel is divided into subsections composed of the main channel and the floodplain sections on either sides (Ackers, 1991; Featherstone and Nalluri, 1982), and Manning's equation is applied to each section separately,

$$Q_i = \frac{1}{n_i} A_i R_i^{\frac{2}{3}} s_i^{\frac{1}{2}} \tag{3}$$

and

$$R_i = \frac{A_i}{P_i}. \tag{4}$$

The discharge is obtained as (Chow, 1959; Featherstone and Nalluri, 1982; Patra, 2011),

$$Q = \sum Q_i \tag{5}$$

The difference in velocity between the fast-moving water in the main channel and the slower-moving water in the floodplain sections generates shear along their boundary (Ackers, 1991; French, 1988). This shear must be considered in order to avoid an underestimation of discharge (French, 1988).

The choice of value for n is made from tables and pictures in the literature. It depends on experience and is thus rather subjective and can be a major source of uncertainty.

3 Methodology

Kiaoni Bridge is a pre-stressed concrete, four-span bridge with a width of 120 m from abutment to abutment (Japan International Cooperation Agency (JICA), (2001). The effective bridge opening was estimated to be 115 m. Considering the impact of the bridge piers on the flow, a fairly straight channel reach 585 m long encompassing the Kiaoni Bridge was chosen. The upstream and downstream ends of the reach were, respectively, 209 and 376 m from the bridge. GIS-enabled equipment was used to take elevations and coordinates at the bridge and high watermarks of the flood. A number of points were chosen in order to produce the upstream and downstream valley cross sections starting at that day's water level up to the line of the high water marks on both sides of the river.

The main channel was approximated to a trapezium and Manning's roughness coefficient determined from Eq. (1) for river discharge of 430 m^3/s on the day of the site visit. This was read off the rating curve for the gauging station at the bridge provided by the Water Resources Authority (WRA). The roughness coefficient for overbank flow was estimated based on the literature and observed ground surface, trees, and other vegetation on the flood plain. The effect of the bridge and buildings was considered especially in respect of their submergence. A roughness of n = 0.05 was adopted for the two overbank sections. The flood peak discharge was calculated using Eqs. (1–5) for a compound channel with fluid shear stress resistance considered.

The errors in inputs into the discharge equation translate into inaccurate estimates of the discharge. Uncertainties in the estimate can be largely attributed to the roughness coefficient and the friction slope. An indication of the degree of error in the value of peak discharge can be found by performing a first-order analysis of variance on Manning's equation for discharge. For a compound channel in which the flood plains are symmetrical about the main channel, the discharge equation can be expressed as (Chow, 1959; Chow et al., 1988).

$$Q = \left[\frac{1}{n_c}A_c^{\frac{5}{3}}P_c^{-\frac{2}{3}} + \frac{2}{n_b}A_b^{\frac{5}{3}}P_b^{-\frac{2}{3}}\right]s^{\frac{1}{2}}. \quad (6)$$

First-order analysis on Eq. (6) gives the coefficient of variation of the discharge as

$$CV_Q^2 = \frac{1}{4}CV_s^2 + \frac{1}{\Psi^2}\mathrm{C}V_{nc}^2 + \left(\frac{\Psi - 1}{\Psi}\right)\mathrm{C}V_{nb}^2. \quad (7)$$

The coefficient of variation for the slope was estimated at 15% (McCuen, 1986) and that for the roughness coefficient at 20% (Chow et al., 1988; McCuen, 1986). Using these values and the adopted values of $n_c = 0.042$ and $n_b = 0.05$, the coefficient of variation of the discharge for the channel was $CV_Q = 0.22$ or 22%.

Manning's roughness coefficient for the main channel was computed from Eq. (1) and was found to be $n = 0.042$ based on the day's discharge of $Q = 430$ m^3/s and measured slope, $s = 0.0012$. This was assumed constant for the channel up to full bank flow. The high watermarks gave a flood slope of 0.013. Based on the literature and observation of vegetation and other features on the flood plain and considering that the bridge was overtopped, a roughness value of $n = 0.05$ was adopted for the flood plains on both sides of the river. The peak discharge was computed at 7076 ± 1557 m^3/s. This estimate flood peak discharge is significantly higher than the discharge of 2900 m^3/s used in the design of the bridge (JICA, 2001) which may now be considered as an underestimate. The event of 24th of April 2018 may be of very high return period. However, the calculated discharge is only an estimation and it is probably a recognition of this fact that some workers who have used the slope-area method have found it necessary to verify the results using other methods (e.g. Okoli et al., 2019; Roy & Mistri, 2013).

4 Conclusions and Recommendations

The flood peak discharge was estimated using the slope-area method for a channel reach encompassing a bridge, a situation not envisaged for the slope-area method. Studies are recommended to establish the impact of riverine structures, such as bridges, on flow patterns, and on the slope-area method.

More studies are recommended to verify the magnitudes, nature, and frequency of high floods on this river while taking into account climate change and the variability of rainfall.

References

Ackers, P. (1991). Hydraulic design of straight compound channels (Vol. 1. Report SR 281).

Benson, M. A., & Dalrymple, T. (1976). General field and office procedures for indirect discharge measurements. *Techniques of water-resources investigations of the United States geological Surveys* (book 3, chapter A1). Geological Survey.

Chow, V. T. (1959). *Open channel hydraulics*.

Chow, V. T., Maidment, D. R., & Mays, L. W. (1988). *Applied hydrology* (1st ed.). McGraw-Hill.

Dalrymple, T., & Benson, M. A. (1976). Measurement of peak discharge by the slope area method. *Techniques of water-resources investigations of the United States geological Surveys* (book 3, chapter A2). Geological Survey.

Featherstone, R. E., & Nalluri, C. (1982). *Civil engineering hydraulics: Essential theory with worked examples*. Collins.

French, R. H. (1988). *Open channel hydraulics*(1st Ed.). New York: McGraw-Hill.

Japan International Cooperation Agency (JICA). (2001). Basic design study report on the project for reconstruction of Athi and Ikutha bridges in the Republic of Kenya.

McCuen, R. H. (2003). *Modelling hydrologic change: statistical methods*. Florida: CRC Press.

Okoli, K., Breinl, K., Mazzoleni, M., & Di Baldassarre, G. (2019). Design flood estimation: Exploring the potentials and limitations of two alternative approaches. *Water, 11*(4), 729. https://doi.org/10.3390/w11040729

Patra, K. C. (2011). *Hydrology and water resources engineering* (2nd ed.). Alpha Science International Ltd.

Roy, S., Mistri B. (2013). Estimation of peak flood discharge for an ungauged river: a case study of the Kunur River, West Bengal. Hindawi Publishing Corporation. *Geography Journal*, *2013*. https://doi.org/10.1155/2013/214140

Water for Mining in the Kingdom of Saudi Arabia: An Overview

Omar K. M. Ouda, Abdulaziz M. Al Shaibani, and Abdulaziz M. Al-Bassam

Abstract

The mining industry has a significant value to national economies and is a major lever to rural development in many countries. Globally, the mining industry is a small water consumer compared to other economic sectors such as agriculture and manufacturing. However, mining requires a substantial volume of water in the mining field, especially in the extraction and processing phases (e.g., 716 cubic meters of water are needed to produce a ton of gold). In some local areas, the mining industry can be the largest water consumer and may impact the availability of water for other economic sectors. In the Kingdom of Saudi Arabia, the mining sector has grown significantly over the last few decades. Going forward, the mining sector will have tremendous growth opportunities in line with Saudi Vision 2030s mining sector goal to have "a mining sector contributing to the national economy at full potential." The present paper provides an overview of the link between water and mining sectors in the Kingdom of Saudi Arabia in light of the National Transformation Program and Saudi Vision 2030 and highlights the ongoing coordination and integration activities to optimize mining water usage in the Kingdom.

Keywords

Water • Mining industry • Kingdom of Saudi Arabia • Best practice • Economic development

1 Introduction

The mining industry is crucial to the growth of the national economy and impacts almost every sector of the global economy. Furthermore, it is a major lever to rural development in many countries. The mining industry has grown substantially in recent decades, and its growth rate has surpassed the economic growth (International Resources Panel, 2020). Its growth rate is expected to maintain the same pace in the future to meet the mineral resource needs of a growing global population that is expected to reach 8.5 billion by 2030, 9.8 billion by 2050, and 11.2 billion by the end of the century (International Resources Panel, 2020). Furthermore, as developing countries try to catch up with the developed ones, the overall demand for minerals will increase as economies grow and technological innovation continues (International Resources Panel, 2020). Water is a major and vital input to the mining industry. Globally, mining is a small water user compared to other economic sectors such as agriculture and manufacturing (Bichueti, 2018) [e.g. less than 1% freshwater withdrawals in the USA in 2015 (USGS, 2020)]. In spite of this fact, the mining industry can be the largest water user at regional and local scales and may impact the availability of water for other economic sectors, especially in rural and remote areas. Mining requires a substantial volume of water in the mine site, especially in the extraction and processing phases [e.g., 716 cubic meters of water to produce a ton of gold (Redix, 2020)]. Most water at the mine site is used to grind and separate minerals from host rocks, to wash and transport materials, to control dust, and to cool drilling machinery (Fred, 2003). Mine water consumption varies greatly depending on a range of factors including climate conditions, ore type, mine management and practices, mining techniques, and the commodity being mined. These facts open wide windows for mining water consumption optimization on site and at regional level. Mining can have significant impacts on the quality of local water resources. The most serious water issues in mining

O. K. M. Ouda (✉) · A. M. Al Shaibani · A. M. Al-Bassam
National Centre for Water Research and Studies, Deputy Ministry of Water, Ministry of Environment, Water and Agriculture, Jeddah, Kingdom of Saudi Arabia
e-mail: oouda@mewa.gov.sa

A. Kallel et al. (eds.), *Selected Studies in Environmental Geosciences and Hydrogeosciences*, Advances in Science, Technology & Innovation, https://doi.org/10.1007/978-3-031-43803-5_57

occur in conjunction with toxic waste disposal resulting from water consumption during the extraction and processing phases (Cook et al., 2011).

The Kingdom of Saudi Arabia (KSA) announced a new strategic vision and comprehensive roadmap for economic development in the Kingdom in April 2016 formally called Saudi Vision 2030, which includes a special program for mining industry development (Government of Saudi Arabia, Vision, 2020; Government of Saudi Arabia, 2020). The mining sector has grown significantly over the last few decades. Going forward, it has tremendous growth opportunities in line with Saudi Vision 2030s goal to have "a mining sector contributing to the national economy at full potential" (Government of Saudi Arabia, Vision, 2020; Government of Saudi Arabia, 2020). The forecasted growth of the sector will increase water demand. The Saudi National Water Strategy 2030 forecasts the mining and industrial water demand to grow at an average annual rate of 2.6%. It is expected to increase from about 1.4 billion cubic meter in 2016 to about 2 billion cubic meter in 2030 (Ministry of Environment, 2020).

This paper provides an overview of the link between water and mining sectors in the Kingdom of Saudi Arabia in light of the National Transformation Program and Saudi Vision 2030 and highlights the ongoing coordination and integration activities to optimize mining water usage in the Kingdom.

2 Overview of Water and Mining Sectors in KSA

2.1 Mining Sector

The KSA government considers the mining sector the third pillar of the country's economy. Accordingly, the government has taken significant steps to boost the mining sector contribution to GDP, provide numerous employment opportunities, enhance localization competencies, and become a global leader in exploration and extraction capabilities.

The Western part of the KSA, comprising basement rocks and geologically known as the Arabian shield, is a major source of precious and basic minerals such as gold, silver, copper, zinc, chromium, manganese, tungsten, lead, tin, aluminum, and iron. On the other hand, the eastern part which consists of extensive sedimentary formations and referred to as the Arabian Platform is rich in industrial minerals such as gypsum, feldspar, mica, sulfur, and salt as shown in Fig. 1.

The mining sector has witnessed significant growth over the last decade. Between 2010 and 2018, gold production grew at a compound annual growth rate (CAGR) of 11.7%; copper at CAGR 60%; zinc at CAGR 23.5%, and metals export grew at CAGR 14% (Ministry of Industry and Mineral Resources, 2020; The U.S.-Saudi Arabian Business Council, 2019). In 2018, the total weight of all extracted mineral ores reached 512 million metric ton (MT); a total of 5574 metallic and non-metallic mineral sites have been discovered; 2045 exploration and development licenses have been issued; and a total of 19 mining projects that have total investments value of about US$ 14 billion are ongoing. In 2018, copper production was about 70 thousand MT; gold production was 11 thousand kilogram (kg); and aluminum production was 932 thousand MT (Ministry of Industry and Mineral Resources, 2020; The U.S.-Saudi Arabian Business Council, 2019); and 98,435 total employees are working in the mining sector (General Authority for Statistics, 2020). In June 2020, the Saudi Cabinet approved of a new Mining Investment Law that aims at facilitating foreign investment in the mining sector (Ministry of Industry and Mineral Resources, 2020). The law aims to increase the mining sector contribution to the Country GDP by $64 billion, reduce the imports by $10 billion, and create 200 thousand direct and indirect job opportunities by 2030 (Ministry of Industry and Mineral Resources, 2020; General Authority for Statistics, 2020).

2.2 Water Sector

The Kingdom of Saudi Arabia (KSA) is facing a challenge where total water demand exceeds the sustainable yield of both conventional and non-conventional water resources in the country (Ouda, 2014). In 2016, the total water consumption reached its peak with a total value of about 25.8 billion m^3 as shown in Fig. 2. The industrial and mining sector water consumption has grown from about 0.65 billion m^3 in 2005 to about 1.55 billion m^3 in 2019, which resulted mainly from the substantial development of industrial and mining sector in the Kingdom as discussed in the previous paragraph.

Renewable water sources in Saudi Arabia are extremely limited and consist mainly of renewable groundwater and surface water that together provide an estimated 6.2 Billion m^3 per year. Saudi Arabia supplements these renewable sources with desalinated seawater, particularly to meet potable and industrial demand. The desalinated seawater added a total supply of about 2.5 Billion m^3 in 2019 (McIlwaine & Ouda, 2020; Ouda, 2014, 2015). The country is also planning to use treated sewage effluent for non-potable uses such as industrial and mining processes, irrigation, and landscaping. Currently, the KSA uses around 17% of the nation's potential treated sewage effluent resource (Chowdhury & Al-Zahrani, 2015). To meet the water demand, the country uses the non-renewable

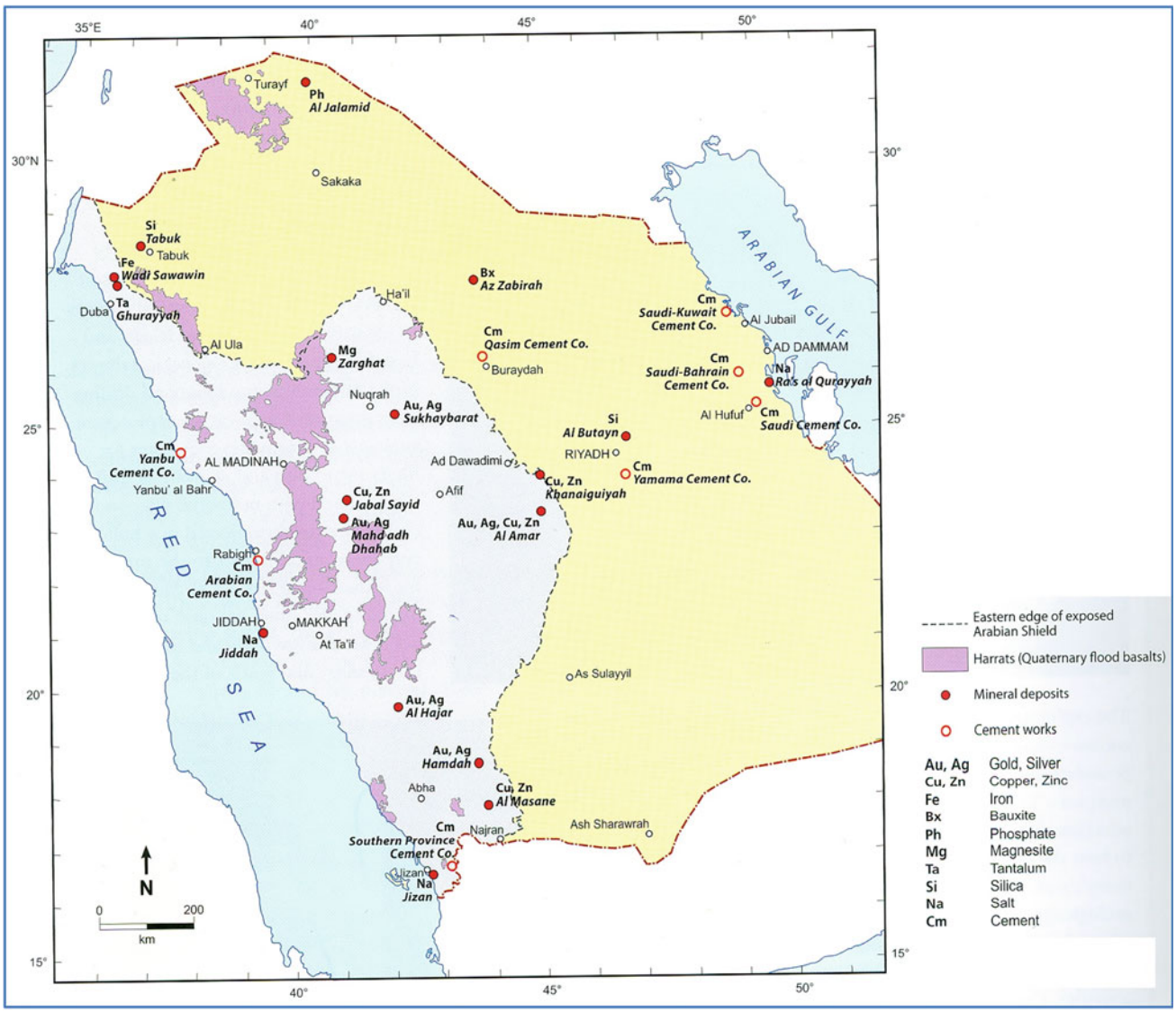

Fig. 1 Mineral reserves in KSA (SGS 2020)

groundwater resources and the total water demand–supply gap is estimated to be around 11.5 Billion m^3 in 2019.

3 Discussion and Coordination Initiatives

The water and mining sectors are mutually dependent. The mining sector is crucial for the Saudi economy. The public and private sectors are investing and planning to invest heavily in the sector over the coming years given its high economic added value to the country. Meanwhile, water resource availability can be somewhat a limiting factor for the country's mining sector development. Accordingly, the country has implemented various initiatives to cope with this challenge including:

- Initiate coordination process at the Ministerial level between the Ministry of Environment, Water and Agriculture (MEWA) and the Ministry of Industry and Mineral Resources (MIMR) to harmonize the mining sector development plan with water supply plans.
- The approval of the National Water Strategy, Water Law, and Mining Investment Law, which together aim for sustainable water and mining sectors with the vision of: "A sustainable water sector, safeguarding the natural resources and the environment of the Kingdom and providing cost-effective supply and high-quality services." (Ministry of Environment, 2020)
- The promotion of the use of non-conventional water resources for the supply of the mining sector demand and the partnership between the water sector and mining

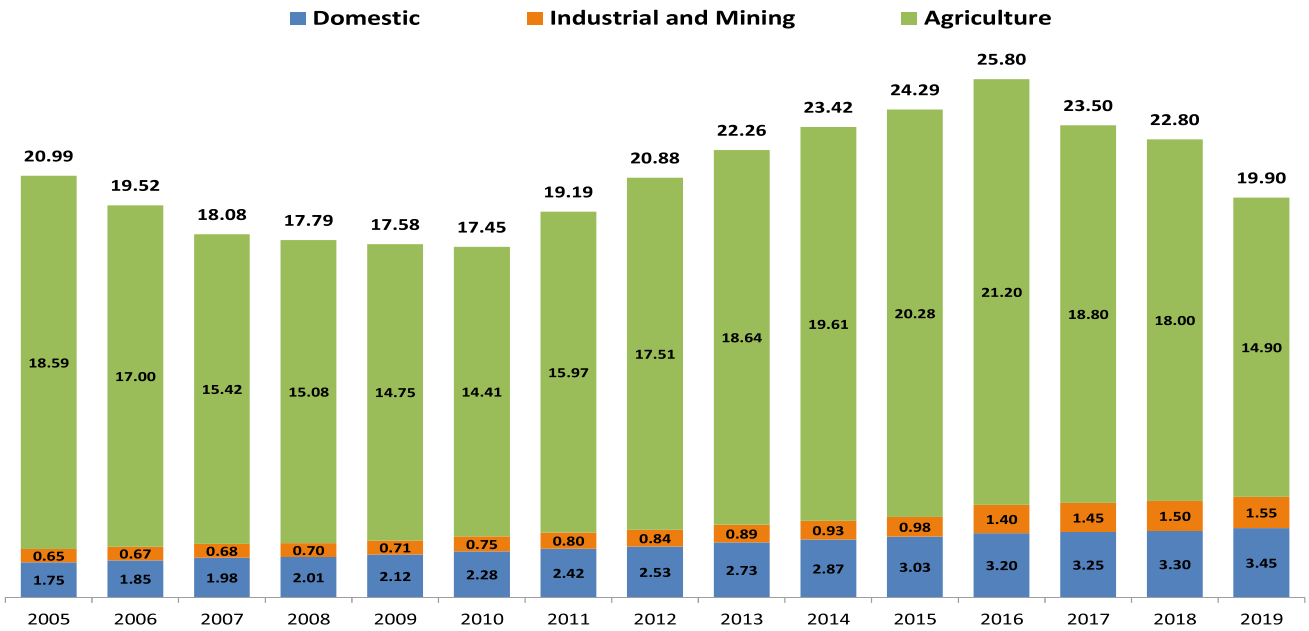

Fig. 2 Total water consumption for all users, updated after (Ministry of Environment, 2020)

sector, which recently resulted in signing an agreement between National Water Company and Madan Mining Company to supply treated wastewater to Waid Al Shamal Mining Project.

- The National Centre for Water Research and Studies is currently conducting research toward optimizing water use in the mining industry, which has shown encouraging results and will be published in the near future.

These initiatives are the right steps in the right direction but will not be enough. There is a need to develop an effective coordination between MEWA and MIMR and the private sector at all professional levels toward achieving the National Transformation Program and Saudi Vision 2030 goals for both water and mining sectors. Additional funds are needed to conduct in-depth technical and socioeconomic research toward optimizing water use in the mining industry.

4 Conclusion

The coordination between the mining and water sectors is crucial for an overall development, economic growth, and sustainability at a global level. The KSA is no exception; the country has substantial mineral reserves and financially capable public and private sectors that are willing to invest in the mining sector. Meanwhile, water scarcity in the Kingdom can be a limiting factor to economic development at a local level, and the growth of the mining sector in particular. The country initiatives to handle this challenge are a good start in the right direction but more initiatives are deemed necessary. In particular, effective coordination mechanisms between MEWA and MIMR and private sector are essential. Research programs that study the economic returns of water use in the mining sector; develop mechanism for optimal allocation of water resources across economic sectors, and water use at the mine level are also needed.

References

Bichueti,† R. S., Gomes, C. M., Kneipp, J. M., Motke, F. D., Perlin, A. P., Kruglianskas, I. (2018). Water use management in the mining industry: A comparison based on company size. *Journal of Environmental Accounting and Management, 6*(2), 135–147.

Chowdhury, S., & Al-Zahrani, M. (2015). Characterizing water resources and trends of sector wise water consumptions in Saudi Arabia. *Journal of King Saudi University: Engineering Sciences, 27*, 68–82.

Cook, A., Finkelman, R. B., Fourie, A. (2011). Mineral and fuel extraction: Health consequences. *Encyclopedia of environmental health* (pp. 781–787).

Kissell, F. N. (2003). Information circular 9465. In *Handbook for dust control in mining*. Pittsburgh Research Laboratory.

General Authority for Statistics, Labor Force Survey, Available at: https://www.stats.gov.sa/en/814. Accessed October 27 2020.

Government of Saudi Arabia, Vision 2030. Available at: www.vision2030.gov.sa/en. Accessed October 27 2020.

Government of Saudi Arabia, National Transformation Program 2020. Available at: https://vision2030.gov.sa/en/programs/NTP. Accessed October 27 2020.

International Resources Panel. (2020). Mineral resource governance in the 21st century: Gearing extractive industries towards sustainable development. A Report by the International Resource Panel. United Nations Environment Programme.

McIlwaine, S. J., Ouda, O. K. M. (2020). Drivers and challenges to water tariff reform in Saudi Arabia. *International Journal of Water*

Resources Development, published online in February 2020. https://doi.org/10.1080/07900627.2020.1720621

Ministry of Industry and Mineral Resources. Mining Investment Law, Available at: https://new.dmmr.gov.sa/mop/pages/InvestmentSystem.aspx. Accessed October 27 2020.

Ministry of Environment, Water and Agriculture. Saudi National Water Strategy 2030. Available at: https://www.mewa.gov.sa/ar/Ministry/Agencies/TheWaterAgency/Topics/Pages/Strategy.aspx. Accessed October 27 2020.

Ouda, O. K. M. (2014). Water demand versus supply in Saudi Arabia: Current and future challenges. *International Journal of Water Resources Development, 30*(2), 335–344.

Ouda, O. K. M. (2015). Domestic water demand in Saudi Arabia: assessment of desalinated water as strategic supply source. *Desalination and Water Treatment*, *56*(11).

Redix, Cubic meter to tone in iron ore, Available at: https://www.fondationgadzarts.ch/rock/716/2019_Sep_29.html. Accessed October 27 2020.

SGS. The geological evolution of Saudi Arabia. A voyage through space and time. Saudi Geological Survey, Available at: https://www.ic.gov.sa/en/invest-in-saudi-arabia/natural-resources/. Accessed October 27 2020.

The U.S.-Saudi Arabian Business Council. (2019). The Saudi Arabian mining sector: ongoing investments propel long-term growth.

USGS, Freshwater Withdrawals in the United States, available at: https://www.usgs.gov/special-topic/water-science-school/science/freshwater-withdrawals-united-states?qt-science_center_objects=0#qt-science_center_objects. Accessed October 27 2020.